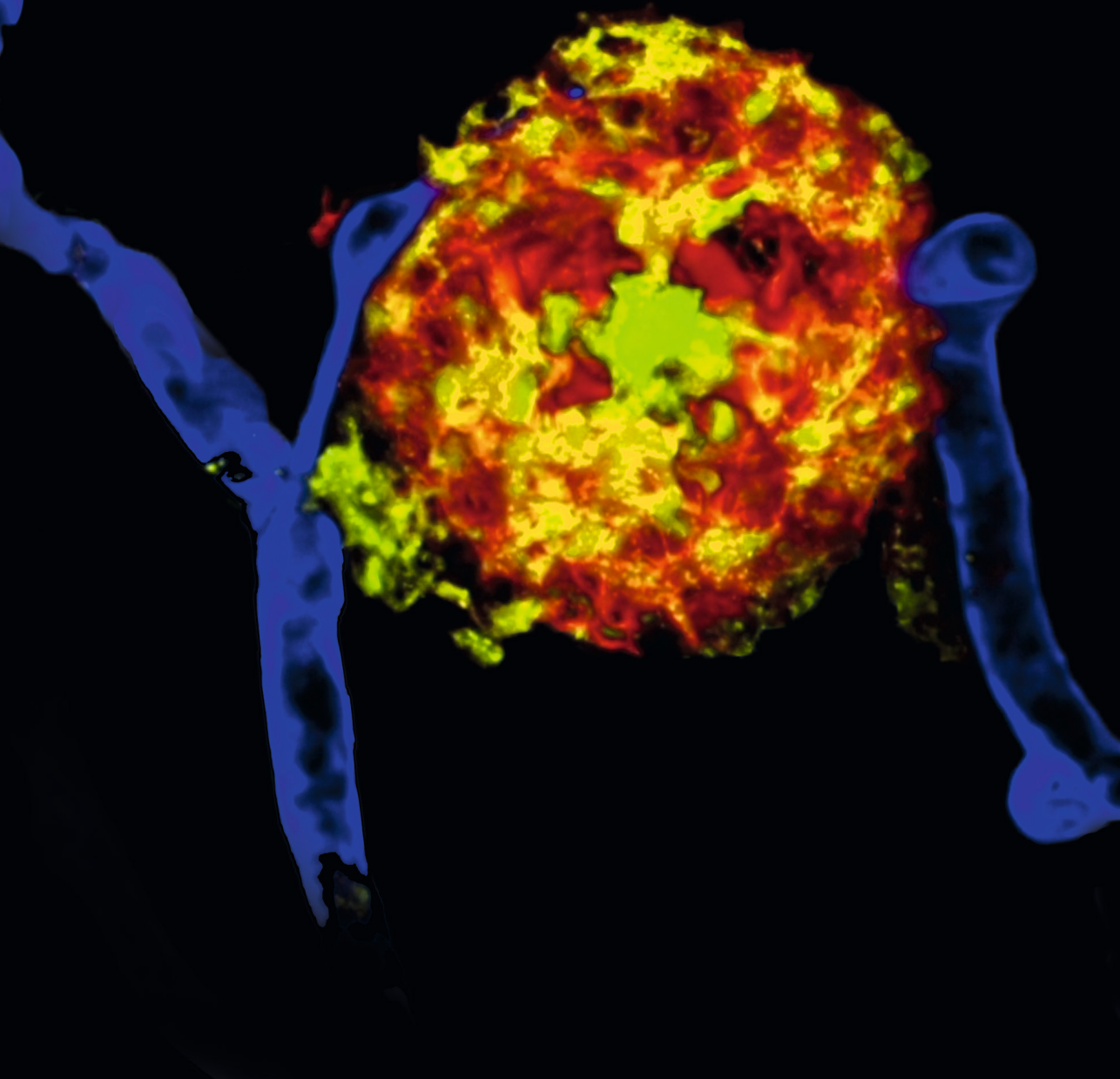


Deciphering neuropathological heterogeneity in Alzheimer's Disease:

Beyond plaques and tangles



Baayla Dimitri Catharina Boon

**DECIPHERING NEUROPATHOLOGICAL
HETEROGENEITY IN ALZHEIMER'S DISEASE:**

Beyond plaques and tangles

Baayla Dimitri Catharina Boon

The research described in this thesis was carried out at the Alzheimer Center Amsterdam and the department of Pathology, Amsterdam UMC (former VU University Medical Center), Amsterdam, the Netherlands. Research of the Alzheimer Center is part of the Neurodegeneration program of Amsterdam Neuroscience and supported by Stichting Alzheimer Nederland and Stichting VUmc Fonds. Several studies were performed within the framework of the Dutch PAGE-AD project and were supported by a ZonMW-Memorabel grant (project #733050104) in the context of the Dutch Deltaplan Dementie. Printing of this thesis was supported by Alzheimer Nederland and Stichting Alzheimer and Neuropsychiatry Foundation.

Cover design: Baayla DC Boon & Birgit Vredenburg

Provided by thesis specialist Ridderprint, ridderprint.nl

Printing: Ridderprint

Layout and design: Birgit Vredenburg, persoonlijkproefschrift.nl

ISBN: 978-94-6416-913-3

Elektronisch ISBN: 978-94-6416-916-4

© Baayla Dimitri Catharina Boon, Neptune Beach, Florida, USA, 2021

All rights reserved. No parts of this publication may be reproduced, stored or transmitted in any way or by any means without the prior permission of the copyright holder, or, when applicable, with permission of the publishers of the scientific journals.

VRIJE UNIVERSITEIT

**DECIPHERING NEUROPATHOLOGICAL HETEROGENEITY IN
ALZHEIMER'S DISEASE: BEYOND PLAQUES AND TANGLES**

ACADEMISCH PROEFSCHRIFT

ter verkrijging van de graad Doctor of Philosophy aan
de Vrije Universiteit Amsterdam,
op gezag van de rector magnificus
prof.dr. C.M. van Praag,
in het openbaar te verdedigen
ten overstaan van de promotiecommissie
van de Faculteit der Geneeskunde
op vrijdag 14 januari 2022 om 13.45 uur
in een bijeenkomst van de universiteit,
De Boelelaan 1105

door

Baayla Dimitri Catharina Boon

geboren te Alkmaar

Voor Van Eyk

*Enjoy your happy little accidents and observe with wonder,
since the true value of Serendipity lies in the eye of its beholder*

Inspired by Bob Ross' quote:

'We don't make mistakes, just **happy little accidents**'

Contents

| | | |
|------------------|---|-----|
| Section 1 | General introduction | 9 |
| Chapter 1 | Introduction | 11 |
| Section 2 | Heterogeneity in Alzheimer's disease pathology: distribution of neuroinflammation in (a)typical AD phenotypes | 29 |
| Chapter 2 | Neuroinflammation is increased in the parietal cortex of atypical Alzheimer's disease | 31 |
| Chapter 3 | A distinct distribution of neuroinflammation, indicating a specific role for reactive astrocytes in clinical atypical Alzheimer's disease | 65 |
| Section 3 | Heterogeneity in Alzheimer's disease pathology: Aβ deposit diversity | 93 |
| Chapter 4 | The coarse-grained plaque: a divergent A β plaque-type in early-onset Alzheimer's disease | 95 |
| Chapter 5 | Label-free vibrational imaging of different A β plaque types in Alzheimer's disease reveals sequential events in plaque development | 153 |
| Chapter 6 | Multimodal, label-free fluorescence and Raman imaging of amyloid deposits in snap-frozen Alzheimer's disease human brain tissue | 191 |
| Section 4 | Translating pathology to the memory clinic via imaging | 243 |
| Chapter 7 | Amyloid- β PET and CSF in an autopsy confirmed cohort | 245 |
| Chapter 8 | Amyloid- β , pTau and reactive microglia load are correlates of MRI cortical atrophy in Alzheimer's disease | |
| Chapter 9 | Can post mortem MRI be used as a proxy for in vivo? A case study | 269 |
| Section 5 | Closing remarks | 297 |
| Chapter 10 | Summary | 321 |
| Chapter 11 | General discussion | 335 |
| Chapter 12 | Dutch summary (Nederlandstalige samenvatting) | 351 |
| Addendum | List of publications | 364 |
| | Alzheimer Center hall of fame | 367 |
| | Acknowledgments (dankwoord) | 372 |
| | About the author | 383 |

Section 1

General introduction

Chapter 1

Introduction

INTRODUCTION

History of Alzheimer's disease

This thesis is focused on the heterogeneity of the most common cause of dementia, which we nowadays refer to as Alzheimer's disease (AD). Since the 'first' description of the disease in 1907 [1], AD heterogeneity has been an ongoing topic of discussion. Therefore, to set the scene for AD heterogeneity, a short history on how AD got to be AD feels in place. Alois Alzheimer was not the first to describe the so well-known AD pathologic hallmarks of plaques and neurofibrillary tangles (NFT). The first description of plaques was done in 1892 by Blocq and Marinesco when they reported 'round heaps' in a group of elderly epileptic patients [6]. The first time these plaques were linked to the clinical picture of (senile) dementia was by dr. Emil Redlich, a professor at the University of Vienna [47]. Interestingly, especially in the current timeframe, Redlich already noted that glial cells were surrounding the plaques. He hypothesized that the brains' innate immune system plays a vital role in forming these plaques. The most extensive evidence linking both plaques and NFT to senile dementia at that time came from dr. Oskar Fischer. He published multiple studies from 1907 till 1912 about senile dementia and its pathological hallmarks, based on a comprehensive cohort of 65 cases [13]. At the same time, Alois Alzheimer published his paper on the 55-year-old Auguste D., a case study in which he described her symptomatology and the post mortem findings of plaques and NFTs throughout the cortex [1]. The name 'Alzheimer's disease' was initiated by dr. Alois Alzheimer's former supervisor, prof. dr. Kraepelin. In the 8th edition of his 'Compendium der Psychiatrie,' he decided to categorize AD as a different disease than the at-that-time well-known dementia senilis [28]. Multiple reasons for Kraepelin to label the disease as a separate entity from the previously known dementia senilis can be thought of. An important reason could be that the clinical picture of Alois Alzheimer's case study was different, as Alois' patient Auguste D. presented at a presenile age with a more aggressive disease course and a more cortical presentation with language disturbances and spastic paraparesis than the initially isolated memory disorder as usually seen in dementia senilis. Another -and maybe even so- important reason was a more political one. Other labs were making a name for themselves by describing presenile dementias such as what we today know as Pick's disease. Dr. Kraepelin did not want to stay behind, and naming a disease after one's employees is definitely a way to put your lab on the map. Interestingly, Alzheimer himself didn't see the disease he described in his case study on Auguste D. as an entity on its own. Instead, he categorized the disease as an atypical form of the dementia senilis when he concluded:

‘Es sind seniele Psychosen, atypische Formen der senielen Demenz’ [2]. In the following times, AD went more or less into oblivion as the presenile dementia only affected ~5% of dementia patients and thus wasn’t diagnosed often. Around the mid-1900s, the field questioned again if AD and senile dementia are the same disease or two different diseases. This time around, the pathological report rather than the clinical characteristics pulled more weight. Since both patients with AD and senile dementia bare the same pathological hallmarks of plaques and NFTs, they were categorized as one disease, now just separated by an early and a late disease-onset [53, 54]. In 1974 the National Institute on Aging (NIA) was established. The head of the NIA, Robert Butler, realized that a disease needs a specific name to get funded for research. Just like the pathologists, leading neurologist Robert Katzman re-categorized AD and senile dementia as one disease in his editorial for the Archives of Neurology journal [24]. However, with Butler’s advice in mind, he now referred to the one disease not as dementia senilis but as AD, making AD suddenly from a rare diagnosis to a major health problem. From then onwards, AD was seen as a prototypical syndrome with various clinical subtypes associated with AD neuropathological change (ADNC) [32, 33]. Nowadays, the field is becoming more and more aware that categorizing the disease as such has implications, not only for its diagnosis but also for studies regarding its etiology and its cure.

Pathogenesis of Alzheimer’s disease

The most leading hypothesis for AD pathogenesis is still the amyloid hypothesis [18, 51]. According to this hypothesis, the disease’s ignition is amyloid-beta ($A\beta$), a peptide that results from the cleavage of the amyloid precursor protein (APP) by β - and subsequently γ -secretase. The excessive extracellular $A\beta$ influences -especially in its oligomeric form- synaptic activity and causes a disbalance in kinase and phosphatase activity in neurons, leading to neurotoxicity and NFT formation of the hyperphosphorylated form of the microtubule-associated protein tau (pTau). The appearance of NFTs is associated with neuronal death. When NFTs are present throughout the neocortex, they lead to such devastating neurodegeneration that the patient suffers from a clinical syndrome we refer to as dementia. The evidence for the amyloid hypothesis is based on the link between autosomal dominant mutations leading to increased $A\beta$ and AD. Due to a triplication of the *APP* gene, persons with Down’s syndrome show an overproduction of $A\beta$ in the brain and show extensive $A\beta$ neuropathology, often accompanied by clinical dementia [12, 38]. Cases with familial AD most often have mutations in either the *APP* gene itself or the genes (*PSEN1* and *PSEN2*) involved in the cleavage process of the APP [30]. Interestingly, a rare

specific missense mutation in the *APP* gene decreases b-secretase-mediated APP cleavage. People with this missense mutation have less risk of developing AD and do not show plaques even when older than 100 years [22, 25]. In sporadic AD, the initiating role for A β in AD is less obvious, and it has even been proposed that not A β but tau might be the initiating factor [9].

Neuropathology of Alzheimer's disease

Despite the ongoing discussion on which protein aggregate comes first, according to current diagnostic guidelines both abnormal proteins must be present for the neuropathological diagnosis of the disease [20, 33, 36]. The pathological hallmarks of AD are intracellular NFTs consisting of aggregated pTau and extracellular A β plaques. Both plaques and NFTs need to be present to a certain degree for the clinical profile of dementia to be caused by AD neuropathological change and both accumulate in the brain according to a proposed spatial-chronological order (Fig. 1) [36]. The ordinal fashion of A β deposit distribution is subdivided into 5 phases as described by Thal et al., starting with deposits observed in the neocortex in phase 1, followed by deposits in the allocortices in phase 2, the diencephalon and striatum in phase 3, inner brain stem nuclei in phase 4 and finally with deposits in the cerebellum in phase 5 [52]. A β pathology is not well correlated with cognitive symptoms, as deposits are observed widespread throughout the cortex even in cases without clinical symptoms [21]. NFTs on the other hand are much better correlated with clinical symptoms than plaques, as their brain regional deposition often aligns with the type of symptoms patients have [40, 42, 44]. In the majority of AD cases with a typical amnesic presentation, these intraneuronal aggregates show an almost opposite spatial distribution compared to A β : NFTs are first observed in the (trans)entorhinal regions, then in the hippocampus and the rest of the allocortex, and finally in the primary areas of the neocortex [7, 8]. Another pathological feature is the neuritic plaque, in which A β and pTau come together in a plaque containing swollen dystrophic neurites. The presence and density of neuritic plaques is graded according to the Consortium to Establish A Registry for Alzheimer's Disease (CERAD) criteria [35]. If A β aggregates in the brain's vasculature, we refer to it as cerebral amyloid angiopathy (CAA). Besides plaques, NFTs, and CAA, we also observe activated microglia and reactive astrocytes in the brains of patients who died with AD. Both cell-types surround A β plaques and activated microglia might even play an active role in the spread of tau pathology [3, 19, 31].

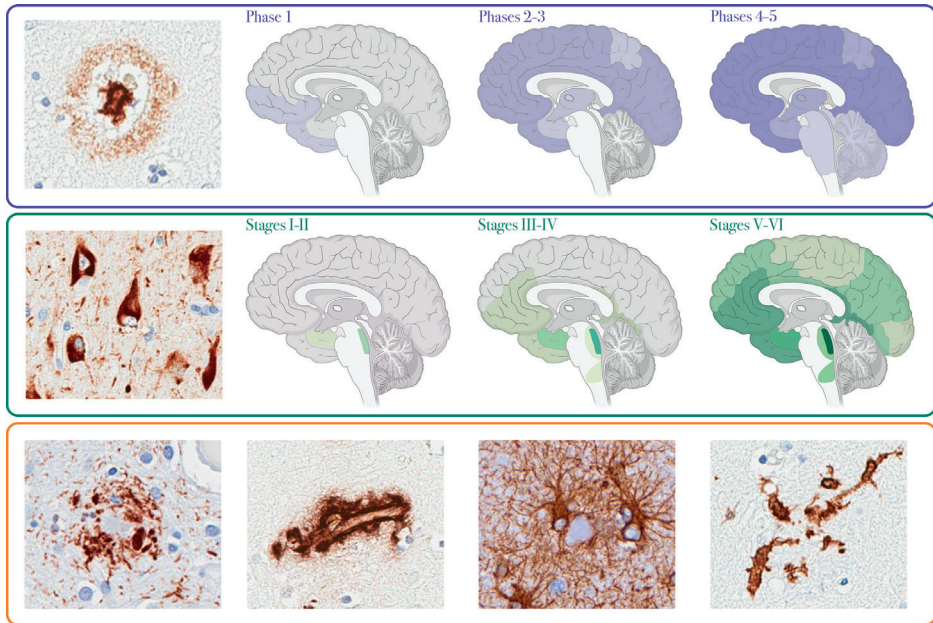


Fig. 1. Pathology in Alzheimer's disease

The top purple outline shows an immunohistochemical picture of the A β plaque (left image), which spreads in a temporospatial manner as described by Thal et al., from the neocortex to finally the cerebellum, as illustrated by the increasing purple coloration of the brain towards the right [52]. The middle green outline shows a pTau NFT (left image), which according to Braak et al., spreads from the (trans)entorhinal regions via the allocortex to the neocortex [7, 8], as illustrated by the increasingly green brain images. The bottom orange outline shows other pathology features frequently seen in AD, such as from left to right: the neuritic plaque, CAA, reactive gliosis, and activated microglia clusters. A β amyloid-beta; AD Alzheimer's disease; CAA cerebral amyloid angiopathy; pTau hyperphosphorylated tau; NFT neurofibrillary tangle. Distribution staging images are adapted from reference [14].

Neuroinflammation

Neuroinflammation involves the recruitment and activation of the central nervous system's immune system, with its key players being microglia and astrocytes. The idea that neuroinflammation plays a vital role in AD is not new, as Redlich already reported on the glia association with plaques in 1898 [47] and Eikelenboom & Stam, as well as Rozemuller et al. described complement immunoreactivity in senile plaques in 1982 and 1989 respectively [11, 48]. The most convincing proof, however, only came in the 21st century with the discovery of AD risk loci in the immune genes CR1, CD33, and TREM2,

which all happened to be involved in the microglial response to A β [5, 23, 29]. While the neuroinflammatory response in AD is very complex and far from understood, the following section only provides a simplified overview. Fibrillar and oligomeric A β can bind to receptors on the microglial surface known to recognize danger- or pathogen-associated molecular patterns. The binding to these receptors, activate the microglia and initiates an inflammatory process. Although being a very heterogeneous process, the goal of this activation is the clearance of A β aggregates. This clearance is facilitated by numerous methods, such as degradation by proteases, cell autophagy after A β internalization, and phagocytosis. Besides a phagocytosis phenotype, the activated microglia take on a spectrum of phenotypes, producing all sorts of pro- and anti-inflammatory mediators such as cytokines, chemokines, and complement factors. Complement factors, in their turn, opsonize the A β plaques and trigger the CR1 receptor on other microglia and astrocytes [55]. Besides microglia, astrocytes are also involved in the inflammatory pathway. They respond to A β by reactive gliosis and upregulation of the glial fibrillary acidic protein (GFAP). Similar to microglia, they release inflammatory mediators and aid in A β clearance, either via direct phagocytosis [57], via transfer of A β via the glymphatic system or across the blood-brain barrier with the help of transport proteins such as apolipoprotein E (apoE) [10]. When A β clearance isn't sufficient, the peptide aggregates either in the brain parenchyma in the form of plaques or in the wall of cerebral blood vessels as CAA.

Imaging Alzheimer's disease pathology

Visualisation of AD pathology is done post mortem using microscopy techniques. The most common technique used for neuropathological diagnosis is brightfield microscopy, which uses white light that is transmitted through the sample. The contrast created by the specimen produces the image. Ordinary brightfield microscopy is suitable for imaging in a 2D plane. For 3D imaging one needs confocal laser scanning microscopy (CLSM). The confocal scanning creates a narrow depth of field, which allows for optical sectioning in z-direction. One can then make multiple thin z-stacks, which the computer can combine into a 3D image. To visualize a specimen with brightfield and CLSM, one first needs to 'label' the subject of interest, such as a protein or compound, by (immuno)histochemical staining experiments performed in the laboratory. Using spectroscopy, which is a label-free technique, one can study the tissue in its most native state. Spectroscopy measures the absorbance or transmittance of the electromagnetic radiation that is transmitted through the specimen. By doing so,

different aspects that can't be studied using microscopy such as protein structure and molecular composition can be analyzed.

In the present day, we can also image the brain in living patients. Such imaging techniques include i.e., magnetic resonance imaging (MRI) and positron emission topography (PET). MRI makes use of a strong magnetic field, magnetic gradients, and electromagnetic radiation to form a structural image of the brain based on the local hydrogen nuclei-density. MRI is non-invasive and with it, we can analyze the brain's structural anatomy [34]. When used in the setting of AD, the severity of neurodegeneration is scaled using the global cortical atrophy scale [43], the medial temporal lobe atrophy score [49], and the posterior atrophy score [27]. In case of PET imaging, a radioactive ligand directed at the substrate of interest, for example $A\beta$ or tau, is injected into the bloodstream. If the substrate is present, the ligand binds in the brain and causes a hyperintense signal visible on the scan. Although these techniques give us insight into the brain's status on a macroscopical level, information on a cellular level is not (yet) feasible.

Alzheimer's disease in the memory clinic

The clinical diagnosis of AD is not only based on the clinical features of memory impairment or the decline of other cognitive abilities but also requires confirmation of the pathological aspects of the disease, including the presence of the two abnormal protein deposits consisting of $A\beta$ (A) and tau (T), and the nonspecific damage indicator, neurodegeneration (N), in the brain [20, 33]. To assess these AT(N) criteria during life, one can use different biomarkers, such as fluid biomarkers and neuroimaging techniques. Both A and T criteria in the brain can, as earlier discussed, be visualized by PET. A and T presence in the brain can also indirectly be reflected by the levels of $A\beta$ and pTau measured in the cerebrospinal fluid (CSF). Biomarkers reflecting the N for neurodegeneration include the degree of atrophy measured with MRI, hypometabolism measured with fluoro-deoxyglucose (FDG) PET, and the levels for total tau in CSF.

Clinical typical Alzheimer's disease

AD typically presents with an isolated anterograde episodic memory deficit when patients are 70 years old [4]. The disease then gradually progresses in ~four years to a state we refer to as dementia by affecting other cognitive abilities such as abstract reasoning and attention, and later on language and visuospatial functioning [16, 56]. The entire disease course from the first objective measurable symptoms to death takes approximately 12 years [56]. Typically, an AD patient who comes to the memory clinic for a diagnostic work-up will have prominent

memory impairment, in combination with a decreased $A\beta_{42}$, increased pTau, increased total tau in CSF, and atrophy being most pronounced in the medial temporal lobe on MRI [39]. If the patient also receives both an amyloid and a tau-PET scan, both scans will be positive, with the tau uptake signal being highest in the medial temporal lobe region [42].

Clinical atypical Alzheimer's disease

One-third of patients who have an early (< 65 years) disease-onset (EOAD) present with a clinical atypical phenotype lacking prominent memory impairment [17, 26]. This atypical presentation can vary with symptoms ranging from disturbed spatial orientation, apraxia, language dysfunction, disturbances of vision, or behavioral change with executive dysfunction. These atypical presentations can be categorized into distinct variants. When patients experience predominant visual processing problems and show prominent atrophy of occipital brain regions but have a relative sparing of the other cognitive functions, the clinical variant is referred to as posterior cortical atrophy (PCA) [50]. When patients initially present with isolated language problems, usually consisting of word-finding difficulties and impaired sentence repetition but intact word understanding, we refer to the atypical clinical syndrome as the logopenic variant of the primary progressive aphasia (lvPPA) [15]. Another atypical clinical variant is the behavioral/dysexecutive variant, a variant that is characterized by more prominent executive dysfunction and behavioral features than the also present memory impairment [41].

Clinicopathological correlations

Besides clinical variability, the AD clinical subtypes show distinct neurodegeneration patterns on MRI. Whereas the atrophy in PCA cases is situated primarily posterior, in lvPPA, atrophy is asymmetrical and located in the left language-dominant hemisphere [39]. These distinct neurodegeneration patterns reflect each subtype's clinical symptomatology. Similar to neurodegeneration, distribution of tau pathology differs between the clinical subtypes as shown both in vivo by tau-PET using tracer [^{18}F]-AV-1451 (Fig. 2) and post mortem by histochemistry [42, 45, 46].

When studying AD from a neuropathological perspective, Murray et al. concluded that AD can be subdivided into three significant subtypes based on their NFT distribution [37]. These three subgroups differed besides their NFT distribution, also in their clinical characteristics. Cases with a hippocampal sparing subtype show relatively more NFTs in the cortex than in the hippocampus, are younger,

more often male, and present more often with an atypical clinical presentation than cases that have a limbic predominant or typical NFT distribution. Although it is pretty well studied that tau pathology differs between AD cases, the cause for variation remains elusive. The distribution of other disease mechanisms such as neuroinflammation is understudied, especially in the light of aberrant tau distribution. In translating pathology findings to the memory clinic, it is assumed that biomarkers such as CSF, PET, and MRI reflect pathology, but studies directly comparing the two are scarce.

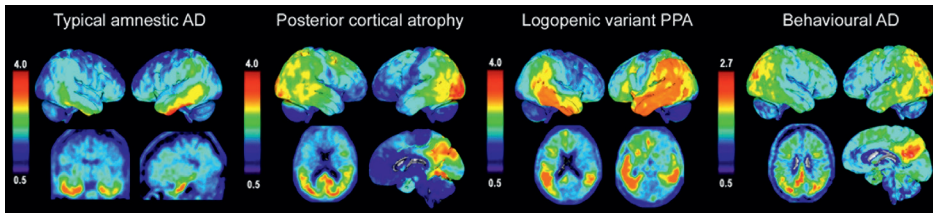


Fig. 2. Tau pathology visualized by [^{18}F]-AV-1451-PET in different clinical subtypes of AD. In typical amnesic AD, tau pathology is predominantly located in the medial temporal lobe. In posterior cortical atrophy, the tau load is mainly found in the posterior brain areas. In the logopenic variant of PPA, tau load is asymmetrically distributed with increased uptake in the language dominant left hemisphere. In behavioural AD, tau was predominantly observed in the parietal cortex. AD Alzheimer's disease; PPA primary progressive aphasia. Figure adapted from reference [42].

Aim of this thesis

The studies described in this thesis are aimed to increase our understanding of the heterogeneity in AD from different angles. First, the pathological heterogeneity in post mortem brain in relation to the clinical presentation of AD was addressed. For this first aim advanced and new imaging techniques were applied, which shed a new perspective on heterogeneity in pathology. Second, in aiming to translate clinical heterogeneity towards a pathological counterpart, the correlation between in vivo and post mortem measures was studied.

Outline of this thesis

The first objective investigating the heterogeneity in pathology of different AD variants, both clinical and neuropathological is described in **section 2**. The studies on the topographical distribution of pathology are described in **chapters 2 and 3**. **Chapter 2** describes the study investigating the distribution of neuroinflammation and the usual AD suspects, $\text{A}\beta$ and pTau, over the temporal and parietal cortex of typical compared to atypical AD. Since case numbers for

pathology studies are small and with the knowledge that pTau distribution is closely related to clinical symptoms, we chose for a so-homogenous group as possible, meaning the atypical AD cases had to have both a clinical atypical presentation during life and an atypical NFT distribution in pathology. In **chapter 3**, we studied if our findings on neuroinflammatory differences discovered in the retrospective cohort, held ground in a cohort that was prospectively collected during this Ph.D. trajectory. In this cohort, typical and atypical AD was solely defined on clinical presentation and not on NFT distribution, facilitating a comparison between clinical symptoms and neuroinflammation without the bias of selecting on pTau distribution.

In **section 3** the microscopical view was expanded by zooming in on AD's most well-known pathological hallmark: the plaque. A prominent fibrillar plaque-type was observed in chapter 2, which was especially prominent in the atypical AD group who had an early disease-onset. The definition of this divergent plaque that I coined the 'coarse-grained plaque' is described in **chapter 4**. The plaque's biology and clinical implications were studied by comparing its characteristics to that of other parenchymal and vascular A β deposits in a cohort of 74 A β pathology positive cases. In **chapters 5** and **6**, spectroscopy - a for-neuropathology-rather-unconventional technique - was used to gain a better understanding of the molecular composition of different plaque-types. This label-free technique enables to study brain tissue in its most native state, as no tissue-manipulating methods such as fixation or histochemical staining procedures are needed. In **chapter 5**, both Fourier-transform infrared (FTIR) and Raman spectroscopy were used to investigate the protein's secondary composition of the proposed sequential plaque-stages. To study the plaque's composition with an increased resolution, both Raman and stimulated Raman spectroscopy (SRS) were used in **chapter 6**. This study compared the dense-cored plaque to the fibrillar - or 'coarse-grained' plaque and shows that the two plaque types differ in their molecular fingerprint of carotenoid content.

In search of a tool that reflects the pathological landscape in the living patient, the correlation between in vivo and post mortem measures was investigated in **section 4**. These translational studies are described in **chapters 7-9**. Although biomarkers measuring A β in the CSF or on PET are assumed to reflect A β pathology in the brain, they do not always correspond with each other. The neuropathology of CSF/PET discordant cases was studied in **chapter 7** to understand what these two modalities exactly reflect. As chapters 2, 3, 4, and 6 teach us that neuroinflammation might be a key-player in AD diversity, **chapter**

8 aims to - in addition to A β and pTau - correlate inflammation with cortical thickness derived from post mortem in situ MRI. However, whether post mortem in situ MRI actually is comparable to MRI measurements performed in vivo has never been studied. By the virtue of the patient described in **chapter 9**, who altruistically chose to donate his brain and participate in research, while deliberately choosing euthanasia, we were able to compare MRIs from both time points with only four days in-between scan procedures.

Chapter 10 summarizes the main findings of this thesis. In **chapter 11**, I end this thesis with a general discussion and recommendations for the future.

REFERENCES

1. Alzheimer A (1907) Über eine eigenartige Erkrankung der Hirnrinde. *Allg Zeitschrift für Psychiatr* 64:146-148
2. Alzheimer A (1911) Über eigenartige Krankheitsfälle des späteren Alters. *Zeitschrift für die Gesamte Neurol und Psychiatr* 4:356-384
3. Asai H, Ikezu S, Tsunoda S, Medalla M, Luebke J, Haydar T, Wolozin B, Butovsky O, Kügler S, Ikezu T (2015) Depletion of microglia and inhibition of exosome synthesis halt tau propagation. *Nat Neurosci* 18:1584-93. doi: 10.1038/nn.4132
4. Barnes J, Dickerson BC, Frost C, Jiskoot LC, Wolk D, Van Der Flier WM (2015) Alzheimer's disease first symptoms are age dependent: Evidence from the NACC dataset. *Alzheimer's Dement* 11:1349-1357. doi: 10.1016/j.jalz.2014.12.007
5. Bertram L, Lange C, Mullin K, Parkinson M, Hsiao M, Hogan MF, Schjeide BMM, Hooli B, Divito J, Ionita I, Jiang H, Laird N, Moscarillo T, Ohlsen KL, Elliott K, Wang X, Hu-Lince D, Ryder M, Murphy A, Wagner SL, Blacker D, Becker KD, Tanzi RE (2008) Genome-wide association analysis reveals putative Alzheimer's disease susceptibility loci in addition to APOE. *Am J Hum Genet* 83:623-632. doi: 10.1016/j.ajhg.2008.10.008
6. Blocq P, Marinesco G (1892) Sur les lésions et la pathogénie de l'épilepsie dite essentielle. *La Sem Médicale* 445-446
7. Braak H, Alafuzoff I, Arzberger T, Kretschmar H, Tredici K (2006) Staging of Alzheimer disease-associated neurofibrillary pathology using paraffin sections and immunocytochemistry. *Acta Neuropathol* 112:389-404. doi: 10.1007/s00401-006-0127-z
8. Braak H, Braak E (1991) Neuropathological staging of Alzheimer-related changes. *Acta Neuropathol* 82:239-59. doi: 10.1007/BF00308809
9. Braak H, Del Tredici K (2011) The pathological process underlying Alzheimer's disease in individuals under thirty. *Acta Neuropathol* 121:171-181. doi: 10.1007/s00401-010-0789-4
10. Deane R, Bell R, Sagare A, Zlokovic B (2009) Clearance of Amyloid- β ; Peptide Across the Blood-Brain Barrier: Implication for Therapies in Alzheimers Disease. *CNS Neurol Disord - Drug Targets* 8:16-30. doi: 10.2174/187152709787601867
11. Eikelenboom P, Stam FC (1982) Immunoglobulins and complement factors in senile plaques. An immunoperoxidase study. *Acta Neuropathol* 57:239-242. doi: 10.1007/BF00685397
12. Glenner GG, Wong CW (1984) Alzheimer's disease and Down's syndrome: sharing of a unique cerebrovascular amyloid fibril protein. *Biochem Biophys Res Commun* 122:1131-1135. doi: 10.1016/0006-291x(84)91209-9
13. Goedert M (2008) Oskar Fischer and the study of dementia. *Brain* 132:1102-1111. doi: 10.1093/brain/awn256
14. Goedert M, Masuda-Suzukake M, Falcon B (2017) Like prions: The propagation of aggregated tau and α -synuclein in neurodegeneration. *Brain* 140:266-278

15. Gorno-Tempini ML, Hillis AE, Weintraub S, Kertesz A, Mendez M, Cappa SF, Ogar JM, Rohrer JD, Black S, Boeve BF, Manes F, Dronkers NF, Vandenberghe R, Rascovsky K, Patterson K, Miller BL, Knopman DS, Hodges JR, Mesulam MM, Grossman M (2011) Classification of primary progressive aphasia and its variants. *Neurology* 76:1006–14. doi: 10.1212/WNL.0b013e31821103e6
16. Grady CL, Haxby J V, Horwitz B, Sundaram M, Berg G, Schapiro M, Friedland RP, Rapoport SI (1988) Longitudinal study of the early neuropsychological and cerebral metabolic changes in dementia of the Alzheimer type. *J Clin Exp Neuropsychol* 10:576–96. doi: 10.1080/01688638808402796
17. Graff-Radford J, Yong KXX, Apostolova LG, Bouwman FH, Carrillo M, Dickerson BC, Rabinovici GD, Schott JM, Jones DT, Murray ME (2021) New insights into atypical Alzheimer’s disease in the era of biomarkers. *Lancet Neurol.* 20:222–234
18. Hardy JA, Higgins GA (1992) Alzheimer’s disease: The amyloid cascade hypothesis. *Science* 256:184–185
19. Heneka MT, Carson MJ, Khoury J El, Landreth GE, Brosseron F, Feinstein DL, Jacobs AH, Wyss-Coray T, Vitorica J, Ransohoff RM, Herrup K, Frautschy SA, Finsen B, Brown GC, Verkhratsky A, Yamanaka K, Koistinaho J, Latz E, Halle A, Petzold GC, Town T, Morgan D, Shinohara ML, Perry VH, Holmes C, Bazan NG, Brooks DJ, Hunot S, Joseph B, Deigendesch N, Garaschuk O, Boddeke E, Dinarello CA, Breitner JC, Cole GM, Golenbock DT, Kummer MP (2015) Neuroinflammation in Alzheimer’s disease. *Lancet Neurol* 14:388–405. doi: 10.1016/S1474-4422(15)70016-5
20. Jack CR, Bennett DA, Blennow K, Carrillo MC, Dunn B, Haeberlein SB, Holtzman DM, Jagust W, Jessen F, Karlawish J, Liu E, Molinuevo JL, Montine T, Phelps C, Rankin KP, Rowe CC, Scheltens P, Siemers E, Snyder HM, Sperling R, Elliott C, Masliah E, Ryan L, Silverberg N (2018) NIA-AA Research Framework: Toward a biological definition of Alzheimer’s disease. *Alzheimer’s Dement.* 14:535–562
21. Jack CR, Wiste HJ, Lesnick TG, Weigand SD, Knopman DS, Vemuri P, Pankratz VS, Senjem ML, Gunter JL, Mielke MM, Lowe VJ, Boeve BF, Petersen RC (2013) Brain β -amyloid load approaches a plateau. *Neurology* 80:890–896. doi: 10.1212/WNL.0b013e3182840bbe
22. Jonsson T, Atwal JK, Steinberg S, Snaedal J, Jonsson P V., Bjornsson S, Stefansson H, Sulem P, Gudbjartsson D, Maloney J, Hoyte K, Gustafson A, Liu Y, Lu Y, Bhangale T, Graham RR, Huttenlocher J, Bjornsdottir G, Andreassen OA, Jonsson EG, Palotie A, Behrens TW, Magnusson OT, Kong A, Thorsteinsdottir U, Watts RJ, Stefansson K (2012) A mutation in APP protects against Alzheimer’s disease and age-related cognitive decline. *Nature* 488:96. doi: 10.1038/nature11283
23. Jonsson T, Stefansson H, Steinberg S, Jonsdottir I, Jonsson P V., Snaedal J, Bjornsson S, Huttenlocher J, Levey AI, Lah JJ, Rujescu D, Hampel H, Giegling I, Andreassen OA, Engedal K, Ulstein I, Djurovic S, Ibrahim-Verbaas C, Hofman A, Ikram MA, van Duijn CM, Thorsteinsdottir U, Kong A, Stefansson K (2013) Variant of TREM2 Associated with the Risk of Alzheimer’s Disease. *N Engl J Med* 368:107–116. doi: 10.1056/nejmoa1211103

24. Katzman R (1976) The Prevalence and Malignancy of Alzheimer Disease: A Major Killer. *Arch Neurol* 33:217-218. doi: 10.1001/archneur.1976.00500040001001
25. Kero M, Paetau A, Polvikoski T, Tanskanen M, Sulkava R, Jansson L, Myllykangas L, Tienari PJ (2013) Amyloid precursor protein (APP) A673T mutation in the elderly Finnish population. *Neurobiol Aging* 34:1518.e1-1518.e3. doi: 10.1016/j.neurobiolaging.2012.09.017
26. Koedam ELGE, Lauffer V, van der Vlies AE, van der Flier WM, Scheltens P, Pijnenburg YAL (2010) Early-versus late-onset Alzheimer's disease: more than age alone. *J Alzheimers Dis* 19:1401-8. doi: 10.3233/JAD-2010-1337
27. Koedam ELGE, Lehmann M, van der Flier WM, Scheltens P, Pijnenburg YAL, Fox N, Barkhof F, Wattjes MP (2011) Visual assessment of posterior atrophy development of a MRI rating scale. *Eur Radiol* 21:2618-25. doi: 10.1007/s00330-011-2205-4
28. Kraepelin E (1910) *Psychiatrie. Ein Lehrbuch für Studierende und Ärzte*, 8th ed. J.A. Barth, Leipzig
29. Lambert JC, Heath S, Even G, Champion D, Sleegers K, Hiltunen M, Combarros O, Zelenika D, Bullido MJ, Tavernier B, Letenneur L, Bettens K, Berr C, Pasquier F, Fiévet N, Barberger-Gateau P, Engelborghs S, De Deyn P, Mateo I, Franck A, Helisalmi S, Porcellini E, Hanon O, De Pancorbo MM, Lendon C, Dufouil C, Jaillard C, Leveillard T, Alvarez V, Bosco P, Mancuso M, Panza F, Nacmias B, Boss P, Piccardi P, Annoni G, Seripa D, Galimberti D, Hannequin D, Licastro F, Soininen H, Ritchie K, Blanché H, Dartigues JF, Tzourio C, Gut I, Van Broeckhoven C, Alperovitch A, Lathrop M, Amouyel P (2009) Genome-wide association study identifies variants at *CLU* and *CR1* associated with Alzheimer's disease. *Nat Genet* 41:1094-1099. doi: 10.1038/ng.439
30. Lanoiselée H-M, Nicolas G, Wallon D, Rovelet-Lecrux A, Lacour M, Rousseau S, Richard A-C, Pasquier F, Rollin-Sillaire A, Martinaud O, Quillard-Muraine M, de la Sayette V, Boutoleau-Bretonniere C, Etcharry-Bouyx F, Chauviré V, Sarazin M, le Ber I, Epelbaum S, Jonveaux T, Rouaud O, Ceccaldi M, Félician O, Godefroy O, Formaglio M, Croisile B, Auriacombe S, Chamard L, Vincent J-L, Sauvée M, Marelli-Tosi C, Gabelle A, Ozsancak C, Pariente J, Paquet C, Hannequin D, Champion D (2017) *APP*, *PSEN1*, and *PSEN2* mutations in early-onset Alzheimer disease: A genetic screening study of familial and sporadic cases. *PLoS Med* 14:e1002270. doi: 10.1371/journal.pmed.1002270
31. Maphis N, Xu G, Kokiko-Cochran ON, Jiang S, Cardona A, Ransohoff RM, Lamb BT, Bhaskar K (2015) Reactive microglia drive tau pathology and contribute to the spreading of pathological tau in the brain. *Brain* 138:1738-55. doi: 10.1093/brain/awv081
32. McKhann G, Drachman D, Folstein M, Katzman R, Price D, Stadlan EM (1984) Clinical diagnosis of alzheimer's disease: Report of the NINCDS-ADRDA work group* under the auspices of department of health and human services task force on alzheimer's disease. *Neurology* 34:939-944. doi: 10.1212/wnl.34.7.939

33. McKhann GM, Knopman DS, Chertkow H, Hyman BT, Jack CR, Kawas CH, Klunk WE, Koroshetz WJ, Manly JJ, Mayeux R, Mohs RC, Morris JC, Rossor MN, Scheltens P, Carrillo MC, Thies B, Weintraub S, Phelps CH, Phelps CH (2011) The diagnosis of dementia due to Alzheimer's disease: recommendations from the National Institute on Aging-Alzheimer's Association workgroups on diagnostic guidelines for Alzheimer's disease. *Alzheimers Dement* 7:263–9. doi: 10.1016/j.jalz.2011.03.005
34. McRobbie DW, Moore EA, Graves MJ, Prince MR (2006) *MRI from Picture to Proton*, 2nd ed. Cambridge University Press
35. Mirra SS, Heyman A, McKeel D, Sumi SM, Crain BJ, Brownlee LM, Vogel FS, Hughes JP, van Belle G, Berg L (1991) The Consortium to Establish a Registry for Alzheimer's Disease (CERAD). Part II. Standardization of the neuropathologic assessment of Alzheimer's disease. *Neurology* 41:479–86. doi: 10.1097/00005072-199405000-00012
36. Montine TJ, Phelps CH, Beach TG, Bigio EH, Cairns NJ, Dickson DW, Duyckaerts C, Frosch MP, Masliah E, Mirra SS, Nelson PT, Schneider JA, Thal DR, Trojanowski JQ, Vinters H V, Hyman BT, National Institute on Aging, Alzheimer's Association (2012) National Institute on Aging-Alzheimer's Association guidelines for the neuropathologic assessment of Alzheimer's disease: a practical approach. *Acta Neuropathol* 123:1–11. doi: 10.1007/s00401-011-0910-3
37. Murray ME, Graff-Radford NR, Ross OA, Petersen RC, Duara R, Dickson DW (2011) Neuropathologically defined subtypes of Alzheimer's disease with distinct clinical characteristics: a retrospective study. *Lancet Neurol* 10:785–796. doi: 10.1016/S1474-4422(11)70156-9
38. Olson MI, Cheng-Mei S (1969) Presenile dementia and Alzheimer's disease in mongolism. *Brain* 92:147–156
39. Ossenkoppele R, Cohn-Sheehy BI, La Joie R, Vogel JW, Möller C, Lehmann M, van Berckel BNM, Seeley WW, Pijnenburg YA, Gorno-Tempini ML, Kramer JH, Barkhof F, Rosen HJ, van der Flier WM, Jagust WJ, Miller BL, Scheltens P, Rabinovici GD (2015) Atrophy patterns in early clinical stages across distinct phenotypes of Alzheimer's disease. *Hum Brain Mapp* 36:4421–37. doi: 10.1002/hbm.22927
40. Ossenkoppele R, Lyoo CH, Sudre CH, van Westen D, Cho H, Ryu YH, Choi JY, Smith R, Strandberg O, Palmqvist S, Westman E, Tsai R, Kramer J, Boxer AL, Gorno-Tempini ML, La Joie R, Miller BL, Rabinovici GD, Hansson O (2020) Distinct tau PET patterns in atrophy-defined subtypes of Alzheimer's disease. *Alzheimer's Dement* 16:335–344. doi: 10.1016/j.jalz.2019.08.201
41. Ossenkoppele R, Pijnenburg YAL, Perry DC, Cohn-Sheehy BI, Scheltens NME, Vogel JW, Kramer JH, Van Der Vlies AE, Joie R La, Rosen HJ, Van Der Flier WM, Grinberg LT, Rozemuller AJ, Huang EJ, Van Berckel BNM, Miller BL, Barkhof F, Jagust WJ, Scheltens P, Seeley WW, Rabinovici GD (2015) The behavioural/dysexecutive variant of Alzheimer's disease: Clinical, neuroimaging and pathological features. *Brain* 138:2732–2749. doi: 10.1093/brain/awv191
42. Ossenkoppele R, Schonhaut DR, Schöll M, Lockhart SN, Ayakta N, Baker SL, O'Neil JP, Janabi M, Lazaris A, Cantwell A, Vogel J, Santos M, Miller ZA, Bettcher BM,

- Vossel KA, Kramer JH, Gorno-Tempini ML, Miller BL, Jagust WJ, Rabinovici GD (2016) Tau PET patterns mirror clinical and neuroanatomical variability in Alzheimer's disease. *Brain* 139:1551-1567. doi: 10.1093/brain/aww027
43. Pasquier F, Leys D, Weerts JG, Mounier-Vehier F, Barkhof F, Scheltens P (1996) Inter- and intraobserver reproducibility of cerebral atrophy assessment on MRI scans with hemispheric infarcts. *Eur Neurol* 36:268-72. doi: 10.1159/000117270
 44. Petersen C, Nolan AL, de Paula França Resende E, Miller Z, Ehrenberg AJ, Gorno-Tempini ML, Rosen HJ, Kramer JH, Spina S, Rabinovici GD, Miller BL, Seeley WW, Heinsen H, Grinberg LT (2019) Alzheimer's disease clinical variants show distinct regional patterns of neurofibrillary tangle accumulation. *Acta Neuropathol* 138:597-612. doi: 10.1007/s00401-019-02036-6
 45. Petersen C, Nolan AL, de Paula França Resende E, Miller Z, Ehrenberg AJ, Gorno-Tempini ML, Rosen HJ, Kramer JH, Spina S, Rabinovici GD, Miller BL, Seeley WW, Heinsen H, Grinberg LT (2019) Alzheimer's disease clinical variants show distinct regional patterns of neurofibrillary tangle accumulation. *Acta Neuropathol* 138:597-612. doi: 10.1007/s00401-019-02036-6
 46. Phillips JS, Das SR, McMillan CT, Irwin DJ, Roll EE, Da Re F, Nasrallah IM, Wolk DA, Grossman M (2018) Tau PET imaging predicts cognition in atypical variants of Alzheimer's disease. *Hum Brain Mapp* 39:691-708. doi: 10.1002/hbm.23874
 47. Redlich E (1898) Über miliare Sklerose der Hirnrinde bei seniler Atrophie. *Jahrbücher für Psychiatr und Neurol* 17:208-216
 48. Rozemuller JM, Eikelenboom P, Stam FC, Befreuther K, Masters CL (1989) A4 Protein in Alzheimer's Disease: Primary and Secondary Cellular Events Extracellular Amyloid Deposition. *Journal of Neuropathology & Experimental Neurology* 48:674-691. doi: 10.1097/00005072-198911000-00009
 49. Scheltens P, Leys D, Barkhof F, Huglo D, Weinstein HC, Vermersch P, Kuiper M, Steinling M, Wolters EC, Valk J (1992) Atrophy of medial temporal lobes on MRI in "probable" Alzheimer's disease and normal ageing: diagnostic value and neuropsychological correlates. *J Neurol Neurosurg Psychiatry* 55:967-72
 50. Schott JM, Lehmann M, Primativo S, Rossor MN, Ryan NS, Shakespeare TJ, Suárez González A, Yong KXX, Fox NC, Rabinovici GD, Lehmann M, Murray M, Snowden JS, Snowden JS, van der Flier WM, Pijnenburg Y, Scheltens P, van der Flier WM, Pijnenburg Y, Scheltens P, Dickerson BC, Vandenberghe R, Ahmed S, Butler C, Bak TH, Boeve BF, Graff-Radford J, Cappa SF, Ceccaldi M, de Souza LC, Dubois B, Felician O, Felician O, Galasko D, Graff-Radford NR, Hof PR, Hof PR, Krolak-Salmon P, Magnin E, Mendez MF, Nestor PJ, Onyike CU, Pelak VS, Pelak VS, Suárez González A, Tang-Wai DF, Carrillo M (2017) Consensus classification of posterior cortical atrophy. *Alzheimer's Dement* 13:870-884. doi: 10.1016/j.jalz.2017.01.014
 51. Selkoe DJ, Hardy J (2016) The amyloid hypothesis of Alzheimer's disease at 25 years. *EMBO Mol Med* 8:1-14. doi: 10.15252/emmm.201606210
 52. Thal DR, Rüb U, Orantes M, Braak H (2002) Phases of Ab-deposition in the human brain and its relevance for the development of AD. *Neurology* 58:1791-800. doi: 10.1212/wnl.58.12.1791

53. Todorov AB, Go RCP, Constantinidis J, Elston RC (1975) Specificity of the clinical diagnosis of dementia. *J Neurol Sci* 26:81-98. doi: 10.1016/0022-510X(75)90116-1
54. Tomlinson BE, Blessed G, Roth M (1970) Observations on the brains of demented old people. *J Neurol Sci* 11:205-242. doi: 10.1016/0022-510X(70)90063-8
55. Veerhuis R, Nielsen HM, Tenner AJ (2011) Complement in the brain. *Mol. Immunol.* 48:1592-1603
56. Vermunt L, Sikkes SAM, van den Hout A, Handels R, Bos I, van der Flier WM, Kern S, Ousset PJ, Maruff P, Skoog I, Verhey FRJ, Freund-Levi Y, Tsolaki M, Wallin ÅK, Olde Rikkert M, Soininen H, Spuru L, Zetterberg H, Blennow K, Scheltens P, Muniz-Terrera G, Visser PJ, Vellas B, Reynish E, Ousset PJ, Andrieu S, Burns A, Pasquier F, Frisoni G, Salmon E, Michel JP, Zekry DS, Boada M, Dartigues JF, Olde-Rikkert MGM, Rigaud AS, Winblad B, Malick A, Sinclair A, Frölich L, Scheltens P, Ribera C, Touchon J, Robert P, Salva A, Waldemar G, Bullock R, Tsolaki M, Rodriguez G, Spuru L, Jones RW, Stiens G, Stoppe G, Eriksdotter Jönhagen M, Cherubini A, Lage PM, Gomez-Isla T, Camus V, Agüera-Morales E, Lopez F, Savy S, Cantet C, Coley N (2019) Duration of preclinical, prodromal, and dementia stages of Alzheimer's disease in relation to age, sex, and APOE genotype. *Alzheimer's Dement* 15:888-898. doi: 10.1016/j.jalz.2019.04.001
57. Wyss-Coray T, Loike JD, Brionne TC, Lu E, Anankov R, Yan F, Silverstein SC, Husemann J (2003) Adult mouse astrocytes degrade amyloid- β in vitro and in situ. *Nat Med* 9:453-457. doi: 10.1038/nm838

Section 2

Heterogeneity in Alzheimer's
disease pathology: distribution of
neuroinflammation in (a)typical AD
phenotypes

Chapter 2

**Neuroinflammation is increased in the
parietal cortex of atypical Alzheimer's
disease**

Baayla DC Boon, Jeroen JM Hoozemans, Boaz Lopuhaä, Kristel N
Eigenhuis, Philip Scheltens, Wouter Kamphorst, Annemieke JM
Rozemuller, Femke H Bouwman

Journal of Neuroinflammation (2018)
doi: 10.1186/s12974-018-1180-y

ABSTRACT

Background: While most patients with Alzheimer's disease (AD) present with memory complaints, 30% of patients with early disease onset present with non-amnesic symptoms. This atypical presentation is thought to be caused by a different spreading of neurofibrillary tangles (NFT) than originally proposed by Braak and Braak. Recent studies suggest a prominent role for neuroinflammation in the spreading of tau pathology.

Methods: We aimed to explore whether an atypical spreading of pathology in AD is associated with an atypical distribution of neuroinflammation. Typical and atypical AD cases were selected based on both NFT distribution and amnesic or non-amnesic clinical presentation. Immunohistochemistry was performed on the temporal pole and superior parietal lobe of 10 typical and 9 atypical AD cases. The presence of amyloid-beta (N-terminal; IC16), pTau (AT8), reactive astrocytes (GFAP), microglia (Iba1, CD68 and HLA-DP/DQ/DR), as well as complement factors (C1q, C3d, C4b, and C5b-9) was quantified by image analysis. Differences in lobar distribution patterns of immunoreactivity were statistically assessed using a linear mixed model.

Results: We found a temporal dominant distribution for amyloid-beta, GFAP, and Iba1 in both typical and atypical AD. Distribution of pTau, CD68, HLA-DP/DQ/DR, C3d, and C4b differed between AD variants. Typical AD cases showed a temporal dominant distribution of these markers, whereas atypical AD cases showed a parietal dominant distribution. Interestingly, when quantifying for the number of amyloid-beta plaques instead of stained surface area, atypical AD cases differed in distribution pattern from typical AD cases. Remarkably, plaque morphology and localization of neuroinflammation within the plaques was different between the two phenotypes.

Conclusions: Our data show a different localization of neuroinflammatory markers and amyloid-beta plaques between AD phenotypes. In addition, these markers reflect the atypical distribution of tau pathology in atypical AD, suggesting that neuroinflammation might be a crucial link between amyloid-beta deposits, tau pathology, and clinical symptoms.

INTRODUCTION

Patients with Alzheimer's disease (AD) typically present with episodic memory impairment followed by deterioration of executive functioning, praxis, and visuospatial skills. However, AD patients may also present with an atypical phenotype [14, 30]. An atypical presentation is seen in 10% of the late-onset AD (LOAD) patients (≥ 65 years of age) and up to 30% of the early-onset (< 65 years) AD (EOAD) patients [24]. So far, three variants of atypical AD have been described: the posterior cortical atrophy (PCA) variant characterized by visuo-perceptual problems [12], the logopenic variant characterized by aphasia [18], and the frontal variant associated with behavioral changes [14, 30]. In addition to clinical differences, these different AD variants show syndrome-specific atrophy patterns on MRI [34].

AD is characterized by the deposition of amyloid-beta plaques and the formation of neurofibrillary tangles (NFT) in the brain. During disease progression, both plaques and NFTs are assumed to spread through the brain in a fixed order [10, 43]. However, the typical NFT distribution as originally described by Braak and Braak [10] does not seem to hold for all AD cases. Clinicopathological studies indicated that AD patients with an atypical phenotype have an atypical NFT distribution [17, 42]. Furthermore, this atypical NFT distribution was demonstrated in living AD patients using the tau tracer (18)F-AV1451 [35]. While the atypical distribution of NFTs corresponds with the observed clinical phenotype, the cause of this difference in NFT spreading between AD variants remains elusive.

There is accumulating evidence that inflammation plays a prominent role in the pathogenesis of AD. Recently, genome-wide association studies have identified several genes involved in inflammation, especially those engaged in microglia function, as risk factors for developing AD [6, 22, 33, 39]. The AD brain shows an increased presence of activated microglia, reactive astrocytes, proinflammatory cytokines, acute phase proteins, and activated complement proteins compared to controls [1]. Complement proteins co-localize with NFTs [29, 37], as well as with amyloid-beta deposits [16], and are actively involved in the formation of these pathological structures. Clusters of activated microglia are found in amyloid plaques, and the presence of activated microglia increases with disease severity [2, 13]. Recent disease models suggest that microglia are actively involved in the spreading of pTau [4, 25, 28]. Tau pathology is heavily reduced in disease-modeled mice that are depleted for microglia compared to their microglia-

positive peers [4, 28]. In the human brain, the presence of activated microglia correlates with Braak staging for NFTs [21].

Evidence for the correlation of pTau, neuroinflammation, and microglia in AD subtypes is lacking. In this study, we aimed to explore whether an atypical spreading of NFT pathology in non-amnesic AD is associated with an atypical distribution of neuroinflammation. In a well-defined cohort of typical and atypical AD, we assessed and compared the presence of pTau, amyloid-beta, (activated) glial cells, and complement proteins in temporal and parietal cortical areas.

METHODS

Post mortem brain tissue

Post mortem brain tissue was obtained from the Netherlands Brain Bank (NBB; Amsterdam, the Netherlands, <https://www.brainbank.nl>). Donors signed informed consent for brain autopsy and the use of brain tissue and medical records for research purposes. Neuropathological diagnosis was based on histochemical stainings including hematoxylin and eosin, congo red staining, Bodian or Gallyas and methenamine silver stainings, and immunohistochemical stainings for amyloid-beta, pTau, alpha-synuclein, and p62. These stainings were performed on formalin-fixed paraffin-embedded (FFPE) brain tissue of multiple brain regions including the frontal cortex, temporal pole, superior parietal lobe, occipital pole, amygdala, and the hippocampus. Neuropathological diagnosis of AD was based on Braak stages for NFT and amyloid [10], Thal phases for amyloid-beta [43], and CERAD criteria for neuritic plaques [31].

Selection of typical and atypical AD cases

Between 1996 and 2014, 352 AD cases came to autopsy and were semi-quantitatively scored by two neuropathologists (WK, AR) for the NFT load using Bodian or Gallyas staining in the temporal pole, the frontal, superior parietal, and occipital cortex as previously described by Hoogendijk et al. [20]. The NFT load was scored in a 0.4 mm² area as being absent (0), sparse (1), mild (2; 2 to 3 NFTs) or severe (3; >3 NFTs) for each brain region separately. From this cohort, we selected cases with an NFT score of 3 in either the temporal or parietal section, or in both sections, resulting in 296 cases (for flowchart, see Fig. 1). For 142 cases, the NFT score was higher in the temporal section than the parietal section. These cases were referred to as having a typical NFT distribution [10]. In 126 of 296 cases, an NFT score of 3 was found in the temporal as well as the

parietal section. A higher NFT score in the parietal compared to the temporal section was observed in 28 cases and was defined as a parietal dominant and thus atypical NFT distribution.

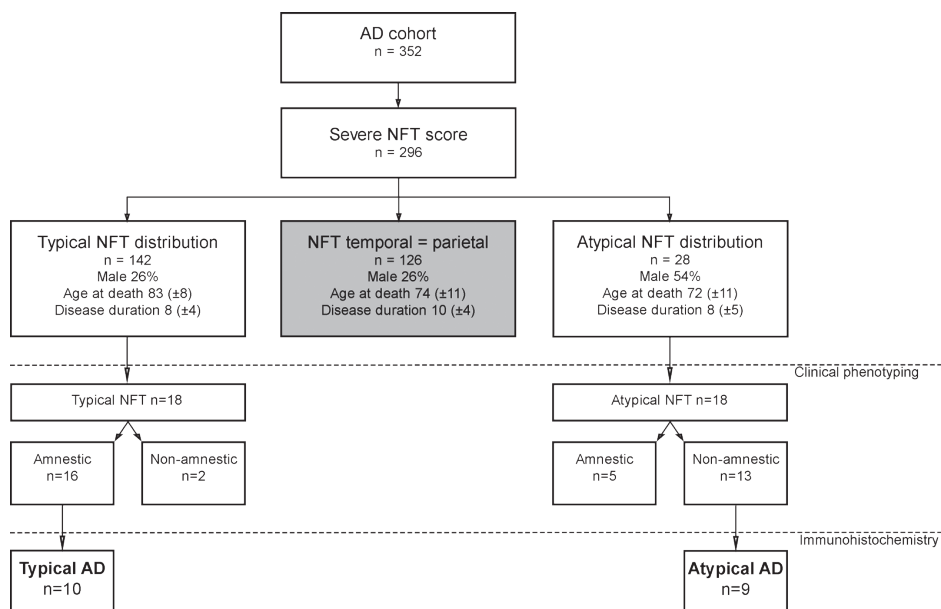


Fig. 1. Flowchart of neuropathologically assessed and semi-quantitatively scored AD cohort. Between 1996 and 2014, 352 AD cases came to autopsy and were semi-quantitatively scored for NFTs as described by Hoogendijk et al. [20]. In 296 cases an NFT score of ≥ 3 in the temporal and/or parietal cortex was observed. Typical NFT distribution was defined as a higher NFT score in the temporal compared to the parietal cortex. Atypical NFT distribution was defined as a higher NFT score in the parietal compared to the temporal section. From the cases with a typical and an atypical NFT distribution, 18 cases per group were selected for which the clinical phenotype was stratified as either amnesic or non-amnesic (results shown in Table 2). From these clinical phenotyped cases, 9 cases with an atypical NFT as well as non-amnesic clinical presentation were compared to 10 cases with an amnesic presentation and typical NFT distribution using immunohistochemistry. Mean \pm SD is shown for age at death and disease duration in years. AD Alzheimer's disease; NFT neurofibrillary tangle.

To study the distribution of neuroinflammation in typical and atypical AD, we further refined our cohort to include only cases with a concordance between clinical presentation and NFT distribution. The clinical phenotype of 36 cases with atypical and typical NFT pathology was retrospectively assessed. In 18 out of 28 cases with an atypical NFT distribution, the available clinical information was sufficient to come to a retrospective clinical diagnosis (see Table 1 for

demographics). To have an equal group for comparison, we randomly chose 18 cases with both typical NFT distribution and sufficient clinical information for clinical phenotyping. Clinical assessment was performed retrospectively and independently by two cognitive neurologists (YP and FB) using the NIA-AA criteria [30]. Both clinicians were blinded to the pathological stratification when assessing the clinical phenotype. The clinical stratification was based on (collateral) history and cognitive examination documented by the clinical neurologist. Cases with first-degree relatives affected by EOAD were excluded to minimize the risk of genetic AD. Other exclusion criteria were sepsis, other neurodegenerative or psychiatric diseases, significant cerebrovascular disease, post mortem interval > 12 hours, and prior known genetic mutations. Due to our exclusion criteria and availability of archived brain tissue samples, our inclusion was limited to nine atypical AD cases and ten typical AD cases of which the temporal pole and superior parietal lobe were assessed by immunohistochemistry (see Fig. 1 for inclusion flowchart; Table 2 for patient details; Table 3 for demographics). Cases were not intentionally matched for disease duration, brain weight, *APOE* status, or post mortem interval.

Table 1. Demographics of 36 cases with typical and atypical NFT distribution for which extensive retrospective clinical assessment was performed

| | Typical NFT distribution <i>n</i> = 18 | | Atypical NFT distribution <i>n</i> = 18 | |
|--|---|---------------------------------|--|----------------------------------|
| | Amnestic (<i>n</i> = 16) | Non-amnestic (<i>n</i> = 2) | Amnestic (<i>n</i> = 5) | Non-amnestic (<i>n</i> = 13) |
| Phenotype | | | | |
| Male, <i>n</i> (%) | 6 (37) | 0 | 3 (60) | 8 (62) |
| Age † | 82 (±7) | 88 (±5) | 71 (±11) | 67 (±7) |
| Disease duration | 8 (±5) | 7 (±4) | 11 (±5) | 8 (±4) |
| NFT stage [10] <i>n</i> per stage IV/V/VI | 2 / 10 / 4 | 1 / 1 / 0 | 0 / 2 / 3 | 0 / 7 / 6 |
| Amyloid stage [10] <i>n</i> per stage O/A/B/C | 0 / 0 / 16 | 0 / 0 / 2 | 0 / 0 / 5 | 0 / 1 / 12 |

Data are mean ± SD. Age at death and disease duration shown in years. NFT neurofibrillary tangle.

Table 2. Clinical and neuropathological characteristics of typical and atypical AD cases

| Case | Phenotype | Symptoms at clinical presentation | Sex | Age † | Disease duration | NFT stage [10] | Amyloid stage [10] | Brain weight (grams) | Cause of death | PMI | APOE |
|------|-------------|--|-----|-------|------------------|----------------|--------------------|----------------------|------------------------------|-------|------|
| 1 | Typical AD | Memory | F | 92 | 8 | V | C | 933 | Heart failure | 7:00 | 34 |
| 2 | Typical AD | Memory, disorientation | F | 84 | 4 | IV | C | 908 | Cardiogenic shock | 4:15 | 23 |
| 3 | Typical AD | Memory, disorientation | F | 84 | 9 | V | C | 827 | Cachexia | 6:40 | 34 |
| 4 | Typical AD | Memory | F | 89 | 5 | V | C | 962 | Pneumonia | 6:28 | 34 |
| 5 | Typical AD | Memory | F | 83 | 6 | VI | C | 1100 | Dehydration | 6:17 | 34 |
| 6 | Typical AD | Memory, behavior | F | 91 | 3 | IV | C | 1026 | Cachexia | 6:25 | 33 |
| 7 | Typical AD | Memory, | F | 77 | 2 | V | C | 999 | Pneumonia | 6:05 | 33 |
| 8 | Typical AD | Memory, behavior | M | 70 | 2 | VI | C | 1261 | Metastasized colon carcinoma | 6:20 | 34 |
| 9 | Typical AD | Memory | F | 76 | 12 | V | C | 1223 | Unknown | 10:45 | 44 |
| 10 | Typical AD | Memory | M | 60 | 2 | VI | C | 1191 | Cachexia | 6:15 | 34 |
| 11 | Atypical AD | Aphasia, dyscalculia, agraphia, left-right agnosia, visuoconstructive problems | F | 65 | 6 | VI | C | 975 | Pneumonia | 5:40 | 33 |
| 12 | Atypical AD | Aphasia, dyslexia, apraxia, visuoconstructive problems | M | 65 | 2 | VI | C | 1057 | Cardiac insufficiency | 8:50 | 44 |
| 13 | Atypical AD | Aphasia, acalculia, finger agnosia, apraxia | M | 64 | 7 | V | C | 1135 | Pneumonia | 4:45 | 42 |
| 14 | Atypical AD | Parkinsonism, falling, alien hand syndrome | F | 67 | 3 | V | C | 817 | Epileptic insult | 7:35 | 33 |
| 15 | Atypical AD | Aphasia, apathy, agitation | M | 59 | 6 | VI | C | 1300 | Cachexia | 5:05 | 44 |

Table 2. Continued.

| Case | Phenotype | Symptoms at clinical presentation | Sex | Age † | Disease duration | NFT stage [10] | Amyloid stage [10] | Brain weight (grams) | Cause of death | PMI | APOE |
|------|-------------|---|-----|-------|------------------|----------------|--------------------|----------------------|-----------------------------|------|------|
| 16 | Atypical AD | Aphasia, dyscalculia, dyslexia, disorientation | M | 62 | 3 | VI | C | 1116 | Malign neuroleptic syndrome | 4:15 | 34 |
| 17 | Atypical AD | Aphasia, dyslexia, apathy, apraxia | M | 65 | 1 | V | C | 1150 | Euthanasia | 6:50 | 34 |
| 18 | Atypical AD | Aphasia, dyslexia, apraxia, visuospatial problems, behavior | M | 62 | 6 | V | B | 1153 | Cachexia | 4:40 | 33 |
| 19 | Atypical AD | Visual hallucinations, psychosis | M | 61 | 6 | VI | C | 1355 | Pneumonia | 5:00 | 34 |

Age at death and disease duration in years; post mortem interval in hours:minutes. Typical AD defined as more NFTs in the temporal compared to the parietal cortex by semi-quantitative scoring as described by Hoogendijk et al. [20] and an amnesic presentation during life. Atypical AD defined as more NFTs assessed by semi-quantitative scoring in the parietal compared to the temporal cortex and a non-amnesic presentation. AD Alzheimer's disease; F female; M male; NFT neurofibrillary tangle; PMI post mortem interval.

Table 3. Demographic characteristics of the AD cases used for immunohistochemical analysis

| | Typical AD (<i>n</i> =10) | Atypical AD (<i>n</i> =9) | <i>p</i> value |
|--|-------------------------------|-------------------------------|----------------|
| Male, <i>n</i> | 2 | 7 | < .05 |
| Age † | 81 (±10) | 63 (±3) | < .01 |
| Disease duration | 5 (±3) | 4 (±2) | .78 |
| Brain weight (grams) | 1043 (±146) | 1117 (±161) | .32 |
| PMI (h:min) | 6:19 (±1:48) | 5:51 (±1:33) | .66 |
| NFT stage [10] <i>n</i> per stage IV/V/VI | 2 / 5 / 3 | 0 / 4 / 5 | .46 |
| Amyloid stage [10] <i>n</i> per stage O/A/B/C | 0 / 0 / 10 | 0 / 1 / 8 | .47 |
| APOE genotype <i>n</i> per category 23/24/33/34/44 | 1 / 0 / 2 / 6 / 1 | 0 / 1 / 3 / 3 / 2 | .48 |

Data in mean (±SD); Age at death and disease duration in years; Mann Whitney *U* for continuous data; Fisher's Exact for categorical data. AD Alzheimer's disease; PMI post mortem interval.

Immunohistochemistry

Immunohistochemistry was performed to detect pTau (AT8); amyloid-beta (N-terminal; IC16); reactive astrocytes (GFAP); microglia (Iba1); activated microglia (CD68 and HLA-DP/DQ/DR); and complement proteins (C1q, C3d, C4b, and C5b-9) (Table 4). FFPE sections (5-µm thick) from the temporal pole and superior parietal lobe of the right hemisphere were used.

Immunohistochemistry for pTau, amyloid-beta, GFAP, and Iba1 was performed using the Ventana BenchMark ULTRA staining system (Roche, Basel, Switzerland). Tissue sections were mounted on TOMO adhesive glass slides (Matsunami, Osaka, Japan) and deparaffinized. After blocking for endogenous peroxidase, antigen retrieval was performed by heating sections at 100°C in Cell Conditioning 1 solution (pH 8.5) (Roche) for different durations per antibody (see Table 4). For detection of primary antibodies with 3,3'-diaminobenzidine tetrahydrochloride (DAB), Optiview DAB IHC detection kit (Roche) was used. Finally, the sections were mounted with coverslipping film (Sakura Tissue-Tek, Leiden, The Netherlands).

Immunohistochemistry for CD68, HLA-DP/DQ/DR, C1q, C3d, C4b, and C5b-9 was performed manually. The sections were mounted on SuperFrost Plus glass slides (Menzel-Gläser, Braunschweig, Germany) and deparaffinized. Subsequently, the sections were blocked for endogenous peroxidase using 0.3% hydrogen peroxide in phosphate buffer saline (PBS; pH 7.4). The sections were immersed in sodium citrate buffer (10 mM sodium citrate, 5 M NaOH, dH₂O,

pH 6.0) and heated to 120 °C in an autoclave for antigen retrieval. Primary antibodies were diluted in normal antibody diluent (ImmunoLogic, Duiven, The Netherlands) and incubated overnight at 4 °C. Primary antibodies were detected using EnVision (Agilent Dako, Glostrup, Denmark). Between steps, the sections were washed in PBS. Subsequently, antibodies were visualized with DAB (Agilent Dako). After counterstaining with hematoxylin, the sections were mounted with Entellan (Merck, Darmstadt, Germany).

Image analyses and quantitative assessment of immunostainings

For quantitative assessment, two regions of interest (ROI) were randomly selected within non-curved areas of each section containing all six cortical layers [3]. Within each ROI, contiguous microscopic fields arranged in columns perpendicular to the cortical surface of the cortex were photographed. Total surface, depending on the width of the cortex, could vary for each ROI and contained at least two columns. Images were taken using a × 10 objective on an Olympus BX 41 photomicroscope with a Leica MC 170 HD digital camera. The presence of DAB staining was quantified with ImageJ (NIH) using the color threshold plugin. Our outcome measurement was the percentage of DAB-stained area per marker, also referred to as immunoreactivity. In addition to immunoreactivity, we also quantified the number of amyloid-beta and C4b plaques. For the amyloid-beta plaques, diffuse deposits were not taken into account and only dense plaques were quantified, defined as particles with an immunoreactive surface area of 100 μm^2 or more [15, 44]. C4b-positive deposits of the same surface area were quantified as a measurement of the atypical appearing plaques as described in the results section.

Fluorescent triple stainings

Co-localization of C4b and CD68 or HLA-DP/DQ/DR with amyloid-beta and thioflavin S was visualized in the parietal section of four atypical AD cases and the temporal section of two typical AD cases. The typical AD cases served as positive controls and reference since localization of complement and microglia in classic cored plaques is widely described in literature (for CD68 [2] / for complement [16,19]).

Table 4. Characteristics of primary antibodies and staining details

| Antibody | Antigen | Species | Origin details | Dilution | Incubation time | Antigen retrieval | Detection method |
|---------------------------|--|-------------|--|----------|-------------------|------------------------------------|------------------|
| pTau, clone AT8 | Tau phosphorylated at Ser202 and Thr205 | Mouse IgG1 | Thermo Fisher, Pittsburgh, USA | 1:10000 | 32 min at 36 °C | Heat-induced (pH 8.5) for 24 min | Optiview |
| Amyloid-beta, clone IC-16 | N-terminus of amyloid-beta (aa 1-16) | Mouse IgG2a | Dr. Carsten Korth, University of Dusseldorf, Germany | 1:25 | 32 min at 36 °C | Heat-induced (pH 8.5) for 24 min | Optiview |
| GFAP, clone EP672Y | Glial fibrillary acidic protein | Mouse | Roche, Basel, Switzerland | 1:2 | 8 min at 37 °C | Heat-induced (pH 8.5) for 32 min | Optiview |
| Iba1 | C-terminus of Iba1 | Rabbit | Wako Pure Chemical Industries, Osaka, Japan | 1:4000 | 32 min at 36 °C | Heat-induced (pH 8.5) for 16 min | Optiview |
| CD68, clone KP1 | CD68 | Mouse IgG1 | Agilent Dako, Glostrup, Denmark | 1:1200 | Overnight at 4 °C | Heat-induced (pH 6.0) by autoclave | EnVision |
| HLA-DP/DR, clone CR3/43 | Alpha and beta-chains of all products of the DP, DQ, and DR subregions | Mouse IgG1 | Agilent Dako | 1:800 | Overnight at 4 °C | Heat-induced (pH 6.0) by autoclave | EnVision |
| C1q | C1q | Rabbit | Agilent Dako | 1:25600 | Overnight at 4 °C | Heat-induced (pH 6.0) by autoclave | EnVision |
| C3d | C3d | Rabbit | Agilent Dako | 1:3200 | Overnight at 4 °C | Heat-induced (pH 6.0) by autoclave | EnVision |
| C4b | C4b | Rabbit | Abcam, Cambridge, United Kingdom | 1:1600 | Overnight at 4 °C | Heat-induced (pH 6.0) by autoclave | EnVision |
| C5b-9, clone WU13-15 | Neopeptide on C9 in the membrane attack complex | Mouse | Hycult Biotech, Plymouth meeting, USA | 1:400 | Overnight at 4 °C | Heat-induced (pH 6.0) by autoclave | EnVision |

After deparaffinization, the sections were submerged in sodium citrate buffer and heated to 120 °C in an autoclave. Subsequently, the sections were incubated using different combinations of primary antibodies: mouse IgG2a-anti-amyloid-beta (1:200), rabbit-anti-C4b (1:200), and mouse IgG1-anti-HLA-DP/DQ/DR (1:25) or mouse IgG1-anti-CD68 (1:300). Antibodies were diluted in normal antibody diluent (ImmunoLogic) and incubated overnight at 4 °C. Subsequently, the sections were incubated with the following secondary antibodies: goat-anti-mouse IgG2a Alexa Fluor dye 594, goat-anti-mouse IgG1 Alexa Fluor dye 647, and donkey-anti-rabbit Alexa Fluor dye 647 (1:250 dilution, Thermo Fisher, Waltham, USA). For visualization of amyloid structures, the sections were counterstained with thioflavin S (1% in dH₂O) and subsequently rinsed in 70% ethanol. Autofluorescence was blocked with 0.1% Sudan black in 70% ethanol for 5 min. Between steps, the sections were rinsed with PBS. Finally, the sections were enclosed with 80% glycerol/20% Tris-buffered saline. Representative pictures were taken with a Leica DMI8 inverted fluorescent microscope equipped with a Leica DFC300 G camera.

Statistical analysis

Demographics of the typical and atypical AD groups were compared using Fisher's exact test for categorical, and Mann-Whitney U test for numerical and not normally distributed data. Outcome measures were compared between the two AD groups by using linear mixed model analysis. Linear mixed model analysis was used to adjust for the nested observations within cases. In the linear mixed model analyses, the group variable (typical versus atypical AD), the region (temporal versus parietal), and the interaction between group and region were added. Correcting for age and sex made the model less stable and was therefore not performed. An assumption to apply a linear mixed model is that residuals of outcome measurements are normally distributed. To meet this assumption, all outcome variables (pTau, amyloid-beta, GFAP, Iba1, HLA-DP/DQ/DR, CD68, C1q, C3d, C4b, number of amyloid-beta plaques, and number of C4b plaques) were transformed by taking the natural log of the (variable + 1). The covariance structure was set to unstructured. Using the linear mixed model, we answered if the difference in outcome measurement over the two regions was different between the two AD phenotypes (region × phenotype), also referred to as interaction effect. Both phenotypes showed a similar distribution over the two regions if no interaction effect was found. Statistical analysis was performed in IBM SPSS statistics version 22.0 (Armonk, NY, USA). Bonferroni correction was used to correct for multiple testing. Since we tested 11 outcome measurements (amyloid-beta, pTau, GFAP, Iba1, CD68, HLA-DP/DQ/DR, C1q, C3d, C4b,

amyloid-beta plaques, and # C4b plaques) statistical significance was set at $p < .0045$ ($p < .05/11$ outcome measurements) for each effect (region \times phenotype and region) of the linear mixed model. Statistical significance was set at $p < .05$ for comparison of baseline characteristics.

RESULTS

Atypical AD cases are younger than typical AD cases

The post mortem cohort used for immunohistochemistry consisted of nine atypical AD cases and ten typical AD cases. For a summary of initial clinical symptoms at presentation for each case, see Table 2. Most atypical AD cases presented with symptoms of aphasia, consisting of word-finding difficulties and spelling mistakes, combined with apraxia. None of our atypical cases retrospectively met the criteria for an isolated primary progressive aphasia [18]. One case presented with Parkinsonism and an alien hand syndrome, fitting a corticobasal syndrome during life. All ten typical AD cases presented with memory complaints as most prominent initial symptom. Demographic characteristics of both AD phenotypes used for immunohistochemical analysis are shown in Table 3. Similar to the large cohort of 296 AD subjects (see Fig. 1), atypical AD patients selected for immunohistochemistry analysis, were younger at age of death and more often male. The disease duration, brain weight, post mortem interval, disease severity, and *APOE* genotype did not differ between groups.

Distribution of pTau and amyloid-beta in typical and atypical AD

Immunohistochemistry for pTau showed neuronal inclusions as well as neuritic threads (Fig. 2A). Typical AD cases showed more pTau immunoreactivity in the temporal compared to the parietal section (Fig. 2C). This was contrary to the pTau distribution in atypical AD cases, in which the parietal section showed more immunoreactivity compared to the temporal section. In addition, the distribution of pTau over the two regions differed significantly between the two phenotypes (Table 5).

Amyloid-beta immunoreactivity was present in the form of diffuse deposits, dense plaques, and classic cored plaques (Fig. 2B). Both the typical and atypical AD group showed more immunoreactivity for amyloid-beta in the temporal than parietal section (Fig. 2D), and no difference in distribution was observed (Table 5). While total immunoreactivity levels did not show differences between the two phenotypes, the number of dense plaques with an immunoreactive surface

area of 100 μm^2 or more did show a significant difference in distribution over the two regions between the two phenotypes (Fig. 2E) (Table 5). In contrast to the typical AD group, more dense plaques were observed in the parietal section of the atypical AD group. Besides a difference in plaque number, we observed a contrast in plaque morphology between the two groups, which will be addressed below.

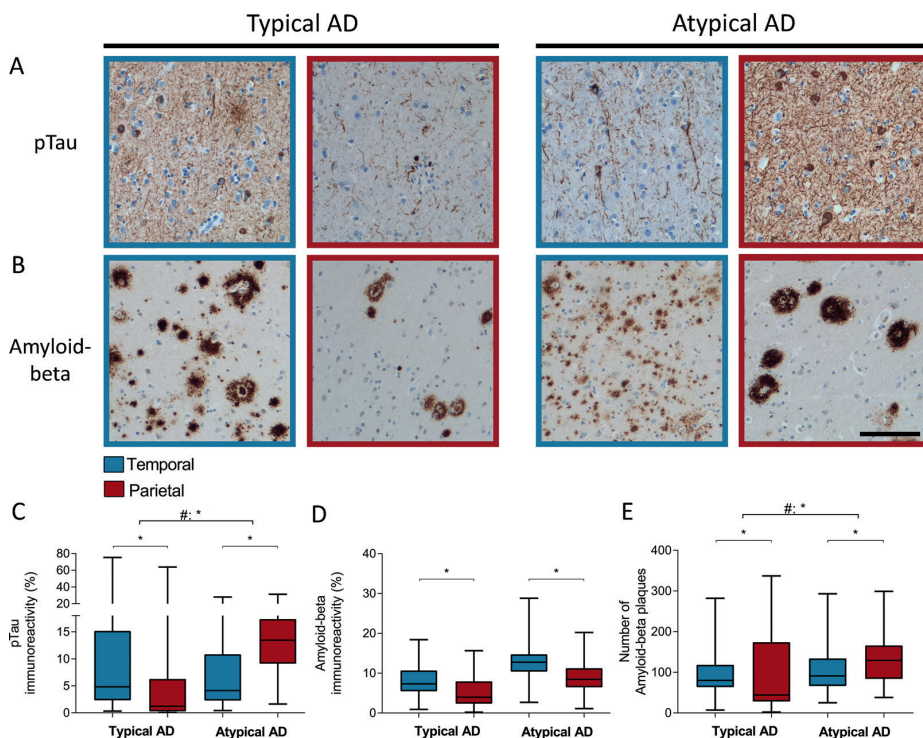


Fig. 2. pTau and amyloid-beta distribution in typical AD and atypical AD

A In typical AD, the temporal cortex (blue border) shows more immunoreactivity for pTau than the parietal cortex (burgundy border). This distribution is inverted in atypical AD (boxplot in C). **B** Although both typical and atypical AD show more overall amyloid-beta immunoreactivity in the temporal cortex compared to the parietal region, the atypical AD group shows increased number of amyloid-beta plaques in the parietal compared to temporal section (boxplot in E). Bar represents 100 μm . **C**, **D**, and **E** Boxplots showing pTau immunoreactive area (%), amyloid-beta immunoreactive area (%), and the number of amyloid-beta plaques, respectively, in the temporal and parietal section of both AD phenotypes. Data shown as median (bar), 1st and 3rd quartile (box boundaries), and min to max (error bars). A difference in distribution over the two regions between the two AD phenotypes is indicated by # (Table 5). AD Alzheimer's disease; pTau phosphorylated tau; * $p < .0045$.

Table 5. Results for the linear mixed model of transformed immunohistochemistry variables

| Transformed variable | Fixed Effect | Phenotype | Results for linear mixed model | |
|---------------------------|--------------------|-------------|--------------------------------|-----------------|
| | | | Beta-coefficient | 95% CI |
| Amyloid-beta | Region × phenotype | | 1.53* | [1.33 - 1.72] |
| | Region | Typical AD | -0.82* | [-0.95 - -0.68] |
| | | Atypical AD | 0.71* | [0.57 - 0.85] |
| GFAP | Region × phenotype | | 0.04 | [-0.06 - 0.15] |
| | Region | Both | -0.46* | [-0.54 - -0.39] |
| Iba1 | Region × phenotype | | 1.25* | [1.02 - 1.48] |
| | Region | Typical AD | -1.71* | [-1.87 - -1.56] |
| | | Atypical AD | -0.46* | [-0.63 - -0.29] |
| CD68 | Region × phenotype | | 0.10 | [0.002 - 0.19] |
| | Region | Both | -0.47* | [-0.53 - -0.41] |
| HLA-DP/DQ/DR | Region × phenotype | | -0.43* | [0.38 - 0.48] |
| | Region | Typical AD | -0.13* | [-0.17 - -0.10] |
| | | Atypical AD | 0.29* | [0.26 - 0.33] |
| C1q | Region × phenotype | | 0.97* | [0.88 - 1.06] |
| | Region | Typical AD | -0.08* | [-0.14 - -0.03] |
| | | Atypical AD | 0.89* | [0.82 - 0.96] |
| C3d | Region × phenotype | | -0.05 | [-0.15 - 0.06] |
| | Region | Both | 0.03 | [-0.05 - 0.10] |
| C4b | Region × phenotype | | 0.74* | [0.62 - 0.86] |
| | Region | Typical AD | -0.39* | [-0.47 - -0.31] |
| | | Atypical AD | 0.36* | [0.26 - 0.45] |
| # of amyloid-beta plaques | Region × phenotype | | 0.95* | [0.84 - 1.07] |
| | Region | Typical AD | -0.24* | [-0.32 - -0.17] |
| | | Atypical AD | 0.71* | [0.62 - 0.80] |
| # of C4b plaques | Region × phenotype | | 0.58* | [0.41 - 0.75] |
| | Region | Typical AD | -0.33* | [-0.44 - -0.21] |
| | | Atypical AD | 0.25* | [0.13 - 0.37] |
| | Region × phenotype | | 1.84* | [1.58 - 2.11] |
| | Region | Typical AD | -0.39* | [-0.56 - -0.22] |
| | | Atypical AD | 1.46* | [1.25 - 1.66] |

Results of the linear mixed model for analyzed immunohistochemistry variables are shown. All variables were transformed: $\ln(\text{variable}+1)$. We tested if the distribution over the two regions was different between the two AD phenotypes, defined as the interaction effect: region × phenotype. When an interaction effect was found, the beta-coefficient is shown per phenotype. To correct for multiple testing, a p value $< .0045$ was considered significant ($p < .05/11$ outcome measurements) and indicated with *. AD Alzheimer's disease; CI confidence interval; # number.

Glial activation is increased in atypical AD

Staining for GFAP-positive astrocytes showed variably sized star-like GFAP-positive structures in all AD cases (Fig. 3A). Both phenotypes showed higher levels of immunoreactivity for GFAP in the temporal section compared to the parietal section. Atypical AD cases showed relatively more GFAP immunoreactivity in the parietal cortex compared to typical AD cases (Fig. 3C; Table 5). Iba1 immunostaining showed positivity in both the cell soma as well as the processes of the microglia, mostly in the form of ramified microglia (Fig. 3B). Both AD groups showed a similar temporal dominance for Iba1.

Activated microglia were stained using CD68 and HLA-DP/DQ/DR. Whereas CD68 positivity was mostly found in the soma of microglia, HLA-DP/DQ/DR showed a prominent staining in the processes of microglia (Fig. 4A and 4B). Both markers showed a different distribution over the two regions between the two AD phenotypes (Fig. 4C, D; Table 5). Atypical AD cases showed more immunoreactivity for CD68 and HLA-DP/DQ/DR in the parietal compared to the temporal section, which was in contrast to the typical AD cases. In addition, the levels of CD68 and HLA-DP/DQ/DR immunoreactivity were relatively high in the parietal section of atypical AD compared to the temporal section of typical AD.

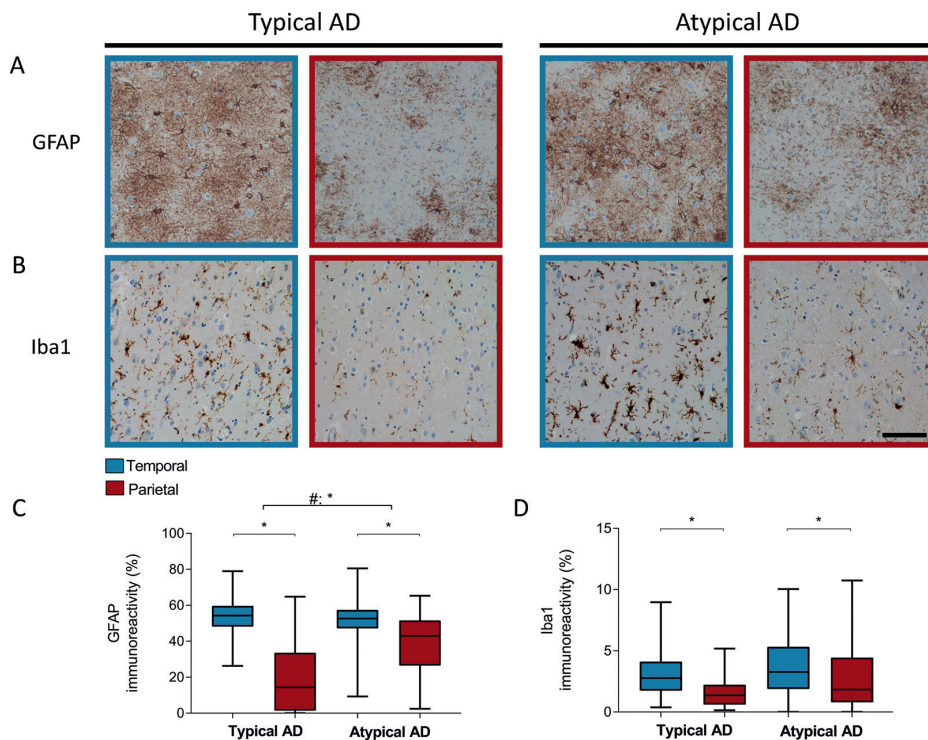


Fig. 3. GFAP and Iba1 immunoreactivity is temporal dominant in both AD phenotypes

A, B The temporal cortex (blue border) shows more GFAP and Iba1 immunoreactivity respectively than the parietal cortex (burgundy border) in typical and atypical AD. Bar represents 100 μ m. **C, D** Boxplots showing GFAP and Iba1 immunoreactive area (%), respectively, in the temporal and parietal section of both AD phenotypes. Atypical AD shows relatively more GFAP immunoreactivity in the parietal cortex than typical AD (Table 5). Iba1 distribution is not different between the two phenotypes. Data shown as median (bar), 1st and 3rd quartile (box boundaries), and min to max (error bars). AD Alzheimer's disease; GFAP glial fibrillary acidic protein * $p < .0045$.

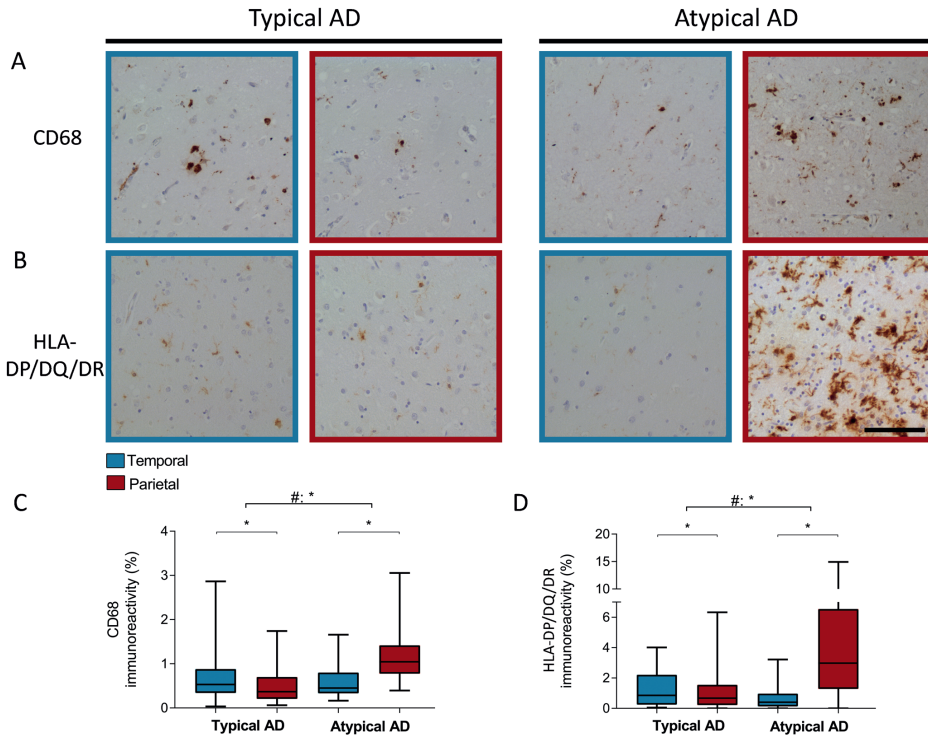


Fig. 4. CD68 and HLA-DP/DQ/DR immunoreactivity show a parietal dominant distribution in atypical AD

A, B In typical AD, the temporal section (blue border) shows more CD68 and HLA-DP/DQ/DR immunoreactivity than the parietal section (burgundy border). In contrast, atypical AD shows more CD68 and HLA-DP/DQ/DR immunoreactivity in the parietal than the temporal section. Note the relative difference in immunoreactivity in the parietal section of atypical AD compared to the temporal section in typical AD. Bar represents 100 μ m. **C, D** Boxplots showing CD68 and HLA-DP/DQ/DR immunoreactive area (%), respectively, in the temporal and parietal section of both AD phenotypes. Linear mixed model shows a different distribution over the two regions between phenotypes (#) (Table 5). AD Alzheimer's disease; * $p < .0045$.

Increased presence of complement proteins in atypical AD

To visualize different parts of the complement cascade, we stained for C1q, C3d, and C4b, representing the start of the cascade, as well as for C5b-9, defining the end-stage of the cascade and forming the membrane attack complex. C1q immunoreactivity was observed as a weak diffuse staining in the form of plaque-like structures, as punctuate staining of the neuropil, and sometimes in neurons (Fig. 5A). While the plaque-like structures were more often observed in the parietal section, the punctuate staining of the neuropil was more prominent in

the temporal section of both AD groups. No difference in C1q immunoreactivity was observed between regions or AD phenotypes (Fig. 5D; Table 5). Compared to C1q, staining for C3d and C4b showed an intense plaque-like staining, which had a morphology resembling that of compact and classic cored plaques (Fig. 5B and 5C). Levels of immunoreactivity for C3d and C4b in typical AD were higher in the temporal compared to the parietal cortex (Fig. 5E, F; Table 5). In contrast, atypical AD showed higher immunoreactivity levels for both markers in the parietal section compared to the temporal section. Analysis of C5b-9 exposed very low to no immunoreactivity in both regions of both phenotypes (data not shown). For this reason, no quantification or statistical analysis was performed for C5b-9. The few structures that were C5b-9 positive included parenchymal and meningeal vessels. The serum within these vessels also stained positive for C5b-9. Our data show a different distribution in temporal and parietal regions between both AD phenotypes for complement factors C3d and C4b. Both complement factors were mostly abundant in the parietal section of atypical AD.

Different plaque appearance in typical and atypical AD

Looking at the morphology of plaques stained by amyloid-beta and C4b, we observed a difference in appearance between the two AD phenotypes. Amyloid-beta and C4b immunoreactive plaques in the parietal section of atypical AD cases showed a more granular composition compared to deposits in the temporal section of this phenotype or compared to deposits in both regions of the typical AD cases (Fig. 6). The surface area positive for C4b of these coarse-grained plaques was larger ($>100 \mu\text{m}^2$) than that of typical plaques. Atypical AD cases had more of these C4b plaques in the parietal compared to the temporal cortex, which was contrary to typical AD cases (Fig. 6I; Table 5).

The coarse-grained plaques observed in the parietal cortex of atypical AD triple-stained for C4b, amyloid-beta, and thioflavin S (Fig. 7). This staining pattern was compared with that of classic cored plaques observed in typical AD. In cored plaques, C4b, amyloid-beta, and thioflavin S co-localized in the core of the plaque, while the corona only stained for amyloid-beta. Compared to cored plaques, coarse-grained plaques showed a fibrillar, less organized morphology with co-localization of C4b, amyloid-beta, and thioflavin S all over the plaque surface. Since an increased presence of activated microglia in atypical AD was observed, the localization of CD68 and HLA-DP/DQ/DR with cored and coarse-grained plaques was compared (Fig. 7). Like cored plaques, coarse-grained plaques were associated with clusters of CD68 and HLA-DP/DQ/DR positive microglia. In cored plaques, activated microglia were located between core and corona of

the plaque. In coarse-grained plaques, the localization of CD68 and HLA-DP/DQ/DR positive microglia was less structured and positive microglia appeared throughout the plaque. This data supports a morphological difference between cored and coarse-grained plaques, of which the latter occurs prominently in atypical AD (Fig. 6I).

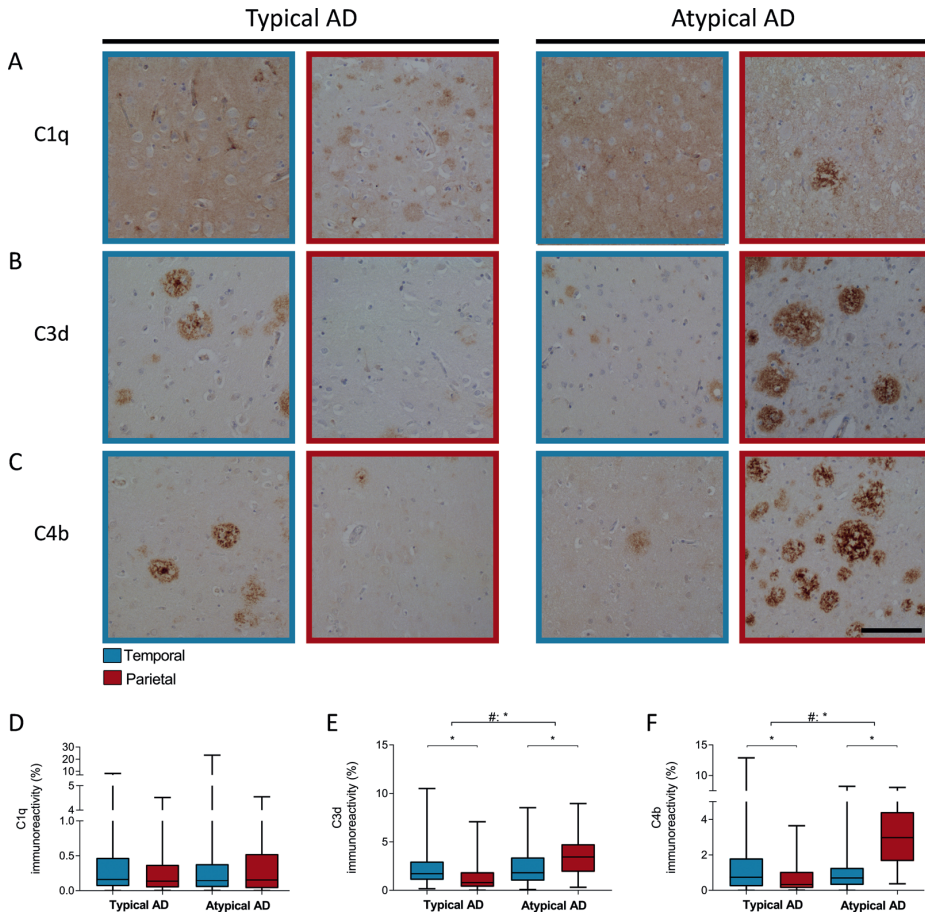


Fig. 5. Distribution of C3d and C4b differs between AD phenotypes
A In both typical and atypical AD, C1q deposition in the temporal cortex (blue border) is more diffuse than in the parietal cortex (burgundy border). **B, C** In typical AD, the temporal cortex shows more immunoreactivity for C3d and C4b than the parietal cortex. This distribution is inverted in atypical AD, showing more immunoreactivity for C3d and C4b in the parietal than temporal section. Bar represents 100 μ m. **D, E,** and **F** Boxplots of immunoreactive area (%) for C1q, C3d, and C4b, respectively, in the temporal and parietal section of both AD phenotypes. Linear mixed model shows a different distribution for C3d and C4b over the two regions between phenotypes (#) (Table 5). AD Alzheimer’s disease; * $p < .0045$.

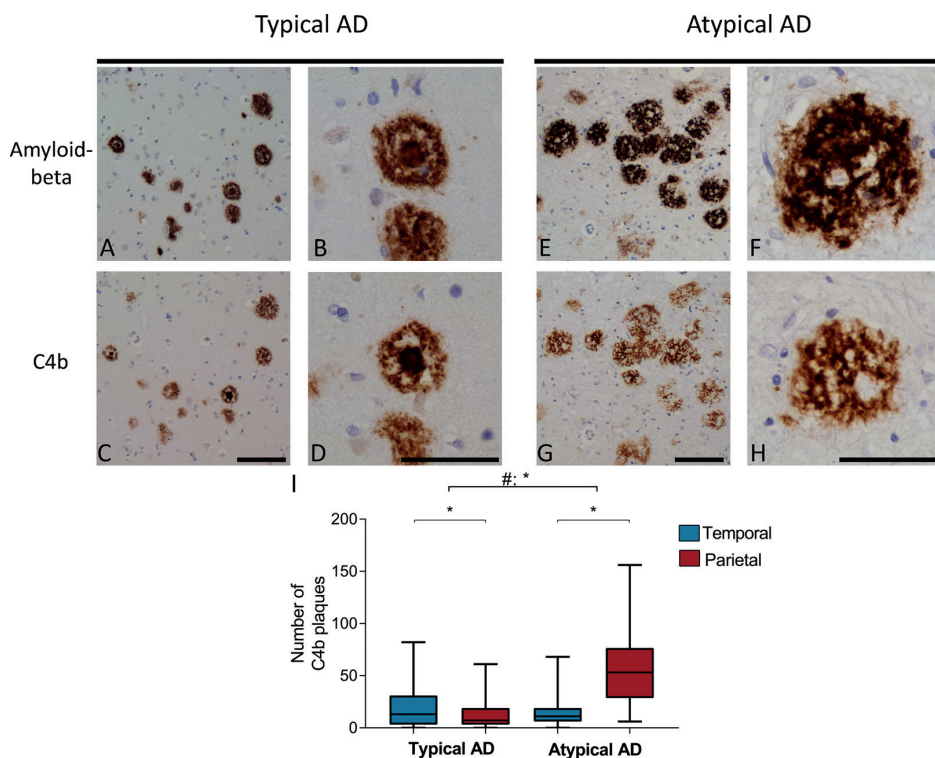


Fig. 6. Plaques in atypical AD show a different morphology compared to plaques in typical AD. **A-D** In typical AD cases, the morphology of amyloid-beta (**A** for overview, **B** for detail) and C4b (**C** for overview, **D** for detail) deposits come in the form of diffuse, dense, and classic cored plaques. **E-H** In atypical AD cases, amyloid-beta (**E** for overview, **F** for detail) and C4b (**G** for overview, **H** for detail) deposits show a distinct morphology, being coarse-grained and affecting a larger surface area ($>100\mu\text{m}^2$) compared to classic cored plaques. Pictures are taken in the region with highest number of amyloid-beta plaques, being temporal for typical AD and parietal for atypical AD (Fig. 2E). Bars represent 100 μm . **I** Boxplot of number of coarse-grained plaques quantified using C4b staining in the temporal and parietal cortex of typical and atypical AD. Linear mixed model shows a different distribution for coarse-grained plaques over the two regions between phenotypes (#) (Table 5). This distribution is parietally dominant in atypical AD. AD Alzheimer's disease; * $p < .0045$.

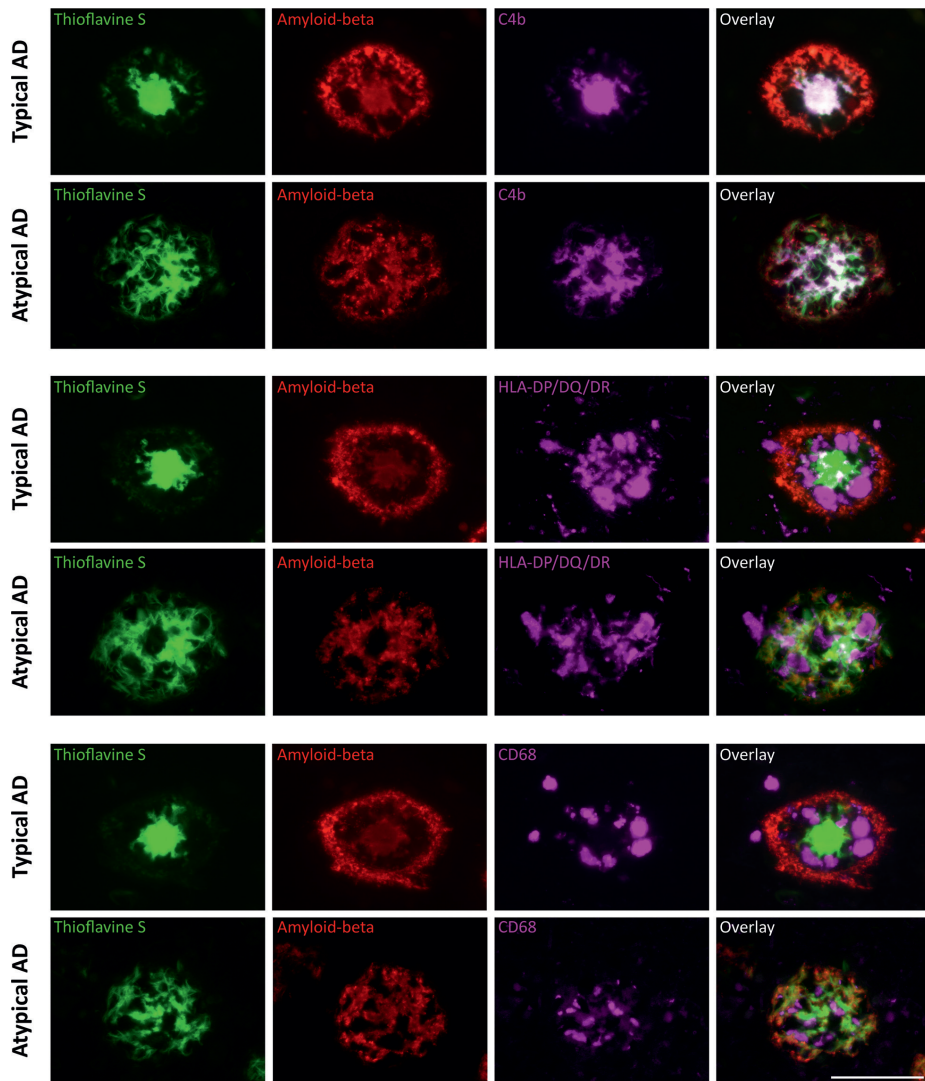


Fig. 7. Different plaque morphology in the parietal cortex of atypical AD

First row: in typical AD, classic cored plaques in the temporal cortex show an organized staining pattern with a corona showing merely amyloid-beta positivity versus a core positive for thioflavine S, amyloid-beta, and C4b. **Second row:** in atypical AD, fibrillar plaques in the parietal cortex show co-localization of thioflavine S, amyloid-beta, and C4b in the form of fibrils throughout the whole plaque. **Third row:** in typical AD, CD68-positive microglia are localized between core and corona of classic cored plaques. **Fourth row:** in atypical AD, CD68-positive microglia localization is less organized. **Fifth + sixth row:** this different distribution within plaques between the two phenotypes also holds for HLA-DP/DQ/DR-positive microglia. Bar is applicable to all images and represents 100 μm . AD Alzheimer's disease.

DISCUSSION

Atypical AD is characterized by a different distribution of NFTs when compared with typical AD. As expected, we observed that also the occurrence of pTau is differently distributed in typical and atypical AD. Here, we show for the first time that the distribution of both activated microglia and complement factors between the temporal and parietal lobe differentiates atypical from typical AD cases. In addition, atypical AD cases are characterized by the presence of plaques with an abnormal morphology, highlighted by an alternative localization of microglia and presence of complement proteins.

In this study, typical and atypical AD were defined according to the distribution of NFTs as well as their clinical presentation. In our cohort, atypical AD cases were younger and more often male than typical AD cases. This was also seen in an earlier study by Murray and colleagues [32], indicating that an atypical distribution of pathology seems to be more common in men and at a younger age. In line with this, another study showed that cases with showed higher mean levels of NFTs in the parietal lobe, when comparing EOAD to LOAD, irrespective of clinical presentation [8]. When taking symptomology into account, this parietal dominant tau distribution is especially common in the PCA variant of atypical AD [11]. Therefore, the current atypical AD cohort defined by parietal dominant NFTs represents only a subgroup of atypical AD. Results from this study do not necessarily apply for patients with a logopenic or behavioral phenotype, as tau pathology seems to be differently distributed in those cases [23, 35]. Besides neuropathological studies, also clinical studies report that an atypical clinical presentation is more common at a younger age [24]. Regarding differences in gender, an atypical presentation is not per se more common in men [24]. However, AD presenting at late onset is more common in women [40], explaining the relative high number of female subjects in typical AD cohorts.

We did not observe a different distribution of total amyloid-beta immunoreactivity between the two AD phenotypes. This is in line with other studies reporting that amyloid-beta distribution is not different between AD subtypes, [5, 8, 41, 42, 45]. However, when quantifying for number of dense amyloid-beta plaques, atypical AD cases showed a parietal dominant distribution compared to typical AD cases, which showed a temporal dominant distribution. This distinction in number of plaques was also reported by Hoff and colleagues who compared cases with PCA to typical AD cases using stereology [19]. These results indicate that although the distribution of overall amyloid-beta immunoreactivity is similar, the number of

dense amyloid-beta plaques may differ between AD phenotypes. In addition to the number of dense amyloid-beta plaques, structural differences in amyloid-beta plaques might be associated with the pathological and clinical differences between typical and atypical AD.

In the present study we observed a clear morphological difference between classic cored plaques in typical AD and dense plaques in atypical AD cases. Dense plaques in atypical AD cases have a coarse-grained structure, as observed with amyloid-beta immunostaining and thioflavin S staining. In addition, these coarse-grained plaques showed a strong immunoreactivity for complement. Multiple studies have reported complement proteins to be associated with amyloid-beta deposits [16, 47]. However, a difference in complement activation between AD subtypes has so far not been described. The increased presence of complement in coarse-grained plaques in atypical AD cases supports a difference in amyloid structure between typical and atypical AD. Most likely, the amyloid structure of fibrillar plaques favors a strong binding and activation of complement factors, which in turn could act as opsonins for phagocytosis carried out by microglia [27, 37, 46]. A structural variation in amyloid-beta fibrils in combination with a difference in binding of amyloid associated proteins may underlie the observed difference in the occurrence of neuroinflammation, pTau, and NFTs between typical and atypical AD. The relation between amyloid-beta, complement, and microglia is underlined by a study in APP transgenic mice deficient for C3 showing less cognitive problems and more amyloid-beta plaques compared to APP mice not deficient for C3 [38]. The amyloid-beta plaques in the C3 knockout mice showed less microglial co-localization. Together, these findings suggest that structural differences in amyloid deposits in atypical AD may directly be related to complement and microglial activation.

The distribution of NFT and pTau pathology is clearly associated with the presence of activated microglia in AD variants. Recent animal studies have shown that microglia are capable of both internalizing [26] and excreting pTau [4, 9], suggesting that microglia contribute to the spreading of the pathology. Indeed, when mice are depleted for microglia, spreading of tau pathology is significantly reduced [4, 28]. In addition, activated microglia could also contribute or induce tau hyperphosphorylation in neurons [7]. These studies indicate that microglial activation drives the spreading of pathology and stimulates neurofibrillary degeneration. Interestingly, recent evidence from a pathological study suggests that activation of microglia may precede tau pathology in chronic traumatic

encephalopathy [11], which implicates that tau pathology may be a consequence, rather than a cause for microglial activation.

The aforementioned demographical differences in age and sex may influence the neuroinflammatory response. Former studies have shown various results on the correlation between sex, age, and microglial activation in both humans and animal models. Schwarz et al showed that during early development, male rats have more microglia within the parietal cortex compared to female rats. However, during juvenile and early adulthood this balance switches, indicating that sex hormones influence microglial colonization at different timepoints in rats [36]. In human studies, contradictory results are published for the effect of age. In healthy controls, aging is correlated with a more primed microglial state. Nevertheless, in diseased cases this was shown to be different, in which increasing age is associated with a diminished neuroinflammatory response [21]. These studies suggest that sex and age influence microglia activation. However, whether differences in sex and age contribute to differences in regional distribution, as observed in the current study between AD subtypes, remains elusive.

Conclusions

Results of this study are in line with the assumption that the fibrillar structure and protein composition of different plaques may be relevant for the difference in regional vulnerability among AD phenotypes. In addition, our results support a role for activated microglia and complement factors in the atypical spreading of pathology in AD subtypes. In this study, we focussed at two brain regions in a subset of atypical AD. It would be interesting to expand this study on the role of neuroinflammation to various brain regions in a larger atypical AD cohort. More clinicopathological studies of AD variants (e.g., logopenic and behavioral frontal) are needed to better understand the relation between amyloid-beta, pTau, and related pathological mechanisms. Future research should focus on how variable disease mechanisms underlie the regional susceptibility in different brain regions leading to different clinical AD subtypes.

ACKNOWLEDGEMENTS

We would like to thank all brain donors and their caregivers for brain donation, the Netherlands Brain Bank and Michiel Kooreman for logistics and help in selecting brain tissue samples, Martijn Heijmans and Wiesje van der Flier for advice on statistical analysis, Robert Veerhuis for help and advice on complement immunostainings, and Yolande Pijnenburg for clinical assessment. This study was funded by ZonMw grant number #733050104. ZonMw had no role in the design of the study, collection, analysis, or interpretation of the data, or writing of the manuscript.

LIST OF ABBREVIATIONS

| | |
|------|---|
| AD | Alzheimer's disease |
| DAB | 3,3'-diaminobenzidine tetrahydrochloride |
| EOAD | early-onset Alzheimer's disease (<65 years) |
| FFPE | formalin-fixed paraffin-embedded |
| GFAP | glial fibrillary acidic protein |
| IQR | inter-quartile range |
| LOAD | late-onset Alzheimer's disease (≥65 year) |
| NBB | Netherlands Brain Bank |
| NFT | neurofibrillary tangles |
| PBS | phosphate buffer saline |
| PCA | posterior cortical atrophy |
| PMI | post mortem interval |
| pTau | phosphorylated tau |
| ROI | region of interest |

REFERENCES

1. Akiyama H, Barger S, Barnum S, Bradt B, Bauer J, Cole GM, Cooper NR, Eikelenboom P, Emmerling M, Fiebich BL, Finch CE, Frautschy S, Griffin WS, Hampel H, Hull M, Landreth G, Lue L, Mrak R, Mackenzie IR, McGeer PL, O'Banion MK, Pachter J, Pasinetti G, Plata-Salaman C, Rogers J, Rydel R, Shen Y, Streit W, Strommeyer R, Tooyoma I, Van Muiswinkel FL, Veerhuis R, Walker D, Webster S, Wegrzyniak B, Wenk G, Wyss-Coray T, Wyss-Coray T (2000) Inflammation and Alzheimer's disease. *Neurobiol Aging* 21:383–421
2. Arends YM, Duyckaerts C, Rozemuller JM, Eikelenboom P, Hauw JJ (2000) Microglia, amyloid and dementia in alzheimer disease. A correlative study. *Neurobiol Aging* 21:39–47. doi: 10.1016/s0197-4580(00)00094-4.
3. Arendt T, Morawski M, Gärtner U, Fröhlich N, Schulze F, Wohmann N, Jäger C, Eisenlöffel C, Gertz H-J, Mueller W, Brauer K (2016) Inhomogeneous distribution of Alzheimer pathology along the isocortical relief. Are cortical convolutions an Achilles heel of evolution? *Brain Pathol* 5:603–611. doi: 10.1111/bpa.12442
4. Asai H, Ikezu S, Tsunoda S, Medalla M, Luebke J, Haydar T, Wolozin B, Butovsky O, Kügler S, Ikezu T (2015) Depletion of microglia and inhibition of exosome synthesis halt tau propagation. *Nat Neurosci* 18:1584–93. doi: 10.1038/nn.4132
5. Beaufils E, Ribeiro MJ, Vierron E, Vercouillie J, Dufour-Rainfray D, Cottier J-P, Camus V, Mondon K, Guilloteau D, Hommet C (2014) The Pattern of Brain Amyloid Load in Posterior Cortical Atrophy Using (18)F-AV45: Is Amyloid the Principal Actor in the Disease? *Dement Geriatr Cogn Dis Extra* 4:431–41. doi: 10.1159/000363761
6. Bertram L, Lange C, Mullin K, Parkinson M, Hsiao M, Hogan MF, Schjeide BMM, Hooli B, Divito J, Ionita I, Jiang H, Laird N, Moscarillo T, Ohlsen KL, Elliott K, Wang X, Hu-Lince D, Ryder M, Murphy A, Wagner SL, Blacker D, Becker KD, Tanzi RE (2008) Genome-wide association analysis reveals putative Alzheimer's disease susceptibility loci in addition to APOE. *Am J Hum Genet* 83:623–32. doi: 10.1016/j.ajhg.2008.10.008
7. Bhaskar K, Konerth M, Kokiko-Cochran ON, Cardona A, Ransohoff RM, Lamb BT (2010) Regulation of tau pathology by the microglial fractalkine receptor. *Neuron* 68:19–31. doi: 10.1016/j.neuron.2010.08.023
8. Bigio EH, Hynan LS, Sontag E, Satumtira S, White CL (2002) Synapse loss is greater in presenile than senile onset Alzheimer disease: implications for the cognitive reserve hypothesis. *Neuropathol Appl Neurobiol* 28:218–227. doi: 10.1046/j.1365-2990.2002.00385.x
9. Bolós M, Llorens-Martín M, Jurado-Arjona J, Hernández F, Rábano A, Avila J (2015) Direct Evidence of Internalization of Tau by Microglia In Vitro and In Vivo. *J Alzheimer's Dis* 50:77–87. doi: 10.3233/JAD-150704
10. Braak H, Braak E (1991) Neuropathological staging of Alzheimer-related changes. *Acta Neuropathol* 82:239–59. doi: 10.1007/BF00308809

11. Cherry JD, Tripodis Y, Alvarez VE, Huber B, Kiernan PT, Daneshvar DH, Mez J, Montenegro PH, Solomon TM, Alosco ML, Stern RA, McKee AC, Stein TD (2016) Microglial neuroinflammation contributes to tau accumulation in chronic traumatic encephalopathy. *Acta Neuropathol Commun* 4:112. doi: 10.1186/s40478-016-0382-8
12. Crutch SJ, Lehmann M, Schott JM, Rabinovici GD, Rossor MN, Fox NC (2012) Posterior cortical atrophy. *Lancet Neurol* 11:170–8. doi: 10.1016/S1474-4422(11)70289-7
13. Dickson DW, Farlo J, Davies P, Crystal H, Fuld P, Yen SH (1988) Alzheimer's disease. A double-labeling immunohistochemical study of senile plaques. *Am J Pathol* 132:86–101
14. Dubois B, Feldman HH, Jacova C, Hampel H, Molinuevo JL, Blennow K, DeKosky ST, Gauthier S, Selkoe D, Bateman R, Cappa S, Crutch S, Engelborghs S, Frisoni GB, Fox NC, Galasko D, Habert M-O, Jicha GA, Nordberg A, Pasquier F, Rabinovici G, Robert P, Rowe C, Salloway S, Sarazin M, Epelbaum S, de Souza LC, Vellas B, Visser PJ, Schneider L, Stern Y, Scheltens P, Cummings JL (2014) Advancing research diagnostic criteria for Alzheimer's disease: the IWG-2 criteria. *Lancet Neurol* 13:614–629. doi: 10.1016/S1474-4422(14)70090-0
15. Duyckaerts C, Delatour B, Potier M-C (2009) Classification and basic pathology of Alzheimer disease. *Acta Neuropathol* 118:5–36. doi: 10.1007/s00401-009-0532-1
16. Eikelenboom P, Stam FC (1982) Immunoglobulins and Complement Factors in Senile Plaques An Immunoperoxidase Study. *Acta Neuropathol* 57:239–242
17. Galton CJ, Patterson K, Xuereb JH, Hodges JR (2000) Atypical and typical presentations of Alzheimer's disease: a clinical, neuropsychological, neuroimaging and pathological study of 13 cases. *Brain* 123:484–98
18. Gorno-Tempini ML, Hillis AE, Weintraub S, Kertesz A, Mendez M, Cappa SF, Ogar JM, Rohrer JD, Black S, Boeve BF, Manes F, Dronkers NF, Vandenberghe R, Rascovsky K, Patterson K, Miller BL, Knopman DS, Hodges JR, Mesulam MM, Grossman M (2011) Classification of primary progressive aphasia and its variants. *Neurology* 76:1006–14. doi: 10.1212/WNL.0b013e31821103e6
19. Hof PR, Vogt BA, Bouras C, Morrison JH (1997) Atypical form of Alzheimer's disease with prominent posterior cortical atrophy: A review of lesion distribution and circuit disconnection in cortical visual pathways. *Vision Res* 37:3609–3625. doi: 10.1016/S0042-6989(96)00240-4
20. Hoogendijk WJ, Sommer IE, Pool CW, Kamphorst W, Hofman MA, Eikelenboom P, Swaab DF (1999) Lack of association between depression and loss of neurons in the locus coeruleus in Alzheimer disease. *Arch Gen Psychiatry* 56:45–51
21. Hoozemans JJ, Rozemuller AJ, van Haastert ES, Eikelenboom P, van Gool WA (2011) Neuroinflammation in Alzheimer's disease wanes with age. *J Neuroinflammation* 8:171. doi: 10.1186/1742-2094-8-171
22. Hu X, Pickering E, Liu YC, Hall S, Fournier H, Katz E, DeChairo B, John S, Van Eerdewegh P, Soares H, Alzheimer's Disease Neuroimaging Initiative the ADN (2011) Meta-analysis for genome-wide association study identifies multiple variants at the BIN1 locus associated with late-onset Alzheimer's disease. *PLoS One* 6:e16616. doi: 10.1371/journal.pone.0016616

23. Josephs KA, Dickson DW, Murray ME, Senjem ML, Parisi JE, Petersen RC, Jack CR, Whitwell JL, Whitwell JL (2013) Quantitative neurofibrillary tangle density and brain volumetric MRI analyses in Alzheimer's disease presenting as logopenic progressive aphasia. *Brain Lang* 127:127-34. doi: 10.1016/j.bandl.2013.02.003
24. Koedam ELGE, Lauffer V, van der Vlies AE, van der Flier WM, Scheltens P, Pijnenburg YAL (2010) Early-versus late-onset Alzheimer's disease: more than age alone. *J Alzheimers Dis* 19:1401-8. doi: 10.3233/JAD-2010-1337
25. Li Y, Liu L, Barger SW, Griffin WST (2003) Interleukin-1 mediates pathological effects of microglia on tau phosphorylation and on synaptophysin synthesis in cortical neurons through a p38-MAPK pathway. *J Neurosci* 23:1605-11
26. Luo W, Liu W, Hu X, Hanna M, Caravaca A, Paul SM (2015) Microglial internalization and degradation of pathological tau is enhanced by an anti-tau monoclonal antibody. *Sci Rep* 5:11161. doi: 10.1038/srep11161
27. Maier M, Peng Y, Jiang L, Seabrook TJ, Carroll MC, Lemere CA (2008) Complement C3 deficiency leads to accelerated amyloid beta plaque deposition and neurodegeneration and modulation of the microglia/macrophage phenotype in amyloid precursor protein transgenic mice. *J Neurosci* 28:6333-41. doi: 10.1523/JNEUROSCI.0829-08.2008
28. Maphis N, Xu G, Kokiko-Cochran ON, Jiang S, Cardona A, Ransohoff RM, Lamb BT, Bhaskar K (2015) Reactive microglia drive tau pathology and contribute to the spreading of pathological tau in the brain. *Brain* 138:1738-55. doi: 10.1093/brain/awv081
29. McGeer PL, Akiyama H, Itagaki S, McGeer EG (1989) Activation of the classical complement pathway in brain tissue of Alzheimer patients. *Neurosci Lett* 107:341-60
30. McKhann GM, Knopman DS, Chertkow H, Hyman BT, Jack CR, Kawas CH, Klunk WE, Koroshetz WJ, Manly JJ, Mayeux R, Mohs RC, Morris JC, Rossor MN, Scheltens P, Carrillo MC, Thies B, Weintraub S, Phelps CH, Phelps CH (2011) The diagnosis of dementia due to Alzheimer's disease: recommendations from the National Institute on Aging-Alzheimer's Association workgroups on diagnostic guidelines for Alzheimer's disease. *Alzheimers Dement* 7:263-9. doi: 10.1016/j.jalz.2011.03.005
31. Mirra SS, Heyman A, McKeel D, Sumi SM, Crain BJ, Brownlee LM, Vogel FS, Hughes JP, van Belle G, Berg L (1991) The Consortium to Establish a Registry for Alzheimer's Disease (CERAD). Part II. Standardization of the neuropathologic assessment of Alzheimer's disease. *Neurology* 41:479-86. doi: 10.1097/00005072-199405000-00012
32. Murray ME, Graff-Radford NR, Ross OA, Petersen RC, Duara R, Dickson DW (2011) Neuropathologically defined subtypes of Alzheimer's disease with distinct clinical characteristics: a retrospective study. *Lancet Neurol* 10:785-796. doi: 10.1016/S1474-4422(11)70156-9
33. Naj AC, Jun G, Beecham GW, Wang L-S, Vardarajan BN, Buross J, Gallins PJ, Buxbaum JD, Jarvik GP, Crane PK, Larson EB, Bird TD, Boeve BF, Graff-Radford NR, De Jager PL, Evans D, Schneider JA, Carrasquillo MM, Ertekin-Taner N, Younkin SG, Cruchaga C, Kauwe JSK, Nowotny P, Kramer P, Hardy J, Huentelman MJ, Myers AJ,

- Barmada MM, Demirci FY, Baldwin CT, Green RC, Rogaeva E, St George-Hyslop P, Arnold SE, Barber R, Beach T, Bigio EH, Bowen JD, Boxer A, Burke JR, Cairns NJ, Carlson CS, Carney RM, Carroll SL, Chui HC, Clark DG, Corneveaux J, Cotman CW, Cummings JL, DeCarli C, DeKosky ST, Diaz-Arrastia R, Dick M, Dickson DW, Ellis WG, Faber KM, Fallon KB, Farlow MR, Ferris S, Frosch MP, Galasko DR, Ganguli M, Gearing M, Geschwind DH, Ghetti B, Gilbert JR, Gilman S, Giordani B, Glass JD, Growdon JH, Hamilton RL, Harrell LE, Head E, Honig LS, Hulette CM, Hyman BT, Jicha GA, Jin L-W, Johnson N, Karlawish J, Karydas A, Kaye JA, Kim R, Koo EH, Kowall NW, Lah JJ, Levey AI, Lieberman AP, Lopez OL, Mack WJ, Marson DC, Martiniuk F, Mash DC, Masliah E, McCormick WC, McCurry SM, McDavid AN, McKee AC, Mesulam M, Miller BL, Miller CA, Miller JW, Parisi JE, Perl DP, Peskind E, Petersen RC, Poon WW, Quinn JF, Rajbhandary RA, Raskind M, Reisberg B, Ringman JM, Roberson ED, Rosenberg RN, Sano M, Schneider LS, Seeley W, Shelanski ML, Slifer MA, Smith CD, Sonnen JA, Spina S, Stern RA, Tanzi RE, Trojanowski JQ, Troncoso JC, Van Deerlin VM, Vinters H V, Vonsattel JP, Weintraub S, Welsh-Bohmer KA, Williamson J, Woltjer RL, Cantwell LB, Dombroski BA, Beekly D, Lunetta KL, Martin ER, Kamboh MI, Saykin AJ, Reiman EM, Bennett DA, Morris JC, Montine TJ, Goate AM, Blacker D, Tsuang DW, Hakonarson H, Kukull WA, Foroud TM, Haines JL, Mayeux R, Pericak-Vance MA, Farrer LA, Schellenberg GD (2011) Common variants at MS4A4/MS4A6E, CD2AP, CD33 and EPHA1 are associated with late-onset Alzheimer's disease. *Nat Genet* 43:436–41. doi: 10.1038/ng.801
34. Ossenkuppele R, Cohn-Sheehy BI, La Joie R, Vogel JW, Möller C, Lehmann M, van Berckel BNM, Seeley WW, Pijnenburg YA, Gorno-Tempini ML, Kramer JH, Barkhof F, Rosen HJ, van der Flier WM, Jagust WJ, Miller BL, Scheltens P, Rabinovici GD (2015) Atrophy patterns in early clinical stages across distinct phenotypes of Alzheimer's disease. *Hum Brain Mapp* 36:4421–37. doi: 10.1002/hbm.22927
35. Ossenkuppele R, Schonhaut DR, Schöll M, Lockhart SN, Ayakta N, Baker SL, O'Neil JP, Janabi M, Lazaris A, Cantwell A, Vogel J, Santos M, Miller ZA, Bettcher BM, Vossel KA, Kramer JH, Gorno-Tempini ML, Miller BL, Jagust WJ, Rabinovici GD (2016) Tau PET patterns mirror clinical and neuroanatomical variability in Alzheimer's disease. *Brain* 139:1551–1567. doi: 10.1093/brain/aww027
36. Schwarz JM, Sholar PW, Bilbo SD (2012) Sex differences in microglial colonization of the developing rat brain. *J Neurochem* 120:948–63. doi: 10.1111/j.1471-4159.2011.07630.x
37. Shen Y, Yang L, Li R (2013) What does complement do in Alzheimer's disease? Old molecules with new insights. *Transl Neurodegener* 2:21. doi: 10.1186/2047-9158-2-21
38. Shi Q, Chowdhury S, Ma R, Le KX, Hong S, Caldarone BJ, Stevens B, Lemere CA (2017) Complement C3 deficiency protects against neurodegeneration in aged plaque-rich APP/PS1 mice. *Sci Transl Med* 9:eaa6295. doi: 10.1126/scitranslmed.aaf6295

39. Sims R, van der Lee SJ, Naj AC, Bellenguez C, Badarinarayan N, Jakobsdottir J, Kunkle BW, Boland A, Raybould R, Bis JC, Martin ER, Grenier-Boley B, Heilmann-Heimbach S, Chouraki V, Kuzma AB, Slegers K, Vronskaya M, Ruiz A, Graham RR, Olaso R, Hoffmann P, Grove ML, Vardarajan BN, Hiltunen M, Nöthen MM, White CC, Hamilton-Nelson KL, Epelbaum J, Maier W, Choi S-H, Beecham GW, Dulary C, Herms S, Smith A V, Funk CC, Derbois C, Forstner AJ, Ahmad S, Li H, Bacq D, Harold D, Satizabal CL, Valladares O, Squassina A, Thomas R, Brody JA, Qu L, Sánchez-Juan P, Morgan T, Wolters FJ, Zhao Y, Garcia FS, Denning N, Fornage M, Malamon J, Naranjo MCD, Majounie E, Mosley TH, Dombroski B, Wallon D, Lupton MK, Dupuis J, Whitehead P, Fratiglioni L, Medway C, Jian X, Mukherjee S, Keller L, Brown K, Lin H, Cantwell LB, Panza F, McGuinness B, Moreno-Grau S, Burgess JD, Solfrizzi V, Proitsi P, Adams HH, Allen M, Seripa D, Pastor P, Cupples LA, Price ND, Hannequin D, Frank-García A, Levy D, Chakrabarty P, Caffarra P, Giegling I, Beiser AS, Giedraitis V, Hampel H, Garcia ME, Wang X, Lannfelt L, Mecocci P, Eiriksdottir G, Crane PK, Pasquier F, Boccardi V, Henández I, Barber RC, Scherer M, Tarraga L, Adams PM, Leber M, Chen Y, Albert MS, Riedel-Heller S, Emilsson V, Beekly D, Braae A, Schmidt R, Blacker D, Masullo C, Schmidt H, Doody RS, Spalletta G, Jr WTL, Fairchild TJ, Bossù P, Lopez OL, Frosch MP, Sacchinelli E, Ghetti B, Yang Q, Huebinger RM, Jessen F, Li S, Kamboh MI, Morris J, Sotolongo-Grau O, Katz MJ, Corcoran C, Dunstan M, Braddel A, Thomas C, Meggy A, Marshall R, Gerrish A, Chapman J, Aguilar M, Taylor S, Hill M, Fairén MD, Hodges A, Vellas B, Soininen H, Kloszewska I, Daniilidou M, Uphill J, Patel Y, Hughes JT, Lord J, Turton J, Hartmann AM, Cecchetti R, Fenoglio C, Serpente M, Arcaro M, Caltagirone C, Orfei MD, Ciarabella A, Pichler S, Mayhaus M, Gu W, Lleó A, Fortea J, Blesa R, Barber IS, Brookes K, Cupidi C, Maletta RG, Carrell D, Sorbi S, Moebus S, Urbano M, Pilotto A, Kornhuber J, Bosco P, Todd S, Craig D, Johnston J, Gill M, Lawlor B, Lynch A, Fox NC, Hardy J, Albin RL, Apostolova LG, Arnold SE, Asthana S, Atwood CS, Baldwin CT, Barnes LL, Barral S, Beach TG, Becker JT, Bigio EH, Bird TD, Boeve BF, Bowen JD, Boxer A, Burke JR, Burns JM, Buxbaum JD, Cairns NJ, Cao C, Carlson CS, Carlsson CM, Carney RM, Carrasquillo MM, Carroll SL, Diaz CC, Chui HC, Clark DG, Cribbs DH, Crocco EA, DeCarli C, Dick M, Duara R, Evans DA, Faber KM, Fallon KB, Fardo DW, Farlow MR, Ferris S, Foroud TM, Galasko DR, Gearing M, Geschwind DH, Gilbert JR, Graff-Radford NR, Green RC, Growdon JH, Hamilton RL, Harrell LE, Honig LS, Huentelman MJ, Hulette CM, Hyman BT, Jarvik GP, Abner E, Jin L-W, Jun G, Karydas A, Kaye JA, Kim R, Kowall NW, Kramer JH, LaFerla FM, Lah JJ, Leverenz JB, Levey AI, Li G, Lieberman AP, Lunetta KL, Lyketsos CG, Marson DC, Martiniuk F, Mash DC, Masliah E, McCormick WC, McCurry SM, McDavid AN, McKee AC, Mesulam M, Miller BL, Miller CA, Miller JW, Morris JC, Murrell JR, Myers AJ, O'Bryant S, Olichney JM, Pankratz VS, Parisi JE, Paulson HL, Perry W, Peskind E, Pierce A, Poon WW, Potter H, Quinn JF, Raj A, Raskind M, Reisberg B, Reitz C, Ringman JM, Roberson ED, Rogaeve E, Rosen HJ, Rosenberg RN,

- Sager MA, Saykin AJ, Schneider JA, Schneider LS, Seeley WW, Smith AG, Sonnen JA, Spina S, Stern RA, Swerdlow RH, Tanzi RE, Thornton-Wells TA, Trojanowski JQ, Troncoso JC, Van Deerlin VM, Van Eldik LJ, Vinters H V, Vonsattel JP, Weintraub S, Welsh-Bohmer KA, Wilhelmsen KC, Williamson J, Wingo TS, Woltjer RL, Wright CB, Yu C-E, Yu L, Garzia F, Golamaully F, Septier G, Engelborghs S, Vandenberghe R, De Deyn PP, Fernandez CM, Benito YA, Thonberg H, Forsell C, Lilius L, Kinhult-Ståhlbom A, Kilander L, Brundin R, Concari L, Helisalmi S, Koivisto AM, Haapasalo A, Dermecourt V, Fievet N, Hanon O, Dufouil C, Brice A, Ritchie K, Dubois B, Himali JJ, Keene CD, Tschanz J, Fitzpatrick AL, Kukull WA, Norton M, Aspelund T, Larson EB, Munger R, Rotter JI, Lipton RB, Bullido MJ, Hofman A, Montine TJ, Coto E, Boerwinkle E, Petersen RC, Alvarez V, Rivadeneira F, Reiman EM, Gallo M, O'Donnell CJ, Reisch JS, Bruni AC, Royall DR, Dichgans M, Sano M, Galimberti D, St George-Hyslop P, Scarpini E, Tsuang DW, Mancuso M, Bonuccelli U, Winslow AR, Daniele A, Wu C-K, Peters O, Nacmias B, Riemenschneider M, Heun R, Brayne C, Rubinsztein DC, Bras J, Guerreiro R, Al-Chalabi A, Shaw CE, Collinge J, Mann D, Tsolaki M, Clarimón J, Sussams R, Lovestone S, O'Donovan MC, Owen MJ, Behrens TW, Mead S, Goate AM, Uitterlinden AG, Holmes C, Cruchaga C, Ingelsson M, Bennett DA, Powell J, Golde TE, Graff C, De Jager PL, Morgan K, Ertekin-Taner N, Combarros O, Psaty BM, Passmore P, Younkin SG, Berr C, Gudnason V, Rujescu D, Dickson DW, Dartigues J-F, DeStefano AL, Ortega-Cubero S, Hakonarson H, Champion D, Boada M, Kauwe JK, Farrer LA, Van Broeckhoven C, Ikram MA, Jones L, Haines JL, Tzourio C, Launer LJ, Escott-Price V, Mayeux R, Deleuze J-F, Amin N, Holmans PA, Pericak-Vance MA, Amouyel P, van Duijn CM, Ramirez A, Wang L-S, Lambert J-C, Seshadri S, Williams J, Schellenberg GD, Williams J, Schellenberg GD (2017) Rare coding variants in *PLCG2*, *ABI3*, and *TREM2* implicate microglial-mediated innate immunity in Alzheimer's disease. *Nat Genet* 49:1373–1384. doi: 10.1038/ng.3916
40. Snyder HM, Asthana S, Bain L, Brinton R, Craft S, Dubal DB, Espeland MA, Gatz M, Mielke MM, Raber J, Rapp PR, Yaffe K, Carrillo MC (2016) Sex biology contributions to vulnerability to Alzheimer's disease: A think tank convened by the Women's Alzheimer's Research Initiative. *Alzheimer's Dement* 12:1186–1196. doi: 10.1016/j.jalz.2016.08.004
41. de Souza LC, Corlier F, Habert M-O, Uspenskaya O, Maroy R, Lamari F, Chupin M, Lehericy S, Colliot O, Hahn-Barma V, Samri D, Dubois B, Bottlaender M, Sarazin M (2011) Similar amyloid- burden in posterior cortical atrophy and Alzheimer's disease. *Brain* 134:2036–2043. doi: 10.1093/brain/awr130
42. Tang-Wai DF, Graff-Radford NR, Boeve BF, Dickson DW, Parisi JE, Crook R, Caselli RJ, Knopman DS, Petersen RC (2004) Clinical, genetic, and neuropathologic characteristics of posterior cortical atrophy. *Neurology* 63:1168–74
43. Thal DR, Rüb U, Orantes M, Braak H (2002) Phases of Ab-deposition in the human brain and its relevance for the development of AD. *Neurology* 58:1791–800. doi: 10.1212/wnl.58.12.1791

44. Walker L, McAleese KE, Johnson M, Khundakar AA, Erskine D, Thomas AJ, McKeith IG, Attems J (2017) Quantitative neuropathology: an update on automated methodologies and implications for large scale cohorts. *J Neural Transm* 124:671–683. doi: 10.1007/s00702-017-1702-2
45. Wang X-D, Lu H, Shi Z, Cai L, Liu S, Liu S, Han T, Wang Y, Zhou Y, Wang X, Gao S, Ji Y (2015) A Pilot Study on Clinical and Neuroimaging Characteristics of Chinese Posterior Cortical Atrophy: Comparison with Typical Alzheimer’s Disease. *PLoS One* 10:e0134956. doi: 10.1371/journal.pone.0134956
46. Wyss-Coray T, Yan F, Lin AH-T, Lambris JD, Alexander JJ, Quigg RJ, Masliah E (2002) Prominent neurodegeneration and increased plaque formation in complement-inhibited Alzheimer’s mice. *Proc Natl Acad Sci U S A* 99:10837–42. doi: 10.1073/pnas.162350199
47. Zanjani H, Finch CE, Kemper C, Atkinson J, McKeel D, Morris JC, Price JL (2005) Complement activation in very early Alzheimer disease. *Alzheimer Dis Assoc Disord* 19:55–66. doi: 10.1097/01.wad.0000165506.60370.94.

Chapter 3

**A distinct distribution of
neuroinflammation, indicating a
specific role for reactive astrocytes in
clinical atypical Alzheimer's disease**

Baayla DC Boon, Irene Frigerio, Danae de Gooijer, Tjado HJ Morrema,
John GJM Bol, Martijn Heymans, Wilma DJ van de berg, Annemieke JM
Rozemuller, Laura E Jonkman, Femke H Bouwman, Jeroen JM Hoozemans

In preparation

ABSTRACT

Background: Besides amyloid-beta ($A\beta$) plaques and hyperphosphorylated tau (pTau) neurofibrillary tangles (NFT), neuroinflammation due to the innate immune system plays an essential role in Alzheimer's disease (AD). Activated microglia and reactive astrocytes are related to both plaques and NFTs. Research shows that in clinical atypical subtypes of AD, the distribution of NFTs, in contrast to the distribution of $A\beta$ plaques, is closely associated with symptomatology. It's unclear, however, how neuroinflammation is distributed in atypical AD.

Methods: In this immunohistochemistry study, we investigated, using immunohistochemistry and image analysis, the distribution and the mutual associations of pTau (AT8), $A\beta$ (4G8), activated microglia using CD68 (KP-1) and MHC-II (CR3/43), and reactive astrocytes using GFAP over 12 brain regions including both limbic and neocortical areas, in a cohort of typical AD ($n = 10$), behavioral/dysexecutive AD ($n = 6$), and posterior cortical atrophy (PCA) ($n = 3$), compared to non-neurological controls ($n = 10$).

Results: A hippocampal-dominant pTau distribution was seen in both typical AD and the behavioural/dysexecutive variant, with increased cortical pTau levels in the latter. In PCA cases, a hippocampal-sparing pTau distribution was observed. For all AD subtypes, $A\beta$ was most pronounced in the neocortex compared to the hippocampus. CD68 and MHC-II showed increased immunoreactivity in the middle frontal gyrus of the behavioural/dysexecutive cases. In this region, MHC-II positively correlated with pTau ($r = 0.62$) in the behavioural/dysexecutive group but not in the other AD subtypes. In PCA cases, GFAP was mainly pronounced in both the inferior and superior parietal cortex and positively correlated with both pTau ($r = 0.54$) and $A\beta$ ($r = 0.76$) in the superior parietal cortex and only with $A\beta$ in the inferior parietal cortex ($r = 0.96$).

Conclusion: This study shows that the involvement of the most prominent players of the inflammatory response, i.e., astrocytes and microglia, differs per clinical AD subtype. Behavioural/dysexecutive AD shows prominent involvement of microglia activation in the frontal cortex, while PCA is associated with strong astroglial involvement in the parietal cortex. Although all AD patients have plaques and NFTs in their brains, the associated neuroinflammatory cells may very well vary and may partly explain the heterogeneity in AD pathology.

INTRODUCTION

Alzheimer's disease (AD) usually presents with predominantly amnesic problems. However, approximately 30% of cases with an early disease onset of AD (EOAD) present with an atypical clinical syndrome [18]. These atypical presentations may vary widely in clinical presentation and can include either more prominent visuospatial problems in case of posterior cortical atrophy (PCA) [7], behaviour or planning and organisation difficulties in case of a behavioural/dysexecutive syndrome [26], or language problems in the primary progressive aphasia subtype of AD [13].

In pathology, AD is characterized by the deposition of extracellular amyloid-beta ($A\beta$) in plaques and intracellular hyperphosphorylated tau (pTau) as neurofibrillary tangles (NFT). Plaques and NFTs are assumed to have distinct ways of spreading [6, 39]. As plaques are detected decades before patients show cognitive decline [2] and $A\beta$ levels seem to plateau before clinical onset [15], $A\beta$ deposition is not well correlated with clinical symptoms. Regional pTau aggregation, on the other hand, very well reflects the topical distribution associated with the patient's clinical phenotype. Atypical clinical phenotypes show distinct distribution pTau patterns compared to typical AD [11, 28, 29].

The activation of the innate immunity as part of the 'neuroinflammation' is associated with AD and is actively involved in the spreading of pathology throughout the brain. Both microglia and astrocytes are observed to surround $A\beta$ plaques [4] and seem to be involved in the constant removal of $A\beta$ on one side and the formation of plaques on the other side [35]. Microglia also contribute to the spreading of pTau and are involved in the process of neuronal loss [3, 36]. While the role of microglia and astrocytes in disease progression is well explored, it is unknown if the activation of the innate immunity differs between various clinical subtypes of AD patients. Here, we investigated the regional distribution of this activation process alongside the AD pathological hallmarks of pTau and $A\beta$ in clinical AD subtypes using immunohistochemistry.

METHODS

Study cohort and clinical assessment

For this study, 29 brain donors including AD cases ($n = 19$) and non-neurological controls ($n = 10$) were used. Post mortem brain tissue was obtained from the Netherlands Brain Bank (NBB; Amsterdam, the Netherlands; <http://brainbank.nl>).

nl) and the Normal Aging Brain Collection Amsterdam (NABCA; Amsterdam, the Netherlands; <http://nabca.eu>). Donors or their next of kin signed informed consent for brain autopsy, the use of brain tissue and medical records for research purposes. AD cases died between 2016 and 2019 and were included based on a clinical dementia syndrome due to AD neuropathological change [20, 22]. AD cases were part of the Amsterdam Dementia Cohort and visited the Alzheimer Center Amsterdam during life for clinical diagnostic purposes, where they received a thorough diagnostic workup, including a standard (neurological) physical examination, extensive cognitive testing and neuropsychological investigation, brain MRI, EEG, standard labs, and lumbar puncture for CSF analysis [9, 10]. The clinical subtype was categorized as typical or atypical based on symptoms reported at the first contact point. Cases were considered to have typical AD ($n = 10$) when memory problems dominated symptomatology. AD was considered to be atypical when problems in other cognitive functions besides memory were dominant. The atypical group consisted of six cases with the behavioural/dysexecutive subtype [26, 42] and three cases with PCA [7]. AD cases were compared to age-matched non-neurological controls ($n = 10$). Controls were obtained from the NABCA and selected if cognitive decline was absent during life and the score for AD neuropathological change was 'low' [21]. For each case, sex, age at symptom onset, disease duration, age at death, post mortem interval, and brain weight is reported. The overall score on the five-point clinical dementia rating (CDR) scale was used to stage global dementia severity around the time of death and is reported when available [23].

Neuropathological assessment

Neuropathological diagnosis was established according to international guidelines of Brain Net Europe II (BNE) consortium (<http://www.brainnet-europe.org>) and NIA-AA criteria for AD neuropathological change [21]. The ABC score for AD neuropathological change [22], Braak stage for NFTs [6], Thal phase for A β [39], Thal stage for cerebral amyloid angiopathy (CAA) [38], and concomitant pathologies, i.e., Lewy body pathology [1], TDP43 pathology [24], and vascular lesions were reported when the respective assessments were readily available from the NBB. Formalin-fixed paraffin-embedded (4% PFA for 4 weeks; FFPE) tissue blocks of the middle frontal gyrus, middle temporal gyrus, superior parietal lobe, inferior parietal lobe, anterior cingulate gyrus, and the hippocampus with entorhinal cortex dissected at the level of the lateral geniculate nucleus were cut 6- μ m and assessed by immunohistochemical staining.

Genotyping

DNA was extracted from blood or brain tissue and *APOE* genotype was determined using methods previously described [10]. Whole-exome sequencing (WES) was performed for AD cases. Exome-DNA was captured using the SeqCap EZ Human Exome Library v3.0 capture Kit or the Agilent SureSelect V6 kit (58 M); 150 bp paired-end reads were generated on the Illumina platform, with a mean depth of coverage of at least 30× across exons. We performed in-house alignment and quality control. The exomes of the genes *APP* (NM_000484.3), *PSEN1* (NM_000021.3), and *PSEN2* (NM_000447.2) were analyzed for likely pathogenic (class 4) or pathogenic (class 5) variants according to variant classification consensus guidelines [32]. Known pathogenic mutations are reported.

Immunohistochemistry (IHC)

Immunohistochemistry was performed to detect pTau (AT8), A β (4G8), activated microglia (CD68, KP1; MHC-II, CR3/43), and reactive astrocytes (GFAP) (see Supplemental Table S1 for antibody and staining characteristics). After deparaffinization, sections were blocked for endogenous peroxidase using 0.3% hydrogen peroxide in phosphate buffer saline (PBS; pH 7.4). Antigen retrieval was performed by immersing sections in sodium citrate buffer (10mM Sodium Citrate, 5M NaOH, dH₂O, pH 6.0) and heated to 120°C in an autoclave. Incubation of primary antibodies diluted in normal antibody diluent (ImmunoLogic, Duiven, The Netherlands) was done at room temperature overnight. Primary antibodies were detected using EnVision (Agilent Dako, Glostrup, Denmark). In between steps, sections were washed in PBS (pH 7.4). Subsequently, antibodies were visualized with 3,3'-diaminobenzidine tetrahydrochloride (DAB) (Agilent Dako). After counterstaining with hematoxylin, sections were mounted with Quick-D (Klinipath, The Netherlands).

Quantitative assessment of pathology

Immunostained slides were digitized using the Vectra Polaris Quantitative Pathology Imaging System (PerkinElmer, Waltham, MA, USA) at 200x magnification. Representative areas were annotated manually using ImageJ ([33]; <https://imagej.net/Fiji>) for Vectra Polaris scanned sections as described by Geut et al. [12]. Representative areas for cortical regions had to include all six cortical layers within non-curved areas. The number of annotated areas per section varied between 1-6 areas. The hippocampal annotation was based on the cellular criteria of Duvernoy [8] and included the following hippocampal subregions: transentorhinal and entorhinal cortex, subiculum, hippocampus proper cornu ammonis (CA) 1

to 4, and fusiform gyrus. Since the differentiation between CA2 and CA3 was unreliable, these regions were taken together as CA2-3 [14]. All TIFF-exported images were analysed in ImageJ using in-house developed scripts quantifying the percentage of DAB-stained area, in this study referred to as immunoreactivity.

Statistical analysis

Demographics were compared between groups (controls, typical AD, behavioural/dysexecutive, and PCA) using a one-way ANOVA for continuous demographical data and Chi-square or Fisher's exact tests for categorical data. Linear mixed model (LMM) analysis was used to test if the distribution of each IHC marker (pTau, A β , CD68, MHC-II, and GFAP) over the different brain regions was different between the groups indicated by an interaction effect for group * region. In case of an interaction effect, the analysis was repeated for the comparison of typical AD versus the atypical AD subtypes and subsequently repeated for the atypical AD subtypes only. The data file was split for groups to study immunoreactivity differences between regions within the groups. Differences in immunoreactivity between regions or diagnostic groups are reported when the *p*-value was < 0.05 after correcting for multiple testing using Bonferroni correction. Correlations between the various neuroinflammatory markers (e.g., GFAP, MHC-II, and CD68) and pathology markers (e.g., pTau and A β) were analyzed in selected cortical regions of interest for the four diagnostic groups using an LMM. The correlation coefficient ($r = (\text{estimate} * \text{SDcovariate}) / \text{SDindependent}$) is reported when *p* < 0.05. Statistical analysis was performed in IBM SPSS statistics version 26.0 (IBM SPSS Statistics, Armonk, NY, USA). Heatmaps visualizing the mean immunoreactivity of each marker per region per diagnostic group and correlation plots were generated using GraphPad Prism version 8.2.1 (GraphPad Software, San Diego, California USA).

RESULTS

Group demographics

Baseline demographics are summarized in Table 1. Individual details per case are summarized in Table S2. As per definition, age at onset, disease duration, CDR-score for global dementia severity, ABC score for AD neuropathological change, Braak stage for NFTs, and Thal phase for A β were different for the controls compared to AD groups. Compared to controls, the typical AD group contained more males. Although the other AD groups also mainly consisted of males, this didn't reach significance when compared to controls. Typical AD, behavioural/dysexecutive, and PCA did not differ from each other. One case in the behavioural/dysexecutive group had a *PSEN1* mutation (c.1254G>T).

Table 1. Group demographics

| | Control | Typical AD | Bv/Dys | PCA | p-value |
|---|--------------------|------------------|------------------|-----------------|----------------------|
| Male, <i>n</i> /total (%) | 4/10 (40%) | 9/10 (90%) | 5/6 (83%) | 3/3 (100%) | 0.029 ^a |
| Age of onset (yrs) | NA | 61 (±8) | 60 (±17) | 57 (±2) | 0.859 |
| Disease duration (yrs) | NA | 8 (±4) | 5 (± 3) | 8 (±1) | 0.258 |
| Age at death (yrs) | 69 (±7) | 70 (±11) | 64 (±16) | 65 (±2.5) | 0.594 |
| Brain weight (grams) | 1226 (±67) | 1273 (±151) | 1270 (±169) | 1220 (±103) | 0.810 |
| PMI (hh:mm) | 09:13 (± 01:58) | 08:39 (± 01:33) | 07:31 (± 01:55) | 07:33 (± 00:52) | 0.241 |
| APOE <i>n</i> per ε4 ⁺ / ε4 ⁻ / ε4 ⁺ | 6/3/0 | 5/4/1 | 1/4/1 | 1/2/0 | 0.553 ^a |
| CDR [23] <i>n</i> per stage 0/1/2/3 | 10/0/0/0* | 0/2/1/3 | 0/2/1/3 | 0/0/1/2/ | 0.001 ^a |
| ABC [21] | | | | | |
| A: <i>n</i> per stage 0/1/2/3 | 3/6/1/0* | 0/0/1/8 | 0/0/0/6 | 0/0/0/3 | 0.001 ^a |
| B: <i>n</i> per stage 0/1/2/3 | 3/7/0/0* | 0/0/3/6 | 0/0/1/5 | 0/0/0/3 | < 0.001 ^a |
| C: <i>n</i> per stage 0/1/2/3 | 10/0/0/0* | 0/0/3/6 | 0/0/1/5 | 0/0/0/3 | < 0.001 ^a |
| Braak NFT [6] <i>n</i> per stage 0/1/II/III/IV/V/VI | 3/6/1/0/0/0/0* | 0/0/0/0/3/2/4 | 0/0/0/0/1/4/1 | 0/0/0/0/1/2 | 0.002 ^a |
| Thal Aβ [39] <i>n</i> per phase 0/1/2/3/4/5 | 3/3/3/1/0/0* | 0/0/0/1/0/8 | 0/0/0/0/0/6 | 0/0/0/0/1/2 | 0.002 ^a |
| CAA-Type [38] NA / 1 / 2 | 8/1/1* | 0/6/2 | 0/5/1 | 0/3/0 | 0.003 ^a |
| Braak stage for LB [1] <i>n</i> per stage 0/1/2/3/4/5/6 ; amygdala only | 10/0/0/0/0/0/0; 0* | 6/0/0/0/0/0/0; 2 | 1/0/0/1/0/2/0; 1 | 3/0/0/0/0/0; 0 | 0.183 |

Age of onset, disease duration, age at death, brain weight, and PMI are expressed as mean ± standard deviation. Statistical analysis was performed using a one-way ANOVA for continuous data and Chi-square or Fisher's exact for categorical data. ^a p-value reported for control versus typical AD. No differences were observed between the three AD groups. Aβ amyloid-beta; AD Alzheimer's disease; Bv/Dys behavioural/dysexecutive variant; CDR clinical dementia rating; LB Lewy body; MCI mild cognitive impairment; PCA posterior cortical atrophy; PMI post mortem interval; NA not applicable or not available; SD standard deviation.

Distribution of AD pathological hallmarks

Results for pTau distribution are visualized in Fig. 1a. The regional distribution of pTau was different between controls and AD groups ($p < 0.001$) and between typical AD and atypical variants ($p = 0.006$), as indicated by the observed interaction effect for group*region. Difference in pTau distribution between the two atypical AD variants (behavioural/dysexecutive and PCA) showed a trend but did not reach statistical significance ($p = 0.084$). The data was split for each diagnostic group and the regions were compared with one another to study what the regional pTau immunoreactivity differences were within each group. In controls, pTau load was low and did not differ between regions. As expected, typical AD showed a hippocampal-dominant pTau distribution. The pTau load was highest in the CA1 area. Both CA1 and transentorhinal cortex showed increased immunoreactivity compared to the CA4 region and the four neocortical regions. In addition, the subiculum and fusiform gyrus both had increased pTau immunoreactivity compared to the middle temporal and superior parietal lobe. In the atypical behavioural/dysexecutive group, the CA1 region also showed the highest pTau load. The other hippocampal areas did not show more pTau than the inferior parietal, superior parietal, and middle frontal section, indicating a more widespread pTau distribution for this AD subtype. The PCA cases showed a widespread pTau distribution but without prominent involvement of the CA1 region. The CA4 area was relatively spared and showed less immunoreactivity than the anterior cingulate and middle temporal gyrus.

Results for A β distribution are visualized in Fig. 1b. An interaction effect for group * region was found for controls versus AD ($p < 0.001$), for typical AD versus the atypical variants ($p = 0.022$), and for behavioural/dysexecutive versus PCA ($p = 0.009$). Controls showed almost no A β immunoreactivity in any region, with the highest immunoreactivity in the middle frontal gyrus compared to the hippocampal areas and the superior parietal lobe. In typical AD, A β was predominantly observed in the neocortical regions (middle temporal, inferior and superior parietal, and middle frontal gyrus) and anterior cingulate gyrus compared to all hippocampal regions. Similar to typical AD, the behavioural/dysexecutive group also had a neocortical dominant A β distribution compared to the hippocampal areas. In this atypical variant, the middle frontal gyrus showed the highest mean for A β immunoreactivity, even when compared to the other (neo)cortical regions. In PCA, the differences between regions were less prominent: A β immunoreactivity was again highest in the middle frontal gyrus, but statistical significance was only reached when compared to the CA2-3

and CA4 and not to the other neocortical areas. The transentorhinal and inferior parietal lobe showed increased A β compared to the CA4 only.

In summary, pTau showed a hippocampal-dominant distribution in typical AD, whereas in behavioural/dysexecutive, a more neocortical involvement was seen, and a sparing of the CA1 region in PCA cases. A β distribution was neocortically predominant in both typical and atypical AD variants. In the behavioural/dysexecutive group, the middle frontal gyrus showed increased A β compared to the other cortical regions.

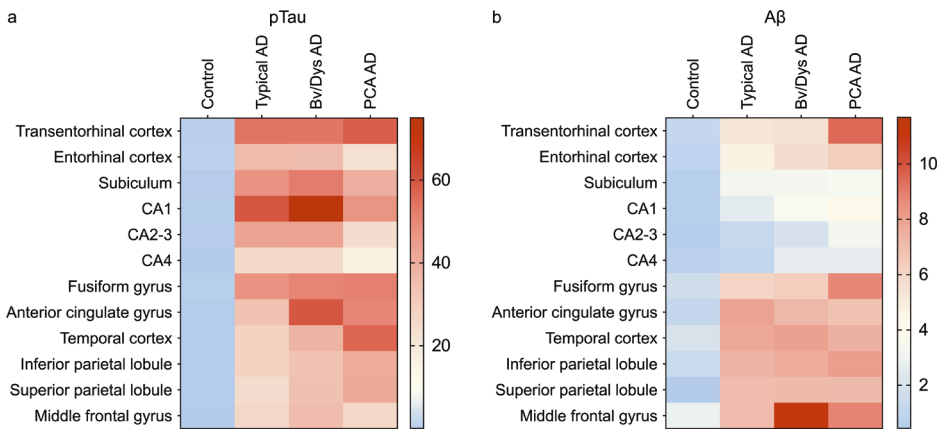


Fig. 1. Heatmaps of the spatial distribution of AD pathology

a Shows the heatmap for pTau. **b** Shows the heatmap for A β . The various diagnostic groups of each separate cohort are represented as columns, the various brain regions as rows. The mean immunoreactive % area was used for color-coding. Study color-scale on the right of each heatmap for scaling. A β amyloid-beta; AD Alzheimer's disease; CA cornu-ammonis; pTau phosphorylated tau.

Distribution of glial immunoreactivity

CD68, a transmembrane glycoprotein that is expressed in phagocytic microglia, was used as a marker for activated microglia. CD68 was differently distributed between controls and AD cases ($p = 0.001$), but not between typical and atypical AD ($p = 0.145$), nor between atypical AD variants ($p = 0.385$). See Fig. 2a for the mean CD68 distribution over the different brain regions for each group. In controls, the CA4 region showed the highest CD68 values when compared to most cortical regions. In typical AD, CD68 was increased in the complete hippocampus. Similar to typical AD, the behavioural/dysexecutive group showed a hippocampus-dominant distribution for CD68. This latter subtype also

showed a relatively high CD68 load in the middle frontal gyrus. The subiculum showed the highest CD68 load in the PCA group. In this subtype, the CD68 hippocampal-dominant distribution was less obvious than in the other AD groups.

MHC-II, representing antigen-presenting microglia, was used as another marker for activated microglia. The distribution of MHC-II over the regions was different between controls and AD groups ($p < 0.001$) and between typical and atypical AD variants ($p = 0.003$). No interaction for region * group was observed for the atypical AD variants ($p = 0.517$). See Fig. 2c for the mean MHC-II distribution over the different brain regions for each group. In controls, the CA4 region showed the highest MHC-II immunoreactivity, whereas the CA1 and superior parietal lobe showed relatively low levels for MHC-II. In both typical and atypical AD variants, wide individual variability in MHC-II immunoreactivity was observed (data not shown). Typical AD showed a hippocampal-dominant presence of MHC-II, similarly to what this phenotype showed for CD68. The behavioural/dysexecutive group did not show a hippocampal-dominant MHC-II distribution, but had increased MHC-II in the middle frontal gyrus compared to the other regions.

The distribution of GFAP immunoreactivity is visualized in Fig. 2c. An interaction effect for group*region was found between controls versus AD groups ($p < 0.001$), typical AD versus atypical AD variants ($p = 0.016$), and atypical AD variants among each other ($p = 0.019$). In the control group, the anterior cingulate gyrus showed most GFAP immunoreactivity. The entorhinal cortex and subiculum also showed relatively high values, which were higher than those observed in the middle temporal and inferior parietal sections. In typical AD, the highest mean value for GFAP was observed in the entorhinal cortex but did not survive multiple testing. Immunoreactivity measured in the middle frontal gyrus was higher than observed in the middle temporal gyrus. The GFAP distribution pattern was different for each atypical AD phenotype. The behavioural/dysexecutive group showed generally low GFAP immunoreactivity without regional differences. The PCA group showed high GFAP values in both the superior and inferior parietal lobes. Immunoreactivity in those regions was higher than in the middle temporal cortex.

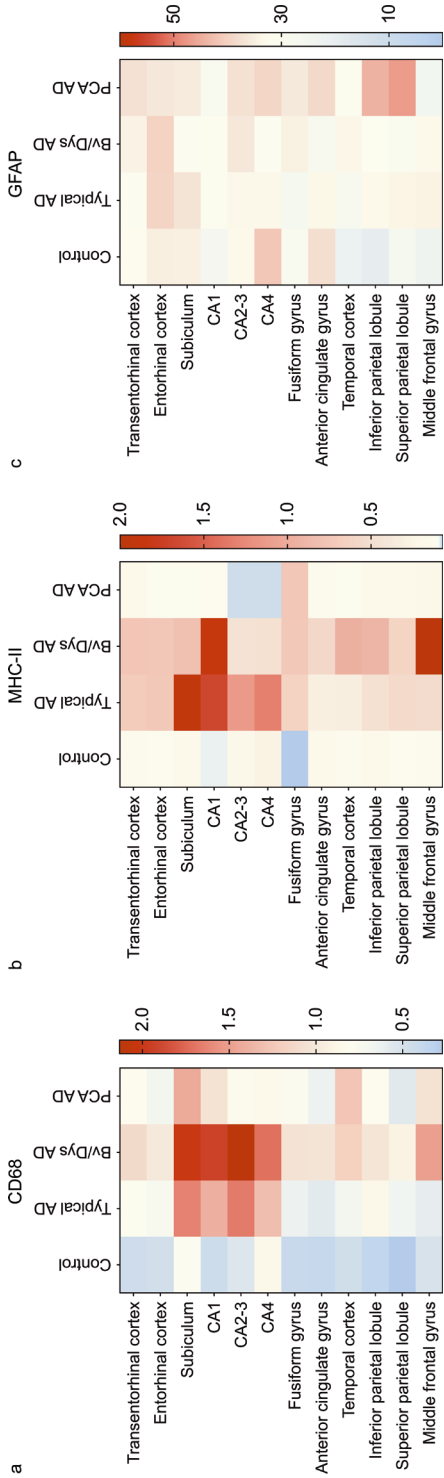


Fig. 2. Heatmaps of the spatial distribution of the various neuroinflammatory markers **a** Shows the heatmap for CD68. **b** Shows the heatmap for MHC-II. **c** Shows the heatmap for GFAP. The various diagnostic groups of each separate cohort are represented as columns, the various brain regions as rows. The mean immunoreactive % area was used for color-coding. Study color-scale on the right of each heatmap for scaling. A β amyloid-beta; AD Alzheimer’s disease; CA cornu-ammonis; pTau phosphorylated tau.

In summary, CD68 distribution only differed between controls and AD groups, whereas MHC-II distribution also differed between typical versus atypical AD variants. Both microglia markers showed increased immunoreactivity in the hippocampal regions of typical AD and in the middle frontal gyrus of the behavioural/dysexecutive variant. CD68 but not MHC-II showed increased immunoreactivity in the hippocampus of behavioural/dysexecutive AD. GFAP distribution differed between typical and atypical AD and also between the two AD atypical variants with especially increased immunoreactivity in the parietal cortices of the PCA cases.

Correlations of neuroinflammation with pathology

Since neuroinflammatory profiles differed between the three AD subtypes, we were interested to see how selected markers correlated with the pTau and A β in selected regions of interest. Although case numbers were small for each subtype, multiple ROIs were selected and analyzed for immunoreactivity in each cortical area of each case, creating multiple measurements per marker. Due to these multiple measures, correlations could be analyzed within the individual groups using an LMM corrected for 'nestedness'. This approach could not be applied to the hippocampal areas as only one measurement per hippocampal subregion was measured.

We analyzed the correlations for the markers CD68 and MHC-II for each group in the middle frontal gyrus as these markers showed increased immunoreactivity in that region for the behavioural/dysexecutive group. CD68 was not correlated with pTau or A β in any of the diagnostic groups (Fig. 3a, b). MHC-II was only for the behavioural/dysexecutive subtype positively correlated in the middle frontal gyrus with pTau ($r = 0.62$; Fig. 3c). We observed that this correlation was significant due to two cases (#21 and #23) with both low pTau and low MHC-II immunoreactivity. Case #21 was a patient with a predominant behavioural presentation by being aggressive and rude at disease onset. Besides AD, no other concomitant pathology was observed. Case #23 had a clinical dysexecutive presentation and showed in addition to AD pathology also extensive Lewy body pathology. No associations were observed between MHC-II and A β .

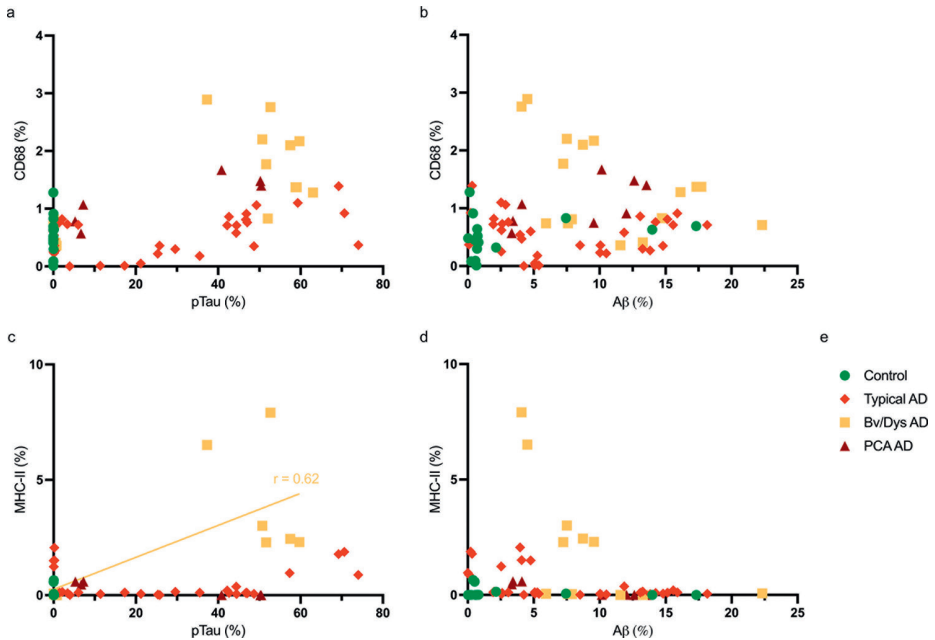


Fig. 3. Correlation plots for CD68 and MHC-II with pTau and A β in the middle frontal gyrus. **a** Shows the correlation plot for CD68 and pTau. **b** Shows the correlation plot for CD68 and A β . **c** Shows the correlation plot for MHC-II and pTau. **d** Shows the correlation plot for MHC-II and A β . **e** Figure legend. All measured ROIs are shown. Since multiple ROIs were taken for each case, there are more data points than the number of cases. A fit line is shown for significant correlations ($p < 0.05$) when tested using an LMM corrected for the multiple measurements within each case, also referred to as nestedness. A β amyloid-beta; LMM linear mixed model; pTau phosphorylated tau; ROI region of interest.

We also analyzed the correlations for GFAP in both the superior and inferior parietal cortex as this marker showed increased immunoreactivity in those regions for the PCA group. In the PCA subgroup, GFAP was correlated with pTau in the inferior parietal cortex ($r = 0.54$) but not in the superior parietal cortex (Fig. 4 a, c). No correlations were observed for GFAP and pTau in the other AD subtypes. Furthermore, GFAP showed a strong positive correlation with A β in both parietal regions of especially the PCA cases ($r = 0.76$ for inferior parietal and $r = 0.96$ for superior parietal; Fig 4b, d, respectively). A weak positive correlation for GFAP and A β was also observed for typical AD in the inferior parietal cortex ($r = 0.36$) and superior parietal cortex ($r = 0.33$), and for controls in the inferior parietal cortex ($r = 0.47$).

These plots show that the associations between the glial markers and the pathology markers differ regionally for the various AD subtypes.

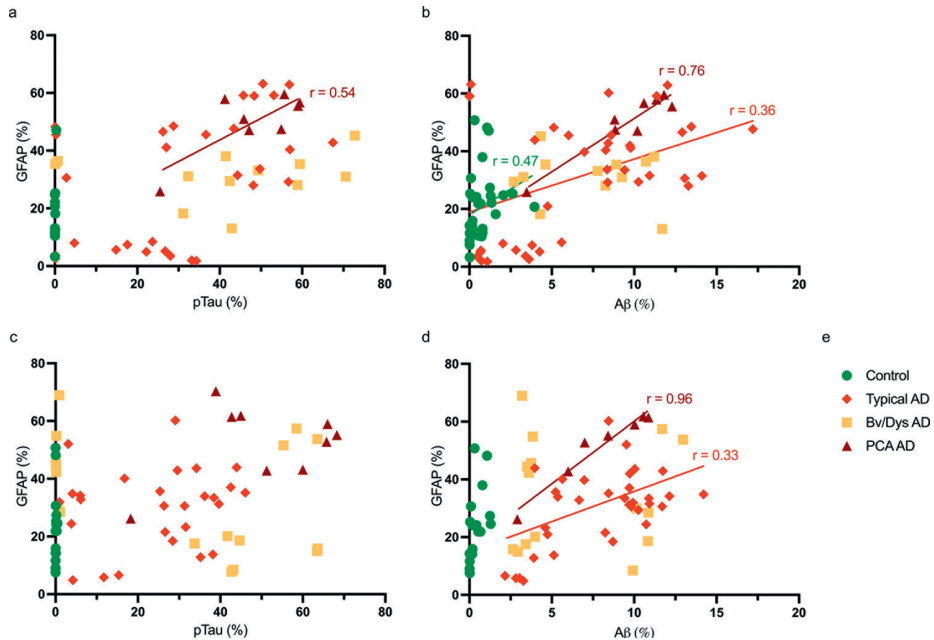


Fig. 4. Correlation plots for GFAP with pTau and A β in the parietal cortices
a Shows the correlation plot for GFAP and pTau in the inferior parietal cortex. **b** Shows the correlation plot for GFAP and A β in the inferior parietal cortex. **c** Shows the correlation plot for GFAP and pTau in the superior parietal cortex. **d** Shows the correlation plot for GFAP and A β in the inferior parietal cortex. **e** Figure legend. Since multiple ROIs were taken for each case, there are more data points than the number of cases. A fit line is shown for significant correlations ($p < 0.05$) when tested using an LMM corrected for the multiple measurements within each case also, referred to as nestedness. A β amyloid-beta; LMM linear mixed model; pTau phosphorylated tau; ROI region of interest.

DISCUSSION

In this study, we investigated, besides A β and pTau, the distribution of different neuroinflammatory markers in various clinical AD subtypes. As expected, we observed different distribution patterns for pTau with a more hippocampal-dominant pattern in typical AD and a more cortical dominant pattern in atypical AD. In all AD groups, A β was more pronounced in the neocortical areas compared to the limbic regions. The activated microglia marker MHC-II showed different distribution patterns in typical compared to atypical

AD, but not between atypical AD variants. Both CD68 and MHC-II showed increased immunoreactivity in the middle frontal gyrus of the behavioural/dysexecutive AD group. The reactive astrocyte distribution measured with GFAP immunoreactivity differentiated not only typical from atypical AD but also atypical AD variants from one another with an increased load in the parietal areas of PCA cases. Our data show that microglia and astrocytes are regionally differently activated in the various AD subtypes. In addition, microglia and astrocytes are differently associated with the presence of pTau and A β within each AD subtype, indicating that the underlying neuroinflammatory profile is different between subtypes.

Like others in the field, we show that the distribution of pTau differs for various clinical subtypes of AD [11, 28–30, 37]. The typical amnesic AD cases showed the typical hippocampal-dominant pTau distribution, whereas the atypical AD cases did not. We could not statistically confirm that the PCA group had a different pTau distribution than our behavioural/dysexecutive cases, most likely due to the small group sizes. Although not statistically confirmed, the PCA cases showed a prominent pTau sparing of the hippocampus proper with a high pTau load in the transentorhinal cortex and temporal cortex and a moderate pTau load in both parietal regions. This similar pattern of a relatively spared hippocampus compared to moderate affected temporoparietal areas was also shown by others investigating pTau in PCA [29, 31]. The behavioural/dysexecutive AD subtype is often referred to as frontal AD due to the observation of pTau and NFTs in the frontal cortex [16, 20, 40]. However, similar to Ossenkopppele et al., we could not confirm that pTau deposition was more pronounced in the frontal cortex than in other cortical regions [27]. In our study, the behavioural/dysexecutive group showed a more diffuse distribution, in which all cortical areas were relatively similarly severely affected, replicating the findings of Petersen et al. [29]. Interestingly, when looking at A β pathology, we did see increased pathology in the frontal section of the behavioural/dysexecutive subtype, which was distinct from that of typical AD. In the current study we assessed overall presence of A β (% immunoreactivity area). Future studies will need to address if the increased A β pathology in the frontal region in this subgroup is correlated with certain types of A β deposits, such as the more common classic cored plaques, the vascular type of A β deposit referred to as CAA, or the recently described coarse-grained plaque, of which its presence is predominantly observed in the frontal cortex [4]. As described previously, we showed that for all AD subtypes, A β distribution is neocortical dominant when compared to the hippocampal regions [19, 34, 40].

The presence of microglia and astrocytes seemed to differ for the various AD subtypes. In typical AD and behavioural/dysexecutive AD, the activated microglia showed a distinct immunoreactivity profile with increased values in the hippocampus. In the behavioural/dysexecutive cases, CD68 and MHC-II also showed increased signal in the middle frontal gyrus, a brain region often mentioned in the context of this phenotype [43, 45]. Interestingly, although A β immunoreactivity showed the highest values in this region and the pTau signal wasn't obviously increased, MHC-II was correlated with pTau and not A β . In PCA, reactive astrocytes showed a distinct parietal distribution. In this subtype, parietal GFAP immunoreactivity is very well associated with A β load and, to a lesser extent, with pTau load. Both observations support the hypothesis that the innate immune system acts as a mediator between A β deposits and pTau pathology. Not many other studies investigated the distribution of neuroinflammation in AD, let alone atypical AD. A recent PET study investigated the distribution of 18kDa translocator protein (TSPO), a protein correlated with neuroinflammation, in EOAD compared to healthy controls [41]. The AD group consisted of six patients with a behavioural presentation, by the authors referred to as frontal AD, and two patients with the PCA variant. TSPO tracer uptake was variable in the frontal AD variant, showing increased uptake predominantly frontally in some and increased uptake throughout all cortices in others. Both PCA cases showed increased uptake in particularly the parieto-occipital regions. Important to note is that TSPO is not cell-type or activation state specific as it can be found both in activated and resting micro- and astroglia [25]. We previously showed that neuroinflammatory distribution is different in atypical AD when comparing the temporal versus parietal cortex [5]. In our previous study, activated microglia and not so much reactive astrocytes distinguished between typical and atypical AD. An essential difference with the current study is that our previous case selection was from a neuropathological perspective, and cases were classified based on NFT distribution. Also, we only investigated two brain regions. A critical finding from the current study, in which more brain regions were analyzed and cases were categorized based on clinical presentation, is that the key cells of the innate immune system differ per subgroup.

The current study has several limitations. The current cohort collection consists of prospectively collected AD cases over a five-year period, resulting in small groups as atypical clinical subtypes are not common. Replication in larger cohorts, including multiple atypical phenotypes, is mandatory. We are very well aware that the neuroinflammatory response is more complex than the three markers tested in this study. Since the microglia-specific markers such as

TMEM119 and TREM2 are more difficult to stain and interpret, we chose more robust immunohistochemistry markers. We stratified our cases based on their symptoms at presentation. However, between disease onset and death patients can show many fluctuations in symptom-trajectory per subtype [17]. Another limitation for pathology studies is their cross-sectional and unilateral aspect. The current ongoing PET studies with tracers directed against, e.g., TSPO for neuroinflammation and MAO-B for astrocytosis could give us more insight into the longitudinal distribution of neuroinflammation in AD [44]. Although combining PET tracers for microglia, astrocytic markers, pTau, and amyloid in one study together is difficult, the correlation between all those markers in different disease phases provides needed insight in AD pathogenesis. It perhaps might also offer a therapeutic window for treatment with specific inflammatory modulating drugs.

Conclusion

This study shows that the spatial distribution of neuroinflammatory cells and AD pathological hallmarks differ for various clinical subtypes of AD. In addition, this study shows that the involvement of the most prominent players of this neuroinflammatory response, i.e., astrocytes and microglia, differs per subtype, indicating that the neuroinflammatory response in AD is more complex than previously assumed. Although all AD patients have plaques and tangles in their brain, their underlying neuroinflammatory profile may very well differ, which has direct consequences for future innate immunity modulating therapies.

LIST OF ABBREVIATIONS

| | |
|-----------|--|
| A β | amyloid-beta |
| AD | Alzheimer's disease |
| BNE | Brain Net Europe II |
| CA | cornu ammonis |
| CAA | cerebral amyloid angiopathy |
| CDR | clinical dementia rating |
| DAB | 3,3'-diaminobenzidine tetrahydrochloride |
| FFPE | formalin-fixed paraffin-embedded |
| LMM | linear mixed model |
| NABCA | Normal Aging Brain Collection Amsterdam |
| NBB | Netherlands Brain Bank |
| NFT | neurofibrillary tangles |
| PBS | phosphate buffer saline |
| PCA | posterior cortical atrophy |
| pTau | phosphorylated tau |
| WES | whole-exome sequencing |
| EOAD | early disease onset of AD |

REFERENCES

1. Alafuzoff I, Ince PG, Arzberger T, Al-Sarraj S, Bell J, Bodi I, Bogdanovic N, Bugiani O, Ferrer I, Gelpi E, Gentleman S, Giaccone G, Ironside JW, Kavantzias N, King A, Korkolopoulou P, Kovács GG, Meyronet D, Monoranu C, Parchi P, Parkkinen L, Patsouris E, Roggendorf W, Rozemuller A, Stadelmann-Nessler C, Streichenberger N, Thal DR, Kretzschmar H (2009) Staging/typing of Lewy body related α -synuclein pathology: A study of the BrainNet Europe Consortium. *Acta Neuropathol* 117:635–652. doi: 10.1007/s00401-009-0523-2
2. Armstrong RA (1995) Beta-amyloid deposition in the medial temporal lobe in elderly non-demented brains and in Alzheimer's disease. *Dement Geriatr Cogn Disord* 6:121–125. doi: 10.1159/000106933
3. Asai H, Ikezu S, Tsunoda S, Medalla M, Luebke J, Haydar T, Wolozin B, Butovsky O, Kügler S, Ikezu T (2015) Depletion of microglia and inhibition of exosome synthesis halt tau propagation. *Nat Neurosci* 18:1584–93. doi: 10.1038/nn.4132
4. Boon BDC, Bulk M, Jonker AJ, Morrema THJ, van den Berg E, Popovic M, Walter J, Kumar S, van der Lee SJ, Holstege H, Zhu X, Van Nostrand WE, Natté R, van der Weerd L, Bouwman FH, van de Berg WDJ, Rozemuller AJM, Hoozemans JJM (2020) The coarse-grained plaque: a divergent A β plaque-type in early-onset Alzheimer's disease. *Acta Neuropathol* 140:811–830. doi: 10.1007/s00401-020-02198-8
5. Boon BDC, Hoozemans JJM, Lopuhaä B, Eigenhuis KN, Scheltens P, Kamphorst W, Rozemuller AJM, Bouwman FH (2018) Neuroinflammation is increased in the parietal cortex of atypical Alzheimer's disease. *J Neuroinflammation* 15:170. doi: 10.1186/s12974-018-1180-y
6. Braak H, Alafuzoff I, Arzberger T, Kretzschmar H, Tredici K (2006) Staging of Alzheimer disease-associated neurofibrillary pathology using paraffin sections and immunocytochemistry. *Acta Neuropathol* 112:389–404. doi: 10.1007/s00401-006-0127-z
7. Crutch SJ, Schott JM, Lehmann M, Primativo S, Rossor MN, Ryan NS, Shakespeare TJ, Suárez González A, Yong KXX, Fox NC, Rabinovici GD, Lehmann M, Murray M, Snowden JS, Snowden JS, van der Flier WM, Pijnenburg Y, Scheltens P, van der Flier WM, Pijnenburg Y, Scheltens P, Dickerson BC, Vandenberghe R, Ahmed S, Butler C, Bak TH, Boeve BF, Graff-Radford J, Cappa SF, Ceccaldi M, de Souza LC, Dubois B, Felician O, Felician O, Galasko D, Graff-Radford NR, Hof PR, Hof PR, Krolak-Salmon P, Magnin E, Mendez MF, Nestor PJ, Onyike CU, Pelak VS, Pelak VS, Suárez González A, Tang-Wai DF, Carrillo M (2017) Consensus classification of posterior cortical atrophy. *Alzheimer's Dement* 13:870–884. doi: 10.1016/j.jalz.2017.01.014
8. Duvernoy HM (1988) *The Human Hippocampus*. J.F. Bergmann-Verlag
9. Van Der Flier WM, Pijnenburg YAL, Prins N, Lemstra AW, Bouwman FH, Teunissen CE, Van Berckel BNM, Stam CJ, Barkhof F, Visser PJ, Van Egmond E, Scheltens P (2014) Optimizing patient care and research: The Amsterdam dementia cohort. *J Alzheimer's Dis* 41:313–327. doi: 10.3233/JAD-132306

10. Van Der Flier WM, Scheltens P (2018) Amsterdam dementia cohort: Performing research to optimize care. *J. Alzheimer's Dis.* 62:1091–1111
11. Galton CJ, Patterson K, Xuereb JH, Hodges JR (2000) Atypical and typical presentations of Alzheimer's disease: a clinical, neuropsychological, neuroimaging and pathological study of 13 cases. *Brain* 123:484–98
12. Geut H, van den Berg E, Boon BDC, Hoozemans JJM, Tunold J-A, Pihlstrøm L, Jonkman LE, Rozemuller AJM, Lemstra AW, van de Berg WDJ Alzheimer's disease copathology in dementia with Lewy bodies is associated with astroglial α -synucleinopathy. Submitted
13. Gorno-Tempini ML, Hillis AE, Weintraub S, Kertesz A, Mendez M, Cappa SF, Ogar JM, Rohrer JD, Black S, Boeve BF, Manes F, Dronkers NF, Vandenberghe R, Rascovsky K, Patterson K, Miller BL, Knopman DS, Hodges JR, Mesulam MM, Grossman M (2011) Classification of primary progressive aphasia and its variants. *Neurology* 76:1006–14. doi: 10.1212/WNL.0b013e31821103e6
14. Harding AJ, Halliday GM, Kril JJ (1998) Variation in hippocampal neuron number with age and brain volume. *Cereb Cortex* 8:710–718. doi: 10.1093/cercor/8.8.710
15. Jack CR, Wiste HJ, Lesnick TG, Weigand SD, Knopman DS, Vemuri P, Pankratz VS, Senjem ML, Gunter JL, Mielke MM, Lowe VJ, Boeve BF, Petersen RC (2013) Brain β -amyloid load approaches a plateau. *Neurology* 80:890–896. doi: 10.1212/WNL.0b013e3182840bbe
16. Johnson JK, Head E, Kim R, Starr A, Cotman CW (1999) Clinical and pathological evidence for a frontal variant of Alzheimer disease. *Arch Neurol* 56:1233–1239. doi: 10.1001/archneur.56.10.1233
17. Jutten RJ, Sikkes SAM, Van der Flier WM, Scheltens P, Visser PJ, Tijms BM (2021) Finding Treatment Effects in Alzheimer Trials in the Face of Disease Progression Heterogeneity. *Neurology* 96:e2673–e2684. doi: 10.1212/wnl.0000000000012022
18. Koedam ELGE, Lauffer V, van der Vlies AE, van der Flier WM, Scheltens P, Pijnenburg YAL (2010) Early-versus late-onset Alzheimer's disease: more than age alone. *J Alzheimers Dis* 19:1401–8. doi: 10.3233/JAD-2010-1337
19. Lehmann M, Ghosh PM, Madison C, Laforce R, Corbetta-Rastelli C, Weiner MW, Greicius MD, Seeley WW, Gorno-Tempini ML, Rosen HJ, Miller BL, Jagust WJ, Rabinovici GD (2013) Diverging patterns of amyloid deposition and hypometabolism in clinical variants of probable Alzheimer's disease. *Brain* 136:844–858. doi: 10.1093/brain/aws327
20. McKhann GM, Knopman DS, Chertkow H, Hyman BT, Jack CR, Kawas CH, Klunk WE, Koroshetz WJ, Manly JJ, Mayeux R, Mohs RC, Morris JC, Rossor MN, Scheltens P, Carrillo MC, Thies B, Weintraub S, Phelps CH, Phelps CH (2011) The diagnosis of dementia due to Alzheimer's disease: recommendations from the National Institute on Aging-Alzheimer's Association workgroups on diagnostic guidelines for Alzheimer's disease. *Alzheimers Dement* 7:263–9. doi: 10.1016/j.jalz.2011.03.005

21. Montine TJ, Phelps CH, Beach TG, Bigio EH, Cairns NJ, Dickson DW, Duyckaerts C, Frosch MP, Masliah E, Mirra SS, Nelson PT, Schneider JA, Thal DR, Trojanowski JQ, Vinters H V, Hyman BT (2012) National Institute on Aging–Alzheimer’s Association guidelines for the neuropathologic assessment of Alzheimer’s disease: a practical approach. *Acta Neuropathol* 123:1–11. doi: 10.1007/s00401-011-0910-3
22. Montine TJ, Phelps CH, Beach TG, Bigio EH, Cairns NJ, Dickson DW, Duyckaerts C, Frosch MP, Masliah E, Mirra SS, Nelson PT, Schneider JA, Thal DR, Trojanowski JQ, Vinters H V, Hyman BT, National Institute on Aging, Alzheimer’s Association (2012) National Institute on Aging–Alzheimer’s Association guidelines for the neuropathologic assessment of Alzheimer’s disease: a practical approach. *Acta Neuropathol* 123:1–11. doi: 10.1007/s00401-011-0910-3
23. Morris JC (1993) The clinical dementia rating (cdr): Current version and scoring rules. *Neurology* 43:2412–2414. doi: 10.1212/wnl.43.11.2412-a
24. Nelson PT, Dickson DW, Trojanowski JQ, Jack CR, Boyle PA, Arfanakis K, Rademakers R, Alafuzoff I, Attems J, Brayne C, Coyle-Gilchrist ITS, Chui HC, Fardo DW, Flanagan ME, Halliday G, Hokkanen SRK, Hunter S, Jicha GA, Katsumata Y, Kawas CH, Keene CD, Kovacs GG, Kukull WA, Levey AI, Makkinejad N, Montine TJ, Murayama S, Murray ME, Nag S, Rissman RA, Seeley WW, Sperling RA, White CL, Yu L, Schneider JA (2019) Limbic-predominant age-related TDP-43 encephalopathy (LATE): Consensus working group report. *Brain* 142:1503–1527
25. Nutma E, Stephenson JA, Gorter RP, De Bruin J, Boucherie DM, Donat CK, Breur M, Van Der Valk P, Matthews PM, Owen DR, Amor S (2019) A quantitative neuropathological assessment of translocator protein expression in multiple sclerosis. *Brain* 142:3440–3455. doi: 10.1093/brain/awz287
26. Ossenkoppele R, Pijnenburg YAL, Perry DC, Cohn-Sheehy BI, Scheltens NME, Vogel JW, Kramer JH, Van Der Vlies AE, Joie R La, Rosen HJ, Van Der Flier WM, Grinberg LT, Rozemuller AJ, Huang EJ, Van Berckel BNM, Miller BL, Barkhof F, Jagust WJ, Scheltens P, Seeley WW, Rabinovici GD (2015) The behavioural/dysexecutive variant of Alzheimer’s disease: Clinical, neuroimaging and pathological features. *Brain* 138:2732–2749. doi: 10.1093/brain/awv191
27. Ossenkoppele R, Pijnenburg YAL, Perry DC, Cohn-Sheehy BI, Scheltens NME, Vogel JW, Kramer JH, Van Der Vlies AE, Joie R La, Rosen HJ, Van Der Flier WM, Grinberg LT, Rozemuller AJ, Huang EJ, Van Berckel BNM, Miller BL, Barkhof F, Jagust WJ, Scheltens P, Seeley WW, Rabinovici GD (2015) The behavioural/dysexecutive variant of Alzheimer’s disease: Clinical, neuroimaging and pathological features. *Brain* 138:2732–2749. doi: 10.1093/brain/awv191
28. Ossenkoppele R, Schonhaut DR, Schöll M, Lockhart SN, Ayakta N, Baker SL, O’Neil JP, Janabi M, Lazaris A, Cantwell A, Vogel J, Santos M, Miller ZA, Bettcher BM, Vessel KA, Kramer JH, Gorno-Tempini ML, Miller BL, Jagust WJ, Rabinovici GD (2016) Tau PET patterns mirror clinical and neuroanatomical variability in Alzheimer’s disease. *Brain* 139:1551–1567. doi: 10.1093/brain/aww027

29. Petersen C, Nolan AL, de Paula França Resende E, Miller Z, Ehrenberg AJ, Gorno-Tempini ML, Rosen HJ, Kramer JH, Spina S, Rabinovici GD, Miller BL, Seeley WW, Heinsen H, Grinberg LT (2019) Alzheimer's disease clinical variants show distinct regional patterns of neurofibrillary tangle accumulation. *Acta Neuropathol* 138:597-612. doi: 10.1007/s00401-019-02036-6
30. Phillips JS, Das SR, McMillan CT, Irwin DJ, Roll EE, Da Re F, Nasrallah IM, Wolk DA, Grossman M (2018) Tau PET imaging predicts cognition in atypical variants of Alzheimer's disease. *Hum Brain Mapp* 39:691-708. doi: 10.1002/hbm.23874
31. Phillips JS, Das SR, McMillan CT, Irwin DJ, Roll EE, Da Re F, Nasrallah IM, Wolk DA, Grossman M (2018) Tau PET imaging predicts cognition in atypical variants of Alzheimer's disease. *Hum Brain Mapp* 39:691-708. doi: 10.1002/hbm.23874
32. Richards S, Aziz N, Bale S, Bick D, Das S, Gastier-Foster J, Grody WW, Hegde M, Lyon E, Spector E, Voelkerding K, Rehm HL (2015) Standards and guidelines for the interpretation of sequence variants: A joint consensus recommendation of the American College of Medical Genetics and Genomics and the Association for Molecular Pathology. *Genet Med* 17:405-424. doi: 10.1038/gim.2015.30
33. Schindelin J, Arganda-Carreras I, Frise E, Kaynig V, Longair M, Pietzsch T, Preibisch S, Rueden C, Saalfeld S, Schmid B, Tinevez JY, White DJ, Hartenstein V, Eliceiri K, Tomancak P, Cardona A (2012) Fiji: An open-source platform for biological-image analysis. *Nat. Methods* 9:676-682
34. de Souza LC, Corlier F, Habert M-O, Uspenskaya O, Maroy R, Lamari F, Chupin M, Lehericy S, Colliot O, Hahn-Barma V, Samri D, Dubois B, Bottlaender M, Sarazin M (2011) Similar amyloid- burden in posterior cortical atrophy and Alzheimer's disease. *Brain* 134:2036-2043. doi: 10.1093/brain/awr130
35. Spangenberg E, Severson PL, Hohsfield LA, Crapser J, Zhang J, Burton EA, Zhang Y, Spevak W, Lin J, Phan NY, Habets G, Rymar A, Tsang G, Walters J, Nespi M, Singh P, Broome S, Ibrahim P, Zhang C, Bollag G, West BL, Green KN (2019) Sustained microglial depletion with CSF1R inhibitor impairs parenchymal plaque development in an Alzheimer's disease model. *Nat Commun* 10:3758. doi: 10.1038/s41467-019-11674-z
36. Spangenberg EE, Lee RJ, Najafi AR, Rice RA, Elmore MRP, Blurton-Jones M, West BL, Green KN, Akama K, Eldik L Van, Akiyama H, Arai T, Kondo H, Tanno E, Haga C, Ikeda K, Ando K, Brion J, Stygelbout V, Suain V, Authelet M, Dedecker R, Asai H, Ikezu S, Tsunoda S, Medalla M, Luebke J, Haydar T, Blinzinger K, Kreutzberg G, Boissonneault V, Filali M, Lessard M, Relton J, Wong G, Rivest S, Bradshaw E, Chibnik L, Keenan B, Ottoboni L, Raj T, Tang A, Buskila Y, Crowe S, Ellis-Davies G, Butovsky O, Jedrychowski M, Moore C, Cialic R, Lanser A, Gabriely G, Cacquevel M, Lebeurrier N, Cheenne S, Vivien D, Cagnin A, Brooks D, Kennedy A, Gunn R, Myers R, Turkheimer F, Centonze D, Muzio L, Rossi S, Cavasinni F, Chiara V De, Bergami A, Chakrabarty P, Li A, Ceballos-Diaz C, Eddy J, Funk C, Moore B, Chapuis J, Hansmannel F, Gistelinc M, Mounier A, Cauwenberghe C Van, Kolen K, Chitu V, Nacu V, Charles J, Henne W, McMahon H, Nandi S, Condello C, Yuan P, Schain A, Grutzendler J, Coniglio S, Eugenin E, Dobrenis K, Stanley E, West B, Symons M,

Costello D, Carney D, Lynch M, Crehan H, Hardy J, Pocock J, Crowe S, Ellis-Davies G, Dagher N, Najafi A, Kayala K, Elmore M, White T, Medeiros R, Dandrea M, Reiser P, Gumula N, Hertzog B, Andrade-Gordon P, DiCarlo G, Wilcock D, Henderson D, Gordon M, Morgan D, Dickson D, Farlo J, Davies P, Crystal H, Fuld P, Yen S, Dong H, Martin M, Chambers S, Csernansky J, Eimer W, Vassar R, Elmore M, Lee R, West B, Green K, Elmore M, Najafi A, Koike M, Dagher N, Spangenberg E, Rice R, Fillit H, Ding W, Buee L, Kalman J, Altstiel L, Lawlor B, Fuhrmann M, Bittner T, Jung C, Burgold S, Page R, Mitteregger G, Gabbita S, Srivastava M, Eslami P, Johnson M, Kobritz N, Tweedie D, Gomez-Nicola D, Fransen N, Suzzi S, Perry V, Grathwohl S, Kalin R, Bolmont T, Prokop S, Winkelmann G, Kaeser S, Grutzendler J, Gan W, Guerreiro R, Wojtas A, Bras J, Carrasquillo M, Rogaeva E, Majounie E, Guillot-Sestier M, Doty K, Gate D, Rodriguez J, Leung B, Rezai-Zadeh K, Hauss-Wegrzyniak B, Lynch M, Vraniak P, Wenk G, Ishizuka K, Kimura T, Igata-yi R, Katsuragi S, Takamatsu J, Miyakawa T, Jankowsky J, Slunt H, Gonzales V, Savonenko A, Wen J, Jenkins N, Jawhar S, Trawicka A, Jenneckens C, Bayer T, Wirths O, Jay T, Miller C, Cheng P, Graham L, Bemiller S, Broihier M, Johansson J, Woodling N, Wang Q, Panchal M, Liang X, Trueba-Saiz A, Kan M, Lee J, Wilson J, Everhart A, Brown C, Hoofnagle A, Kim T, Cavnar M, Cohen N, Sorenson E, Greer J, Seifert A, Kim W, Li H, Ruberu K, Chan S, Elliott D, Low J, Kitazawa M, Cheng D, Tsukamoto M, Koike M, Wes P, Vasilevko V, Kitazawa M, Oddo S, Yamasaki T, Green K, LaFerla F, Kiyota T, Okuyama S, Swan R, Jacobsen M, Gendelman H, Ikezu T, Klein D, Patzko A, Schreiber D, Hauwermeiren A van, Baier M, Groh J, Koenigsknecht-Talboo J, Landreth G, Lambert J, Heath S, Even G, Campion D, Slegers K, Hiltunen M, Leinenga G, Gotz J, Li R, Shen Y, Yang L, Lue L, Finch C, Rogers J, Mattiace L, Davies P, Yen S, Dickson D, McGeer E, McGeer P, Meda L, Cassatella M, Szendrei G, Otvos L, Baron P, Villalba M, Medway C, Morgan K, Mok S, Koya R, Tsui C, Xu J, Robert L, Wu L, Myczek K, Yeung S, Castello N, Baglietto-Vargas D, LaFerla F, Naj A, Jun G, Beecham G, Wang L, Vardarajan B, Buros J, Neely K, Green K, LaFerla F, Oakley H, Cole S, Logan S, Maus E, Shao P, Craft J, Pan X, Zhu Y, Lin N, Zhang J, Ye Q, Huang H, Parachikova A, Vasilevko V, Cribbs D, LaFerla F, Green K, Peters A, Kaiserman-Abramof I, Pyonteck S, Akkari L, Schuhmacher A, Bowman R, Sevenich L, Quail D, Rice R, Berchtold N, Cotman C, Green K, Rice R, Spangenberg E, Yamate-Morgan H, Lee R, Arora R, Hernandez M, Robinson J, Molina-Porcel L, Corrada M, Raible K, Lee E, Lee V, Rodriguez-Ortiz C, Hoshino H, Cheng D, Liu-Yescevitiz L, Blurton-Jones M, Wolozin B, Rozemuller J, Eikelenboom P, Stam F, Scheff S, Price D, Schmitt F, Mufson E, Schreiner B, Romanelli E, Liberski P, Ingold-Heppner B, Sobottka-Brillout B, Hartwig T, Seshadri S, Fitzpatrick A, Ikram M, DeStefano A, Gudnason V, Boada M, Shaftel S, Kyrkanides S, Olschowka J, Miller J, Johnson R, O'Banion M, Spires-Jones T, Meyer-Luehmann M, Osetek J, Jones P, Stern E, Bacskai B, Srivatsan S, Swiecki M, Otero K, Cella M, Shaw A, Tap W, Wainberg Z, Anthony S, Ibrahim P, Zhang C, Healey J, Valdearcos M, Robblee M, Benjamin D, Nomura D, Xu A, Koliwad S, Wake H, Moorhouse A, Jinno S, Kohsaka S, Nabekura J, Wang Y, Cella M, Mallinson K, Ulrich J, Young K, Robinette M, Webster S, Yang A,

- Margol L, Garzon-Rodriguez W, Glabe C, Tenner A, Xu Q, Li Y, Cyras C, Sanan D, Cordell B, Yamanaka M, Ishikawa T, Griep A, Axt D, Kummer M, Heneka M, Ziehn M, Avedisian A, Tiwari-Woodruff S, Voskuhl R (2016) Eliminating microglia in Alzheimer's mice prevents neuronal loss without modulating amyloid- β pathology. *Brain* 139:1265–81. doi: 10.1093/brain/aww016
37. Tang-Wai DF, Graff-Radford NR, Boeve BF, Dickson DW, Parisi JE, Crook R, Caselli RJ, Knopman DS, Petersen RC (2004) Clinical, genetic, and neuropathologic characteristics of posterior cortical atrophy. *Neurology* 63:1168–74
 38. Thal DR, Griffin WST, de Vos RAI, Ghebremedhin E (2008) Cerebral amyloid angiopathy and its relationship to Alzheimer's disease. *Acta Neuropathol* 115:599–609. doi: 10.1007/s00401-008-0366-2
 39. Thal DR, Rüb U, Orantes M, Braak H (2002) Phases of Ab-deposition in the human brain and its relevance for the development of AD. *Neurology* 58:1791–1800
 40. Therriault J, Pascoal TA, Savard M, Benedet AL, Chamoun M, Tissot C, Lussier F, Kang MS, Thomas E, Terada T, Rej S, Massarweh G, Nasreddine Z, Vitali P, Soucy JP, Saha-Chaudhuri P, Gauthier S, Rosa-Neto P (2021) Topographic Distribution of Amyloid-b, Tau, and Atrophy in Patients With Behavioral/Dysexecutive Alzheimer Disease. *Neurology* 96:e81–e92. doi: 10.1212/WNL.0000000000011081
 41. Tondo G, Iaccarino L, Caminiti SP, Presotto L, Santangelo R, Iannaccone S, Magnani G, Perani D (2020) The combined effects of microglia activation and brain glucose hypometabolism in early-onset Alzheimer's disease. *Alzheimer's Res Ther* 12:1–10. doi: 10.1186/s13195-020-00619-0
 42. Townley RA, Graff-Radford J, Mantyh WG, Botha H, Polsinelli AJ, Przybelski SA, Machulda MM, Makhoul AT, Senjem ML, Murray ME, Reichard RR, Savica R, Boeve BF, Drubach DA, Josephs KA, Knopman DS, Lowe VJ, Jack CR, Petersen RC, Jones DT (2020) Progressive dysexecutive syndrome due to Alzheimer's disease: a description of 55 cases and comparison to other phenotypes. *Brain Commun* 2. doi: 10.1093/braincomms/fcaa068
 43. Villain N, Dubois B (2019) Alzheimer's Disease Including Focal Presentations. *Semin Neurol* 39:213–226. doi: 10.1055/s-0039-1681041
 44. Villemagne VL, Harada R, Dore V, Furumoto S, Mulligan RS, Kudo Y, Burnham SC, Krishnadas N, Huang K, Yanai K, Rowe CC, Okamura N (2020) Evaluation of the novel 18 F-labeled PET tracer SMBT-1 for imaging astrogliosis in healthy elderly controls and A+/T+/(N+) Alzheimer's disease patients . *Alzheimer's Dement* 16. doi: 10.1002/alz.039858
 45. Woodward M, Jacova C, Black SE, Kertesz A, Mackenzie IR, Feldman H, Gauthier S, Bouchard RW, Loy-English I, Hogan D, Rockwood K, Hsiung GYR (2010) Differentiating the frontal variant of Alzheimer's disease. *Int J Geriatr Psychiatry* 25:732–738. doi: 10.1002/gps.2415

SUPPLEMENTARY DATA

Table S1. Antibody characteristics

| Antibody | Antigen | Species | Origin details | Dilution |
|-------------------------|---|--------------|-------------------------------|----------|
| pTau, clone AT8 | Tau phosphorylated at Ser202 and Thr205 | Mouse, IgG1 | ThermoFisher, Pittsburgh, USA | 1:800 |
| Amyloid-beta, clone 4G8 | N-terminus of amyloid-beta (aa 17-24) | Mouse, IgG2b | Biologend, San Diego, USA | 1:8000 |
| CD68, clone KP1 | CD68 | Mouse, IgG1 | Dako, Glostrup, Denmark | 1:1200 |
| MHC-II, clone CR3/43 | HLA-DP/DQ/DR | Mouse igG1 | Dako, Glostrup, Denmark | 1:800 |
| GFAP | GFAP | Rabbit | Dako, Glostrup, Denmark | 1:3000 |
| C4b | C4b | Rabbit | Abcam, Cambridge, UK | 1:1600 |

Table S2. Individual case details

| Case # | Group | CDR [23] | Sex | Onset age (yrs) | Disease duration (yrs) | Age † (yrs) | Cause † |
|--------|---------------------|----------|-----|-----------------|------------------------|-------------|--------------------------|
| 1 | Control | 0 | M | NA | NA | 68 | Euthanasia |
| 2 | Control | 0 | F | NA | NA | 63 | Euthanasia |
| 3 | Control | 0 | F | NA | NA | 72 | Heart failure |
| 4 | Control | 0 | F | NA | NA | 69 | Pulmonary embolism |
| 5 | Control | 0 | M | NA | NA | 59 | Euthanasia |
| 6 | Control | 0 | M | NA | NA | 77 | Pneumonia |
| 7 | Control | 0 | F | NA | NA | 78 | Unknown |
| 8 | Control | 0 | F | NA | NA | 59 | Euthanasia |
| 9 | Control | 0 | F | NA | NA | 71 | Lung carcinoma |
| 10 | Control | 0 | M | NA | NA | 74 | Euthanasia |
| 11 | Typical AD | 2 | M | 58 | 2 | 60 | Euthanasia |
| 12 | Typical AD | 3 | M | 62 | 6 | 68 | Euthanasia |
| 13 | Typical AD | 3 | M | 58 | 11 | 69 | Respiratory failure |
| 14 | Typical AD | 1 | F | 73 | 7 | 80 | Euthanasia |
| 15 | Typical AD | | M | 48 | 5 | 53 | Palliative sedation |
| 16 | Typical AD | 3 | M | 52 | 12 | 64 | Cachexia and dehydration |
| 17 | Typical AD | | M | | 84 | 84 | Euthanasia |
| 18 | Typical AD | | M | 67 | 10 | 77 | Suicide by drugs |
| 19 | Typical AD | | M | | 65 | 65 | Euthanasia |
| 20 | Typical AD | 1 | M | 71 | 13 | 84 | Euthanasia |
| 21 | Atypical AD; Bv/Dys | 1 | M | 73 | 4 | 77 | Euthanasia |
| 22 | Atypical AD; Bv/Dys | 3 | M | 63 | 10 | 73 | Cachexia and dehydration |
| 23 | Atypical AD; Bv/Dys | 2 | M | | | 59 | Euthanasia |
| 24 | Atypical AD; Bv/Dys | 3 | F | 74 | 4 | 78 | Cachexia and dehydration |
| 25 | Atypical AD; Bv/Dys | 1 | M | 32 | 5 | 37 | Euthanasia |
| 26 | Atypical AD; Bv/Dys | 3 | M | 56 | 3 | 59 | Dysphagia |
| 27 | Atypical AD; PCA | 3 | M | 54 | 8 | 62 | Palliative sedation |
| 28 | Atypical AD; PCA | 3 | M | 58 | 9 | 67 | Cachexia and dehydration |
| 29 | Atypical AD; PCA | 2 | M | 58 | 7 | 65 | Cardiac arrest |

A β amyloid-beta; AD Alzheimer's disease; Amy amygdala; Bv/Dys behavioural/dysexecutive; CAA cerebral amyloid angiopathy; CDR clinical dementia rating scale; F female; LB Lewy body; M male; NA non-applicable; NFT neurofibrillary tangle; PCA posterior cortical atrophy; PMI post mortem interval; † death; # number.

| PMI (hh:mm) | Brain weight (grams) | APOE | ABC [22] | Braak NFT stage [6] | Thal A β phase [39] | CAA- Type [38] | Braak LB [1] |
|----------------|----------------------------|------|----------|------------------------|------------------------------|-------------------|--------------------|
| 08:40 | 1322 | 34 | A1 B1 C0 | I | 2 | 2 | 0 |
| 08:10 | 1269 | NA | A0 B0 C0 | 0 | 0 | 0 | 0 |
| 07:20 | 1205 | 33 | A0 B0 C0 | 0 | 0 | 0 | 0 |
| 13:00 | 1155 | 33 | A1 B1 C0 | I | 1 | 0 | 0 |
| 08:00 | 1322 | 34 | A1 B1 C0 | I | 2 | 0 | 0 |
| 11:40 | 1260 | 23 | A1 B1 C0 | I | 1 | 0 | 0 |
| 10:00 | 1175 | 33 | A1 B1 C0 | I | 1 | 0 | 0 |
| 08:10 | 1145 | 33 | A0 B0 C0 | 0 | 0 | 0 | 0 |
| 06:50 | 1165 | 34 | A1 B1 C0 | I | 2 | 1 | 0 |
| 10:20 | 1245 | 33 | A2 B1 C0 | II | 3 | 0 | 0 |
| 08:35 | 1395 | 33 | A3 B3 C3 | VI | 5 | 1 | 0 |
| 09:15 | 1365 | 33 | A3 B3 C3 | V | 5 | 2 | 0 |
| 11:55 | 1210 | 34 | A3 B3 C3 | V | 5 | 1 | |
| 07:05 | 1007 | 33 | A3 B2 C2 | IV | 5 | 1 | 0 |
| 09:00 | 1505 | 33 | A3 B3 C3 | VI | 5 | 1 | 0 |
| 07:55 | 1236 | 34 | A3 B3 C3 | VI | 5 | 2 | Amy predominant |
| 08:35 | 1212 | 33 | A2 B2 C2 | IV | 3 | na | |
| 09:05 | 1150 | 44 | A3 B3 C3 | VI | 5 | 1 | |
| 09:20 | 1380 | 34 | A3 B3 C3 | V | 5 | 1 | Amy only |
| 05:53 | | 34 | A3 B2 C2 | IV | 5 | 1 | 0 |
| 07:00 | 1318 | 34 | A3 B2 C2 | IV | 5 | 2 | 0 |
| 07:20 | 1175 | 34 | A3 B3 C3 | V | 5 | 1 | 5 |
| 06:30 | 1305 | 44 | A3 B3 C3 | V | 5 | 1 | 5 |
| 07:30 | 1040 | 34 | A3 B3 C3 | V | 5 | 1 | 3 |
| 11:11 | 1545 | 23 | A3 B3 C3 | VI | 5 | 1 | Amy only |
| 05:35 | 1236 | 34 | A3 B3 C3 | V | 5 | 1 | |
| 08:15 | 1105 | 34 | A3 B3 C3 | VI | 5 | 1 | 0 |
| 06:35 | 1250 | 34 | A3 B3 C3 | VI | 5 | 1 | 0 |
| 07:50 | 1305 | 33 | A3 B3 C3 | V | 4 | 1 | 0 |

Section 3

Heterogeneity in Alzheimer's disease
pathology: A β deposit diversity

Chapter 4

The coarse-grained plaque: a divergent A β plaque-type in early-onset Alzheimer's disease

Baayla DC Boon, Marjolein Bulk, Allert J Jonker, Tjado HJ Morrema, Emma van den Berg, Marko Popovic, Jochen Walter, Sathish Kumar, Sven J van der Lee, Henne Holstege, Xiaoyue Zhu, William E Van Nostrand, Remco Natté, Louise van der Weerd, Femke H Bouwman, Wilma DJ van de Berg, Annemieke JM Rozemuller*, Jeroen JM Hoozemans*

Acta Neuropathologica (2020)
doi: 10.1007/s00401-020-02198-8

* Authors contributed equally

ABSTRACT

Alzheimer's disease (AD) is characterized by amyloid-beta ($A\beta$) deposits, which come in myriad morphologies with varying clinical relevance. Previously, we observed an atypical $A\beta$ deposit, referred to as the coarse-grained plaque. In this study, we evaluate the plaque's association with clinical disease and perform in-depth immunohistochemical and morphological characterization. The coarse-grained plaque, a relatively large ($\varnothing \approx 80 \mu\text{m}$) deposit, characterized as having multiple cores and $A\beta$ -devoid pores, was prominent in the neocortex. The plaque was semi-quantitatively scored in the middle frontal gyrus of $A\beta$ -positive cases ($N = 74$), including non-demented cases ($n = 15$), early-onset (EO)AD ($n = 38$), and late-onset (LO)AD cases ($n = 21$). The coarse-grained plaque was only observed in cases with clinical dementia and more frequently present in EOAD compared to LOAD. This plaque was associated with a homozygous *APOE* $\epsilon 4$ status and cerebral amyloid angiopathy (CAA). In-depth characterization was done by studying the coarse-grained plaque's neuritic component (pTau, APP, PrP^C), $A\beta$ isoform composition ($A\beta_{40}$, $A\beta_{42}$, $A\beta_{N3pE}$, pSer8A β), its neuroinflammatory component (C4b, CD68, MHC-II, GFAP), and its vascular attribution (laminin, collagen IV, norrin). The plaque was compared to the classic cored plaque, cotton wool plaque, and CAA. Similar to CAA but different from classic cored plaques, the coarse-grained plaque was predominantly composed of $A\beta_{40}$. Furthermore, the coarse-grained plaque was distinctly associated with both intense neuroinflammation and vascular (capillary) pathology. Confocal laser scanning microscopy (CLSM) and 3D analysis revealed for most coarse-grained plaques a particular $A\beta_{40}$ shell structure and a direct relation with vessels. Based on its morphological and biochemical characteristics, we conclude that the coarse-grained plaque is a divergent $A\beta$ plaque-type associated with EOAD. Differences in $A\beta$ processing and aggregation, neuroinflammatory response, and vascular clearance may presumably underlie the difference between coarse-grained plaques and other $A\beta$ deposits. Disentangling specific $A\beta$ deposits between AD subgroups may be important in the search for disease-mechanistic-based therapies.

INTRODUCTION

Amyloid-beta ($A\beta$) plaques and hyperphosphorylated tau (pTau) tangles are the main pathological hallmarks of Alzheimer's disease (AD). $A\beta$ plaques originate from the accumulation and aggregation of the $A\beta$ peptide, which is formed by the sequential cleavage of the amyloid precursor protein (APP) by β - and γ -secretases [22]. Depending on the cleavage site of γ -secretase, the $A\beta$ peptide length may vary from 36 to 43 amino acids, with $A\beta_{40}$ and $A\beta_{42}$ being the most common forms found in AD. The longer $A\beta_{42}$ is more prone to aggregate and is predominantly found in parenchymal plaques, whereas the shorter $A\beta_{40}$ is secreted by cells in higher levels and is the major $A\beta$ isoform deposited in the cerebral vasculature, referred to as cerebral amyloid angiopathy (CAA) [5, 6, 29]. The $A\beta$ peptide can undergo several post-translational modifications resulting e.g., in truncated pyroglutamate $A\beta$ ($A\beta_{N3pE}$) and $A\beta$ phosphorylated at serine 8 (pSer8 $A\beta$) [31–33]. These different $A\beta$ isoforms are associated with clinical disease progression and are considered to mark sequential phases of plaque and CAA maturation [21, 44, 53].

Since the first description of AD, many different types of amyloid deposits have been described, which vary in their association with clinical symptoms [18, 19, 40, 49, 50]. The currently used categorization scheme for both cerebral parenchymal and vascular $A\beta$ deposits, referred to as plaques and CAA respectively, are both described by Thal et al. [49, 50]. The first categorization step for plaques is based on their fibril content, since the fibrillar type is better associated with clinical dementia than the non-fibrillar type [11, 45]. Fibrillar plaques can range in size from 30 to 100 μm cross-sectionally and contain $A\beta$ in a β -pleated sheet secondary conformation, also referred to as amyloid. Amyloid plaques are further ordered into compact or cored-only plaques, and classic cored plaques [16, 49]. Non-fibrillar or better known as diffuse plaques, can range from 10 to $> 100 \mu\text{m}$ cross-sectionally with a great variation in morphology [49]. Contrary to fibrillar plaques, diffuse plaques are often present in cases without cognitive impairment [3, 12, 41]. The next categorization step is the presence of a neuritic component. A plaque is considered neuritic when the focal $A\beta$ deposit contains degenerating axons and dendrites referred to as dystrophic neurites. The load of these neuritic plaques in the neocortex correlates well with clinical disease severity [35]. Besides the common plaque variants, more rare plaque-types such as the cotton wool plaque are described. These plaques are clinically relevant as, although reported in a few sporadic cases, they are predominantly described in patients with specific *PSEN1* mutations [10, 48]. For vascular $A\beta$ deposits, CAA

is categorized as either CAA-Type 1 involving cortical capillaries in addition to leptomenigeal and cortical arteries and arterioles, and CAA-Type 2 not involving cortical capillaries [50].

We recently observed a plaque morphology that did not fit the afore mentioned descriptions [7]. Comparing AD related pathology in a small cohort of different AD subtypes, we observed a relatively large plaque with a coarse-grained structure using anti-A β immunostaining. According to our knowledge, these coarse-grained plaques have not yet been well-described. In the current study, we describe the coarse-grained plaque and investigate its presence in a cohort ($N = 74$) of EOAD, LOAD, and A β -positive non-demented cases. We further characterize the coarse-grained plaque by comparing it to other clinically relevant A β deposits, being the classic cored plaque, the cotton wool plaque, and CAA-Type 1. CLSM was used to image the coarse-grained plaque in 3D.

METHODS

Post mortem brain tissue

Post mortem brain tissue was obtained from the Netherlands Brain Bank (NBB; Amsterdam, the Netherlands, <https://www.brainbank.nl>) and the Normal Aging Brain Collection (NABCA; Amsterdam UMC - location VUmc, Amsterdam, The Netherlands, <http://nabca.eu>). In compliance with all ethical standards, brain donors signed informed consent regarding the usage of their brain tissue and clinical records for research purposes. The local medical ethics committee of the VUmc approved the brain donor programs of the NBB and NABCA. Brain dissection and neuropathological diagnosis were performed according to international guidelines of Brain Net Europe II (BNE) consortium (<http://www.brainnet-europe.org>) and NIA-AA [36]. A β -positive cases were selected if cognitive decline was not reported during life, A β deposits were present in the brain, i.e., A β -positive, and total AD neuropathologic score according to the NIA-AA was 'low' [36]. A β -positive cases were age- and sex-matched to LOAD cases. AD cases were selected based on dementia diagnosis during life in combination with an intermediate or high score for AD pathology [36]. This resulted in a cohort of 15 A β -positive cases, 38 EOAD -, and 21 LOAD cases. Additional cases, containing cotton wool plaques ($n = 4$) and CAA-Type 1 ($n = 3$) were included for the comparison to different types of A β deposits. For all cases, Thal phase for A β [52], Braak stage for neurofibrillary tangles [8], Thal stage for CAA [51] and concomitant pathologies i.e., Lewy bodies [1], TDP43 pathology [37], and vascular lesions were reported when the respective assessment was

readily available from the brain bank (for case details see Supplementary Table S1, online resource).

Formalin (4%) -fixed paraffin-embedded (FFPE) tissue blocks of the right middle frontal gyrus were used. In addition, for 14 cases (Supplementary Table S1, online resource) also FFPE blocks of the right temporal -, parietal -, occipital-, olfactory cortex, pre- and postcentral gyrus, amygdala, hippocampus (including CA1-CA4, dentate gyrus, subiculum, and entorhinal cortex), caudate nucleus, putamen, substantia nigra, locus coeruleus, pons, medulla oblongata, and cerebellum were used. For 1 of 4 cotton wool cases, the superior parietal lobule region was included due to tissue region availability within the NBB. For CAA-Type 1 comparison, the occipital cortex was used, as this region is most prone to CAA pathology [6]. FFPE tissue was cut at 6 μm thickness for immunohistochemistry and at 5 μm thickness for multi-label immunofluorescence. Formalin-fixed free-floating (FFFF) (4% formalin; for 24-36 hours) tissue from the left middle frontal gyrus of 5 AD cases (Supplementary Table 1, online resource) was used for 3D multi-label immunofluorescence confocal imaging. FFFF tissue was put on sucrose (15%; 30%) for cryopreservation, stored at -80°C and cut on a sliding microtome in 60 mm-thick sections.

Genotyping

DNA was extracted from blood or brain tissue and apolipoprotein E genotype (*APOE*) was determined for 72 of 74 cases and 3 of 4 cotton wool cases using methods previously described (Supplementary Table S1, online resource) [20]. Whole-exome sequencing (WES) was performed for 64 of 74 cases and for 3 of 4 cotton wool cases. For WES, exome-DNA was captured using the SeqCap EZ Human Exome Library v3.0 capture Kit or the Agilent SureSelect V6 kit (58M); 150bp paired-end reads were generated on the Illumina platform, with a mean depth of coverage of at least 30x across exons. We performed in house alignment and quality control. The exomes of the genes *APP* (NM_000484.3), *PSEN1* (NM_000021.3), and *PSEN2* (NM_000447.2) were analyzed for likely pathogenic (class 4) or pathogenic (class 5) variants according to variant classification consensus guidelines [43]. Known pathogenic mutations are reported (Supplementary Table S1, online resource).

(Immuno)histochemistry

(Immuno)histochemistry was performed on sequential sections for hematoxylin and eosin (H&E), Congo red, $\text{A}\beta$ (aa 8-17), $\text{A}\beta_{40}$, $\text{A}\beta_{42}$, $\text{A}\beta_{\text{N3pE}}$, pSer8A β , APP, PrP^C, pTau, C4b, MHC-II, GFAP, norrin, laminin, collagen IV, and ApoE (see

Supplementary Table S2 for antibody - and staining specifics, online resource). After deparaffinization, (immuno)histochemistry was performed according to the following protocols. H&E was performed by submerging sections in hematoxylin (5 min), followed by submerging in eosin (3 min). Histochemistry for Congo red was performed by incubation with a saturated sodium chloride solution (3% NaCl in 80% ethanol and 1% 1M NaOH) followed by incubation with a saturated Congo red solution (0.25% Congo red in 80% ethanol and 1% 1M NaOH), both for 20 min at room temperature. Endogenous peroxidase was quenched using 0.3% H₂O₂ in either phosphate buffered saline (PBS; pH 7.4) or methanol. This was followed by the appropriate antigen retrieval and primary antibody incubation. Subsequently, sections were incubated with a secondary antibody, followed by color development using 3,3'-diaminobenzidine (DAB) (Agilent-Dako) and counterstained using hematoxylin. In between steps, sections were rinsed in PBS. Finally, sections were mounted with Quick-D (Klinipath) or Entellan (Sigma-Aldrich) and coverslipped. The omission of primary antibodies was used as negative control.

Multi-label immunofluorescence

Multi-labeling on 5 µm sections was performed on case #18, 32, 35, 39, 56, 64, 68, and all cotton wool cases (#75, 76, 77, 78) for neuroinflammatory markers and vascular-associated markers. Double-labeling for Aβ₄₀ and Aβ₄₂ was in addition to the above-mentioned cases, also performed on case #79, 80, 81. See Supplementary Table S2, online resource, for antibody and staining details. After deparaffinization, sections stained for markers reflecting neuroinflammation were heated in citrate buffer (pH 6.0) using an autoclave and subsequently incubated overnight with a cocktail of antibodies directed against C4b, CD68, and GFAP. The following day, sections were incubated for 1 h with a cocktail of the appropriate secondary antibodies (dilution 1:250). Antibody retrieval for sections stained for vascular-associated markers entailed submerging sections in Tris-EDTA buffer (pH 9.0) and heating them using an autoclave. Primary antibody incubation was done sequentially, since both primary antibodies for vascular-associated markers were raised in rabbit. First, sections were incubated with anti-laminin overnight, followed by incubation with EnVision (Dako), rinsed in Tris-buffered saline (TBS pH 7.6) and color development by tyramide reagent Alexa 568 (1:100 in 0.0015% H₂O₂ in TBS). Sections were heated in Tris-EDTA buffer using a microwave to ensure primary antibody detachment. Subsequently, sections were incubated with anti-norrin and anti-Aβ aa 1-16 directly labelled Alexa 488. Norrin was visualized by incubating sections for 1 h with secondary antibody goat-anti-rabbit Alexa 647 (dilution 1:250). Multi-label staining for Aβ

isoform staining was performed by submerging sections in 98% formic acid for 5 min, followed by incubation with a cocktail of primary antibodies overnight and secondary antibodies the next day for 1 h. All sections were enclosed with 80% glycerol/20% TBS. In between steps, sections were rinsed in PBS. All antibodies were diluted in normal antibody dilution (ImmunoLogic).

Multi-labeling on 60 μm FFFF sections was performed on case #29, 30, 42, 53, and 74. Sections were stained for neuroinflammatory markers (CD68 and GFAP together with $\text{A}\beta$ aa 1-16), vascular markers (norrin and laminin together with $\text{A}\beta$ aa 1-16), or $\text{A}\beta_{40}$ together with $\text{A}\beta_{42}$ (see Supplementary Table S2, online resource). Antigen retrieval was performed for neuroinflammatory and vascular markers by heating sections in a water bath to 95 °C for 30 min in either citrate buffer (pH 6.0) or Tris-EDTA buffer (pH 9.0). Sections double-labeled for $\text{A}\beta_{40}$ and $\text{A}\beta_{42}$ were submerged in formic acid 99% for 10 min. All sections were rinsed in 2% bovine serum albumin (BSA) in TBS to block non-specific binding sites in the tissue sample and prevent non-specific antibody binding. Since some primary antibodies were raised in the same species, staining for neuroinflammatory and vascular markers was performed for each antigen sequentially using consecutive incubation steps. After the first primary antibody incubation with either anti-CD68 or anti-laminin, sections were incubated with a biotinylated secondary antibody directed against the appropriate species. This was followed by the ABC method and color development using tyramide reagent (Alexa 594 for CD68; Alexa 555 for laminin). Sections were re-heated in the water bath to 95 °C for 30 min to ensure the detachment of the primary antibody. The potential residual primary antibody sites were then blocked by incubation for 1 h with normal serum (2%) of the appropriate species. This was followed by incubation with the next primary antibody (anti-GFAP or anti-norrin) and secondary antibody (goat-anti-chicken Alexa 555 or goat-anti-rabbit Alexa 647). The staining procedure was finalized by incubation with anti- $\text{A}\beta$ aa 1-16 directly labeled Alexa 488. Staining for $\text{A}\beta_{40}$ and $\text{A}\beta_{42}$ was performed using a cocktail of antibodies and visualized with goat-anti-mouse-IgG2 Alexa 488 and goat-anti-mouse-IgG1 Alexa 647. All sections were mounted with 0.3% gelatin in Tris-HCl (0,05 M; pH 7,6), enclosed with Mowiol and DABCO and coverslipped. In between steps, sections were rinsed in TBS. For all multi-labeling experiments, the omission of primary antibodies was used as a negative control and the color development step with tyramide was performed after the detachment step to check if primary antibody detachment was successful.

Confocal imaging

CLSM was performed with a Nikon A1R HD microscope (Nikon, Amsterdam, the Netherlands) using a CFI Plan Achromat λ 100 \times oil, NA 1.45, WD 0.13 objective lens. Scanning was done using galvano with scan size 1024 \times 1024 pixels, pixel size: 0.12 μm , and a pixel dwell time of 1.1 μs . Signal detection was performed using an A1-DUS spectral detector unit. Pinhole size was adjusted per experiment. The pinhole size was set to 57.5 μm for all immunofluorescence stained FFPE sections (5 μm). For FFFF sections (60 μm), the pinhole radius was set to 20.4 μm for $\text{A}\beta_{40}$ and $\text{A}\beta_{42}$ combination, to 66.4 μm for neuroinflammatory marker combination ($\text{A}\beta$, CD68, and GFAP), and to 63.9 μm for vascular marker combination ($\text{A}\beta$, laminin, and norrin). Sections were irradiated with a laser combination of wavelength 488, 514, 594, and 640 nm, depending on fluorochrome combination. FFPE sections (5 μm) were imaged in 2D. For a 3D reconstruction of coarse-grained plaques, z-steps of 0.25 μm were taken during the scanning of FFFF sections. For FFPE sections, no line integration was performed. For FFFF sections, line integration was set to 8 \times for neuroinflammatory marker stained sections, to 4 \times for vascular marker stained sections, and to 4 \times for $\text{A}\beta_{40}$ and $\text{A}\beta_{42}$ stained sections. The spectrum profile of each fluorochrome was acquired from single stains. The autofluorescent spectrum was acquired from negative control sections. Images were spectrally unmixed using the appropriate spectra in the NIS-Elements AR software (Nikon).

3D Image processing and qualitative analysis of coarse-grained plaques

Coarse-grained plaques were selected and subsequently scanned based on their 2D morphology in $\text{A}\beta$ aa 1-16, $\text{A}\beta_{40}$, or norrin staining with the CSLM. In total, 118 plaques were qualitatively analyzed in 5 cases (Supplementary Table S3, online resource). The GFAP - Alexa 555 signal that was used for the neuroinflammation protocol in FFFF sections, decreased along the z-axis due to spherical aberration. This effect was post-imaging corrected in Imaris software (version 9.3.1, Oxford Instruments) by normalizing all layers. Post-imaging processing was performed for all FFFF z-stacks using the denoise.AI algorithm in NIS-Elements imaging software (version 5.20.01, Nikon). Movies were annotated using Adobe After Effects (version 16.1, Adobe Systems Incorporated). All figures were composed using Adobe Photoshop (CS6, Adobe Systems Incorporated).

Semi-quantitative scoring of the coarse-grained plaque

In anti- $\text{A}\beta$ immunohistochemistry, the coarse-grained plaque is defined by its size (30-100 μm), coarse-grainy deposits with multiple intensely stained cores, $\text{A}\beta$ -devoid pores, and an ill-defined border (see Results section). Its presence

was semi-quantitatively scored independently by two assessors (BDCB, MB) after anti-A β (aa 8-17; 6F/3D) staining. The assessors were blinded for group (A β -positive cases, EOAD, or LOAD) during the scoring process. Interrater reliability for the semi-quantitative scoring of the coarse-grained plaque was substantial (Cohen's $\kappa = 0.78$) [9]. The scoring system was comprised of the following 4 categories: 0, no coarse-grained plaques; 1, sparse (> 0 and < 6 coarse-grained plaques per 1 cm²); 2, moderate (≥ 6 and ≤ 30 coarse-grained plaques per 1 cm²); and 3, frequent (>30 coarse-grained plaques per 1 cm²). See Supplementary Fig. S4, online resource, for representative figures per category.

Laser-capture microdissection of coarse-grained plaques for ELISA analysis

Snap-frozen brain tissue of 2 cases with a frequent score for coarse-grained plaques (#18 and 32) was sectioned at 25 μm and mounted on Leica Frame Slides (Leica Microsystems, Danvers, MA, USA). Mounted brain sections were stained with thioflavin S to identify fibrillar amyloid plaques. Per case, a total of 1200 individual coarse-grained amyloid plaques were identified, excised, and captured using a laser-capture microdissection microscope LMD6 (Leica Microsystems) (See Supplementary Fig. S5, online resource, for visualization of plaque laser microdissection). The microdissected plaques were collected into 100 μl of 10 mM sodium phosphate buffer, pH 7.2, containing 0.01% sodium azide.

A β ELISA analysis of captured coarse-grained plaques

For the analysis of A β composition, 10 μl of the collected plaque suspension was added to 90 μl 5M Guanidine HCl, 50 mM Tris-HCl, pH 8.0. The samples were then diluted 1:200 and subjected to sandwich ELISA analysis for the measurement of A β_{40} and A β_{42} peptides as described [13, 30]. Briefly, in the sandwich ELISAs A β_{40} and A β_{42} were captured using their respective carboxyl-terminal specific antibodies mAb2G3 and mAb21F12 and biotinylated m3D6, specific for N-terminus of human A β , was used for detection [30]. Each plaque collection sample was measured in triplicate and compared to linear standard curves generated with known concentrations of human A β_{40} and A β_{42} using a Spectramax M2 plate reader (Molecular Devices, Sunnyvale, CA).

Statistical analysis

Demographics of A β -positive cases, EOAD, and LOAD were compared using Chi square test for categorical data and ANOVA for numerical data. Since A β -positive cases were age- and sex- matched to LOAD, age and sex comparison was only performed for EOAD versus LOAD. Chi square test was performed to study the presence of coarse-grained plaques in relation to group (A β -positive

cases, EOAD, and LOAD), *APOE* $\epsilon 4$ status (non-carrier, $\epsilon 4$ heterozygous, and $\epsilon 4$ homozygous), and CAA-Type (no CAA, CAA-Type 1, and CAA-Type 2). Post-hoc Chi-square test was performed when initial test was significant. A *p*-value of < 0.05 was considered significant. Statistical analysis was performed in IBM SPSS version 22.0.

RESULTS

Description and localization of the coarse-grained plaque

Morphologically the coarse-grained plaque showed a multi-cored, coarse-grainy appearance with pores devoid of $A\beta$ (Fig. 1a). The coarse-grained plaque is usually relatively large, with a diameter (\emptyset) ranging between 50-100 μm . However, smaller variants ($\emptyset \approx 30 \mu\text{m}$) were also observed. Tubular-like or trabecular structures were seen within the plaque. Immunostaining directed against $A\beta$ (aa 8-17; 6F/3D) revealed a somewhat ill-defined plaque border (Fig. 1a; Fig. 3a). The plaques were predominantly found in layers II-IV, but when frequently present also in layers V and VI. The coarse-grained plaques were mostly observed in clusters in the fundi of cortical sulci (Fig. 1b) and near CAA-affected vessels (Fig. 1c). In summary, using anti- $A\beta$ immunohistochemistry the coarse-grained plaque can be distinguished by its size (30-100 μm), coarse-grainy deposits with the appearance of multiple cores, $A\beta$ -devoid pores, and a vague rim. In a subset of cases ($n = 14$) the plaque's presence was scored in 20 brain regions additional to the middle frontal gyrus (Supplementary Fig. S6, online resource). The coarse-grained plaque was predominantly found in the frontal and parietal regions and to a lesser extent also in the temporal and occipital regions of the neocortex. The coarse-grained plaque was moderately observed in the limbic regions, being mostly the olfactory cortex and amygdala and occasionally the hippocampus. The coarse-grained plaque was not observed in the basal ganglia. In one case, a few coarse-grained plaques were observed in the olivary nuclei and in another case one coarse-grained plaque was seen in the cerebellum. Other cases did not show coarse-grained plaques in the brain stem areas or cerebellum.

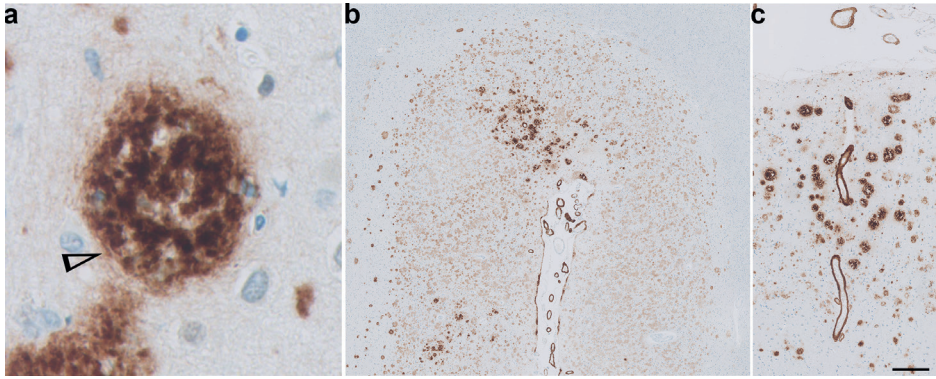


Fig. 1. The coarse-grained plaque and its localization

a The coarse-grained plaque was defined using anti-A β immunohistochemistry (aa 8-17; 6F/3D) by its size (30-100 μ m), coarse-grainy deposits with the appearance of multiple cores, A β -devoid pores, and a vague rim. Tubular-like structures (arrowhead) were seen within the plaque. **b** The coarse-grained plaque was predominantly found in layers II-IV of sulcal fundi and **c** near CAA-affected vessels. Scale bar is applicable to all images and represents 10 μ m in **a**, 400 μ m in **b**, and 200 μ m in **c**. A β amyloid-beta; CAA cerebral amyloid angiopathy.

Clinical relevance of the coarse-grained plaque

Cohort description

We investigated the clinical relevance of the coarse-grained plaque by scoring the plaque in a cohort including EOAD and LOAD cases as well as non-demented A β -positive cases (see Supplementary Table S1, online resource, for individual case details; Table 1 for group demographics; Fig. 2a for coarse-grained plaque scoring results per group). The EOAD group differed from the A β -positive group in their age at death and, as per definition, disease duration and AD pathology. EOAD cases had higher Braak stages for neurofibrillary tangles compared to LOAD cases ($p < 0.01$). Parenchymal CAA was seen in 66% of A β -positive cases, in 100% of EOAD, and in 91% of LOAD. Of the A β -positive cases that were tested for *APOE*, only 31% had an $\epsilon 4$ allele and all $\epsilon 4$ carriers were heterozygous. In the EOAD group 58% of cases was $\epsilon 4$ positive compared to 86% of LOAD cases. The EOAD $\epsilon 4$ positive group consisted of relatively more $\epsilon 4$ homozygous cases (36%) than the LOAD $\epsilon 4$ group (17%). In 5 cases of the EOAD group an autosomal dominant mutation was found in either the *PSEN1* ($n = 4$) or *APP* gene ($n = 1$) (Supplementary Table S1, online resource).

Table 1. Group demographics

| | Aβ-positive cases | EOAD | LOAD |
|---|---|------------------------------|------------------------------|
| | <i>n</i> = 15 | <i>n</i> = 38 | <i>n</i> = 21 |
| Male, <i>n</i> (%) | 8 (53) | 25 (66) | 9 (43) |
| Age of onset | NA | 55 (\pm 8) ^{***} | 76 (\pm 6) ^{***} |
| Disease duration | NA | 10 (\pm 6) ^{***} | 8 (\pm 3) |
| Age at death | 80 (\pm 9) | 65 (\pm 9) ^{***} | 85 (\pm 6) ^{***} |
| ABC [36] | | | |
| A: <i>n</i> per stage 0/1/2/3 | 0/13/2/0 | 0/0/0/38 ^{***} | 0/0/0/21 |
| B: <i>n</i> per stage 0/1/2/3 | 1/11/3/0 | 0/0/0/38 ^{***} | 0/0/4/17 ^{**} |
| C: <i>n</i> per stage 0/1/2/3 | 11/4/0/0 | 0/0/3/35 ^{***} | 0/2/4/15 |
| CAA-Type [51] NA/1/2 | 5/4/6 | 0/25/13 ^{***} | 2/17/2* |
| APOE <i>n</i> per ϵ4^{-/-} / ϵ4^{+/-} / ϵ4^{+/+} | 9/4/0 | 16/14/8 | 3/15/3* |

Data are mean \pm SD; age at onset, disease duration, and age at death shown in years; A β -positive cases were age- and sex-matched to LOAD. Statistical analysis was performed for group differences between A β -positive cases versus EOAD and EOAD versus LOAD using ANOVA for continuous data and (post-hoc) Chi-square test for categorical data. Abbreviations: A β amyloid-beta; EOAD early-onset Alzheimer's disease; LOAD late-onset Alzheimer's disease; NA non-applicable

* $p < 0.05$; ** $p < 0.01$; *** $p < 0.001$.

The coarse-grained plaque is associated with an early disease onset and a homozygous APOE ϵ 4 status

Coarse-grained plaques were not observed in the A β -positive cases (with the exception of 1 coarse-grained plaque in the middle frontal gyrus of case #7). In contrast, the plaque was present in 66% of LOAD and in 95% of EOAD patients (Fig. 2a). Cases with EOAD had more coarse-grained plaques compared to LOAD ($p < 0.01$). Extensive genotyping for (likely) pathogenic mutations in the *APP*, *PSEN1*, and *PSEN2* genes was performed for 64 cases. In 5 genotyped cases with such a mutation, coarse-grained plaques were observed in either a sparse ($n = 2$), moderate ($n = 1$) or frequent ($n = 2$) amount (Supplementary Table S1, online resource). Although coarse-grained plaques were observed in both ϵ 4 carriers and ϵ 4 non-carrier cases AD cases, the plaque was especially prevalent in individuals homozygous for the ϵ 4 allele ($p < 0.01$) (Fig. 2b). Moreover, homozygous carriers of the ϵ 4 allele ($n = 11$; 3 LOAD, 8 EOAD), always showed a moderate to frequent number of coarse-grained plaques.

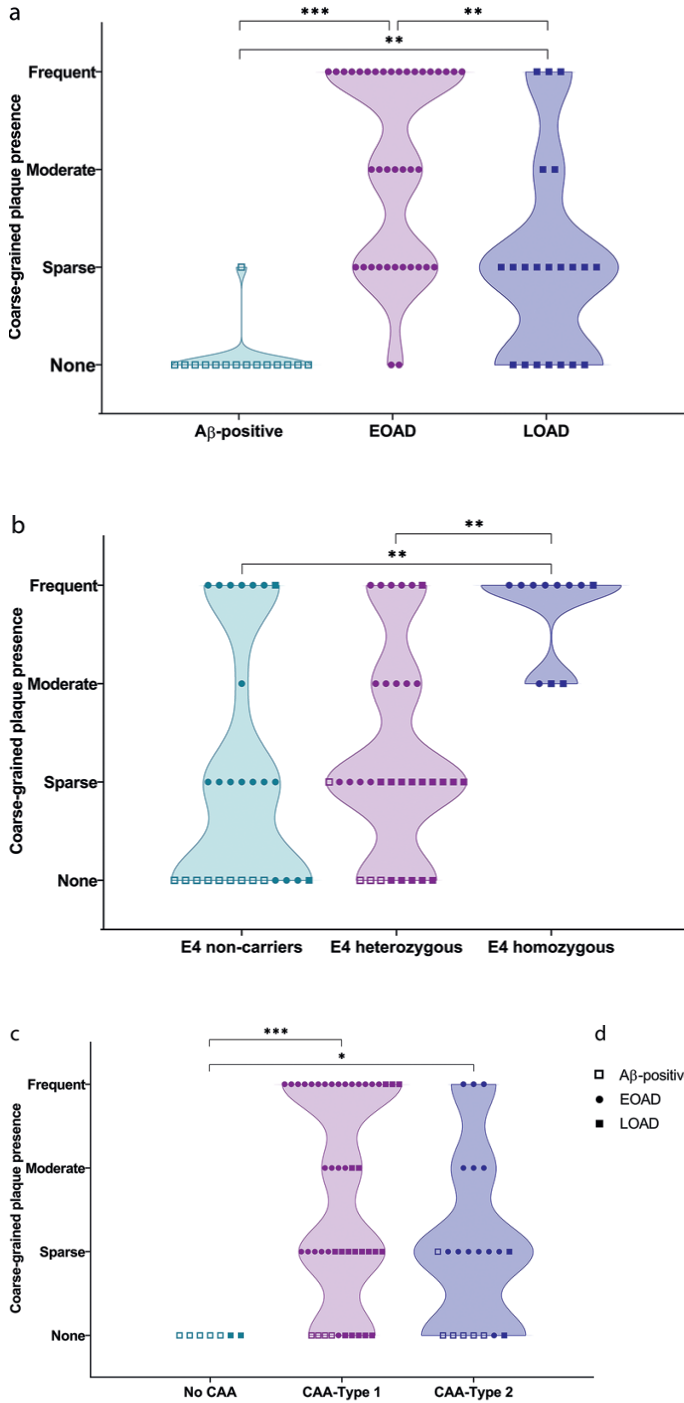


Fig. 2. Clinical relevance of coarse-grained plaques

a Coarse-grained plaques were generally not observed in Aβ-positive non-demented cases, except for 1 coarse-grained plaque in 1 case. Coarse-grained plaques were more frequently seen in EOAD compared to LOAD. **b** The plaque's presence was related to a homozygous APOE ε4 status. APOE status was known for 72 of 74 cases. **c** The coarse-grained plaque was not observed in cases devoid of CAA. **d** Figure legend is applicable to all 3 previous graphs. Aβ amyloid-beta; CAA cerebral amyloid angiopathy; EOAD early-onset Alzheimer's disease; LOAD late-onset Alzheimer's disease. Statistical analysis was performed using (post-hoc) Chi-square test; * $p < 0.05$; ** $p < 0.01$; *** $p < 0.001$.

The coarse-grained plaque is associated with CAA-Type 1

Due to our previous observation that coarse-grained plaques often neighbored CAA-affected vessels, we investigated the co-occurrence of coarse-grained plaques with the presence and type of CAA [50] (Fig. 2c). Note that only 7 cases were devoid of CAA, of which 2 were cases with clinical AD. The coarse-grained plaque was only observed in cases with CAA. A frequent degree of coarse-grained plaques was observed in 47% of cases with CAA-Type 1 and in 14% of cases with CAA-Type 2. The presence of CAA-Type 1 was correlated to the presence of coarse-grained plaques ($p < 0.001$).

In-depth characterization of the coarse-grained plaque

Coarse-grained plaques are different from cotton wool and classic cored plaques

In-depth (immuno)histochemical characterization was performed by comparing the coarse-grained plaque to other clinically relevant plaques, i.e., the cotton wool plaque and the classic cored plaque (Fig. 3, 4, 5, 6, 7, and 8). See Table 2 for a complete summary of each (immuno)histochemical staining per investigated plaque-type. After H&E staining, the coarse-grained plaque showed tissue distortion without a sharply defined outline (Fig. 3b). The plaque contained amyloid fibrils as visualized by Congo red staining (Fig. 3c). Neuropil threads positive for pTau were always observed in and around the coarse-grained plaque (Fig. 3d). Dystrophic neurites positive for pTau were often, but not always visible within coarse-grained plaques. When present, the neurites were relatively less swollen compared to neurites seen in classic cored plaques. Also, the center of the coarse-grained plaque was devoid of pTau staining in the presence of neurites. Of note, all cases with a high load of the coarse-grained plaque in the middle frontal gyrus section showed extensive pTau immunoreactivity. In addition, the coarse-grained plaque was, similarly to the classic cored plaque, immunoreactive for ApoE, APP, and PrP^C (Fig. 4). Immunohistochemical staining confirmed that the coarse-grained plaque was not immunoreactive for PrP^{Sc} (See Supplementary Fig. S7, online resource).

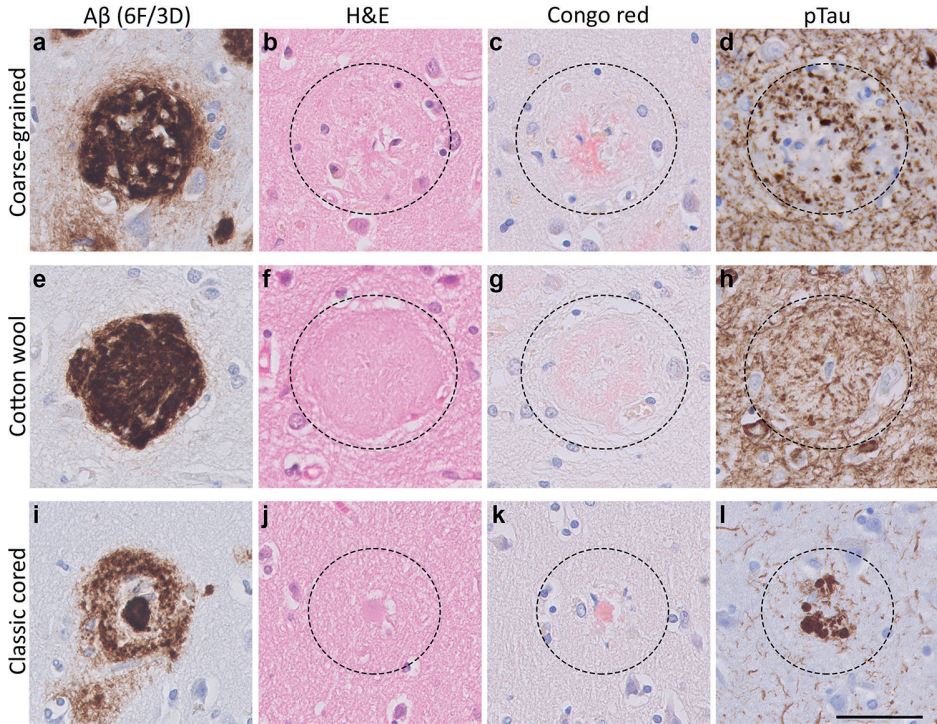


Fig. 3. Histology of the coarse-grained plaque compared to the cotton wool and classic cored plaque

a Anti-A β (6F/3D) staining showed that the coarse-grained plaque is relatively large ($\approx 80 \mu\text{m}$), contains A β -devoid pores, and has an ill-defined border. **b** The plaque showed tissue distortion in H&E. **c** Congo red staining for the coarse-grained plaque demonstrated fibrillar amyloid not condensed in one core. **d** When the coarse-grained plaque contained pTau immunoreactive dystrophic neurites, the plaque-center was often devoid of pTau immunoreactivity. **e, f** The cotton wool plaque showed a distinct circumscribed border in both anti-A β (6F/3D) as well as H&E staining. **g** The cotton wool plaque lacked clear amyloid. **h** Neuritic threads indicated by pTau immunoreactivity, but not dystrophic neurites were seen within the cotton wool plaque. **i** The classic cored plaque demonstrated a central amyloid core, which was surrounded by a corona of non-fibrillar A β . **j, k, l** The central pit in classic cored plaques was visible in H&E as well as Congo red staining and was often surrounded by dystrophic neurites (pTau). Scale bar represents $50 \mu\text{m}$ and is applicable to all images. A β amyloid-beta; H&E hematoxylin-eosin; pTau hyperphosphorylated tau.

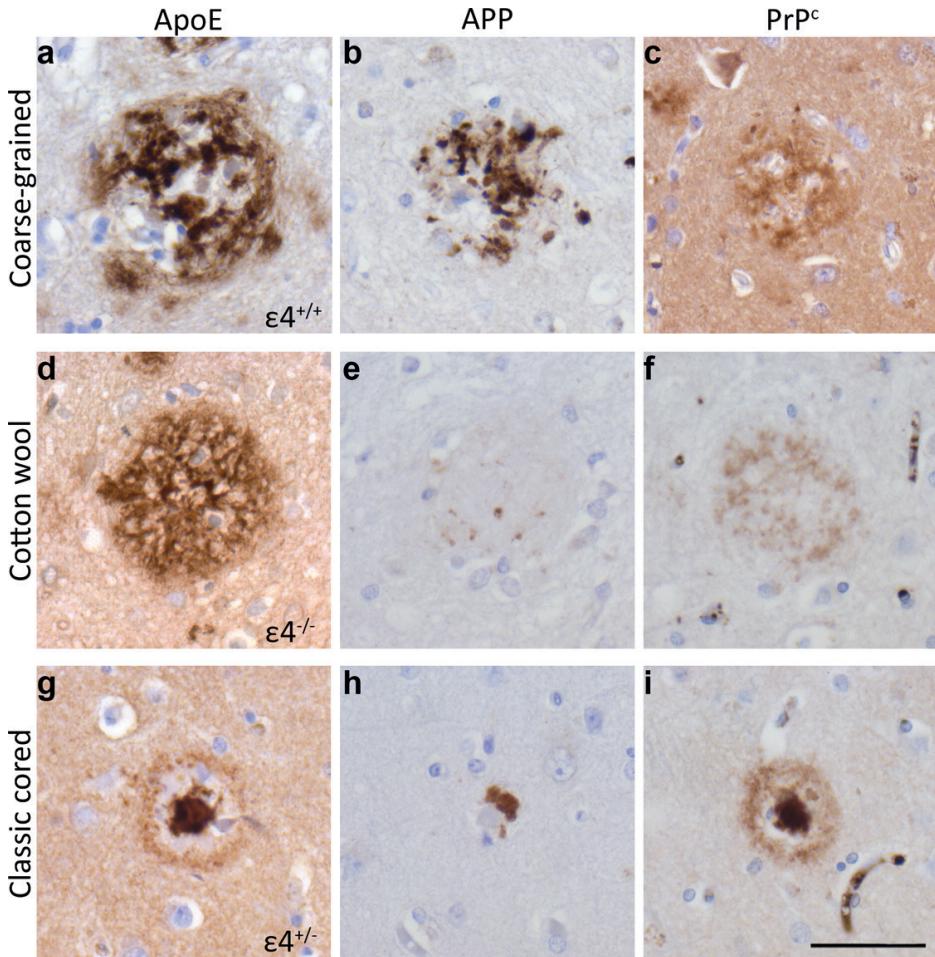


Fig. 4. ApoE, APP, and PrP^C immunoreactivity of the coarse-grained plaque compared to the cotton wool and classic cored plaque

a ApoE was abundantly present all through the coarse-grained plaque. **b** Dystrophic neurites immunoreactive for APP were found throughout the coarse-grained plaque. **c** The coarse-grained plaque was immunoreactive for PrP^C. **d** The cotton wool plaque stained positive for ApoE. **e** APP dystrophic neurites were negligibly visible in the cotton wool plaques. **f** PrP^C was observed in cotton wool plaques. **g** ApoE was found in both the corona and core of the classic cored plaque. ApoE staining intensity was highest in the core. **h** APP dystrophic neurites could be seen surrounding the core of classic cored plaques. **i** The classic cored plaque was immunoreactive for PrP^C. *APOE* genotype of respective case is shown in right lower corner of images of plaques stained for ApoE. Scale bar represents 50 μ m and is applicable to all images. ApoE apolipoprotein E; APP amyloid precursor protein; PrP^C cellular prion protein.

Table 2. Staining summary per plaque-type

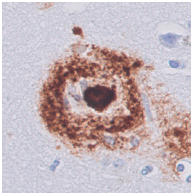
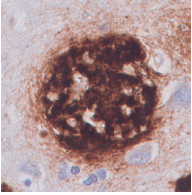
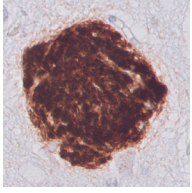
| Staining | The coarse-grained plaque | The cotton wool plaque | The classic cored plaque |
|---|---|---|---|
| Aβ (aa 8-17; 6E/3D) |  |  |  |
| H&E | Tissue distortion | Circumscribed defined patches | Visible core |
| Congo red | ++; fibrillar amyloid throughout the plaque | -; not fibrillar | ++; fibrillar amyloid condensed into a core |
| pTau | ++; neuropil threads +; dystrophic neurites | ++; neuropil threads | +; dystrophic neurites |
| APP | +; dystrophic neurites | - | +; dystrophic neurites |
| ApoE | ++; throughout the plaque | ++; throughout the plaque | ++; in the core; +- in the corona |
| PrP^C | +; throughout the plaque | +; throughout the plaque | ++; in the core; +- in the corona |
| Aβ₄₀ | ++; fibrillary or tubular structures; 61% as shell surrounding the lesser A β ₄₂ | ++; homogenous throughout the plaque | ++; in the core; +- in the corona |
| Aβ₄₂ | +; in the plaque center, sometimes co-localizing with A β ₄₀ | +; outer ring | ++; in both the core and the corona |
| Aβ_{N3pE} | ++ | ++ | ++ |
| pSer8Aβ | ++ | ++; intense stained plaque with diffuse halo | ++ |
| C4b | ++; throughout the plaque | +; outer ring | +; in the core; +- in the corona |
| CD68 | ++; within A β -devoid pores | +; occasionally 1 cell body within the plaque | +; in-between the core and the corona |

Table 2. Continued.

| Staining | The coarse-grained plaque | The cotton wool plaque | The classic cored plaque |
|--------------------|--|---|---|
| MHC-II | ++; within A β -devoid pores | +; occasionally 1 cell body within the plaque | +; in-between the core and the corona |
| GFAP | +; cell bodies are often found within the plaque | +; disrupted processes mostly staining the outer plaque-edges | + |
| Norrin | ++; fibril-like throughout the plaque | ++; homogenous throughout the plaque | - |
| Laminin | +; small punctate dots throughout the plaque | +; as small punctate dots throughout the plaque | +; small punctate dots surrounding the core |
| Collagen IV | - | - | +; small punctate dots surrounding the core |

(Immunohistochemical staining summary per plaque-type is given and indicated as follows: - = no staining; +- = some positive staining; ++ prominent positive staining. See Supplementary Table S1 for antibody and staining details.

The coarse-grained plaque has unique characteristics compared to the cotton wool and classic cored plaque (Fig. 3 a-l). At first sight, the coarse-grained plaque looks similar to the cotton wool plaque due to its size and morphology observed with A β (aa 8-17; 6F/3D) immunostaining. However, the coarse-grained plaque had a less-defined border compared to the distinct circumscribed cotton wool plaque. The cotton wool plaque is visible in both A β (Fig. 3e) and in H&E as cotton wool-like patches (Fig. 3f). Furthermore, the cotton wool plaque is only faintly visible in Congo red (Fig. 3g) and seldom contains dystrophic neurites (Fig. 3h). The coarse-grained plaque also differed from the classic cored plaque (Fig. 3i-l). The most obvious difference is in \emptyset and morphology, while the \emptyset of classic cored plaques is commonly 30-50 μm with a central core surrounded by a corona of diffuse A β , the \emptyset of the coarse-grained plaques is mostly 50-100 μm and lacks this central core. Both plaque types contained fibrillar amyloid and could contain dystrophic neurites. In the classic cored plaque, the swollen dystrophic neurites surround the amyloid that is condensed into a central core. In addition, classic cored plaques are more often observed in the deeper cortical layers (V-VI) than in the more superficial layers [14, 46].

The coarse-grained plaque has a distinct A β isoform composition, being predominantly A β_{40} immunoreactive

The coarse-grained plaque showed strong immunoreactivity for A β_{40} , A $\beta_{\text{N3pE}'}$ and pSer8A β throughout the entire plaque (Fig. 5a, c, d). Interestingly, the coarse-grained plaque showed only little A β_{42} positivity (Fig. 5b). This weak A β_{42} immunoreactivity was observed more in the center than in the periphery of the plaque. Quantitative ELISA on laser-dissected coarse-grained plaques in two cases with a high load confirmed the relatively higher levels of A β_{40} compared to A β_{42} . The coarse-grained plaques in case #18 contained 324.94 pg/ μl of A β_{40} and 13.59 pg/ μl of A β_{42} , making the A β_{40} /A β_{42} ratio = 23.91. The coarse-grained plaques in case #32 contained 264.24 pg/ μl of A β_{40} and 9 pg/ μl of A β_{42} , making the A β_{40} /A β_{42} ratio = 29.36.

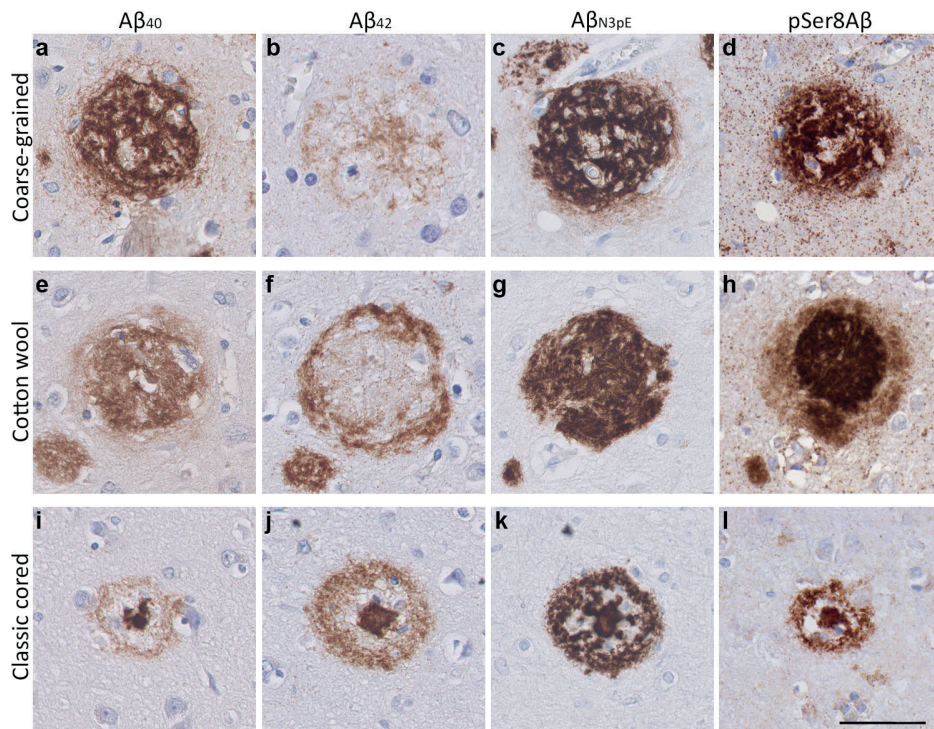


Fig. 5. A β isoform composition of the coarse-grained plaque compared to the cotton wool and classic cored plaque

a, b The coarse-grained plaque was predominantly A β_{40} immunoreactive compared to A β_{42} . **c, d** Strong immunostaining was also seen for A β_{N3pE} and pSer8A β . This A β composition differed from that of the cotton wool plaque (**e-h**) and the classic cored plaque (**i-l**). **e, f** The cotton wool plaque showed a central staining for A β_{40} that was surrounded by an A β_{42} immunoreactive ring. **g, h** The cotton wool plaque was immunoreactive for A β_{N3pE} and displayed a distinct halo immunoreactive for pSer8A β . **i, j** Classic cored plaques were predominantly A β_{42} compared to A β_{40} immunoreactive. **k, l** Both A β_{N3pE} and pSer8A β were detected in the entire classic cored plaque. Scale bar represents 50 μ m and is applicable to all images. A β_{40} amyloid-beta 40; A β_{42} amyloid-beta 42; A β_{N3pE} truncated pyroglutamate A β ; pSer8A β phosphorylated A β at serine 8.

The A β isoforms composition and distribution in the coarse-grained plaque were different from that of other plaques (Fig. 5e-h for the cotton wool plaque and Fig. 5i-l for the classic cored plaque). Similar to the coarse-grained plaque, the cotton wool plaque was predominantly A β_{40} , A β_{N3pE} , and pSer8A β positive. However, in the cotton wool plaque, the A β_{42} was observed as a small outer ring surrounding the A β_{40} -positive center. In the cotton wool plaque, pSer8A β immunoreactivity showed a dense center surrounded by a less prominent halo. A β_{N3pE} distribution in cotton wool plaques was similarly as in coarse-grained

plaques seen throughout the plaque. The difference between the coarse-grained and classic cored plaque was most prominent in their $A\beta_{40}$ and $A\beta_{42}$ composition. The classic cored plaque consisted predominantly of $A\beta_{42}$, which was seen both in the core and corona of the plaque. $A\beta_{40}$ was mostly seen in the core and occasionally little in the corona.

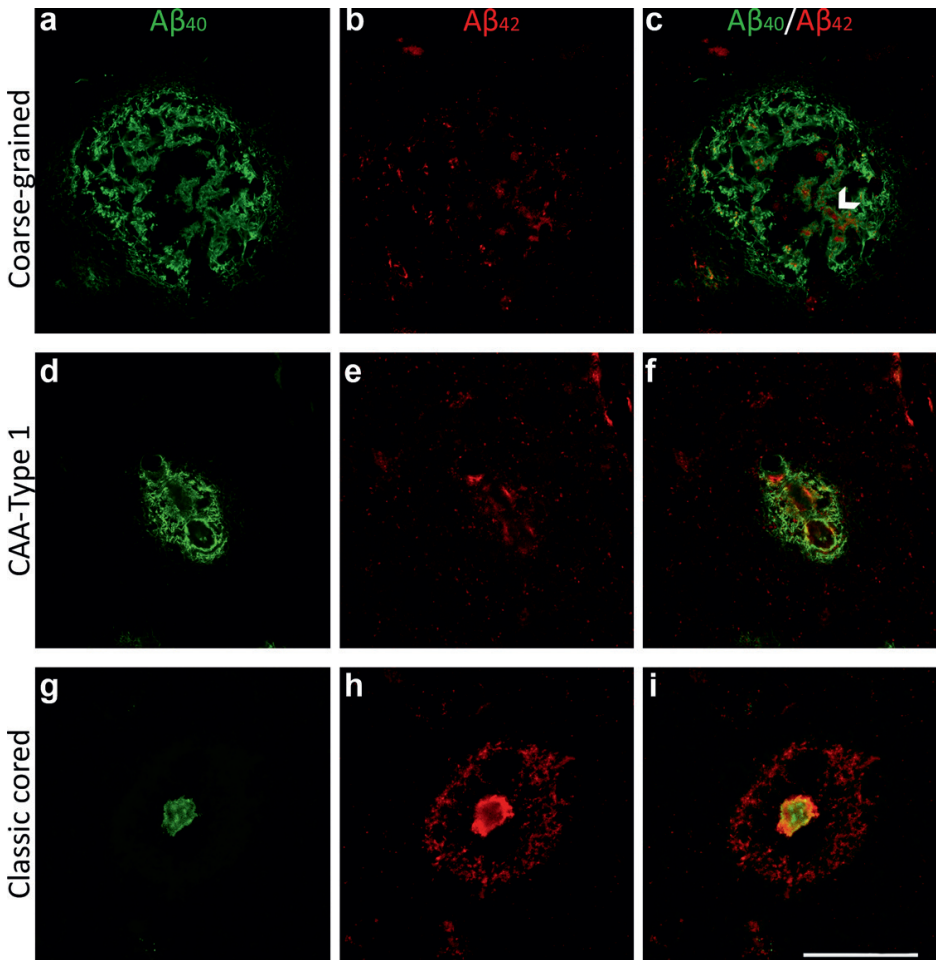


Fig. 6. Immunofluorescence for $A\beta_{40}$ and $A\beta_{42}$ in the coarse-grained plaque compared to CAA-Type 1 and the classic cored plaque

a-c Double immunofluorescence labelling for $A\beta_{40}$ (green) and $A\beta_{42}$ (red) confirmed the $A\beta_{40}$ predominance in coarse-grained plaques. **c** White arrowhead indicates an $A\beta_{40}$ tubular-like structure filled with $A\beta_{42}$. **d-f** CAA-Type 1 showed a similar $A\beta_{40}$ to $A\beta_{42}$ ratio as the coarse-grained plaque. **g-i** Classic cored plaques were predominantly $A\beta_{42}$ immunoreactive. Scale bar represents 50 μm and is applicable to all images. $A\beta_{40}$ amyloid-beta 40; $A\beta_{42}$ amyloid-beta 42; CAA cerebral amyloid angiopathy.

Although the location of coarse-grained plaques is different from that of CAA, we directly compared the $A\beta_{40}$ and $A\beta_{42}$ composition of the coarse-grained plaque to that of CAA due to a similar $A\beta_{40}$ -predominance (Fig. 6). The classic cored plaque was used as a reference for plaque $A\beta$ -isoform composition. In coarse-grained plaques, $A\beta_{40}$ staining was somewhat tubular or trabecular-like. The $A\beta_{40}$ immunoreactive trabeculae occasionally surrounded the rarer $A\beta_{42}$ (Fig. 6c arrowhead). The coarse-grained plaque $A\beta_{40}$ to $A\beta_{42}$ ratio resembled that what is seen in CAA-Type 1, which showed a predominant presence of $A\beta_{40}$ (Fig. 6d-f). As shown earlier, this was quite the opposite from what is seen in classic cored plaques (Fig. 6g-i).

The coarse-grained plaque is associated with intense neuroinflammation and vascular pathology

To study $A\beta$ -related disease mechanisms, immunostainings were performed for neuroinflammatory markers against complement (complement factor C4b), activated microglia (MHC-II / CD68), and reactive astrocytes (GFAP). These well-established markers have been shown to increase with AD pathology and are strongly associated with $A\beta$ deposition [7, 25, 26]. The coarse-grained plaque showed intense immunoreactivity for C4b and activated microglia (Fig. 7a, b). C4b was seen throughout the plaque in a similar pattern as $A\beta$ as observed in our previous study [7]. MHC-II staining showed intense microglial activation covering the complete coarse-grained plaque. GFAP staining indicated the presence of reactive astrocytes around the coarse-grained plaque with mostly disrupted GFAP-positive processes within the plaque (Fig. 7c).

The neuroinflammatory response appeared to be different in the coarse-grained plaque compared to the cotton wool (Fig. 7d-f) or classic cored plaque (Fig. 7g-i). In the cotton wool plaque, C4b (Fig. 7d) showed a ring-like immunostaining resembling the previous mentioned $A\beta_{42}$ staining (Fig. 5f). Microglial activation was negligible and astrocytic processes seemed to encapsulate the cotton wool plaque (Fig. 7e, f, respectively). In the classic cored plaque, C4b was found predominantly in the core and to a lesser extent in the corona and activated microglia were located between the $A\beta$ core and corona. Astrocytic processes in the classic cored plaque seemed less disrupted than in the coarse-grained plaque. In Supplementary Fig. S8, online resource, comparable results for all three plaque-types are shown but then visualized by triple immunofluorescence staining for C4b, CD68, and GFAP.

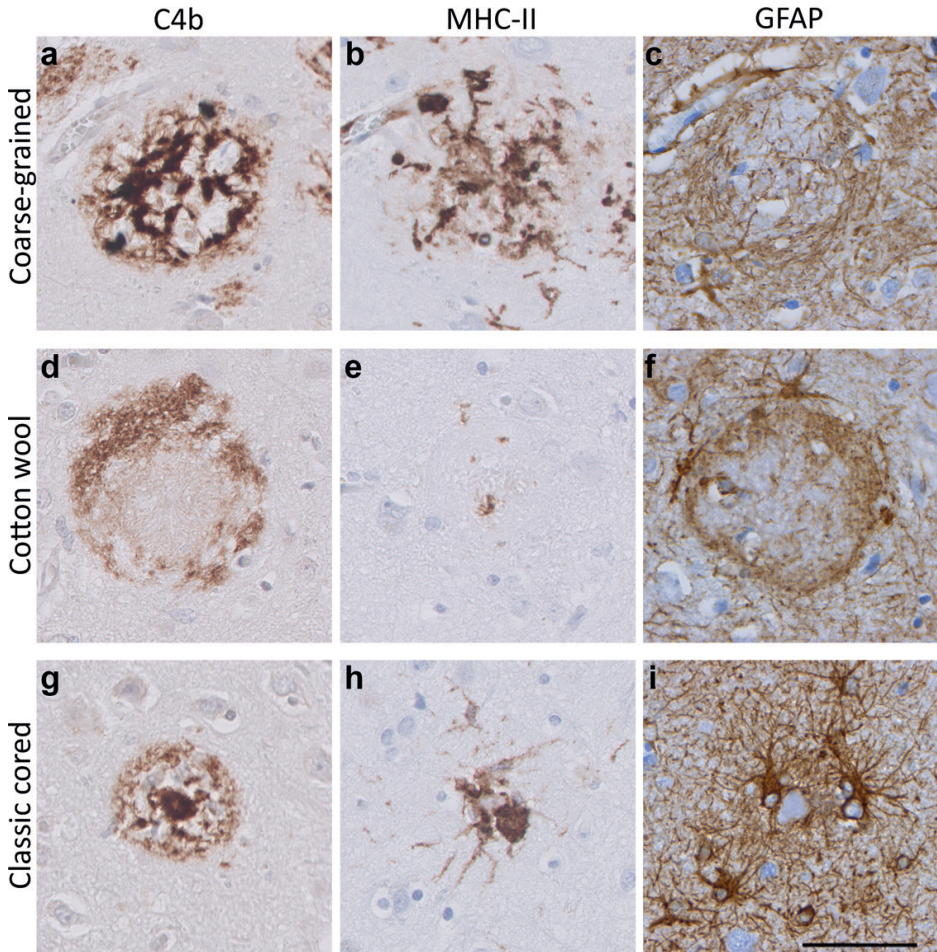


Fig. 7. Neuroinflammatory response in the coarse-grained plaque compared to the cotton wool and classic cored plaque

a, b In the coarse-grained plaque, C4b was seen throughout the plaque with intense MHC-II immunoreactivity. **c** GFAP-positive astrocytes showed disrupted processes. **d-i** C4b, MHC-II, and GFAP showed a different staining pattern in the cotton wool (**d-f**) and classic cored plaque (**g-i**). Scale bar represents 50 μm and is applicable to all images.

To study if the coarse-grained plaque was related to vascular pathology, we immunohistochemically stained sequential sections for $A\beta_{40}$, the capillary-pathology-associated marker norrin [24], and vascular basement membrane markers (laminin and collagen IV [54]) (See Fig.8). The coarse-grained plaque was both $A\beta_{40}$ and norrin positive throughout the entire plaque. Anti-laminin

staining showed small punctate dots in areas where coarse-grained plaques were found in the adjacent section. Collagen IV was not observed in coarse-grained plaques. The same markers were assessed in the cotton wool plaque (Fig. 8e-h) and the classic cored plaque (Fig. 8i-l). The most striking difference was observed after immunostaining for norrin. Although cotton wool plaques also showed norrin immunoreactivity, the staining had a more homogenous appearance than in coarse-grained plaques. Classic cored plaques were not immunoreactive for norrin. All three plaque-types showed a punctate staining for laminin (Fig. 8c, g, k). Whereas in coarse-grained plaques the laminin dots were seen throughout the plaque, in cotton wool plaques the dots were visible at the outer edges and in classic cored plaques the dots surrounded the core. Only in classic cored plaques, collagen IV positivity was sometimes vaguely seen as punctate dots surrounding the core (Fig. 8d, h, l). In Supplementary Fig. S9, online resource, comparable results for all three plaque-types are shown but then visualized by triple immunofluorescence staining for A β aa 1-16, norrin, and laminin.

3D visualization of the coarse-grained plaque

To gain a deeper understanding of the coarse-grained plaque, we scanned the plaque in 3D using high-resolution CLSM in the right middle frontal gyrus of five different cases with coarse-grained plaques (Supplementary Table S1 for case details; Supplementary Table S3 for # plaques per individual case, online resource). The combination of markers that was scanned was (1) A β_{40} & A β_{42} ; (2) A β , CD68, GFAP; (3) A β , norrin, laminin. Important to note for 3D interpretation is that due to fixation and pretreatment the tissue deforms and shrinks, especially in z-direction [15]. As a result, the originally 60 μ m cut FFFF-sections measured after mounting approximately 40 μ m for combination 1 (A β_{40} & A β_{42}) and 30 μ m for combination 2 (A β , CD68, GFAP) and 3 (A β , norrin, laminin). Due to this ‘flattening’ in z-direction, the plaque, which is assumed to be a sphere, appeared as an ovoid.

3D analysis of large coarse-grained plaques reveals an A β_{40} shell structure

A total of 38 coarse-grained plaques stained for A β_{40} & A β_{42} were scanned (see Supplementary Table S3, online resource). 3D CLSM imaging showed that the predominant A β_{40} staining showed a trabecular-like and sometimes tubular-like morphology in the coarse-grained plaque, confirming our 2D observations (Fig. 9 and Supplementary Video S10 and S11, online resource). This trabecular appearance was most prominent at the surface of the plaque. Interestingly, in 61% of all scanned coarse-grained plaques, the A β_{40} formed an outer shell around the lesser A β_{42} (Supplementary Table S3, online resource). This was

especially prominent in the larger coarse-grained plaques ($\varnothing \approx 80 \mu\text{m}$; larger plaque in Fig. 9 and Supplementary Video S10, online resource, and the plaque in Supplementary Video S11, online resource). In the smaller coarse-grained plaques ($\varnothing \approx 50 \mu\text{m}$), the $A\beta$ isoform segregation was less present and $A\beta_{40}$ and $A\beta_{42}$ more often co-localized (smaller plaque in Fig. 9, and Supplementary Video S10, online resource).

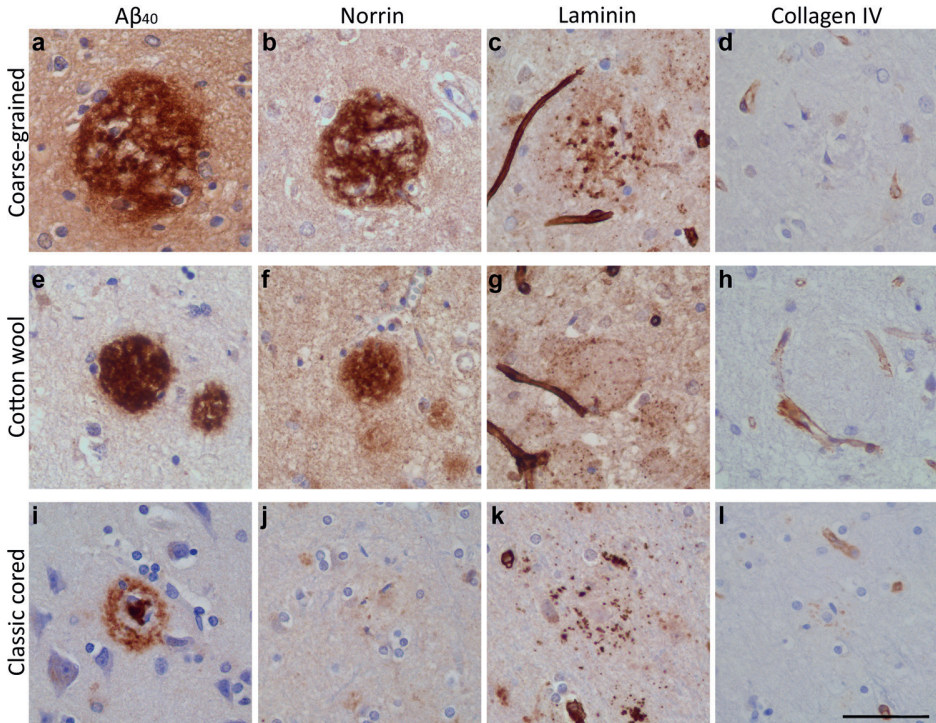


Fig. 8. Vascular association of the coarse-grained plaque compared to the cotton wool and classic cored plaque

a-d The coarse-grained plaque showed immunoreactivity for $A\beta_{40}$, norrin, and laminin but not for collagen IV. **e-h** Although the cotton wool plaque was positive for the same markers, staining morphology differed compared to the coarse-grained plaque. **i-l** The classic cored plaque had an $A\beta_{40}$ positive core, was not immunoreactive for norrin, and showed a punctate staining for both laminin and collagen IV. Scale bar represents $50 \mu\text{m}$ and is applicable to all images. $A\beta_{40}$ amyloid-beta 40.

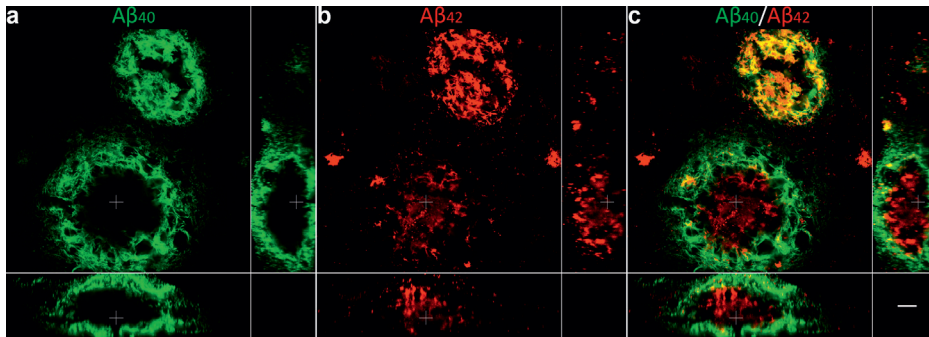


Fig. 9. 3D composition of $A\beta_{40}$ and $A\beta_{42}$ in the coarse-grained plaque

CLSM 3D image of two coarse-grained plaques stained for $A\beta_{40}$ (a; green) and $A\beta_{42}$ (b; red) with $A\beta_{40}/A\beta_{42}$ overlay in c, is shown. In the smaller coarse-grained plaque (upper plaque) $A\beta_{40}$ and $A\beta_{42}$ is co-localized. In the larger coarse-grained plaques (lower plaque) $A\beta_{40}$ showed an outer shell structure, surrounding the lesser present $A\beta_{42}$. White cross in XY indicates the same point in space as the white cross in XZ and YZ. Scale bar represents 10 μm and is applicable to all images. $A\beta_{40}$ amyloid-beta 40; $A\beta_{42}$ amyloid-beta 42; CLSM confocal laser scanning microscopy.

Neuroinflammatory response is seen throughout the coarse-grained plaque

A total of 36 coarse-grained plaques stained for neuroinflammatory markers ($A\beta$, CD68, and GFAP) were scanned (Supplementary Table S3, online resource). Although not all $A\beta$ -devoid pores were filled with CD68 or GFAP, both markers were found throughout the plaque in a rather unorganized manner, confirming our 2D-based observations (Fig. 10 upper row a-d; Supplementary Video S12 and S13, online resource).

3D analysis hints to a vascular component in the coarse-grained plaque

Forty-four coarse-grained plaques stained for vascular markers ($A\beta$, norrin, and laminin) were scanned (Supplementary Table S3, online resource). Based on 2D observations of the plaque's $A\beta_{40}$ and norrin immunoreactivity, the tubular structures, and the association with CAA-affected vessels, we expected CAA vessels to penetrate the coarse-grained plaque in 3D. This was however not observed with CLSM analysis. We did observe that at least 37/44 (84%) of scanned coarse-grained plaques were in direct contact with a vessel (Fig. 10 bottom row e-h; Supplementary Video S14 and S15, online resource). Seven of the 44 scanned plaques were not in direct contact with a vessel. Five of those seven could not be completely scanned in z-direction, and therefore, their potential vessel connection could be missed, making the 84% most likely an underestimation. A little bulge in laminin, possibly reflecting the localization of a pericyte (mean

width $\approx 7 \mu\text{m}$) [4], was often observed where the plaque touched the vessel. Although the touching vessel was not immunoreactive for norrin, norrin positive threads within the plaque were closely connected to the vessel (Supplementary Video S14 and S15, online resource). In addition, similar to what was observed in 2D DAB staining, laminin staining was seen as punctate dots although with lesser intensity.

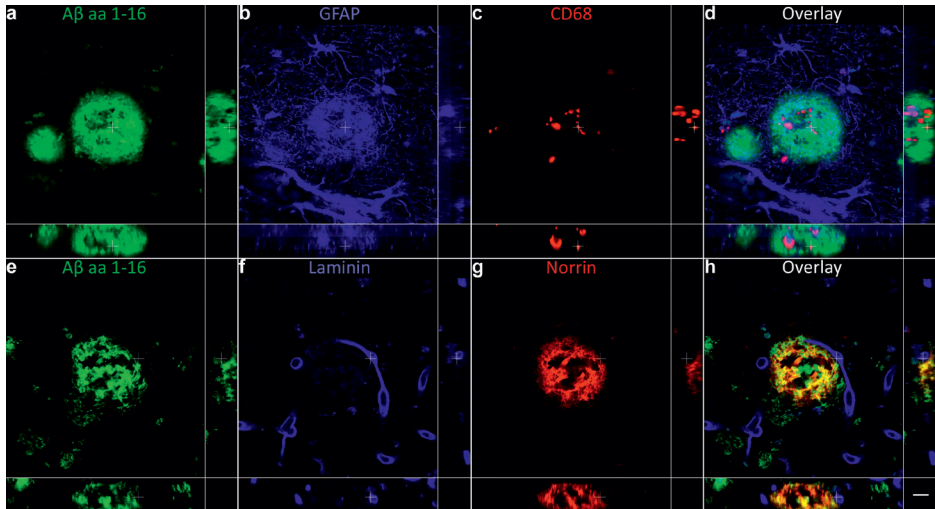


Fig. 10. 3D composition of neuroinflammation and vascular attribution in the coarse-grained plaque.

Representative CLSM 3D images are shown for neuroinflammation (**top row**) and vascular attribution (**bottom row**) in and near the coarse-grained plaque. White cross in XY indicates the same point in space as the white cross in XZ and YZ. Scale bar represents $10 \mu\text{m}$ and is applicable to all images. A β amyloid-beta; CLSM confocal laser scanning microscopy.

DISCUSSION

In this study we defined a divergent plaque-type, called the coarse-grained plaque, with distinct characteristics compared to earlier described plaques. Using anti-A β immunostaining, the coarse-grained plaque was defined by its size ($30\text{-}100 \mu\text{m}$), multi-cored coarse-grainy appearance, A β -devoid pores, and an ill-defined border. Increased presence of the coarse-grained plaque was related to an early disease onset in AD, a homozygous *APOE* $\epsilon 4$ status, and CAA-Type 1. The coarse-grained plaque was not observed in A β -positive clinically non-demented cases. Together, these results highlight the association of this plaque-type with the clinical manifestation of AD. In-depth characterization revealed

that the plaque contains fibrillar amyloid, was mostly composed of $A\beta_{40}$ and showed strong immunoreactivity for neuroinflammation- as well as vascular pathology-associated markers. In-depth 3D assessment exposed an $A\beta_{40}$ shell structure in the larger coarse-grained plaques and a direct vascular connection.

Based on the plaque's characteristics observed in this study, we hypothesize that the coarse-grained plaque evolves at the parenchymal border of the capillary blood-brain barrier as illustrated in Fig. 11. To discuss the placement of the coarse-grained plaque, we made a direct comparison with the classic cored plaque and CAA-Type 1 as a reference for parenchymal and vascular deposited $A\beta$, respectively. In the classic cored plaques predominant $A\beta_{42}$ precipitates, after neuronal excretion, in the brain parenchyma, most likely due to the increased aggregation properties and decreased drainage of $A\beta_{42}$ compared to $A\beta_{40}$ [29]. The aggregated $A\beta$ becomes increasingly fibrillar and is then associated with complement factors, reactive astrocytes, and activated microglia [7, 17, 27, 55]. Dystrophic neurites immunoreactive for APP or pTau can be observed near the amyloid containing aggregates [16]. In case of CAA, the excessive $A\beta$ is also produced neuronally [23]. However, the excreted $A\beta$ than consists mainly of $A\beta_{40}$ which is hypothesized to travel further than the plaque-associated $A\beta_{42}$ due to increased solubility and only aggregates once it reaches the (peri) vasculair drainage system [23]. The complement cascade becomes also activated and dystrophic neurites can be found surrounding the congophilic vessels [38, 39, 56]. However, different from plaques, microglial and macrophage activity markers in CAA do not seem to be increased compared to control vessels [56]. Only when $A\beta$ is found to be dyshoric, meaning the $A\beta$ is deposited in the parenchyma around the amyloid-laden vessel, microglia activation is present in CAA [42]. When CAA is located in the capillaries, referred to as CAA-Type 1, the vessels are immunoreactive for the norrin protein [24]. We placed the coarse-grained plaque between the classic cored plaque and CAA-Type 1, since it showed similarities and differences with both types of $A\beta$ deposits. Similar to the classic cored plaque, the coarse-grained plaque is localized within the brain parenchyma and is immunoreactive for complement and associated with activated microglia and astrocytes [7]. The amyloid structure of the coarse-grained plaque most likely favours a strong binding and activation of complement factors, which in turn could act as opsonins for phagocytosis carried out by microglia [34, 47, 57]. APP and PrP^C immunoreactivity in the coarse-grained plaque could reflect dystrophic neurites, indicating damage to the surrounding axons. Similar to CAA-Type 1, the coarse-grained plaque mainly consists of $A\beta_{40}$ and is immunoreactive for norrin [6, 24]. Different to CAA, the

vascular morphology in coarse-grained plaques is not so obvious. However, using anti-A β immunostaining we did observe tubular-like structures in the coarse-grained plaque. Together with the dot-like laminin immunoreactivity, we speculate these tubular structures to be vascular remnants with the laminin representing the collapsed vascular basement membrane. Furthermore, the coarse-grained plaque was predominantly observed in sulcal fundi, in which the vascular density is higher than in gyral crowns [2]. Although CAA-affected vessels were often noted in the proximity of coarse-grained plaques and most coarse-grained plaques were in direct contact with a vessel, these vessels were not affected by CAA nor did they penetrate the plaque. For these reasons, we assume that the A β aggregation in coarse-grained plaque does not start within the vessel wall as in CAA, but rather starts at the parenchymal border of the capillary blood-brain barrier, which is similar to the location of dyschoric A β in CAA-Type 1. Why the A β_{40} in case of CAA is capable of crossing the blood brain barrier and in case of the coarse-grained plaque is not, remains elusive. The observed A β_{40} shell structure surrounding the lesser A β_{42} in larger coarse-grained plaques is remarkable. Although we are unsure of the essence of the shell structure, we hypothesize it to be related to the aggregation properties and the development of the coarse-grained plaque.

Similar amyloid plaque structures as what we define here as the coarse-grained plaque have sporadically been described by others. The coarse-grained plaque is comparable to the previously described 'fibrous' or 'fibrillar' plaque described by Schmidt et al. and Dickson & Vickers, respectively [14, 46]. Although studied in a small cohort, both groups show that this type of plaque is associated with clinical symptoms of dementia, which is in line with our results. This association was not found for the classic cored plaque, since this plaque was also observed in cases without clinical symptoms [14]. Furthermore, Schmidt et al. concluded that these fibrous - or what we deemed 'coarse-grained' - plaques are rare in AD, but are particular common in Down syndrome cases with AD pathology [46]. With a mean age of death at 78 years, it is most likely that the AD cohort studied by Schmidt et al. mainly consisted of LOAD cases. After the reported observation 25 years ago, the coarse-grained plaque escaped attention and was not included in the currently most used plaque categorization scheme [49, 52]. To our knowledge, we are the first to perform such in-depth characterization for the coarse-grained plaque and to report that this plaque is especially prominent in EOAD.

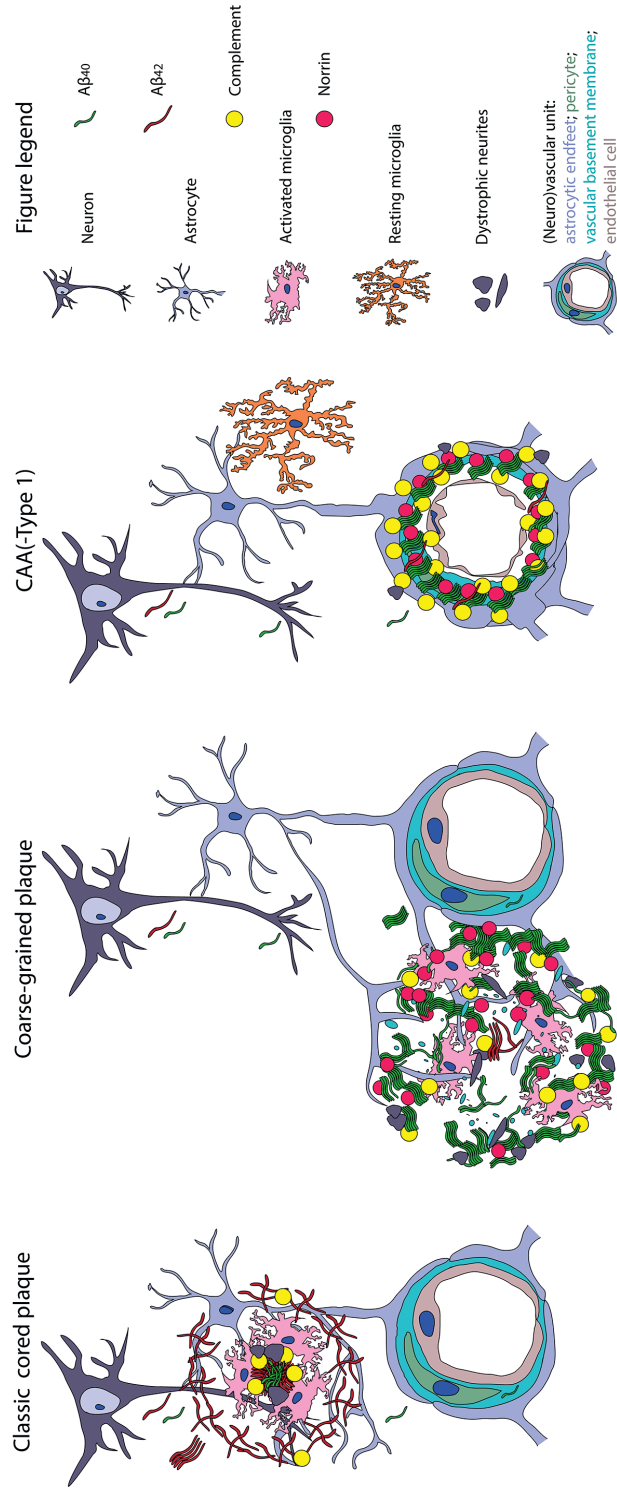


Fig. 11. Hypothetical illustration of the coarse-grained plaque's origin. This figure illustrates the coarse-grained plaques' similarities and differences with the two other forms of A β deposits, being parenchymal plaques illustrated by the classic cored plaque and vascular-located A β illustrated by CAA. We placed the coarse-grained plaque in-between parenchymal and vascular aggregates, based on its parenchymal perivascular localization, microglial activation, A β_{40} predominance, and norrin immunoreactivity. See Discussion section for explanation. A β amyloid-beta; A β_{40} amyloid-beta 40; A β_{42} amyloid-beta 42; CAA cerebral amyloid angiopathy.

As A β pathology starts long before clinical symptoms arise and comes in a myriad of different morphologies [28, 49], it is important to study A β deposits that are clinically relevant. The fact that coarse-grained plaques were only observed in cases with clinical symptoms of AD and not in non-demented A β -positive cases, indicates the clinical relevance of this plaque type. In addition, the coarse-grained plaque contains A β isoforms that correlate with clinical disease progression. Previously, Upadhya et al. showed that both A β_{42} and A β_{40} was detected in brain homogenates of A β -positive but cognitively-healthy cases [44]. In cases with pre-clinical AD, A β_{N3pE} was also detectable, while pSer8A β was only detected in cases with clinical dementia due to AD. The immunoreactivity of the coarse-grained plaque for pSer8A β is in line with the observation that this plaque is only seen in clinically demented cases. This could be a relevant finding for exploring biomarkers reflecting specific A β deposits that could distinguish between clinical subgroups in AD.

As EOAD cases are likely to be genetically predisposed, the occurrence of the coarse-grained plaque could be related to genetic factors. However, extensive genetic screening for the known mendelian mutations in *APP*, *PSEN1*, and *PSEN2* for AD could not link the coarse-grained plaque to the functional impairment in one of those genes such as found for the cotton wool plaque, which is linked to an exon 9 deletion in the *PSEN1* gene [10]. We did observe an association with the most prevalent genetic risk factor for AD, being *APOE* $\epsilon 4$. Interestingly, mice transgenic for human *APOE* $\epsilon 4$ and a familial *APP* mutation (E4FAD mice) show both larger plaques and increased neuroinflammation compared to *APOE* $\epsilon 4$ negative FAD mice [2]. Although at first sight the plaques stained with thioflavin S in E4FAD mice may resemble the coarse-grained plaque, the mouse plaques are predominantly A β_{42} positive, which is an important difference with our coarse-grained plaque. In our view it is too soon to draw any conclusions on the functional correlation with *APOE* $\epsilon 4$, especially since at least one third of the cases with a frequent degree of coarse-grained plaques lacked any $\epsilon 4$ allele. This makes it most likely that besides *APOE* also other (genetic) factors come into play. Since the coarse-grained plaque was more prevalent in EOAD than in LOAD, the plaque is likely to be genetically predisposed. Therefore, it would be interesting for future studies to investigate whether we can identify additional genetic mutations or variants in individuals with coarse-grained plaques.

Some limitations may apply to this work. We are well aware that post mortem studies are cross-sectional, making our hypothesis on plaque-development speculative. It would be interesting to study the plaque's development in a

mechanistic model. However, this would require more in-depth background on the pathology (e.g., proteome) of the plaque, the genotype, and the clinical phenotype of cases with coarse-grained plaques. In this study, CD68 was used as a microglial activation marker in 3D visualization. It would be interesting to extend this microglia marker panel with other activation markers as well as more microglia specific markers (e.g., P2Y12, TMEM119, Iba1) to gain better insights on the microglial involvement.

We observed the coarse-grained plaque to be especially prominent in the neocortex, which is one of the first regions to develop A β pathology [52]. The coarse-grained plaque, similar to other plaques, is likely to be region specific [7, 52]. In this study, we observed that the coarse-grained plaque was predominantly found in the frontal and parietal regions and to a lesser extent also in the temporal and occipital regions of the neocortex. Future work could focus on the presence of coarse-grained plaques in different pathology stages, as well as in different clinical AD phenotypes.

Conclusion

In this study, we describe and define a new type of A β deposit, referred to as the ‘coarse-grained plaque’. Its characteristics are different from other A β deposits. We provide a morphological and biochemical definition for the coarse-grained plaque, supporting that this deposit is unique, with specific clinical and etiological associations. Associated disease mechanisms such as neuroinflammation and vascular attribution, as well as the structure and biochemical composition of A β may lie at the cause of morphological differences between A β deposits. Disentangling specific A β deposits between AD subgroups may be important in the search for disease-mechanistic-based therapies in the near future.

ACKNOWLEDGEMENTS

We would like to acknowledge all brain donors and their caregivers, and the Netherlands Brain Bank (NBB) and Normal Aging Brain Collection Amsterdam (NABCA) for providing well-defined brain tissue. We thank Ingrid Hegeman-Kleinn, Chris van Geffen, and Evelien Timmermans-Huisman for technical assistance with tissue preparation and immunohistochemistry. We thank both the clinical genetics department of the Amsterdam UMC, location VUmc for exome sequencing and especially Marc Hulsman for helping out with the genetic data. We thank dr. Nienke de Wit for providing labelled anti-A β antibodies.

We thank David Giling and Vasco Vicente for help with Adobe After Effects and prof.dr. Piet Eikelenboom for in-depth discussions. This study was funded by grants from Alzheimer Nederland (#NL-16054, #WE.15-2019-13), ZonMw (#733050104), Alzheimer Forschung Initiative (AFI) e.V. grant (#17011), Deutsche Forschungsgemeinschaft (DFG) (#WA1477/6-6), and NIH (#1R01AG061775).

LIST OF ABBREVIATIONS

| | |
|------------------|---|
| A β | amyloid-beta |
| A β_{40} | amyloid-beta 40 |
| A β_{42} | amyloid-beta 42 |
| A β_{N3pE} | truncated pyroglutamate A β |
| AD | Alzheimer's disease |
| ApoE | apolipoprotein E |
| <i>APOE</i> | apolipoprotein E gene |
| APP | amyloid precursor protein |
| BSA | bovine serum albumin |
| BNE | Brain Net Europe II |
| CAA | cerebral amyloid angiopathy |
| CLSM | confocal laser scanning microscopy |
| DAB | 3,3'-diaminobenzidine |
| EOAD | early onset Alzheimer's disease |
| FFFF | formalin-fixed free-floating |
| FFPE | formalin-fixed paraffin-embedded |
| GFAP | glial fibrillary acidic protein |
| LOAD | late onset Alzheimer's disease |
| NBB | Netherlands Brain Bank |
| NABCA | Normal Aging Brain Collection Amsterdam |
| PBS | phosphate buffered saline |
| PMI | post mortem interval |
| PrP ^C | cellular prion protein |
| <i>PSEN1</i> | presenilin 1 gene |
| <i>PSEN2</i> | presenilin 2 gene |
| pSer8A β | Ab phosphorylated at serine 8 |
| pTau | phosphorylated tau |
| TBS | Tris-buffered saline |
| WES | whole-exome sequencing |

REFERENCES

1. Alafuzoff I, Ince PG, Arzberger T, Al-Sarraj S, Bell J, Bodi I, Bogdanovic N, Bugiani O, Ferrer I, Gelpi E, Gentleman S, Giaccone G, Ironside JW, Kavantzias N, King A, Korkolopoulou P, Kovács GG, Meyronet D, Monoranu C, Parchi P, Parkkinen L, Patsouris E, Roggendorf W, Rozemuller A, Stadelmann-Nessler C, Streichenberger N, Thal DR, Kretschmar H (2009) Staging/typing of Lewy body related α -synuclein pathology: A study of the BrainNet Europe Consortium. *Acta Neuropathol* 117:635–652. doi: 10.1007/s00401-009-0523-2
2. Arendt T, Morawski M, Gärtner U, Fröhlich N, Schulze F, Wohmann N, Jäger C, Eisenlöffel C, Gertz H-J, Mueller W, Brauer K (2016) Inhomogeneous distribution of Alzheimer pathology along the isocortical relief. Are cortical convolutions an Achilles heel of evolution? *Brain Pathol* 5:603–611. doi: 10.1111/bpa.12442
3. Armstrong RA (1995) Beta-amyloid deposition in the medial temporal lobe in elderly non-demented brains and in Alzheimer's disease. *Dement Geriatr Cogn Disord* 6:121–125. doi: 10.1159/000106933
4. Armulik A, Genové G, Betsholtz C (2011) Pericytes: Developmental, Physiological, and Pathological Perspectives, Problems, and Promises. *Dev. Cell* 21:193–215
5. Asami-Odaka A, Ishibashi Y, Kikuchi T, Kitada C, Suzuki N (1995) Long amyloid beta-protein secreted from wild-type human neuroblastoma IMR-32 cells. *Biochemistry* 34:10272–8. doi: 10.1021/bi00032a022
6. Attems J, Jellinger K, Thal DR, Van Nostrand W (2011) Review: Sporadic cerebral amyloid angiopathy. *Neuropathol Appl Neurobiol* 37:75–93. doi: 10.1111/j.1365-2990.2010.01137.x
7. Boon BDC, Hoozemans JJM, Lopuhaä B, Eigenhuis KN, Scheltens P, Kamphorst W, Rozemuller AJM, Bouwman FH (2018) Neuroinflammation is increased in the parietal cortex of atypical Alzheimer's disease. *J Neuroinflammation* 15:170. doi: 10.1186/s12974-018-1180-y
8. Braak H, Alafuzoff I, Arzberger T, Kretschmar H, Tredici K (2006) Staging of Alzheimer disease-associated neurofibrillary pathology using paraffin sections and immunocytochemistry. *Acta Neuropathol* 112:389–404. doi: 10.1007/s00401-006-0127-z
9. Cohen J (1960) A Coefficient of Agreement for Nominal Scales. *Educ Psychol Meas* 20:37–46. doi: 10.1177/001316446002000104
10. Crook R, Verkoniemi A, Perez-Tur J, Mehta N, Baker M, Houlden H, Farrer M, Hutton M, Lincoln S, Hardy J, Gwinn K, Somer M, Paetau A, Kalimo H, Ylikoski R, Pöyhönen M, Kucera S, Haltia M (1998) A variant of Alzheimer's disease with spastic paraparesis and unusual plaques due to deletion of exon 9 of presenilin 1. *Nat Med* 4:452–5. doi: 10.1038/nm0498-452
11. Delaère P, Duyckaerts C, He Y, Piette F, Hauw JJ (1991) Subtypes and differential laminar distributions of β A4 deposits in Alzheimer's disease: relationship with the intellectual status of 26 cases. *Acta Neuropathol* 81:328–335. doi: 10.1007/BF00305876

12. Delaère P, He Y, Fayet G, Duyckaerts C, Hauw JJ (1993) β A4 deposits are constant in the brain of the oldest old: An immunocytochemical study of 20 french centenarians. *Neurobiol Aging* 14:191-194. doi: 10.1016/0197-4580(93)90096-T
13. DeMattos RB, O'dell MA, Parsadanian M, Taylor JW, Harmony JAK, Bales KR, Paul SM, Aronow BJ, Holtzman DM (2002) Clusterin promotes amyloid plaque formation and is critical for neuritic toxicity in a mouse model of Alzheimer's disease. *Proc Natl Acad Sci U S A* 99:10843-10848. doi: 10.1073/pnas.162228299
14. Dickson TC, Vickers JC (2001) The morphological phenotype of beta-amyloid plaques and associated neuritic changes in Alzheimer's disease. *Neuroscience* 105:99-107. doi: 10.1016/s0306-4522(01)00169-5
15. Dorph-Petersen KA, Nyengaard JR, Gundersen HJ (2001) Tissue shrinkage and unbiased stereological estimation of particle number and size. *J Microsc* 204:232-46. doi: 10.1046/j.1365-2818.2001.00958.x
16. Duyckaerts C, Delatour B, Potier M-C (2009) Classification and basic pathology of Alzheimer disease. *Acta Neuropathol* 118:5-36. doi: 10.1007/s00401-009-0532-1
17. Eikelenboom P, Rozemuller JM, Kraal G, Stam FC, McBride PA, Bruce ME, Fraser H (1991) Cerebral amyloid plaques in Alzheimer's disease but not in scrapie-affected mice are closely associated with a local inflammatory process. *Virchows Arch B Cell Pathol Incl Mol Pathol* 60:329-336. doi: 10.1007/BF02899564
18. Fischer O (1907) Miliare Nekrosen mit drusigen Wucherungen der Neurofibrillen, eine regelmässige Veränderung der Hirnrinde bei seniler Demenz. *Eur Neurol* 22:361-372. doi: 10.1159/000211873
19. Fischer O (1910) Die presbyophrene Demenz, deren anatomische Grundlage und klinische Abgrenzung. *Zeitschrift für die Gesamte Neurol und Psychiatr* 3:371-471
20. Van Der Flier WM, Pijnenburg YAL, Prins N, Lemstra AW, Bouwman FH, Teunissen CE, Van Berckel BNM, Stam CJ, Barkhof F, Visser PJ, Van Egmond E, Scheltens P (2014) Optimizing patient care and research: The Amsterdam dementia cohort. *J Alzheimer's Dis* 41:313-327. doi: 10.3233/JAD-132306
21. Gerth J, Kumar S, Rijal Upadhaya A, Ghebremedhin E, von Arnim CAF, Thal DR, Walter J (2018) Modified amyloid variants in pathological subgroups of β -amyloidosis. *Ann Clin Transl Neurol* 5:815-831. doi: 10.1002/acn3.577
22. Haass C, Selkoe DJ (2007) Soluble protein oligomers in neurodegeneration: Lessons from the Alzheimer's amyloid β -peptide. *Nat Rev Mol Cell Biol* 8:101-112. doi: 10.1038/nrm2101
23. Herzig MC, Winkler DT, Burgermeister P, Pfeifer M, Kohler E, Schmidt SD, Danner S, Abramowski D, Stürchler-Pierrat C, Bürki K, Van Duinen SG, Maat-Schieman MLC, Staufenbiel M, Mathews PM, Jucker M (2004) $A\beta$ is targeted to the vasculature in a mouse model of hereditary cerebral hemorrhage with amyloidosis. *Nat Neurosci* 7:954-960. doi: 10.1038/nrn1302
24. Hondius DC, Eigenhuis KN, Morrema THJ, van der Schors RC, van Nierop P, Bugiani M, Li KW, Hoozemans JJM, Smit AB, Rozemuller AJM (2018) Proteomics analysis identifies new markers associated with capillary cerebral amyloid angiopathy in Alzheimer's disease. *Acta Neuropathol Commun* 6:46. doi: 10.1186/s40478-018-0540-2

25. Hoozemans JJ, Rozemuller AJ, van Haastert ES, Eikelenboom P, van Gool WA (2011) Neuroinflammation in Alzheimer's disease wanes with age. *J Neuroinflammation* 8:171. doi: 10.1186/1742-2094-8-171
26. Hopperton KE, Mohammad D, Trépanier MO, Giuliano V, Bazinet RP (2018) Markers of microglia in post-mortem brain samples from patients with Alzheimer's disease: A systematic review. *Mol. Psychiatry* 23:177-198
27. Itagaki S, McGeer PL, Akiyama H, Zhu S, Selkoe D (1989) Relationship of microglia and astrocytes to amyloid deposits of Alzheimer disease. *J Neuroimmunol* 24:173-182. doi: 10.1016/0165-5728(89)90115-X
28. Jack CR, Knopman DS, Jagust WJ, Shaw LM, Aisen PS, Weiner MW, Petersen RC, Trojanowski JQ (2010) Hypothetical model of dynamic biomarkers of the Alzheimer's pathological cascade. *Lancet Neurol* 9:119-128. doi: 10.1016/S1474-4422(09)70299-6
29. Jarrett JT, Berger EP, Lansbury PT (1993) The Carboxy Terminus of the β Amyloid Protein Is Critical for the Seeding of Amyloid Formation: Implications for the Pathogenesis of Alzheimer's Disease. *Biochemistry* 32:4693-4697. doi: 10.1021/bi00069a001
30. Johnson-Wood K, Lee M, Motter R, Hu K, Gordon G, Barbour R, Khan K, Gordon M, Tan H, Games D, Lieberburg I, Schenk D, Seubert P, McConlogue L (1997) Amyloid precursor protein processing and A β 42 deposition in a transgenic mouse model of Alzheimer disease. *Proc Natl Acad Sci U S A* 94:1550-1555. doi: 10.1073/pnas.94.4.1550
31. Kumar S, Rezaei-Ghaleh N, Terwel D, Thal DR, Richard M, Hoch M, Mc Donald JM, Wüllner U, Glebov K, Heneka MT, Walsh DM, Zweckstetter M, Walter J (2011) Extracellular phosphorylation of the amyloid β 2-peptide promotes formation of toxic aggregates during the pathogenesis of Alzheimer's disease. *EMBO J* 30:2255-2265. doi: 10.1038/emboj.2011.138
32. Kumar S, Wirths O, Theil S, Gerth J, Bayer TA, Walter J (2013) Early intraneuronal accumulation and increased aggregation of phosphorylated Abeta in a mouse model of Alzheimer's disease. *Acta Neuropathol* 125:699-709. doi: 10.1007/s00401-013-1107-8
33. Kummer MP, Heneka MT (2014) Truncated and modified amyloid-beta species. *Alzheimer's Res Ther* 6:28. doi: 10.1186/alzrt258
34. Maier M, Peng Y, Jiang L, Seabrook TJ, Carroll MC, Lemere CA (2008) Complement C3 deficiency leads to accelerated amyloid beta plaque deposition and neurodegeneration and modulation of the microglia/macrophage phenotype in amyloid precursor protein transgenic mice. *J Neurosci* 28:6333-41. doi: 10.1523/JNEUROSCI.0829-08.2008
35. Mirra SS, Heyman A, McKeel D, Sumi SM, Crain BJ, Brownlee LM, Vogel FS, Hughes JP, van Belle G, Berg L (1991) The Consortium to Establish a Registry for Alzheimer's Disease (CERAD). Part II. Standardization of the neuropathologic assessment of Alzheimer's disease. *Neurology* 41:479-86. doi: 10.1097/00005072-199405000-00012

36. Montine TJ, Phelps CH, Beach TG, Bigio EH, Cairns NJ, Dickson DW, Duyckaerts C, Frosch MP, Masliah E, Mirra SS, Nelson PT, Schneider JA, Thal DR, Trojanowski JQ, Vinters H V, Hyman BT, National Institute on Aging, Alzheimer's Association (2012) National Institute on Aging-Alzheimer's Association guidelines for the neuropathologic assessment of Alzheimer's disease: a practical approach. *Acta Neuropathol* 123:1-11. doi: 10.1007/s00401-011-0910-3
37. Nelson PT, Dickson DW, Trojanowski JQ, Jack CR, Boyle PA, Arfanakis K, Rademakers R, Alafuzoff I, Attems J, Brayne C, Coyle-Gilchrist ITS, Chui HC, Fardo DW, Flanagan ME, Halliday G, Hokkanen SRK, Hunter S, Jicha GA, Katsumata Y, Kawas CH, Keene CD, Kovacs GG, Kukull WA, Levey AI, Makkinejad N, Montine TJ, Murayama S, Murray ME, Nag S, Rissman RA, Seeley WW, Sperling RA, White CL, Yu L, Schneider JA (2019) Limbic-predominant age-related TDP-43 encephalopathy (LATE): Consensus working group report. *Brain* 142:1503-1527
38. Oshima K, Uchikado H, Dickson DW (2008) Perivascular neuritic dystrophy associated with cerebral amyloid angiopathy in Alzheimer's disease - PubMed. *Int J Clin Exp Pathol* 1:403-408
39. Peers MC, Lenders MB, Défossez A, Delacourte A, Mazzuca M (1988) Cortical angiopathy in Alzheimer's disease: The formation of dystrophic perivascular neurites is related to the exudation of amyloid fibrils from the pathological vessels. *Virchows Arch A Pathol Anat Histopathol* 414:15-20. doi: 10.1007/BF00749733
40. Perusini G (1909) Über klinisch und histologisch eigenartige psychische Erkrankungen des späteren Lebensalters. *Histol und Histopathol Arb über die Gehirnrinde III*:297-351
41. Price JL, Davis PB, Morris JC, White DL (1991) The distribution of tangles, plaques and related immunohistochemical markers in healthy aging and Alzheimer's disease. *Neurobiol Aging* 12:295-312. doi: 10.1016/0197-4580(91)90006-6
42. Richard E, Carrano A, Hoozemans JJ, Van Horssen J, Van Haastert ES, Eurelings LS, De Vries HE, Thal DR, Eikelenboom P, Van Gool WA, Rozemuller AJM (2010) Characteristics of dyschoric capillary cerebral amyloid angiopathy. *J Neuropathol Exp Neurol* 69:1158-1167. doi: 10.1097/NEN.0b013e3181fab558
43. Richards S, Aziz N, Bale S, Bick D, Das S, Gastier-Foster J, Grody WW, Hegde M, Lyon E, Spector E, Voelkerding K, Rehm HL (2015) Standards and guidelines for the interpretation of sequence variants: A joint consensus recommendation of the American College of Medical Genetics and Genomics and the Association for Molecular Pathology. *Genet Med* 17:405-424. doi: 10.1038/gim.2015.30
44. Rijal Upadhaya A, Kosterin I, Kumar S, von Arnim CAF, Yamaguchi H, Fändrich M, Walter J, Thal DR (2014) Biochemical stages of amyloid- β peptide aggregation and accumulation in the human brain and their association with symptomatic and pathologically preclinical Alzheimer's disease. *Brain* 137:887-903. doi: 10.1093/brain/awt362

45. Rozemuller JM, Eikelenboom P, Stam FC, Beyreuther K, Masters CL (1989) A4 protein in Alzheimer's disease: primary and secondary cellular events in extracellular amyloid deposition. *J Neuropathol Exp Neurol* 48:674–91. doi: 10.1097/00005072-198911000-00009
46. Schmidt ML, Robinson KA, Lee VM, Trojanowski JQ (1995) Chemical and immunological heterogeneity of fibrillar amyloid in plaques of Alzheimer's disease and Down's syndrome brains revealed by confocal microscopy. *Am J Pathol* 147:503–15
47. Shen Y, Yang L, Li R (2013) What does complement do in Alzheimer's disease? Old molecules with new insights. *Transl Neurodegener* 2:21. doi: 10.1186/2047-9158-2-21
48. Tabira T, Chui DH, Nakayama H, Kuroda S, Shibuya M (2002) Alzheimer's disease with spastic paresis and cotton wool type plaques. *J Neurosci Res* 70:367–72. doi: 10.1002/jnr.10392
49. Thal DR, Capetillo-Zarate E, Del Tredici K, Braak H (2006) The development of amyloid beta protein deposits in the aged brain. *Sci Aging Knowledge Environ* 2006:re1. doi: 10.1126/sageke.2006.6.re1
50. Thal DR, Ghebremedhin E, Rüb U, Yamaguchi H, Del Tredici K, Braak H (2002) Two types of sporadic cerebral amyloid angiopathy. *J Neuropathol Exp Neurol* 61:282–293. doi: 10.1093/jnen/61.3.282
51. Thal DR, Griffin WST, de Vos RAI, Ghebremedhin E (2008) Cerebral amyloid angiopathy and its relationship to Alzheimer's disease. *Acta Neuropathol* 115:599–609. doi: 10.1007/s00401-008-0366-2
52. Thal DR, Rüb U, Orantes M, Braak H (2002) Phases of A β -deposition in the human brain and its relevance for the development of AD. *Neurology* 58:1791–800. doi: 10.1212/wnl.58.12.1791
53. Thal DR, Walter J, Saido TC, Fändrich M (2015) Neuropathology and biochemistry of A β and its aggregates in Alzheimer's disease. *Acta Neuropathol.* 129:167–182
54. Thomsen MS, Routle LJ, Moos T (2017) The vascular basement membrane in the healthy and pathological brain. *J. Cereb. Blood Flow Metab.* 37:3300–3317
55. Veerhuis R, van der Valk P, Janssen I, Zhan SS, Eikelenboom P, Van Nostrand WE, Eikelenboom P (1995) Complement activation in amyloid plaques in Alzheimer's disease brains does not proceed further than C3. *Virchows Arch* 426:603–610. doi: 10.1007/BF00192116
56. Verbeek MM, Otte-Höller I, Veerhuis R, Ruiten DJ, De Waal RMW (1998) Distribution of A β -associated proteins in cerebrovascular amyloid of Alzheimer's disease. *Acta Neuropathol* 96:628–636. doi: 10.1007/s004010050944
57. Wyss-Coray T, Yan F, Lin AH-T, Lambris JD, Alexander JJ, Quigg RJ, Masliah E (2002) Prominent neurodegeneration and increased plaque formation in complement-inhibited Alzheimer's mice. *Proc Natl Acad Sci U S A* 99:10837–42. doi: 10.1073/pnas.162350199

SUPPLEMENTARY DATA

Table S1. Case details

| Case # | Group | Sex | Onset age | Disease duration | Age † | Cause † | PMI | APOE | Pathogenic mutation in <i>APP</i> , <i>PSEN1</i> , or <i>PSEN2</i> |
|--------|-------|-----|-----------|------------------|-------|----------------------------------|-------|------|--|
| 1 | Ab + | M | NA | NA | 82 | Lung carcinoma | 05:30 | NA | NA |
| 2 | Ab + | M | NA | NA | 93 | Heart failure | 08:30 | NA | NA |
| 3 | Ab + | M | NA | NA | 82 | Euthanasia | 07:30 | 34 | NA |
| 4 | Ab + | F | NA | NA | 64 | Relapsing pneumothorax | 05:40 | 23 | NA |
| 5 | Ab + | F | NA | NA | 91 | Brain stem infarction | 03:47 | 33 | NA |
| 6 | Ab + | F | NA | NA | 89 | Euthanasia | 06:30 | 34 | NA |
| 7 | Ab + | M | NA | NA | 71 | Pancreas carcinoma | 08:55 | 34 | None |
| 8 | Ab + | F | NA | NA | 70 | Pneumonia by pulmonary carcinoma | 06:15 | 33 | None |
| 9 | Ab + | F | NA | NA | 70 | Cachexia by pancreas carcinoma | 07:35 | 33 | None |
| 10 | Ab + | F | NA | NA | 78 | Pneumonia | 04:35 | 33 | None |
| 11 | Ab + | M | NA | NA | 79 | Euthanasia | 05:45 | 33 | None |
| 12 | Ab + | M | NA | NA | 79 | Euthanasia | 06:30 | 23 | None |
| 13 | Ab + | M | NA | NA | 83 | Myocardial infarct | 05:15 | 33 | None |
| 14 | Ab + | M | NA | NA | 95 | Heart failure | 07:15 | 24 | None |
| 15 | Ab + | F | NA | NA | 78 | Euthanasia | 07:10 | 33 | None |
| 16 | EOAD | M | 56 | 8 | 64 | Cachexia/dehydration | 4:40 | 24 | None |
| 17 | EOAD | F | 64 | 3 | 67 | Epileptic insult | 4:45 | 33 | None |
| 18 | EOAD | M | 48 | 11 | 59 | Cachexia/dehydration | 7:35 | 44 | None |
| 19 | EOAD | M | 59 | 6 | 65 | Pneumonia | 03:32 | 33 | NM_000021.3 (PSEN1):c.791C>T (p.Pro264Leu) |
| 20 | EOAD | M | 56 | 6 | 62 | Cachexia/dehydration | 04:40 | 33 | None |
| 21 | EOAD | M | 58 | 2 | 60 | Euthanasia | 08:35 | 33 | NM_000021.3 (PSEN1):c.786G>C p.(Leu262Phe) |
| 22 | EOAD | M | 62 | 6 | 68 | Euthanasia | 09:15 | 33 | None |
| 23 | EOAD | F | 56 | 10 | 66 | Sedatives and pneumonia | 08:01 | 33 | None |

| ABC [36] | Thal Ab [52] | Braak NFT [8] | CAA-Type [51] | Braak LB [1] | LATE-NC [37] | Vascular lesions | Coarse-grained plaque score | FFPE region | FFFF region |
|----------|--------------|---------------|---------------|------------------|--------------|--|-----------------------------|-------------|-------------|
| A1B1C0 | 1 | 2 | 1 | NA | NA | None | None | MFG | |
| A1B2C0 | 1 | 3 | 2 | 6 | 1 | None | None | MFG | |
| A1B1C0 | 1 | 1 | 0 | 4 | 0 | None | None | MFG | |
| A1B0C0 | 1 | 0 | 0 | 0 | NA | None | None | MFG | |
| A1B1C0 | 2 | 2 | 2 | 0 | NA | Multiple i's | None | MFG | |
| A1B1C0 | 1 | 3 | 2 | 0 | NA | Multiple i's | None | MFG | |
| A2B1C1 | 3 | 2 | 2 | 0; Amygdala only | NA | None | Sparse | MFG | |
| A1B1C0 | 1 | 2 | 1 | 0 | NA | None | None | MFG | |
| A1B1C0 | 1 | 2 | 2 | 0 | NA | None | None | MFG | |
| A1B2C1 | 2 | 3 | 2 | 0 | NA | Hypertensive vasculopathy; mi | None | MFG | |
| A1B1C1 | 1 | 3 | 1 | 0 | NA | Calcified vessels in WM | None | MFG | |
| A1B1C0 | 1 | 2 | 0 | 0; Amygdala only | NA | None | None | MFG | |
| A1B1C0 | 1 | 1 | 0 | 1 | NA | i | None | MFG | |
| A2B1C0 | 3 | 2 | 1 | 1 | NA | Hypertensive vasculopathy; multiple mi's | None | MFG | |
| A1B1C0 | 1 | 1 | 0 | 0 | NA | None | None | MFG | |
| A3B3C3 | ≥4 | 5 | 2 | 0 | NA | None | Sparse | MFG | |
| A3B3C3 | ≥4 | 5 | 2 | 0 | NA | Gliotic scars | Sparse | MFG | |
| A3B3C3 | ≥4 | 6 | 1 | 0 | NA | None | Frequent | MFG | |
| A3B3C3 | 5 | 6 | 1 | 0; Amygdala only | NA | None | Sparse | MFG | |
| A3B3C3 | ≥4 | 5 | 1 | 0; Amygdala only | 0 | Small vessel disease | Sparse | MFG | |
| A3B3C3 | 5 | 6 | 1 | 0 | NA | None | Sparse | MFG | |
| A3B3C3 | 5 | 5 | 2 | 0 | NA | None | Sparse | MFG | |
| A3B3C3 | 5 | 6 | 2 | 0 | 0 | Hypertensive vasculopathy; mi | Sparse | MFG | |

Table S1. Continued.

| Case # | Group | Sex | Onset age | Disease duration | Age † | Cause † | PMI | APOE | Pathogenic mutation in <i>APP</i> , <i>PSEN1</i> , or <i>PSEN2</i> |
|--------|-------|-----|-----------|------------------|-------|------------------------------|-------|------|--|
| 24 | EOAD | M | 58 | 7 | 65 | Cardiac arrest | 07:51 | 33 | NA |
| 25 | EOAD | M | 64 | 9 | 73 | NA | 06:37 | 34 | NA |
| 26 | EOAD | F | 55 | 10 | 65 | Euthanasia | 06:41 | 33 | None |
| 27 | EOAD | M | 56 | 6 | 62 | Malign neuroleptic syndrome | 4:15 | 34 | None |
| 28 | EOAD | M | 63 | 7 | 70 | Metastasized colon carcinoma | 6:20 | 34 | None |
| 29 | EOAD | M | 54 | 8 | 62 | Palliative sedation | 08:15 | 34 | None |
| 30 | EOAD | M | 58 | 9 | 67 | Dehydration | 06:35 | 34 | None |
| 31 | EOAD | F | 59 | 6 | 65 | Cachexia/dehydration | 5:40 | 33 | None |
| 32 | EOAD | M | 60 | 5 | 65 | Cardiac insufficiency | 8:50 | 44 | None |
| 33 | EOAD | M | 62 | 3 | 65 | Euthanasia | 6:50 | 34 | None |
| 34 | EOAD | M | 52 | 9 | 61 | Pneumonia | 05:00 | 34 | None |
| 35 | EOAD | M | 58 | 17 | 75 | Cachexia/dehydration | 03:05 | 44 | None |
| 36 | EOAD | M | 53 | 11 | 64 | Pneumonia | 04:35 | 33 | None |
| 37 | EOAD | M | 58 | 11 | 69 | Pneumonia | 11:55 | 34 | None |
| 38 | EOAD | M | < 58 | NA | 59 | Euthanasia | 06:31 | 44 | None |
| 39 | EOAD | F | 61 | 13 | 74 | Cachexia/dehydration | 05:15 | 44 | None |
| 40 | EOAD | F | 47 | 15 | 62 | Palliative sedation | 06:25 | 44 | NA |
| 41 | EOAD | M | 32 | 5 | 37 | Euthanasia | 11:11 | 23 | NM_000021.3 (PSEN1):c.1254G>T (p.Leu418Phe) |
| 42 | EOAD | M | 53 | 5 | 58 | Cachexia/dehydration | 08:55 | 34 | None |
| 43 | EOAD | F | 56 | 15 | 71 | Pneumonia | 03:30 | 24 | None |
| 44 | EOAD | M | 60 | 11 | 71 | Cachexia/dehydration | 06:35 | 33 | None |
| 45 | EOAD | F | 40 | 27 | 67 | Cerebrovascular accident | 04:30 | 34 | None |

| ABC [36] | Thal Ab [52] | Braak NFT [8] | CAA-Type [51] | Braak LB [1] | LATE-NC [37] | Vascular lesions | Coarse-grained plaque score | FFPE region | FFFF region |
|----------|--------------|---------------|---------------|-------------------------|--------------|--|-----------------------------|-------------|-------------|
| A3B3C3 | 4 | 5 | 1 | 0 | ≥2 | Multiple mi's | Sparse | MFG | |
| A3B3C3 | 5 | 6 | 1 | 0 | 0 | None | Sparse | MFG | |
| A3B3C2 | 5 | 5 | 2 | 0 | NA | None | None | MFG | |
| A3B3C3 | ≥4 | 6 | 1 | 0 | NA | None | Moderate | MFG | |
| A3B3C3 | ≥4 | 6 | 1 | 0 | NA | None | Moderate | MFG; + | |
| A3B3C3 | 5 | 6 | 1 | 0 | 0 | None | Moderate | MFG; + | MFG |
| A3B3C3 | 5 | 6 | 1 | 0 | NA | None | Moderate | MFG; + | MFG |
| A3B3C3 | ≥4 | 6 | 2 | 0 | NA | None | Frequent | MFG | |
| A3B3C3 | ≥4 | 6 | 1 | 0 | NA | None | Frequent | MFG | |
| A3B3C3 | ≥4 | 5 | 1 | 0 | NA | None | Frequent | MFG; + | |
| A3B3C3 | 4 | 6 | 1 | 0; Amygdala predominant | NA | None | Frequent | MFG; + | |
| A3B3C3 | 5 | 6 | 2 | 0 | NA | None | Frequent | MFG; + | |
| A3B3C3 | 5 | 6 | 1 | 0; Amygdala predominant | NA | None | Frequent | MFG; + | |
| A3B3C3 | 5 | 5 | 1 | 0 | NA | None | Frequent | MFG; + | |
| A3B3C3 | 5 | 5 | 1 | 5 | 0 | Extensive calcifications in basal nuclei and hippocampus | Frequent | MFG; + | |
| A3B3C3 | 5 | 6 | 2 | 0; Amygdala only | 0 | None | Frequent | MFG; + | |
| A3B3C3 | 5 | 6 | 1 | 0 | 0 | None | Frequent | MFG | |
| A3B3C3 | 5 | 6 | 1 | 0; Amygdala only | 0 | None | Frequent | MFG; + | |
| A3B3C3 | 5 | 4 | 1 | 0 | 0 | None | Frequent | MFG; + | MFG |
| A3B3C3 | ≥4 | 6 | 2 | 0 | NA | None | Sparse | MFG | |
| A3B3C3 | ≥4 | 6 | 1 | 0 | NA | None | None | MFG | |
| A3B3C3 | 4 | 6 | 2 | 4 | NA | i | Sparse | MFG | |

Table S1. Continued.

| Case # | Group | Sex | Onset age | Disease duration | Age † | Cause † | PMI | APOE | Pathogenic mutation in <i>APP</i> , <i>PSEN1</i> , or <i>PSEN2</i> |
|--------|-------|-----|-----------|------------------|-------|-------------------------------------|-------|------|--|
| 46 | EOAD | F | 54 | 7 | 61 | Cachexia/dehydration | 05:10 | 44 | None |
| 47 | EOAD | F | 34 | 37 | 43 | Cachexia/dehydration | 04:15 | 33 | NM_000021.3 (PSEN1):c.617G>A (p.Gly206Asp) |
| 48 | EOAD | F | 60 | 13 | 73 | NA | 07:17 | 33 | None |
| 49 | EOAD | M | 61 | 11 | 72 | Pneumonia and stomach bleed | 05:15 | 34 | None |
| 50 | EOAD | F | 64 | 27 | 91 | NA | 04:20 | 33 | None |
| 51 | EOAD | M | 47 | 12 | 59 | Euthanasia | 05:25 | 33 | APP duplication |
| 52 | EOAD | F | 51 | 21 | 70 | Cachexia/dehydration | 04:20 | 44 | None |
| 53 | EOAD | M | 63 | 10 | 73 | Cachexia/dehydration | 07:00 | 34 | None |
| 54 | LOAD | F | 75 | 9 | 84 | Cardiac arrest after cachexia | 6:30 | 34 | None |
| 55 | LOAD | F | 81 | 10 | 91 | Acute abdomen | 10:45 | 34 | None |
| 56 | LOAD | F | 74 | 15 | 89 | Cardiogenic shock | 6:30 | 34 | None |
| 57 | LOAD | M | 73 | 9 | 82 | Pneumonia | 04:15 | 34 | None |
| 58 | LOAD | M | 70 | 10 | 80 | Sudden death | 10:51 | 34 | None |
| 59 | LOAD | F | 74 | 4 | 78 | Cachexia/dehydration | 07:31 | 34 | None |
| 60 | LOAD | F | 73 | 7 | 80 | Euthanasia | 07:05 | 33 | None |
| 61 | LOAD | M | 71 | 13 | 84 | Euthanasia | 05:53 | 34 | None |
| 62 | LOAD | M | 71 | 7 | 78 | Fever eci, cachexia/ dehydration | 6:35 | 44 | None |
| 63 | LOAD | F | 84 | 8 | 92 | Heart failure | 7:00 | 34 | None |
| 64 | LOAD | F | 85 | 6 | 91 | Cachexia/dehydration | 5:05 | 33 | None |
| 65 | LOAD | M | 77 | 11 | 88 | Cachexia /dehydration | 05:30 | 34 | None |
| 66 | LOAD | F | 79 | 6 | 85 | Cachexia/dehydration | 04:05 | 34 | None |
| 67 | LOAD | M | 78 | 8 | 86 | Cachexia/dehydration | 05:10 | 34 | None |
| 68 | LOAD | M | 71 | 10 | 81 | Cachexia/dehydration | 07:50 | 34 | None |
| 69 | LOAD | F | 80 | 8 | 88 | Cachexia/dehydration | 04:40 | 34 | None |

| ABC [36] | Thal Ab [52] | Braak NFT [8] | CAA-Type [51] | Braak LB [1] | LATE-NC [37] | Vascular lesions | Coarse-grained plaque score | FFPE region | FFFF region |
|----------|--------------|---------------|---------------|-------------------------|--------------|--|-----------------------------|-------------|-------------|
| A3B3C2 | ≥4 | 6 | 2 | 0 | NA | None | Moderate | MFG | |
| A3B3C3 | 5 | 6 | 2 | 0; Amygdala predominant | NA | None | Moderate | MFG | |
| A3B3C3 | 5 | 6 | 1 | 0; Amygdala only | NA | None | Frequent | MFG | |
| A3B3C2 | 5 | 6 | 1 | 0; Amygdala predominant | NA | Lobar bl; i | Frequent | MFG | |
| A3B3C3 | 5 | 6 | 1 | 0 | NA | i's | Frequent | MFG | |
| A3B3C3 | 5 | 5 | 1 | 0; Amygdala only | NA | None | Frequent | MFG | |
| A3B3C3 | 5 | 6 | 1 | 0 | NA | i; hippocampal sclerosis | Frequent | MFG | |
| A3B3C3 | 5 | 5 | 2 | 5 | 0 | mi's | Moderate | MFG; + | MFG |
| A3B3C3 | ≥4 | 5 | 1 | 0 | NA | None | Sparse | MFG | |
| A3B3C3 | ≥4 | 5 | 1 | 0 | NA | Ischemic foci | Sparse | MFG | |
| A3B3C3 | ≥4 | 5 | 1 | 0 | NA | i | Sparse | MFG | |
| A3B3C3 | ≥4 | 5 | 2 | 1 | NA | None | None | MFG | |
| A3B3C3 | 5 | 6 | 1 | 4; Amygdala predominant | ≥2 | Lobar bl; i's | Sparse | MFG | |
| A3B3C3 | 5 | 5 | 1 | 3 | 0 | mi's; calcinosis hippocampal vasculature | Sparse | MFG | |
| A3B2C2 | 5 | 4 | 1 | 0 | ≥1 | None | None | MFG | |
| A3B2C2 | 5 | 4 | 1 | 0 | 0 | None | Sparse | MFG | |
| A3B3C3 | ≥4 | 5 | 1 | 0; Amygdala only | NA | None | Moderate | MFG | |
| A3B3C3 | ≥4 | 5 | 1 | 0 | NA | None | Frequent | MFG | |
| A3B3C3 | ≥4 | 4 | 1 | 0 | NA | None | Frequent | MFG | |
| A3B3C2 | ≥4 | 6 | 1 | 0 | NA | None | Sparse | MFG | |
| A3B3C3 | ≥4 | 5 | 2 | 0 | NA | Ischemic defects | Sparse | MFG | |
| A3B3C1 | 5 | 5 | 1 | 0; Amygdala only | NA | i's | None | MFG | |
| A3B3C3 | 5 | 6 | 1 | 0 | NA | None | None | MFG | |
| A3B3C3 | 5 | 6 | 1 | 0 | NA | None | None | MFG | |

Table S1. Continued.

| Case # | Group | Sex | Onset age | Disease duration | Age † | Cause † | PMI | APOE | Pathogenic mutation in <i>APP</i> , <i>PSEN1</i> , or <i>PSEN2</i> |
|-----------------|------------|-----|-----------|------------------|-------|---|-------|------|--|
| 70 | LOAD | F | 89 | 7 | 96 | Heart failure and myelodysplastic syndrome | 07:55 | 34 | None |
| 71 | LOAD | F | > 65 | NA | 82 | NA | 04:35 | 34 | None |
| 72 | LOAD | F | 85 | 5 | 90 | Cerebrovascular accident or gastro-intestinal bleed | 03:55 | 23 | NA |
| 73 | LOAD | M | 69 | 4 | 73 | NA | 04:45 | 44 | None |
| 74 | LOAD | M | 67 | 10 | 77 | Suicide by overdose | 09:05 | 44 | None |
| 75 ^a | CWP | M | 69 | 8 | 77 | Cardiogenic shock | 05:44 | NA | NA |
| 76 ^a | CWP | M | 46 | 11 | 57 | Aspiration pneumonia and toxic hepatitis | 05:45 | 33 | NM_000021.3 (PSEN1):c.791C>T (p.Pro264Leu) |
| 77 ^a | CWP | F | 65 | 11 | 76 | Palliative sedation | 06:20 | 34 | None |
| 78 ^a | CWP | M | 64 | 6 | 70 | Cachexia/dehydration | 09:20 | 44 | None |
| 79 ^a | CAA-Type 1 | F | 86 | 10 | 96 | Cachexia/dehydration | 04:20 | NA | NA |
| 80 ^a | CAA-Type 1 | M | 45 | 19 | 74 | Sudden death | 03:25 | NA | NA |
| 81 ^a | CAA-Type 1 | F | 63 | 12 | 75 | Cachexia/dehydration | 06:00 | NA | NA |

APOE genotype and pathogenic mutations are reported when available. ^aThese cases were not included in the semiquantitative scoring for coarse-grained plaques and were only used for comparison with other specific Ab deposits, being cotton wool plaques and CAA-Type 1 as indicated by the 'group' column. Ab + amyloid-beta positive cases; bl bleed; CWP cotton wool plaque; EOAD early-onset Alzheimer's disease; F female; FFFF formalin-fixed free-floating (4%; 24-36 hours); FFPE formalin-fixed paraffin embedded (4%); i infarct; LATE-NC limbic-predominant age-related TDP-43 encephalopathy-neuropathological changes; LB Lewy body; LOAD late-onset Alzheimer's disease; M male; MFG middle frontal gyrus; mi microinfarct; NA not available; NFT neurofibrillary tangle; OCC Occipital lobe; PMI post-mortem interval; SPL superior parietal lobe; WM white matter; † death; # number; + temporal -, parietal -, occipital-, olfactory cortex, pre- and post-central gyrus, hippocampus (including CA1-CA4, dentate gyrus, subiculum, and entorhinal cortex), amygdala, caudate nucleus, putamen, substantia nigra, locus coeruleus, pons, medulla oblongata and cerebellum.

| ABC [36] | Thal Ab [52] | Braak NFT [8] | CAA-Type [51] | Braak LB [1] | LATE-NC [37] | Vascular lesions | Coarse-grained plaque score | FFPE region | FFFF region |
|----------|--------------|---------------|---------------|-------------------------|--------------|---------------------------|-----------------------------|-------------|-------------|
| A3B2C2 | 4 | 4 | 1 | 6 | NA | None | Sparse | MFG | |
| A3B2C1 | 4 | 4 | 0 | 0 | 3 | i; hippocampal sclerosis | None | MFG | |
| A3B3C3 | 5 | 6 | 0 | 0; Amygdala only | NA | i's | None | MFG | |
| A3B3C3 | 4 | 5 | 1 | 0; Amygdala predominant | NA | Hypertensive vasculopathy | Moderate | MFG | |
| A3B3C3 | 5 | 5 | 1 | 0; Amygdala only | NA | None | Frequent | MFG; + | MFG |
| A3B3C3 | 5 | 5 | 1 | 0 | NA | None | | MFG | |
| A3B3C3 | 5 | 6 | 1 | 0 | NA | None | | MFG | |
| A3B3C3 | ≥4 | 5 | 1 | 6 | NA | None | | MFG | |
| A3B3C3 | 5 | 6 | 1 | 0; Amygdala only | NA | None | | SPL | |
| A3B3C2 | ≥4 | 5 | 1 | 0 | NA | None | | OCC | |
| A3B3C3 | ≥4 | 5 | 1 | 0; Amygdala only | NA | None | | OCC | |
| A3B3C3 | ≥4 | 5 | 1 | 0 | NA | None | | OCC | |

Table S2. Antibody characteristics and staining details

| Antigen | Antibody | Source | Host | Isotype | Tissue | Method |
|---------------------------|----------|---|---------|----------------|-------------------|--------|
| A β (aa 1-16) | IC-16 | Prof. Dr. Carsten Korth, Heinrich Heine Universität Düsseldorf, Germany | Mouse | IgG2a | FFPE (5 μ m) | IF |
| | | | | | FFFF (60 μ m) | IF |
| A β (aa 8-17) | 6F/3D | Dako | Mouse | IgG1 κ | FFPE (6 μ m) | IHC |
| A β_{40} (aa 32-40) | MBC40 | Prof. Dr. Haruyasu Yamaguchi, Gunma University School of Health Sciences, Maebashi, Japan | Mouse | | FFPE (6 μ m) | IHC |
| A β_{40} | G2-10 | Sigma-Aldrich | Mouse | IgG2b κ | FFPE (5 μ m) | IF |
| | | | | | FFFF (60 μ m) | IF |
| A β_{42} (aa 37-42) | MBC42 | Prof. Dr. Haruyasu Yamaguchi | Mouse | | FFPE (6 μ m) | IHC |
| A β_{42} | G2-11 | Sigma-Aldrich | Mouse | IgG1 κ | FFPE (5 μ m) | IF |
| | | | | | FFFF (60 μ m) | IF |
| A β_{N3pE} | 33748 | BioLegend | Mouse | IgG1 κ | FFPE (6 μ m) | IHC |
| ApoE | E6D7 | Abcam | Mouse | IgG1 | FFPE (6 μ m) | IHC |
| APP | 3E9 | ThermoFisher | Mouse | IgG1 | FFPE (6 μ m) | IHC |
| C4b | #AB66791 | Abcam | Rabbit | IgG | FFPE (6 μ m) | IHC |
| | | | | | FFPE (5 μ m) | IF |
| CD68 | KP1 | Dako | Mouse | IgG1 | FFPE (5 μ m) | IF |
| | | | | | FFFF (60 μ m) | IF |
| Collagen IV | CIV 22 | Dako | Mouse | IgG1 κ | FFPE (6 μ m) | IHC |
| GFAP | 6F2 | Monosan | Mouse | IgG1 | FFPE (6 μ m) | IHC |
| GFAP | #AB5541 | EMD Millipore | Chicken | IgY | FFPE (5 μ m) | IF |

| Dilution | Antigen retrieval ^a | Incubation | Secondary step ^b |
|---------------------------------|---|-------------|--|
| 1:200 | HIER in citrate buffer pH 6.0 or Tris-EDTA pH 9.0 | 24 hr at RT | Primary directly labeled Alexa 488 |
| 1:200 in 2% BSA/TBS+0,2% Triton | HIER in citrate buffer pH 6.0 or Tris-EDTA pH 9.0 | 24 hr at RT | Primary directly labeled Alexa 488 |
| 1:20 | FA 85% (1 hour) + 0.1% trypsin (30 minutes at 37°C) | 24 hr at RT | Biotinylated rabbit anti-mouse (1:200), followed by ABC (1:400) |
| 1:100 | FA 99% (5 min) | 24 hr at RT | Biotinylated rabbit anti-mouse (1:200), followed by ABC (1:400) |
| 1:100 | FA 99% (5 min) | 24 hr at RT | goat-anti-mouse-IgG2 Alexa 488 |
| 1:100 in 2% BSA/TBS+0,2% Triton | FA 99% (10 min) | 24 hr at RT | goat-anti-mouse-IgG2 Alexa 488 |
| 1:200 | FA 99% (5 min) | 24 hr at RT | Biotinylated rabbit anti-mouse (1:200), followed by ABC (1:400) |
| 1:100 | FA 99% (5 min) | 24 hr at RT | goat-anti-mouse-IgG1 Alexa 647 |
| 1:100 in 2% BSA/TBS+0,2% Triton | FA 99% (10 min) | 24 hr at RT | goat-anti-mouse-IgG1 Alexa 647 |
| 1:800 | HIER in citrate buffer pH 6.0 | 24 hr at RT | EnVision (Dako) |
| 1:3200 | HIER in citrate buffer pH 6.0 | 24 hr at RT | EnVision (Dako) |
| 1:6000 | HIER in citrate buffer pH 6.0 | 24 hr at RT | EnVision (Dako) |
| 1:1600 | HIER in citrate buffer pH 6.0 | 24 hr at RT | EnVision (Dako) |
| 1:200 | HIER in citrate buffer pH 6.0 | 24 hr at RT | goat-anti-rabbit Alexa 647 |
| 1:300 | HIER in citrate buffer pH 6.0 | 24 hr at RT | goat-anti-mouse Alexa 488 |
| 1:300 in 2% BSA/TBS+0,2% Triton | HIER in citrate buffer pH 6.0 | 48 hr at RT | Biotinylated goat anti-mouse (1:500), followed by ABC (1:400) and tyramide reagent Alexa 594 (1:100 in 0,0015% H ₂ O ₂ in TBS) |
| 1:25 | HIER in citrate buffer pH 6.0 | 24 hr at RT | EnVision (Dako) |
| 1:500 | HIER in citrate buffer pH 6.0 | 24 hr at RT | EnVision (Dako) |
| 1:750 | HIER in citrate buffer pH 6.0 | 24 hr at RT | goat-anti-chicken Alexa 555 |

Table S2. Continued.

| Antigen | Antibody | Source | Host | Isotype | Tissue | Method |
|--------------------------------------|--------------|--|--------|-------------------|--------------|--------|
| | | | | | FFFF (60 μm) | IF |
| MHC-II | CR3/43 | Dako | Mouse | IgG1 | FFPE (6 μm) | IHC |
| Laminin | #NB300-144SS | Novus Biologicals | Rabbit | IgG | FFPE (6 μm) | IHC |
| | | | | | FFPE (5 μm) | IF |
| | | | | | FFFF (60 μm) | IF |
| Norrin | #NBP1-59305 | Novus Biologicals | Rabbit | IgG | FFPE (6 μm) | IHC |
| | | | | | FFPE (5 μm) | IF |
| Norrin (mid-domain) | Custom made | GeneScript | Rabbit | | FFFF (60 μm) | IF |
| p-Aβ at Ser8 | 1E4E11 [31] | Prof. Dr. Jochen Walter, University Hospital Bonn, Bonn, Germany | Mouse | IgG1κ | FFPE (6 μm) | IHC |
| PrP ^C , PrP ^{Sc} | 3F4 | Covance | Mouse | IgG2 _A | FFPE (6 μm) | IHC |
| pTau at Ser202 and Thr205 | AT8 | ThermoFisher | Mouse | IgG1 | FFPE (6 μm) | IHC |

^aPrimary antibodies were diluted in either PBS or normal antibody diluent (ImmunoLogic).

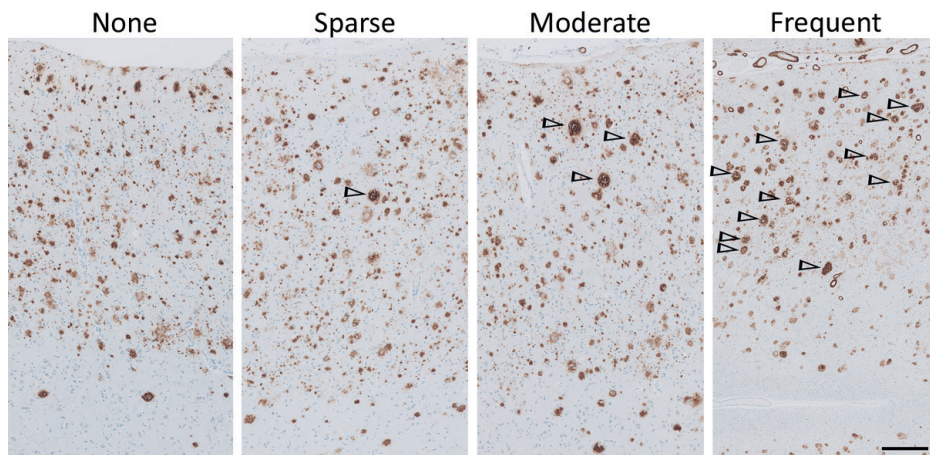
^bHIER was done by autoclave (FFPE) or by water bath 95 °C for 30 minutes (FFFF). ^cSecondary antibodies were diluted 1:250 in either PBS or normal antibody diluent (ImmunoLogic) (FFPE) or in TBS (FFFF) unless stated otherwise; secondary antibodies were incubated for 1 hour (FFPE) or 4 hours (FFFF), unless stated otherwise. aa amino-acid; Aβ amyloid-beta; APP amyloid precursor protein; ApoE apolipoprotein E; FA formic acid; FFFF formalin-fixed (4%; 24-36 hours) free-floating; FFPE formalin-fixed (4%) paraffin-embedded; GFAP glial fibrillary acidic protein; HIER heat-induced epitope retrieval; IF immunofluorescence; IHC immunohistochemistry; ON overnight; PBS phosphate buffered saline; PrP^C cellular prion protein; PrP^{Sc} abnormal scrapie isoform of the prion protein; RT room temperature; TBS Tris-buffered saline.

| Dilution | Antigen retrieval ^a | Incubation | Secondary step ^b |
|---------------------------------------|---|-------------|--|
| 1:750 in 2% BSA/TBS+0,2% Triton | HIER in citrate buffer pH 6.0 | 48 hr at RT | goat-anti-chicken Alexa 555 (in TBS+0,2% Triton) |
| 1:800 | HIER in citrate buffer pH 6.0 | 24 hr at RT | EnVision (Dako) |
| 1:500 | HIER in citrate buffer pH 6.0 | 24 hr at RT | EnVision (Dako) |
| 1:200 | HIER in Tris-EDTA buffer pH 9.0 | 24 hr at RT | EnVision and tyramide reagent Alexa 594 (1:100 in 0,0015% H ₂ O ₂ in TBS) |
| 1:500 in 2% BSA/TBS+0,2% Triton | HIER in Tris-EDTA buffer pH 9.0 | 24 hr at RT | Biotinylated goat anti- rabbit (1:500), followed by ABC (1:400) and tyramide reagent Alexa 555 (1:100 in 0,0015% H ₂ O ₂ in TBS) for 30 min |
| 1:400 | HIER in citrate buffer pH 6.0 | 24 hr at RT | EnVision (Dako) |
| 1:400 | HIER in Tris-EDTA buffer pH 9.0 | 24 hr at RT | goat-anti-rabbit Alexa 647 |
| 1:400 in 2% BSA/TBS+0,2% Triton | HIER in Tris-EDTA buffer pH 9.0 | 24 hr at RT | goat-anti-rabbit Alexa 647 |
| 1:100 | HIER in citrate buffer pH 6.0 | 24 hr at RT | EnVision (Dako) |
| 1:300 | Pre-treatment with FA for 5 min and HIER in citrate buffer pH 6.0 + Proteinase K (Dako) for 5 min for PrP ^{Sc} detection | 1 hr at RT | EnVision (Dako) |
| 1:800 | HIER in citrate buffer pH 6.0 | 24 hr at RT | EnVision (Dako) |

Table S3. Overview of coarse-grained plaques scanned using CLSM

| Case # | # Plaques for $A\beta_{40}/A\beta_{42}$ | | # Plaques for $A\beta/$ CD68/GFAP | # Plaques for $A\beta/$ norrin/laminin |
|--------------|---|---|--------------------------------------|--|
| | | # Plaques with $A\beta_{40}$ shell/total plaques | | # Plaques in direct contact with vessel/total plaques |
| 29 | 7 | 6/7 | 7 | 9 9 / 9 |
| 30 | 6 | 3/6 | 7 | 8 5 / 8 |
| 42 | 9 | 5/9 | 7 | 7 7 / 7 |
| 53 | 9 | 6/9 | 6 | 11 10 / 11 |
| 74 | 7 | 3/7 | 9 | 9 6 / 9 |
| Total | 38 | 23/38 (61%) | 36 | 44 37 / 44 (84%)^a |

Shown are the # of plaques per case that were scanned in z-axis using CLSM per antibody combination (See Table 1 for case details). In a subset of plaques stained for $A\beta_{40}/A\beta_{42}$ an $A\beta_{40}$ shell structure was observed, indicated in the 3rd column. Indicated in the 6th column is the number of coarse-grained plaques that was in direct contact with a vessel. ^aOf the 7 plaques not in direct contact with a vessel, only 2 plaques were completely scanned in z-axis. $A\beta$ amyloid-beta; $A\beta_{40}$ amyloid-beta 40; $A\beta_{42}$ amyloid-beta 42; CLSM Confocal laser scanning microscopy; # number.

**Fig. S4.** Semi-quantitative categories for coarse-grained plaque presence in $A\beta$ (6F/3D) immunostaining

Ascending categories of coarse-grained plaque semi-quantitative stages are shown: none; sparse (<6 plaques per 1 cm²); moderate (≥ 6 and ≤ 30 plaques per 1 cm²); and frequent (>30 plaques per 1 cm²). Arrowheads indicate coarse-grained plaques. Not all coarse-grained plaques in the last panel are marked due to readability reasons. Scale bar represents 200 μ m and is applicable to all images.

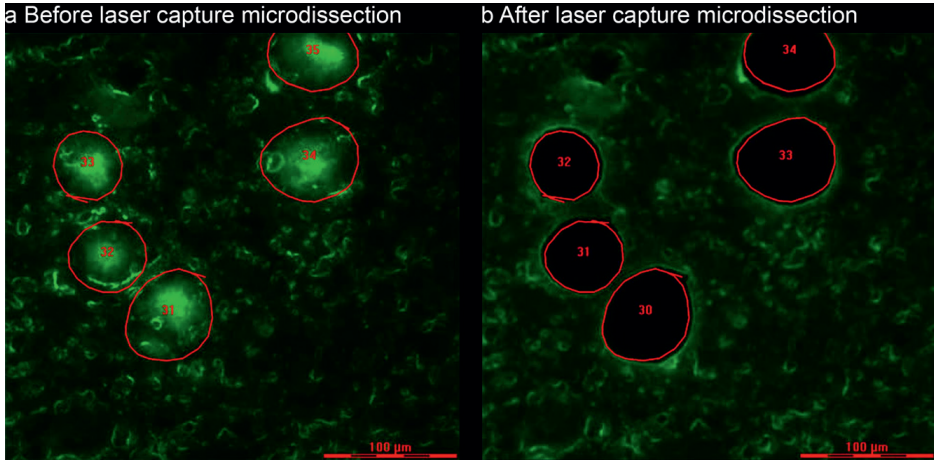


Fig. S5. Visualization of laser-capture microdissection of coarse-grained plaques
a Snap-frozen brain sections of case #18 and #32 (Supplementary Table 1 for case details) were stained using thioflavin S. **b** Preparatory to ELISA analysis for $A\beta_{40}$ and $A\beta_{42}$, coarse-grained plaques were laser captured. $A\beta_{40}$ amyloid-beta 40; $A\beta_{42}$ amyloid-beta 42.

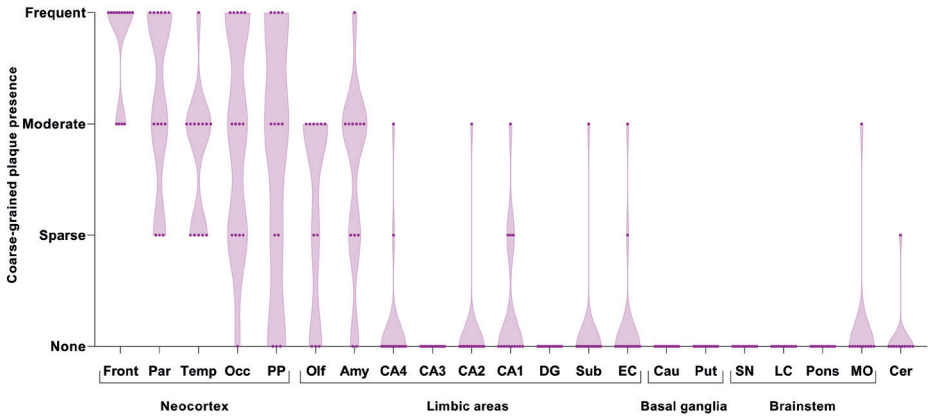


Fig. S6. Distribution of the coarse-grained plaque over different brain regions
 The coarse-grained plaque was semi-quantitatively scored (y-axis for scoring categories) in multiple brain regions of 14 cases who had a moderate to frequent score for the coarse-grained plaque in the middle frontal gyrus section. Amy amygdala; Cau caudate nucleus; Cer cerebellum; DG dentate gyrus; EC entorhinal cortex; Front middle frontal gyrus; LC locus coeruleus; MO medulla oblongata; Occ occipital cortex; Olf olfactory cortex; Par parietal cortex; PP pre-/post central gyrus; SN substantia nigra; Sub subiculum; Temp temporal cortex.

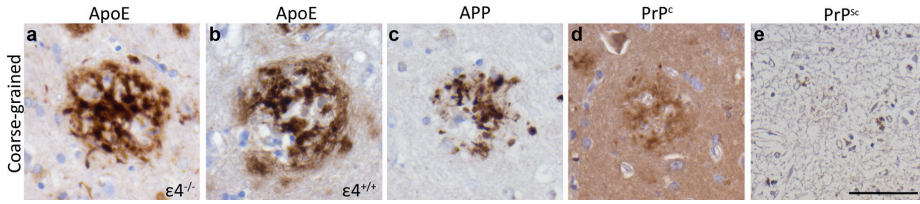


Fig. S7. Immunoreactivity for apoE, APP, PrP^C, and PrP^{Sc} in the coarse-grained plaque
a, b The coarse-grained plaque was immunoreactive for ApoE in both *APOE* ε4^{-/-} (**a**) and *APOE* ε4^{+/+} (**b**) cases. **c** APP dystrophic neurites were found within the coarse-grained plaque. **d, e** The coarse-grained plaque was immunoreactive for PrP^C and not for PrP^{Sc}. Scale bar represents 50 μm and is applicable to all images. APP amyloid precursor protein; ApoE apolipoprotein E; PrP^C cellular prion protein; PrP^{Sc} scrapie isoform of prion protein.

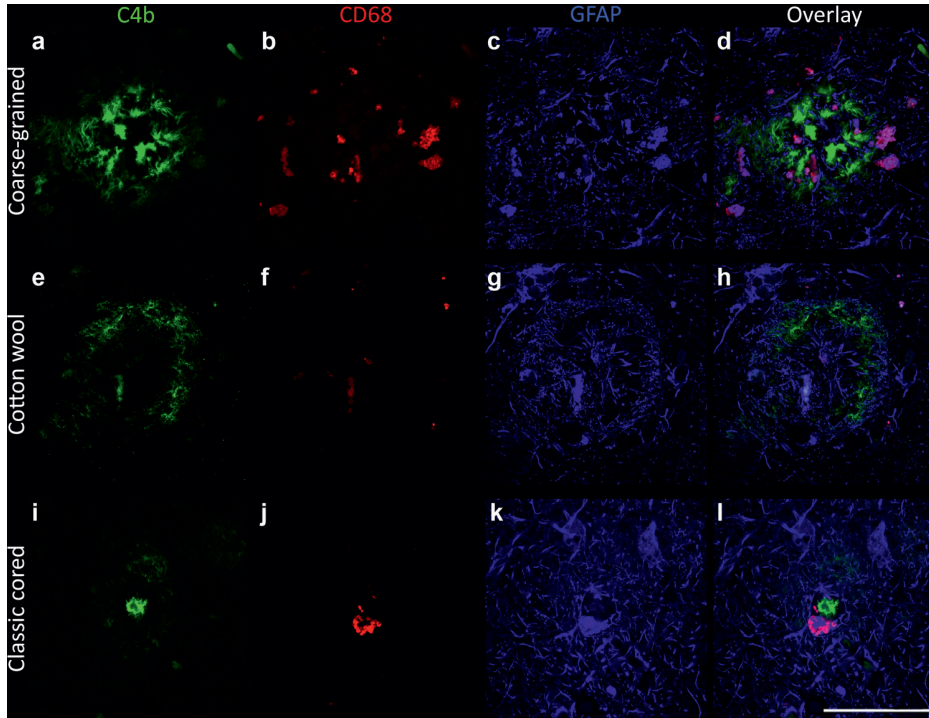


Fig. S8. Triple immunofluorescence for the neuroinflammatory response in the coarse-grained plaque (**a-d**) compared to the cotton wool (**e-h**) and classic cored plaque (**i-l**). Sections were immunostained using anti-complement factor C4b (green), anti-CD68 (red), and anti-GFAP (blue). The overlay is shown in the last column. Scale bar represents 50 μm and is applicable to all images.

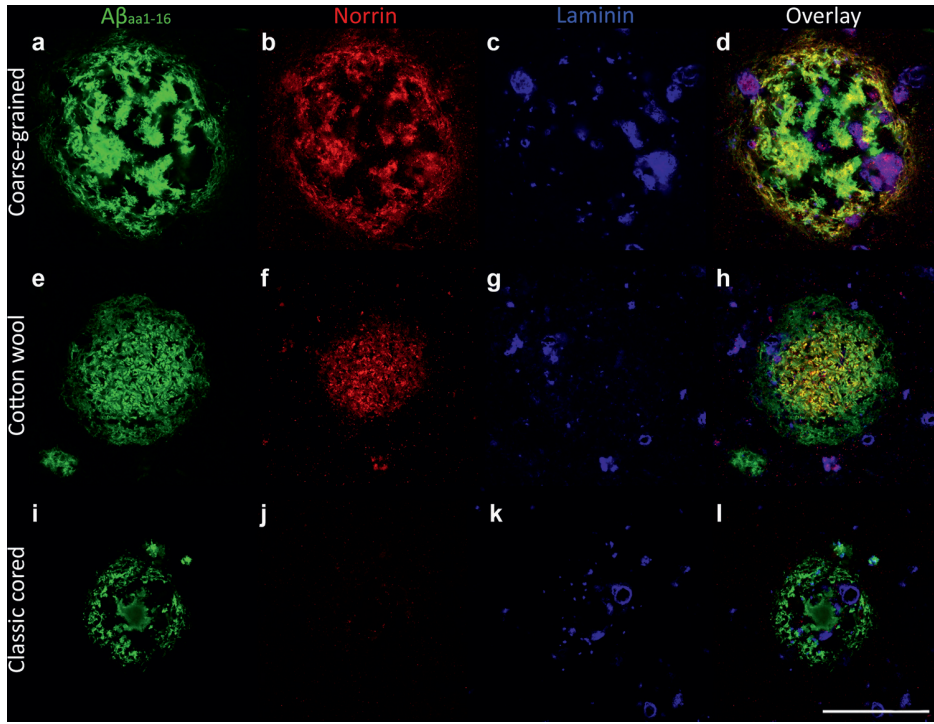


Fig. S9. Triple immunofluorescence for vascular-associated markers in the coarse-grained plaque (a-d) compared to the cotton wool (e-h) and classic cored plaque (i-l). Sections were immunostained using anti-A β aa 1-16 (green), anti-norrin (red), and anti-laminin (blue). The overlay is shown in the last column. Scale bar represents 50 μ m and is applicable to all images.

Supplementary Video S10-S15 available at: <https://link.springer.com/article/10.1007/s00401-020-02198-8#additional-information>

Supplementary Video S10. $A\beta_{40}$ / $A\beta_{42}$ in a coarse-grained plaque in case #30
3D Movie of two coarse-grained plaques stained for $A\beta_{40}$ (green) and $A\beta_{42}$ (red) acquired using confocal laser scanning microscopy. In the smaller coarse-grained plaque, $A\beta_{40}$ and $A\beta_{42}$ is co-localized. In the larger coarse-grained plaque, $A\beta_{40}$ showed an outer shell structure, surrounding the lesser present $A\beta_{42}$. Tubular-like structures are visible in $A\beta_{40}$.

Supplementary Video S11. $A\beta_{40}$ / $A\beta_{42}$ in a coarse-grained plaque in case #53
3D Movie of a coarse-grained plaque stained for $A\beta_{40}$ (green) and $A\beta_{42}$ (red) acquired using confocal laser scanning microscopy. The coarse-grained plaque has an $A\beta_{40}$ outer shell structure, surrounding the lesser present $A\beta_{42}$. Tubular-like structures are visible in $A\beta_{40}$.

Supplementary Video S12. $A\beta$ / CD68 / GFAP in a coarse-grained plaque in case #53

3D Movie of a coarse-grained plaque stained for $A\beta$ (green), GFAP (blue), and CD68 (red) acquired using confocal laser scanning microscopy. GFAP and CD68 signal is seen inside the $A\beta$ -devoid pores of the plaque.

Supplementary Video S13. $A\beta$ / CD68 / GFAP in a coarse-grained plaque in case #29

3D Movie of two coarse-grained plaques stained for $A\beta$ (green), GFAP (blue), and CD68 (red) acquired using confocal laser scanning microscopy. GFAP and CD68 signal is seen inside the $A\beta$ -devoid pores of both plaques.

Supplementary Video S14. $A\beta$ / norrin / laminin in a coarse-grained plaque in case #53

3D Movie of a coarse-grained plaque stained for $A\beta$ (green), laminin (blue), and norrin (red) acquired using confocal laser scanning microscopy. The coarse-grained plaque was in direct contact with a string vessel. A thread of norrin seemed to be connected to the vessel.

Supplementary Video S15. $A\beta$ / norrin / laminin in a coarse-grained plaque in case #29

3D Movie of a coarse-grained plaque stained for $A\beta$ (green), laminin (blue), and norrin (red) acquired using confocal laser scanning microscopy. The coarse-

grained plaque was in direct contact with a vessel. A thread of norrin seemed to be connected to the vessel.

REFERENCES SUPPLEMENTARY DATA

1. Alafuzoff I, Ince PG, Arzberger T, Al-Sarraj S, Bell J, Bodi I, Bogdanovic N, Bugiani O, Ferrer I, Gelpi E, Gentleman S, Giaccone G, Ironside JW, Kavantzias N, King A, Korkolopoulou P, Kovács GG, Meyronet D, Monoranu C, Parchi P, Parkkinen L, Patsouris E, Roggendorf W, Rozemuller A, Stadelmann-Nessler C, Streichenberger N, Thal DR, Kretzschmar H (2009) Staging/typing of Lewy body related α -synuclein pathology: A study of the BrainNet Europe Consortium. *Acta Neuropathol* 117:635–652
2. Braak H, Alafuzoff I, Arzberger T, Kretzschmar H, Tredici K (2006) Staging of Alzheimer disease-associated neurofibrillary pathology using paraffin sections and immunocytochemistry. *Acta Neuropathol* 112:389–404
3. Kumar S, Rezaei-Ghaleh N, Terwel D, Thal DR, Richard M, Hoch M, Mc Donald JM, Wüllner U, Glebov K, Heneka MT, Walsh DM, Zweckstetter M, Walter J (2011) Extracellular phosphorylation of the amyloid β 2-peptide promotes formation of toxic aggregates during the pathogenesis of Alzheimer's disease. *EMBO J* 30:2255–2265
4. Mirra SS, Heyman A, McKeel D, Sumi SM, Crain BJ, Brownlee LM, Vogel FS, Hughes JP, van Belle G, Berg L (1991) The Consortium to Establish a Registry for Alzheimer's Disease (CERAD). Part II. Standardization of the neuropathologic assessment of Alzheimer's disease. *Neurology* 41:479–86
5. Montine TJ, Phelps CH, Beach TG, Bigio EH, Cairns NJ, Dickson DW, Duyckaerts C, Frosch MP, Masliah E, Mirra SS, Nelson PT, Schneider JA, Thal DR, Trojanowski JQ, Vinters H V, Hyman BT, National Institute on Aging, Alzheimer's Association (2012) National Institute on Aging-Alzheimer's Association guidelines for the neuropathologic assessment of Alzheimer's disease: a practical approach. *Acta Neuropathol* 123:1–11
6. Thal DR, Capetillo-Zarate E, Del Tredici K, Braak H (2006) The development of amyloid beta protein deposits in the aged brain. *Sci Aging Knowledge Environ* 2006:re1
7. Thal DR, Griffin WST, de Vos RAI, Ghebremedhin E (2008) Cerebral amyloid angiopathy and its relationship to Alzheimer's disease. *Acta Neuropathol* 115:599–609

Chapter 5

Label-free vibrational imaging of different A β plaque types in Alzheimer's disease reveals sequential events in plaque development

Dominik Röhr, Baayla DC Boon, Martin Schuler, Kristin Kremer, Jeroen JM Hoozemans, Femke H Bouwman, Samir F El-Mashtoly, Andreas Nabers, Frederik Großerueschkamp, Annemieke JM Rozemuller, Klaus Gerwert

Acta Neuropathologica Communications (2020)
doi: 10.1186/s40478-020-01091-5

ABSTRACT

Background: The neuropathology of Alzheimer's disease (AD) is characterized by hyperphosphorylated tau neurofibrillary tangles (NFTs) and amyloid-beta ($A\beta$) plaques. $A\beta$ plaques are hypothesized to follow a development sequence starting with diffuse plaques, which evolve into more compact plaques and finally mature into the classic cored plaque type. A better molecular understanding of $A\beta$ pathology is crucial, as the role of $A\beta$ plaques in AD pathogenesis is under debate.

Methods: Here, we studied the deposition and fibrillation of $A\beta$ in different plaque types with label-free infrared and Raman imaging. Fourier-transform infrared (FTIR) and Raman imaging was performed on native snap-frozen brain tissue sections from AD cases and non-demented control cases. Subsequently, the scanned tissue was stained against $A\beta$ and annotated for the different plaque types by an AD neuropathology expert. In total, 160 plaques (68 diffuse, 32 compact, and 60 classic cored plaques) were imaged with FTIR and the results of selected plaques were verified with Raman imaging.

Results: In diffuse plaques, we detect evidence of short antiparallel β -sheets, suggesting the presence of $A\beta$ oligomers. $A\beta$ fibrillation significantly increases alongside the proposed plaque development sequence. In classic cored plaques, we spatially resolve cores containing predominantly large parallel β -sheets, indicating $A\beta$ fibrils.

Conclusions: Combining label-free vibrational imaging and immunohistochemistry on brain tissue samples of AD and non-demented cases provides novel insight into the spatial distribution of the $A\beta$ conformations in different plaque types. This way, we reconstruct the development process of $A\beta$ plaques in human brain tissue, provide insight into $A\beta$ fibrillation in the brain, and support the plaque development hypothesis.

INTRODUCTION

Alzheimer's disease (AD) is the most common neurodegenerative disease and is pathologically characterized by hyperphosphorylated tau neurofibrillary tangles (NFTs) and amyloid beta (A β) plaques. A β originates from the cleavage of the amyloid precursor protein (APP) and is secreted to the extracellular space. The most accepted hypothesis for AD pathogenesis is the amyloid cascade hypothesis [32, 66]. According to this hypothesis, A β aggregates in the neuropil as plaques, due to an imbalance of A β production and clearance. The A β monomers misfold and form β -sheet-rich oligomers, which then form protofibrils that stack into highly organized amyloid fibrils [38, 50]. The aggregation of A β causes synaptic stress and induces an inflammatory response. Simultaneously, synaptic and neuronal injury leads to the hyperphosphorylation of tau, which aggregates within neurons as NFTs that finally cause neuronal death. As the disease spreads and progresses, there is extensive neuronal death throughout the brain, which ultimately leads to dementia. The amyloid cascade hypothesis is currently under debate. While it is proposed that A β is the initial trigger of pathological processes, NFTs are considered to be the progressive force of the disease [55]. The discussion is fueled by several failed clinical studies of A β -targeting antibodies, as well as encouraging results of most recent anti-A β drug studies [77, 12, 67].

A β plaques show different morphologies. Here, we consider (i) the diffuse type, (ii) the compact (or primitive) type, and (iii) the classic cored type [76]. It is proposed that these different morphologies represent the progressive stages of A β fibrillation [7, 34, 62, 75]. Plaque formation is proposed to start as diffuse amorphous structures that mainly consist of aggregated A β oligomers and protofibrils. Then, with the progression of A β fibrillation, the plaque shows an increasingly compact morphology with a more clearly defined outline. An inflammatory response, driven mainly by microglia, is strongly associated with the early stages of A β plaque formation and even considered to drive the continuing build-up of amyloid fibrils and the accompanied neurotoxic effects [48, 61, 74]. The final fibrillation stage is reached when A β is condensed to a core that contains mostly A β fibrils.

Here, we applied Fourier transform infrared (FTIR) and Raman imaging to snap-frozen thin sections of human brain tissue. These label-free methods are much less invasive towards the sample than staining methods because the tissue is examined without chemical alterations [30]. The vibrational microspectroscopy approach provides spatially resolved spectra that reflect the

biochemical fingerprint of analyzed samples, including the protein secondary structure [21, 26, 31]. Raman is a complementary spectroscopic technique to FTIR and is used here to verify the FTIR results. The major constituents of brain tissue are proteins and lipids [53]. The secondary structure of proteins can be determined by analyzing the amide I absorbance band (C=O stretching vibration of the protein backbone). The amide I absorbance band is indicative for the secondary structure. It consists of several bands, each associated with distinct secondary structures [28, 29, 37]. The position of the main β -sheet-band at 1630 cm^{-1} shifts towards lower wavenumbers, when the strands become arranged in parallel β -sheets [9, 47, 78]. Accordingly, amyloid fibrils often absorb at a lower wavenumber than native β -sheet proteins [83]. For instance, oligomeric A β with typically antiparallel β -sheet structure absorbs at 1630 cm^{-1} , whereas a shift to lower wavenumbers has been reported for A β fibrils [5, 41, 54, 63, 64]. Furthermore, antiparallel β -sheets display a characteristic band at 1693 cm^{-1} . This band is not observed in A β fibrils with predominantly parallel β -sheets [8, 10]. Here, the accumulation of β -sheet-rich A β oligomers and fibrils in plaques is studied, analyzing the amide I band. Apart from that, lipids constitute about 40% of the grey matter dry weight [56] and show characteristic absorbance bands as well. The fatty acids in lipids consist mostly of methylene and methyl (CH_2 and CH_3 groups, which also occur in protein side chains) that generate stretching vibration bands in the region $3000\text{-}2800\text{ cm}^{-1}$. The head groups of most phospholipids, which make up $\sim 70\%$ of the lipid content, contain ester groups that generate the lipid-associated band (ester C=O stretching vibration) at 1738 cm^{-1} [18, 43].

In this study, the progression of A β fibrillation, alongside the proposed development sequence of A β plaques (diffuse, compact, classic cored) in AD is studied with spatial and molecular resolution, using label-free imaging. Post mortem sections from snap-frozen brain tissue were analyzed by FTIR and Raman imaging without chemical tissue treatment to stay as close to the brain's conditions as possible. Particularly, the secondary structure-sensitive amide I band was analyzed spatially resolved in different A β plaque types. Plaques in the analyzed region were subsequently confirmed by anti-A β immunohistochemistry (A β -IHC) on the same tissue section. We observed increased A β fibril contents alongside the ascending plaque stages. The spectral image analysis provides insight into the spatial distribution of A β structure in different plaque types, contributing evidence for the current hypotheses on plaque development.

METHODS

Post mortem human brain tissue

Post mortem brain tissue was selected from the Netherlands Brain Bank (the NBB; Amsterdam, the Netherlands, <https://www.brainbank.nl>). Donors or their next of kin signed informed consent for the usage of brain tissue and clinical information for research purposes. The Institutional Review Board and Medical Ethical Board from the Vrije University Medical Center approved the procedures of the NBB. Neuropathological diagnosis was performed (by AJMR) and was based on multiple (immuno)histochemical stainings of diversified brain regions according to the standard operating procedures of the NBB and BrainNet Europe consortium. AD cases ($n = 5$) were selected when clinical and neuropathological information fulfilled the criteria of the National Institute on Aging-Alzheimer's Association (NIA-AA) for AD and no other neurodegenerative or psychiatric disease was present [51]. Two additional AD cases with the vascular type were included – also referred to as CAA-Type 1. These cases do not fit the typical NIA-AA criteria, since amyloid and tau depositions are vascular related. Controls were selected when no cognitive decline was reported during life and AD pathology was absent or 'low' (supplementary Table 1). Snap-frozen tissue of the superior parietal lobule (LPS) was used, as this neocortical area shows the plaque types of interest. Sections (20 μm) were mounted on CaF₂ slides for vibrational imaging and subsequent A β -IHC. Tissue sections were stored at -80 °C in-between experiments in order to minimize sample degradation [46].

FTIR imaging

FTIR was conducted with a Cary 670 spectrometer (Agilent Technologies), coupled to a Cary 620 microscope (Agilent Technologies) in transmission mode. The microscope features a 128 \times 128-element focal plane array detector and a 15 \times (0.62 NA) objective. In high magnification mode (5 \times optical increase), the instrument yields a nominal pixel size of 1.1 μm . Each 128 \times 128-element data acquisition provided a field of view (FOV) of approximately 141 \times 141 μm . Interferograms were obtained as a mean of 128 scans. Using Blackman-Harris-4-term apodisation, power phase correction and zero-filling factor 2 for Fourier-transformation, the resulting spectral range was 3700-948 cm^{-1} at a spectral sampling interval of 1.9 cm^{-1} . For background correction, a clean area of each CaF₂ slide was measured (1024 scans) and subsequently subtracted from sample measurements. The software Resolutions Pro 5.3 was used for image acquisition. The instruments and the sample cavity were continuously purged with dry air to reduce atmospheric water vapor contribution and to maintain

the samples in a conserving dry state. We checked for spectral alterations that may have been caused by prolonged exposure to the dry air environment during the experiments. None of the bands used here for plaque analysis showed noteworthy alterations (supplementary Fig. 1).

Immunohistochemical staining

Following spectral measurements, the sample was placed into a container filled with argon at a temperature of 36 °C for one hour to increase the tissue adherence whilst maintaining dry conditions. The sample was fixated in ethanol for 10 min, and dipped in a gelatin solution (0.3% in 50 mM Tris-HCL buffer) to further increase tissue adherence. After washing (3 × 5 min in PBS (Thermo Fisher)), the sample was incubated with the primary antibody mouse-anti-A β directed against aa1-16 (clone IC16) for 1 h. After washing, the sample was incubated with EnVision (Agilent Dako) for 1 h and washed. Color development was done using 3,3'-diaminobenzidine tetrahydrochloride (DAB) (Agilent Dako). The section was dehydrated in an ethanol series (70%-96%-100%), mounted with Euporal (Roth) and coverslipped. The stained sample was subsequently imaged with an Olympus BX61VS slide scanner, using the UPlanSApo 20 × 0.75 NA objective (Olympus). The exemplary classic cored plaque appears to have a hollow core in the A β -IHC image (Fig. 2A₄). This phenomenon was described before [65] and may derive from incomplete antibody penetration into the plaque core during the A β -IHC staining procedure. Another classic cored plaque with a homogeneously stained core exhibits similar distributions of (β -sheet) protein (supplementary Fig. 2).

Image alignment

In order to link spectral data with A β -IHC images, both modalities were precisely overlaid. We used a homemade software (written in Matlab) to determine an affine 2D transformation that warps the A β -IHC image onto the coordinate system of the vibrational images, based on reference coordinates given by the user. The quality of the overlay was visually verified, based on tissue morphology. Subsequently, a region of interest (ROI) within the spectral coordinates was chosen for each plaque. The ROI of the spectral image and the corresponding region of the A β -IHC image were cut out and saved for further analysis. Exemplary cutouts are shown in Fig. 1.

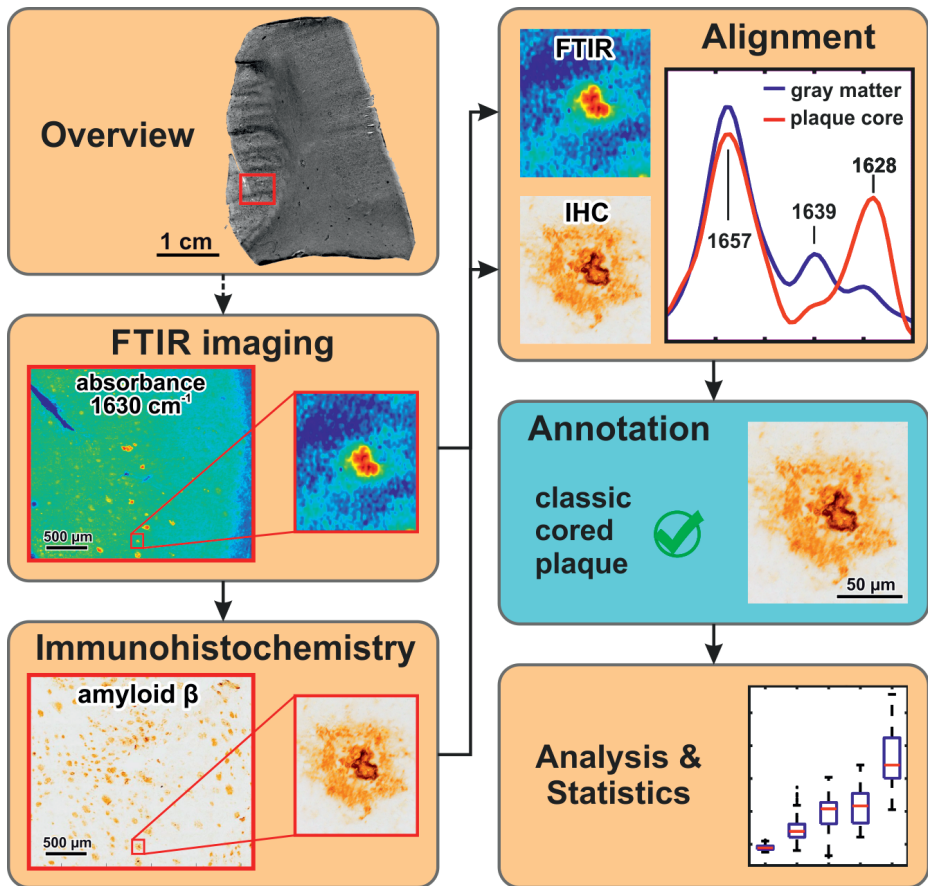


Fig. 1. Workflow

FTIR and Raman imaging were applied to selected sample areas. Subsequently, the sample was immunostained against A β and imaged with light microscopy. The resulting (spectral) images were spatially aligned to generate a precisely overlaid, unified dataset. An expert in AD neuropathology (BDCB) annotated A β -IHC images to the different plaque types. Based on this data, spectral analysis was conducted and statistically evaluated. A β Amyloid-beta; AD Alzheimer's disease; FTIR Fourier-transform infrared; IHC immunohistochemistry.

Plaque annotation

The cutouts of the A β -IHC image, containing one plaque each, were transferred to an AD neuropathology expert (BDCB) who has extensive experience with plaque morphologies. No further information was given; the expert was blinded regarding case numbers and disease stages. The expert assigned each plaque to one of the following classes: 1. diffuse plaque; 2. compact plaque; 3. classic cored plaque; 4. Miscellaneous; 5. no assignment possible. In this study, only plaques of the diffuse, compact, and classic cored type were used.

FTIR spectral data preparation

Spectra, which were not suitable for analysis, were determined by their noise level ($\text{SNR} < 100$). In addition, spectra with strong scattering contribution ($A_{\text{silent region}} > A_{1655}/2$) were excluded. Scattering appears as apparent absorbance in the so-called “silent region” (e.g., 2300-1800 cm^{-1}), where biological samples usually display no absorbance (supplementary Fig. 3). Thus, a small fraction of spectra was excluded from analysis in order to prevent statistical distortions by outlier spectra. All remaining spectra were subjected to Mie scattering correction, based on extended multiplicative signal correction (EMSC) [42, 70]. Supplementary Fig. 3 presents exemplary plaque spectra before and after the application of EMSC. In order to identify spectra within a hypercuboid, that correspond to a plaque (more precisely “A β positive area”); a binary mask was generated from the A β -IHC image cutouts (supplementary Fig. 4), using Otsu’s method (Matlab Image Processing Toolbox) [57]. The henceforth-called plaque spectrum is the arithmetic mean of all pixel-spectra within this mask. Another mask was generated, that describes a ring-shape with a radial thickness of 100 μm , surrounding the plaque, excluding A β -positive pixel, which were again detected by using Otsu’s method. The arithmetic means of the spectra corresponding to the latter mask is henceforth called surrounding spectrum.

FTIR spectral data analysis

For the structural analysis of each classic cored plaque, the respective spectral image cutout was separated using hierarchical cluster analysis (HCA) (Matlab, Statistics toolbox). Spectra were thereby grouped into 10 subgroups based on spectral similarity. The subgroups belonging to the core or the corona were each selected by visual comparison to the corresponding A β -IHC image and merged, if applicable. The arithmetic means of spectra belonging to the core were used in further analysis and are being referred to as core spectra of the inner core. Difference spectra were calculated between plaque spectra and surrounding spectra. For the analysis of the amide region, a linear baseline was subtracted from the spectra within the range 1800-1480 cm^{-1} . Whereas, for the detailed investigation of the band at 1630 cm^{-1} , a linear baseline was subtracted from the amide I bands within the range 1690-1610 cm^{-1} . The bands were subsequently area-normalized in the range 1690-1610 cm^{-1} and subtracted from each other. Arithmetic means of all difference spectra from a respective plaque-type were calculated and interpolated with a spline for display. Second derivatives of spectra were calculated, using a Savitzki-Golay filter with a third-degree polynomial and a frame size of five (Matlab, Signal Processing toolbox).

FTIR band assignment and interpretation

We determined spectroscopic ratios between FTIR absorbance bands that correspond to vibrational modes of the protein backbone, CH₂, and CH₃ groups (supplementary Table 2). The protein accumulation is quantified by the amide II peak (A_{1545} , N-H bending vibration) of the protein backbone vibration [45], in proportion to the absorbance in the CH-stretching region, as proxy for total absorbance from lipids and proteins. The β -sheet levels are quantified by the ratio A_{1630}/A_{1655} of respective bands representing β -sheets and non- β -sheet secondary structures. The band positions were derived from second derivatives. The band at 1655 cm⁻¹ is commonly associated with α -helical proteins, but as e.g., unordered structures may also contribute to the band, we use the term non- β -sheets here.

Statistical analysis

The spectroscopic ratios and band height differences in second derivatives were used for statistical analysis. Additional to the A β plaques, 208 randomly selected small (approximately 100 \times 100 μ m), A β -negative areas from the grey matter of control cases constituted the control group. Furthermore, core spectra were included as a separate group. In between each group, *p*-values were calculated alongside the proposed development sequence (Matlab, Statistics toolbox), according to Student's *t*-test [71]. The confidence levels were determined according to *p*-values < 0.05 (*), < 0.01 (**), and < 0.001 (***). The correlation between the ratios was quantified by the Pearson correlation coefficient *R* [44] (Matlab, Statistics toolbox), using only plaques spectra and core spectra. We investigated the statistical influence of cases, which contributed high amounts of plaques to the respective types (cases 7 and 9, supplementary Table 1). We found that case 7 has little impact on the statistical analysis of diffuse plaques, whereas the classic cored plaques of case 9 shift the respective distributions slightly downwards, by approximately - 0.16 points for protein and approximately - 0.09 points for β -sheets. Further, we found no notable alterations in the spectral data of case 7, which had the longest post mortem interval (10.45 h).

RESULTS

We developed a workflow that combines FTIR, Raman, and A β -IHC imaging within the same tissue thin section, thereby integrating label-free imaging with the neuropathology gold standard for plaque detection (Fig. 1). For each sample, areas of about 20 mm² were measured by FTIR imaging. Additionally, smaller subareas of about 0.2 mm² were imaged by Raman. Subsequently, the same tissue section was immunostained against A β and imaged by light microscopy. By spatial overlay of vibrational and A β -IHC images, A β plaques were clear-cut identified in FTIR and Raman images. AD neuropathology experts annotated each scanned plaque in A β -IHC images to differentiate between the plaque types. We present the spectral analysis of 68 diffuse plaques [80], 32 compact plaques [16], and 60 classic cored plaques [69], measured in 20 μ m thick native post mortem brain sections of seven AD cases. The plaques were compared to their surrounding tissue (supplementary Fig. 4) and A β -negative grey matter of three non-demented control cases (supplementary Table 1). None of the bands used here for analysis showed alterations during the measurements (supplementary Fig. 1), ruling out sample degradation.

FTIR imaging reveals the distribution of β -sheet protein in different plaque types

We present exemplary plaques of each type in A β -IHC images (Fig. 2A). Healthy control tissue is shown as a reference (Fig. 2A₁). The FTIR results of the same tissue areas are visualized in pseudo-color images that display protein accumulation (Fig. 2B). We observed increased protein concentrations in all plaque types, compared to control tissue. We assign this aggregated protein mostly to A β , as indicated by the respective A β -IHC images (Fig. 2A). Due to the cellular composition of brain tissue, the protein concentration in control tissue is not homogeneous (Fig. 2B₁). The diffuse plaque shows protein accumulations that are randomly distributed within the plaque area (Fig. 2B₂). In the compact plaque, protein is accumulated in the center (Fig. 2B₃). Overall, compact plaques displayed a wide range of protein distributions, spanning from homogeneous dispersions to centralized accumulations. Interestingly, in some compact plaques we even noted core-like protein structures (Fig. 2B₃), which were not visible in corresponding A β -IHC images (Fig. 2A₃). Classic cored plaques, recognized by their typical core in A β -IHC images (Fig. 2A₄), present in FTIR data a core with high protein content that is surrounded by a corona with less aggregated protein (Fig. 2B₄).

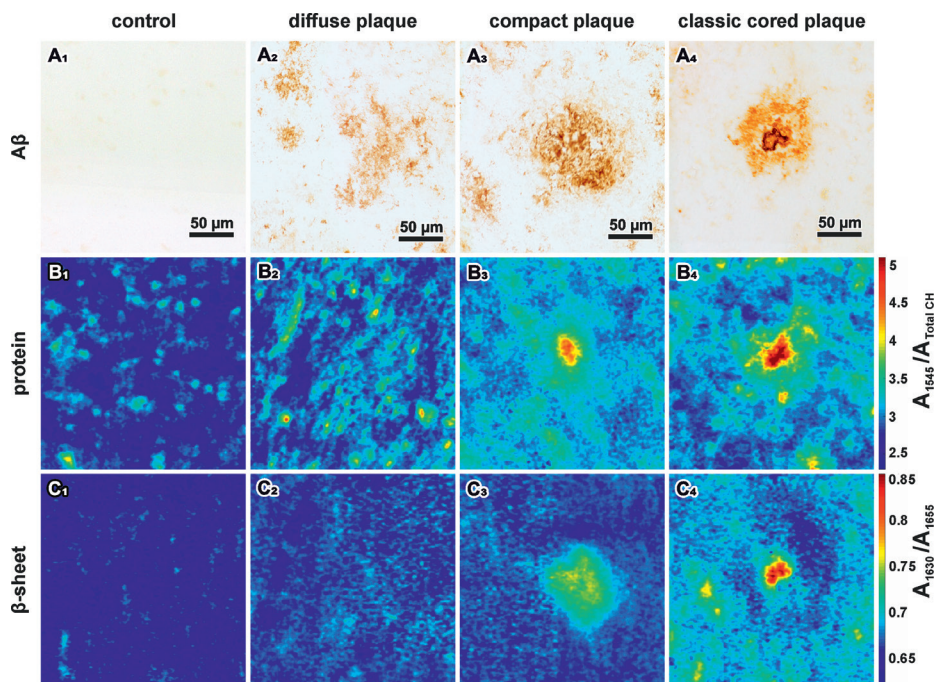


Fig. 2. Immunohistochemical and FTIR imaging of control tissue (A₁), diffuse (A₂), compact (A₃) and classic cored (A₄) plaques

A Immunohistochemical staining against A β . **B**. Ratio between the amide II and CH stretching bands. Red indicates high protein concentrations. **C** Ratio between the main β -sheet band and non- β -sheet band of the amide I. Red indicates high β -sheet levels. A β Amyloid-beta.

In the next step, we analyzed the secondary structure composition of A β in the different plaque types to evaluate β -sheet levels (Fig. 2C). This is elaborated from the ratio between the amide I bands of β -sheets and non- β -sheets. Healthy grey matter shows no β -sheet aggregations (Fig. 2C₁). In diffuse plaques, we observed slightly increased β -sheet levels (Fig. 2C₂). The compact plaque shows increased β -sheet levels across the plaque area (Fig. 2C₃). The classic cored plaque shows aggregated β -sheet protein, condensed in its core (Fig. 2C₄). Interestingly, the surrounding corona displays low levels of β -sheets, similar to diffuse deposits. Two selected classic cored plaques were additionally analyzed with Raman imaging, confirming FTIR observations (supplementary Fig. 6).

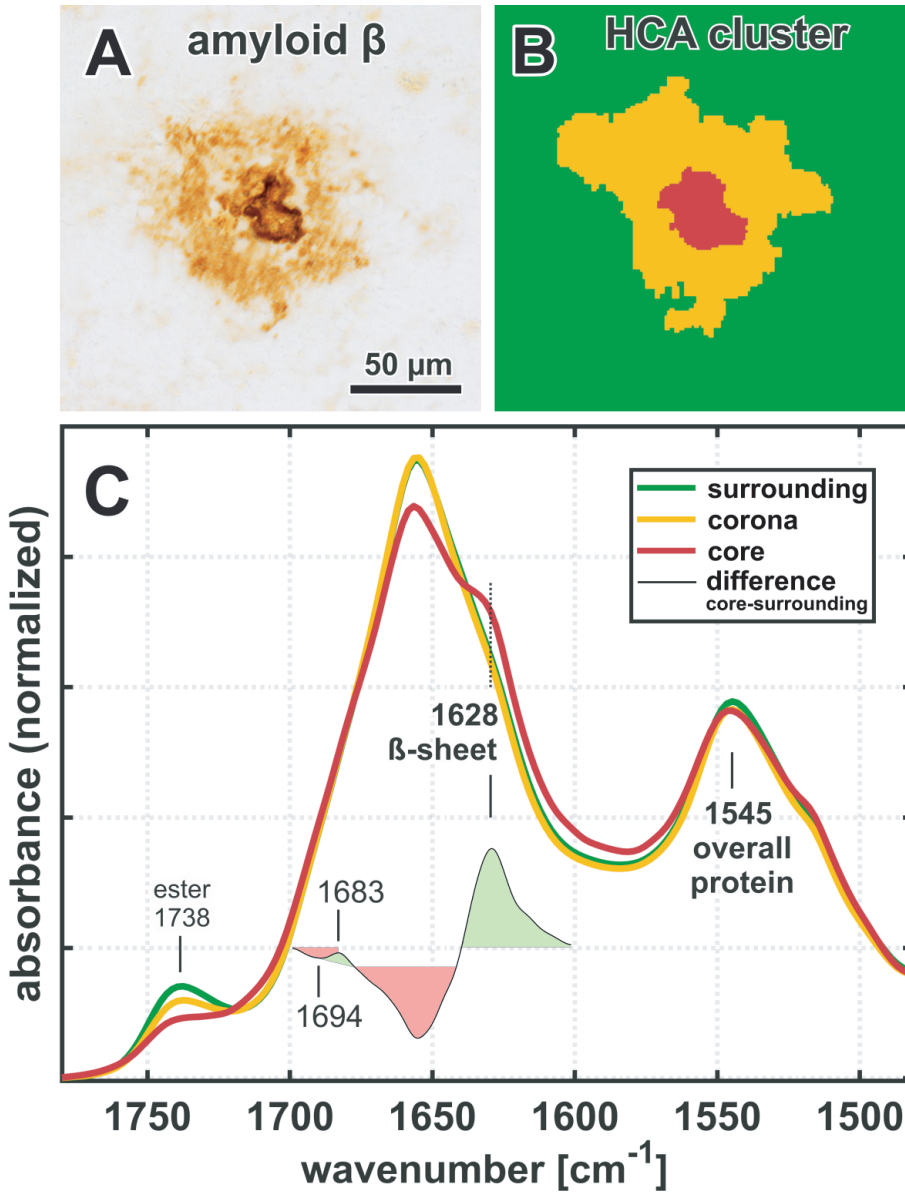


Fig. 3. FTIR analysis of an exemplary classic cored plaque and its compartments **A** Anti- $\text{A}\beta$ immunostaining **B** Areas of spectral similarity, identified by HCA, that correspond to surrounding tissue (green), corona (yellow), and core (red). **C** Area-normalized FTIR spectra in the range 1780-1480 cm^{-1} . The red core spectrum shows a prominent shoulder at 1628 cm^{-1} and reduced absorbance at 1655 cm^{-1} . A difference spectrum (black) in the range 1700-1600 cm^{-1} reveals minor bands at 1683 cm^{-1} and 1694 cm^{-1} . The lipid-associated ester band at 1738 cm^{-1} is decreased in both the corona and the core. $\text{A}\beta$ Amyloid-beta; HCA hierarchical cluster analysis.

The characteristic core and corona structure of classic cored plaques was analyzed in more detail (Fig. 3). Plaque cores and coronas were distinguished from each other and from the surrounding tissue, based on their spectral properties, using hierarchical cluster analysis (HCA). We performed HCA on spectral hypercuboids of all included classic cored plaques ($n = 60$). Thereby, we separated pixel that correspond to the core of each plaque and generated core spectra of 52 out of the 60 classic cored plaques. The remaining cores were either too small to be resolved in FTIR or were discarded due to insufficient data quality. HCA results for the exemplary classic cored plaque are shown (Fig. 3A, B). Fig. 3C shows only the most relevant spectral range, containing the amide I ($\sim 1655 \text{ cm}^{-1}$), amide II ($\sim 1545 \text{ cm}^{-1}$), and the lipid-associated ester band ($\sim 1738 \text{ cm}^{-1}$). The ester band is decreased in the corona (yellow) and even more in the core (red). However, we note that the ester band does not disappear entirely, indicating a residual lipid content within the core. The structure-sensitive amide I band of the corona is nearly identical to that of the surrounding tissue (green), indicating low β -sheet levels in the corona. In contrast, the core spectrum displays a strong shoulder at 1628 cm^{-1} . A difference spectrum between the core and the surrounding tissue is shown (Fig. 3C). It reveals positive bands at 1683 cm^{-1} and 1628 cm^{-1} , as well as negative bands at 1694 cm^{-1} and 1655 cm^{-1} .

The amide I band reveals structural properties of the A β in plaques

A detailed analysis of the amide I band reveals further differences between the plaque types (Fig. 4). The previously described, increased absorbance at 1630 cm^{-1} manifests in a shoulder on the right side of the amide I band (Fig. 4A). Difference spectra between plaque spectra and surrounding spectra reveal that the 1630 cm^{-1} band shifts to the right, alongside the proposed plaque development sequence (diffuse, compact, classic cored) (Fig. 4B). The band position reaches 1628 cm^{-1} in core spectra. Additionally, the right flank of the band broadens, showing increased absorbance at 1620 cm^{-1} . The shift to lower wavenumbers is reproduced in second derivative spectra (Fig. 4C), which reveal additionally bands at 1693 cm^{-1} , 1682 cm^{-1} , 1657 cm^{-1} , and 1639 cm^{-1} . The band at 1682 cm^{-1} is slightly increased, whereas the band at 1693 cm^{-1} does not change and the bands at 1657 cm^{-1} , and 1639 cm^{-1} are decreased. In accordance, we observe a positive band at 1683 cm^{-1} and a negative band at 1694 cm^{-1} emerging in difference spectra (supplementary Fig. 5).

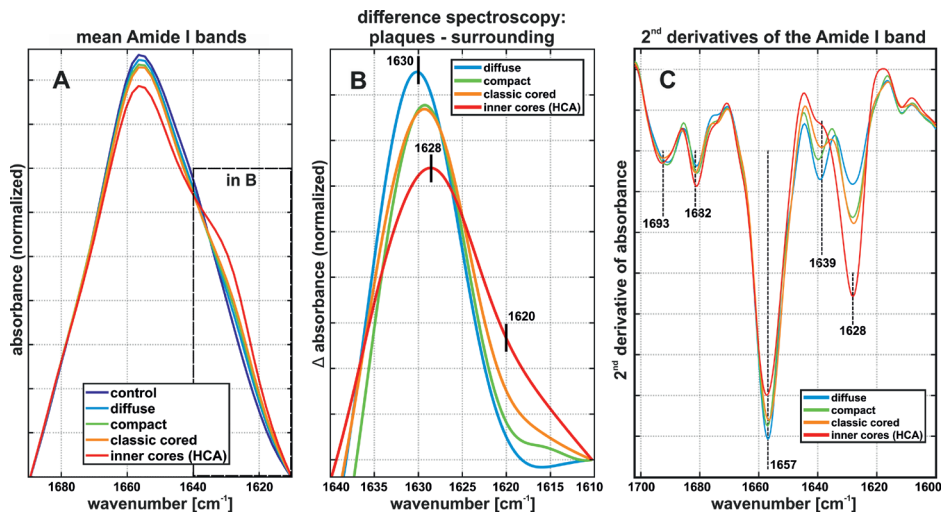


Fig. 4. Amide I band analysis

A Mean amide I bands of all plaque spectra from each plaque type, core spectra generated by HCA, and grey matter control spectra. The shoulder at 1628 cm^{-1} indicates β -sheet protein. **B** Cutout of mean difference spectra between plaque spectra and their respective surrounding spectra. Note the shift to lower wavenumbers and the increased absorbance at 1620 cm^{-1} . **C** Visualization of sub-bands of the amide I in the region $1700\text{--}1600\text{ cm}^{-1}$. The marked local minima indicate bands that are relevant for protein secondary structure. Note the substantial increase of the band at 1628 cm^{-1} alongside the plaque development sequence. The band at 1693 cm^{-1} displays little change, whereas the band at 1682 cm^{-1} increases, and the bands at 1657 cm^{-1} , and 1639 cm^{-1} decrease.

Since the biochemical composition of the grey matter is inhomogeneous, especially during disease processes, it is essential to include a viable number of plaques from a representative cohort for statistical analysis (Fig. 5). The accumulation of protein, as well as the level of β -sheets increase along the sequence from (i) grey matter control, to (ii) diffuse plaques, (iii) compact plaques, and peak in the (vi) cores of classic cored plaques (Fig. 5A, B). The β -sheet levels in diffuse plaques display some outliers (black crosses in Fig. 5B). We associate these outliers with unusually high misfolding levels with the two oldest cases in this study (cases 5 and 6, supplementary Table 1). Further research will be necessary to elaborate if there is a correlation between age and β -sheet levels in diffuse plaques. Notably, we detect no significant differences between plaque spectra of compact plaques and classic cored plaques, neither regarding protein nor β -sheet levels. Remarkably, protein and β -sheet levels correlate ($R = 0.73$) in plaques (Fig. 5C). Furthermore, the height difference between the bands at 1628 cm^{-1} and 1693 cm^{-1} increases significantly alongside the plaque development sequence (Fig. 5D), indicating an increasing dominance of the 1628 cm^{-1} band over the 1693 cm^{-1} band in mature plaques.

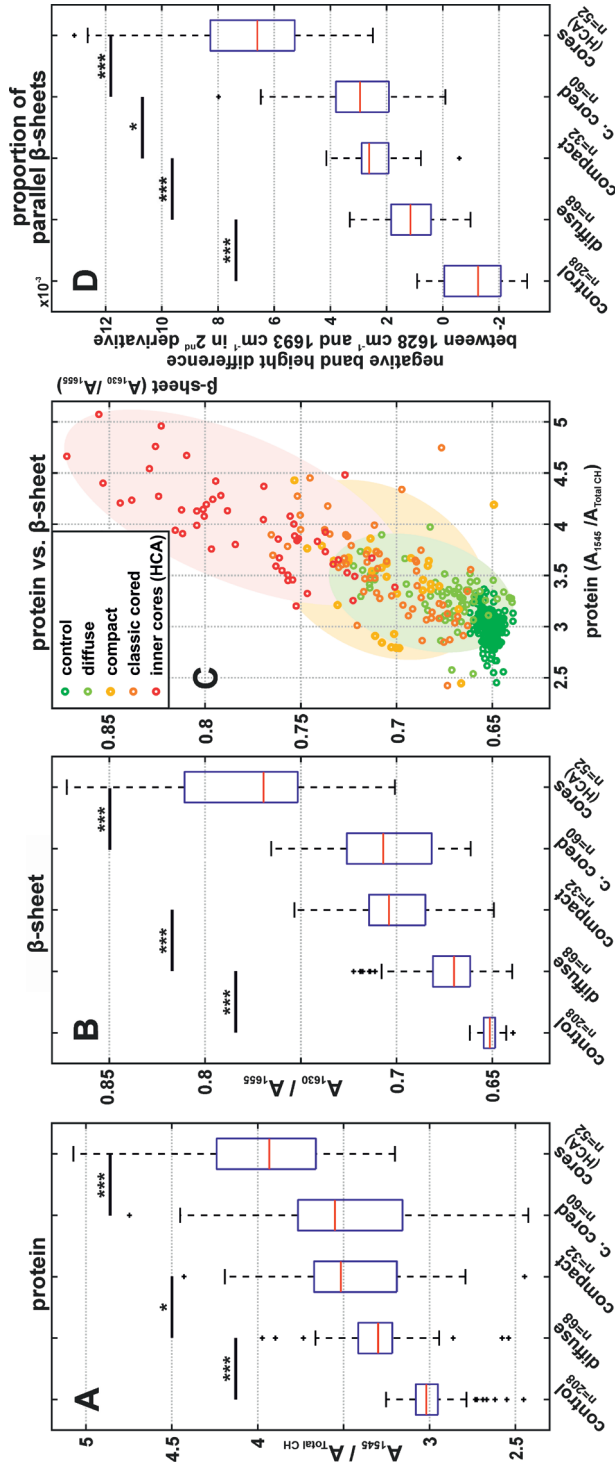


Fig. 5. Statistical analysis

The boxplots present spectroscopic ratios derived from control, plaque, and core spectra. The red bar indicates the median value, the blue boxes range between the first and third quartile. The black whiskers show the extremes of the distribution, excluding outliers (black crosses). The significance bars announce the confidence levels. **A** Ratios between the amide II band and the CH stretching bands, indicating protein accumulation. **B** Ratios between the amide I band of β -sheets and non- β -sheet structures, indicating β -sheet levels. **C** The scatterplot illustrates the correlation between protein and β -sheet levels in plaques. A successive accumulation of β -sheet protein alongside the plaque development sequence is apparent. **D** The negative height difference of the bands at 1628 and 1693 cm^{-1} in 2nd derivative spectra indicates increased proportions of parallel β -sheets.

DISCUSSION

We observed the accumulation of A β with a β -sheet structure in plaques, which centralizes successively alongside the proposed plaque development sequence (Fig. 2). With increasing A β density, plaque spectra show a shift of the band at 1630 cm⁻¹ towards lower wavenumbers and a decreasing band at 1693 cm⁻¹ (Fig. 3, 4). This behavior is consistent across cases and shows a steady transition along the proposed plaque development sequence (Fig. 5).

Several studies have already applied vibrational spectroscopy to analyze amyloid brain deposits and thereby provided insight into protein misfolding in tissue. The tissue sections were usually not immunostained against A β , as the staining of brain tissue on non-adhesive crystal slides is difficult. Therefore, a differential analysis of A β plaque types has not been performed yet. We have overcome this challenge with an optimized staining protocol (see methods) and now present a detailed analysis of the most common A β plaque types. Most previous studies used mouse models of AD, as the tissue of transgenic mice is more easily available than human tissue and usually contains dense amyloid deposits [24, 35, 41, 45, 58, 59, 72, 73]. Much has been elaborated about the properties of plaques this way. Surowka et al. report increased β -sheet levels in mature plaques in mice, using FTIR [74]. Fonseca et al. detect lipid-rich cell-sized depositions surrounding mature plaques using Raman microspectroscopy [24].

However, as the transferability of findings between mouse models and humans remains unclear, we investigate A β plaques in human brain tissue here, in order to resemble the disease course and pathology in human brains. This is particularly relevant for the interplay between A β and the various surrounding cell types, which is considered to be crucial in plaque development [2, 60, 62, 79, 82]. Several groups have applied vibrational imaging to human AD brain tissue before [1, 6, 22, 23, 39, 46, 49]. For instance, Benseny-Cases et al. report an increased 1630 cm⁻¹ to 1650 cm⁻¹ ratio in thioflavin T-positive deposits from the human brain [6], which aligns well with our results on classic cored plaques (Fig. 2C_d). Michael et al. report a shift of the Raman amide I band towards 1666 cm⁻¹ in amyloid deposits [49], which aligns with our observations in plaque cores (supplementary Fig. 6). Klementieva et al. recently detected increased β -sheet levels in neuron models of AD, using second derivatives of optical photothermal infrared spectra [40], which reveal a structure of the amide I band that is similar to the here presented data (Fig. 4C). Some of the spectroscopic studies on amyloid deposits in formaldehyde-fixated human brain tissue reported elevated lipid

bands in ring-like shapes around amyloid cores, which were proposed to originate from microglia [6, 39, 49]. As we do not observe similar structures in our snap-frozen samples, we suspect that the described lipid-like signal might be caused by the fixation procedure with formaldehyde, which is known to bind to proteins and show lipid-like absorbance [11]. Two studies report FTIR measurements on amyloid deposits in native human brain tissue [23, 46]. The therein-presented spectra show visibly increased absorbance at 1630 cm^{-1} and decreased absorbance at 1738 cm^{-1} , which is in nice agreement with our results (Fig. 3C).

By analyzing the amide I band in plaques, we conclude a successive accumulation of A β with β -sheet structure from increased absorbance at 1630 cm^{-1} (Fig. 2, 5A, B) alongside the proposed plaque development sequence (diffuse, compact, classic cored). Additionally, we observe an increased peak at 1683 cm^{-1} (Fig. 3C, 4C) that is associated with β -turns in β -sheet proteins [27], confirming the accumulation of β -sheet protein. In contrast, we do not observe increased absorbance at 1693 cm^{-1} (Fig. 4C), which would be expected if the deposited A β were in an antiparallel β -sheet formation [8, 10]. On the contrary, difference spectra reveal a decreased contribution of the 1693 cm^{-1} band in compact and classic cored plaques (Fig. 3C and supplementary Fig. 5). We deduce that A β adopts a parallel β -sheets structure during plaque development [8, 9]. Further, we observe a shift of the amide I band from 1630 cm^{-1} to 1628 cm^{-1} , accompanied by increased absorbance at 1620 cm^{-1} (Fig. 4B). This shift is associated with a growing number of strands in parallel β -sheets [9, 47, 78]. We conclude that increasing fractions of A β is in extended parallel β -sheet conformation (Fig. 4, 5D). Such a shift was described for the formation of A β fibrils [5, 54, 41, 63]. The absorbance of amyloid fibrils at low wavenumbers was described *in vitro* [3, 81, 83] as well as for A β fibrils in cell culture [4, 41]. In summary, we conclude the growth of parallel β -sheet fibrils alongside the plaque development sequence, in agreement with other reports [79, 82]. The extensive knowledge about A β fibrillation from spectroscopic studies [5, 41, 54, 63, 64] allows us this careful analysis of A β in the brain, with respect to the limitations set by the complex conditions in tissue. Thus, to the best of our knowledge, we report the first evidence of A β fibril growth alongside the proposed plaque development sequence in the human brain.

We observed protein clusters in diffuse plaques (Fig. 2B₂), which might originate from parenchymal A β depositions or A β -enriched cells, which would align with descriptions of internalized A β prior to parenchymal infestation [13, 25,

33]. Diffuse plaques displayed increased β -sheet levels compared to control tissue (Fig. 5B). The main β -sheet band is symmetric at 1630 cm^{-1} (Fig. 4B). The marker band 1693 cm^{-1} for anti-parallel β -sheets is not notably decreased in difference spectra (supplementary Fig. 5). Taken together, this indicates that the $A\beta$ in diffuse plaques is primarily arranged in antiparallel β -sheets and parallel β -sheets with a low number of strands. We conclude that diffuse plaques contain mostly oligomeric and protofibrillar $A\beta$, yet in low concentrations (Fig. 6B₁). This aligns well with the assumption that diffuse plaques are the starting point of plaque development [34].

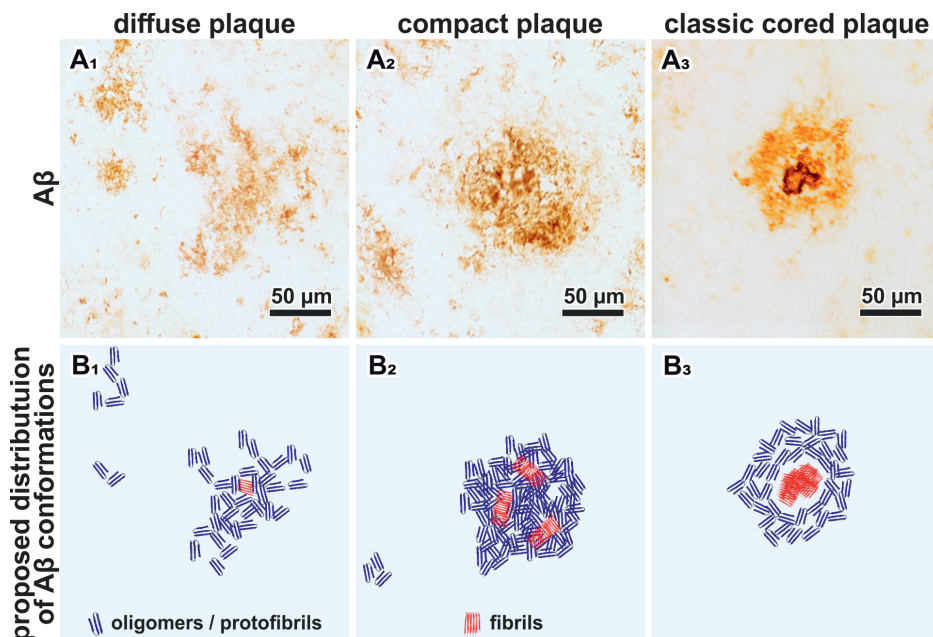


Fig. 6. Proposal of $A\beta$ conformations in the different plaque types

A depicts the exemplary plaques from Fig. 2. **B** Based on our observations, we propose the depicted composition of $A\beta$ conformations in the different plaque types. The symbols are used to indicate the hypothetical location, density, and mixture of $A\beta$ conformation in a simplified fashion. $A\beta$ Amyloid-beta.

Compact plaques usually displayed homogeneously distributed β -sheet levels, while protein levels appeared either homogenous or centrally localized (Fig. 2B₃). Those centralized protein clusters were usually indistinguishable in $A\beta$ -IHC and β -sheet images (Fig. 2A₃, C₃). FTIR imaging might be capable of detecting an emerging core in these plaques. However, the observed protein might also originate from proteins other than $A\beta$. Further investigations are

necessary to clarify the origin of these observations. Furthermore, we observe a broad distribution of β -sheet levels in compact plaques (Fig. 5B). This aligns with reports, which state that not all compact plaques stain positive with Congo Red or thioflavin S [19, 20]. The amide I band analysis indicates a significantly increased contribution of large parallel β -sheet structures in compact plaques (Fig. 4, 5). Thereby, we deduce that compact plaques contain an increased content of β -sheet A β , including varying amounts of A β fibrils (Fig. 6C₂). Therefore, we propose that compact plaques are a heterogeneous group of intermediate states in plaque development, which cannot easily be differentiated with the most common anti-A β staining methods.

The cores of classic cored plaques display high levels of β -sheet A β (Fig. 2). The strong band at 1628 cm⁻¹ and the decreased band at 1693 cm⁻¹ imply high levels of large parallel β -sheet structures. From this, we conclude an abundance of A β fibrils in the cores (Fig. 6C₃). This is consistent with amyloid-marker-based studies [2, 15, 65]. Nevertheless, our data suggests that plaque cores are not spheres of pure A β , as their usually dense appearance in A β -IHC images may suggest. FTIR measurements detect lipids within the cores (Fig. 3C), which aligns with a previous report [46]. This may imply (i) cellular involvement, for example of infiltrating microglia or astrocytes extensions [2, 14], or the presence of processes that (ii) actively or (iii) passively integrate membranous material in the cores. Neighboring neurites may also contribute to the lipid signal, as the spatial resolution of FTIR imaging is limited. Recently, evidence for lipids and membranous material in Lewy bodies in Parkinson's disease has been reported [68]. Despite the ubiquitous abundance of lipids in the brain, this similarity of the two pathological phenomena is interesting, because it indicates cellular involvement in their respective developments; either as unintentional incorporation of e.g., cell fragments, or by cell-driven deposition [52]. Further research will be necessary to better understand the cellular involvement in the formation of A β plaques and other protein aggregates.

In contrast to the central plaque core, we observed low levels of β -sheets in the corona of classic cored plaques (Fig. 2, 3), indicating a low content of β -sheet A β in the corona. This appears to be the reason why we do not observe significant differences between compact plaques and classic cored plaques in the statistical analysis (Fig. 5). The statistical analysis is based on the mean spectra of plaques, which include the core and corona, in case of the classic cored plaques (supplementary Fig. 4). Accordingly, the relatively large corona appears to compensate for the highly fibrillar core. This implies that the A β composition

in the corona is similar to that in diffuse plaques; featuring low contents of mainly oligomeric and protofibrillar A β (Fig. 6C₃). The substantial differences between cores and coronas may be due to the influence of inflammatory cells and the subsequent disaggregation and/or displacement of A β fibrils. Several studies have placed activated microglia in the focus of plaque core formation [2, 60, 61, 82]. We observe the characteristic gaps that glia cells leave in A β -IHC images of plaques (Fig. 2A), indicating glial involvement in the here investigated plaques. Microglia have been shown to dissolve A β fibrils into oligomers [36]. We suspect that such A β oligomers may be contained in the corona. Microglial involvement may also be a reason for the relatively low protein levels, which we observe in coronas (Fig. 2B₄), as the infiltrating microglia might displace protein with their lipid-rich cell bodies [2, 58, 82]. Additionally, several studies have found neurites and various dystrophic cell fragments in the corona [17, 19], which presumably contribute to A β displacement.

Raman data of identical tissue areas validate FTIR results on classic cored plaques and reproduces the distribution of β -sheet protein in a side-by-side comparison to FTIR (supplementary Fig. 6). As similar results were obtained with an independent technique, our findings are verified, confirming the reliability of our label-free approach.

In conclusion, our novel approach allowed us to track the progression of A β fibrillation alongside the plaque development sequence, for the first-time label-free, in human brain tissue thin sections. Our observations of successive accumulation and fibrillation of β -sheet structured A β could give implications for therapeutic approaches and supports that the proposed plaque-type sequence (diffuse, compact, classic cored plaques) describes the development stages of A β plaques in AD.

ACKNOWLEDGEMENTS

The anti-A β antibody clone IC-16 was kindly provided by Prof. Carsten Korth, Heinrich Heine Universität Düsseldorf, Germany. We would like to thank dr. Wilma D.J. van de Berg for recommending the use of gelatin as tissue adhesive and we acknowledge Allert J. Jonker for technical assistance with tissue preparation. This research was supported by the Protein Research Unit Ruhr within Europe (PURE), funded by the Ministry of Innovation, Science and Research (MIWF) of North-Rhine Westphalia, Germany (grant number: 233-1.08.03.03-031-68079), the Center for Protein Diagnostics (PRODI), funded by the Ministry of Culture and Science (MKW) of the State of North Rhine-Westphalia, Germany (#111.08.03.05-133974), Alzheimer Nederland (#WE.15-2019-13), ZonMw (#733050104), and NIH (#1R01AG061775).

LIST OF ABBREVIATIONS

| | |
|----------------|---|
| A β | amyloid-beta |
| A β -IHC | anti-A β immunohistochemistry |
| AD | Alzheimer's disease |
| APP | amyloid precursor protein |
| DAB | 3,3'-diaminobenzidine tetrahydrochloride |
| EMSC | extended multiplicative signal correction |
| FOV | field of view |
| FTIR | Fourier-transform infrared |
| HCA | hierarchical cluster analysis |
| LPS | superior parietal lobule |
| NFT | neurofibrillary tangle |
| ROI | region of interest |

REFERENCES

1. Araki K, Yagi N, Ikemoto Y, Yagi H, Choong C-J, Hayakawa H, et al. (2015) Synchrotron FTIR micro-spectroscopy for structural analysis of Lewy bodies in the brain of Parkinson's disease patients. *Sci Rep* 5:17625. doi: 10.1038/srep17625
2. Arends YM, Duyckaerts C, Rozemuller JM, Eikelenboom P, Hauw JJ (2000) Microglia, amyloid and dementia in Alzheimer disease: A correlative study. *Neurobiol Aging* 21:39-47. doi: 10.1016/S0197-4580(00)00094-4
3. Barth A (2007) Infrared spectroscopy of proteins. *Biochim Biophys Acta - Bioenerg* 1767:1073-1101. doi: 10.1016/j.bbabi.2007.06.004
4. Benseny-Cases N, Álvarez-Marimon E, Castillo-Michel H, Cotte M, Falcon C, Cladera J (2018) Synchrotron-Based Fourier Transform Infrared Microspectroscopy (μ FTIR) Study on the Effect of Alzheimer's A β Amorphous and Fibrillar Aggregates on PC12 Cells. *Anal Chem* 90:2772-2779. doi: 10.1021/acs.analchem.7b04818
5. Benseny-Cases N, Cócera M, Cladera J (2007) Conversion of non-fibrillar β -sheet oligomers into amyloid fibrils in Alzheimer's disease amyloid peptide aggregation. *Biochem Biophys Res Commun* 361:916-921. doi: 10.1016/j.bbrc.2007.07.082
6. Benseny-Cases N, Klementieva O, Cotte M, Ferrer I, Cladera J (2014) Microspectroscopy (μ FTIR) Reveals Co-localization of Lipid Oxidation and Amyloid Plaques in Human Alzheimer Disease Brains. *Anal Chem* 86:12047-12054. doi: 10.1021/ac502667b
7. Bugiani O, Giaccone G, Frangione B, Ghetti B, Tagliavini F (1989) Alzheimer patients: preamyloid deposits are more widely distributed than senile plaques throughout the central nervous system. *Neurosci Lett* 103:263-268. doi: 10.1016/0304-3940(89)90110-9
8. Cerf E, Sarroukh R, Tamamizu-Kato S, Breydo L, Derclayes S, Dufrênes YF, et al. (2009) Antiparallel β -sheet: A signature structure of the oligomeric amyloid β -peptide. *Biochem J* 421:415-423. doi: 10.1042/BJ20090379
9. Chirgadze YN, Nevskaya NA (1976) Infrared spectra and resonance interaction of amide-I vibration of the parallel-chain pleated sheet. *Biopolymers* 15:627-636. doi: 10.1002/bip.1976.360150403
10. Chirgadze YN, Nevskaya NA (1976) Infrared spectra and resonance interaction of amide-I vibration of the antiparallel-chain pleated sheet. *Biopolymers* 15:607-625. doi: 10.1002/bip.1976.360150402
11. Craver C (1982) *The Coblentz Society Desk Book of Infrared Spectra*, 2nd ed. The Coblentz Society, Kirkwood, MO
12. Cummings J, Lee G, Ritter A, Sabbagh M, Zhong K (2019) Alzheimer's disease drug development pipeline: 2019. *Alzheimer's Dement Transl Res Clin Interv* 5:272-293. doi: 10.1016/j.trci.2019.05.008
13. D'Andrea MR (2016) *Intracellular Consequences of Amyloid in Alzheimer's Disease*. Elsevier, Wilmington, DE, USA

14. D'Andrea MR, Cole GM, Ard MD (2004) The microglial phagocytic role with specific plaque types in the Alzheimer disease brain. *Neurobiol Aging* 25:675–683. doi: 10.1016/j.neurobiolaging.2003.12.026
15. D'Andrea MR, Nagele RG (2010) Morphologically distinct types of amyloid plaques point the way to a better understanding of Alzheimer's disease pathogenesis. *Biotech Histochem* 85:133–147. doi: 10.3109/10520290903389445
16. Dickson DW (1997) The Pathogenesis of Senile Plaques. *J Neuropathol Exp Neurol* 56:321–339. doi: 10.1097/00005072-199704000-00001
17. Dickson TC, Vickers JC (2001) The morphological phenotype of β -amyloid plaques and associated neuritic changes in Alzheimer's disease. *Neuroscience* 105:99–107. doi: 10.1016/S0306-4522(01)00169-5
18. Dreissig I, Machill S, Salzer R, Krafft C (2009) Quantification of brain lipids by FTIR spectroscopy and partial least squares regression. *Spectrochim Acta - Part A Mol Biomol Spectrosc* 71:2069–2075. doi: 10.1016/j.saa.2008.08.008
19. Duyckaerts C, Delatour B, Potier M-C (2009) Classification and basic pathology of Alzheimer disease. *Acta Neuropathol* 118:5–36. doi: 10.1007/s00401-009-0532-1
20. Duyckaerts C, Dickson D (2011) Neuropathology of Alzheimer's Disease and its variants. In: Dickson DW, Weller RO (eds) *Neurodegeneration: The Molecular Pathology of Dementia and Movement Disorders*. Wiley-Blackwell, Oxford, UK, pp 62–91
21. El-Mashtoly SF, Petersen D, Yosef HK, Mosig A, Reinacher-Schick A, Kötting C, et al. (2014) Label-free imaging of drug distribution and metabolism in colon cancer cells by Raman microscopy. *Analyst* 139:1155. doi: 10.1039/c3an01993d
22. Fabian H, Choo LPI, Szendrei GI, Jackson M, Halliday WC, Otvos L, et al. (1993) Infrared spectroscopic characterization of Alzheimer plaques. *Appl Spectrosc* 47:1513–1518. doi: 10.1366/0003702934067469
23. Findlay CR, Wiens R, Rak M, Sedlmair J, Hirschmugl CJ, Morrison J, et al. (2015) Rapid biodiagnostic ex vivo imaging at 1 μ m pixel resolution with thermal source FTIR FPA. *Analyst* 140:2493–2503
24. Fonseca EA, Lafetá L, Cunha R, Miranda H, Campos J, Medeiros HG, et al. (2019) A fingerprint of amyloid plaques in a bitransgenic animal model of Alzheimer's disease obtained by statistical unmixing analysis of hyperspectral Raman data. *Analyst* 144:7049–7056. doi: 10.1039/C9AN01631G
25. Friedrich RP, Tepper K, Ronicke R, Soom M, Westermann M, Reymann K, et al. (2010) Mechanism of amyloid plaque formation suggests an intracellular basis of A pathogenicity. *Proc Natl Acad Sci* 107:1942–1947. doi: 10.1073/pnas.0904532106
26. Garczarek F, Gerwert K (2006) Functional waters in intraprotein proton transfer monitored by FTIR difference spectroscopy. *Nature* 439:109–112. doi: 10.1038/nature04231
27. Goormaghtigh E, Cabiaux V, Ruyschaert JM (1994) Determination of soluble and membrane protein structure by Fourier transform infrared spectroscopy. II. Experimental aspects, side chain structure, and H/D exchange. *Subcell Biochem* 23:363–403. doi: 10.1007/978-1-4615-1863-1_9

28. Goormaghtigh E, Derenne A, Bénard A, Gasper R, Raussens V (2010) Data processing in FTIR imaging of cells: Towards protein secondary structure imaging. *Spectroscopy* 24:51–54. doi: 10.3233/SPE-2010-0403
29. Goormaghtigh E, Ruyschaert J-M, Raussens V (2006) Evaluation of the Information Content in Infrared Spectra for Protein Secondary Structure Determination. *Biophys J* 90:2946–2957. doi: 10.1529/biophysj.105.072017
30. Großerueschkamp F, Bracht T, Diehl HC, Kuepper C, Ahrens M, Kallenbach-Thieltges A, et al. (2017) Spatial and molecular resolution of diffuse malignant mesothelioma heterogeneity by integrating label-free FTIR imaging, laser capture microdissection and proteomics. *Sci Rep* 7:44829. doi: 10.1038/srep44829
31. Güldenhaupt J, Adigüzel Y, Kuhlmann J, Waldmann H, Kötting C, Gerwert K (2008) Secondary structure of lipidated Ras bound to a lipid bilayer. *FEBS J* 275:5910–5918. doi: 10.1111/j.1742-4658.2008.06720.x
32. Haass C, Selkoe DJ (2007) Soluble protein oligomers in neurodegeneration: Lessons from the Alzheimer's amyloid β -peptide. *Nat. Rev. Mol. Cell Biol.* 8:101–112
33. Head E, Garzon-Rodriguez W, Johnson JK, Lott IT, Cotman CW, Glabe C (2001) Oxidation of A β and plaque biogenesis in Alzheimer's disease and Down syndrome. *Neurobiol Dis* 8:792–806. doi: 10.1006/nbdi.2001.0431
34. Ikeda S-I, Yanagisawa N, Allsop D, Glenner GG (1990) Early senile plaques in Alzheimer's disease demonstrated by histochemistry, immunocytochemistry, and electron microscopy. *Hum Pathol* 21:1221–1226. doi: 10.1016/S0046-8177(06)80034-1
35. Ji M, Arbel M, Zhang L, Freudiger CW, Hou SS, Lin D, et al. (2018) Label-free imaging of amyloid plaques in Alzheimer's disease with stimulated raman scattering microscopy. *Sci Adv* 4:1–9. doi: 10.1126/sciadv.aat7715
36. Joshi P, Turola E, Ruiz A, Bergami A, Libera DD, Benussi L, et al. (2014) Microglia convert aggregated amyloid- β into neurotoxic forms through the shedding of microvesicles. *Cell Death Differ* 21:582–593. doi: 10.1038/cdd.2013.180
37. Kauffmann E, Austin R, Gerwert K (2001) Probing protein folding with time-resolved FTIR spectroscopy - Novel techniques for the investigation of changes in protein conformation. *BIF Futur* 16:152–158
38. Kirschner DA, Inouye H, Duffy LK, Sinclair A, Lind M, Selkoe DJ (1987) Synthetic peptide homologous to beta protein from Alzheimer disease forms amyloid-like fibrils in vitro. *Proc Natl Acad Sci U S A* 84:6953–6957. doi: 10.1073/pnas.84.19.6953
39. Kiskis J, Fink H, Nyberg L, Thyr J, Li JY, Enejder A (2015) Plaque-associated lipids in Alzheimer's diseased brain tissue visualized by nonlinear microscopy. *Sci Rep* 5:1–9. doi: 10.1038/srep13489
40. Klementieva O, Sandt C, Martinsson I, Kansiz M, Gouras GK, Borondics F (2020) Super-Resolution Infrared Imaging of Polymorphic Amyloid Aggregates Directly in Neurons. *Adv Sci* 7. doi: 10.1002/advs.201903004
41. Klementieva O, Willén K, Martinsson I, Israelsson B, Engdahl A, Cladera J, et al. (2017) Pre-plaque conformational changes in Alzheimer's disease-linked A β and APP. *Nat Commun* 8:14726. doi: 10.1038/ncomms14726

42. Konevskikh T, Lukacs R, Kohler A (2018) An improved algorithm for fast resonant Mie scatter correction of infrared spectra of cells and tissues. *J Biophotonics* 11:1–10. doi: 10.1002/jbio.201600307
43. Krafft C, Neudert L, Simat T, Salzer R (2005) Near infrared Raman spectra of human brain lipids. *Spectrochim Acta - Part A Mol Biomol Spectrosc* 61:1529–1535. doi: 10.1016/j.saa.2004.11.017
44. Lee Rodgers J, Nicewander WA (1988) Thirteen Ways to Look at the Correlation Coefficient. *Am Stat* 42:59–66. doi: 10.1080/00031305.1988.10475524
45. Leskovjan AC, Lanzirotti A, Miller LM (2009) Amyloid plaques in PSAPP mice bind less metal than plaques in human Alzheimer's disease. *Neuroimage* 47:1215–1220. doi: 10.1016/j.neuroimage.2009.05.063
46. Liao CR, Rak M, Lund J, Unger M, Platt E, Albenis BC, et al. (2013) Synchrotron FTIR reveals lipid around and within amyloid plaques in transgenic mice and Alzheimer's disease brain. *Analyst* 138:3991–3997. doi: 10.1039/c3an00295k
47. Lomont JP, Ostrander JS, Ho J-J, Petti MK, Zanni MT (2017) Not All β -Sheets Are the Same: Amyloid Infrared Spectra, Transition Dipole Strengths, and Couplings Investigated by 2D IR Spectroscopy. *J Phys Chem B* 121:8935–8945. doi: 10.1021/acs.jpcc.7b06826
48. McGeer PL, Itagaki S, Tago H, McGeer EG (1987) Reactive microglia in patients with senile dementia of the Alzheimer type are positive for the histocompatibility glycoprotein HLA-DR. *Neurosci Lett* 79:195–200. doi: 10.1016/0304-3940(87)90696-3
49. Michael R, Lenferink A, Vrensen GFJM, Gelpi E, Barraquer RI, Otto C (2017) Hyperspectral Raman imaging of neuritic plaques and neurofibrillary tangles in brain tissue from Alzheimer's disease patients. *Sci Rep* 7:1–11. doi: 10.1038/s41598-017-16002-3
50. Michaels TCT, Šarić A, Curk S, Bernfur K, Arosio P, Meisl G, et al. (2020) Dynamics of oligomer populations formed during the aggregation of Alzheimer's A β 42 peptide. *Nat Chem* 12:445–451. doi: 10.1038/s41557-020-0452-1
51. Montine TJ, Phelps CH, Beach TG, Bigio EH, Cairns NJ, Dickson DW, et al. (2012) National institute on aging-Alzheimer's association guidelines for the neuropathologic assessment of Alzheimer's disease: A practical approach. *Acta Neuropathol* 123:1–11. doi: 10.1007/s00401-011-0910-3
52. Moors TE, Maat CA, Niedieker D, Mona D, Petersen D, Timmermans-Huisman E, et al. (2018) Subcellular orchestration of alpha-synuclein variants in Parkinson's disease brains revealed by 3D multicolor STED microscopy. *bioRxiv* 470476. doi: 10.1101/470476
53. Morell P, Quarles R (1999) Characteristic composition of myelin. In: Siegel G, Agranoff R, Albers R (eds) *Basic Neurochemistry: Molecular, Cellular and Medical Aspects*, 6th ed. Lippincott-Raven, Philadelphia
54. Nabers A, Ollesch J, Schartner J, Kötting C, Genius J, Hafermann H, et al. (2016) Amyloid- β -Secondary Structure Distribution in Cerebrospinal Fluid and Blood Measured by an Immuno-Infrared-Sensor: A Biomarker Candidate for Alzheimer's Disease. *Anal Chem* 88:2755–2762. doi: 10.1021/acs.analchem.5b04286

55. Nelson PT, Alafuzoff I, Bigio EH, Bouras C, Braak H, Cairns NJ, et al. (2012) Correlation of alzheimer disease neuropathologic changes with cognitive status: A review of the literature. *J Neuropathol Exp Neurol* 71:362–381. doi: 10.1097/NEN.0b013e31825018f7
56. O'Brien JS, Sampson EL (1965) Lipid composition of the normal human brain: gray matter, white matter, and myelin. *J Lipid Res* 6:537–544
57. Otsu N (1979) A Threshold Selection Method from Gray-Level Histograms. *IEEE Trans Syst Man Cybern* 9:62–66. doi: 10.1109/TSMC.1979.4310076
58. Palombo F, Tamagnini F, Jeynes JCG, Mattana S, Swift I, Nallala J, et al. (2018) Detection of A β plaque-associated astrogliosis in Alzheimer's disease brain by spectroscopic imaging and immunohistochemistry. *Analyst* 143:850–857. doi: 10.1039/C7AN01747B
59. Rak M, Del Bigio MR, Mai S, Westaway D, Gough KM (2007) Dense-core and diffuse A β plaques in TgCRND8 mice studied with synchrotron FTIR microspectroscopy. *Biopolymers* 87:207–217. doi: 10.1002/bip.20820
60. Rozemuller AJM, Jansen C, Carrano A, Van Haastert ES, Hondius D, Van Der Vies SM, et al. (2012) Neuroinflammation and common mechanism in Alzheimer's disease and prion amyloidosis: Amyloid-associated proteins, neuroinflammation and neurofibrillary degeneration. *Neurodegener Dis* 10:301–304. doi: 10.1159/000335380
61. Rozemuller JM, Eikelenboom P, Stam FC (1986) Role of microglia in plaque formation in senile dementia of the Alzheimer type - An immunohistochemical study. *Virchows Arch B Cell Pathol Incl Mol Pathol* 51:247–254. doi: 10.1007/BF02899034
62. Rozemuller JM, Eikelenboom P, Stam FC, Beyreuther K, Masters CL (1989) A4 Protein in Alzheimer's Disease: Primary and Secondary Cellular Events in Extracellular Amyloid Deposition. *J Neuropathol Exp Neurol* 48:674–691. doi: 10.1097/00005072-198911000-00009
63. Sarroukh R, Cerf E, Derclaye S, Dufrêne YF, Goormaghtigh E, Ruyschaert JM, et al. (2011) Transformation of amyloid β (1-40) oligomers into fibrils is characterized by a major change in secondary structure. *Cell Mol Life Sci* 68:1429–1438. doi: 10.1007/s00018-010-0529-x
64. Sarroukh R, Goormaghtigh E, Ruyschaert JM, Raussens V (2013) ATR-FTIR: A "rejuvenated" tool to investigate amyloid proteins. *Biochim Biophys Acta - Biomembr* 1828:2328–2338. doi: 10.1016/j.bbmem.2013.04.012
65. Schmidt ML, Robinson KA, Lee VMY, Trojanowski JQ (1995) Chemical and immunological heterogeneity of fibrillar amyloid in plaques of Alzheimer's disease and Down's syndrome brains revealed by confocal microscopy. *Am J Pathol* 147:503–15
66. Selkoe DJ (1989) Amyloid β protein precursor and the pathogenesis of Alzheimer's disease. *Cell* 58:611–612. doi: 10.1016/0092-8674(89)90093-7
67. Sevigny J, Chiao P, Bussière T, Weinreb PH, Williams L, Maier M, et al. (2016) The antibody aducanumab reduces A β plaques in Alzheimer's disease. *Nature* 537:50–56. doi: 10.1038/nature19323

68. Shahmoradian SH, Lewis AJ, Genoud C, Hench J, Moors TE, Navarro PP, et al. (2019) Lewy pathology in Parkinson's disease consists of crowded organelles and lipid membranes. *Nat Neurosci* 22:1099-1109. doi: 10.1038/s41593-019-0423-2
69. Sheng JG, Zhou XQ, Mrak RE, Griffin WST (1998) Progressive neuronal injury associated with amyloid plaque formation in Alzheimer disease. *J Neuropathol Exp Neurol* 57:714-717. doi: 10.1097/00005072-199807000-00008
70. Solheim JH, Gunko E, Petersen D, Großertüschkamp F, Gerwert K, Kohler A (2019) An open-source code for Mie extinction extended multiplicative signal correction for infrared microscopy spectra of cells and tissues. *J Biophotonics* 12. doi: 10.1002/jbio.201800415
71. Student (W.S. Gosset) (1908) The Probable Error of a Mean. *Biometrika* 6:1. doi: 10.2307/2331554
72. Summers KL, Fimognari N, Hollings A, Kiernan M, Lam V, Tidy RJ, et al. (2017) A Multimodal Spectroscopic Imaging Method To Characterize the Metal and Macromolecular Content of Proteinaceous Aggregates ("Amyloid Plaques"). *Biochemistry* 56:4107-4116. doi: 10.1021/acs.biochem.7b00262
73. Surowka AD, Pilling M, Henderson A, Boutin H, Christie L, Szczerbowska-Boruchowska M, et al. (2017) FTIR imaging of the molecular burden around A β deposits in an early-stage 3-Ig-APP-PSP1-TAU mouse model of Alzheimer's disease. *Analyst* 142:156-168. doi: 10.1039/c6an01797e
74. T. Griffin WS, Sheng JG, Roberts GW, Mrak RE (1995) Interleukin-1 Expression in Different Plaque Types in Alzheimer's Disease. *J Neuropathol Exp Neurol* 54:276-281. doi: 10.1097/00005072-199503000-00014
75. Tagliavini F, Giaccone G, Frangione B, Bugiani O (1988) Preamyloid deposits in the cerebral cortex of patients with Alzheimer's disease and nondemented individuals. *Neurosci Lett* 93:191-196. doi: 10.1016/0304-3940(88)90080-8
76. Thal DR (2006) The Development of Amyloid beta Protein Deposits in the Aged Brain. *Sci Aging Knowl Environ* 2006:re1. doi: 10.1126/sageke.2006.6.re1
77. Tolar M, Abushakra S, Hey JA, Porsteinsson A, Sabbagh M (2020) Aducanumab, gantenerumab, BAN2401, and ALZ-801 - The first wave of amyloid-targeting drugs for Alzheimer's disease with potential for near term approval. *Alzheimer's Res Ther* 12:1-10. doi: 10.1186/s13195-020-00663-w
78. Welch WRW, Kubelka J, Keiderling TA (2013) Infrared, vibrational circular dichroism, and raman spectral simulations for β -sheet structures with various isotopic labels, interstrand, and stacking arrangements using density functional theory. *J Phys Chem B* 117:10343-10358. doi: 10.1021/jp4056126
79. Xie H, Hou S, Jiang J, Sekutowicz M, Kelly J, Bacskai BJ (2013) Rapid cell death is preceded by amyloid plaque-mediated oxidative stress. *Proc Natl Acad Sci U S A* 110:7904-7909. doi: 10.1073/pnas.1217938110
80. Yamaguchi H, Hirai S, Morimatsu M, Shoji M, Harigaya Y (1988) Diffuse type of senile plaques in the brains of Alzheimer-type dementia. *Acta Neuropathol* 77:113-119. doi: 10.1007/BF00687420

Chapter 5

81. Yamaguchi KI, Takahashi S, Kawai T, Naiki H, Goto Y (2005) Seeding-dependent propagation and maturation of amyloid fibril conformation. *J Mol Biol* 352:952–960. doi: 10.1016/j.jmb.2005.07.061
82. Yuan P, Condello C, Keene CD, Wang Y, Bird TD, Paul SM, et al. (2016) TREM2 Haplodeficiency in Mice and Humans Impairs the Microglia Barrier Function Leading to Decreased Amyloid Compaction and Severe Axonal Dystrophy. *Neuron* 90:724–739. doi: 10.1016/j.neuron.2016.05.003
83. Zandomenighi G, Krebs MRH, McCammon MG, Fändrich M (2004) FTIR reveals structural differences between native beta-sheet proteins and amyloid fibrils. *Protein Sci* 13:3314–21. doi: 10.1110/ps.041024904

SUPPLEMENTARY DATA

Materials and Methods - Raman

Raman microspectroscopy

Raman spectral imaging was performed using the WITec alpha300 RA confocal Raman microscope (WITec, Ulm, Germany) as described before [1, 10]. A single-frequency diode laser of 785 nm (Toptica Photonics AG, Munich, Germany) was utilized for excitation with an output power of approximately 300 mW. The laser beam was collimated with an achromatic lens, passed through a holographic band-pass filter and subsequently focused on the sample with a Nikon S Plan Fluor (20 \times / 0.45) dry-objective. The sample was placed on a piezoelectrically driven scanning stage and the back-scattered light was collected with the same objective and passed through the holographic edge filter into a multimode fiber (d = 50 μ m). A 300 mm focal length monochromator with a 600/mm grating, blazed at 750 nm was utilized and the Raman spectra were detected by a back-illuminated deep-depletion charge-coupled device (-60 $^{\circ}$ C). Dry air was continuously purged onto the sample to avoid sample degradation. Raman spectra were acquired with a pixel resolution of 1 μ m and 1 sec integration time per pixel. Due to the small area covered by Raman and difficulties to localize plaques in unstained tissue, even when guided by adjacent A β -IHC stained sections, only two classic cored plaques were measured. Given the restricted plaque quantity, Raman data was used for validation of FTIR, rather than providing new results.

Raman spectral data preparation and data analysis

All spectra were smoothed by Savitzky-Golay algorithm, baseline-corrected using a fourth-order polynomial with a noise threshold of 3 and a custom spectral fit mask with the Project FOUR software (WITec, Ulm, Germany). Raman spectra of the tissue regions that displayed strong (auto-)fluorescence or noise were excluded from data analysis. Cosmic peak correction was done by replacing peaks with neighboring values in the spectra. Peak ratios were calculated to visualize the ratio between protein and lipids, as well as the degree of protein misfolding, analog to FTIR analysis (supplementary Table 2). We used the ratio I_{1665}/I_{1654} of the Raman-active sub-bands of the amide I band to evaluate the degree of protein misfolding in Raman, analog to the A_{1630}/A_{1655} ratio in FTIR. The ratio $I_{1659}/I_{CH\ Total}$ compares the total amide I band of the protein back bone and the CH₂ & CH₃ deformation bands, mostly of fatty acids and protein side chains. The selected bands represent the same molecular classes in Raman and FTIR, namely protein for the amide bands, and a sum of lipid and protein for the CH₂ & CH₃ groups.

Tables

Table 1. Case details

| Case # | Group | Gender | Onset age | Age † | Cause of † | PMI h:mm | ABC [7] | # diffuse plaques | # compact plaques | # classic cored plaques |
|--------|------------------------|--------|-----------|-------|----------------------------------|-------------|------------------------------------|----------------------|----------------------|----------------------------|
| 1 | Control | Male | NA | 83 | Myocardial infarct | 5:15 | A1 B1 C0 | NA | NA | NA |
| 2 | Control | Female | NA | 92 | Heart failure | 6:35 | A0 B2 C0 | NA | NA | NA |
| 3 | Control | Female | NA | 78 | Euthanasia | 7:10 | A1 B1 C0 | NA | NA | NA |
| 4 | AD | Male | 60 | 65 | Cardiac insufficiency | 8:50 | A3 B3 C3 | 0 | 1 | 1 |
| 5 | AD vascular variant | Male | 77 | 80 | Dehydration | 5:05 | A3 B3 C0 ^a | 3 | 9 | 7 |
| 6 | AD | Female | 75 | 84 | Cardiac arrest after cachexia | 6:30 | A3 B3 C3 | 8 | 5 | 16 |
| 7 | AD | Female | 64 | 76 | Unclear | 10:45 | A3 B3 C3 | 45 | 6 | 4 |
| 8 | AD | Male | 48 | 59 | Dehydration / cachexia | 7:35 | A3 B3 C3 | 0 | 6 | 4 |
| 9 | AD | Male | 59 | 65 | Pneumonia | 3:32 | A3 B3 C3 | 4 | 1 | 26 |
| 10 | AD vascular variant | Female | 75 | 78 | Dehydration / cachexia | 4:20 | A3 NA ^b C0 ^a | 8 | 4 | 2 |

AD Alzheimer's disease; NA not applicable; PMI post mortem interval; # number of; † death; ^a no plaques but only dystrophic angiopathy in Gallyas staining; ^b severe tauopathy related to vascular amyloid, not qualifying Braak staging.

Table 2. Nomenclature of mean values

| Nomenclature | Observed vibration | Peak range | Baseline range |
|-----------------------|---|-------------|----------------|
| A ₁₅₄₅ | Amide II [4] | 1535 - 1555 | 1345 - 1780 |
| A ₁₆₃₀ | Amide I of β -sheets [2] | 1630 | - |
| A ₁₆₅₅ | Amide I of non- β -sheets | 1655 | - |
| A _{Total CH} | CH ₂ and CH ₃ stretching | 2800 - 2995 | 2750 - 3100 |
| I ₁₆₅₉ | Amide I total | 1650 - 1673 | - |
| I ₁₆₅₄ | Amide I of non- β -sheets | 1644 - 1659 | - |
| I ₁₆₆₅ | Amide I of β -sheets | 1664 - 1679 | - |
| I _{Total CH} | CH ₂ and CH ₃ deformation | 1430 - 1446 | - |

The mean absorbance A or mean Raman intensity I was calculated within the respective peak range. A linear baseline correction was applied to FTIR spectra within the ranges stated.

FIGURES

Investigation of spectral alterations in native brain samples during long measurements

We carefully prevented chemical alterations of our samples to approach in vivo conditions as close as possible. Nonetheless, the samples were kept in dried air during defrosting and spectral measurements, which usually lasted for several days. As we analyze minute chemical changes, some of which associated to oxidation processes, the ambient oxygen constitutes a potentially disruptive factor.

In order to characterize possible spectral changes that originate from prolonged exposure to dry air, we conducted a simple experiment. We measured a sample with FTIR, as described above, and instead of staining right away, we kept the sample in a closed, dry-air-purged container for about three weeks, repeated the FTIR measurement afterwards and then stained subsequently. We extracted plaque spectra from ten plaques, contained in both measurements to conduct a precise comparison. The mean plaque spectra are presented in supplementary Fig. 1. After prolonged dry air exposure, we observe the emergence of bands at 1322 cm⁻¹, 1160 cm⁻¹ and 1095 cm⁻¹. The assignment of these bands is difficult, because of the multitude of overlapping bands in the fingerprint region. From literature we deduce, that a possible origin of the bands might be the stretching vibrations of C-O-R groups, whereas R represents a manifold of possible extensions [8]. Fortunately, the spectral ranges we used for the analysis of plaques do not show alterations after a prolonged exposure to dry air.

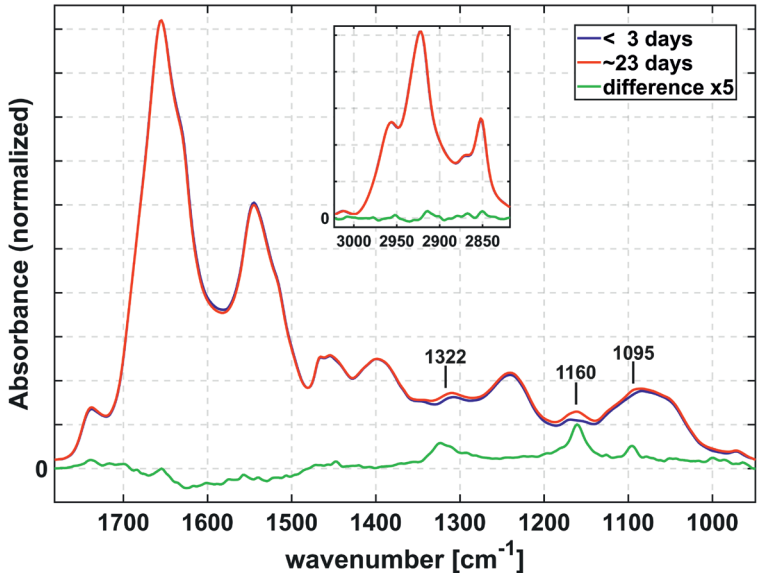


Fig. 1. Sample ageing
 Area-normalized mean plaque spectra from FTIR measurements shortly after defrosting (blue) and about three weeks later (red). The 5-fold difference of both spectra is plotted in green.

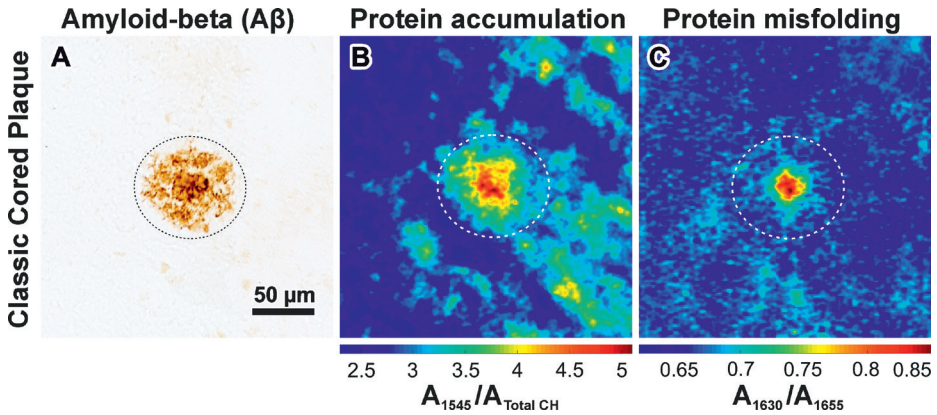


Fig. 2. Further exemplary classic cored plaque
 Analog to Fig. 2 in main text.

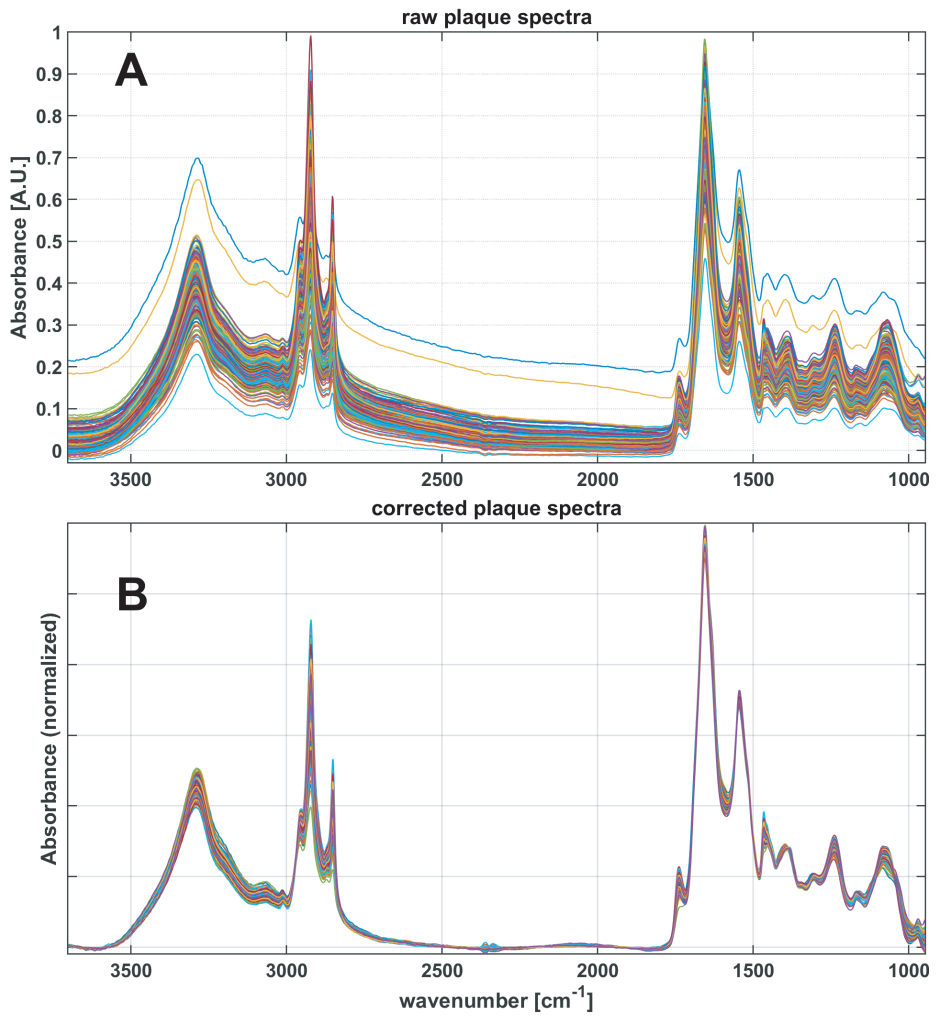


Fig. 3. Mie Correction

Typical spectra before and after application of Mie scattering correction based on extended multiplicative signal correction (EMSC) [9].

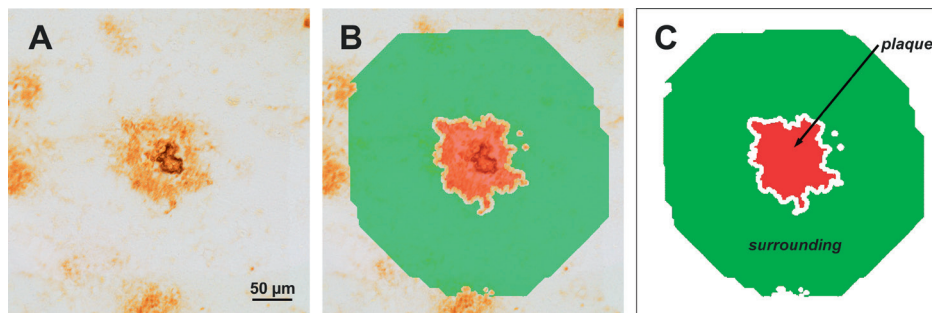


Fig. 4. Plaque masks

A Original A β -IHC staining. **B** Overlay of staining image and masks. **C** Masks for the plaque area (red) and the surrounding area (green).

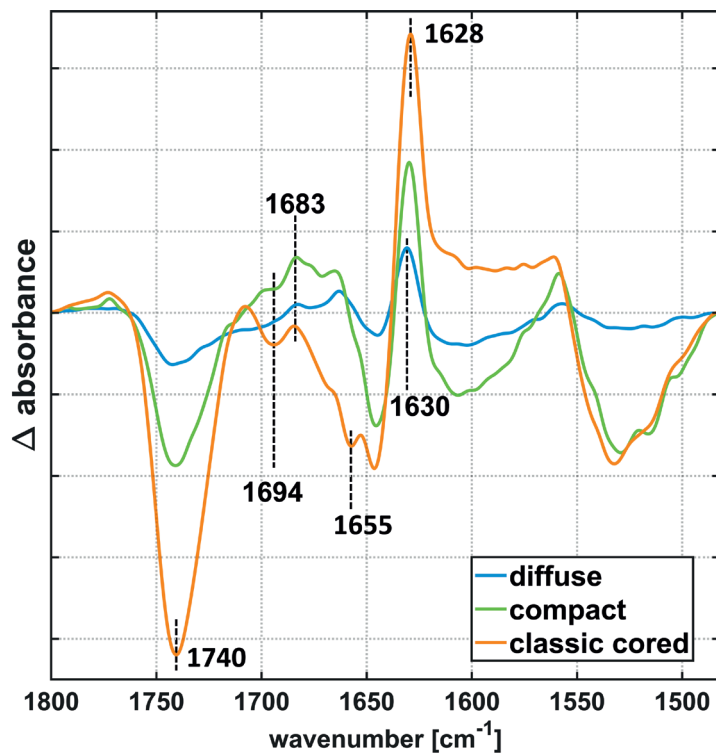


Fig. 5. Difference spectroscopy

Difference spectra between mean plaque spectra and their corresponding surrounding spectra. Relevant bands are marked. At 1694 cm^{-1} , we observe (i) no clear band in diffuse plaques, (ii) a dip in compact plaques, and (iii) a clear local minimum in classic cored plaques. All plaque types display local maxima at 1683 cm^{-1} and 1630 cm^{-1} .

Validation with Raman

In the Raman measurements (supplementary Fig. 6), we observed auto-fluorescence in small parts of the tissue that might originate from lipofuscin deposits [5]. However, Raman data can still be used to confirm the findings of FTIR. One distinction between FTIR and Raman concerns the amide I band. The respective bands of β -sheets are most prominent at 1666 cm^{-1} in Raman and at 1630 cm^{-1} in FTIR [6]. The observed amide I band shift in the plaque of human tissue in the present Raman study (supplementary Fig. 6A₃) is consistent with that monitored by stimulated Raman scattering using fresh frozen AD mouse brain sections [3]. Furthermore, a major difference between FTIR and Raman is the confocality as well as higher spatial resolution provided by Raman imaging. These differences are visible in the integrated absorption signal of all tissue layers as shown for the FTIR images (supplementary Fig. 6B₁, C₁), but a z-layer specific emission intensity is displayed in the Raman images (supplementary Fig. 6B₂, C₂), resulting in an altered appearance of the plaque in Raman images. This includes the formation of β -sheet rich structures, most likely A β fibrils, in classic cored plaques.

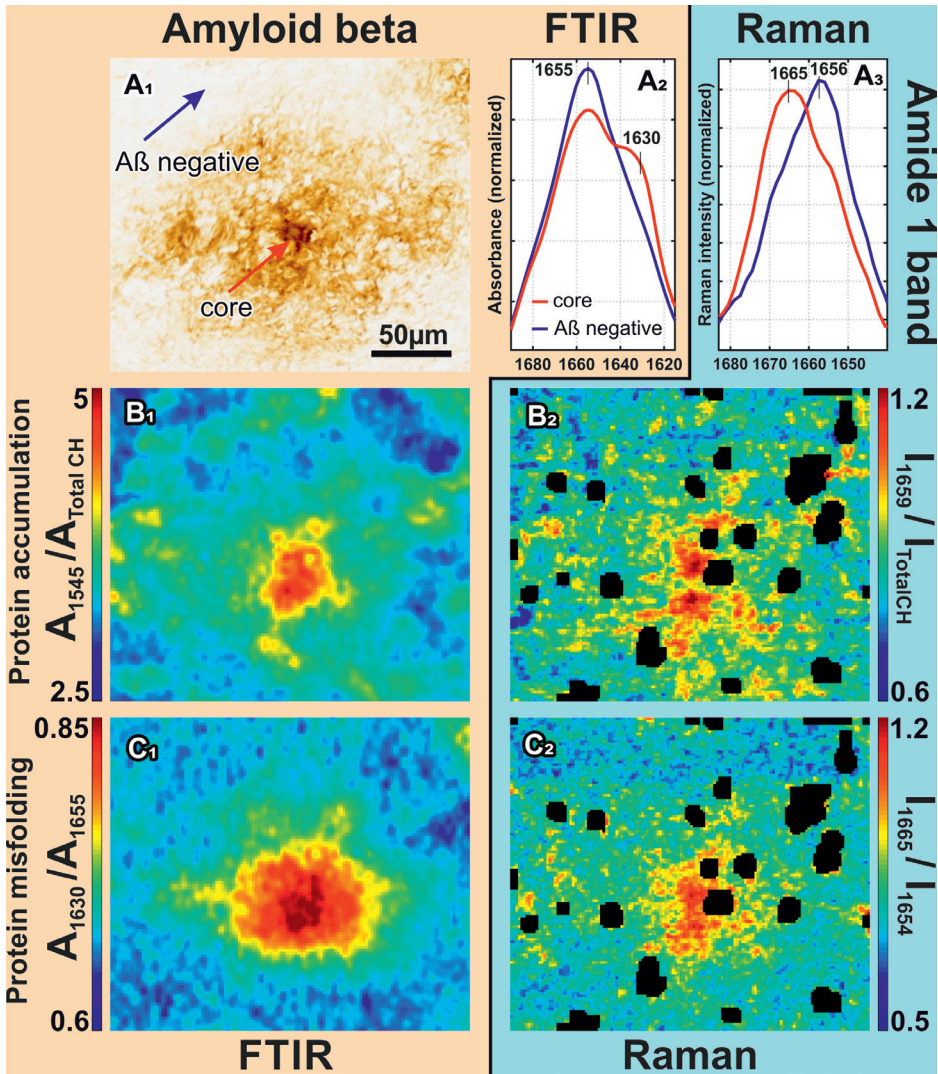


Fig. 6. Raman spectral analysis of a classic cored plaque in direct comparison to FTIR. A_1 anti- $A\beta$ staining of the plaque. The red and blue arrows indicate the regions corresponding to the spectra in A_2 and A_3 . A_2 FTIR amide I band of the plaque core (red) and the $A\beta$ negative region (blue). A_3 Raman amide I band of the plaque core (red) and the $A\beta$ negative region (blue). All bands were extracted from corrected spectra and normalized on the same area under the line within the displayed ranges. B_1 , C_1 display the protein accumulation and misfolding within the tissue, determined by FTIR, analog to Fig. 2B, C in the main text. B_2 , C_2 show the protein accumulation and misfolding within the plaque as determined by Raman. The blackened areas indicate pixel spectra, which were unsuitable for analysis due to strong fluorescence artefacts.

REFERENCES SUPPLEMENTARY DATA

1. Aljakouch K, Lechtonen T, Yosef HK, Hammoud MK, Alsaidi W, Kötting C, et al. (2018) Raman Microspectroscopic Evidence for the Metabolism of a Tyrosine Kinase Inhibitor, Neratinib, in Cancer Cells. *Angew Chemie - Int Ed* 57:7250–7254. doi: 10.1002/anie.201803394
2. Goormaghtigh E, Ruyschaert J-M, Raussens V (2006) Evaluation of the Information Content in Infrared Spectra for Protein Secondary Structure Determination. *Biophys J* 90:2946–2957. doi: 10.1529/biophysj.105.072017
3. Ji M, Arbel M, Zhang L, Freudiger CW, Hou SS, Lin D, et al. (2018) Label-free imaging of amyloid plaques in Alzheimer's disease with stimulated raman scattering microscopy. *Sci Adv* 4:1–9. doi: 10.1126/sciadv.aat7715
4. Leskovjan AC, Lanzirotti A, Miller LM (2009) Amyloid plaques in PSAPP mice bind less metal than plaques in human Alzheimer's disease. *Neuroimage* 47:1215–1220. doi: 10.1016/j.neuroimage.2009.05.063
5. Lochocki B, Morrema THJ, Ariese F, Hoozemans JJM, de Boer JF (2020) The search for a unique Raman signature of amyloid-beta plaques in human brain tissue from Alzheimer's disease patients. *Analyst* 145:1724–1736. doi: 10.1039/C9AN02087J
6. Miyazawa T, Blout ER (1961) The Infrared Spectra of Polypeptides in Various Conformations: Amide I and II Bands. *J Am Chem Soc* 83:712–719. doi: 10.1021/ja01464a042
7. Montine TJ, Phelps CH, Beach TG, Bigio EH, Cairns NJ, Dickson DW et al (2012) National Institute on Aging-Alzheimer's Association guidelines for the neuropathologic assessment of Alzheimer's disease: a practical approach. *Acta Neuropathol* 123:1–11. doi: 10.1007/s00401-011-0910-3
8. Socrates G (2001) *Infrared and Raman Characteristic Group Frequencies: Tables and Charts*, 3rd ed. J.Wiley and Sons LTD, Chichester
9. Solheim JH, Gunko E, Petersen D, Großerüschkamp F, Gerwert K, Kohler A (2019) An open-source code for Mie extinction extended multiplicative signal correction for infrared microscopy spectra of cells and tissues. *J Biophotonics* 12. doi: 10.1002/jbio.201800415
10. Yosef HK, Frick T, Hammoud MK, Maghnoij A, Hahn S, Gerwert K, et al. (2018) Exploring the efficacy and cellular uptake of sorafenib in colon cancer cells by Raman micro-spectroscopy. *Analyst* 143:6069–6078. doi: 10.1039/c8an02029a

Chapter 6

Multimodal, label-free fluorescence and Raman imaging of amyloid deposits in snap-frozen Alzheimer's disease human brain tissue

Benjamin Lochocki, Baayla DC Boon, Sander R Verheul, Liron Zada,
Jeroen JM Hoozemans, Freek Ariese, Johannes F de Boer

Communications Biology (2021)
doi: 10.1038/s42003-021-01981-x

ABSTRACT

Background: Alzheimer's disease (AD) neuropathology is characterized by hyperphosphorylated tau containing neurofibrillary tangles and amyloid-beta ($A\beta$) plaques. Normally these hallmarks are studied by (immuno-) histological techniques requiring chemical pretreatment and indirect labelling. Label-free imaging enables one to visualize normal tissue and pathology in its native form. Therefore, these techniques could contribute to a better understanding of the disease.

Methods: Here, we present a comprehensive study of high-resolution fluorescence imaging (before and after staining) and spectroscopic modalities (Raman mapping under pre-resonance conditions and stimulated Raman scattering (SRS)) of amyloid deposits in snap-frozen AD human brain tissue. We performed fluorescence and spectroscopic imaging and subsequent thioflavin-S staining of the same tissue slices to provide direct confirmation of plaque location and correlation of spectroscopic biomarkers with plaque morphology.

Results: Differences were observed between cored and fibrillar plaques. The SRS results showed a protein peak shift towards the β -sheet structure in cored amyloid deposits. In the Raman maps recorded with 532 nm excitation we identified the presence of carotenoids as a unique marker to differentiate between a cored amyloid plaque area versus a non-plaque area without prior knowledge of their location.

Conclusions: The observed presence of carotenoids suggests a distinct neuroinflammatory response to misfolded protein accumulations.

INTRODUCTION

Dementia affects memory, cognitive abilities, and behavior of mainly elderly people. Alzheimer's disease (AD) is the most common type and contributes to around 65% of the dementia cases [90]. Together with hyperphosphorylated tau deposits, the accumulation of amyloid-beta ($A\beta$), commonly referred to as amyloid plaque, is one of the main pathological hallmarks of AD [8, 35, 79]. Within the plaque, misfolded protein chains, cleaved off from the amyloid precursor protein (APP), aggregate in an insoluble, anti-parallel β -sheet structure which subsequently leads to different pathological amyloid plaque types [85]. Attempts at in vivo diagnosis include the targeting of $A\beta$ in the brain [34, 39, 50], in cerebrospinal fluid (CSF) [2, 57, 66] and recently also in blood or serum [23, 64, 66, 72, 77]. However, these techniques always rely on the indirect binding of $A\beta$ by an antibody or labeling compound and thus provide no specific information on the intrinsic properties of the pathological substrate. Although at least partially invasive, these methodologies cannot provide a definitive diagnosis of AD. At the moment, conclusive assessment of AD can only be obtained post mortem by (immuno-) histochemical staining on brain tissue [28, 38]. Staining protocols are often labor-intensive and time-consuming, and there may be risk of dehydration, heat and deformation. A label-free characterization of the molecular composition of fresh tissue could provide a fast assessment of pathology and potentially an option for in vivo AD diagnosis in e.g., the retina [28, 29]. Such non-invasive or minimally invasive techniques include among others FTIR-spectroscopy [70], coherent anti-Stokes Raman spectroscopy (CARS) [49] and surface-enhanced Raman spectroscopy (SERS) [27]. These techniques could generate new possibilities to detect and follow pathology while giving new insights in the composition of the pathological substrate. While in most of the available AD related literature and research, transgenic AD mice were used, Hodge et al. [37] stressed the importance of studying human tissue as the differences from cell types in mouse tissue are extensive. Recently, we investigated whether Raman spectroscopy ($\lambda_{exc} = 785 \text{ nm}$) could be used for the detection of $A\beta$ plaques in fixed human brain tissue. Despite the potential of vibrational spectroscopic techniques for a label-free and non-invasive characterization of biomolecular composition, a unique $A\beta$ associated spectrum could not be determined [54]. In the present study, we report on data obtained from post mortem, snap-frozen human AD tissue. We used auto-fluorescence microscopy, followed by spontaneous Raman spectroscopy using a 532 nm excitation source to examine the unstained plaque tissue sections. Afterward, we recorded stimulated Raman scattering (SRS) [30, 42] images of the same tissue areas. To the best of our knowledge, it is the first

time that various imaging and spectroscopic modalities were used consecutively on the same native AD tissue section. Moreover, each examined tissue section was eventually stained with thioflavin-S to confirm plaque pathology and the exact locations within the tissue.

RESULTS AND DISCUSSION

The results are presented in the following order: first, we demonstrate that amyloid plaques can be identified based on their (auto-) fluorescence properties in native-unstained tissue confirmed by subsequent thioflavin-S staining. Secondly, we show that cored amyloid accumulations can be identified by conventional Raman spectroscopy using 532 nm excitation. We identified unique spectral hallmarks that enabled us to detect plaques within tissue without prior knowledge of their location. These spectral features are further characterized in the next section. Thirdly, we present SRS measurements, looking specifically for a protein peak shift when measuring within an amyloid plaque compared to blank background tissue.

It is worth to note that all samples were subject to the same conditions: the Raman settings, the hardware used, the laser power reaching the samples, the staining protocol and data processing were identical to reduce possible experimental variability. The same is true for the SRS measurements, where objective, laser power, and pixel dwell time were kept constant. The experimental work flow is illustrated in Fig. 1. Table ST1, presented in the Supplementary Information, gives an overview, which imaging modality was applied to which section.

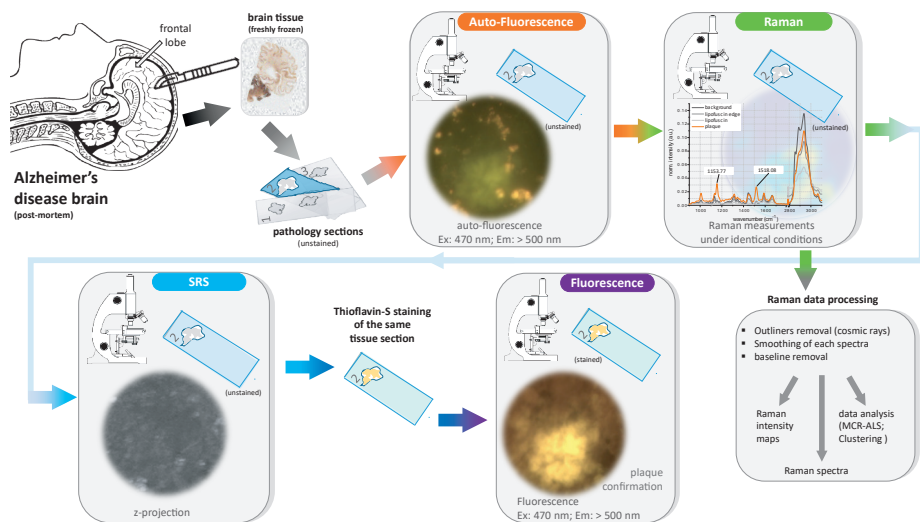


Fig. 1. Experimental work-flow

Brain autopsy is performed within 9 hours post mortem and the tissue is immediately snap-frozen to -80°C . Next, the tissue is cut at $20\ \mu\text{m}$ and mounted on CaF_2 microscope slides. Afterwards, the section is imaged under the fluorescence microscope. Subsequently, Raman maps are recorded. Hereafter, the tissue is measured across the amide-I protein peak using the SRS microscope. Following SRS, the tissue section is stained with thioflavin-S and imaged under the fluorescence microscope for plaque confirmation. Finally, the data is processed and analyzed. SRS stimulated Raman scattering.

Fluorescence microscopy

In Fig. 2, we show a column-wise overview of three measured tissue sections, characterized in Table 1. The remaining cases are shown in Fig. S3. Fig. 2a shows the auto-fluorescence images of the freshly cut tissue, acquired with the fluorescence microscope using a $\times 20$ and $\times 40$ objective for the first and second row, respectively. The bright, yellow/orange and uniformly distributed spots, which can be seen in all auto-fluorescence tissue samples (some spots are indicated by blue arrows in Fig. 2a and Fig. 3) are lipofuscin granular deposits [54, 65]. Lipofuscin, an age-related metabolic waste product, is highly unlikely an indicator or hallmark of AD since it is also found in control cases with a similar distribution [16, 54] (See also controls in Fig. S4). Lipofuscin auto-fluorescence properties are well known from brain tissue [40, 43, 52, 65, 71, 86, 96] and retinal imaging [17, 93] and are not further investigated here. In the areas of interest (yellow and red dashed boxes), the auto-fluorescence of amyloid accumulations appears greenish (seen best in the 2nd row of Fig. 2a), either in a compact and dense shape (#1a, #1b) or as a cloudy fibrillar haze

(#2). It should be mentioned that these green spots were more easily spotted by eye under the microscope than in the recorded RGB images. Some areas show a faint dark greenish patchy background without substantial features. In order to provide further evidence, the enlarged images of the red dashed boxed areas are shown in the Supplementary Information in Fig. S2. In Fig. 2b the fluorescence images of the same tissue sections are shown after thioflavin-S staining to highlight amyloid deposits. The positively stained thioflavin-S areas (bright yellow areas) match perfectly the greenish auto-fluorescent areas, while the rest of the tissue is observed as a uniform dark background. The colocalization of the thioflavin-S staining and the green auto-fluorescence tissue areas indicates that these are amyloid plaques. The auto-fluorescence signal of the lipofuscin that was bright in the images of Fig. 2a) now remains hidden in the background due to the high thioflavin-S fluorescence signal and the reduction in auto-fluorescence of lipofuscin over time (but is still sometimes seen as weak, light orange fluorescence). The additional cases are shown in Fig. S3. Fig. 3 is an enlarged, side-by-side comparison of distinct plaque locations (yellow dashed boxes in Fig. 2 for the cases #1a, #1b and #2), comparing the auto-fluorescence images with the subsequently acquired fluorescence images after thioflavin-S staining. Fig. 3 confirms the perfect match between greenish auto-fluorescence area and the thioflavin-S positive staining of the tissue. No green emission was observed in the tissue samples from control cases ($n = 5$, see Fig. S4). The greenish appearance observed in the present study agrees with a recent publication on AD mice tissue where various excitation sources in the range of 460 to 490 nm were used and plaque locations emitted in green (510 nm and 530 - 550 nm) [25]. Others reported similar results when illuminating with a 475 ± 10 nm source. Due to their additional NIR measurements they concluded amyloid fibers as source of the luminescence, while stating that “the underlying basic phenomena remain mostly unknown” [71]. However, the authors could not exactly specify the peak emission wavelength since the emission was recorded with a rather broad bandpass filter, ± 50 nm, centered at 530 nm. Thal et al. measured auto-fluorescence when illuminating human AD brain tissue with UV (330 to 385 nm) and deep blue (400 to 410 nm) and recorded emission images above 420 nm and 455 nm, respectively, therefore the plaques appeared in (dark) blue [83]. However, no emission curve was presented by the authors.

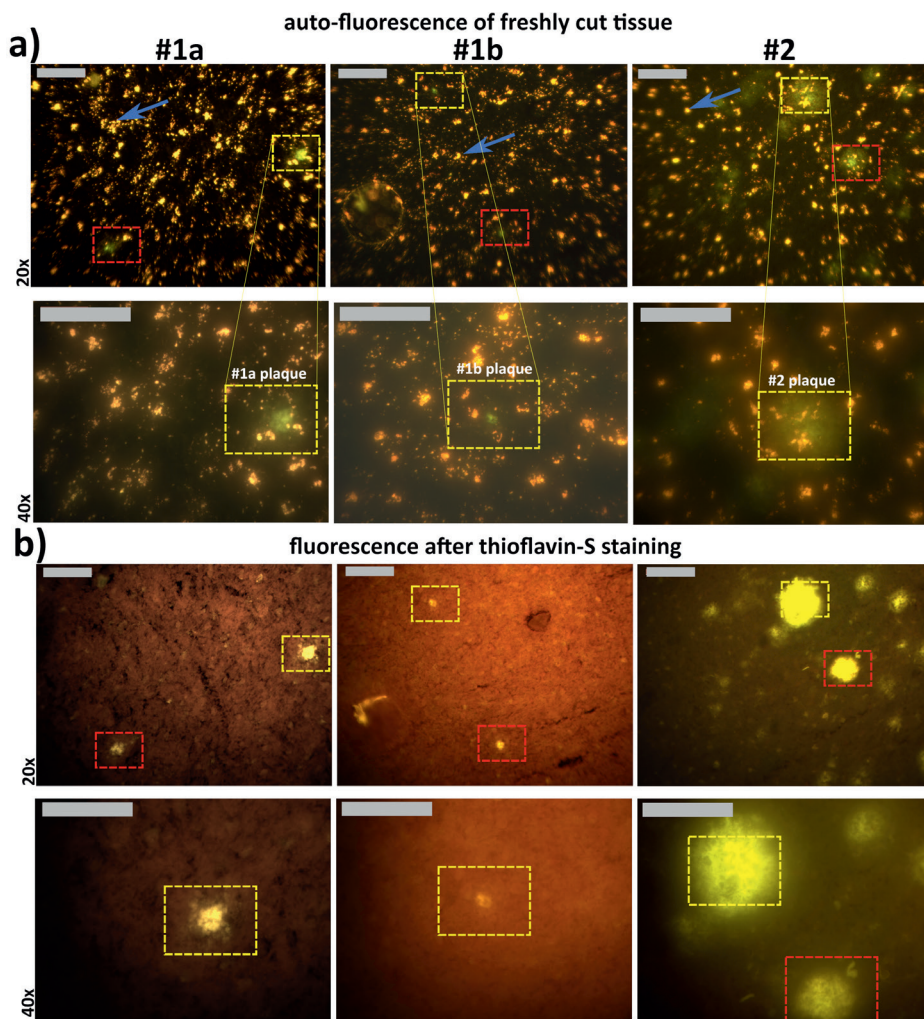


Fig. 2. Fluorescence images of AD cases 1 and 2, before and after staining, at 20x and 40x magnification

a) Auto-fluorescence images of freshly cut tissue. Greenish dense cores (#1a and #1b) and greenish patches (#2) are clearly visible. The uniformly distributed yellow spots (blue arrows, just one is identified in each image) are lipofuscin deposits [54]. **b)** Fluorescence images of the same tissue sections and areas stained with thioflavin-S. Here, the yellow bright spot areas are the positively stained amyloid accumulations. All images were taken with the full field fluorescence microscope and an illumination source of 470 nm. Yellow and red dashed boxes mark the measured plaque areas. # Refers to AD donor number and plaque in Table 1. Scale bars: 100 μm . The 40x image pairs of the red dashed boxes are shown in the Supplementary Information, Fig. S2. Enlarged images of each plaque is shown in Fig. 3. The image pairs of cases 3 to 5 are shown in Fig. S3. AD Alzheimer's disease.

Table 1. Demographics of AD brain donors and imaged plaques

| Case | Sex | Age † | NFT stage [11] | Amyloid [11] | Region | PMD | Plaque ref. | Plaque type |
|------|-----|-------|----------------|--------------|------------------------|------|-------------|---------------------------|
| #1 | F | 90 | 5 | C | Middle frontal gyrus | 4:00 | a | Cored amyloid deposit |
| | | | | | | | b | Cored amyloid deposit |
| #2 | M | 72 | 5 | C | Middle frontal gyrus | 6:00 | | Fibrillar amyloid deposit |
| #3 | M | 84 | 4 | B | Middle frontal gyrus | 5:53 | a | Cored amyloid deposit |
| | | | | | | | b | Fibrillar amyloid deposit |
| | | | | | | | c | Cored amyloid deposit |
| #4 | M | 65 | 6 | C | Superior frontal gyrus | 8:50 | a | Fibrillar amyloid deposit |
| | | | | | | | b | Fibrillar amyloid deposit |
| | | | | | | | c | Fibrillar amyloid deposit |
| #5 | F | 84 | 6 | C | Middle frontal gyrus | 6:30 | | Cored amyloid deposit |
| c#1 | F | 62 | 1 | B | Middle frontal gyrus | 7:55 | a | <i>Control</i> |
| | | | | | | | b | |
| | | | | | | | c | |
| c#2 | M | 64 | 1 | A | Middle frontal gyrus | 8:25 | a | <i>Control</i> |
| | | | | | | | b | |

A total of ten plaques in five different AD donors were measured. The last two rows are the control cases. Age in years. AD Alzheimer's disease; F female; M male; NFT neurofibrillary tangle; PMD post mortem delay in hours; ref. reference.

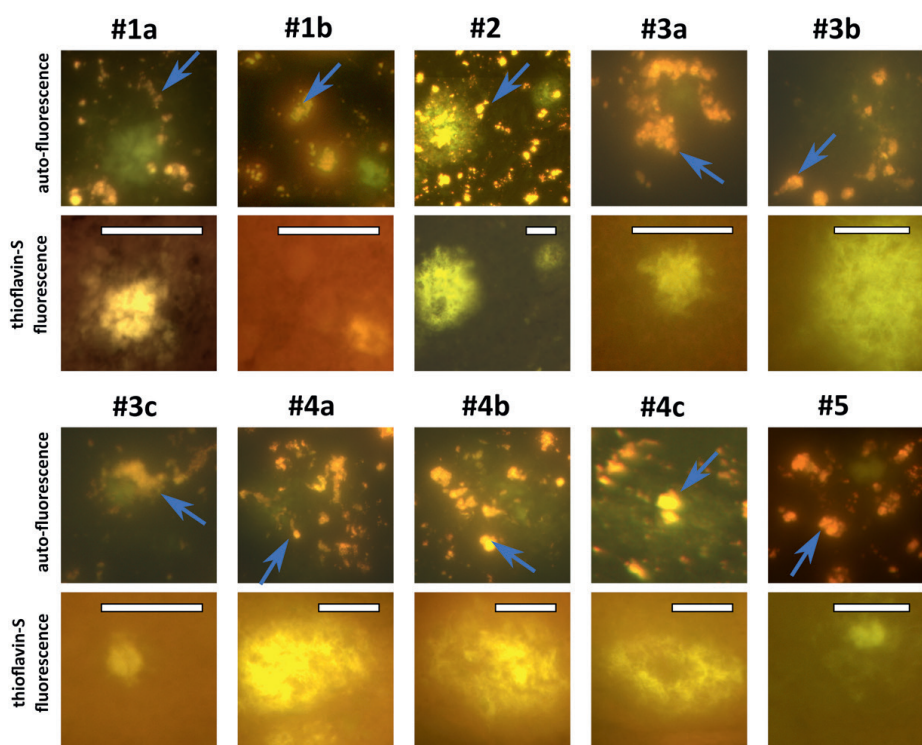


Fig. 3. Side-by-side comparison

Side-by-side comparison of plaque locations (as indicated by the yellow dashed boxes in Fig. 2 for cases #1a, #1b and 2) of auto-fluorescence images and the same location after staining with thioflavin-S. The blue arrows point to lipofuscin deposits, which are not visible in the thioflavin-S-stained images since the fluorescence of thioflavin-S is stronger. Scale bars: 40 μm .

To determine the spectral response of amyloid deposits we measured the green emission with a confocal microscope in spectral detection mode, using an excitation source of 488 nm, close to the 470 nm LED of the full-field fluorescence microscope. Amyloid deposits in adjacent sections of cases #3 and #4 were investigated, resulting in a total of 3 cored and 2 fibrillar amyloid deposits. In Fig. 4 the results for one of the cored and one of the fibrillar amyloid deposit measurements are shown. The emission of the core plaque peaks around 540 nm and for the fibrillar plaque around 549 nm (mean values). Lipofuscin peaks in both cases around 566 nm. Similar emission curves of the three additionally measured plaques are shown in the Supplementary Information in Fig. S5.

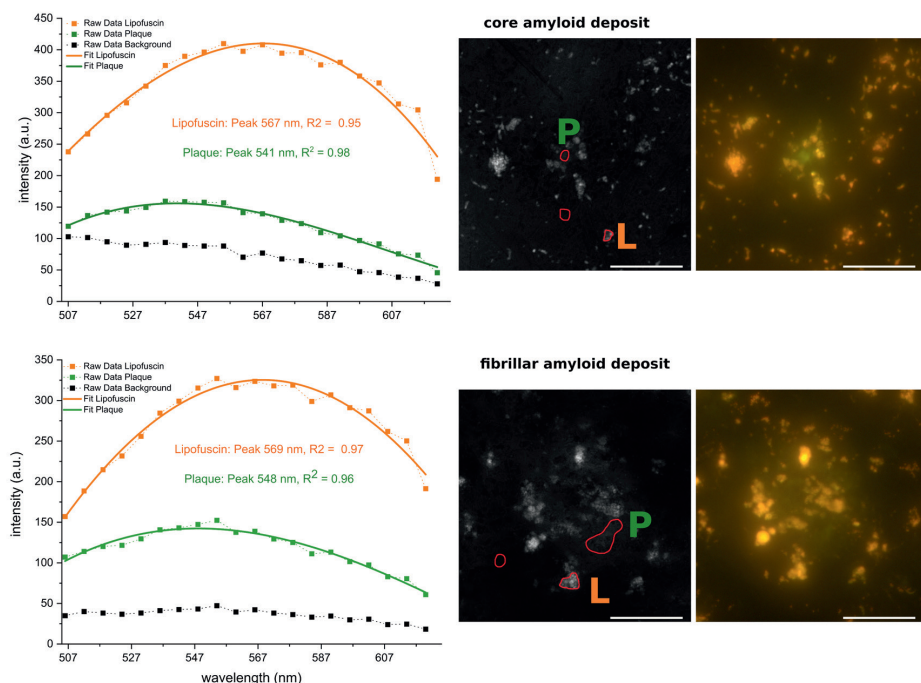


Fig. 4. Fluorescence emission spectra of plaque areas excited with a 488 nm source. Top row: cored amyloid deposit. Bottom row: fibrillary amyloid deposit. Symbols connected with a dashed line are the measured data. The solid lines are the corresponding 3rd order polynomial fits; peak position and R^2 values are indicated. The right half shows the corresponding z-projection of the emission images and the locations where the data points for plaque (P), lipofuscin (L) and background were taken, next to it the corresponding full-field auto-fluorescence images. Corresponding thioflavin-S images are not shown. Scale bar: 40 μm .

It is important to mention that we also observed a few greenish auto-fluorescence areas of different appearance which did not stain positive for amyloid deposit with thioflavin-S. These looked similar in terms of density and color but had a spherical shape and were smaller with a diameter of 10-15 μm . In Fig. S6 (Supplementary Information) we show two of those spots, comparing the auto-fluorescence before and the fluorescence image after thioflavin-S staining. As can be noted, the green bubble-like structures are not stained by thioflavin-S and are therefore not positive for amyloid. We hypothesize that these intracellular bodies are corpora amylacea. In agreement with the literature, the observed cellular bodies match size, luminescence and the lack of $A\beta$ [4, 5, 12]. Furthermore, corpora amylacea are known for their abundance in neurodegenerative diseases [5] and were recently proposed as “containers to remove waste products” [73].

Spontaneous Raman spectroscopy

After recording the Raman maps, the spectral data were analyzed and visualized. In columns 2-6 in Fig. 5, the processed images are compared to the acquired (auto-) fluorescence images of column 1. The Raman mapping images were taken in 1- μm step size and cover an area of $61 \times 61 \mu\text{m}$ for plaques #1a, #1b, #3a and #3b, $201 \times 201 \mu\text{m}$ for plaque #2, $81 \times 81 \mu\text{m}$ for plaques #3b and 5 and $101 \times 101 \mu\text{m}$ for #4. The overview for the control cases can be found in the Supplementary Information, Fig. S7. The total intensity images (meaning the integrated spectra per pixel) are shown in column 2 of Fig. 5, emphasizing areas with underlying fluorescent lipofuscin granules (orange-red spots in the images in the first column) while the rest of the tissue shows an almost uniform background. Columns 3 and 4 show the Raman peak intensity images (after data pre-processing but before MCR-ALS and clustering) of the protein and lipid bands. In addition, the ratio maps [51] of plaques #1a and #1b are shown in the Supplementary Information (Fig. S8). The protein and lipid mapping images highlight, similar to the total intensity images but in an inverse manner, the granular lipofuscin accumulations but they do not provide any visual evidence of potential increased β -sheet deposits. For the areas that were at a later stage confirmed with thioflavin-S staining to contain amyloid-plaque (see below) we then looked for any substantial changes in the Raman spectra at protein wavenumbers. This was triggered by other studies that provided evidence of a distinct protein peak shift towards the expected β -sheet peak when using either SRS on mice tissue [42] or conventional Raman scattering on human AD brain tissue [74] or CSF and blood samples [67]. In the Supplementary Information Fig. S9, we show the Amide-I band ($1640 - 1680 \text{ cm}^{-1}$) for all AD cases, where we compare the Raman spectrum of plaque locations to the averaged non-plaque spectrum, based on the MCR-ALS cluster spectra. The detected β -shifts were not as prominent as expected and were not found in all AD cases. Although the overall study size was limited, our results suggest that conventional Raman mapping at protein or lipid wavenumbers or peak ratio imaging, as commonly used for tissue analysis [24, 46, 59], does not appear to be such a robust method for the detection of amyloid plaques in brain tissue. On the other hand, strong Raman peaks at 1518 cm^{-1} and 1154 cm^{-1} , indicative of carotenoid compounds, were detected specifically at the cored plaque locations, as shown in the peak intensity images in columns 5 and 6 of Fig. 5. These two unique Raman peaks enable the spectral differentiation of the cored plaque areas from the surrounding tissue. This is further illustrated in Fig. 6, where we plot the full spectra (orange lines) associated with each plaque. The spectral origin is discussed in more detail in section 0. In none of the plaques of AD donor #2 and

#4 the carotenoid-specific spectrum was observed. The measured plaques in those two cases were of the fibrillar plaque type. Only one fibrillar plaque (#3b) showed clear carotenoid peaks within the fibrillar amyloid deposit. Interestingly, in this AD donor the majority of plaque types was of the dense cored type whereas in case #2 and #4 the majority of plaques were of the fibrillar type. This suggests that the carotenoid signal differs in plaque types and might especially be associated with dense cored plaques.

The last column in Fig. 5 shows the fluorescence images of the same tissue slice and area after thioflavin-S staining. Amyloid deposits are stained positively in yellow, matching not only the green auto-fluorescence areas in the unstained images but also the Raman peak intensity images (1154 cm^{-1} and 1518 cm^{-1}) at carotenoid wavenumbers and the cluster images column 7) and therefore confirm the actual presence of plaques in the measured tissue areas.

In Fig. 6 we compare the obtained spectra after clustering of the MCR-ALS data, depicting the plaque associated spectra in orange. In all cored plaques (#1a, #1b, #3a, #3c, #5) and in plaque #3b we have an identical spectral distribution with the peaks around 1154 cm^{-1} and 1518 cm^{-1} (and also the elevated peak around 1008 cm^{-1} which partially overlaps with the phenylalanine peak at 1003 cm^{-1}). These Raman peaks are well-known to be associated with carotenoids [1, 69], which can be found in the human body, including in the brain [95] and also in the retinal macular pigment [20, 26]. For further discussion and analysis of carotenoids in amyloid plaques, please see section 0. The spectral data of the background (dark and medium dark gray) differ only slightly in intensity with no peak variations observed. The background exhibits the main common tissue peaks at 1660 cm^{-1} (protein), 1445 cm^{-1} (lipids) and others. The lipofuscin spectrum (light gray) is the lowest in overall intensity but shows the same vibrational modes for proteins and lipids across the spectrum. Its apparent lower intensity can be explained as a consequence of the background removal algorithm. The raw spectral data of lipofuscin areas contain the highest fluorescence background and relatively little Raman scattering on top of it [54]. The background removal algorithm subtracts most of the underlying fluorescence, resulting in a low intensity Raman spectrum for the lipofuscin spots.

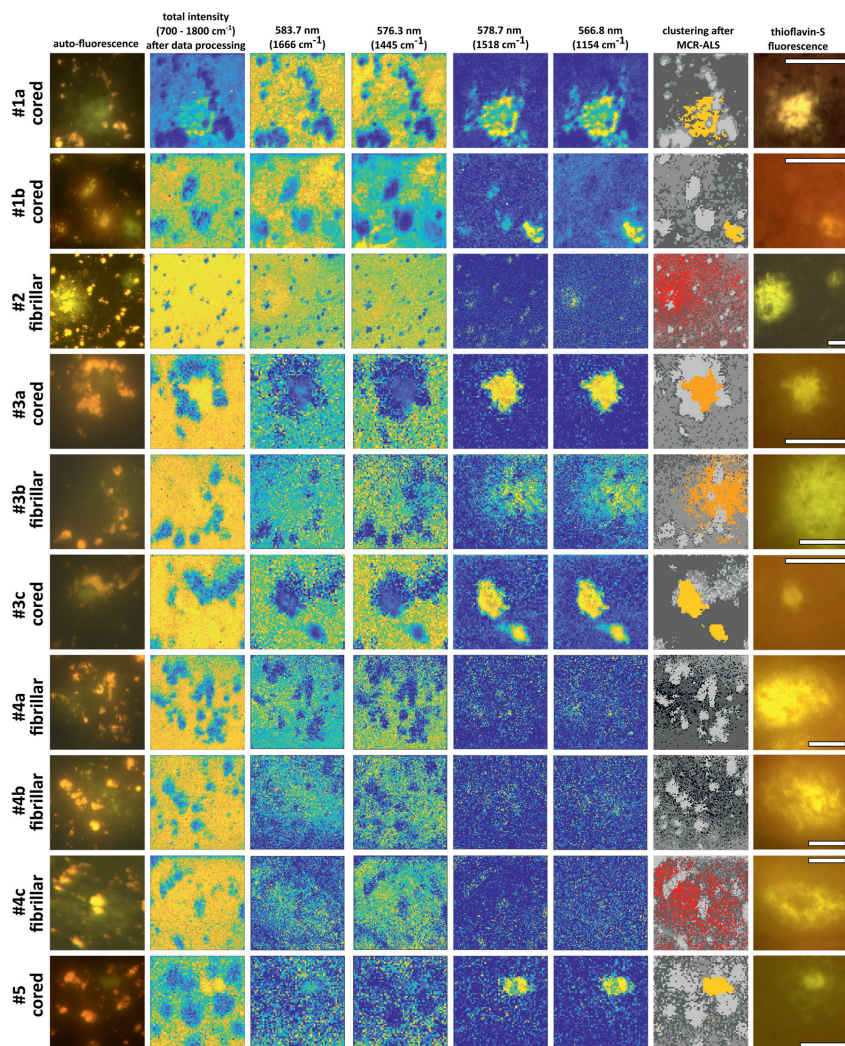


Fig. 5. Overview of fluorescence and Raman images

Each row represents one tissue section. 1st column: Auto-fluorescence images of the presumed plaque (green) areas. 2nd column: The total intensity image of the spectral Raman data after data pre-processing. 3rd and 4th column: Raman peak intensity images of the protein (1666 cm^{-1}) and lipid (1445 cm^{-1}) bands. 5th and 6th column: Raman peak intensity images at two prominent carotenoid wavenumbers (1518 cm^{-1} and 1154 cm^{-1}). 7th column: 4-cluster images of the Raman data after MCR-ALS computing, highlighting the plaque locations in orange (#1) and red (#2 and #4c). Last column (8th): Fluorescence image of the thioflavin-S stained tissue, confirming anticipated plaque locations by yellow fluorescence. Note for cored plaques #1a, #1b, #3a, #3c and #5 how well the carotenoid peak images and the cluster analysis match the stained plaque depositions. Scale bars: $40\text{ }\mu\text{m}$; color coding: blue (low) to yellow (high). MCR-ALS multivariate curve resolution-alternating least squares.

When analyzing the spectral clustering of fibrillar plaques #2 and #4(a, b and c), the above-mentioned carotenoid peaks were not detected. The red area in the cluster image of #2 and #4c show the points which largely cover the locations where a plaque was confirmed by thioflavin-S staining but the associated spectra do not show any carotenoid peaks. All 4-cluster spectra show roughly the same spectral distribution with very similar peaks and only minor intensity variations. The peaks at 1659 cm^{-1} and 1439 cm^{-1} are most likely slightly shifted amide-I (protein) and lipid bands. Together with the 1005 cm^{-1} phenylalanine peak, they represent the general Raman peaks of human brain tissue. Even though we do not observe carotenoid peaks in most of the fibrillar amyloid plaques, there are other spectral peaks, which are also present but to a lesser extent in the spectra of other plaques. Common peaks are at 760 cm^{-1} , associated with DNA or protein; at 1130 cm^{-1} , associated with C-N stretching of proteins and overlapping with the phosphatidylcholine lipid band; at 1311 cm^{-1} , the CH_2 twisting mode of lipid combined with the Amide-III mode and at 1586 cm^{-1} , most likely associated with retinoid compounds [14, 22]. The 4-cluster spectra of the control cases were obtained in a similar manner but show no sign of carotenoid peaks. The cluster images and corresponding spectra of the control cases can be found in the Supplementary Information (Fig. S10).

Multimodal, label-free fluorescence and Raman imaging of amyloid deposits

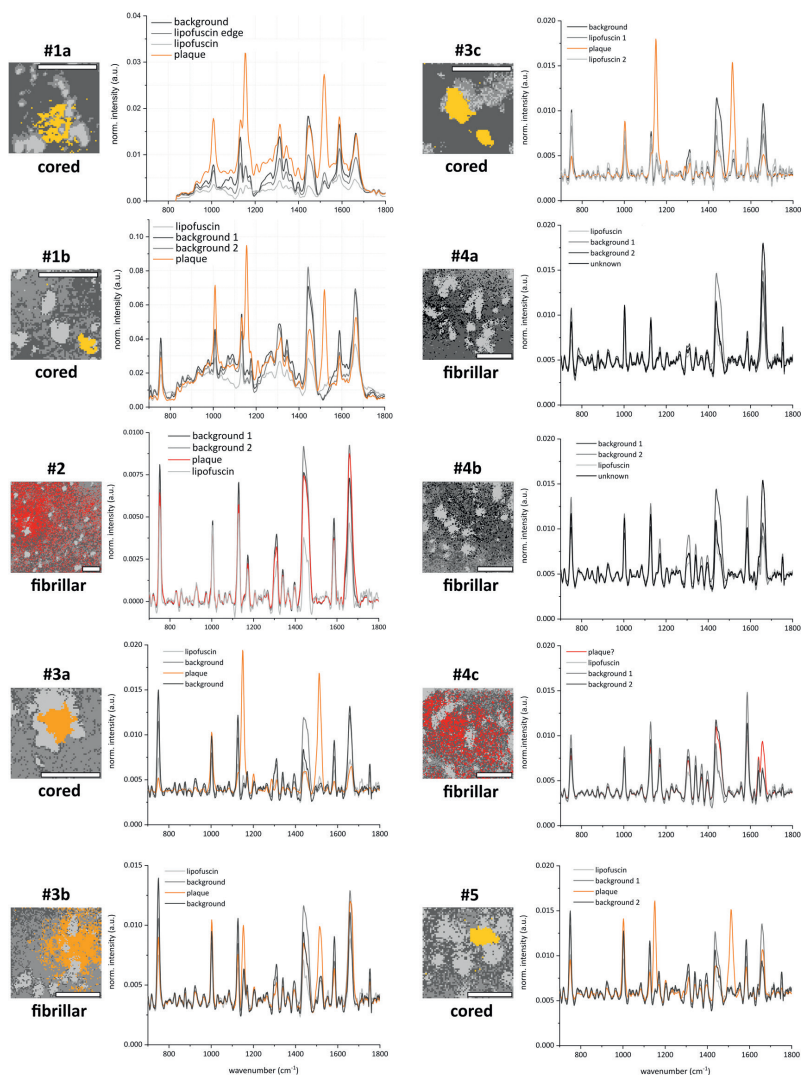


Fig. 6. 4-cluster images of all plaques and their corresponding spectra after complete data processing

The orange solid lines, obtained from the cored plaques and from fibrillar plaque #3b, exhibit a distinguishable spectrum with clear carotenoid associated peaks. However, in plaques #2 and #4(a, b, and c) no carotenoid peaks were detectable. The red area, which largely overlaps with the later confirmed plaque location, corresponds to the spectrum (red line) on the right which is not associated with carotenoids. (The whole recorded spectra of #1a including the CH-stretch range can be found in the Supplementary Information, Fig. S11). Scale bars: 40 μm .

Resonance Enhancement

In the Supplementary Information, Fig. S12, we show a spectral Raman clustering comparison between the 532 nm and 785 nm excitation source of the identical tissue area (plaque #1b), demonstrating the absence of detectable carotenoid peaks when using the NIR source. Similar observations were reported before, when Raman spectroscopy with different excitation sources was used to study colon cancer tissue [80]. In our recent work [54], we were not able to reveal unique spectral differences between plaque and non-plaque areas within formalin-fixed AD tissue. Although in principle the fixation of the tissue might be responsible for the unsuccessful distinction of amyloid plaques, the more likely reason is the use of a different Raman excitation source of $\lambda = 785$ nm. In order to assess the effect of the Raman excitation wavelength, we recorded the absorption spectra of two carotenoid compounds β -carotene and lutein (Sigma Aldrich) dissolved in hexane. We observed that the compounds have similar UV-VIS spectra, with two substantial peaks at around 450 (443) and 478 (472) nm, respectively (see Fig. S13 in the Supplementary Information) in agreement with literature [6, 26, 58]. Therefore, using a 532 nm Raman excitation source is expected to enhance the carotenoid Raman signals relative to those of the other tissue components through the so-called pre-resonance effect [92]. The green 532 nm laser lies at the edge of the absorption flank of carotenoids, whereas there will be practically no resonance enhancement with a NIR source. We found a factor of roughly 38 times increased efficiency for beta-carotene and 30 times for lutein when using a 532-nm source in comparison with the 785-nm laser (see Fig. S14 in the Supplementary Information, normalized to the solvent Raman intensity to correct for differences in laser power and other factors). Note that this enhancement factor at 532 nm may be different for other carotenoid compounds with a shifted absorption spectrum. In the absence of any substantial resonance enhancement, the carotenoid levels are too low to be detected with 785 nm excitation. Previous studies on carotenoids suggest to use a laser wavelength in the deep blue range to increase the resonance effect even further by better matching the excitation wavelength with the absorption band [21]. Beta-carotene and lutein are weakly fluorescent (see Fig. S15, in agreement with reference [45]) and their emission wavelength range matches that of the greenish auto-fluorescence of the plaque areas (under 488 nm excitation, see Fig. S4 and S5) quite well. However, it cannot be excluded that another plaque-associated compound, present at lower level but with a higher fluorescence quantum yield, is mainly responsible for this green emission. The molecular origin of the green fluorescence must be different from that of the blue emission

observed under UV excitation by Thal et al. [83], indicating that there are at least two separate fluorescent compounds associated with plaques.

In Fig. S16, we compare the obtained Raman plaque spectra of #1a with Raman measurements of β -carotene dissolved in hexane. Beta-carotene is commonly used as reference sample for carotenoids while lutein, together with zeaxanthin, is one of the main carotenoids found in human brain tissue [3, 44]. The three typical carotenoid peaks [41], approximately at 1007 cm^{-1} , 1156 cm^{-1} and $1523/6\text{ cm}^{-1}$, clearly match the extra peaks observed in plaques, see in Fig. S12 (bottom left) the averaged Raman spectra of plaque and non-plaque areas. This provides further proof that carotenoids are present at elevated levels within amyloid accumulations. The exact Raman peak positions may slightly vary, depending on the polyene chain length, side groups and aggregation state of the specific carotenoid molecule [58, 69]. In vitro and in vivo animal carotenoid studies suggest that carotenoids in general have antioxidant and anti-inflammatory effects [48, 62] and lutein was observed to have a “strong suppressive impact on $A\beta$ formations” [47, 62, 81]. Our results are in line with the observation that amyloid accumulation in AD brain is associated with an inflammatory process [7, 10, 32, 36, 75], and activated microglia are localized next to (the core of) plaques [9, 10, 18, 40, 76]. Also, others reported carotenoid associated Raman spectra in AD formalin-fixed human brain tissue [53] and in blood plasma [31] which supports the suggestion that the presence of carotenoids may be associated with an ongoing inflammatory process [36]. Carotenoids cannot be synthesized de novo by mammals and therefore must be obtained from diet [33]. Due to their lipophilic nature, they are expected to occur at a resting level in cell membranes and lipoprotein components [82]. Literature suggests that carotenoids, similar to microglia, are accumulating at sites of local inflammation (here, protein aggregation in AD), to fight oxidative damage and reactive oxygen species (ROS)[48, 82, 91]. This might explain the elevated levels of carotenoids found at locations with high $A\beta$ accumulations. As an indication that similar processes may have occurred in the AD cases of our study, we show microglia activity next to a core amyloid deposit, imaged in an adjacent section of sample #3c (see Fig. S17). Interestingly, retinal imaging studies in AD patients have shown that the macula pigment volume, consisting of carotenoids, is significantly lower compared to control patients [68].

Stimulated Raman scattering microscopy

Recently, Ji et al. [42], reported a protein peak shift towards the expected β -sheet peak (1670 cm^{-1}) in freshly frozen transgenic mouse brain tissue (with

AD pathology) using SRS micro-spectroscopy. Here, we applied a comparable SRS methodology to human AD samples, using the same tissue sections and areas of interest as in the previous sections. The results are given in Fig. 7 and for the control cases in Fig. S18 in the Supplementary Information. The plaques were raster scanned at different wavenumber settings across the protein peak in 3 cm^{-1} steps (with smaller step sizes around the 1660 cm^{-1} region, while plaque #1a was obtained using a larger step size). The data for the averaged background were taken within the yellow dashed circles, the red dashed lines encompass the plaque areas. The data per plaque were normalized for a better comparison of the background and plaque curves. Please note that for the SRS measurements, the tissue sections on the microscope slides were not protected with a cover slip but only covered with deionized water. Therefore, the $20 \text{ }\mu\text{m}$ thick tissue might be slightly bloated and therefore appears non-flat under the microscope, which complicates the depth sensitive SRS measurements in terms of homogenous field of view observation. That is the reason why we could not obtain SRS measurements from samples #3c, #4c and from control sample c#1b. In AD tissue sections #1b, #3a and #3b we observe a strong and unique protein peak shift towards the expected β -sheet peak. The intensity of the background data has a maximum at 1659 cm^{-1} while the plaque curve peaks at 1666 cm^{-1} . This is in agreement with the above mentioned results from mouse brain tissue, where the examined plaque deposits can be described as ultra-dense and compact [42]. For tissue sections #1a, #4a and #5, the protein peak shift is less pronounced compared to the former sections. Finally, for tissue section #2 and #4b the extensive spread of the amyloid fibrils with a presumably low molecular density hampers any clear spectroscopic distinction; the data appear very noisy and do not allow any unambiguous statement about a potential peak shift. In general, the results suggest that all cored plaques (#1a, #1b, #3a and #5) that were found to contain carotenoid accumulations also display a protein peak shift when measured with SRS. In addition, a similar behavior can be observed for the amyloid deposit #3b, which we classified as fibrillar deposit based on its thioflavin-S staining pattern. As expected, the control cases do not show a protein peak shift within the imaged areas (as shown in Fig. S18 in the Supplementary Information). In summary, the obtained results are largely in agreement with published results on mice [42], with the peak shifts observed in the conventional Raman data (Fig. S9 in the Supplementary Information) and with our findings on carotenoid levels. Nevertheless, we are still far away from a label-free detection method for plaques in AD tissue via SRS since only a few of the plaques could be clearly identified, mostly the ones with a very high concentration of amyloid. Furthermore, it is worth to mention that our current

data do not reveal a pronounced lipid halo surrounding the plaques as recently reported by several studies [42, 70, 78].

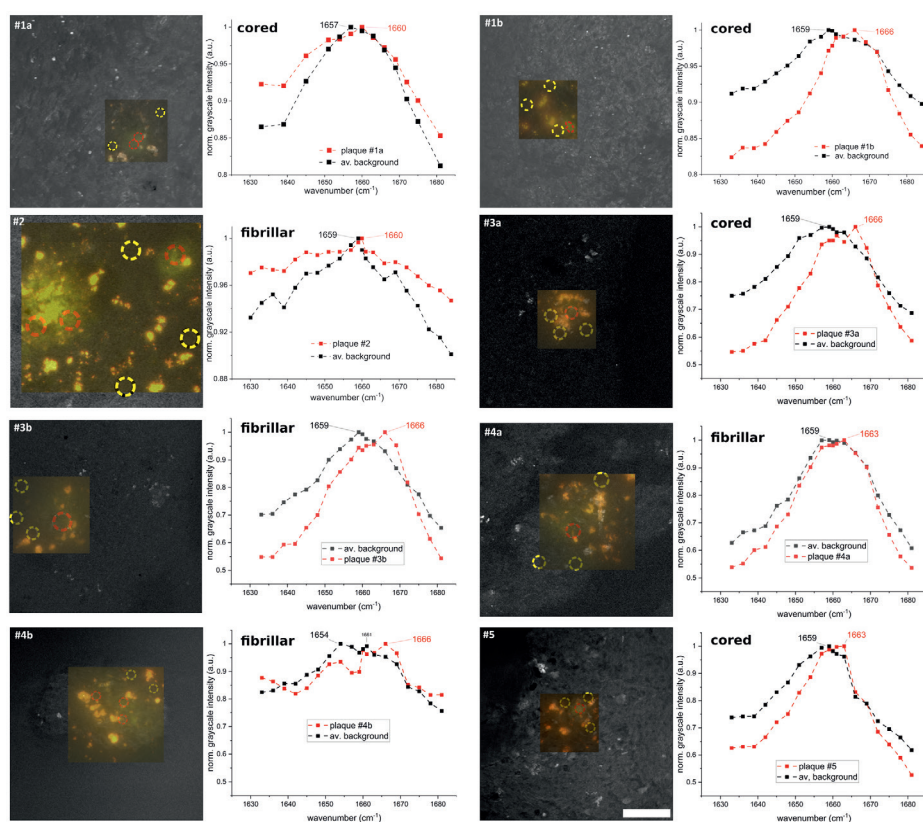


Fig. 7. SRS images obtained while scanning across the protein peak for each plaque. Auto-fluorescence images overlaid on SRS max. intensity projection images (@ 1666 cm^{-1}) with the plaque locations shown as green spots. Next to the images are the SRS response graphs of averaged sweeps across the protein peak per plaque. A clear shift from the “normal” 1659 cm^{-1} protein peak towards the β -sheet peak at 1666 cm^{-1} is only observed in plaques featuring a dense cored plaque. This shift was not observed in plaque #2 and less visible in #1a (which was measured with bigger step sizes). The yellow circles indicate areas where data was taken for the background, the red circles indicate the areas for plaques. Scale bar: 50 μm . SRS stimulated Raman scattering.

In summary, we sequentially applied multimodal and label-free imaging techniques on human AD brain tissue to identify different phenotypes of amyloid plaques. Mere auto-fluorescence imaging of snap-frozen, unstained AD gray matter tissue suggests the possibility of rapid visual assessment and localization

of plaque pathology. The RGB camera of our full-field fluorescence microscope (rather than a single-wavelength bandpass filter) helped to distinguish the plaque's greenish auto-fluorescence from the stronger yellow-orange emission of the lipofuscin deposits. Thal et al. [83] reported that plaques areas show blue auto-fluorescence upon irradiation in the UV range. A comparative study should be carried out to find out which wavelength settings in excitation and emission would offer the best sensitivity and selectivity in label-free fluorescence microscopy applications for fast direct pathological examination of AD tissue. The label-free identification of amyloid plaques by its auto-fluorescence signal could provide a promising basis for *in vivo* (auto-) fluorescence brain and potential retinal imaging as the eye provides a clear optical window for human studies [13, 15, 55].

Despite its extended acquisition time, spontaneous Raman mapping under (pre-) resonance conditions adds vital and complementary information about the chemical specificity of the examined biomolecules. We identified the presence of carotenoids as a unique spectral feature associated with the location of (cored) plaques, which allowed us to differentiate areas with accumulations of amyloid protein from the surrounding tissue.

In the near future, advanced and rapid tissue imaging using SRS for amyloid plaques identification by monitoring and detecting a potential spectral shift from protein to β -sheet might have some potential pitfalls. In this preliminary study, only the cored amyloid plaques showed a peak shift, while fibrillar plaques showed no or only limited evidence of such a protein peak shift. Certainly, more research is needed to better understand the underlying causes why the expected peak shift towards β -sheet deposits was not observable in all plaques. A major advantage of SRS over spontaneous Raman is of course the much higher mapping speed: even when the same area is imaged at tens of different wavenumber settings (as in this study) it is still about two orders of magnitude faster. Furthermore, SRS does not suffer from background fluorescence. Advanced strategies e.g. via deep learning [56] might be able to enhance the information value of SRS imaging results. At the same time, future research should investigate the presence of carotenoids in AD tissue using advanced (VIS) SRS systems with at least one of the laser wavelengths closer to the carotenoids' absorption band [58]. Under such pre-resonance SRS conditions, we anticipate an improved sensitivity and selectivity of the carotenoids within AD tissue and an even higher mapping speed as compared to detecting a potential protein peak shift with NIR SRS [89].

Overall, the detection of carotenoids in amyloid accumulations indicates a neuroinflammatory response associated with misfolded protein aggregations and its involvement in neuropathological structures in dementia. However, the implications of carotenoids co-localized with A β accumulations remains unanswered and further investigations are necessary to understand their role and why some plaques appear to have non-detectable carotenoid levels.

METHODS

Brain tissue and tissue preparation

Post mortem brain tissue was obtained from the Netherlands Brain Bank (NBB, Amsterdam, the Netherlands, <https://www.brainbank.nl>). All brain tissue was collected from donors with written informed consent for brain autopsy and the use of brain tissue and clinical information for research purposes. The brain donor program of the NBB was approved by the local medical ethics committee of the Vrije Universiteit medical center (Ref#2009/148). Neuropathological diagnosis was based on histochemical stainings including hematoxylin and eosin, Congo red staining, Bodian or Gallyas and Methenamine silver stainings and immunohistochemical stainings for A β , p-tau, alpha-synuclein, and p62. These stainings were performed on formalin-fixed, paraffin embedded (FFPE) brain tissue of multiple brain regions including the frontal cortex, temporal pole, superior parietal lobe, occipital pole, amygdala and the hippocampus. Neuropathological diagnosis of AD was based on Braak stages for neurofibrillary tangles (NFT) and amyloid [11], Thal phases for A β [84], as well as CERAD criteria for neuritic plaques [60]. We selected cases with a high score of AD pathology according to the NIA-AA criteria [63]. Based on post mortem diagnosis, we excluded cases with other neurodegenerative diseases. Snap-frozen brain tissue sections (20 μ m) from five selected cases were obtained from the frontal lobe. The area of interest was the gray matter region where plaques are expected and their presence was confirmed using histochemistry with thioflavin-S in the same section and immunohistochemistry against A β in sequential sections (see Fig. S1 for anti-A β staining in the Supplementary Information). Here, we report on the results of plaques imaged from five different AD brain donors. In total, ten amyloid plaques have been assessed. Patient demographics and plaque characteristics, based on their thioflavin-S-stained pattern (cored vs. fibrillar), can be found in Table 1. The characterization of the five control sections from two donors can be found at the last rows in Table 1.

Fluorescence microscopy

Full field fluorescence microscopy

Auto-fluorescence images were acquired with a Leica DM2000 fluorescence microscope. The illumination source was a blue LED with a wavelength of about 470 nm. The color images were obtained for wavelengths above 500 nm using the attached Leica DFC450 C camera and the Leica application suite lite software. The same microscope and filter settings were used for the thioflavin-S-stained tissue sections after spontaneous Raman and SRS imaging.

Confocal fluorescence scanning microscopy

A confocal fluorescence scanning microscope (Nikon A1) with an A1-DUS spectral detector unit was used. The characterization of the emission curve of plaque locations was done using a 488 nm excitation source (close to the 470 nm LED source of the full-field fluorescence microscope) and a $\times 20$ objective (0.8 NA). The power was kept constant at 1 mW with a pixel dwell time of 2.4 μ s. The recorded emission ranged from 507 to 621 nm with a step size of 6 nm, resulting in 20 data points.

Raman spectroscopy

The spontaneous Raman measurements were recorded in mapping mode using a commercially available Raman spectrometer, Renishaw inVia, with an excitation wavelength of 532 nm. The attached Leica microscope was equipped with a $\times 50$ objective (Leica HC PL FLUOTAR) with a NA of 0.8. The following settings were kept constant for each measured plaque. The laser power was set to 5% corresponding to 3 mW at the sample plane with a spot size of less than 1 μ m. Per pixel, two or three accumulations were recorded with an exposure time of 1 s. The tissue sustained no detectable damage during the measurement. We recorded the fingerprint region from around 850 to 1850 cm^{-1} with a resolution of approximately 4 cm^{-1} FWHM. The total Raman spectra acquisition time per sample was up to 23 hours, depending on the mapped area. Based on the prior acquired auto-fluorescence images, we mapped an area around the plaque location in 1 μ m steps. To analyze and compare the resonance enhancement, additional measurements were done with an excitation source of 785 nm and the laser power set to 100%, measured as 82 mW at the sample plane.

Stimulated Raman Scattering microscopy

For Stimulated Raman Scattering (SRS) measurements, we used an in-house built picosecond system as described in more detail in previous works [30, 61, 94]. In short, the Stokes beam ($\lambda = 1064$ nm, 80 MHz repetition rate, power 25 mW at

the sample plane) was amplitude modulated at 3.6 MHz. The pump beam from the OPO was tuned from 901 to 907 nm to cover the amide-I protein peak in the fingerprint region (around 1660 cm^{-1}), with a power measured as 55 mW at the sample plane. The spectral resolution in this wavelength range is approximately 4 cm^{-1} . The tissue section was placed below the objective (Zeiss, C-Achroplan W, $\times 32$, 0.85 NA, water immersion) and covered with deionized water. During the recording the pixel dwell time per image was kept constant and set to $177.32\text{ }\mu\text{s}$. Furthermore, the lock-in amplifier settings with a scale factor of +445.5 (a.u.), offset +0.100 mV, low-pass filter order 8 and a time constant of $25\text{ }\mu\text{s}$, were kept constant throughout all measurements. The obtained raster scanned images are an average of two measurements.

Thioflavin-S staining

Thioflavin-S staining was performed for confirmation of amyloid deposits, but only after auto-fluorescence imaging, spontaneous Raman imaging and SRS imaging. First, the tissue was fixed using formalin (4 %) (10 min) to secure tissue on the microscope slide. Subsequently, the tissue sections were incubated with 1% thioflavin-S (Sigma-Aldrich) solution (demineralized water) for 10 min, followed by rinsing off excess thioflavin-S using 70% alcohol. Tissue sections were then washed using PBS and covered using Tris-buffered saline (TBS)/glycerol mounting medium, as described previously [28], and covered with a coverslip. Thioflavin-S binds to $\text{A}\beta$ that is stacked into a beta-pleated confirmation, also referred to as amyloid. This amyloid is present in cored and fibrillary plaques. Any possible non-fibrillary plaques [85] are likely not stained and hence the plaque might appear smaller than expected from well-known $\text{A}\beta$ staining. Thioflavin-S staining is commonly used to identify plaque in tissue [19, 42, 49].

Data processing

The spectral data recorded from the Raman spectrometer were processed entirely using OCTAVVS (version 0.0.28) [87], a recently developed open chemometrics toolkit consisting of three steps: (data) pre-processing, multivariate curve resolution-alternating least squares (MCR-ALS) and clustering. In the preprocessing step, the spectra were de-noised (Savitzky-Golay filter with a window size of 9 data points corresponding to approximately 9.4 cm^{-1} and a 3rd order polynomial), baseline corrected (using the asymmetric reweighted penalized least squares (arPLS) algorithm) and normalized (area under the curve). In step two, a single value decomposition (SVD) for 8 components was performed (with 5% noise allowed). Afterward, the MCR-ALS was started

using the non-negatively constrained least squares iteration algorithm to reach a tolerance below 0.1 %. The final clustering step was performed based on the pure spectra calculated by MCR-ALS. Eventually, the computed spectra were clustered in 4 groups using area normalization and the Mini Batch K-Means algorithm. For a more detailed description of these processing algorithms we refer to the paper of the OCTAVVS developers [88].

ACKNOWLEDGEMENTS

The authors would like to thank Tjado H. J. Morrema for technical assistance and C. Troein for his software support. This research is supported by the Dutch Technology Foundation STW (grant number 13935, I-READ), which is part of the Netherlands Organization of Scientific Research (NWO), and which is partly founded by the Ministry of Economic Affairs.

LIST OF ABBREVIATIONS

| | |
|-----------|---|
| A β | amyloid-beta |
| AD | Alzheimer's disease |
| APP | amyloid precursor protein |
| arPLS | asymmetric reweighted penalized least squares |
| CARS | coherent anti-Stokes Raman spectroscopy |
| CSF | cerebrospinal fluid |
| Ex | excitation |
| Em | emission |
| MCR-ALS | multivariate curve resolution-alternating least squares |
| ROS | reactive oxygen species |
| SERS | surface-enhanced Raman spectroscopy |
| SRS | stimulated Raman scattering |
| SVD | single value decomposition |
| TBS | Tris-buffered saline |

REFERENCES

1. Adar F (2017) Carotenoids - Their Resonance Raman Spectra and How They Can Be Helpful in Characterizing a Number of Biological Systems. *Spectroscopy* 32:12-20
2. Andreasen N, Zetterberg H (2008) Amyloid-Related Biomarkers for Alzheimer 's Disease. *Curr Med Chem* 15:766-771
3. Arteni AA, Fradot M, Galzerano D, Mendes-Pinto MM, Sahel JA, Picaud S, Robert B, Pascal AA (2015) Structure and conformation of the carotenoids in human retinal macular pigment. *PLoS One* 10. doi: 10.1371/journal.pone.0135779
4. Augé E, Bechmann I, Llor N, Vilaplana J, Krueger M, Pelegrí C (2019) Corpora amylacea in human hippocampal brain tissue are intracellular bodies that exhibit a homogeneous distribution of neo-epitopes. *Sci Rep* 9. doi: 10.1038/s41598-018-38010-7
5. Augé E, Cabezón I, Pelegrí C, Vilaplana J (2017) New perspectives on corpora amylacea in the human brain. *Sci Rep* 7. doi: 10.1038/srep41807
6. Bernstein PS, Yoshida MD, Katz NB, McClane RW, Gellermann W (1998) Raman detection of macular carotenoid pigments in intact human retina. *Invest Ophthalmol Vis Sci* 39:2003-2011
7. Bevan-Jones WR, Cope TE, Jones PS, Kaalund SS, Passamonti L, Allinson K, Green O, Hong YT, Fryer TD, Arnold R, Coles JP, Aigbirhio FI, Larner AJ, Patterson K, O'Brien JT, Rowe JB (2020) Neuroinflammation and protein aggregation co-localize across the frontotemporal dementia spectrum. *Brain* 143:1010-1026. doi: 10.1093/brain/awaa033
8. Beyreuther K, Masters CL (1991) Amyloid Precursor Protein (APP) and B2A4 Amyloid in the Etiology of Alzheimer's Disease: Precursor-Product Relationships in the Derangement of Neuronal Function. *Brain Pathol* 1:241-251. doi: 10.1111/j.1750-3639.1991.tb00667.x
9. Boon BDC, Bulk M, Jonker AJ, Morrema THJ, van den Berg E, Popovic M, Walter J, Kumar S, van der Lee SJ, Holstege H, Zhu X, Van Nostrand WE, Natté R, van der Weerd L, Bouwman FH, van de Berg WDJ, Rozemuller AJM, Hoozemans JJM (2020) The coarse-grained plaque: a divergent A β plaque-type in early-onset Alzheimer's disease. *Acta Neuropathol* 140:811-830. doi: 10.1007/s00401-020-02198-8
10. Boon BDC, Hoozemans JJM, Lopuhaä B, Eigenhuis KN, Scheltens P, Kamphorst W, Rozemuller AJM, Bouwman FH (2018) Neuroinflammation is increased in the parietal cortex of atypical Alzheimer's disease. *J Neuroinflammation* 15:170. doi: 10.1186/s12974-018-1180-y
11. Braak H, Braak E Neuropathological stageing of Alzheimer-related changes. *Acta Neuropathol* 82:239-259. doi: 10.1007/BF00308809
12. Cavanagh JB (1999) Corpora-amylacea and the family of polyglucosan diseases. *Brain Res. Rev.* 29:265-295
13. Cerquera-Jaramillo MA, Nava-Mesa MO, González-Reyes RE, Tellez-Conti C, De-La-Torre A (2018) Visual features in Alzheimer's disease: From basic mechanisms to clinical overview. *Neural Plast.* 2018

14. Chen AJ, Li J, Jannasch A, Mutlu AS, Wang MC, Cheng JX (2018) Fingerprint Stimulated Raman Scattering Imaging Reveals Retinoid Coupling Lipid Metabolism and Survival. *ChemPhysChem* 19:2500–2506. doi: 10.1002/cphc.201800545
15. Csincsik L, MacGillivray TJ, Flynn E, Pellegrini E, Papanastasiou G, Barzegar-Befroei N, Csutak A, Bird AC, Ritchie CW, Peto T, Lengyel I (2018) Peripheral Retinal Imaging Biomarkers for Alzheimer's Disease: A Pilot Study. *Ophthalmic Res* 59:182–192. doi: 10.1159/000487053
16. D'Andrea MR, Nagele RG, Gumula NA, Reiser PA, Polkovitch DA, Hertzog BM, Andrade-Gordon P (2002) Lipofuscin and A β 42 exhibit distinct distribution patterns in normal and Alzheimer's disease brains. *Neurosci Lett* 323:45–49. doi: 10.1016/S0304-3940(01)02444-2
17. Delori FC, Dorey CK, Staurenghi G, Arend O, Goger DG, Weiter JJ (1995) In vivo fluorescence of the ocular fundus exhibits retinal pigment epithelium lipofuscin characteristics. *Investig Ophthalmol Vis Sci* 36:718–729
18. Dickson DW, Farlo J, Davies P, Crystal H, Fuld P, Yen SH (1988) Alzheimer's disease. A double-labeling immunohistochemical study of senile plaques. *Am J Pathol* 132:86–101
19. Dickson TC, Vickers JC (2001) The morphological phenotype of beta-amyloid plaques and associated neuritic changes in Alzheimer's disease. *Neuroscience* 105:99–107. doi: 10.1016/s0306-4522(01)00169-5
20. Ermakov I V., Ermakova MR, Gellermann W (2005) Simple raman instrument for in vivo detection of macular pigments. *Appl Spectrosc* 59:861–867. doi: 10.1366/0003702054411616
21. Ermakov I V., McClane RW, Gellermann W, Bernstein PS (2001) Resonant Raman detection of macular pigment levels in the living human retina. *Opt Lett* 26:202. doi: 10.1364/ol.26.000202
22. Failloux N, Bonnet I, Baron MH, Perrier E (2003) Quantitative Analysis of Vitamin A Degradation by Raman Spectroscopy. *Appl Spectrosc* 57:1117–1122. doi: 10.1366/00037020360695973
23. Fišar Z, Jiráček R, Zvěřová M, Setnička V, Habartová L, Hroudová J, Vaníčková Z, Raboch J (2019) Plasma amyloid beta levels and platelet mitochondrial respiration in patients with Alzheimer's disease. *Clin Biochem* 72:71–80. doi: 10.1016/j.clinbiochem.2019.04.003
24. Frank CJ, McCreery RL, Redd DCB (1995) Raman Spectroscopy of Normal and Diseased Human Breast Tissues. *Anal Chem* 67:777–783. doi: 10.1021/ac00101a001
25. Gao Y, Liu Q, Xu L, Zheng N, He X, Xu F (2019) Imaging and Spectral Characteristics of Amyloid Plaque Autofluorescence in Brain Slices from the APP/PS1 Mouse Model of Alzheimer's Disease. *Neurosci Bull* 35:1126–1137. doi: 10.1007/s12264-019-00393-6
26. Gellermann W, Ermakov I V., Ermakova MR, McClane RW, Zhao D-Y, Bernstein PS (2002) In vivo resonant Raman measurement of macular carotenoid pigments in the young and the aging human retina. *J Opt Soc Am A* 19:1172. doi: 10.1364/josaa.19.001172

27. Guerrini L, Arenal R, Mannini B, Chiti F, Pini R, Matteini P, Alvarez-Puebla RA (2015) SERS detection of amyloid oligomers on metallorganic-decorated plasmonic beads. *ACS Appl Mater Interfaces* 7:9420–9428. doi: 10.1021/acsami.5b01056
28. den Haan J, Morrema THJ, Rozemuller AJ, Bouwman FH, Hoozemans JJM (2018) Different curcumin forms selectively bind fibrillar amyloid beta in post mortem Alzheimer's disease brains: Implications for in-vivo diagnostics. *Acta Neuropathol Commun* 6:75. doi: 10.1186/s40478-018-0577-2
29. den Haan J, Morrema THJ, Verbraak FD, de Boer JF, Scheltens P, Rozemuller AJ, Bergen AAB, Bouwman FH, Hoozemans JJ (2018) Amyloid-beta and phosphorylated tau in post-mortem Alzheimer's disease retinas. *Acta Neuropathol Commun* 6:147. doi: 10.1186/s40478-018-0650-x
30. van Haasterecht L, Zada L, Schmidt RW, de Bakker E, Barbé E, Leslie HA, Vethaak AD, Gibbs S, de Boer JF, Niessen FB, van Zuijlen PPM, Groot ML, Ariese F (2020) Label-free stimulated Raman scattering imaging reveals silicone breast implant material in tissue. *J Biophotonics* 13. doi: 10.1002/jbio.201960197
31. Habartová L, Hruběšová K, Syslová K, Vondroušová J, Fišar Z, Jiráček R, Raboch J, Setnička V (2019) Blood-based molecular signature of Alzheimer's disease via spectroscopy and metabolomics. *Clin Biochem* 72:58–63. doi: 10.1016/j.clinbiochem.2019.04.004
32. Hamlett ED, Ledreux A, Potter H, Chial HJ, Patterson D, Espinosa JM, Bettcher BM, Granholm AC (2018) Exosomal biomarkers in Down syndrome and Alzheimer's disease. *Free Radic. Biol. Med.* 114:110–121
33. Hammond BR, Renzi LM (2013) Carotenoids. *Adv Nutr* 4:474–476. doi: 10.3945/an.113.004028
34. Hanseeuw BJ, Betensky RA, Jacobs HIL, Schultz AP, Sepulcre J, Becker JA, Cosio DMO, Farrell M, Quiroz YT, Mormino EC, Buckley RF, Papp KV, Amariglio RA, Dewachter I, Ivanoiu A, Huijbers W, Hedden T, Marshall GA, Chhatwal JP, Rentz DM, Sperling RA, Johnson K (2019) Association of Amyloid and Tau with Cognition in Preclinical Alzheimer Disease: A Longitudinal Study. *JAMA Neurol* 76:915–924. doi: 10.1001/jamaneurol.2019.1424
35. Hardy J, Allsop D (1991) Amyloid deposition as the central event in the aetiology of Alzheimer's disease. *Trends Pharmacol. Sci.* 12:383–388
36. Heppner FL, Ransohoff RM, Becher B (2015) Immune attack: The role of inflammation in Alzheimer disease. *Nat. Rev. Neurosci.* 16:358–372
37. Hodge RD, Bakken TE, Miller JA, Smith KA, Barkan ER, Graybuck LT, Close JL, Long B, Penn O, Yao Z, Eggermont J, Holt T, Levi BP, Shehata SI, Aevermann B, Beller A, Bertagnolli D, Brouner K, Casper T, Cobbs C, Dalley R, Dee N, Ding S-L, Ellenbogen RG, Fong O, Garren E, Goldy J, Gwinn RP, Hirschstein D, Keene CD, Keshk M, Ko AL, Lathia K, Mahfouz A, Maltzer Z, McGraw M, Nguyen TN, Nyhus J, Ojemann JG, Oldre A, Parry S, Reynolds S, Rimorin C, Shapovalova N V., Somasundaram S, Szafer A, Thomsen ER, Tieu M, Scheuermann RH, Yuste R, Sunkin SM, Lelieveldt B,

- Feng D, Ng L, Bernard A, Hawrylycz M, Phillips J, Tasic B, Zeng H, Jones AR, Koch C, Lein ES (2019) Conserved cell types with divergent features between human and mouse cortex. *Nature* 573:61–68. doi: 10.1101/384826
38. Ikeda S, Allsop D, Glenner GG (1989) Morphology and distribution of plaque and related deposits in the brains of Alzheimer's disease and control cases. An immunohistochemical study using amyloid β -protein antibody. *Lab Invest* 60:113–122
 39. Ikonomic MD, Klunk WE, Abrahamson EE, Mathis CA, Price JC, Tsopelas ND, Lopresti BJ, Ziolkowski S, Bi W, Paljug WR, Debnath ML, Hope CE, Isanski BA, Hamilton RL, DeKosky ST (2008) Post-mortem correlates of in vivo PiB-PET amyloid imaging in a typical case of Alzheimer's disease. *Brain* 131:1630–1645. doi: 10.1093/brain/awn016
 40. Itagaki S, P.L. Akiyama SM (1989) Relationship of microglia and astrocytes to amyloid deposits of Alzheimer disease. *J Neuroimmunol* 24:173–182. doi: 10.1017/CBO9781107415324.004
 41. Jehlička J, Edwards HGM, Oren A (2014) Raman spectroscopy of microbial pigments. *Appl. Environ. Microbiol.* 80:3286–3295
 42. Ji M, Arbel M, Zhang L, Freudiger CW, Hou SS, Lin D, Yang X, Bacskai BJ, Sunney Xie X (2018) Label-free imaging of amyloid plaques in Alzheimer's disease with stimulated Raman scattering microscopy. *Sci Adv* 4. doi: 10.1126/sciadv.aat7715
 43. Ji M, Lewis S, Camelo-Piragua S, Ramkissoon SH, Snuderl M, Venneti S, Fisher-Hubbard A, Garrard M, Fu D, Wang AC, Heth JA, Maher CO, Sanai N, Johnson TD, Freudiger CW, Sagher O, Xie XS, Orringer DA (2015) Detection of human brain tumor infiltration with quantitative stimulated Raman scattering microscopy. *Sci Transl Med* 7. doi: 10.1126/scitranslmed.aab0195
 44. Johnson EJ (2012) A possible role for lutein and zeaxanthin in cognitive function in the elderly. *Am. J. Clin. Nutr.* 96
 45. Kandori H, Sasabe H, Mimuro M (1994) Direct Determination of a Lifetime of the S2State of β -Carotene by Femtosecond Time-Resolved Fluorescence Spectroscopy. *J Am Chem Soc* 116:2671–2672. doi: 10.1021/ja00085a078
 46. Kast R, Auner G, Yurgelevic S, Broadbent B, Raghunathan A, Poisson LM, Mikkelsen T, Rosenblum ML, Kalkanis SN (2015) Identification of regions of normal grey matter and white matter from pathologic glioblastoma and necrosis in frozen sections using Raman imaging. *J Neurooncol* 125:287–295. doi: 10.1007/s11060-015-1929-4
 47. Katayama S, Ogawa H, Nakamura S (2011) Apricot carotenoids possess potent anti-amyloidogenic activity in vitro. *J Agric Food Chem* 59:12691–12696. doi: 10.1021/jf203654c
 48. Kaulmann A, Bohn T (2014) Carotenoids, inflammation, and oxidative stress-implications of cellular signaling pathways and relation to chronic disease prevention. *Nutr. Res.* 34:907–929
 49. Kiskis J, Fink H, Nyberg L, Thyer J, Li JY, Enejder A (2015) Plaque-associated lipids in Alzheimer's diseased brain tissue visualized by nonlinear microscopy. *Sci Rep* 5. doi: 10.1038/srep13489

50. Klunk WE, Engler H, Nordberg A, Wang Y, Blomqvist G, Holt DP, Bergström M, Savitcheva I, Huang GF, Estrada S, Ausén B, Debnath ML, Barletta J, Price JC, Sandell J, Lopresti BJ, Wall A, Koivisto P, Antoni G, Mathis CA, Långström B (2004) Imaging Brain Amyloid in Alzheimer's Disease with Pittsburgh Compound-B. *Ann Neurol* 55:306–319. doi: 10.1002/ana.20009
51. Kumar S, Verma T, Mukherjee R, Ariese F, Somasundaram K, Umapathy S (2016) Raman and infra-red microspectroscopy: Towards quantitative evaluation for clinical research by ratiometric analysis. *Chem. Soc. Rev.* 45:1879–1900
52. Kwan AC, Duff K, Gouras GK, Webb WW (2009) Optical visualization of Alzheimer's pathology via multiphoton-excited intrinsic fluorescence and second harmonic generation. *Opt Express* 17:3679. doi: 10.1364/oe.17.003679
53. Lobanova EG, Lobanov S V., Triantafilou K, Langbein W, Borri P (2018) Quantitative chemical imaging of amyloid- β plaques with Raman micro-spectroscopy in human Alzheimer's diseased brains
54. Lochocki B, Morrema THJ, Ariese F, Hoozemans JJM, De Boer JF (2020) The search for a unique Raman signature of amyloid-beta plaques in human brain tissue from Alzheimer's disease patients. *Analyst* 145:1724–1736. doi: 10.1039/c9an02087j
55. MacGillivray T, McGrory S, Pearson T, Cameron J (2018) Retinal imaging in early Alzheimer's disease. In: *Neuromethods*. Humana Press Inc., pp 199–212
56. Manifold B, Thomas E, Francis AT, Hill AH, Fu D (2019) Denoising of stimulated Raman scattering microscopy images via deep learning. *Biomed Opt Express* 10:3860. doi: 10.1364/boe.10.003860
57. Mecocci P, Paolacci L, Boccardi V (2018) Biomarkers of dementia: from bench to clinical side. *Geriatr Care* 4. doi: 10.4081/gc.2018.7718
58. Meinhardt-Wollweber M, Suhr C, Kniggendorf AK, Roth B (2018) Absorption and resonance Raman characteristics of β -carotene in water-ethanol mixtures, emulsion and hydrogel. *AIP Adv* 8:1126. doi: 10.1063/1.5025788
59. Michael R, Otto C, Lenferink A, Gelpi E, Montenegro GA, Rosandić J, Tresserra F, Barraquer RI, Vrensen GFJM (2014) Absence of amyloid-beta in lenses of Alzheimer patients: A confocal Raman microspectroscopic study. *Exp Eye Res* 119:44–53. doi: 10.1016/j.exer.2013.11.016
60. Mirra SS, Heyman A, McKeel D, Sumi SM, Crain BJ, Brownlee LM, Vogel FS, Hughes JP, van Belle G, Berg L, Ball MJ, Bierer LM, Claasen D, Hansen LR, Hart M, Hedreen J, Baltimore B, Hen Derson V, Hyman BT, Joachim C, Mark-Esbery W, Mar Tinez AJ, McKee A, Miller C, Moosy J, Nochlin D, Perl D, Petito C, Rao GR, Schelper RL, Slager U, Terry RD (1991) The Consortium to Establish a Registry for Alzheimer's Disease (CERAD). Part II. Standardization of the neuropathologic assessment of Alzheimer's disease. *Neurology* 41:479–486. doi: 10.1212/wnl.41.4.479
61. Moester MJ, Ariese F, De Boer JF (2015) Optimized signal-to-noise ratio with shot noise limited detection in stimulated raman scattering microscopy. *J Eur Opt Soc* 10:15022. doi: 10.2971/jeos.2015.15022

62. Mohammadzadeh Honarvar N, Saedisomeolia A, Abdolahi M, Shayeganrad A, Taheri Sangsari G, Hassanzadeh Rad B, Muench G (2017) Molecular Anti-inflammatory Mechanisms of Retinoids and Carotenoids in Alzheimer's Disease: a Review of Current Evidence. *J. Mol. Neurosci.* 61:289–304
63. Montine TJ, Phelps CH, Beach TG, Bigio EH, Cairns NJ, Dickson DW, Duyckaerts C, Frosch MP, Masliah E, Mirra SS, Nelson PT, Schneider JA, Thal DR, Trojanowski JQ, Vinters H V., Hyman BT (2012) National Institute on Aging–Alzheimer's Association guidelines for the neuropathologic assessment of Alzheimer's disease: a practical approach. *Acta Neuropathol* 123:1–11. doi: 10.1007/s00401-011-0910-3
64. Mordechai S, Shufan E, Porat Katz BS, Salman A (2017) Early diagnosis of Alzheimer's disease using infrared spectroscopy of isolated blood samples followed by multivariate analyses. *Analyst* 142:1276–1284. doi: 10.1039/c6an01580h
65. Moreno-García A, Kun A, Calero O, Medina M, Calero M (2018) An overview of the role of lipofuscin in age-related neurodegeneration. *Front. Neurosci.* 12
66. Nabers A, Hafermann H, Wiltfang J, Gerwert K (2019) A β and tau structure-based biomarkers for a blood- and CSF-based two-step recruitment strategy to identify patients with dementia due to Alzheimer's disease. *Alzheimer's Dement Diagnosis, Assess Dis Monit* 11:257–263. doi: 10.1016/j.dadm.2019.01.008
67. Nabers A, Perna L, Lange J, Mons U, Schartner J, Güldenhaupt J, Saum K, Janelidze S, Holleccek B, Rujescu D, Hansson O, Gerwert K, Brenner H (2018) Amyloid blood biomarker detects Alzheimer's disease. *EMBO Mol Med* 10. doi: 10.15252/emmm.201708763
68. Nolan JM, Loskutova E, Howard AN, Moran R, Mulcahy R, Stack J, Bolger M, Dennison J, Akuffo KO, Owens N, Thurnham DI, Beatty S (2014) Macular pigment, visual function, and macular disease among subjects with alzheimer's disease: An exploratory study. *J Alzheimer's Dis* 42:1191–1202. doi: 10.3233/JAD-140507
69. de Oliveira VE, Castro H V., Edwards HGM, de Oliveira LFC (2010) Carotenes and carotenoids in natural biological samples: A Raman spectroscopic analysis. *J Raman Spectrosc* 41:642–650. doi: 10.1002/jrs.2493
70. Palombo F, Tamagnini F, Jeynes JCG, Mattana S, Swift I, Nallala J, Hancock J, Brown JT, Randall AD, Stone N (2018) Detection of A β plaque-associated astrogliosis in Alzheimer's disease brain by spectroscopic imaging and immunohistochemistry. *Analyst* 143:850–857. doi: 10.1039/c7an01747b
71. Pansieri J, Jossierand V, Lee SJ, Rongier A, Imbert D, Sallanon MM, Kövari E, Dane TG, Vendrely C, Chaix-Pluchery O, Guidetti M, Vollaie J, Fertin A, Usson Y, Rannou P, Coll JL, Marquette C, Forge V (2019) Ultraviolet-visible-near-infrared optical properties of amyloid fibrils shed light on amyloidogenesis. *Nat Photonics* 13:473–479. doi: 10.1038/s41566-019-0422-6
72. Paraskevaidi M, Morais CLM, Halliwell DE, Mann DMA, Allsop D, Martin-Hirsch PL, Martin FL (2018) Raman Spectroscopy to Diagnose Alzheimer's Disease and Dementia with Lewy Bodies in Blood. *ACS Chem Neurosci* 9:2786–2794. doi: 10.1021/acscchemneuro.8b00198

73. Riba M, Augé E, Campo-Sabariz J, Moral-Anter D, Molina-Porcel L, Ximelis T, Ferrer R, Martín-Venegas R, Pelegrí C, Vilaplana J (2019) Corpora amylacea act as containers that remove waste products from the brain. *Proc Natl Acad Sci U S A* 116:26038–26048. doi: 10.1073/pnas.1913741116
74. Röhr D, Boon BDC, Schuler M, Kremer K, Hoozemans JJM, Bouwman FH, El-Mashtoly SF, Nabers A, Großerueschkamp F, Rozemuller AJM, Gerwert K (2020) Label-free vibrational imaging of different A β plaque types in Alzheimer's disease reveals sequential events in plaque development. *Acta Neuropathol Commun* 8:1–13. doi: 10.1186/s40478-020-01091-5
75. Roy ER, Wang B, Wan YW, Chiu G, Cole A, Yin Z, Propson NE, Xu Y, Jankowsky JL, Liu Z, Lee VMY, Trojanowski JQ, Ginsberg SD, Butovsky O, Zheng H, Cao W (2020) Type I interferon response drives neuroinflammation and synapse loss in Alzheimer disease. *J Clin Invest* 130:1912–1930. doi: 10.1172/JCI133737
76. Rozemuller JM, Eikelenboom P, Stam FC (1986) Role of microglia in plaque formation in senile dementia of the Alzheimer type - An immunohistochemical study. *Virchows Arch B Cell Pathol Incl Mol Pathol* 51:247–254. doi: 10.1007/BF02899034
77. Ryzhikova E, Kazakov O, Halamkova L, Celmins D, Malone P, Molho E, Zimmerman EA, Lednev IK (2015) Raman spectroscopy of blood serum for Alzheimer's disease diagnostics: Specificity relative to other types of dementia. *J Biophotonics* 8:584–596. doi: 10.1002/jbio.201400060
78. Schweikhard V, Baral A, Krishnamachari V, Hay W, Fuhrmann M (2019) Label-free characterization of Amyloid- β -plaques and associated lipids in brain tissues using stimulated Raman scattering microscopy. *bioRxiv* 789248. doi: 10.1101/789248
79. Selkoe DJ (1991) The Molecular Pathology of Alzheimer's Disease. *Neuron* 6:487–498. doi: 10.1016/0896-6273(91)90052-2
80. Synytsya A, Judexova M, Hoskovec D, Miskovicova M, Petruzalka L (2014) Raman spectroscopy at different excitation wavelengths (1064, 785 and 532 nm) as a tool for diagnosis of colon cancer. *J Raman Spectrosc* 45:903–911. doi: 10.1002/jrs.4581
81. Takasaki J, Ono K, Yoshiike Y, Hirohata M, Ikeda T, Morinaga A, Takashima A, Yamada M (2011) Vitamin A has anti-oligomerization effects on amyloid- β in vitro. *J Alzheimer's Dis* 27:271–280. doi: 10.3233/JAD-2011-110455
82. Tapiero H, Townsend DM, Tew KD (2004) The role of carotenoids in the prevention of human pathologies. *Biomed Pharmacother* 58:100–110. doi: 10.1016/j.biopha.2003.12.006
83. Thal DR, Ghebremedhin E, Haass C, Schultz C (2002) UV light-induced autofluorescence of full-length A β -protein deposits in the human brain. *Clin Neuropathol* 21:35–40
84. Thal DR, Rüb U, Orantes M, Braak H (2002) Phases of A β -deposition in the human brain and its relevance for the development of AD. *Neurology* 58:1791–1800
85. Thal DR, Rüb U, Schultz C, Sassin I, Ghebremedhin E, Del Tredici K, Braak E, Braak H (2000) Sequence of A β -protein deposition in the human medial temporal lobe. *J Neuropathol Exp Neurol* 59:733–748. doi: 10.1093/jnen/59.8.733

86. Thériault P, Rivest S (2016) Microglia: Senescence Impairs Clearance of Myelin Debris. *Curr. Biol.* 26:R772–R775
87. Troein C (2020) Open Chemometrics Toolkit for Analysis and Visualization of Vibrational Spectroscopy data (ocatvvs)
88. Troein C, Siregar S, Op De Beeck M, Peterson C, Tunlid A, Persson P (2020) Octavvs: A graphical toolbox for high-throughput preprocessing and analysis of vibrational spectroscopy imaging data. *Methods Protoc* 3:1–15. doi: 10.3390/mps3020034
89. Wei L, Min W (2018) Electronic Preresonance Stimulated Raman Scattering Microscopy. *J. Phys. Chem. Lett.* 9:4294–4301
90. WHO (2017) Global action plan on the public health response to dementia 2017 - 2025. https://www.who.int/mental_health/neurology/dementia/action_plan_2017_2025/en/
91. Wong WT (2013) Microglial aging in the healthy CNS: Phenotypes, drivers, and rejuvenation. *Front. Cell. Neurosci.* 7
92. Yeung ES, Heiling M, Small GJ (1975) Pre-resonance Raman intensities. *Spectrochim Acta Part A Mol Spectrosc* 31:1921–1931. doi: 10.1016/0584-8539(75)80248-0
93. Yung M, Klufas MA, Sarraf D (2016) Clinical applications of fundus autofluorescence in retinal disease. *Int. J. Retin. Vitre.* 2
94. Zada L, Leslie HA, Vethaak AD, Tinnevelt GH, Jansen JJ, de Boer JF, Ariese F (2018) Fast microplastics identification with stimulated Raman scattering microscopy. *J Raman Spectrosc* 49:1136–1144. doi: 10.1002/jrs.5367
95. Zhou Y, Liu C-H, Wu B, Yu X, Cheng G, Zhu K, Wang K, Zhang C, Zhao M, Zong R, Zhang L, Shi L, Alfano RR (2019) Optical biopsy identification and grading of gliomas using label-free visible resonance Raman spectroscopy. *J Biomed Opt* 24:1. doi: 10.1117/1.jbo.24.9.095001
96. Zipfel WR, Williams RM, Christiet R, Nikitin AY, Hyman BT, Webb WW (2003) Live tissue intrinsic emission microscopy using multiphoton-excited native fluorescence and second harmonic generation. *Proc Natl Acad Sci U S A* 100:7075–7080. doi: 10.1073/pnas.0832308100

SUPPLEMENTARY DATA

Table ST1. Overview of imaging modalities applied to each plaque/control

| Plaque/control | #1a | #1b | #2 | #3a | #3b | #3c | #4a | #4b | #4c | #5 | #c1a | #c1b | #c1c | #c2a | #c2b |
|---------------------------|-----|-----|----|-----|-----|-----|-----|-----|-----|----|------|------|------|------|------|
| Auto-fluorescence | ● | ● | ● | ● | ● | ● | ● | ● | ● | ● | ● | ● | ● | ● | ● |
| Pre-Resonance Raman | ● | ● | ● | ● | ● | ● | ● | ● | ● | ● | ● | ● | ● | ● | ● |
| SRS | ● | ● | ● | ● | ● | ○ | ● | ● | ○ | ● | ● | ○ | ● | ● | ● |
| Thioflavin-S fluorescence | ● | ● | ● | ● | ● | ● | ● | ● | ● | ● | ● | ● | ● | ● | ● |

Plaque # refers to AD donor # + plaque reference letter derived from Table 1. All AD and control sections were imaged using auto-fluorescence, pre-resonance Raman and subsequent fluorescence imaging after thioflavin-S staining. All cases were imaged using SRS, except AD cases #3c and #4c, and control case c#1b. AD Alzheimer's disease; SRS Stimulated Raman scattering; ● available; ○ not available.

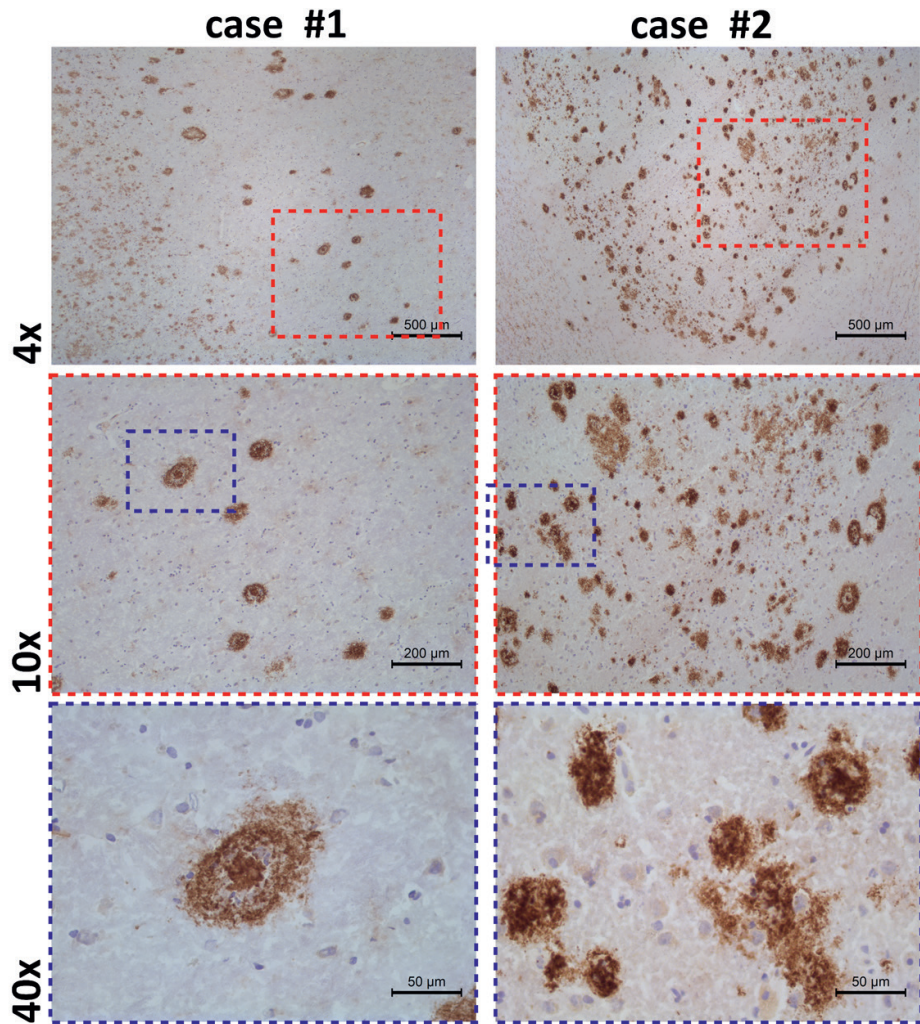


Fig. S1. A β immunostainings

A β immunostainings (clone IC-16) of nearby sections of case #1 and #2 (Table 1). Pictures were taken with a $\times 4$ objective (**top row**), $\times 10$ objective (**middle row**), and $\times 40$ objective (**bottom row**). The sections are not directly adjacent to the sections presented in the manuscript but are shown here as a visual impression of the number and type of amyloid-b plaques present in the tissue. Case #1 shows a clear presence of classic cored plaques whereas case #2 has mainly fibrillary amyloid-beta deposits. Similar images were obtained for the other AD cases (not shown). A β amyloid-beta; AD Alzheimer's disease.

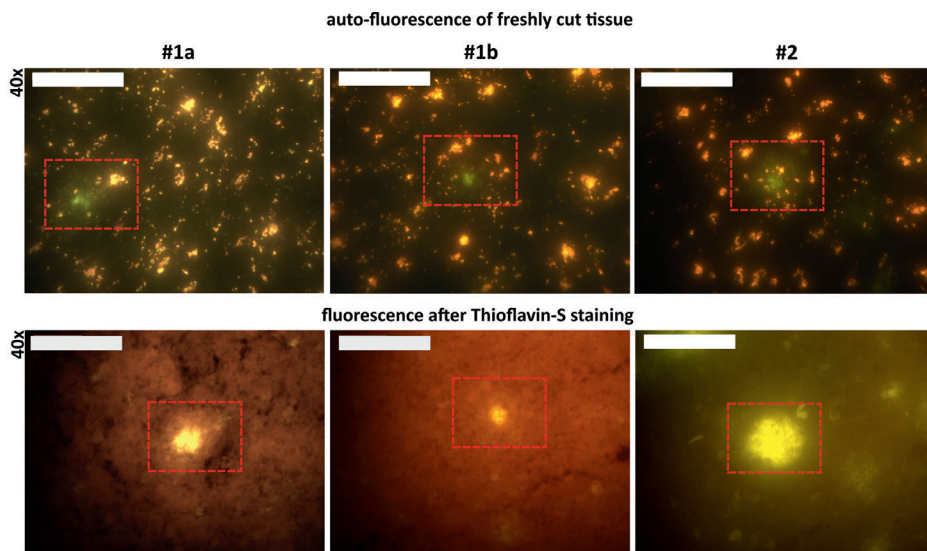


Fig. S2. Additional examples of fluorescence images before and after staining
Top row: Auto-fluorescence images of unstained tissue. Red boxes highlight areas with greenish auto-fluorescence (see also Figure 2 in manuscript). **Bottom row:** The same tissue after thioflavin-S staining, confirming that areas which appeared green were indeed amyloid plaques. All images taken with a $\times 40$ objective using the same microscope and a 470 nm illumination source. Scale bars 100 μm .

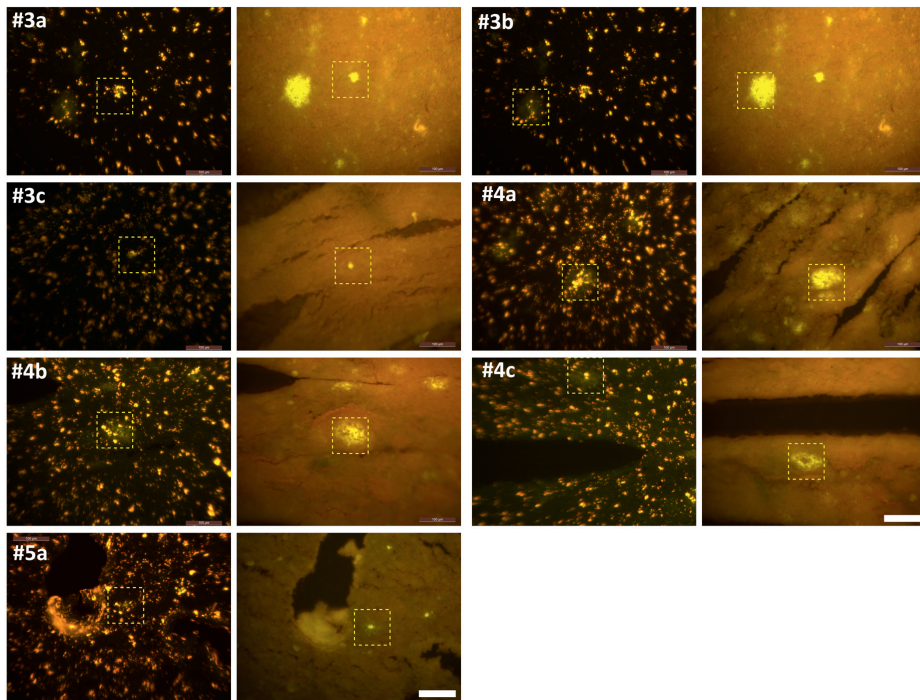


Fig. S3. Fluorescence images of AD cases #3 to #5 before and after staining. Yellow dashed boxes mark roughly the same area (just for viewing purpose). Detailed areas can be seen in Fig.3. Plaque # is AD donor # + plaque reference letter derived from Table 1. Scale bars: 100 μ m. AD Alzheimer's disease.

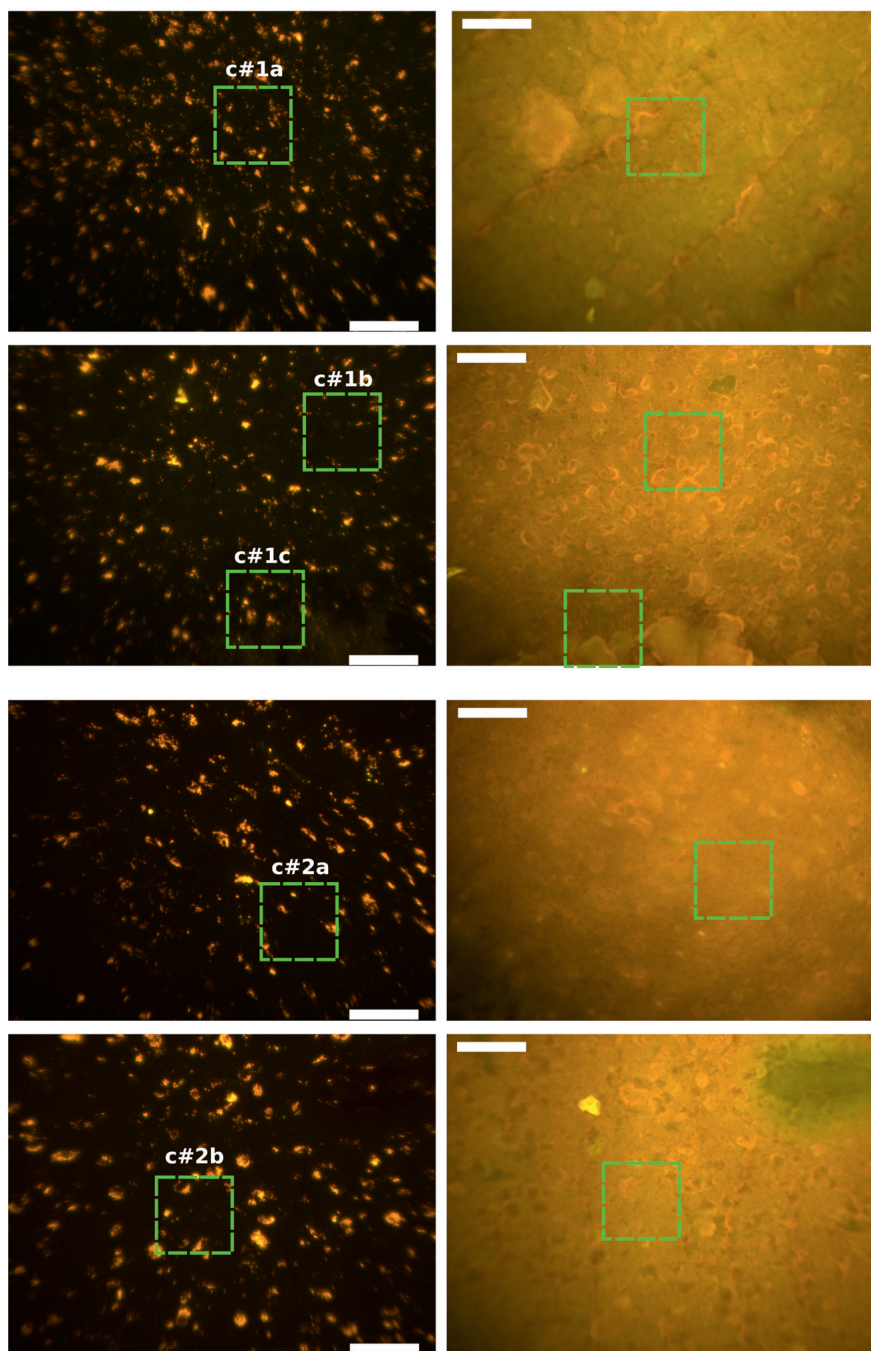


Fig. S4. Fluorescence images of control cases
Fluorescence images of all control cases before and after staining, showing the absence of green emission in the unstained slices (**left panels**). The green dashed boxed mark the area

where all the image modalities were performed. Please note that lipofuscin is also found in the control tissue and therefore supports the claim that lipofuscin deposits are not a hallmark to identify Alzheimer's disease. Plaque # is AD donor # + plaque reference letter derived from Table 1. Scale bars: 100 μm .

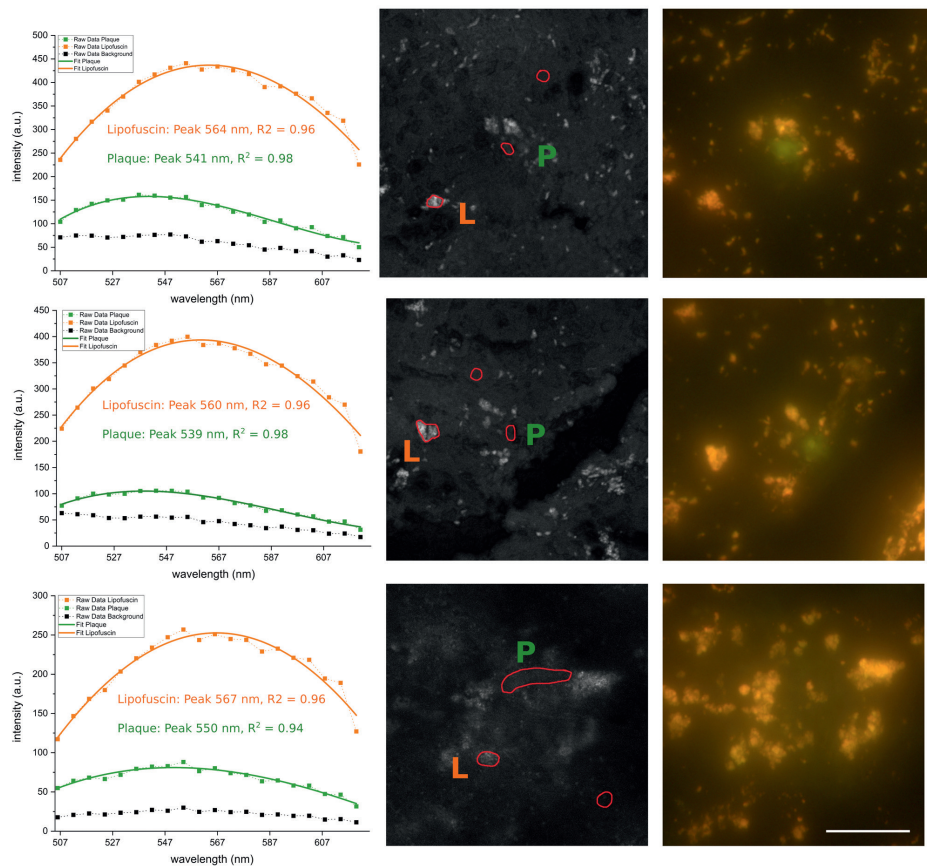


Fig.S5. Fluorescence emission spectra of plaques

Fluorescence emission spectra are shown of two dense core amyloid deposits (**top and middle row**, adjacent slice of case #3) and one fibrillar amyloid deposit (bottom row, adjacent slice of case #4) when excited with 488 nm. Symbols connected with a dashed line are the measured data. The solid lines are the corresponding 3rd order polynomial fits; peak position and R^2 values are indicated. The **right half** shows the corresponding z-projection of the emission images and the locations where the data points for plaque (P), lipofuscin (L), and background were taken, with the corresponding full-field auto-fluorescence images next to it. Corresponding thioflavin-S images are not shown. Scale bar: 40 μm .

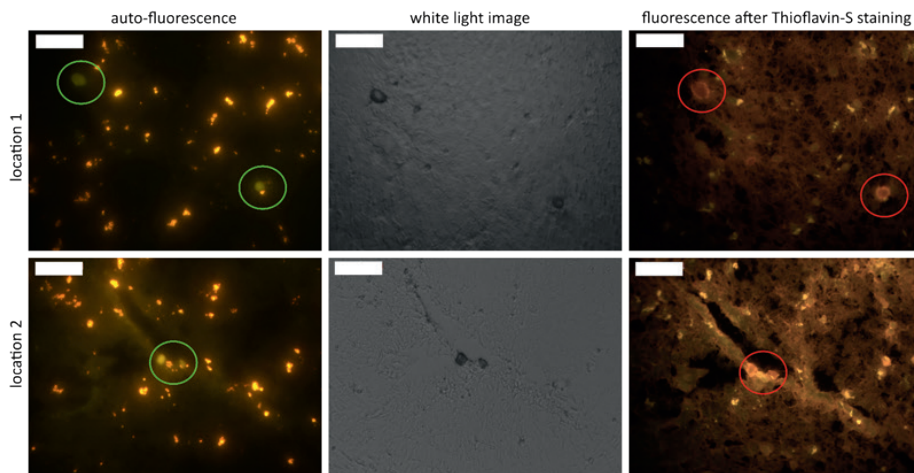


Fig. S6. Greenish auto-fluorescence examples

Example of two locations within the same tissue section (adjacent slice of #1a) with similar greenish auto-fluorescence (**left column**). Compared to plaques they are homogenously filled and geometrically shaped and similar to corpora amylacea. **Middle column**: white light images; **right column**: after staining with thioflavin-S, these spots do not show bright yellow emission. Scale bar: 50 μm .

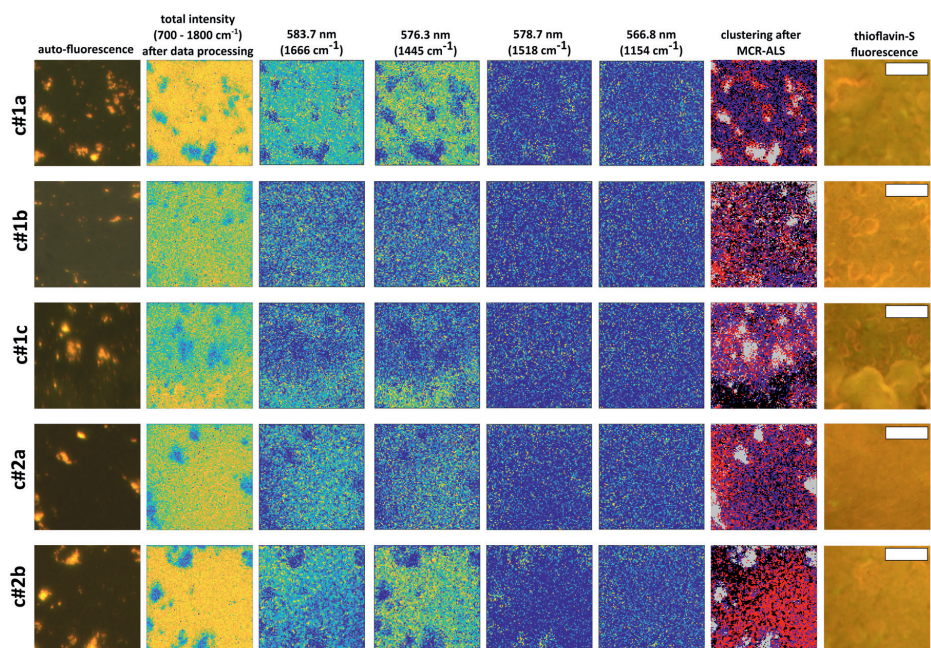


Fig. S7. Overview of fluorescence and Raman images of the control cases ($101 \times 101 \mu\text{m}$) Each row represents one tissue section. **1st column:** auto-fluorescence images. **2nd column:** the total intensity image of the spectral Raman data after data pre-processing. **3rd and 4th column:** Raman peak intensity images of the protein (1666 cm^{-1}) and lipid (1445 cm^{-1}) bands. **5th and 6th column:** Raman peak intensity images at two prominent carotenoid wavenumbers (1518 cm^{-1} and 1154 cm^{-1}). **7th column:** 4-cluster images of the Raman data after MCR-ALS computing, highlighting lipofuscin spots in gray. **8th column:** fluorescence image of the thioflavin-S-stained tissue, confirming the absence of plaque in these tissues. Plaque # is AD donor # + plaque reference letter derived from Table 1. Scale bars: $40 \mu\text{m}$. MCR-ALS Multivariate curve resolution alternating least square.

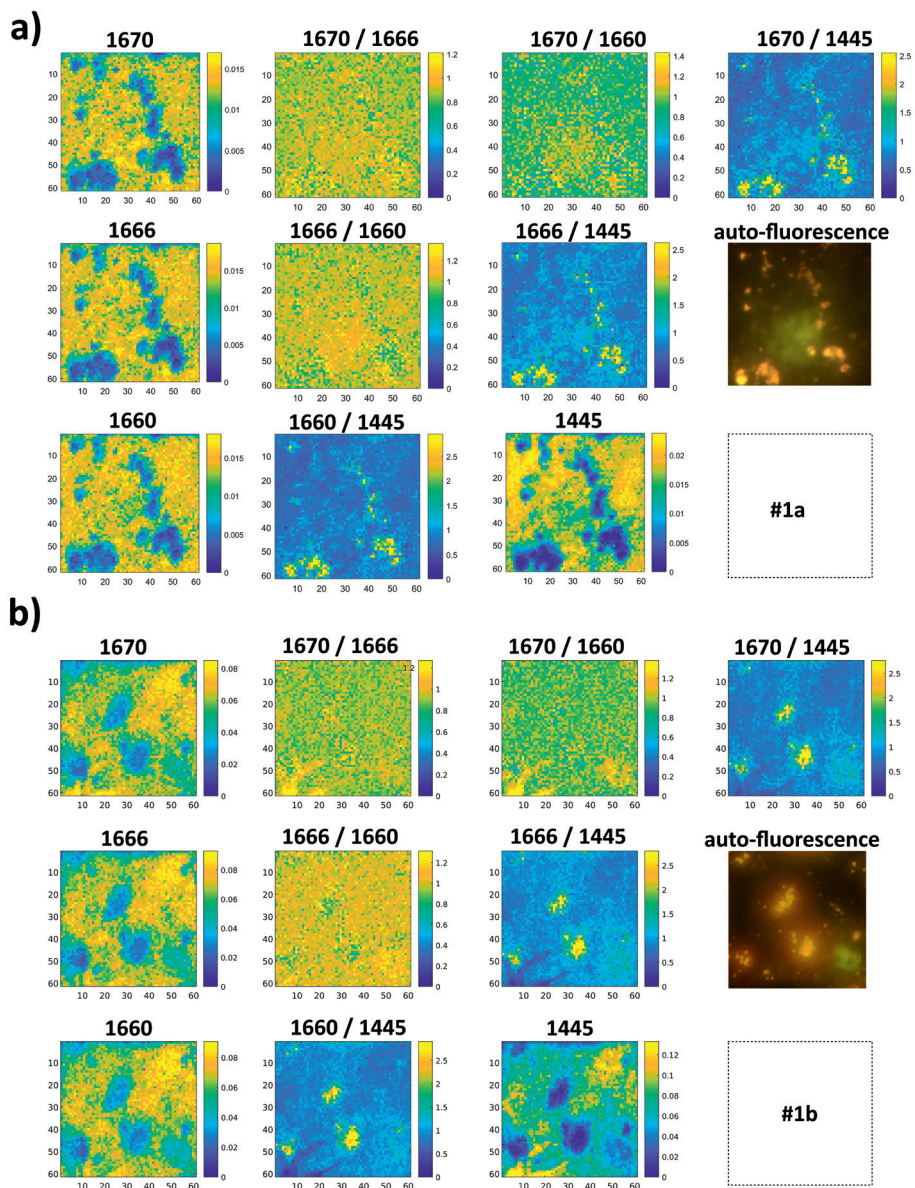


Fig. S8. Raman peak intensity ratio images of plaques a) #1a and b) #1b

Images computed after smoothing, baseline removal and normalization (as described in the data processing paragraph). For the other AD cases we observe similar images but these are not shown here. Plaque # is AD donor # + plaque reference letter derived from Table 1. AD Alzheimer's disease.

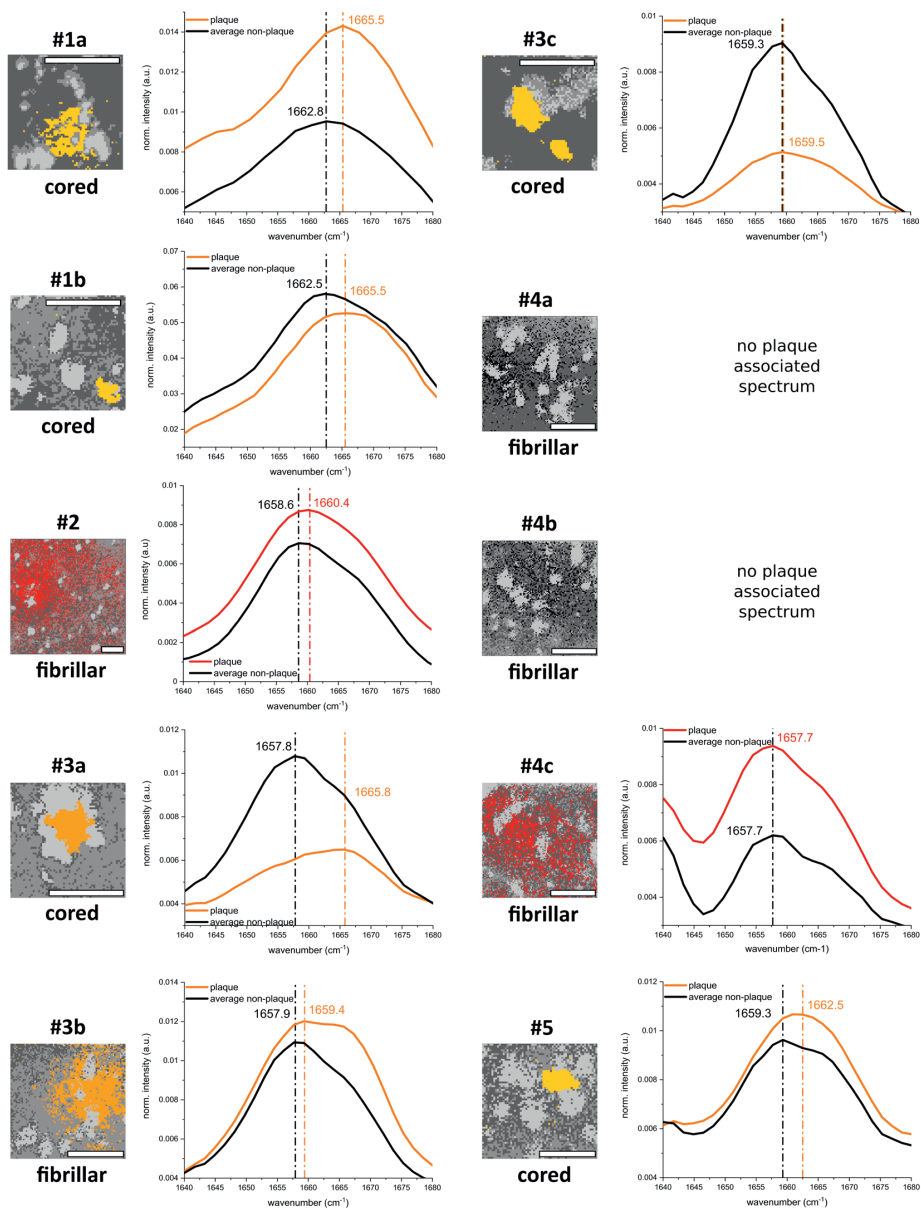


Fig. S9. Spontaneous Raman amide-I band

Spontaneous Raman amide-I band comparison of each plaque spectrum (orange/red line) to the averaged non-plaque spectrum (black line) based on the spectra obtained after the MCR-ALS cluster analysis. The cored plaque cases and fibrillar plaque #3b exhibit in general a small shift towards higher wavenumbers. For the fibrillar plaques #2 and #4c the results are not clear but the results should be interpreted carefully since the plaque associated spectrum hardly matches the area which was later stained positive with thioflavin-S. Plaques #4a and

#4b do not show an associated spectrum after the data processing steps (see also Fig. 6). Plaque # is AD donor # + plaque reference letter derived from Table 1. Scale bars: 40 μm . AD Alzheimer's disease; MCR-ALS Multivariate curve resolution alternating least square.

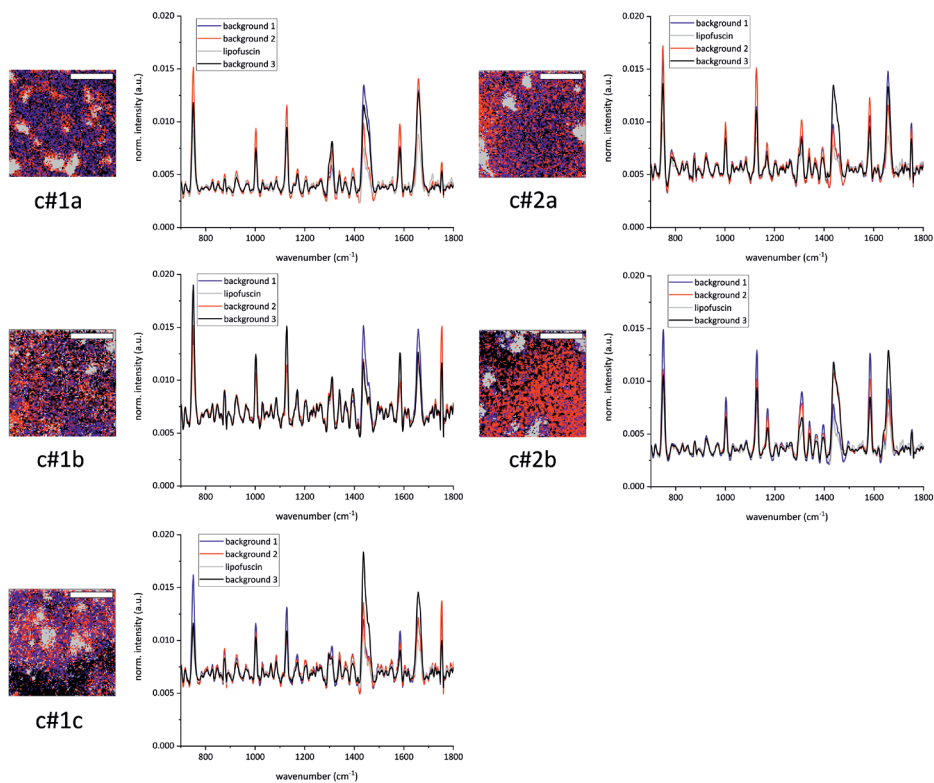


Fig. S10. 4-cluster images of all control cases and their corresponding spectra processed as described for Fig. 6. There are intensity variations in each spectrum but no additional peaks are observed. Plaque # is AD donor # + plaque reference letter derived from Table 1. Scale bar: 40 μm . AD Alzheimer's disease.

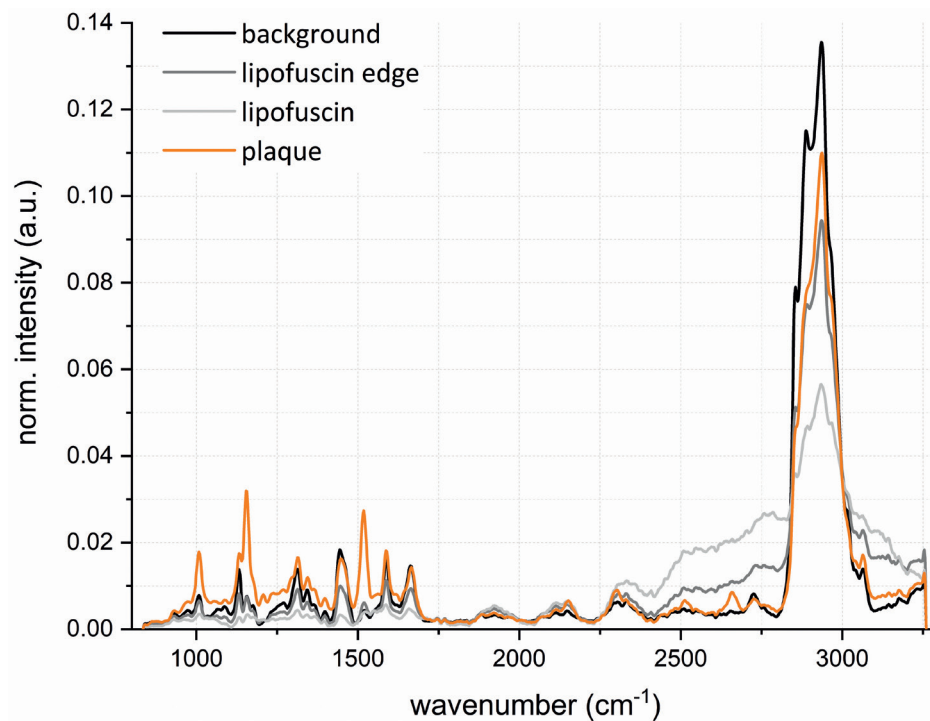


Fig. S11. Full recorded Raman spectral range of #1a

Full recorded Raman spectral range of #1a (as partially shown in Fig. 6). In the CH-stretch range we observe, apart from the intensity changes, fewer spectral differences than in the fingerprint range.

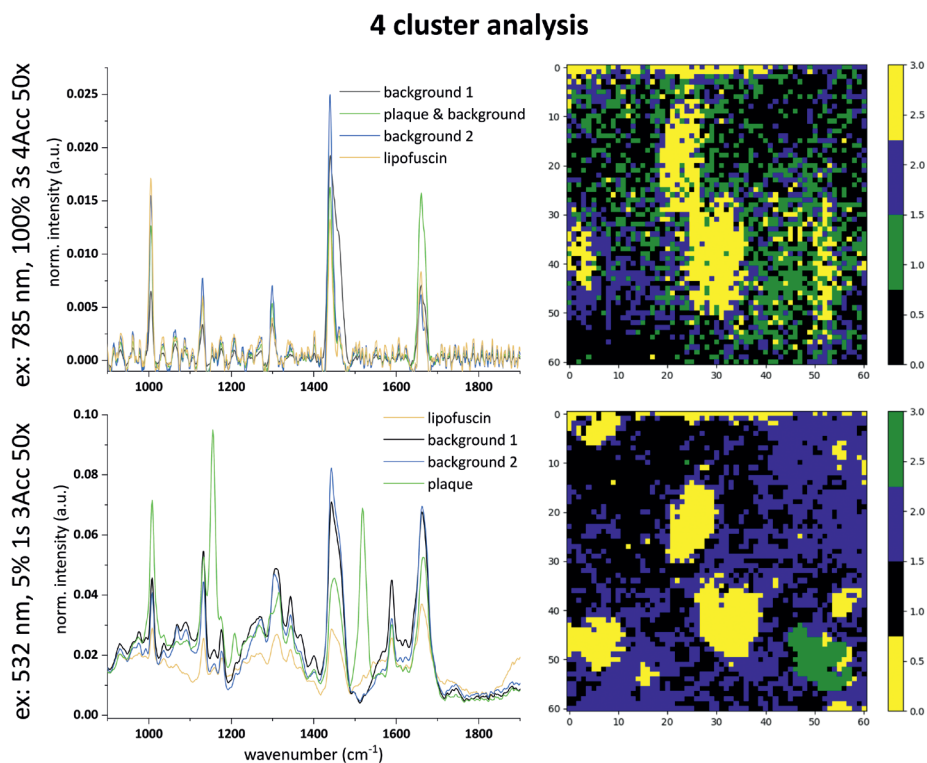


Fig. S12. 4-cluster analysis

The **left column** depicts the comparison of the Raman spectra, recorded at the same core plaque location (case #1b, see also Figs. 5 and 6) using 785 nm (top) and 532 nm (bottom) as Raman excitation source. The **right column** depicts the corresponding 4-cluster images after the raw data were processed in the same manner. The carotenoid associated peaks (around 1150 cm^{-1} and 1520 cm^{-1}) are very prominent in the spectra of the plaque areas with 532-nm excitation (green curve), but are not visible in the spectra obtained with the 785 nm source. Please note that the overall mapping time for the 785 nm source was three times longer. Size of the images is $61 \times 61 \mu\text{m}$. ex excitation.

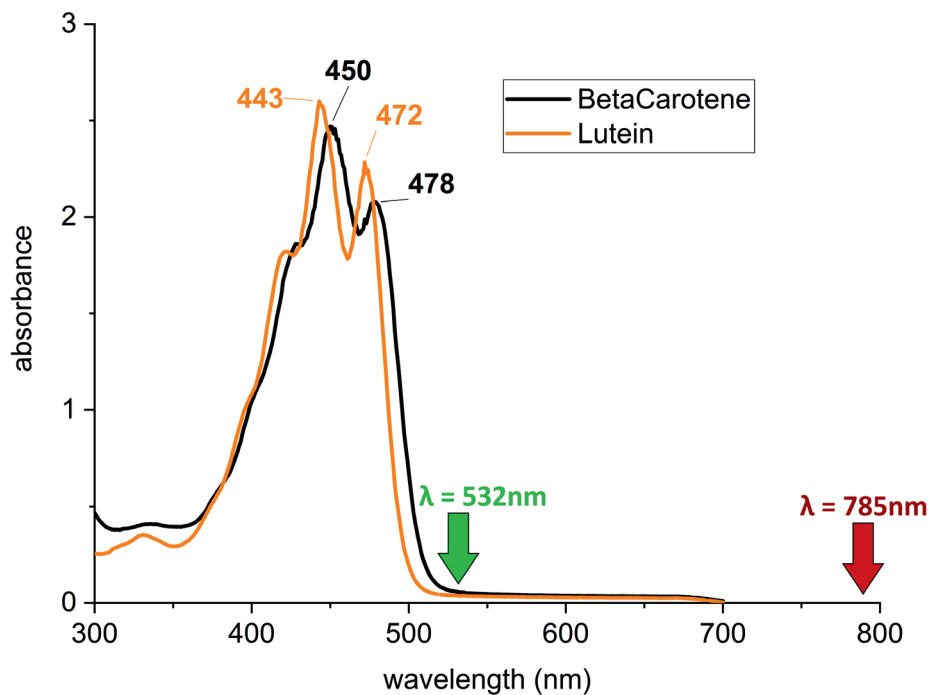


Fig. S13. Absorption spectrum

Absorption spectrum of beta-carotene dissolved in hexane, concentration = 1.76×10^{-5} M and lutein, concentration = 1.63×10^{-5} M. The arrows illustrate the proximity of the green Raman laser to the absorption band (offering pre-resonance enhancement) as opposed to the NIR laser. (Cary 50 single-beam spectrometer; 1 nm spectral bandwidth; 10-mm quartz cuvette; hexane reference).

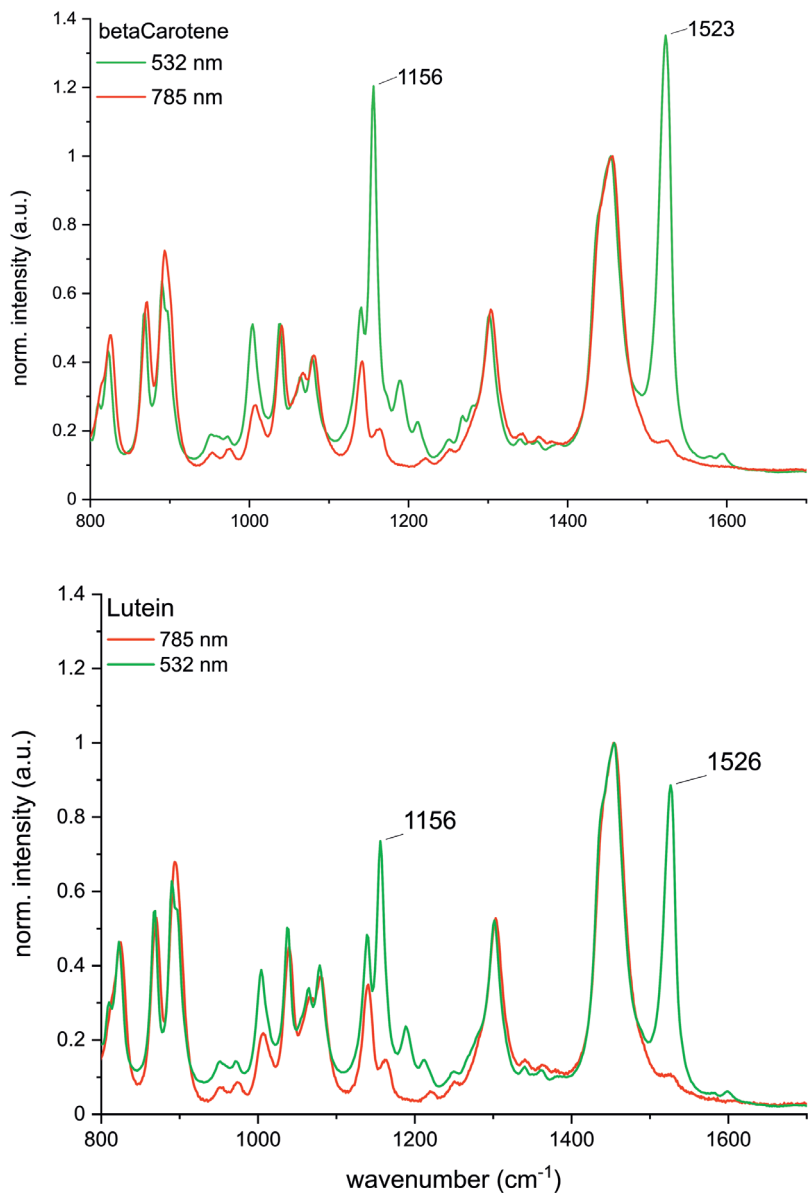


Fig. S14. Illustration of the pre-resonance enhancement Raman spectra of beta-carotene (top) and lutein (bottom) recorded with a 532 nm (green line) and 785 nm (red line) excitation source; concentration_{betaCarotene} = 1.76×10^{-5} M and concentration_{Lutein} = 1.63×10^{-5} M in hexane. The spectra were normalized to the solvent peak at 1455 cm^{-1} , measured in pure hexane (using both excitation sources) and subsequently a baseline has been removed. A pre-resonance enhancement factor of 38 for beta-carotene and of 30 for lutein was determined from the relative intensities of the $1523/6 \text{ cm}^{-1}$ peak.

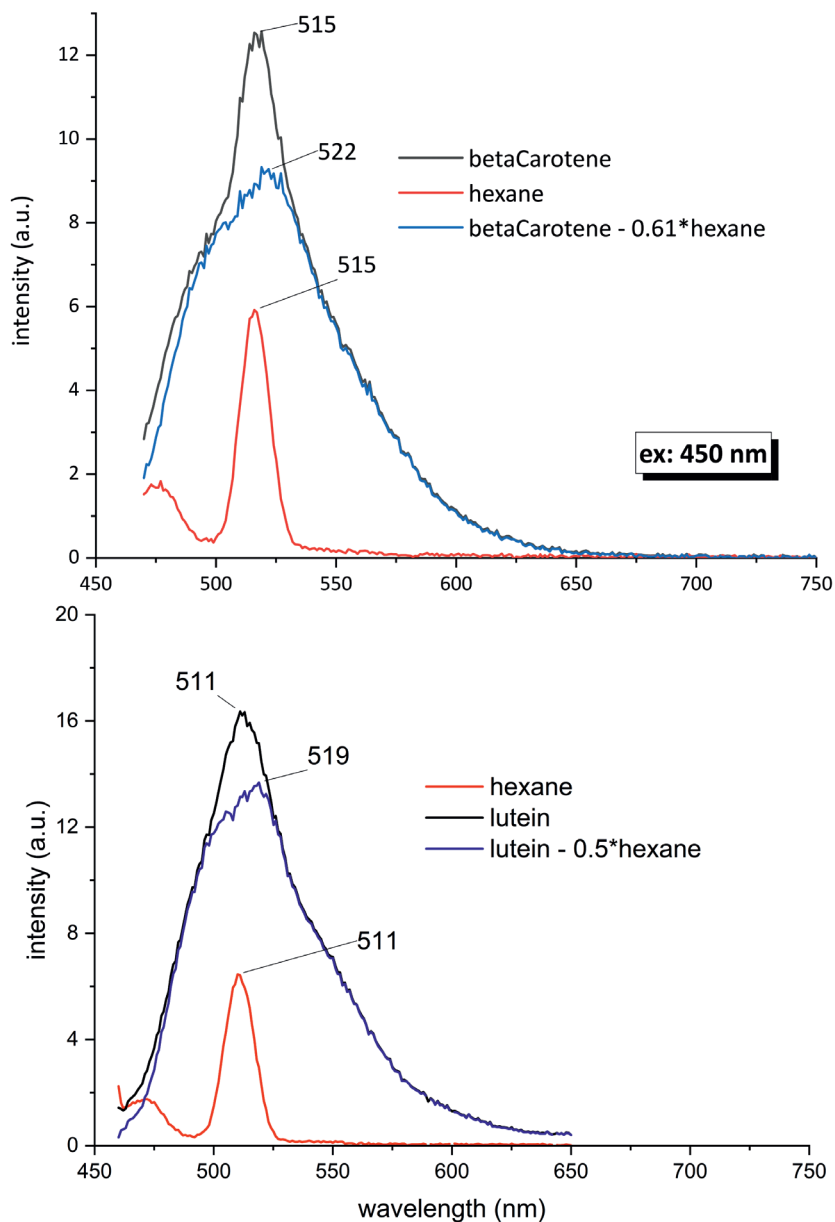


Fig. S15. Fluorescence spectra of beta-carotene (top) and lutein (bottom) dissolved in hexane (black line) and of pure hexane (red line) using 450 nm excitation. The blue line shows the pure carotenoid emission spectrum after scaled subtraction of the hexane Raman background. The concentration was 6.2×10^{-6} M for beta-carotene and 6.9×10^{-6} M for lutein. (Cary Eclipse spectrofluorimeter; 10-mm quartz cuvette; exc/em slit widths 10/10 nm). Ex excitation.

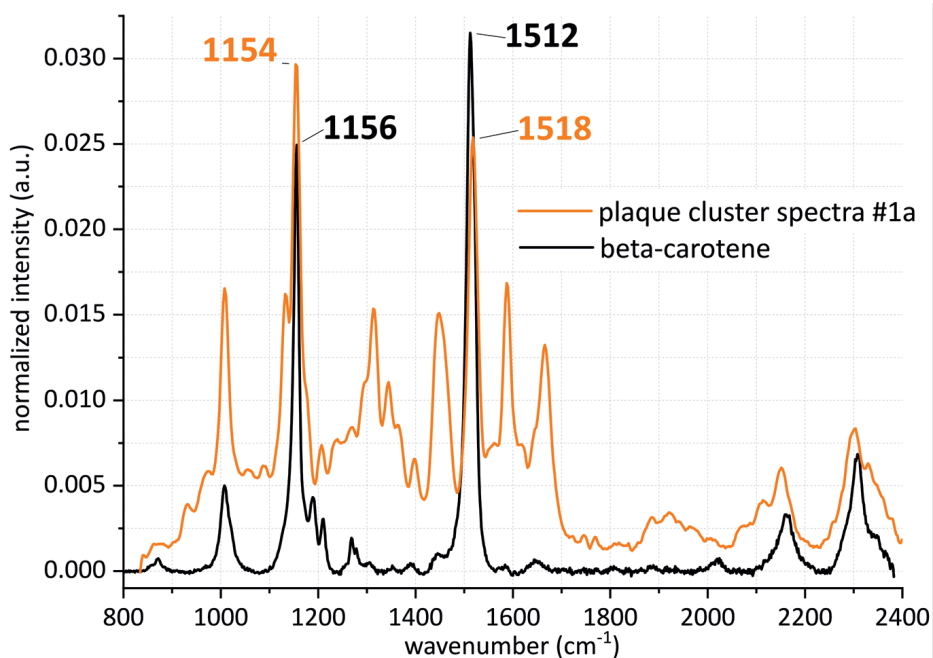


Fig. S16. Raman spectral comparison of beta-carotene

Raman spectral comparison of beta-carotene (6.2×10^{-5} M in hexane) with the cluster spectra of plaque #1a, showing a nearly perfect match of the carotenoid peaks with the obtained spectral plaque peaks (around 1007 cm^{-1} , 1150 cm^{-1} and 1520 cm^{-1}). The other peaks in the plaque spectrum also occur in non-plaque areas (see Fig. 6) and correspond to proteins, lipids, and other common tissue components.

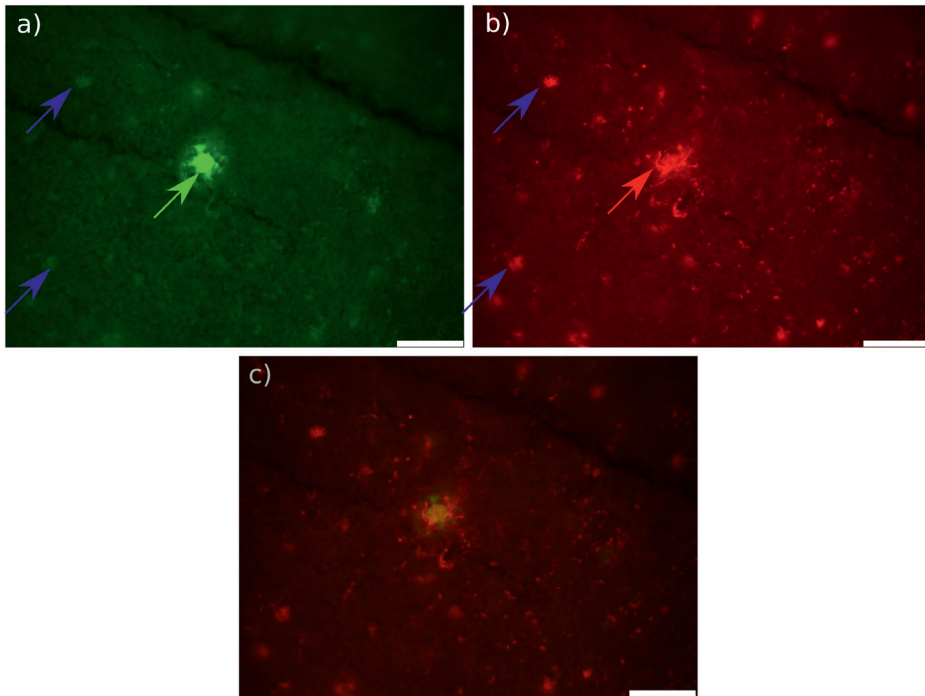


Fig. S17. Double staining detection of microglia activity

Fluorescence images of an adjacent section of sample #3c. Image a) shows the thioflavin-S positive cored amyloid plaque (green arrow; ex: 480 nm, em: > 512 nm). Image b) shows the tissue stained for microglia (Iba1) activity (red arrow; ex: 560 nm, em: > 593 nm). The blue arrows indicate locations, which are most likely lipofuscin auto-fluorescence. Image c) shows an overlay of images a) and b), highlighting microglia activity next to the cored amyloid deposit. Scale bar: 50 μm .

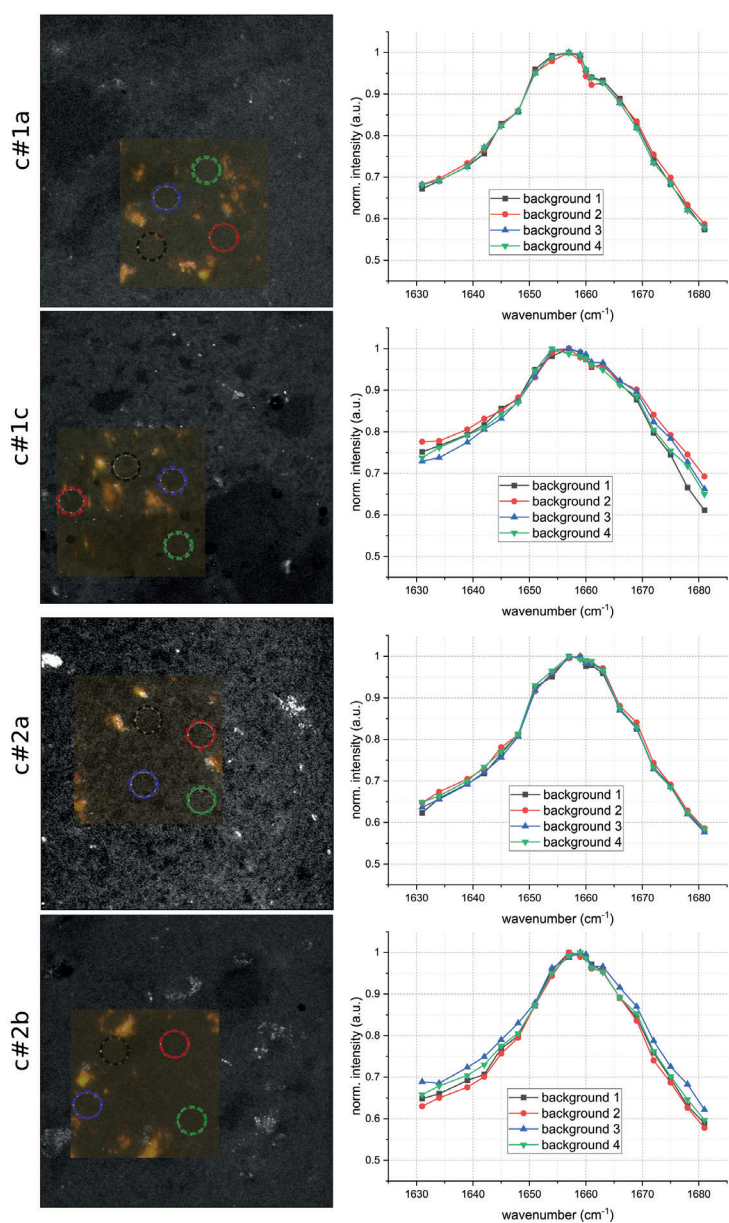


Fig. S18. SRS imaging across the protein peak for control cases (no SRS was recorded for c#1b). Random locations were picked (colored circles) and their protein sweep is shown on the right half. As expected, no protein shift was observed. Image size: $204 \times 204 \mu\text{m}$. SRS stimulated Raman scattering.

Section 4

Translating pathology to the memory
clinic via imaging

Chapter 7

Amyloid- β PET and CSF in an autopsy confirmed cohort

Juhan Reimand, Baayla DC Boon, Lyduine E Collij, Charlotte E Teunissen, Annemieke JM Rozemuller, Bart NM van Berckel, Philip Scheltens, Rik Ossenkoppele, Femke Bouwman

Annals of Clinical and Translational Neurology (2020)
doi: 10.1002/acn3.51195

ABSTRACT

Objective: Accumulation of amyloid- β is among the earliest changes in Alzheimer's disease (AD). Amyloid- β positron emission tomography (PET) and $A\beta_{42}$ in cerebrospinal fluid (CSF) both assess amyloid- β pathology in vivo, but 10-20% of cases show discordant (CSF+/PET- or CSF-/PET+) results. The neuropathological correspondence with amyloid- β CSF/PET discordance is unknown.

Methods: We included 21 patients from our tertiary memory clinic who had undergone both CSF $A\beta_{42}$ analysis and amyloid- β PET, and had neuropathological data available. Amyloid- β PET and CSF results were compared with neuropathological ABC scores (comprising of Thal (A), Braak (B) and CERAD (C) stage, all ranging from 0 [low] to 3 [high]) and neuropathological diagnosis.

Results: Neuropathological diagnosis was AD in 11 (52%) patients. Amyloid- β PET was positive in all A3, C2 and C3 cases and in one of the two A2 cases. CSF $A\beta_{42}$ was positive in 92% of \geq A2 and 90% of \geq C2 cases. PET and CSF were discordant in 3/21 (14%) cases: CSF+/PET- in a patient with granulomatosis with polyangiitis (A0B0C0), CSF+/PET- in a patient with FTLN-TDP type B (A2B1C1), and CSF-/PET+ in a patient with AD (A3B3C3). Two CSF+/PET+ cases had a non-AD neuropathological diagnosis, i.e., FTLN-TDP type E (A3B1C1) and adult-onset leukoencephalopathy with axonal spheroids (A1B1C0).

Interpretation: Our study demonstrates neuropathological underpinnings of amyloid- β CSF/PET discordance. Furthermore, amyloid- β biomarker positivity on both PET and CSF did not invariably result in an AD diagnosis at autopsy, illustrating the importance of considering relevant co-morbidities when evaluating amyloid- β biomarker results.

INTRODUCTION

Among the earliest neuropathological events in Alzheimer's disease (AD) is the accumulation and aggregation of amyloid- β , which occurs decades before symptom onset [3]. Amyloid- β can aggregate in the brain parenchyma as plaques or in the cerebral vasculature as cerebral amyloid angiopathy (CAA). Two methods are currently employed to assess amyloid- β pathology in vivo. A β_{42} levels in the cerebrospinal fluid (CSF) reflect the concentrations of soluble amyloid- β , which has been shown to correlate with amyloid- β deposits in the brain [40]. Alternatively, positron emission tomography (PET) with amyloid- β radiotracers can be used to visualize cerebral amyloid- β deposits [7, 16, 35]. These two methods are considered interchangeable for the assessment of amyloid pathology in vivo and for the diagnosis of AD in both clinical practice and research [17, 25].

In the majority of cases, amyloid- β PET and CSF are concordant, but 10-20% of patients show discordant (CSF+/PET- or CSF-/PET+) results [10, 48]. One possible hypothesis for the amyloid- β CSF/PET discordance is that soluble CSF A β_{42} decreases before significant fibrillar amyloid- β deposits can be detected by PET [32, 46]. Although studies have been performed to compare either amyloid- β PET or CSF A β_{42} to neuropathological examination results [7, 16, 35, 40], so far, no head-to-head cohort studies have been performed to compare in vivo amyloid- β CSF and PET results to neuropathological findings. Previously, two case reports of patients with discordant amyloid- β CSF/PET (both CSF+/PET-) and available neuropathology have been published, [4, 38] in which the negative PET signal was attributed to the lack of neuritic plaques at autopsy. Further investigating the correspondence between amyloid- β PET, CSF and neuropathology ('standard of truth') is important to shed light on the underlying cause of amyloid- β CSF/PET discordance. Also, if CSF+/PET- amyloid- β status is an indicator of early amyloid- β pathology, this could be instrumental for future disease modifying therapies [14]. Therefore, the aim of this study was to investigate the concordance between PET and CSF amyloid- β status in a sample with available neuropathological results and to characterize the amyloid- β CSF/PET discordant cases neuropathologically.

METHODS

Participants

We retrospectively included 21 autopsy cases from the Amsterdam Dementia Cohort who had undergone both CSF $A\beta_{42}$ analysis and amyloid- β PET during life. Patients visiting our tertiary memory center are screened according to a standardized protocol [11], including a clinical and neuropsychological evaluation, *APOE* genotyping, magnetic resonance imaging (MRI), and a lumbar puncture (LP) for CSF biomarker analysis. Clinical diagnosis is determined during a multidisciplinary meeting.

Amyloid- β PET and CSF analyses were performed between 2007 and 2016 and neuropathological diagnosis was performed between 2011 and 2019 (Fig. 1). In this sample, LP for CSF analysis always preceded amyloid- β PET and, the median CSF-PET time was 28 [interquartile range (IQR): 18, 56] days. The median time difference between amyloid- β PET and patient death was 3.0 (IQR: 1.7, 6.5) years and the time difference between LP and patient death was 3.3 (IQR: 2.0, 6.7) years.

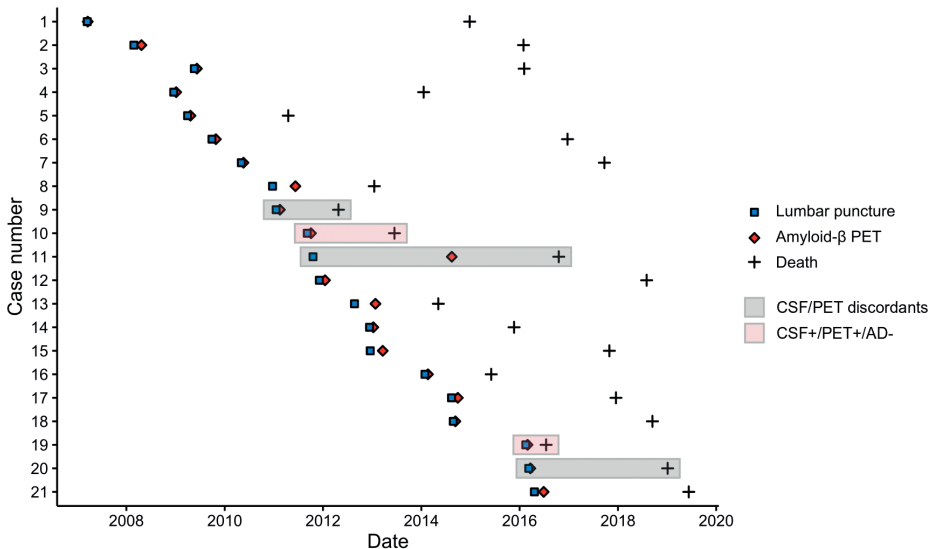


Fig. 1. Time between lumbar puncture, amyloid- β PET and patient death
AD Alzheimer’s disease; CSF cerebrospinal fluid; PET positron emission tomography.

Cerebrospinal fluid

CSF was obtained during life by LP between L3/4 and L5/S1, using a 25-gauge needle and a syringe [9]. Samples were collected in polypropylene collection tubes and centrifuged at 1800 g for 10 min at 4 °C and thereafter frozen at -20 °C until routine biomarker analysis. Manual analyses of A β_{42} , total tau (t-tau) and phosphorylated tau (p-tau) were performed using sandwich ELISAs (Innotest assays: β -amyloid1-42, tTAU-Ag and PhosphoTAU-181p; Fujirebio) in the Neurochemistry Laboratory of the Department of Clinical Chemistry of Amsterdam UMC. If two CSF results were available, we used the result closest to the amyloid- β PET (three cases, all with concordant A β_{42} status between two samples). As median CSF A β_{42} values of our cohort have been gradually increasing over the years, we were unable to use the original CSF A β_{42} values [36]. Therefore, we used CSF A β_{42} values that have been adjusted for the longitudinal upward drift with a uniform cut-off of 813 pg/ml (< 813 pg/mL considered as CSF amyloid- β positive) [43]. Additionally, as it has been previously shown that the ratio of CSF A β_{42} with CSF (p-)tau is superior to CSF A β_{42} in predicting the diagnosis of AD [8], we also used a CSF p-tau/A β_{42} ratio with a previously validated cut-off of 0.054 [49]. This cut-off was obtained by mixture modelling of 2711 CSF results of the Amsterdam Dementia Cohort, similar to previous work [43].

Amyloid- β positron emission tomography

Amyloid- β PET was performed using the following PET scanners: ECAT EXACT HR+ scanner (Siemens Healthcare, Germany), Gemini TF PET/CT, Ingenuity TF PET-CT and Ingenuity PET/MRI (Philips Medical Systems, the Netherlands). We included fifteen cases with [¹¹C]Pittsburgh Compound-B (PiB) [31], three with [¹⁸F]florbetaben [47], and three with [¹⁸F]flutemetamol [51]. Amyloid- β PET status (positive or negative) was determined by a majority visual read of three reads. All scans were initially read by an expert nuclear medicine physician (BvB, from 2007 to 2016, read 1). In addition, in 2019 the scans were reread for this study by BvB (read 2) and LC (with extensive experience in reading amyloid- β PET scans, read 3), while being blinded to the results of other visual reads, CSF, and neuropathological results. The three amyloid- β PET visual reads were concordant (either +/+/+ or -/-/-) in 18/21 cases. In the three remaining cases (#5, #10, #19), two of the three visual reads were positive, and as such these cases were considered PET-positive.

Neuropathology

Autopsies were performed by the Department of Pathology of Amsterdam UMC; location VUmc for the Netherlands Brain Bank (NBB, Amsterdam, the Netherlands, <https://www.brainbank.nl>) or for VUmc. Brain donors or their next of kin signed informed consent regarding the usage of brain tissue and clinical records for research purposes. Brain autopsies and neuropathological diagnosis were performed according to international guidelines of Brain Net Europe II consortium (<http://www.brainnet-europe.org>) and the applicable diagnostic criteria [23, 27]. For this particular study, every case also without suspicion of AD pathology during life, was scored by AR and BB for AD neuropathological changes according to the ABC scoring system by AR and BB [27], in which the A stands for amyloid- β Thal phase [42], B for Braak stage for neurofibrillary tangles [3], and C for CERAD criteria for neuritic plaques [26]. When present, CAA was classified as Type 1 (including capillaries in the parenchyma) or Type 2 (leptomeningeal/cortical without capillary involvement) and staged according to Thal et al. [41].

Statistical analysis

Statistical analysis was conducted using R software (Version 3.6.1). We used descriptive statistics to characterize the sample. We used the Cochran-Armitage trend test to examine the associations between amyloid- β biomarkers and the neuropathological ABC scores [1], which allowed us to compare both PET and CSF to neuropathology as we had only binarized results available for amyloid- β PET.

RESULTS

Study population

In our sample of 21 cases, 16 (76%) were male and 10 (48%) were carriers of an *APOE* ϵ 4 allele (Table 1). Mean age at death was 65 ± 8 years and the average last known Mini-Mental State Examination (MMSE, median 2.0 years before death) was 20 ± 6 . Eleven (52%) patients had a clinical diagnosis of AD, which was in accordance with neuropathological diagnosis in all AD cases. Two cases (#4 and #15, both CSF/PET concordant) carried an autosomal dominant mutation associated with AD. In 15 (71%) cases, CAA (11 CAA-Type 1, 4 CAA-Type 2) was observed at neuropathological examination.

In vivo amyloid- β status

Thirteen (62%) cases were defined as amyloid- β positive based on PET, 14 (67%) based on CSF A β_{42} and 11 (52%) based on CSF p-tau/A β_{42} ratio. In our sample, CSF A β_{42} and amyloid- β PET were concordant in 18 (86%) cases. CSF p-tau/A β_{42} ratio was concordant with amyloid- β PET in 17 (81%) cases and with CSF A β_{42} in 16 (76%) cases.

Discordance between amyloid- β PET, CSF and neuropathological diagnosis

Of the three cases discordant for CSF A β_{42} and amyloid- β PET, two were CSF+/PET- (case #9, clinical diagnosis: frontotemporal dementia [neuropathological diagnosis: frontotemporal lobar degeneration (FTLD)-TDP type B, ABC score: A2B1C1] and case #20 with vasculitis [granulomatosis with polyangiitis, A0B0C0], and one was CSF-/PET+ (case #11 with AD [AD, A3B3C3], Fig. 2A-C). The three amyloid- β CSF/PET discordant patients all had an *APOE* $\epsilon 3/\epsilon 3$ genotype. In addition, there were two CSF+/PET+ cases with a non-AD primary neuropathological diagnosis, i.e., case #10 with semantic dementia [FTLD-TDP type E, A3B1C1; CAA-Type 1 stage 2]; and case #20 with adult-onset leukoencephalopathy with axonal spheroids (HDLS) [leukodystrophy due to HDLS, A1B1C0; CAA-Type 1 stage 1] (Fig. 2D-E).

Association between biomarkers and ABC scores

CSF A β_{42} (Fig. 3A) was positive in 12/13 (92%) and CSF p-tau/A β_{42} ratio (Fig. 3B) in 10/13 (77%) of the A2/A3 cases. Both CSF A β_{42} and p-tau/A β_{42} ratio were positive in 10/11 (91%) B2/B3 cases and 9/10 (90%) C2/C3 cases. Amyloid- β PET (Fig. 3C) was positive in one of the two A2 cases, and in all A3 and/or B2/B3 and/or C2/C3 cases. Cochran trend analyses showed that there is an increasing proportion of biomarker-positive cases from score 0 to 3 across all ABC scores for amyloid- β PET (Z -score = -3.93 for A, Z = -3.81 for B, Z = -3.68 for C, all p < 0.001) and CSF A β_{42} (Z = -2.92, p = 0.003 for A; Z = -2.46, p = 0.014 for B; Z = -2.60, p = 0.009 for C). In *APOE* $\epsilon 4$ carriers, both CSF A β_{42} and amyloid- β PET were positive in all A2/A3 and/or B2/B3 and/or C2/C3 cases. In *APOE* $\epsilon 4$ non-carriers, CSF A β_{42} was positive in 80% of A2/A3, 75% of B2/B3 and 75% of C2/C3 cases, and amyloid- β PET was positive in 80% A2/A3 cases and all B2/B3 and/or C2/C3 cases.

Table 1. Case characteristics

| Nr | Sex | Age at † | APOE genotype | Clinical diagnosis | CSF A β ₄₂ | CSF Amyloid- β PET | CSF/PET status | Neuropathology | | CAA-Type |
|------|-----|----------|---------------|----------------------|-----------------------------|--------------------------|----------------|----------------|-------------------------|----------|
| | | | | | | | | ABC | Primary diagnosis | |
| 1 | m | 75 | E4E4 | AD | 810 | positive | CSF+/PET+ | A3B3C3 | AD | 2 |
| 2 | m | 65 | E3E3 | AD | 640 | positive | CSF+/PET+ | A3B3C3 | AD | 2 |
| 3 | m | 65 | E3E3 | CBS | 940 | negative | CSF-/PET- | A0B1C0 | FTLD-TDP type A | - |
| 4 | f | 43 | E3E3 | AD | 554 | positive | CSF+/PET+ | A3B3C3 | AD | 1 |
| 5 | f | 64 | E4E4 | AD | 619 | positive | CSF+/PET+ | A2B2C2 | AD | 1 |
| 6 | m | 69 | E3E4 | AD | 504 | positive | CSF+/PET+ | A3B3C3 | AD | 1 |
| 7 | m | 76 | E3E4 | FTD | 1110 | negative | CSF-/PET- | A1B0C0 | FTLD-TDP type A | - |
| 8 | m | 60 | - | Dementia unspecified | 1136 | negative | CSF-/PET- | A0B0C0 | Autoimmune encephalitis | - |
| * 9 | m | 75 | E3E3 | FTD | 787 | negative | CSF+/PET- | A2B1C1 | FTLD-TDP type B | - |
| ^ 10 | m | 64 | E4E4 | SD | 739 | positive | CSF+/PET+ | A3B1C1 | FTLD-TDP type E | 1 |
| * 11 | m | 68 | E3E3 | AD | 828 | positive | CSF-/PET+ | A3B3C3 | AD | 2 |
| 12 | m | 68 | E3E3 | Dementia unspecified | 1167 | negative | CSF-/PET- | A0B1C0 | LBD | - |
| 13 | m | 65 | E2E3 | FTD | 1708 | negative | CSF-/PET- | A1B1C0 | FTLD/MND TDP type B | 1 |
| 14 | m | 70 | E3E4 | AD | 755 | positive | CSF+/PET+ | A3B3C3 | AD | 2 |
| 15 | f | 62 | E4E4 | AD | 681 | positive | CSF+/PET+ | A3B3C3 | AD | 1 |
| 16 | f | 61 | E3E4 | FTD | 862 | negative | CSF-/PET- | A1B0C0 | FTLD-TDP type E | 1 |
| 17 | m | 73 | E3E4 | AD | 644 | positive | CSF+/PET+ | A3B2C1 | AD | 1 |
| 18 | m | 53 | E3E3 | AD | 587 | positive | CSF+/PET+ | A3B3C3 | AD | 1 |

Table 1. Continued.

| Nr | Sex | Age at † | APOE genotype | Clinical diagnosis | CSF Aβ ₄₂ | Amyloid-β PET | CSF/PET status | ABC | Neuropathology | |
|----|-----|----------|---------------|--------------------|----------------------|---------------|----------------|--------|----------------------------------|----------|
| | | | | | | | | | Primary diagnosis | CAA-Type |
| 19 | m | 50 | E3E3 | HDLS | 676 | positive | CSF+/PET+ | A1B1C0 | Leukodystrophy due to HDLS | 1 |
| 20 | f | 65 | E3E3 | Vasculitis | 646 | negative | CSF+/PET- | A0B0C0 | Granulomatosis with polyangiitis | - |
| 21 | m | 65 | E3E4 | AD | 397 | positive | CSF+/PET+ | A3B3C3 | AD | 1 |

* in the first column highlight CSF/PET discordant cases and ^ highlight CSF+/PET+ cases with a non-AD neuropathological diagnosis. Values under 813 pg/mL for CSF Aβ₄₂ indicate amyloid-β pathology. Amyloid-β PET positivity was determined by majority visual read. Neuropathological ABC scoring system entails amyloid-β Thal (A) phase, Braak (B) stage for neurofibrillary tangles and CERAD (C) criteria for neuritic plaques. CAA column indicates the neuropathological type of cerebral amyloid angiopathy: Type 1 (capillary) or Type 2 (leptomeningeal/cortical). AD Alzheimer's disease; CAA cerebral amyloid angiopathy; CBS corticobasal syndrome; CSF cerebrospinal fluid; FTD frontotemporal dementia; FTLD frontotemporal lobar degeneration; HDLS Adult-onset leukoencephalopathy with axonal spheroids; LBD Lewy body dementia; MND motoneuron disease; PET positron emission tomography; SD semantic dementia.

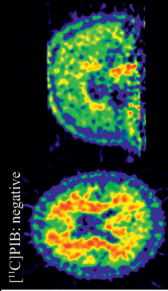
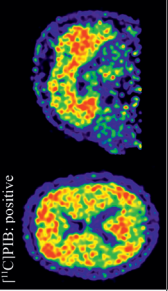
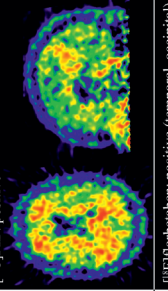
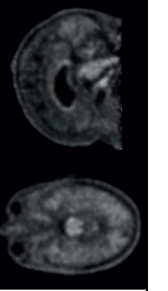
| | Clinical findings | CSF | Amyloid- β PET | Neuropathology | Explanations for discordance |
|---------------------|--|--|--|---|---|
| A case 9 | 74 y/o man was referred for compulsive and anti-social character change. MMSE was 24/30. On MRI, left hippocampal atrophy (MTA 2), and extensive white matter damage (Fazlkas III) with two possible small lacunes were seen. Amyloid- β PET was performed for research and was negative. The patient was diagnosed with possible bvFTD. | $A\beta_{42}$: 787 t-tau: 279 p-tau: 41 | ¹¹ C]PIB: negative  | Diagnosis: FTLD-TDP type B ABC score: A2B1C1 Additional findings: N/A | CSF+/PET-/AD- > CSF detected amyloid co-pathology > CSF $A\beta_{42}$ could be false-positive as it is close to the cut-off (individual CSF $A\beta_{42}$ production or pre-analytical factors) |
| B case 11 | 63 y/o man visited our center with memory complaints. MMSE was 30/30. The neuropsychological exam confirmed memory dysfunction. The MRI was normal and the CSF analysis was inconclusive. Amnesic MCI was diagnosed. During follow-up there was a slow decline in memory and executive functioning and after 3 years amyloid- β PET was requested. The PET scan was read positive and the patient was diagnosed with AD. | $A\beta_{42}$: 828 t-tau: 498 p-tau: 66 | ¹¹ C]PIB: positive  | Diagnosis: AD ABC score: A3B3C3 Additional findings: CAA-Type 2 (stage 1) | CSF-/PET+/AD+ > CSF $A\beta_{42}$ is false negative as it is close to the cut-off and CSF tau levels were already increased (individual variation of CSF $A\beta_{42}$ or pre-analytical factors) > The long time difference between CSF analysis and amyloid PET could be an additional contributing factor |
| C case 20 | 62 y/o woman was referred because of apathy and tiredness. MMSE was 30/30. White-matter lesions and a lacune in the right thalamus were found on the MRI. A β PET was performed and was negative. CSF pleocytosis was found and $A\beta_{42}$ was decreased. An autoimmune cause was suspected. Over the next 2 years there was subacute cognitive decline and progression of vascular damage based on MRI. FDG PET showed increased uptake in the thoracic aorta, indicative of vasculitis. | $A\beta_{42}$: 646 t-tau: 251 p-tau: 40 | ¹⁸ F]florbetaben: negative  | Diagnosis: Granulomatosis with polyangiitis ABC score: A0B0C0 Additional findings: $A\beta$ -positive axons in the substantia nigra and in the sub-thalamic nucleus, corresponding to leakage of amyloid precursor protein. | CSF+/PET-/AD- > Decreased CSF $A\beta_{42}$ due to neuroinflammation |
| D case 10 | 53 y/o man was referred because of severe word finding problems and behavioral change. MMSE was 18/30. Family history was positive for early-onset dementia. The CSF analysis was considered normal (prior adjustment for $A\beta_{42}$ longitudinal drift) and MRI showed anterotemporal atrophy (MTA: left 2, right 1). FDG PET showed bilateral frontal and left temporal hypometabolism. A β PET was clinically requested and initially read as negative. Patient was diagnosed with SD. | $A\beta_{42}$: 739 t-tau: 362 p-tau: 38 | ¹¹ C]PIB: positive  | Diagnosis: FTLD-TDP type E ABC score: A3B1C1 Additional findings: CAA-Type 1 (stage 2) | CSF+/PET+/AD- > Detection of amyloid co-pathology by both CSF and PET > Possible detection of CAA |
| E case 19 | 49 y/o man was referred to our memory clinic due to multi-domain (memory, executive functioning, visuospatial, behavioral) cognitive decline over 1-2 years. MMSE was 24/40. Familial history was positive for early-onset dementia. MRI showed extensive parietal atrophy and white matter lesions. Amyloid- β PET was requested for research and was initially read as negative. Genetic analysis found CSF IR mutation and HDLS was diagnosed. | $A\beta_{42}$: 676 t-tau: 528 p-tau: 33 | ¹⁸ F]florbetaben: positive (temporal, occipital)  | Diagnosis: Leukodystrophy due to HDLS ABC score: A1B1C0 Additional findings: CAA-Type 1 (stage 1) | CSF-/PET+/AD- > Detection of CAA by PET and CSF |

Fig. 2. Discordance between amyloid- β CSF, PET and autopsy

Vignettes illustrating amyloid- β CSF/PET discordant cases (A, B, C) and CSF+/PET+ cases with a non-AD neuropathological diagnosis (D, E). CSF values for $A\beta_{42}$ <813 pg/mL, for phosphorylated tau (p-tau) >52 pg/mL, and for total tau (t-tau) >375 pg/mL are pathological (indicated by bold). Amyloid- β PET scans in cases 10 and 19 were initially read as amyloid-negative, but for this study the scans were considered amyloid-positive based on majority visual read. AD Alzheimer's disease; CAA cerebral amyloid angiopathy; CSF cerebrospinal fluid; FDG Fluorodeoxyglucose; FTD frontotemporal dementia; FTLD frontotemporal lobar degeneration; HDLS Adult-onset leukoencephalopathy with axonal spheroids; MCI Mild cognitive impairment; MMSE Mini-Mental State Examination; MRI Magnetic resonance imaging; MTA Medial temporal lobe atrophy; PET positron emission tomography; SD semantic dementia; TDP transactive response DNA binding protein.

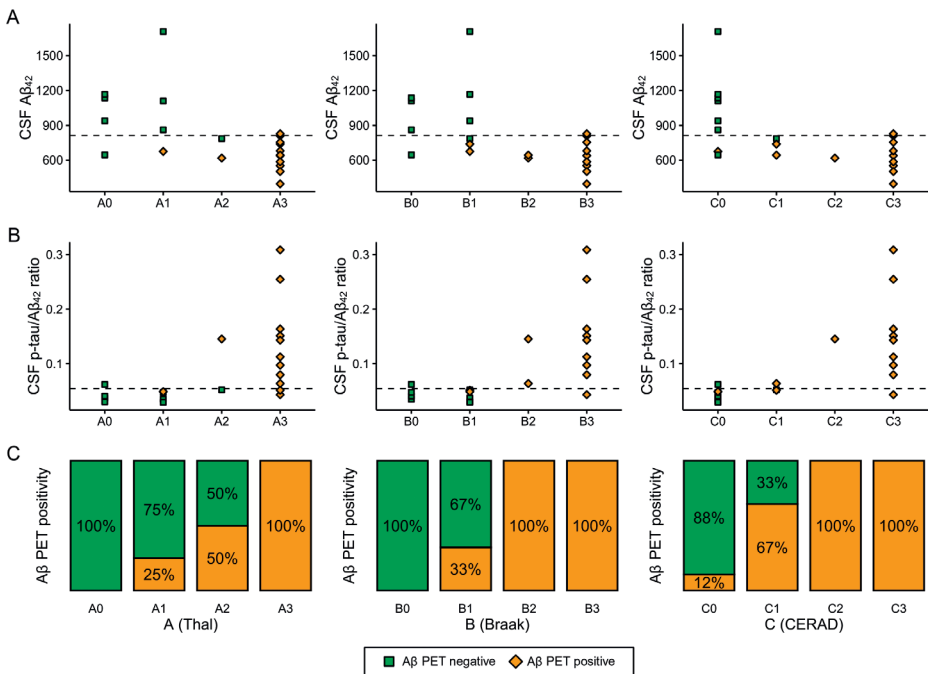


Fig. 3. Correspondence of CSF $A\beta_{42}$ (A), CSF p-tau/ $A\beta_{42}$ ratio (B), and amyloid- β (A β) PET (C) to neuropathological ABC scoring

Neuropathological ABC scoring system entails amyloid- β Thal phase (A0-A3), Braak stage for neurofibrillary tangles (B0-B3), and CERAD criteria for neuritic plaques (C0-C3). Dashed lines represent cut-offs for CSF $A\beta_{42}$ (813 pg/mL) and CSF p-tau/ $A\beta_{42}$ ratio (0.054).

Association between biomarkers and neuropathological diagnosis

Finally, we investigated the association between binarized biomarker results and neuropathological diagnosis. Amyloid- β PET was positive in all AD cases, but also indicated amyloid- β pathology in two cases without AD as

neuropathological diagnosis (Fig. 4). Both CSF $A\beta_{42}$ and p-tau/ $A\beta_{42}$ were positive in 10/11 AD cases. Decreased CSF $A\beta_{42}$ with a normal CSF p-tau/ $A\beta_{42}$ ratio was seen in three non-AD cases (HDLS [A1B1C0], FTLD-TDP type B [A2B1C1], FTLD-TDP type E [A3B1C1]) and one AD case (A3B3C3). There were three cases with a non-AD neuropathological diagnosis (HDLS, FTLD-TDP type E, FTLD/MND-TDP type B) with normal levels of CSF p-tau but with increased CSF t-tau.

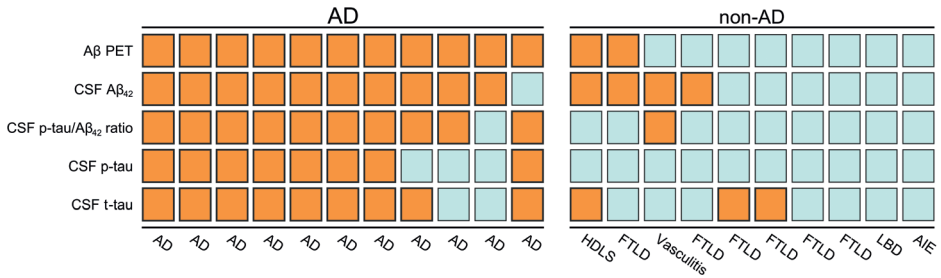


Fig. 4. Biomarker status by primary neuropathological diagnosis
 Colors indicate binarized status of biomarkers: orange for biomarker-positive, blue for biomarker-negative. Aβ Amyloid-β; AD Alzheimer’s disease; AIE autoimmune encephalitis; CSF cerebrospinal fluid; FTLD frontotemporal lobar degeneration; HDLS Adult-onset leukoencephalopathy with axonal spheroids; PET positron emission tomography.

DISCUSSION

The primary aim of this study was to investigate the concordance between PET and CSF amyloid-β status in a sample with available neuropathological results in order to enhance our understanding of the amyloid-β CSF/PET discordant cases. We found that although both CSF and PET generally captured AD pathological change, there was still 14% (3/21) discordance between the two modalities. In our sample, possible reasons for amyloid-β CSF/PET discordance included neuroinflammation (CSF+/PET- in a case of granulomatosis with polyangiitis, A0B0C0), detection of amyloid-β co-pathology (CSF+/PET- in FTLD-TDP type B, A2B1C1) and additional factors influencing CSF $A\beta_{42}$ levels (CSF-/PET+ in AD, A3B3C3). Additionally, we described two CSF+/PET+ non-AD cases illustrating that amyloid-β biomarker positivity on both PET and CSF does not invariably result in an AD diagnosis at autopsy. This highlights that it is important to consider other comorbidities when evaluating the results of amyloid-β biomarkers, especially since molecular biomarkers for non-AD neurodegenerative diseases are currently lacking.

Although in the majority of cases, amyloid- β PET and CSF A β_{42} show concordant results, 10-20% discordant CSF/PET status has repeatedly been shown [10, 33, 48]. As amyloid- β CSF/PET discordance rates are highest in patients with early disease, it has been hypothesized that CSF/PET discordance might be partly explained by early decreases of CSF A β_{42} that precede amyloid- β depositions visible by PET [32, 46]. On the other hand, amyloid- β CSF/PET discordance in patients with dementia could be explained by one modality detecting beginning amyloid- β co-pathology in non-AD cases [48]. To our knowledge, this is the first serial study including patients who have both amyloid- β PET and CSF A β_{42} in addition to neuropathological data available. In line with previous in vivo studies, we found a 14% (3/21) CSF/PET discordance rate. We reported a CSF+/PET- patient with A2B1C1 FTLD-TDP type B, where it is feasible that the reduction of CSF A β_{42} is caused by concomitant amyloid- β pathology. However, as the A β_{42} value was relatively close to the cut-off, it is not possible to entirely exclude individual CSF A β_{42} dynamics (i.e., this patient intrinsically producing less A β_{42}) [12] or pre-analytical factors [13]. Previously, two CSF+/PET- case reports with available neuropathology have been published. First, a negative PiB PET scan was reported in a 91-year-old patient with abnormal CSF A β_{42} and tau biomarkers with sporadic AD [4]. The negative amyloid- β PET status was attributed to the absence of a significant amount of fibrillar plaques (i.e., with a fibrillar core that the tracer binds to), although diffuse plaques were present. Second, low PiB PET retention with decreased CSF A β_{42} was reported in a familial AD case with arctic amyloid precursor protein (*APP*) mutation, thought to be caused by the lack of fibrillar amyloid- β plaques characteristic for this mutation [38]. Future studies with neuropathological data are needed to further validate whether amyloid- β CSF+/PET- status is caused by beginning amyloid- β depositions and explore additional neuropathological substrates for CSF/PET discordance, such as differences in distribution, load and morphology of amyloid- β plaques and possible influences of co-pathologies.

In our sample, there were two cases with amyloid- β CSF+/PET+ biomarker status who did not meet neuropathological criteria for AD. The first had a diagnosis of FTLD-TDP type E with a high Thal score but only sparse neuritic plaques (A3B1C1). It is feasible that in this case both biomarkers detected concomitant amyloid- β co-pathology as increased PiB PET signal has been shown to be related to fibrillar plaque load even in case of sparse neuritic plaques [22, 29]. The patient was also diagnosed with CAA-Type 1 stage 2, which could also contribute to the amyloid-positivity, as CAA has been shown to affect both amyloid- β PET tracer uptake [18] and CSF A β_{42} levels [5]. The second CSF+/

PET+ patient with a low score for AD pathology (A1B1C0) was diagnosed with HDLS, an autosomal dominant white matter disease due to mutations in the gene encoding colony stimulating factor 1 receptor (*CSF1R*) [50]. Previous case reports of HDLS including CSF analyses have provided no evidence for alterations in $A\beta_{42}$ levels [20, 39]. It is also unlikely that pre-analytical assay effects caused the decrease of CSF $A\beta_{42}$ in this case as the patient had a separate CSF $A\beta_{42}$ sample with decreased $A\beta_{42}$ four months earlier. Similar to the previous patient, CAA-Type 1 was present and might have contributed to the positive amyloid- β biomarker status, especially since PET tracer uptake was seen predominantly in the occipital region, a predilection site for CAA pathology [18]. This illustrates that even concordant positivity of two amyloid- β biomarkers does not always result in a neuropathological diagnosis of AD, and relevant co-pathologies should always be considered.

There were four cases where CSF $A\beta_{42}$ was decreased without a neuropathological diagnosis of AD. In three of them there was neuropathological evidence for amyloid- β co-pathology, but we also we described a CSF+/PET- case with granulomatosis with polyangiitis (formerly known as Wegener's granulomatosis), which is in line with literature, as neuroinflammation [28, 44] as well as infection [19, 24] have been previously shown to cause decreased CSF $A\beta_{42}$ without presence of AD pathology. This highlights that in select cases, there might be unspecific decreases in CSF $A\beta_{42}$ levels without AD, although these cases might be distinguished from AD pathology based on clinical findings and MR imaging. In our particular case, after $A\beta$ immunostaining, $A\beta$ immunoreactive axons were seen, which can be attributed to the leakage of APP that is reported in various conditions such as ischemia, traumatic brain injury and - similar to this case - inflammation [15]. The possible connection of this finding with the decrease of CSF $A\beta_{42}$ is unclear, although it is tempting to hypothesize that the loss of APP leads to the interruption of the APP pathway and the reduction of its product $A\beta_{42}$ in the CSF. We were unable to find previous case reports of vasculitis with available CSF $A\beta_{42}$ analysis, but primary angiitis of the central nervous system has been associated with decreased APP in the CSF [34], lending support to that speculative theory.

CSF p-tau/ $A\beta_{42}$ ratio was slightly more specific than CSF $A\beta_{42}$ for capturing the neuropathological diagnosis of AD, which has been previously shown in studies involving living subjects [8]. In the CSF-/PET+ discordant case we presented, the patient with a clinically advanced AD dementia had a CSF $A\beta_{42}$ value just above the cut-off, but CSF p-tau/ $A\beta_{42}$ ratio was in the pathological range. In this

case, CSF $A\beta_{42}$ was likely false-negative, possibly due to individual differences in CSF dynamics, as both CSF t-tau and p-tau were already increased. This also highlights the advantage of using continuous measurements as opposed to binarized data, as the distance from cut-off includes additional information. Although (p-)tau/ $A\beta_{42}$ ratio may be superior to $A\beta_{42}$ when predicting clinically advanced disease with increased (p-)tau levels, this may hamper the detection of merely amyloid- β pathology, where tau tangle pathology has not yet begun. This may become clinically significant if anti-amyloid treatment arrives in the future. Finally, we reported an isolated increase of CSF t-tau with normal CSF p-tau levels in three non-AD cases (two FTLD, one HDLS). Although CSF t-tau and p-tau are highly correlated, this finding supports the notion that CSF t-tau can increase in other brain pathologies [37] and CSF p-tau is more AD-specific [30].

The primary strength of our study is the availability of two amyloid- β biomarkers and a neuropathological assessment in a relatively large patient cohort that allowed us to compare the two in vivo amyloid- β biomarkers to neuropathological change. Although PET and CSF were usually performed close in time, there was a median 3-year delay between the amyloid- β biomarkers and autopsy, as is often the case with studies involving in vivo biomarkers and autopsy data. While this might have impacted our results, a major change over three years is unlikely, given the remarkably slow course of AD [45]. We used standardized uptake value ratio images for PET visual read, which could have an impact on our results as non-displaceable binding potential images have been shown to be more reliable in detecting early amyloid- β pathology [2, 6]. Another limitation is that we included subjects from the year 2006, and over time technologic advancement has taken place, leading to both increased image quality of PET scans and understanding of pre-analytical factors influencing CSF (leading to longitudinal drift of median values, in our cohort). Finally, correcting CSF $A\beta_{42}$ values with CSF $A\beta_{40}$ has been shown to account for the individual variation in the production of amyloid- β [21]. As CSF $A\beta_{40}$ values were only available for seven patients (and none of them were among the discordant cases), we did not include a $A\beta_{42}/_{40}$ ratio in our analyses.

Conclusion

In conclusion, our findings illustrate a range of reasons for the amyloid- β CSF/PET discordance, and that even concordant amyloid- β biomarker positivity accurately reflecting amyloid- β pathology does not always equal a definite neuropathological diagnosis of AD. Thus, it is important to consider comorbidities as well as other neurodegenerative diseases when using amyloid- β

biomarkers for clinical diagnosis, especially since molecular biomarkers for non-AD neurodegenerative diseases are currently lacking.

ACKNOWLEDGMENTS

The institutional review board of the VU University Medical Center approved all studies from which the current data was gathered and retrospectively analyzed. All patients provided written informed consent for their data to be used for research purposes. The Alzheimer Center Amsterdam is supported by Alzheimer Nederland and Stichting VUmc fonds. Research performed at the Alzheimer Center Amsterdam is part of the neurodegeneration research program of Amsterdam Neuroscience. JR would like to thank Sergei Nazarenko, the International Atomic Energy Agency (IAEA) and the North Estonia Medical Centre for their contribution to his professional development.

LIST OF ABBREVIATIONS

| | |
|-------|---|
| AD | Alzheimer's disease |
| APP | amyloid precursor protein |
| CAA | cerebral amyloid angiopathy |
| CBS | corticobasal syndrome |
| CSF | cerebrospinal fluid |
| CSF1R | colony stimulating factor 1 receptor |
| FTD | frontotemporal dementia; |
| FTLD | frontotemporal lobar degeneration; |
| HDLS | adult-onset leukoencephalopathy with axonal spheroids |
| MRI | magnetic resonance imaging |
| LBD | Lewy body dementia |
| LP | lumbar puncture |
| MND | motoneuron disease |
| PET | positron emission tomography |
| PiB | Pittsburgh compound B |
| p-tau | phosphorylated tau |
| SD | semantic dementia |
| t-tau | total tau |

REFERENCES

1. Armitage P (1955) Tests for Linear Trends in Proportions and Frequencies. *Biometrics* 11:375. doi: 10.2307/3001775
2. Van Berckel BNM, Ossenkoppele R, Tolboom N, Yaqub M, Foster-Dingley JC, Windhorst AD, Scheltens P, Lammertsma AA, Boellaard R (2013) Longitudinal amyloid imaging using 11C-PiB: Methodologic considerations. *J Nucl Med* 54:1570–1576. doi: 10.2967/jnumed.112.113654
3. Braak H, Braak E Neuropathological staging of Alzheimer-related changes. *Acta Neuropathol* 82:239–259. doi: 10.1007/BF00308809
4. Cairns NJ, Ikonovic MD, Benzinger T, Storandt M, Fagan AM, Shah AR, Reinwald LT, Carter D, Felton A, Holtzman DM, Mintun MA, Klunk WE, Morris JC (2009) Absence of Pittsburgh compound B detection of cerebral amyloid β in a patient with clinical, cognitive, and cerebrospinal fluid markers of Alzheimer disease: A case report. *Arch Neurol* 66:1557–1562. doi: 10.1001/archneurol.2009.279
5. Charidimou A, Friedrich JO, Greenberg SM, Viswanathan A (2018) Core cerebrospinal fluid biomarker profile in cerebral amyloid angiopathy: A meta-analysis. *Neurology* 90:e754–e762. doi: 10.1212/WNL.0000000000005030
6. Collij LE, Konijnenberg E, Reimand J, Kate M ten, Braber A den, Alves IL, Zwan M, Yaqub M, van Assema DME, Wink AM, Lammertsma AA, Scheltens P, Visser PJ, Barkhof F, van Berckel BNM (2019) Assessing Amyloid Pathology in Cognitively Normal Subjects Using 18 F-Flutemetamol PET: Comparing Visual Reads and Quantitative Methods. *J Nucl Med* 60:541–547. doi: 10.2967/jnumed.118.211532
7. Curtis C, Gamez JE, Singh U, Sadowsky CH, Villena T, Sabbagh MN, Beach TG, Duara R, Fleisher AS, Frey KA, Walker Z, Hunjan A, Holmes C, Escovar YM, Vera CX, Agronin ME, Ross J, Bozoki A, Akinola M, Shi J, Vandenberghe R, Ikonovic MD, Sherwin PF, Grachev ID, Farrar G, Smith APL, Buckley CJ, McLain R, Salloway S (2015) Phase 3 trial of flutemetamol labeled with radioactive fluorine 18 imaging and neuritic plaque density. *JAMA Neurol* 72:287–294. doi: 10.1001/jamaneurol.2014.4144
8. Duits FH, Teunissen CE, Bouwman FH, Visser P-J, Mattsson N, Zetterberg H, Blennow K, Hansson O, Minthon L, Andreasen N, Marcusson J, Wallin A, Rikkert MO, Tsolaki M, Parnetti L, Herukka S-K, Hampel H, De Leon MJ, Schröder J, Aarsland D, Blankenstein MA, Scheltens P, van der Flier WM (2014) The cerebrospinal fluid “Alzheimer profile”: Easily said, but what does it mean? *Alzheimer’s Dement* 10:713–723. doi: 10.1016/j.jalz.2013.12.023
9. Engelborghs S, Niemantsverdriet E, Struyfs H, Blennow K, Brouns R, Comabella M, Dujmovic I, van der Flier W, Frölich L, Galimberti D, Gnanapavan S, Hemmer B, Hoff E, Hort J, Iacobaeus E, Ingelsson M, Jan de Jong F, Jonsson M, Khalil M, Kuhle J, Lleó A, de Mendonça A, Molinuevo JL, Nagels G, Paquet C, Parnetti L, Roks G,

- Rosa-Neto P, Scheltens P, Skårsgard C, Stomrud E, Tumani H, Visser PJ, Wallin A, Winblad B, Zetterberg H, Duits F, Teunissen CE (2017) Consensus guidelines for lumbar puncture in patients with neurological diseases. *Alzheimer's Dement Diagnosis, Assess Dis Monit* 8:111-126. doi: 10.1016/j.dadm.2017.04.007
10. Ewers M, Mattsson N, Minthon L, Molinuevo JL, Antonell A, Popp J, Jessen F, Herukka S-K, Soininen H, Maetzler W, Leyhe T, Bürger K, Taniguchi M, Urakami K, Lista S, Dubois B, Blennow K, Hampel H (2015) CSF biomarkers for the differential diagnosis of Alzheimer's disease: A large-scale international multicenter study. *Alzheimer's Dement* 11:1306-1315. doi: 10.1016/j.jalz.2014.12.006
 11. Van Der Flier WM, Pijnenburg YAL, Prins N, Lemstra AW, Bouwman FH, Teunissen CE, Van Berckel BNM, Stam CJ, Barkhof F, Visser PJ, Van Egmond E, Scheltens P (2014) Optimizing patient care and research: The Amsterdam dementia cohort. *J Alzheimer's Dis* 41:313-327. doi: 10.3233/JAD-132306
 12. Hansson O, Lehmann S, Otto M, Zetterberg H, Lewczuk P (2019) Advantages and disadvantages of the use of the CSF Amyloid β (A β) 42/40 ratio in the diagnosis of Alzheimer's Disease. *Alzheimer's Res. Ther.* 11:1-15
 13. Hansson O, Mikulskis A, Fagan AM, Teunissen C, Zetterberg H, Vanderstichele H, Molinuevo JL, Shaw LM, Vandijck M, Verbeek MM, Savage M, Mattsson N, Lewczuk P, Batrla R, Rutz S, Dean RA, Blennow K (2018) The impact of preanalytical variables on measuring cerebrospinal fluid biomarkers for Alzheimer's disease diagnosis: A review. *Alzheimer's Dement.* 14:1313-1333
 14. Hardy J, Bogdanovic N, Winblad B, Portelius E, Andreasen N, Cedazo-Minguez A, Zetterberg H (2014) Pathways to Alzheimer's disease. *J Intern Med* 275:296-303. doi: 10.1111/joim.12192
 15. Hayashi T, Ago K, Nakamae T, Higo E, Ogata M (2015) Two different immunostaining patterns of beta-amyloid precursor protein (APP) may distinguish traumatic from nontraumatic axonal injury. *Int J Legal Med* 129:1085-1090. doi: 10.1007/s00414-015-1245-8
 16. Ikonovic MD, Klunk WE, Abrahamson EE, Mathis CA, Price JC, Tsopelas ND, Lopresti BJ, Ziolkowski S, Bi W, Paljug WR, Debnath ML, Hope CE, Isanski BA, Hamilton RL, DeKosky ST (2008) Post-mortem correlates of in vivo PiB-PET amyloid imaging in a typical case of Alzheimer's disease. *Brain* 131:1630-1645. doi: 10.1093/brain/awn016
 17. Jack CR, Bennett DA, Blennow K, Carrillo MC, Dunn B, Haeberlein SB, Holtzman DM, Jagust W, Jessen F, Karlawish J, Liu E, Molinuevo JL, Montine T, Phelps C, Rankin KP, Rowe CC, Scheltens P, Siemers E, Snyder HM, Sperling R, Elliott C, Masliah E, Ryan L, Silverberg N (2018) NIA-AA Research Framework: Toward a biological definition of Alzheimer's disease. *Alzheimer's Dement* 14:535-562. doi: 10.1016/j.jalz.2018.02.018
 18. Johnson KA, Gregas M, Becker JA, Kinnecom C, Salat DH, Moran EK, Smith EE, Rosand J, Rentz DM, Klunk WE, Mathis CA, Price JC, DeKosky ST, Fischman AJ, Greenberg SM (2007) Imaging of amyloid burden and distribution in cerebral amyloid angiopathy. *Ann Neurol* 62:229-234. doi: 10.1002/ana.21164

19. Krut JJ, Zetterberg H, Blennow K, Cinque P, Hagberg L, Price RW, Studahl M, Gisslén M (2013) Cerebrospinal fluid Alzheimer's biomarker profiles in CNS infections. *J Neurol* 260:620–626. doi: 10.1007/s00415-012-6688-y
20. Levin J, Tiedt S, Arzberger T, Biskup S, Schuberth M, Stenglein-Krapf G, Kreth FW, Högen T, La Fougère C, Linn J, Van Der Knaap MS, Giese A, Kretschmar HA, Danek A (2014) Diffuse leukoencephalopathy with spheroids: Biopsy findings and a novel mutation. *Clin Neurol Neurosurg* 122:113–115. doi: 10.1016/j.clineuro.2014.04.022
21. Lewczuk P, Matzen A, Blennow K, Parnetti L, Molinuevo JL, Eusebi P, Kornhuber J, Morris JC, Fagan AM (2017) Cerebrospinal Fluid A β 42/40 Corresponds Better than A β 42 to Amyloid PET in Alzheimer's Disease. *J Alzheimer's Dis* 55:813–822. doi: 10.3233/JAD-160722
22. Lowe VJ, Lundt ES, Albertson SM, Przybelski SA, Senjem ML, Parisi JE, Kantarci K, Boeve B, Jones DT, Knopman D, Jack CR, Dickson DW, Petersen RC, Murray ME (2019) Neuroimaging correlates with neuropathologic schemes in neurodegenerative disease. *Alzheimer's Dement* 15:927–939. doi: 10.1016/j.jalz.2019.03.016
23. MacKenzie IRA, Neumann M, Bigio EH, Cairns NJ, Alafuzoff I, Kril J, Kovacs GG, Ghetti B, Halliday G, Holm IE, Ince PG, Kamphorst W, Revesz T, Rozemuller AJM, Kumar-Singh S, Akiyama H, Baborie A, Spina S, Dickson DW, Trojanowski JQ, Mann DMA (2010) Nomenclature and nosology for neuropathologic subtypes of frontotemporal lobar degeneration: An update. In: *Acta Neuropathologica*. pp 1–4
24. Mattsson N, Bremell D, Anckarsäter R, Blennow K, Anckarsäter H, Zetterberg H, Hagberg L (2010) Neuroinflammation in Lyme neuroborreliosis affects amyloid metabolism. *BMC Neurol* 10. doi: 10.1186/1471-2377-10-51
25. McKhann GM, Knopman DS, Chertkow H, Hyman BT, Jack CR, Kawas CH, Klunk WE, Koroshetz WJ, Manly JJ, Mayeux R, Mohs RC, Morris JC, Rossor MN, Scheltens P, Carrillo MC, Thies B, Weintraub S, Phelps CH, Phelps CH (2011) The diagnosis of dementia due to Alzheimer's disease: recommendations from the National Institute on Aging-Alzheimer's Association workgroups on diagnostic guidelines for Alzheimer's disease. *Alzheimer's Dement* 7:263–9. doi: 10.1016/j.jalz.2011.03.005
26. Mirra SS, Heyman A, McKeel D, Sumi SM, Crain BJ, Brownlee LM, Vogel FS, Hughes JP, Belle G v., Berg L (1991) The Consortium to Establish a Registry for Alzheimer's Disease (CERAD): Part II. Standardization of the neuropathologic assessment of Alzheimer's disease. *Neurology* 41:479–479. doi: 10.1212/WNL.41.4.479
27. Montine TJ, Phelps CH, Beach TG, Bigio EH, Cairns NJ, Dickson DW, Duyckaerts C, Frosch MP, Masliah E, Mirra SS, Nelson PT, Schneider JA, Thal DR, Trojanowski JQ, Vinters H V., Hyman BT (2012) National Institute on Aging–Alzheimer's Association guidelines for the neuropathologic assessment of Alzheimer's disease: a practical approach. *Acta Neuropathol* 123:1–11. doi: 10.1007/s00401-011-0910-3
28. Mori F, Rossi S, Sancesario G, Codecá C, Mataluni G, Monteleone F, Buttari F, Kusayanagi H, Castelli M, Motta C, Studer V, Bernardi G, Koch G, Bernardini S, Centonze D (2011) Cognitive and cortical plasticity deficits correlate with altered amyloid-B CSF levels in multiple sclerosis. *Neuropsychopharmacology* 36:559–568. doi: 10.1038/npp.2010.187

29. Murray ME, Lowe VJ, Graff-Radford NR, Liesinger AM, Cannon A, Przybelski SA, Rawal B, Parisi JE, Petersen RC, Kantarci K, Ross OA, Duara R, Knopman DS, Jack CR, Dickson DW (2015) Clinicopathologic and 11 C-Pittsburgh compound B implications of Thal amyloid phase across the Alzheimer's disease spectrum. *Brain* 138:1370–1381. doi: 10.1093/brain/awv050
30. Olsson B, Lautner R, Andreasson U, Öhrfelt A, Portelius E, Bjerke M, Hölttä M, Rosén C, Olsson C, Strobel G, Wu E, Dakin K, Petzold M, Blennow K, Zetterberg H (2016) CSF and blood biomarkers for the diagnosis of Alzheimer's disease: a systematic review and meta-analysis. *Lancet Neurol* 15:673–684. doi: 10.1016/S1474-4422(16)00070-3
31. Ossenkoppele R, Prins ND, Pijnenburg YAL, Lemstra AW, Van Der Flier WM, Adriaanse SF, Windhorst AD, Handels RLH, Wolfs CAG, Aalten P, Verhey FRJ, Verbeek MM, Van Buchem MA, Hoekstra OS, Lammertsma AA, Scheltens P, Van Berckel BNM (2013) Impact of molecular imaging on the diagnostic process in a memory clinic. *Alzheimer's Dement* 9:414–421. doi: 10.1016/j.jalz.2012.07.003
32. Palmqvist S, Schöll M, Strandberg O, Mattsson N, Stomrud E, Zetterberg H, Blennow K, Landau S, Jagust W, Hansson O (2017) Earliest accumulation of β -amyloid occurs within the default-mode network and concurrently affects brain connectivity. *Nat Commun* 8. doi: 10.1038/s41467-017-01150-x
33. Reimand J, Collij L, Scheltens P, Bouwman F, Ossenkoppele R (2020) Amyloid- β CSF/PET discordance vs tau load 5 years later: It takes two to tangle. doi: 10.1101/2020.01.29.20019539
34. Ruland T, Wolbert J, Gottschalk MG, König S, Schulte-Mecklenbeck A, Minnerup J, Meuth SG, Groß CC, Wiendl H, zu Hörste GM (2018) Cerebrospinal fluid concentrations of neuronal proteins are reduced in primary angiitis of the central nervous system. *Front Neurol* 9. doi: 10.3389/fneur.2018.00407
35. Sabri O, Sabbagh MN, Seibyl J, Barthel H, Akatsu H, Ouchi Y, Senda K, Murayama S, Ishii K, Takao M, Beach TG, Rowe CC, Leverenz JB, Ghetti B, Ironside JW, Catafau AM, Stephens AW, Mueller A, Koglin N, Hoffmann A, Roth K, Reininger C, Schulz-Schaeffer WJ (2015) Florbetaben PET imaging to detect amyloid beta plaques in Alzheimer's disease: Phase 3 study. *Alzheimer's Dement* 11:964–974. doi: 10.1016/j.jalz.2015.02.004
36. Schindler SE, Sutphen CL, Teunissen C, McCue LM, Morris JC, Holtzman DM, Mulder SD, Scheltens P, Xiong C, Fagan AM (2018) Upward drift in cerebrospinal fluid amyloid β 42 assay values for more than 10 years. *Alzheimer's Dement* 14:62–70. doi: 10.1016/j.jalz.2017.06.2264
37. Schöll M, Maass A, Mattsson N, Ashton NJ, Blennow K, Zetterberg H, Jagust W (2019) Biomarkers for tau pathology. *Mol. Cell. Neurosci.* 97:18–33
38. Scholl M, Wall A, Thordardottir S, Ferreira D, Bogdanovic N, Langstrom B, Almkvist O, Graff C, Nordberg A (2012) Low PiB PET retention in presence of pathologic CSF biomarkers in Arctic APP mutation carriers. *Neurology* 79:229–236. doi: 10.1212/WNL.0b013e31825fdf18

39. Spitzer P, Kohl Z, Golitz P, Coras R, Blumcke I, Bruck W, Dorfler A, Maihofner C (2014) Biochemical markers of neurodegeneration in hereditary diffuse leucoencephalopathy with spheroids. *Case Reports* 2014:bcr2012008510–bcr2012008510. doi: 10.1136/bcr-2012-008510
40. Strozyk D, Blennow K, White LR, Launer LJ (2003) CSF Abeta 42 levels correlate with amyloid-neuropathology in a population-based autopsy study. *Neurology* 60:652–656. doi: 10.1212/01.WNL.0000046581.81650.D0
41. Thal DR, Ghebremedhin E, Rüb U, Yamaguchi H, Del Tredici K, Braak H (2002) Two types of sporadic cerebral amyloid angiopathy. *J Neuropathol Exp Neurol* 61:282–293. doi: 10.1093/jnen/61.3.282
42. Thal DR, Rüb U, Orantes M, Braak H (2002) Phases of A β -deposition in the human brain and its relevance for the development of AD. *Neurology* 58:1791–800. doi: 10.1212/WNL.58.12.1791
43. Tijms BM, Willemse EAJ, Zwan MD, Mulder SD, Visser PJ, Van Berckel BNM, Van Der Flier WM, Scheltens P, Teunissen CE (2018) Unbiased approach to counteract upward drift in cerebrospinal fluid amyloid- β 1–42 analysis results. *Clin Chem* 64:576–585. doi: 10.1373/clinchem.2017.281055
44. Trysberg E, Höglund K, Svenungsson E, Blennow K, Tarkowski A (2004) Decreased levels of soluble amyloid beta-protein precursor and beta-amyloid protein in cerebrospinal fluid of patients with systemic lupus erythematosus. *Arthritis Res Ther* 6. doi: 10.1186/ar1040
45. Villemagne VL, Burnham S, Bourgeat P, Brown B, Ellis KA, Salvado O, Szoek C, Macaulay SL, Martins R, Maruff P, Ames D, Rowe CC, Masters CL (2013) Amyloid β deposition, neurodegeneration, and cognitive decline in sporadic Alzheimer's disease: A prospective cohort study. *Lancet Neurol* 12:357–367. doi: 10.1016/S1474-4422(13)70044-9
46. Vlassenko AG, McCue L, Jasielc MS, Su Y, Gordon BA, Xiong C, Holtzman DM, Benzinger TLS, Morris JC, Fagan AM (2016) Imaging and cerebrospinal fluid biomarkers in early preclinical alzheimer disease. *Ann Neurol* 80:379–387. doi: 10.1002/ana.24719
47. de Wilde A, van der Flier WM, Pelkmans W, Bouwman F, Verwer J, Groot C, van Buchem MM, Zwan M, Ossenkoppele R, Yaqub M, Kunneman M, Smets EMA, Barkhof F, Lammertsma AA, Stephens A, van Lier E, Biessels GJ, van Berckel BN, Scheltens P (2018) Association of Amyloid Positron Emission Tomography With Changes in Diagnosis and Patient Treatment in an Unselected Memory Clinic Cohort. *JAMA Neurol* 75:1062. doi: 10.1001/jamaneurol.2018.1346
48. De Wilde A, Reimand J, Teunissen CE, Zwan M, Windhorst AD, Boellaard R, Van Der Flier WM, Scheltens P, Van Berckel BNM, Bouwman F, Ossenkoppele R (2019) Discordant amyloid- β PET and CSF biomarkers and its clinical consequences. *Alzheimer's Res Ther* 11. doi: 10.1186/s13195-019-0532-x
49. Willemse EAJ, Tijms BM, van Berckel BNM, Scheltens P, Teunissen CE Optimal use of cerebrospinal fluid amyloid-beta(1-42) in the memory clinic: use of biomarker ratios across immunoassays. (in prep)

Chapter 7

50. Zhuang L-P, Liu C-Y, Li Y-X, Huang H-P, Zou Z-Y (2020) Clinical features and genetic characteristics of hereditary diffuse leukoencephalopathy with spheroids due to CSF1R mutation: a case report and literature review. *Ann Transl Med* 8:11-11. doi: 10.21037/atm.2019.12.17
51. Zwan MD, Bouwman FH, Konijnenberg E, Van Der Flier WM, Lammertsma AA, Verhey FRJ, Aalten P, Van Berckel BNM, Scheltens P (2017) Diagnostic impact of [18F]flutemetamol PET in early-onset dementia. *Alzheimer's Res Ther* 9. doi: 10.1186/s13195-016-0228

Chapter 8

**A β , p-tau, and reactive microglia load
are correlates of MRI cortical atrophy in
Alzheimer's disease**

Irene Frigerio, Baayla DC Boon, Chen-Pei Lin, Yvon Galis-de Graaf,
John GJM Bol, Paolo Preziosa, Jos Twisk, Frederik Barkhof, Jeroen JM
Hoozemans, Femke H Bouwman, Annemieke JM Rozemuller, Wilma DJ
van de Berg, Laura E Jonkman

Accepted for publication in Brain Communications

ABSTRACT

Background: This study aimed to identify the histopathological correlates of cortical atrophy as measured by magnetic resonance imaging (MRI) in (a)typical Alzheimer's disease (AD) donors.

Methods: 19 AD and 10 control donors underwent post mortem in situ 3T-3DT1-MRI, from which cortical thickness was calculated. Upon subsequent autopsy, 21 cortical brain regions were selected and immunostained against amyloid-beta ($A\beta$), phosphorylated-tau (p-tau), and reactive microglia. MRI-pathology associations were assessed using linear mixed models. Post mortem MRI was compared to ante mortem MRI when available.

Results: Higher $A\beta$ load was weakly correlated with a higher cortical thickness globally. P-tau strongly correlated with cortical atrophy in frontotemporal regions. Reactive microglia load strongly correlated with cortical atrophy in the parietal region. Post mortem scans showed high concordance with ante mortem scans acquired < 1 year before death.

Conclusions: Distinct histopathological markers correlate differently with cortical atrophy, highlighting their different roles in the neurodegenerative process. This study contributes to the understanding of pathological underpinnings in MRI atrophy patterns.

INTRODUCTION

Alzheimer's disease (AD) is a progressive neurodegenerative disease with a heterogeneous clinical presentation. Clinically, AD is defined as typical when memory deficits are the first complaints, and atypical when memory is initially spared while other symptoms are more prominent, such as visuospatial impairment, aphasia, or behavioral/dysexecutive dysfunction [18]. On magnetic resonance imaging (MRI), typical AD is characterized by hippocampal and temporoparietal atrophy [49], whereas atypical presentations may show initial hippocampal sparing, and cortical atrophy in regions corresponding to clinical symptoms [37]. Although hippocampal and temporoparietal atrophy are commonly used MRI biomarkers in AD, reliable imaging biomarkers ideally reflect disease state as well as underlying pathophysiological mechanisms in AD, and should be validated in a cohort of neuropathologically-confirmed AD subjects.

Pathologically, AD is characterised by the accumulation of amyloid-beta (A β) plaques and phosphorylated-tau (p-tau) neurofibrillary tangles (NFT) in the grey matter [10, 46]. In addition, neuroinflammation plays a key role in AD [2, 20]. Reactive microglia tend to proliferate and increase with disease progression [2, 20] and seem to reflect p-tau deposition sites [7].

Studies combining MRI and positron emission tomography (PET) imaging as a proxy for pathology showed that the load and neuroanatomical distribution of tau tracers correlate with cortical atrophic patterns on MRI [30, 36, 38, 39, 48], while widespread cortical A β deposition [38] does not correlate with cortical atrophy nor clinical presentation in clinically-defined AD cases [25, 42]. The effect of reactive microglia load on cortical atrophy remains elusive, since the few studies that investigated its association with MRI atrophic patterns report contrasting results [14, 35]. Unfortunately, PET imaging cannot evaluate different pathological processes together, but just one at each exam. As such, post mortem histopathological examination remains the gold standard to diagnose AD and to evaluate the combination of different markers [31].

The aim of the current study was to assess the association between post mortem in situ (within the skull) MRI cortical thickness and histopathological hallmarks in clinically-defined and pathologically-confirmed AD subjects. Additionally, due to the clinical heterogeneity in AD, we explored the association between neuroanatomical distribution of MRI and pathological patterns in clinically-

defined typical and atypical AD phenotypes [15]. Lastly, we investigated the coherence between ante mortem and post mortem patterns in a subset of these patients. The results of this study will increase our knowledge on the histopathological correlates of cortical atrophy, thereby contributing to the understanding of the pathological underpinnings of MRI atrophy patterns.

METHODS

Detailed methods are described in Supplementary Methods.

Donor inclusion

In collaboration with the Netherlands Brain Bank (NBB; <http://brainbank.nl>) we included 19 AD donors from the Amsterdam Dementia Cohort [16]. The AD donors could be further subdivided into 10 typical and 9 atypical AD donors based on clinical symptoms, of which 6 were diagnosed with the behavioural/dysexecutive variant (B/D) [37], and 3 with posterior cortical atrophy (PCA) [12]. Neuropathological diagnosis was confirmed by an expert neuropathologist (AJMR) and performed according to the international guidelines of the Brain Net Europe II (BNE) consortium (<http://www.brainnet-europe.org>) [3, 4]. Additionally, 10 age-matched pathologically confirmed non-neurological controls were selected from the Normal Aging Brain Collection Amsterdam (NABCA; <http://nabca.eu>) [27]. All donors signed an informed consent for brain donation and the use of material and clinical information for research purposes. The procedures for brain tissue collection of NBB and NABCA have been approved by the Medical Ethical Committee of the VUmc. For donor characteristics, see Table S1.

Post mortem in situ and ante mortem in vivo MRI acquisition

Post mortem 3T brain in situ MRI acquisition was acquired according to a previously described pipeline [28] and explained in detail in the Supplementary Methods. Briefly, 3T MRI was acquired on a magnetic resonance scanner (Signa-MR750, General Electric Medical Systems, United States) with an eight-channel phased-array head-coil. The cortical surface was reconstructed with FreeSurfer, version 6.0 (<http://surfer.nmr.mgh.harvard.edu>) [13]. Moreover, 14 out of 19 AD patients included in our study had ante mortem in vivo 3T MRI scans available, and these were included for comparison with post mortem MRI. Details about these scans can be found in Table S2.

Tissue sampling

Formalin-fixed paraffin-embedded (4%; 4 weeks fixation) tissue blocks from the following regions of the right hemisphere were used: superior and middle frontal gyrus, anterior and posterior cingulate gyrus, middle temporal gyrus, superior and inferior parietal gyrus, precuneus, occipital cortex (primary visual cortex), and hippocampus (including the entorhinal cortex, parahippocampal, and fusiform gyrus as described before [1]). Additionally, for 13 AD cases (7 typical and 6 atypical), 9 formalin-fixed paraffin-embedded (4%; 24-36 hours fixation) tissue blocks from the left hemisphere were available from the same regions as described above except for the hippocampus and posterior cingulate gyrus, adding the superior temporal gyrus.

Immunohistochemistry and image analysis

The immunohistological procedures are explained in detail in the Supplementary Methods. Briefly, 6- μ m thick sections were cut from the above-mentioned regions. The sections from the right hemisphere were stained against A β (clone 4G8), p-tau (clone AT8), and reactive microglia (CD68, clone KP1). The sections from the left hemisphere were additionally collected and stained for A β (4G8) and p-tau (AT8) (see Table S3 for information on primary antibodies). Images were taken using a whole-slide scanner (Vectra Polaris, 20 \times objective) and quantified using Fiji ImageJ Version 1.52r (<https://imagej.nih.gov/ij>). Regions of interest (ROIs) containing all cortical layers were delineated in straight areas of the cortex to avoid over- or underestimation of pathology in sulci and gyri, respectively [5]. After colour deconvolution, used to separate hematoxylin and 3,3'-Diaminobenzidine (DAB) channels, the immunoreactivity of DAB staining was quantified using the auto-threshold plugin "maximum entropy" [29]. The outcome measure was the % of DAB-stained area per ROIs of each section per marker. For an overview of our workflow, see Fig. 1.

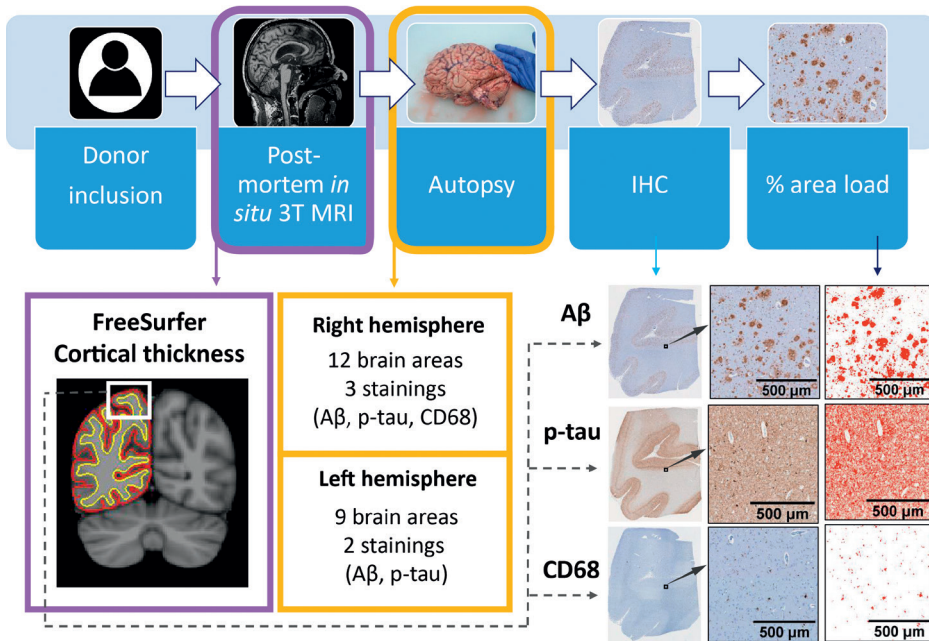


Fig. 1. Workflow of the post mortem MRI-pathology pipeline

Once the donors were included in the study, they received a post mortem *in situ* 3T MRI, and cortical thickness was calculated with FreeSurfer [13] from the 3D T1w image (purple box). After the MRI scan, autopsy was performed, and brain tissue was processed for immunohistochemistry against $A\beta$, p-tau and CD68 (yellow boxes), which were quantified using ImageJ. The correlation between cortical thickness and % area of immunoreactivity was investigated via linear mixed models (dashed grey arrow). $A\beta$ amyloid-beta; IHC immunohistochemistry; p-tau phosphorylated-tau.

Statistics

Statistical analyses are detailed in the Supplementary Methods, and were performed in IBM SPSS statistics version 26.0 (Armonk, NY, USA). Cortical thickness between groups and its association with pathology was tested with linear mixed models (LMM) with age, gender, and post mortem delay as covariates, and Bonferroni post-hoc correction for multiple testing. Pathological outcome measures were compared across groups with LMM, using age and gender as covariates. Statistics at the brain area level were corrected for multiple comparisons using the false discovery rate (FDR) approach [6], and the corrected *p*-values were expressed as *q*-values.

RESULTS

Donor characteristics

Demographical, clinical, radiological, and pathological data of AD and non-neurological control donors are summarized in Table 1. Age, disease duration, and post mortem delay did not differ between groups, whereas gender differed between controls and AD cases ($p = 0.032$). On MRI, normalized brain volume (-5.4% in AD compared to controls, $p = 0.040$), and normalized grey matter volume (-11.6%, $p = 0.001$), but not normalized white matter volume ($p = 0.735$) were lower in AD cases compared to controls. As per definition, AD cases had higher Braak NFT stage ($p < 0.001$), Thal A β phase ($p < 0.001$) and ABC score ($p < 0.001$) than controls. Regarding AD phenotypes, typical and atypical AD did not differ in demographical, radiological, or pathological data. *APOE* genotype did not differ between AD phenotypes ($p = 0.315$).

MRI cortical atrophy of the temporo-parietal region in AD

AD donors had significantly more cortical atrophy compared to controls (-5.7%, $p = 0.011$, see Table S4), in the inferior ($q = 0.004$), middle ($q = 0.008$) and superior temporal gyrus ($q = 0.012$), entorhinal cortex ($q = 0.001$), fusiform gyrus ($q = 0.050$), inferior parietal gyrus ($q = 0.020$), insular cortex ($q = 0.043$), supramarginal cortex ($q = 0.020$) and precuneus ($q = 0.028$) in the left hemisphere, and in the entorhinal cortex ($q = 0.025$) and inferior temporal gyrus ($q = 0.042$) in the right hemisphere (Fig. 2A). Compared to controls, atypical AD cases showed significant global cortical atrophy (-6.2%, $p = 0.039$), while typical AD cases did not ($p = 0.116$) (Fig. 2B). No significant difference in atrophy was found between AD phenotypes ($p = 1.000$) (Table S4).

Table 1. Clinical, radiological, and pathological characteristics of included donors

| | Control | AD | Typical AD | Atypical AD |
|---|---------------|----------------|---------------|------------------|
| Clinical characteristics | | | | |
| <i>n</i> (phenotype) | 10 | 19 | 10 | 9 (6 B/D, 3 PCA) |
| Gender M/F (%M) | 4/6 (40%) | 16/3 (84%) * | 9/1 (90%) | 7/2 (78%) |
| APOE genotype <i>n</i> | 9 | 19 | 10 | 9 |
| ε4 non-carrier | 5 (56%) | 7 (37%) | 5 (50%) | 2 (22%) |
| ε4 heterozygous | 4 (44%) | 10 (53%) | 4 (40%) | 6 (67%) |
| ε4 homozygous | - | 2 (10%) | 1 (10%) | 1 (11%) |
| Age at disease onset years; mean ± SD | - | 60 ± 10 | 61 ± 8 | 59 ± 13 |
| Age at death years; mean ± SD | 69 ± 7 | 67 ± 12 | 70 ± 11 | 64 ± 12 |
| Disease duration years; mean ± SD | - | 8 ± 5 | 10 ± 6 | 6 ± 3 |
| Post mortem delay Min; mean ± SD | 549 ± 114 | 478 ± 116 | 520 ± 95 | 432 ± 124 |
| Radiologic characteristics | | | | |
| NBV (L) mean ± SD | 1.49 ± 0.06 | 1.41 ± 0.13 * | 1.42 ± 0.13 | 1.40 ± 0.14 |
| NGMV (L) mean ± SD | 0.76 ± 0.04 | 0.67 ± 0.09 ** | 0.68 ± 0.07 | 0.67 ± 0.11 * |
| NWMV (L) mean ± SD | 0.72 ± 0.03 | 0.73 ± 0.08 | 0.73 ± 0.09 | 0.73 ± 0.08 |
| Pathological characteristics | | | | |
| ABC score [33] <i>n</i> | 10 | 19 | 10 | 9 |
| A 0/1/2/3 | 3/6/1/0 | 0/0/0/19 *** | 0/0/0/10 *** | 0/0/0/9 *** |
| B 0/1/2/3 | 3/7/0/0 | 0/0/4/15 *** | 0/0/3/7 *** | 0/0/1/8 *** |
| C 0/1/2/3 | 10/0/0/0 | 0/0/4/15 *** | 0/0/3/7 *** | 0/0/1/8 *** |
| Thal Aβ phase [46] <i>n</i> | 10 | 19 *** | 10 *** | 9 ** |
| 0/1/2/3/4/5 | 3/3/3/1/0/0 | 0/0/0/1/1/17 | 0/0/0/1/0/9 | 0/0/0/0/1/8 |
| Braak NFT stage [10] <i>n</i> | 10 | 19 *** | 10 *** | 9 ** |
| 0/I/II/III/IV/V/VI | 3/6/1/0/0/0/0 | 0/0/0/0/4/8/7 | 0/0/0/0/3/3/4 | 0/0/0/0/1/5/3 |
| CAA Type <i>n</i> | 10 | 18 | 10 | 9 |
| 1/ 2 (% type 1) | 0/0 | 15/3 (83%) | 7/2 (78%) | 8/1 (89%) |

AD Alzheimer's disease; B/D behavioral/dysexecutive variant; CAA cerebral amyloid angiopathy; F female; L liter; M male; *n* sample size; NBV normalized brain volume; NFT neurofibrillary tangles; NGMV normalized grey matter volume; NWMV normalized white matter volume; PCA posterior cortical atrophy; SD standard deviation; **p* < 0.05, ***p* < 0.01, ****p* < 0.001 when compared to controls.

Load and distribution of AD pathological hallmarks

As expected, AD cases had significantly higher A β ($p < 0.001$) and p-tau load ($p < 0.001$) compared to controls (see Table S5). By subgroup, both typical and atypical AD had higher A β ($p = 0.012$ and $p = 0.001$, respectively) (Fig. 3A-C) and p-tau load ($p = 0.002$ and $p < 0.001$, respectively) (Fig. 3D-F) compared to controls, whereas typical and atypical AD did not differ in A β ($p = 1.000$) or p-tau load ($p = 1.000$) from one another.

AD cases showed a higher load of reactive microglia compared to controls ($p = 0.002$, see Table S5). By subgroup, atypical AD cases had a higher reactive microglia load than controls ($p = 0.001$), whereas typical AD cases did not ($p = 0.104$) (Fig. 3G-I), suggesting that the significant difference in reactive microglia load between AD and controls was driven by the atypical AD group. No difference was found between AD phenotypes ($p = 0.199$). For an overview of the correlations between pathological markers, see table Table S6.

Cortical thickness associates with Thal A β and Braak NFT staging

In the whole cohort, the average whole-brain cortical thickness correlated negatively with both Thal A β phase ($r_s = -0.39$, $R^2 = 15\%$, $p = 0.037$) and Braak NFT stage ($r_s = -0.40$, $R^2 = 16\%$, $p = 0.030$, Fig. S1), suggesting an increase in cortical atrophy with disease progression.

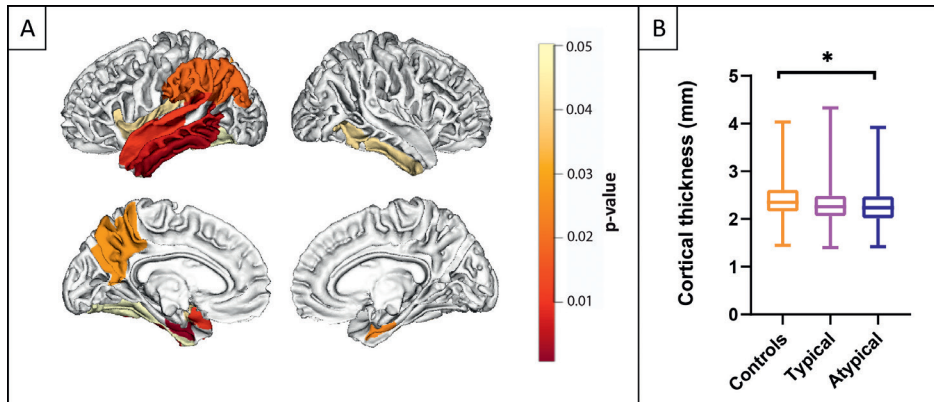


Fig. 2. MRI cortical atrophy in AD

A The atrophy patterns in AD (typical and atypical combined) compared to controls are shown across the whole cortex. The scale bar represents the p -values with increasing significance from yellow to red. No significant differences in atrophy patterns were found between typical and atypical AD. **B** Boxplot visualizing the range of global cortical thickness in controls, typical, and atypical AD. The boxplot represents the median, the upper and lower quartile, and the minimum and maximum values. AD Alzheimer's disease; * $p < 0.05$ when compared to controls. For detailed information, see Table S4.

A β load weakly correlates with less cortical atrophy in AD

A weak positive correlation between A β load and cortical thickness was found in the AD group across regions ($r = 0.19$, $R^2 = 3\%$, $p = 0.010$; Table S7, Fig. 4A) but not in controls ($p = 0.165$). A similar association was found in typical AD ($r = 0.22$, $R^2 = 5\%$, $p = 0.022$), but not in the atypical AD ($p = 0.200$). We found no associations within brain areas for any group. Overall, A β load weakly correlated with less cortical atrophy in AD.

P-tau load strongly correlates with regional cortical atrophy

No associations were found between p-tau load and cortical thickness in AD ($p = 0.477$), AD phenotypes ($p = 0.144$ for typical, and $p = 0.856$ for atypical), or controls ($p = 0.755$) across regions. However, within regions, we observed strong significant correlations in the middle ($r = -1.00$, $R^2 = 100\%$, $q = 0.001$) and superior frontal gyrus ($r = -0.76$, $R^2 = 58\%$, $q = 0.018$), and the middle temporal gyrus ($r = -0.84$, $R^2 = 71\%$, $q = 0.001$) in the AD group only (Table S8, Fig. 4C-E). Overall, p-tau load strongly correlated with cortical atrophy in frontal and temporal regions in AD.

Reactive microglia load contributes to cortical atrophy in the parietal region

No associations were found between reactive microglia load and cortical thickness in the AD group ($p = 0.487$) nor controls ($p = 0.242$) across regions. Similarly, we found no associations in typical ($p = 0.747$) and atypical ($p = 0.285$) AD phenotypes. However, within regions, we found a strong negative significant association in the right inferior parietal gyrus in AD donors ($r = -0.94$, $R^2 = 89\%$, $q < 0.001$) (Fig. 4B), which also survived when p-tau load was included in the model as covariate ($r = -0.86$, $R^2 = 74\%$, $q < 0.001$). Overall, reactive microglia load strongly correlated with cortical atrophy in the inferior parietal gyrus in AD.

Combined contribution of pathological hallmarks to cortical thickness

A regression model was run to investigate the combined contribution of A β , p-tau, and reactive microglia load on cortical thickness of each brain area, and to investigate which marker had the strongest association with cortical atrophy. While we found no associations in controls, we found significant associations in AD in the middle frontal gyrus ($r = 0.88$, $R^2 = 77\%$, $q = 0.031$), and the inferior parietal gyrus ($r = 0.92$, $R^2 = 84\%$, $q < 0.001$), explaining up to 84% of the variance in cortical thickness. In AD, p-tau load was the major contributor in the middle frontal gyrus ($q = 0.007$), while load of reactive microglia was the main contributor in the inferior parietal gyrus ($q = 0.001$). When the AD group was split up in typical and atypical AD, no areas showed significant regression models.

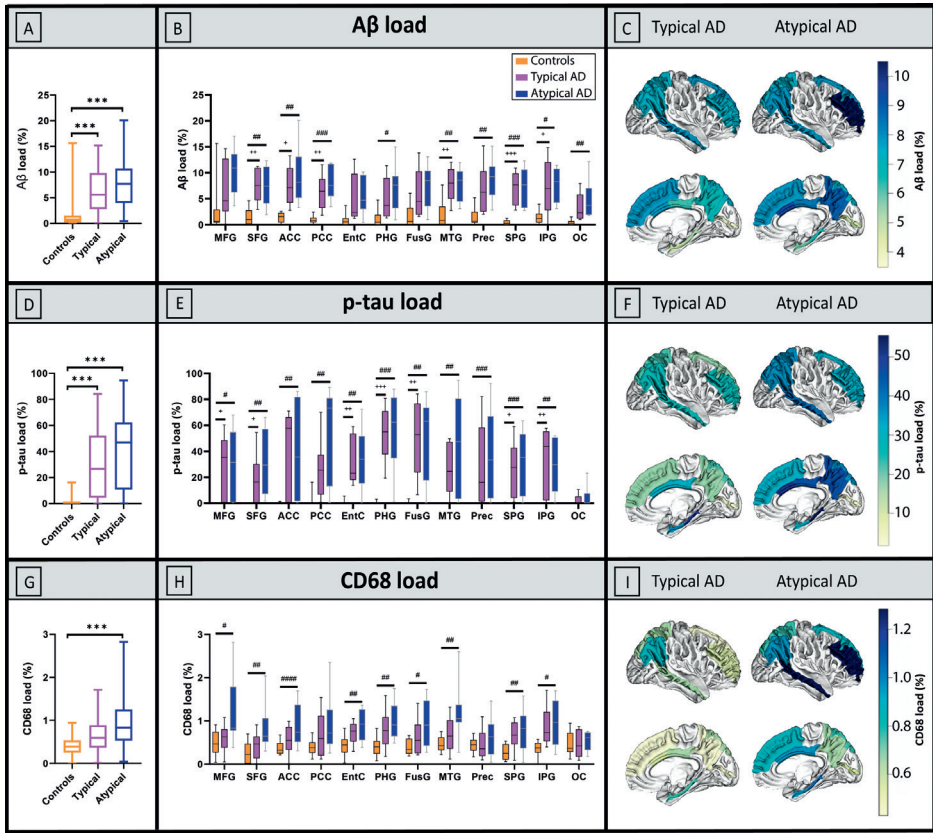


Fig. 3. Load and distribution of pathological hallmarks in AD phenotypes and controls. A-C represent the % load of A β , D-F of p-tau, and G-I of reactive microglia in the right hemisphere. In the first column (A, D, and G) show group differences in overall pathological load with boxplots showing median, upper and lower quartile, and minimum and maximum values for each group; the middle column (B, E, and H) show group differences across regions; C, E, and I visually show the mean pathological load on the cortical surface in typical and atypical AD phenotypes, i.e., the same data graphically showed in the middle column. A β amyloid-beta; ACC anterior cingulate cortex; AD Alzheimer’s disease; EntC entorhinal cortex; FusG fusiform gyrus; IPG inferior parietal gyrus; MFG middle frontal gyrus; MTG middle temporal gyrus; OC occipital cortex; PCC posterior cingulate cortex; PHG parahippocampal gyrus, Prec precuneus; p-tau phosphorylated tau; SFG superior frontal gyrus; SPG superior parietal gyrus. In the first column: * $p < 0.05$; ** $p < 0.010$; *** $p < 0.001$ when compared to controls. In the middle column, FDR corrected p -values: + $q < 0.05$; ++ $q < 0.010$; +++ $q < 0.001$ typical AD compared to controls; # $q < 0.05$; ### $q < 0.010$; #### $q < 0.001$ atypical AD compared to controls.

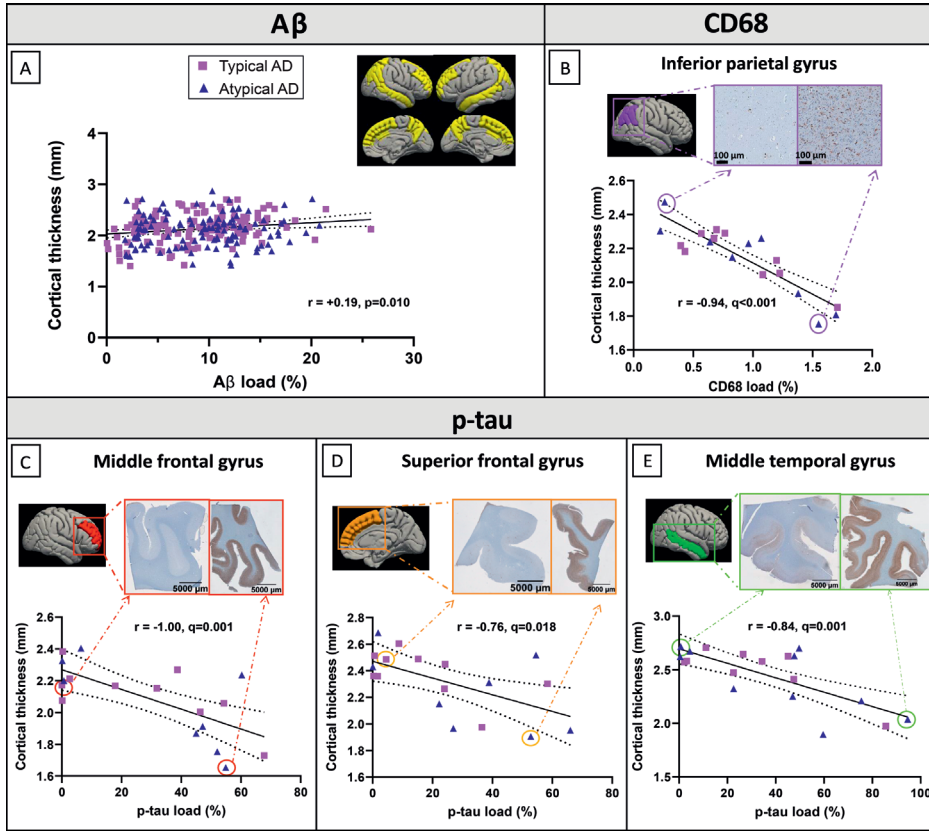


Fig. 4. MRI-pathology associations in AD

A $A\beta$ load and cortical thickness show a weak positive correlation in the AD group across regions (shown in yellow). B Reactive microglia load and cortical thickness showed a strong negative correlation in the inferior parietal gyrus (purple). C p-tau load and cortical thickness showed a strong negative correlation in the middle frontal gyrus (red), D superior frontal gyrus (orange), E and middle temporal gyrus (green). On the top right of each graph, two tissue sections representing a low (left) and high (right) pathological load are shown. Purple squares represent typical AD cases; blue triangles represent atypical AD cases. A fit-line with 95% confidence interval (dashed lines) is shown for each correlation. $A\beta$ amyloid-beta; AD Alzheimer’s disease; p-tau phosphorylated tau.

From post mortem in situ to ante mortem in vivo

Additionally, we investigated the association between ante mortem in vivo and post mortem in situ MRI scans of the same donor. Cortical thickness assessment of scans acquired < 1 year before death tended to have a stronger correlation with post mortem cortical thickness than ante mortem scans acquired 8-10 years before death (r ranged from 0.98 in ante mortem scan with a 2-year interval from

death to 0.69 in ante mortem scan with a 10-year interval from death, $p < 0.001$ for all, Table S9). Moreover, we investigated the correlation between p-tau load and both ante mortem and post mortem cortical thickness in the 3 brain areas that showed significant correlations in our study (see Fig. 4 C, D, E). Cortical thickness measured from ante mortem scans acquired shortly before death (< 1 year, $n = 3$) showed high concordance with post mortem cortical thickness and its relationship with histopathology, while cortical thickness measured from ante mortem scans acquired 8-10 years before death ($n = 2$) showed less concordance with post mortem cortical thickness, especially in the middle temporal gyrus (Fig. S2A-B). One AD case had 3 ante mortem scans. Within this case, we observed increasing concordance between ante mortem and post mortem measured cortical thickness in ante mortem scans closer to death (Fig. S2C).

DISCUSSION

Using a combined post mortem in situ MRI and histopathology approach, we investigated the associations between MRI cortical thickness and A β , p-tau, and reactive microglia load in clinically-defined and pathologically-confirmed AD and control donors. In addition, we explored the mentioned associations in typical and atypical AD phenotypes. Associations between the histopathological hallmarks and MRI cortical atrophy were found in the AD group, and not in controls. In AD, A β and p-tau load contributed differently to cortical thickness: A β associated weakly and diffusely with reduced cortical atrophy, while p-tau accumulation strongly associated with specific regional cortical atrophy. In the cortex of AD donors, the strongest contributors to cortical atrophy were p-tau load in the frontal and temporal cortices, and reactive microglia load in the parietal region.

On MRI, our AD cohort showed pronounced cortical atrophy in the temporoparietal region of the left hemisphere, consistent with the classic AD signature and independent of the phenotypical presentation [37, 38, 49].

We found a higher A β load in both AD phenotypes compared to controls, but we did not observe a difference in A β load nor distribution between AD phenotypes, which is in line with previous studies [7, 38]. Furthermore, we found a high p-tau load in AD excluding the occipital cortex, consistent with the fact that this region is the last affected according to Braak NFT staging [10]. We did not find any significant differences in p-tau load nor distribution in clinically-defined AD

phenotypes, although a difference in distribution has been described previously [7, 34, 41, 43]. However, most of those studies used pathologically-defined AD donors as opposite to our clinically-defined cohort [7, 34, 43], and the only study that used clinically-defined phenotypes did not find any significant difference in NFT load or distribution in the B/D variant compared to typical AD cases [41], which represents 6 out of 9 cases of our atypical AD cohort.

In line with the literature [2, 20], we show that atypical AD cases had a higher reactive microglia load compared to controls. Our results indicate that neuroinflammation not only tends to be stronger in relatively younger compared to older AD patients [21], but that this also differs per subtype [8]. As such, the underlying disease mechanisms that lead to an increased inflammatory response remains to be elucidated.

When associating our MRI findings with AD pathological hallmarks, we found a weak positive association between $A\beta$ load and cortical thickness in AD, suggesting that a higher $A\beta$ load associated to a slightly decreased global cortical atrophy. Previous studies also reported that $A\beta$ deposition is widespread across the cortex in AD, however they were not consistent in the association with cortical atrophy nor in the direction of the association. Some PET studies showed no correlation between $A\beta$ and cortical thickness or grey matter volume [36, 38, 48, 50], while other cerebrospinal fluid (CSF) studies found a - similar to us - positive correlation [17, 19, 26, 32, 40]. The latter argued the existence of a “two-phase phenomenon” along the AD continuum, according to which cortical thickness follows a biphasic trajectory: in preclinical phases there is a cortical thickening, suggesting a relationship with amyloid deposition, and in the late clinical phases cortical atrophy occurs, indicating the (additional) influence of p-tau accumulation [17, 19, 24, 26, 32, 40]. Our results being similar to these latter CSF studies is not due to the inclusion of preclinical AD cases, since the positive association was found in our clinical AD group, but more likely due to the use of immunohistochemical quantification. In fact, immunohistochemistry is sensitive to pick up even small diffuse accumulations of $A\beta$ (which is limited with PET imaging [11, 23, 45]). Therefore, it is possible that our study revealed a positive association between $A\beta$ and cortical thickness in late clinical AD similar to preclinical AD.

We found that the regional increase in p-tau load strongly associated with cortical atrophy in frontal and temporal regions in AD (Fig. 5). These results are in line with several tau PET studies which reported regional correlations

between tau tracer uptake and cortical thickness or grey matter volume [30, 36, 38, 39, 48, 50]. Even if the exact mechanisms of p-tau-mediated neurodegeneration are still unclear, p-tau has been shown to be closely related to axonal transports deficits and neuronal and synaptic loss, leading to volume loss, hence cortical atrophy [47]. A striking finding in our study is the variance in cortical thickness explained by p-tau load, which ranges between 58% in the superior frontal gyrus to 100% in the middle frontal gyrus, suggesting that p-tau load is indeed one of the main contributors to cortical atrophy in AD. While temporal regions are expected to be hit by p-tau-associated atrophy in AD [37], our results indicate that frontal regions are also particularly vulnerable to p-tau pathology, which might be due to our inclusion of atypical AD cases of the B/D phenotype.

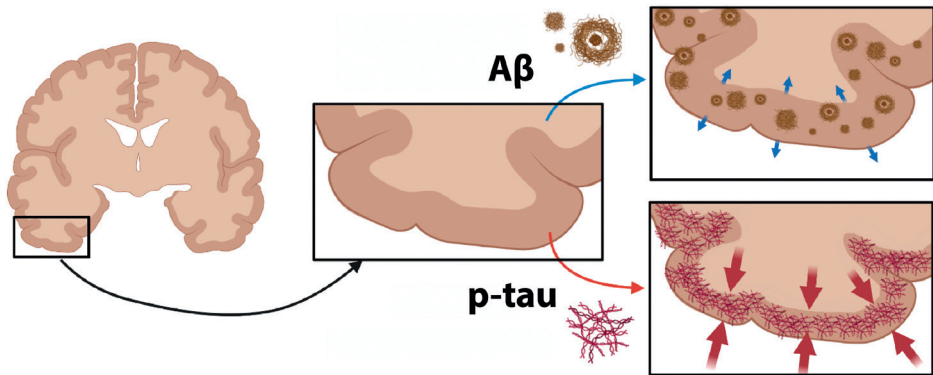


Fig. 5. Summary Figure differential effects of p-tau and A β load on cortical thickness in AD. A β weakly correlates with a reduced cortical atrophy (**top**; small blue arrows), while p-tau load strongly correlates with cortical atrophy (**bottom**; big red arrows) in AD.

We found a strong association between reactive microglia load and cortical atrophy in the parietal region in AD. Similar findings have been reported in a PET study, where the PET marker $^{11}\text{CPK11195}$ for microglial activation correlated with parieto-occipital thinning in AD, including the inferior parietal gyrus [35]. The temporoparietal region reveals neuroinflammation in AD [44], which can contribute to structural damage. Since the temporal region is one of the first to be affected [10], any correlational analysis with structural imaging is likely to suffer from a floor effect in end-stage AD cases [35]. Therefore, cortical thinning is, most likely, significantly correlated with neuroinflammation only in parietal areas. When chronically activated, microglia tend to transform to a dystrophic, senescent phenotype, which brings them to lose their neuroprotective functions and to become detrimental and neurotoxic, thus accelerating the disease course

[20]. Senescent reactive microglia are known to release cytokines, reactive oxygen species and pro-inflammatory factors [2], which can contribute to synaptic and neuronal loss [20], hence neurodegeneration.

To further validate our results, we explored the correlation between post mortem and ante mortem cortical thickness extrapolated from scans acquired shortly before death and several years prior to it, and its correlation to histopathology. Our findings show that post mortem in situ scans showed high concordance with ante mortem in vivo scans acquired few months prior to death. On the other hand, when the ante mortem scans were acquired with increasing years before death, the associations showed increasing discrepancies. To conclude, this confirms that cortical thickness derived from post mortem MRI can be used as a proxy for that of in vivo MRI [9].

The main strength of this study is that MRI and gold-standard immunohistological data were collected from the same donor at the same moment in time. All donors had pathological confirmation of clinical diagnosis, as clinical-pathological discrepancies occur in 10% of cases [22], and may obscure in vivo studies. In addition, comprehensive clinical and pathological datasets were available, and both ante mortem and post mortem MRI were collected for a subset of patients, making this study encompassing clinical, pathological, and radiological data. However, there are also limitations, such as the small group sample sizes, the heterogeneity of our atypical AD cohort, and the fact that the ante mortem MRI scans have not been collected systematically, having therefore slightly different parameters. Additionally, since we used only one antibody for p-tau, glial and neuronal tau could not be differentiated, and similarly, different A β variants were not differentiated. Moreover, we investigated three markers that might contribute to cortical thickness changes, while it is likely that also other cellular and molecular components contribute to cortical atrophy, such as synaptic and axonal degeneration. Future research should therefore investigate the MRI-pathology associations in a larger cohort and include more neurodegenerative markers to further validate MRI atrophy patterns in AD.

Taken together, our findings show that in AD, A β load correlates to a reduced global cortical atrophy, while p-tau load is the strongest contributor to regional cortical atrophy in fronto-temporal regions, and reactive microglia load is a strong correlate of cortical atrophy in the parietal region. An exploration within AD phenotypes showed an increased reactive microglia load in atypical AD, but not in typical AD, even though no or only subtle differences were found in

MRI-pathology associations, indicating that the histopathological correlates of cortical atrophy might be similar between AD phenotypes included in our study. Moreover, we show that post mortem in situ MRI derived cortical thickness can be used as proxy for ante mortem in vivo MRI. In conclusion, our results show that distinct histopathological markers correlate differently with cortical atrophy, highlighting their different roles in the neurodegenerative process, therefore contributing to the understanding of the pathological underpinnings of MRI atrophic patterns.

ACKNOWLEDGEMENTS

We would like to thank all brain donors and their next of kin for brain donation, the NBB and NABCA autopsy teams, Tjado HJ Morrema and Danae de Gooijer for cutting sections, and Martijn Steenwijk for the lesion filling MRI script. FB is supported by the NIHR biomedical research centre at UCLH. This study was funded by PAGE-AD Alzheimer Association (Research Fellowship AARF-18-566,459), ZonMW Memorabel (grant # 733050102), and MJFF (grant # 17253).

LIST OF ABBREVIATIONS

| | |
|-----------|--|
| A β | amyloid-beta |
| AD | Alzheimer's disease |
| B/D | behavioural/dysexecutive variant |
| BNE | Brain Net Europe II |
| CSF | cerebrospinal fluid |
| DAB | 3,3'-diaminobenzidine tetrahydrochloride |
| FDR | false discovery rate |
| LMM | linear mixed models |
| MRI | magnetic resonance imaging |
| NABCA | Normal Aging Brain Collection Amsterdam |
| NBB | Netherlands Brain Bank |
| NFT | neurofibrillary tangles |
| p-tau | phosphorylated tau |
| PCA | posterior cortical atrophy |
| PET | positron emission tomography |
| ROI | region of interest |

REFERENCES

1. Adler DH, Pluta J, Kadivar S, Craige C, Gee JC, Avants BB, Yushkevich PA (2014) Histology-derived volumetric annotation of the human hippocampal subfields in postmortem MRI. *Neuroimage* 84:505–523. doi: 10.1016/j.neuroimage.2013.08.067
2. Akiyama H, Barger S, Barnum S, Bradt B, Bauer J, Cole GM, Cooper NR, Eikelenboom P, Emmerling M, Fiebich BL, Finch CE, Frautschy S, Griffin WST, Hampel H, Hull M, Landreth G, Lue LF, Mrazek R, MacKenzie IR, McGeer PL, O'Banion MK, Pachter J, Pasinetti G, Plata-Salaman C, Rogers J, Rydel R, Shen Y, Streit W, Strohmeyer R, Tooyoma I, Van Muiswinkel FL, Veerhuis R, Walker D, Webster S, Wegrzyniak B, Wenk G, Wyss-Coray T (2000) Inflammation and Alzheimer's disease. *Neurobiol. Aging* 21:383–421
3. Alafuzoff I, Arzberger T, Al-Sarraj S, Bodi I, Bogdanovic N, Braak H, Bugiani O, Del-Tredici K, Ferrer I, Gelpi E, Giaccone G, Graeber MB, Ince P, Kamphorst W, King A, Korkolopoulou P, Kovács GG, Larionov S, Meyronet D, Monoranu C, Parchi P, Patsouris E, Roggendorf W, Seilhean D, Tagliavini F, Stadelmann C, Streichenberger N, Thal DR, Wharton SB, Kretschmar H (2008) Staging of neurofibrillary pathology in Alzheimer's disease: a study of the BrainNet Europe Consortium. *Brain Pathol* 18:484–96. doi: 10.1111/j.1750-3639.2008.00147.x
4. Alafuzoff I, Thal DR, Arzberger T, Bogdanovic N, Al-Sarraj S, Bodi I, Boluda S, Bugiani O, Duyckaerts C, Gelpi E, Gentleman S, Giaccone G, Graeber M, Hortobagyi T, Höftberger R, Ince P, Ironside JW, Kavantzias N, King A, Korkolopoulou P, Kovács GG, Meyronet D, Monoranu C, Nilsson T, Parchi P, Patsouris E, Pikkarainen M, Revesz T, Rozemuller A, Seilhean D, Schulz-Schaeffer W, Streichenberger N, Wharton SB, Kretschmar H (2009) Assessment of β -amyloid deposits in human brain: A study of the BrainNet Europe Consortium. *Acta Neuropathol* 117:309–320. doi: 10.1007/s00401-009-0485-4
5. Arendt T, Morawski M, Gärtner U, Fröhlich N, Schulze F, Wohmann N, Jäger C, Eisenlöffel C, Gertz H-J, Mueller W, Brauer K (2016) Inhomogeneous distribution of Alzheimer pathology along the isocortical relief. Are cortical convolutions an Achilles heel of evolution? *Brain Pathol* 5:603–611. doi: 10.1111/bpa.12442
6. Benjamini Y, Hochberg Y (1995) Controlling the False Discovery Rate: A Practical and Powerful Approach to Multiple Testing. *J R Stat Soc Ser B* 57:289–300. doi: 10.1111/j.2517-6161.1995.tb02031.x
7. Boon BDC, Hoozemans JJM, Lopuhaä B, Eigenhuis KN, Scheltens P, Kamphorst W, Rozemuller AJM, Bouwman FH (2018) Neuroinflammation is increased in the parietal cortex of atypical Alzheimer's disease. *J Neuroinflammation* 15:170. doi: 10.1186/s12974-018-1180-y
8. Boon BDC, Hoozemans JJM, Lopuhaä B, Eigenhuis KN, Scheltens P, Kamphorst W, Rozemuller AJM, Bouwman FH (2018) Neuroinflammation is increased in the parietal cortex of atypical Alzheimer's disease. *J Neuroinflammation* 15:170. doi: 10.1186/s12974-018-1180-y

9. Boon BDC, Pouwels PJW, Jonkman LE, Keijzer MJ, Preziosa P, van de Berg WDJ, Geurts JJG, Scheltens P, Barkhof F, Rozemuller AJM, Bouwman FH, Steenwijk MD (2019) Can post-mortem MRI be used as a proxy for in vivo? A case study. *Brain Commun* 1:1-10. doi: 10.1093/braincomms/fcz030
10. Braak H, Braak E Neuropathological staging of Alzheimer-related changes. *Acta Neuropathol* 82:239-259. doi: 10.1007/BF00308809
11. Cairns NJ, Ikonomic MD, Benzinger T, Storandt M, Fagan AM, Shah AR, Reinwald LT, Carter D, Felton A, Holtzman DM, Mintun MA, Klunk WE, Morris JC (2009) Absence of Pittsburgh compound B detection of cerebral amyloid β in a patient with clinical, cognitive, and cerebrospinal fluid markers of Alzheimer disease: A case report. *Arch Neurol* 66:1557-1562. doi: 10.1001/archneurol.2009.279
12. Crutch SJ, Schott JM, Lehmann M, Primativo S, Rossor MN, Ryan NS, Shakespeare TJ, Suárez González A, Yong KXX, Fox NC, Rabinovici GD, Lehmann M, Murray M, Snowden JS, Snowden JS, van der Flier WM, Pijnenburg Y, Scheltens P, van der Flier WM, Pijnenburg Y, Scheltens P, Dickerson BC, Vandenberghe R, Ahmed S, Butler C, Bak TH, Boeve BF, Graff-Radford J, Cappa SF, Ceccaldi M, de Souza LC, Dubois B, Felician O, Felician O, Galasko D, Graff-Radford NR, Hof PR, Hof PR, Krolak-Salmon P, Magnin E, Mendez MF, Nestor PJ, Onyike CU, Pelak VS, Pelak VS, Suárez González A, Tang-Wai DF, Carrillo M (2017) Consensus classification of posterior cortical atrophy. *Alzheimer's Dement* 13:870-884. doi: 10.1016/j.jalz.2017.01.014
13. Dale AM, Fischl B, Sereno MI (1999) Cortical surface-based analysis: I. Segmentation and surface reconstruction. *Neuroimage* 9:179-194. doi: 10.1006/ning.1998.0395
14. Daniela Femminella G, Dani M, Wood M, Fan Z, Calsolaro V, Atkinson R, Edginton T, Hinz R, Brooks DJ, Edison P (2019) Microglial activation in early Alzheimer trajectory is associated with higher gray matter volume. doi: 10.1212/WNL.0000000000007133
15. Dubois B, Feldman HH, Jacova C, Hampel H, Molinuevo JL, Blennow K, DeKosky ST, Gauthier S, Selkoe D, Bateman R, Cappa S, Crutch S, Engelborghs S, Frisoni GB, Fox NC, Galasko D, Habert M-O, Jicha GA, Nordberg A, Pasquier F, Rabinovici G, Robert P, Rowe C, Salloway S, Sarazin M, Epelbaum S, de Souza LC, Vellas B, Visser PJ, Schneider L, Stern Y, Scheltens P, Cummings JL (2014) Advancing research diagnostic criteria for Alzheimer's disease: the IWG-2 criteria. *Lancet Neurol* 13:614-629. doi: 10.1016/S1474-4422(14)70090-0
16. Van Der Flier WM, Scheltens P (2018) Amsterdam dementia cohort: Performing research to optimize care. *J. Alzheimer's Dis.* 62:1091-1111
17. Fortea J, Vilaplana E, Alcolea D, Carmona-Iragui M, Sánchez-Saudinos MB, Sala I, Antón-Aguirre S, González S, Medrano S, Pegueroles J, Morenas E, Clarimón J, Blesa R, Lleó A (2014) Cerebrospinal fluid β -amyloid and phospho-tau biomarker interactions affecting brain structure in preclinical Alzheimer disease. *Ann Neurol* 76:223-230. doi: 10.1002/ana.24186
18. Graff-Radford J, Yong KXX, Apostolova LG, Bouwman FH, Carrillo M, Dickerson BC, Rabinovici GD, Schott JM, Jones DT, Murray ME (2021) New insights into atypical Alzheimer's disease in the era of biomarkers. *Lancet Neurol.* 20:222-234

19. Harrison TM, Du R, Klencklen G, Baker SL, Jagust WJ (2020) Distinct effects of beta-amyloid and tau on cortical thickness in cognitively healthy older adults. *Alzheimer's Dement* alz.12249. doi: 10.1002/alz.12249
20. Heppner FL, Ransohoff RM, Becher B (2015) Immune attack: The role of inflammation in Alzheimer disease. *Nat. Rev. Neurosci.* 16:358–372
21. Hoozemans JJ, Rozemuller AJ, van Haastert ES, Eikelenboom P, van Gool WA (2011) Neuroinflammation in Alzheimer's disease wanes with age. *J Neuroinflammation* 8:171. doi: 10.1186/1742-2094-8-171
22. Ikonomic MD, Buckley CJ, Heurling K, Sherwin P, Jones PA, Zanette M, Mathis CA, Klunk WE, Chakrabarty A, Ironside J, Ismail A, Smith C, Thal DR, Beach TG, Farrar G, Smith APL (2016) Post-mortem histopathology underlying β -amyloid PET imaging following flutemetamol F 18 injection. *Acta Neuropathol Commun* 4:130. doi: 10.1186/s40478-016-0399-z
23. Ikonomic MD, Klunk WE, Abrahamson EE, Mathis CA, Price JC, Tsopelas ND, Lopresti BJ, Ziolkowski S, Bi W, Paljug WR, Debnath ML, Hope CE, Isanski BA, Hamilton RL, DeKosky ST (2008) Post-mortem correlates of in vivo PiB-PET amyloid imaging in a typical case of Alzheimer's disease. *Brain* 131:1630–1645. doi: 10.1093/brain/awn016
24. Ingala S, De Boer C, Masselink LA, Vergari I, Lorenzini L, Blennow K, Chételat G, Di Perri C, Ewers M, van der Flier WM, Fox NC, Gispert JD, Haller S, Molinuevo JL, Muniz-Terrera G, Mutsaerts HJMM, Ritchie CW, Ritchie K, Schmidt M, Schwarz AJ, Vermunt L, Waldman AD, Wardlaw J, Wink AM, Wolz R, Wottschel V, Scheltens P, Visser PJ, Barkhof F (2021) Application of the ATN classification scheme in a population without dementia: Findings from the EPAD cohort. *Alzheimer's Dement.* doi: 10.1002/alz.12292
25. Jack CR, Lowe VJ, Senjem ML, Weigand SD, Kemp BJ, Shiung MM, Knopman DS, Boeve BF, Klunk WE, Mathis CA, Petersen RC (2008) 11C PiB and structural MRI provide complementary information in imaging of Alzheimer's disease and amnesic mild cognitive impairment. *Brain* 131:665–680. doi: 10.1093/brain/awn336
26. Johnson SC, Christian BT, Okonkwo OC, Oh JM, Harding S, Xu G, Hillmer AT, Wooten DW, Murali D, Barnhart TE, Hall LT, Racine AM, Klunk WE, Mathis CA, Bendlin BB, Gallagher CL, Carlsson CM, Rowley HA, Hermann BP, Dowling NM, Asthana S, Sager MA (2014) Amyloid burden and neural function in people at risk for Alzheimer's Disease. *Neurobiol Aging* 35:576–584. doi: 10.1016/j.neurobiolaging.2013.09.028
27. Jonkman LE, Graaf YG de, Bulk M, Kaaij E, Pouwels PJW, Barkhof F, Rozemuller AJM, van der Weerd L, Geurts JGG, van de Berg WDJ (2019) Normal Aging Brain Collection Amsterdam (NABCA): A comprehensive collection of postmortem high-field imaging, neuropathological and morphometric datasets of non-neurological controls. *NeuroImage Clin* 22. doi: 10.1016/j.nicl.2019.101698
28. Jonkman LE, Kenkhuis B, Geurts JGG, van de Berg WDJ (2019) Post-Mortem MRI and Histopathology in Neurologic Disease: A Translational Approach. *Neurosci Bull* 35:229–243. doi: 10.1007/s12264-019-00342-3

29. Kapur JN, Sahoo PK, Wong AKC (1985) A new method for gray-level picture thresholding using the entropy of the histogram. *Comput Vision, Graph Image Process* 29:273–285. doi: 10.1016/0734-189X(85)90125-2
30. Mak E, Bethlehem RAI, Romero-Garcia R, Cervenka S, Rittman T, Gabel S, Surendranathan A, Bevan-Jones RW, Passamonti L, Vázquez Rodríguez P, Su L, Arnold R, Williams GB, Hong YT, Fryer TD, Aigbirhio FI, Rowe JB, O'Brien JT (2018) In vivo coupling of tau pathology and cortical thinning in Alzheimer's disease. *Alzheimer's Dement Diagnosis, Assess Dis Monit* 10:678–687. doi: 10.1016/j.dadm.2018.08.005
31. Mirra SS, Heyman A, McKeel D, Sumi SM, Crain BJ, Brownlee LM, Vogel FS, Hughes JP, van Belle G, Berg L, Ball MJ, Bierer LM, Claassen D, Hansen LR, Hart M, Hedreen J, Baltimore B, Hen Derson V, Hyman BT, Joachim C, Mark-Esbery W, Mar Tinez AJ, McKee A, Miller C, Moossy J, Nochlin D, Perl D, Petito C, Rao GR, Schelper RL, Slager U, Terry RD (1991) The consortium to establish a registry for Alzheimer's disease (CERAD). Part II. Standardization of the neuropathologic assessment of Alzheimer's disease. *Neurology* 41:479–486. doi: 10.1212/wnl.41.4.479
32. Montal V, Vilaplana E, Alcolea D, Pegueroles J, Pasternak O, González-Ortiz S, Clarimón J, Carmona-Iragui M, Illán-Gala I, Morenas-Rodríguez E, Ribosa-Nogué R, Sala I, Sánchez-Saudinós MB, García-Sebastian M, Villanúa J, Izagirre A, Estanga A, Ecay-Torres M, Iriondo A, Clerigue M, Tainta M, Pozueta A, González A, Martínez-Heras E, Llufríu S, Blesa R, Sanchez-Juan P, Martínez-Lage P, Lleó A, Fortea J (2018) Cortical microstructural changes along the Alzheimer's disease continuum. *Alzheimer's Dement* 14:340–351. doi: 10.1016/j.jalz.2017.09.013
33. Montine TJ, Phelps CH, Beach TG, Bigio EH, Cairns NJ, Dickson DW, Duyckaerts C, Frosch MP, Masliah E, Mirra SS, Nelson PT, Schneider JA, Thal DR, Trojanowski JQ, Vinters H V, Hyman BT, National Institute on Aging, Alzheimer's Association (2012) National Institute on Aging-Alzheimer's Association guidelines for the neuropathologic assessment of Alzheimer's disease: a practical approach. *Acta Neuropathol* 123:1–11. doi: 10.1007/s00401-011-0910-3
34. Murray ME, Graff-Radford NR, Ross OA, Petersen RC, Duara R, Dickson DW (2011) Neuropathologically defined subtypes of Alzheimer's disease with distinct clinical characteristics: a retrospective study. *Lancet Neurol* 10:785–796. doi: 10.1016/S1474-4422(11)70156-9
35. Nicastro N, Malpetti M, Mak E, Williams GB, Bevan-Jones WR, Carter SF, Passamonti L, Fryer TD, Hong YT, Aigbirhio FI, Rowe JB, O'Brien JT (2020) Gray matter changes related to microglial activation in Alzheimer's disease. *Neurobiol Aging* 94:236–242. doi: 10.1016/j.neurobiolaging.2020.06.010
36. Ossenkoppele R, Lyoo CH, Sudre CH, van Westen D, Cho H, Ryu YH, Choi JY, Smith R, Strandberg O, Palmqvist S, Westman E, Tsai R, Kramer J, Boxer AL, Gorno-Tempini ML, La Joie R, Miller BL, Rabinovici GD, Hansson O (2020) Distinct tau PET patterns in atrophy-defined subtypes of Alzheimer's disease. *Alzheimer's Dement* 16:335–344. doi: 10.1016/j.jalz.2019.08.201

37. Ossenkoppele R, Pijnenburg YAL, Perry DC, Cohn-Sheehy BI, Scheltens NME, Vogel JW, Kramer JH, Van Der Vlies AE, Joie R La, Rosen HJ, Van Der Flier WM, Grinberg LT, Rozemuller AJ, Huang EJ, Van Berckel BNM, Miller BL, Barkhof F, Jagust WJ, Scheltens P, Seeley WW, Rabinovici GD (2015) The behavioural/dysexecutive variant of Alzheimer's disease: Clinical, neuroimaging and pathological features. *Brain* 138:2732-2749. doi: 10.1093/brain/awv191
38. Ossenkoppele R, Schonhaut DR, Schöll M, Lockhart SN, Ayakta N, Baker SL, O'Neil JP, Janabi M, Lazaris A, Cantwell A, Vogel J, Santos M, Miller ZA, Bettcher BM, Vossel KA, Kramer JH, Gorno-Tempini ML, Miller BL, Jagust WJ, Rabinovici GD (2016) Tau PET patterns mirror clinical and neuroanatomical variability in Alzheimer's disease. *Brain* 139:1551-1567. doi: 10.1093/brain/aww027
39. Ossenkoppele R, Smith R, Ohlsson T, Strandberg O, Mattsson N, Insel PS, Palmqvist S, Hansson O (2019) Associations between tau, A β , and cortical thickness with cognition in Alzheimer disease. *Neurology* 92:e601-e612. doi: 10.1212/WNL.0000000000006875
40. Pegueroles J, Vilaplana E, Montal V, Sampedro F, Alcolea D, Carmona-Iragui M, Clarimon J, Blesa R, Lleó A, Fortea J (2017) Longitudinal brain structural changes in preclinical Alzheimer's disease. *Alzheimer's Dement* 13:499-509. doi: 10.1016/j.jalz.2016.08.010
41. Petersen C, Nolan AL, de Paula França Resende E, Miller Z, Ehrenberg AJ, Gorno-Tempini ML, Rosen HJ, Kramer JH, Spina S, Rabinovici GD, Miller BL, Seeley WW, Heinsen H, Grinberg LT (2019) Alzheimer's disease clinical variants show distinct regional patterns of neurofibrillary tangle accumulation. *Acta Neuropathol* 138:597-612. doi: 10.1007/s00401-019-02036-6
42. Rabinovici GD, Jagust WJ, Furst AJ, Ogar JM, Racine CA, Mormino EC, O'Neil JP, Lal RA, Dronkers NF, Miller BL, Gorno-Tempini ML (2008) A β amyloid and glucose metabolism in three variants of primary progressive aphasia. *Ann Neurol* 64:388-401. doi: 10.1002/ana.21451
43. Tang-Wai DF, Graff-Radford NR, Boeve BF, Dickson DW, Parisi JE, Crook R, Caselli RJ, Knopman DS, Petersen RC (2004) Clinical, genetic, and neuropathologic characteristics of posterior cortical atrophy. *Neurology* 63:1168-74. doi: 10.1212/01.WNL.0000140289.18472.15
44. Terada T, Yokokura M, Obi T, Bunai T, Yoshikawa E, Ando I, Shimada H, Suhara T, Higuchi M, Ouchi Y (2019) In vivo direct relation of tau pathology with neuroinflammation in early Alzheimer's disease. *J Neurol* 266:2186-2196. doi: 10.1007/s00415-019-09400-2
45. Thal DR, Attems J, Ewers M (2014) Spreading of amyloid, tau, and microvascular pathology in Alzheimer's disease: Findings from neuropathological and neuroimaging studies. *J. Alzheimer's Dis.* 42:S421-S429
46. Thal DR, Rüb U, Orantes M, Braak H (2002) Phases of A β -deposition in the human brain and its relevance for the development of AD. *Neurology* 58:1791-1800. doi: 10.1212/WNL.58.12.1791

47. Wang Y, Mandelkow E (2016) Tau in physiology and pathology. *Nat. Rev. Neurosci.* 17:5–21
48. Whitwell JL, Graff-Radford J, Tosakulwong N, Weigand SD, Machulda MM, Senjem ML, Spychalla AJ, Vemuri P, Jones DT, Drubach DA, Knopman DS, Boeve BF, Ertekin-Taner N, Petersen RC, Lowe VJ, Jack CR, Josephs KA (2018) Imaging correlations of tau, amyloid, metabolism, and atrophy in typical and atypical Alzheimer's disease. *Alzheimer's Dement* 14:1005–1014. doi: 10.1016/j.jalz.2018.02.020
49. Whitwell JL, Jack CR, Przybelski SA, Parisi JE, Senjem ML, Boeve BF, Knopman DS, Petersen RC, Dickson DW, Josephs KA (2011) Temporoparietal atrophy: A marker of AD pathology independent of clinical diagnosis. *Neurobiol Aging* 32:1531–1541. doi: 10.1016/j.neurobiolaging.2009.10.012
50. Xia C, Makaretz SJ, Caso C, McGinnis S, Gomperts SN, Sepulcre J, Gomez-Isla T, Hyman BT, Schultz A, Vasdev N, Johnson KA, Dickerson BC (2017) Association of in vivo [18F]AV-1451 tau PET imaging results with cortical atrophy and symptoms in typical and atypical Alzheimer disease. *JAMA Neurol* 74:427–436. doi: 10.1001/jamaneurol.2016.5755

SUPPLEMENTARY DATA

MRI acquisition

The following post mortem sequences were acquired for all subjects: i) a sagittal 3D T1-weighted fast spoiled gradient echo sequence (repetition time (TR) = 7 ms, echo time (TE) = 3 ms, flip angle = 15°, 1-mm-thick axial slices, in-plane resolution= 1.0 × 1.0 mm²); ii) and a sagittal 3D fluid attenuation inversion recovery (FLAIR) sequence (TR = 8000 ms, TE = 130 ms, inversion time (TI) = 2000-2500 ms, 1.2-mm-thick axial slices, in-plane resolution= 1.11 × 1.11 mm²), with TI corrected for post mortem delay (PMD). Subsequently to MRI acquisition, the autopsy was immediately performed, resulting in a total PMD within 10 hours for all brain donors.

Ante mortem sequences were retrospectively obtained from the Amsterdam Dementia Cohort, from two different scanners (3T GE MR750 and Philips 3T Achieva). The parameters were slightly different between scanners, with TR varying between 7.8 and 7.9 ms, and TE between 2.9 and 5.2 ms, and voxel size was fixed at 1mm³ (Table S2 for the sequence details).

Filling of white matter hyperintensities on MRI

Post mortem T1w images were lesion filled to reduce lesion effects on subsequent automated segmentations. Segmentation of white matter abnormalities was performed on FLAIR images using multi-view convolutional neural network with batch normalization followed by manual editing, obtaining lesion maps, which were registered to the 3D T1 images. The refilling of the lesions was done using LEAP [1].

MRI cortical thickness assessment

Images underwent inhomogeneity correction, removal of non-brain tissue, and segmentation into grey and white matter. Parcellation of the brain was done using the Desikan-Killany atlas [2]. Cortical thickness was measured as the distance from the grey/white matter boundary to corresponding pial surface. The reconstructed datasets were visually inspected, and segmentation errors were corrected.

MRI brain volume assessment

For all donors, post mortem normalized brain volume, normalized grey, and white matter volumes were measured from the T1w images using Structural Image Evaluation, using Normalisation, of Atrophy (SIENAX) (part of FSL 5.0.9;

<http://fsl.fmrib.ox.ac.uk/>), which estimates brain tissue volume normalized for skull size [3].

Immunohistochemistry (IHC)

The sections were cut and mounted on superfrost+ glass slides (Thermo Scientific, USA). The sections were blocked for endogenous peroxidase using 0.3% hydrogen peroxide and 0.1% sodium azide in phosphate buffer saline (PBS; pH 7.4). The sections were immersed in 10mM Citrate buffer pH 6.0 and heated to 120°C in an autoclave for antigen retrieval. Primary antibodies were diluted (as indicated in Table S2) in normal antibody diluent (ImmunoLogic, Duiven, The Netherlands) and incubated overnight at 4°C. Primary antibodies were detected using EnVision (Dako, Glostrup, Denmark). Afterwards, antibodies were visualized using 3,3'-Diaminobenzidine (DAB, Dako) with Imidazole (50 mg DAB, 350 mg Imidazole and 30 μ L of H₂O₂ per 100 mL of Tris-HCl 30mM, pH 7.6). In between steps, PBS was used to wash the sections. After counterstaining with haematoxylin, the sections were mounted with Entellan (Merck, Darmstadt, Germany). To visualize the line of Gennari in the occipital cortex and therefore identify the striate area, we further performed a Kluver staining on these sections.

Statistics

Normality was tested, and subsequently demographics between AD and controls, and between typical and atypical AD, were compared using a Student t-test or Mann-Whitney U test for continuous data, and Fisher exact test for categorical data. The association between cortical thickness and Braak stages/Thal phases was calculated with Spearman's correlation. MRI-pathology associations were carried out firstly in the whole cohort to investigate whether they were independent of diagnosis, then in the AD and control group separately, and then within AD phenotype groups with age, gender and PMD as covariates.

REFERENCES SUPPLEMENTARY DATA

1. Chard DT, Jackson JS, Miller DH, Wheeler-Kingshott CAM (2010) Reducing the impact of white matter lesions on automated measures of brain gray and white matter volumes. *J Magn Reson Imaging* 32:223–228. doi: 10.1002/jmri.22214
2. Desikan RS, Ségonne F, Fischl B, Quinn BT, Dickerson BC, Blacker D, Buckner RL, Dale AM, Maguire RP, Hyman BT, Albert MS, Killiany RJ (2006) An automated labeling system for subdividing the human cerebral cortex on MRI scans into gyral based regions of interest. *Neuroimage* 31:968–980. doi: 10.1016/J.NEUROIMAGE.2006.01.021
3. Jenkinson M, Beckmann CF, Behrens TEJ, Woolrich MW, Smith SM (2012) FSL. *Neuroimage* 62:782–90. doi: 10.1016/j.neuroimage.2011.09.015

Chapter 9

Can post mortem MRI be used as a proxy for in vivo? A case study

Baayla DC Boon, Petra JW Pouwels, Laura E Jonkman, Matthijs J Keijzer, Paolo Preziosa, Wilma DJ van de Berg, Jeroen JG Geurts, Philip Scheltens, Frederik Barkhof, Annemieke JM Rozemuller, Femke H Bouwman, Martijn D Steenwijk

Brain Communications (2019)
doi: [10.1093/braincomms/fcz030](https://doi.org/10.1093/braincomms/fcz030)

ABSTRACT

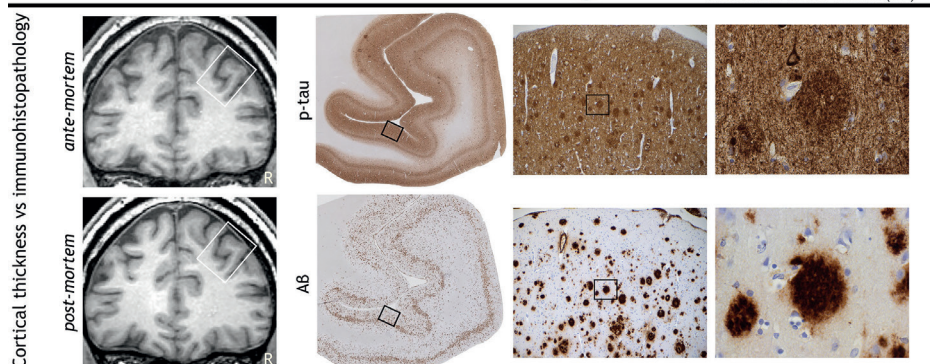
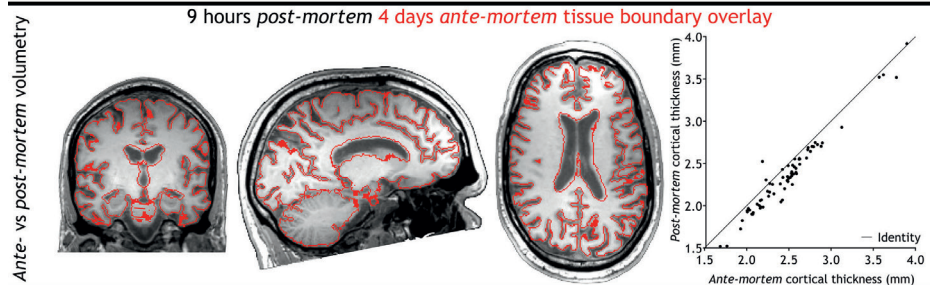
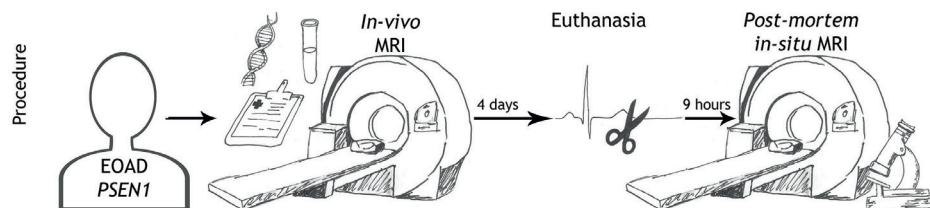
Background: *Post mortem in situ* MRI has been used as an intermediate between brain histo(patho)logy and *in vivo* imaging. However, it is not known how comparable *post mortem in situ* is to *ante mortem* imaging.

Methods: We report the unique situation of a patient with familial early-onset Alzheimer's disease due to a *PSEN1* mutation, who underwent *ante mortem* brain MRI and *post mortem in situ* imaging only 4 days apart. T1-weighted and diffusion MRI was performed at 3-Tesla at both time points. Visual atrophy rating scales, brain volume, cortical thickness, and diffusion measures were derived from both scans and compared.

Results: *Post mortem* visual atrophy scores decreased 0.5-1 point compared with *ante mortem*, indicating an increase in brain volume. This was confirmed by quantitative analysis; showing a 27% decrease of ventricular and 7% increase of whole-brain volume. This increase was more pronounced in the cerebellum and supratentorial white matter than in grey matter. Furthermore, axial and radial diffusivity decreased up to 60% *post mortem* whereas average fractional anisotropy of white matter increased approximately 10%.

Conclusions: This unique case study shows that the process of dying affects several imaging markers. These changes need to be taken into account when interpreting *post mortem* MRI to make inferences on the *in vivo* situation.

GRAPHICAL ABSTRACT



INTRODUCTION

Brain MRI is used to visualize tissue damage in numerous neurological diseases. MRI measures such as atrophy and white matter lesions often correlate with clinical outcome measurements of physical or cognitive disability [21, 29]. However, the nature of the actual underlying pathophysiology of these *in vivo* imaging measurements may vary and requires histopathological validation. Due to the time lag between *in vivo* imaging and histology, several studies have evaluated the sensitivity, specificity, and substrate of *in vivo* imaging markers by combining *post mortem ex cranium* and *in situ* brain MRI with histology [13].

Whether imaging markers obtained from *post mortem* MRI are comparable to those obtained *ante mortem*, has thus far only been studied in animals [2, 20, 28]. However, these animal studies perform *post mortem* imaging after fixation or decapitation, introducing physiological and methodological differences in the *post mortem* to *ante mortem* imaging comparison. Therefore, it remains undefined how comparable human *post mortem* and *ante mortem* imaging is, specifically in the *in situ* situation, which has the brain still *in cranium*, only hours after death.

In this case study, we report on several imaging markers derived 9 h *post mortem in situ*, compared with the *ante mortem* situation, which was obtained 4 days before death.

METHODS

Case study

The patient visited the Alzheimer Center Amsterdam 4 days prior to death, to undergo a research work-up, including a detailed history, cognitive neurological examination, lumbar puncture, genotyping using whole-exome sequencing, and brain MRI. The patient was considered mentally competent in his request for euthanasia, which was granted by his general practitioner, according to the Dutch guidelines [15]. He decided to donate his brain to science via the Netherlands Brain Bank (NBB; Amsterdam, the Netherlands, <https://www.brainbank.nl>), for which he and his wife signed informed consent. In addition, they signed informed consent for this specific case report. The institutional ethics review board of the Amsterdam UMC, location VUmc, approved the study. Euthanasia was performed using thiopental and rocuronium, leading to death 20 min after drug administration. Nine hours after death, MRI was repeated with the brain *in situ*.

MRI acquisition

Both MRI examinations were performed on the same 3-Tesla whole body system (General Electric Discovery MR750, Milwaukee) using an eight-channel phased-array head coil. To assure consistency, the scanning was performed by the same operators (MDS and MJK) using an identical protocol, involving a 3D T1-weighted fast spoiled gradient-recalled echo sequence for tissue segmentation and atrophy quantification (repetition time = 6.7 ms, echo time = 2.9 ms, inversion time = 450 ms, flip angle = 15°, sagittal 1.0 mm slices, and 1 × 1 mm² in-plane resolution), a 3D fluid-attenuated inversion-recovery sequence for detection of white matter hyperintensities (repetition time = 8000 ms, echo time = 130 ms, inversion time = 2350 ms *ante mortem* and 2064 ms *post mortem*, sagittal 1.2 mm slices, and 0.98 × 0.98 mm² in-plane resolution), and a 3D susceptibility-weighted imaging spoiled gradient-recalled echo sequence for visualization of lacunes and microbleeds (repetition time = 31 ms, echo time = 25 ms, flip angle = 15°, slice thickness = 3.0 mm, 0.65 × 0.65 mm² in-plane resolution). The inversion time of the *post mortem* fluid-attenuated inversion-recovery sequence was optimized to compensate for the decrease in temperature and assure good suppression of cerebrospinal fluid (CSF) signal [34]. Finally, 2D echo-planar diffusion-tensor images (repetition time = 8000 ms, echo time = 85 ms, slice thickness = 2.0 mm, 2.0 × 2.0 mm² in-plane resolution) were acquired, including 30 diffusion gradient directions ($b = 900 \text{ s/mm}^2$) and five non-diffusion-weighted measurements. Similar images with bottom-up and top-down phase-encoding directions were acquired to correct for echo-planar imaging distortions. The 3D images were corrected for geometrical distortions due to gradient nonlinearity prior to further analysis.

Visual MRI assessment

Both *ante-* and *post mortem* MRI scans were visually assessed by an experienced neuroradiologist (FB). Blinding was not possible due to a difference in *post mortem* vessel signal (Supplementary Fig. S1). Visual rating scales were scored for: medial temporal lobe atrophy [27], posterior cortical atrophy [16], global cortical atrophy [22], and white matter hyperintensities [6]. In addition, the number of lacunes, microbleeds, and infarcts was scored.

Quantitative MRI assessment

Image analysis was performed by an experienced operator (MDS). In short, white matter lesions were automatically segmented using the kNN-TTP algorithm [32]. To assure correct segmentation, white matter hyperintensity segmentation was manually adjusted by an experienced rater (PP). Then, hypointense regions on

the T1-weighted images were filled with signal intensity of normal white matter to minimize the impact of white matter abnormalities on volume measurements [1]. Subsequently, volumetry and cortical thickness were measured using the longitudinal processing scheme of FreeSurfer 5.3 [24].

At both time points, the diffusion-weighted images were corrected for movement and eddy current distortions, using FMRIB's Diffusion Toolbox (part of FSL 5.0.9: <https://fsl.fmrib.ox.ac.uk>). Subsequently, the fractional anisotropy, mean, axial, and radial diffusivity were calculated. Grey matter and white matter masks from FreeSurfer were linearly registered to diffusion space (FSL FLIRT, six degrees of freedom, nearest neighbour interpolation) and used to calculate average diffusion measures within the grey and white matter. In addition, the skeletonized diffusion data were analysed after applying the tract-based spatial statistics pre-processing pipeline [31]. This allowed us to measure the average diffusion measures within centres of the white matter tracts.

Neuropathological diagnosis

Neuropathological diagnosis was performed according to NIA-AA guidelines (Montine et al., 2012). The extent of Alzheimer's disease pathology was summarized by an 'ABC score', which is a composite of 3 scores: (A) for amyloid-beta ($A\beta$) Thal phase, (B) for Braak stage of neurofibrillary tangles, and (C) for Consortium to Establish a Registry for Alzheimer Disease (CERAD) score of neuritic plaques.

Quantitative immunohistochemistry

Immunohistochemistry was performed for Alzheimer's disease pathology consisting of hyperphosphorylated tau (p-tau; AT8 antibody, Thermo Fisher Scientific) and $A\beta$ (4G8 antibody, Biogen) on formalin-fixed paraffin-embedded tissue sections (6 μ m thick) of the following 11 regions: superior frontal gyrus, medial frontal gyrus, medial temporal gyrus, superior and inferior parietal lobule, precuneus, occipital pole, anterior and posterior cingulate gyrus, hippocampus, and entorhinal cortex from the right hemisphere. After deparaffinization, sections were blocked for endogenous peroxidase using 0.3% H_2O_2 in phosphate buffered saline pH 7.4 (PBS) for 30 min. Antigen retrieval was performed with 10 mM/L pH 6.0 sodium citrate buffer heated by autoclave. Incubation with primary antibodies (AT8, dilution 1:800; 4G8, dilution 1:8000) diluted in normal antibody diluent (Immunologic) was performed overnight at 4°C. EnVision (Agilent Dako) was used as a secondary step. Colour development was accomplished with 3,3'-diaminobenzidine (DAB). Mayers hematoxylin

was used for nuclear counterstaining. Sections were then dehydrated and coverslipped using quick-D (Klinipath). Sections were digitally scanned at 20x using the Vectra Polaris Automated Quantitative Pathology Imaging System (PerkinElmer). Regions of interest (ROI) containing all grey matter layers, were selected in the digital scans, using ImageJ (NIH). Using the ImageJ colour threshold plugin, immunoreactivity for p-tau and A β was quantified as the percentage of DAB-stained area compared to total surface area for each ROI.

Statistical analysis

Pearson's correlation was calculated to assess the correlation between *ante mortem* and *post mortem* cortical thickness. Statistical analysis was performed using IBM SPSS version 22.0 (Armonk, NY, USA).

RESULTS

Case history

The patient was a right-handed 37-yrs-old Caucasian male suffering from Alzheimer's disease. At the age of 32, the patient and his wife noticed loss of oversight and initiative, difficulties in structuring narratives while working as a journalist and less recognition of emotions. The family history reported that the patient's father died of Alzheimer's disease at the age of 44. No other relatives were affected. Neuropsychological examination of the patient at the age of 35 showed concentration difficulties, verbal and visual memory problems, and decreased social cognition. CSF indicated Alzheimer's disease based on decreased A β_{42} and elevated p-tau $_{181}$ levels. Genotyping revealed a heterozygous *PSEN1* mutation (c. 1254G > C). After 5 years of disease progression, living at home became increasingly difficult. When visiting the memory clinic 4 days before death, the patient made a cognitively impaired impression. He was orientated in place but inconsistently orientated in time. He was easily distracted and repeatedly trailed off in the middle of sentences. Praxis was slightly disturbed and psychomotor tempo was slowed. The patient's memory was severely disturbed. In the language domain, word-finding difficulties, semantic paraphasia, and neologisms were observed. In addition, comprehension of spoken language was slightly disturbed. Executive functioning as well as visuoconstruction was impaired. The patient showed disease awareness, but not insight. He scored 17/30 on the Mini-Mental State Examination. Global disease severity was rated as 2.0 on the Clinical Dementia Rating scale [12]. Suffering from his degenerating capabilities and outlook on life with an incurable disease, the patient requested for euthanasia.

Neuropathological diagnosis

Neuropathology confirmed Alzheimer's disease pathology, with maximum stages for A β plaques, neurofibrillary tangles, and neuritic plaques resulting in an A3B3C3 score [19]. Immunohistochemistry for p-tau (AT8) showed pathology mostly in the form of neuritic plaques (Fig. 1). For A β (6F/3D) a wide morphological variety of pathology was seen, including capillary cerebral amyloid angiopathy (type 1; stage 3) [33], classic cored plaques, and compact plaques with a homogenous aspect (Fig. 1). Furthermore, in hematoxylin-eosin (H&E) staining many neurons had shrunken eosophilic cytoplasm and condensed nuclei, indicating hypoxia. Retraction artefacts were seen between cell bodies and myelin or neuropil (Fig. 1), suggesting cellular oedema. Vascular congestion (seen in H&E) was present throughout the brain, indicating vasogenic oedema. These findings point to more extensive agonal changes, which are not seen after acute death [7, 10].

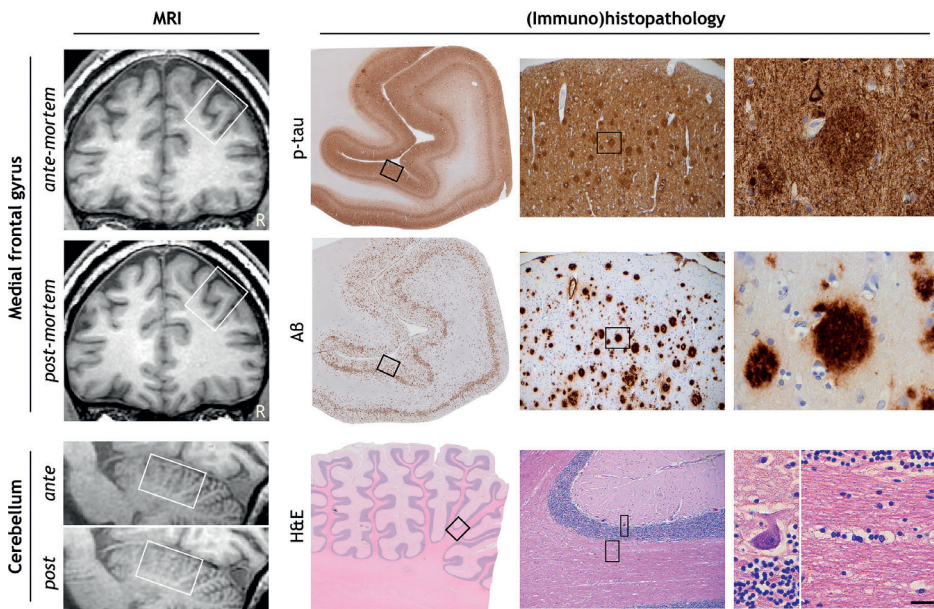


Fig. 1. MRI and corresponding (immuno)histopathology of the presented case. Hyperphosphorylated tau (p-tau; AT8) shows many neuritic plaques, threads, and neurofibrillary tangles in the medial frontal gyrus. Amyloid-beta (A β ; 6F/3D) deposits are mostly found as homogenous compact plaques in the medial frontal gyrus. Hematoxylin-eosin (H&E) staining of the cerebellum shows agonal changes, visualized by shrunken eosinophilic cytoplasm of the Purkinje cell and retraction artefacts enclosing cells in both grey and white matter. Bordered areas represent the image-region of the consecutive column. Bar is applicable to all (immuno)histopathology images and represents 2 mm, 144 μ m, and 23 μ m from left to right in consecutive columns.

Visual MRI assessment

The result of the visual MRI assessment is shown in Table 1. Rating scales for medial temporal lobe atrophy, parietal cortical atrophy, and global cortical atrophy decreased by 0.5 - 1 point *post mortem* compared to *ante mortem*, signifying an increase in brain volume. No clinically meaningful white matter hyperintensities, lacunes, or infarcts were observed on either scan. Although one microbleed was observed on both occasions, the *post mortem* susceptibility-weighted image looked drastically different with a darker vessel signal due to blood stasis and deoxygenation (Supplementary Fig. S1).

Quantitative MRI assessment

Volumetric measures

Results of the volumetric analysis are displayed in Table 1. Fig. 2 and Video 1 show both *ante mortem* and *post mortem* T1-weighted images registered in the same space. Total brain volume increased by 7% *post mortem*. This was mainly driven by an increase in white matter volume (+ 9%) and to a lesser extent by an increase in grey matter volume (+ 5%). The cerebellum showed a relatively large volume increase (+ 13%) compared with total brain volume. Cortical grey matter showed a smaller increase in volume relative to subcortical grey matter structures (+ 3% versus + 7%, respectively). Notably, the increase in cortical grey matter was particularly driven by enlargement of white / grey matter surface (+ 7%) while a thinning of the cortex was observed (- 5%). The cortical thinning was equally pronounced over different areas ($r = 0.975$, $p < 0.001$; see Fig. 3). Except for the putamen (- 8%), all subcortical grey matter structures showed increased volumes, ranging from an increase of 3% in the caudate to 17% in the pallidum.

Diffusion measures

The results of the diffusivity measurements are shown in Table 1. In all tissue compartments, diffusivity measures decreased 50-60% *post mortem* compared with *ante mortem*. Simultaneously, fractional anisotropy increased with 11% in white matter and 25% in grey matter. This increase was driven by a slightly larger relative decrease of radial diffusivity compared with axial diffusivity, especially in grey matter. Tract-based spatial statistics analysis of the white matter skeleton showed an approximately linear relationship between *ante mortem* and *post mortem* diffusion measures throughout the brain (see Supplementary Fig. S2).

Table 1. MRI measurements

| | Ante mortem | Post mortem | Change |
|---|-------------|-------------|-----------|
| <i>Clinical rating scales</i> | | | |
| Medial temporal lobe atrophy [27]; right / left | 1 / 2 | 1 / 1 | - 0.5 |
| Parietal cortical atrophy [16]; right / left | 1 / 2 | 1 / 1 | - 0.5 |
| Global cortical atrophy [22] | 1 | 0 | - 1 |
| White matter hyperintensities [6] | 0 | 0 | 0 |
| Nr of lacunes / microbleeds / infarcts | 0 / 1 / 0 | 0 / 1 / 0 | 0 / 0 / 0 |
| <i>Volumetric measurements</i> | | | |
| Total brain (L) | 1.18 | 1.26 | + 7% |
| White matter abnormality volume (mL) | 2.70 | 2.45 | - 9% |
| Grey matter volume (mL) | 678.40 | 714.70 | + 5% |
| Cortical volume (mL) | 492.90 | 509.00 | + 3% |
| Cortical thickness (mm) | 2.39 | 2.24 | - 6% |
| Cortical surface area (dm ²) | 17.98 | 19.28 | + 7% |
| Subcortical volume (mL) | 58.84 | 63.08 | + 7% |
| Amygdala (mL) ^a | 1.61 | 1.69 | + 5% |
| Caudate (mL) ^a | 4.63 | 4.77 | + 3% |
| Hippocampus (mL) ^a | 4.40 | 4.69 | + 7% |
| Pallidum (mL) ^a | 1.67 | 1.96 | + 17% |
| Putamen (mL) ^a | 4.60 | 4.23 | - 8% |
| Thalamus (mL) ^a | 7.26 | 8.21 | + 13% |
| White matter volume (mL) | 501.70 | 544.90 | + 9% |
| Total cerebellar volume (mL) | 161.70 | 182.20 | + 13% |
| Lateral, 3rd and 4th ventricle volume (mL) | 48.43 | 35.49 | - 27% |
| <i>Diffusion measurements</i> | | | |
| Grey matter | | | |
| Fractional anisotropy | 0.16 | 0.20 | + 25% |
| Mean diffusivity ^b | 110.7 | 50.3 | - 55% |
| Axial diffusivity ^b | 126.5 | 59.2 | - 53% |
| Radial diffusivity ^b | 102.8 | 45.8 | - 56% |
| White matter | | | |
| Fractional anisotropy | 0.34 | 0.38 | + 11% |
| Mean diffusivity ^b | 82.3 | 31.8 | - 61% |
| Axial diffusivity ^b | 114.0 | 44.4 | - 61% |
| Radial diffusivity ^b | 66.5 | 25.5 | - 62% |
| CSF | | | |
| Fractional anisotropy | 0.12 | 0.20 | + 77% |
| Mean diffusivity ^b | 192.5 | 91.2 | - 53% |
| Axial diffusivity ^b | 211.0 | 109.4 | - 48% |
| Radial diffusivity ^b | 183.3 | 82.2 | - 55% |

Table 1. Continued.

| | Ante mortem | Post mortem | Change |
|---------------------------------------|-------------|-------------|--------|
| Tract Based Spatial Statistics | | | |
| Fractional anisotropy | 0.32 | 0.40 | + 23% |
| Mean diffusivity ^b | 94.7 | 36.6 | - 61% |
| Axial diffusivity ^b | 125.9 | 50.5 | - 60% |
| Radial diffusivity ^b | 79.1 | 29.7 | - 63% |

^aVolumes of the left and right structure were averaged. ^bMean, axial, and radial diffusivity are reported in $\times 10^{-5}$ mm²/s. CSF cerebrospinal fluid.

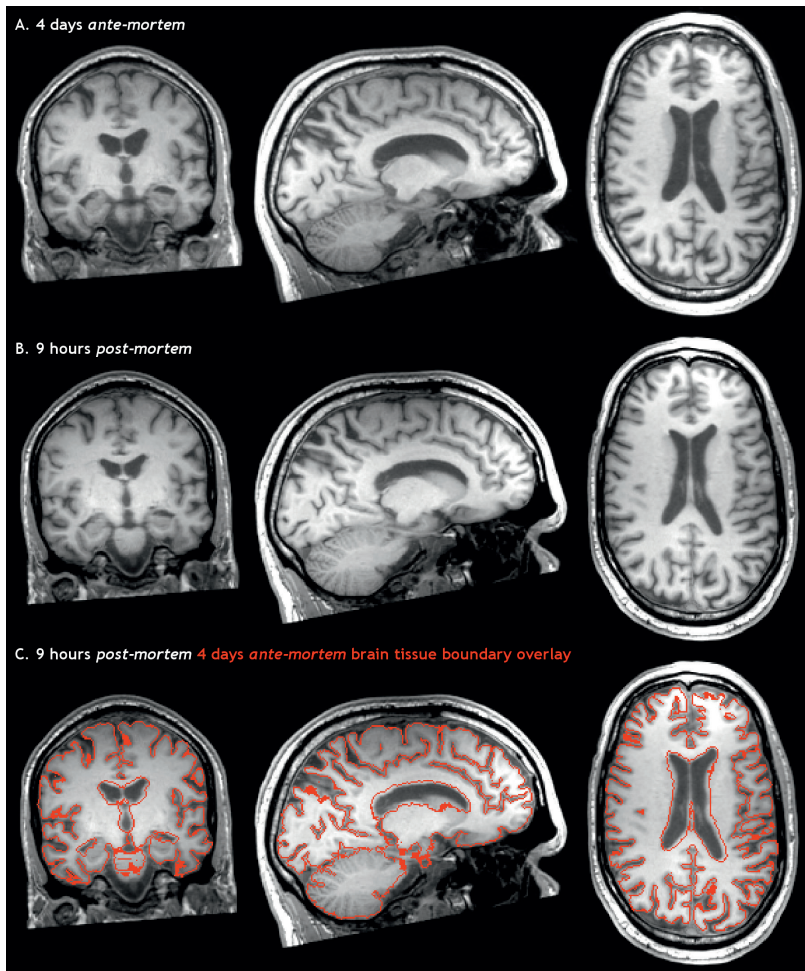


Fig. 2. Ante mortem and post mortem T1-weighted images of the brain 3D T1-weighted images of the brain, 4 days ante mortem (A) and 9 h post mortem (B) registered in the same space. The fusion of both images (C) clearly shows an increase in brain volume post mortem, particularly evident by smaller ventricles and the swollen cerebellum.

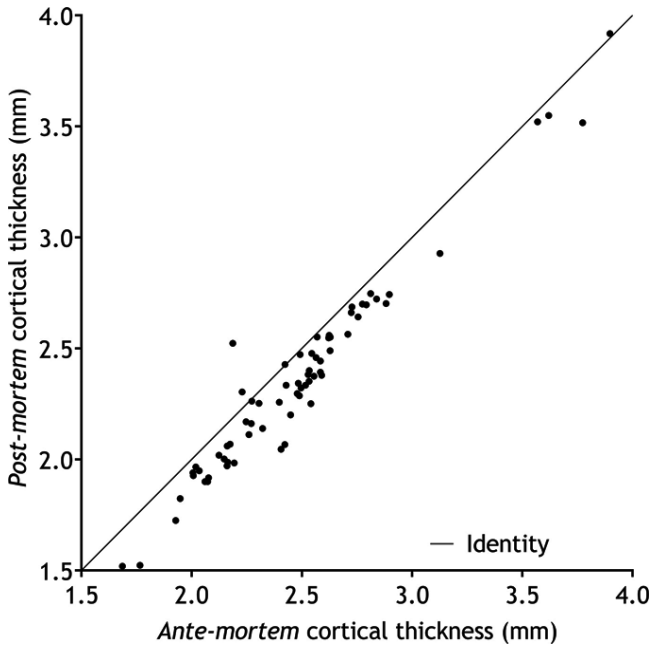


Fig. 3. Scatterplot of the *ante mortem* versus *post mortem* cortical thickness
Scatterplot of the *ante mortem* versus *post mortem* cortical thickness (A) in 68 different brain regions [3], using the longitudinal stream in FreeSurfer [24]. Pearson's $r = 0.975$, $p < 0.001$.

MRI in relation to immunohistopathology

Fig. 4 shows the scatterplot for cortical thickness at both time points versus immunohistopathology for $A\beta$ and p-tau in the corresponding region. $A\beta$ and p-tau scatterplot show a similar shape for *ante mortem* and *post mortem* imaging, indicating that *post mortem* cortical thickness and histology results show a similar relationship as *ante mortem* cortical thickness and histology results within the same patient.

DISCUSSION

In this study comparing *post mortem in situ* to *ante mortem* MRI of the same donor, we showed that volumetric, cortical thickness, and diffusion MRI markers differ between time points. Cortical thickness and diffusion measures show compatibility for the comparison between *post mortem* and *ante mortem* MRI due to a consequent difference on whole-brain level.

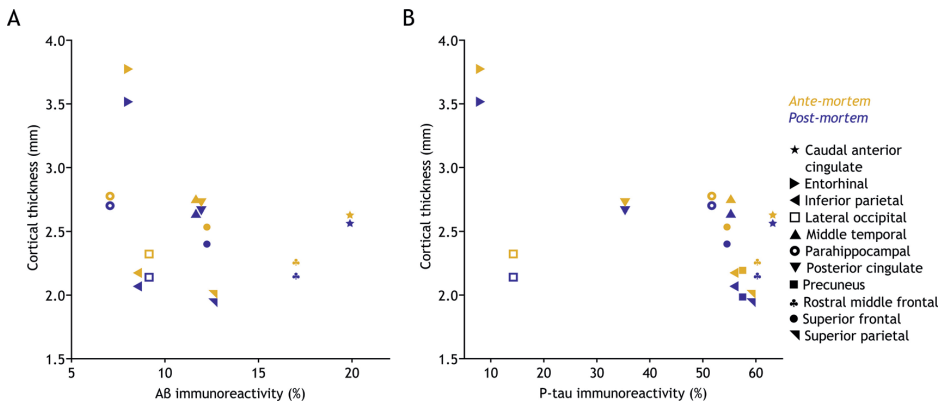


Fig. 4. Scatterplots of cortical thickness versus immunohistopathology

The scatterplots of *ante-* and *post mortem* cortical thickness versus immunohistopathology for amyloid-beta ($A\beta$) immunoreactivity (**A**) and hyperphosphorylated tau (p-tau) immunoreactivity (**B**). Both scatterplots show the same shape for the two timepoints. The symbol legend for brain regions on the far right is applicable to both plots.

The most notable finding was a *post mortem* increase in brain volume predominantly of the cerebellum and white matter. This volume increase may be due to a combination of vasogenic and cytotoxic oedema, as indicated by the pathological findings of congested vessels as well as eosinophilic neurons and retraction artefacts enclosing cell bodies. By implementing the knowledge on brain oedema in ischemic stroke [9], we speculate that the prolonged duration of the agonal state, in this case 20 min, led to a longer hypoxic state than in acute death, which may be an important factor in the extent of the oedema [7, 10]. The extracellular space of the white matter being larger (80 nm) than that of the grey matter (20 nm) [26], and the cerebellum being one of the most sensitive regions to hypoxia [7], may clarify for the more pronounced volume increase in these regions. Since the *post mortem* volume increase is disproportional between regions, this measurement is according to our results not directly suitable as a proxy for the *in vivo* situation.

Though cortical volume was also increased *post mortem*, this was accompanied by a reduction of cortical thickness and an enlargement of the cortical surface, suggesting that the cortex was stretched by swelling of the white matter (as a balloon), rather than swelling of the grey matter. The observed differences for cortical thickness were larger than the normal variance of 2% that can be expected from test-retest performance on all cortical regions of the FreeSurfer longitudinal stream in normal individuals [14, 24]. In addition, the expected annual cortical

thinning in familial Alzheimer's disease is 7% [35], making it unlikely that our observed 5% thinning within 4 days is due to the disease process itself. Therefore, we believe our findings are indeed the consequence of both agonal and *post mortem* effects. Of note, the reduction in cortical thickness was quite consistent between regions, suggesting that the post mortem cortical thinning takes place at the whole-brain level and thus can be used to compare regions within a subject. Similar scatterplots were found for immunohistopathology versus cortical thickness for both timepoints. Therefore, based on this case report, the use of *post mortem* cortical thickness as an intermediate between histopathology and *in vivo* imaging is justifiable.

We found that *post mortem* diffusivity measures were reduced compared with *ante mortem*. As diffusivity measures show an inter-session within-subjects variation of only 3% when using similar pre-processing and tensor fitting as ours [18], other causes had to play a role. Consistent with the literature, we observed that the decrease in diffusivity vectors was disproportionate, resulting in a net increase of fractional anisotropy [4, 30]. A reduction of diffusivity was expected since body temperature decreases *post mortem* and the diffusion coefficient of water is temperature-dependent [17]. Diffusivity of water was calculated to reduce with 15% (<https://dtrx.de/od/diff/>), when estimating body temperature at time of *post mortem* scanning to be 27°C (Δ temperature = *post mortem* delay in hours + 1 [8]). A similar decrease in the CSF was expected due to its large water content and isotropic aspect. However, *post mortem* a 50% reduction of diffusivity in CSF was observed, suggesting that besides temperature, other processes such as tissue decomposition, CSF absorption cessation, and viscosity changes influence diffusivity [11, 25]. The disproportionate diffusivity decrease in the grey matter being larger than in the white matter may be explained by partial volume effects of a disproportionate diffusivity decrease in CSF [5]. It is important to note that diffusion measures were altered approximately linear throughout the white matter. As with cortical thickness, this indicates that the *post mortem* effect particularly induces diffusion differences at the whole-brain level. This suggests that *post mortem* diffusion measures can still be used to compare between regions within a subject.

Some limitations apply to this work. First, although the increase in brain volume is readily appreciated from visual inspection, subtle differences in imaging contrast of the T1-weighted image may have contributed to the differences observed in the volumetric analysis. We tried to minimize this effect by using multi-time point initialization and normalization embedded in the longitudinal

FreeSurfer processing scheme. Second, our results are based on a single patient. We realize that certain factors influencing *post mortem* results might be very specific to this case such as; the Alzheimer's disease condition, the fact that euthanasia was performed, the type of euthanica that were given [23], and aspects that influence *post mortem* body temperature.

Imaging markers have been postulated to serve as a bridge between the clinical situation and histopathology. Although the current experimental setup (i.e., *post mortem* with the brain *in situ*) is quite possibly as close to both the *in vivo* and histopathological situation as one can get, we observe that *post mortem in situ* MRI measurements differ substantially from that of *ante mortem* MRI. These irreconcilable differences occur on a global whole-brain level, but show consistency across regions on a local level for cortical thickness and diffusion measurements. Therefore, future *post mortem* MRI studies referring to the *in vivo* situation should focus on regional analysis, and statistical (e.g., multilevel) models to accommodate for within-subject (nested) data.

ACKNOWLEDGEMENTS

Our thoughts go out to the family of the patient who donated his brain for this study. We thank them for their support and interest in research. In addition, we thank the Netherlands Brain Bank for providing the brain tissue and the department of clinical genetics of the Amsterdam UMC, VUmc for genetic screening of the donor. We acknowledge the Normal Aging Brain Collection (NABCA; www.nabca.eu) team for developing and optimizing the *post mortem* MRI-pathology pipeline. This study was funded by ZonMw grant #733050104. PJW Pouwels receives research support from the Dutch MS Research Foundation, grant #14-876. LE Jonkman is financially supported by a grant from the Alzheimer's Association (AARF-18-566459). WDJ van de Berg was financially supported by grants from Amsterdam Neuroscience, ZonMW Memorabel, ZonMW Technology Hotel, Stichting Parkinson Fonds, Alzheimer Netherlands-LECMA and contract research for Roche Pharma, Lysosomal Therapeutics, Crossbeta Sciences. Ph Scheltens is supported by Piramal. F Barkhof is supported by the National Institute for Health Research biomedical research centre at University College London Hospital.

LIST OF ABBREVIATIONS

| | |
|-----------|--|
| A β | amyloid-beta |
| DAB | 3,3'-diaminobenzine |
| CSF | cerebrospinal fluid |
| CERAD | Consortium to Establish a Registry for Alzheimer Disease |
| H&E | hematoxylin-eosin |
| p-tau | phosphorylated tau |
| PBS | phosphate buffered saline |
| ROI | region of interest |

REFERENCES

1. Chard DT, Jackson JS, Miller DH, Wheeler-Kingshott CAM (2010) Reducing the impact of white matter lesions on automated measures of brain gray and white matter volumes. *J Magn Reson Imaging* 32:223–228. doi: 10.1002/jmri.22214
2. D'Arceuil HE, Westmoreland S, de Crespigny AJ (2007) An approach to high resolution diffusion tensor imaging in fixed primate brain. *Neuroimage* 35:553–565. doi: 10.1016/j.neuroimage.2006.12.028
3. Desikan RS, Ségonne F, Fischl B, Quinn BT, Dickerson BC, Blacker D, Buckner RL, Dale AM, Maguire RP, Hyman BT, Albert MS, Killiany RJ (2006) An automated labeling system for subdividing the human cerebral cortex on MRI scans into gyral based regions of interest. *Neuroimage* 31:968–980. doi: 10.1016/J.NEUROIMAGE.2006.01.021
4. Eggen MD, Swingen CM, Iaizzo PA (2012) Ex vivo diffusion tensor MRI of human hearts: Relative effects of specimen decomposition. *Magn Reson Med* 67:1703–1709. doi: 10.1002/mrm.23194
5. Falconer JC, Narayana PA (1997) Cerebrospinal fluid-suppressed high-resolution diffusion imaging of human brain. *Magn Reson Med* 37:119–123. doi: 10.1002/mrm.1910370117
6. Fazekas F, Chawluk J, Alavi A, Hurtig H, Zimmerman R (1987) MR signal abnormalities at 1.5 T in Alzheimer's dementia and normal aging. *Am J Roentgenol* 149:351–356. doi: 10.2214/ajr.149.2.351
7. Graham DI (1977) Pathology of hypoxic brain damage in man. *J Clin Pathol Suppl (R Coll Pathol)* 11:170–80
8. Guharaj P V., Chandran MR (2003) Forensic medicine. Orient Longman
9. Hacke W, Schwab S, Horn M, Spranger M, De Georgia M, von Kummer R (1996) "Malignant" middle cerebral artery territory infarction: clinical course and prognostic signs. *Arch Neurol* 53:309–15
10. Hardy JA, Wester P, Winblad B, Gezelius C, Bring G, Eriksson A (1985) The patients dying after long terminal phase have acidotic brains; implications for biochemical measurements on autopsy tissue. *J Neural Transm* 61:253–264. doi: 10.1007/BF01251916
11. Hasan KM, Lincoln JA, Nelson FM, Wolinsky JS, Narayana PA (2015) Lateral ventricular cerebrospinal fluid diffusivity as a potential neuroimaging marker of brain temperature in multiple sclerosis: a hypothesis and implications. *Magn Reson Imaging* 33:262–9. doi: 10.1016/j.mri.2014.11.002
12. Hughes CP, Berg L, Danziger WL, Coben LA, Martin RL (1982) A new clinical scale for the staging of dementia. *Br J Psychiatry* 140:566–72
13. Jonkman LE, Kenkhuis B, Geurts JJG, van de Berg WDJ (2019) Post-Mortem MRI and Histopathology in Neurologic Disease: A Translational Approach. *Neurosci Bull* 35:229–243. doi: 10.1007/s12264-019-00342-3

14. Jovicich J, Marizzoni M, Sala-Llonch R, Bosch B, Bartrés-Faz D, Arnold J, Benninghoff J, Wiltfang J, Roccatagliata L, Nobili F, Hensch T, Tränkner A, Schönknecht P, Leroy M, Lopes R, Bordet R, Chanoine V, Ranjeva J-P, Didic M, Gros-Dagnac H, Payoux P, Zoccatelli G, Alessandrini F, Beltramello A, Bargalló N, Blin O, Frisoni GB (2013) Brain morphometry reproducibility in multi-center 3 T MRI studies: A comparison of cross-sectional and longitudinal segmentations. *Neuroimage* 83:472–484. doi: 10.1016/j.NEUROIMAGE.2013.05.007
15. KNMG; KNMP (Institution/Organisation) (2012) KNMG/KNMP Guideline Performance of euthanasie and physician-assisted suicide [in Dutch]. KNMG website
16. Koedam ELGE, Lehmann M, van der Flier WM, Scheltens P, Pijnenburg YAL, Fox N, Barkhof F, Wattjes MP (2011) Visual assessment of posterior atrophy development of a MRI rating scale. *Eur Radiol* 21:2618–25. doi: 10.1007/s00330-011-2205-4
17. Kozak L, Bango M, Szabo M, Rudas G, Vidnyanszky Z, Nagy Z (2009) Using diffusion MRI for measuring the temperature of cerebrospinal fluid within the lateral ventricles. *Acta Paediatr* 99:237–43. doi: 10.1111/j.1651-2227.2009.01528.x
18. Liu X, Yang Y, Sun J, Yu G, Xu J, Niu C, Tian H, Lin P (2014) Reproducibility of diffusion tensor imaging in normal subjects: an evaluation of different gradient sampling schemes and registration algorithm. *Neuroradiology* 56:497–510. doi: 10.1007/s00234-014-1342-2
19. Montine TJ, Phelps CH, Beach TG, Bigio EH, Cairns NJ, Dickson DW, Duyckaerts C, Frosch MP, Masliah E, Mirra SS, Nelson PT, Schneider JA, Thal DR, Trojanowski JQ, Vinters H V, Hyman BT, National Institute on Aging, Alzheimer’s Association (2012) National Institute on Aging-Alzheimer’s Association guidelines for the neuropathologic assessment of Alzheimer’s disease: a practical approach. *Acta Neuropathol* 123:1–11. doi: 10.1007/s00401-011-0910-3
20. Oguz I, Yaxley R, Budin F, Hoogstoel M, Lee J, Maltbie E, Liu W, Crews FT (2013) Comparison of Magnetic Resonance Imaging in Live vs. Post Mortem Rat Brains. *PLoS One* 8:e71027. doi: 10.1371/journal.pone.0071027
21. Ossenkoppele R, Cohn-Sheehy BI, La Joie R, Vogel JW, Möller C, Lehmann M, van Berckel BNM, Seeley WW, Pijnenburg YA, Gorno-Tempini ML, Kramer JH, Barkhof F, Rosen HJ, van der Flier WM, Jagust WJ, Miller BL, Scheltens P, Rabinovici GD (2015) Atrophy patterns in early clinical stages across distinct phenotypes of Alzheimer’s disease. *Hum Brain Mapp* 36:4421–37. doi: 10.1002/hbm.22927
22. Pasquier F, Leys D, Weerts JGE, Mounier-Vehier F, Barkhof F, Scheltens P (1996) Inter-and Intraobserver Reproducibility of Cerebral Atrophy Assessment on MRI Scans with Hemispheric Infarcts. *Eur Neurol* 36:268–272. doi: 10.1159/000117270
23. Pierozan P, Jernerén F, Ransome Y, Karlsson O (2017) The Choice of Euthanasia Method Affects Metabolic Serum Biomarkers. *Basic Clin Pharmacol Toxicol* 121:113–118. doi: 10.1111/bcpt.12774
24. Reuter M, Schmansky NJ, Rosas HD, Fischl B (2012) Within-subject template estimation for unbiased longitudinal image analysis. *Neuroimage* 61:1402–18. doi: 10.1016/j.neuroimage.2012.02.084

25. Sakka L, Coll G, Chazal J (2011) Anatomy and physiology of cerebrospinal fluid. *Eur Ann Otorhinolaryngol Head Neck Dis* 128:309–316. doi: 10.1016/J.ANORL.2011.03.002
26. Saukko P, Knight B (2004) *Knight's Forensic Pathology*, Third edit. Hodder Education Publishers
27. Scheltens P, Leys D, Barkhof F, Huglo D, Weinstein HC, Vermersch P, Kuiper M, Steinling M, Wolters EC, Valk J (1992) Atrophy of medial temporal lobes on MRI in "probable" Alzheimer's disease and normal ageing: diagnostic value and neuropsychological correlates. *J Neurol Neurosurg Psychiatry* 55:967–72
28. Schilling K, Gao Y, Stepniewska I, Choe AS, Landman BA, Anderson AW (2017) Reproducibility and variation of diffusion measures in the squirrel monkey brain, in vivo and ex vivo. *Magn Reson Imaging* 35:29–38. doi: 10.1016/j.mri.2016.08.015
29. Schippling S (2017) MRI for multiple sclerosis diagnosis and prognosis. *Neurodegener Dis Manag* 7:27–29. doi: 10.2217/nmt-2017-0038
30. Shepherd TM, Flint JJ, Thelwall PE, Stanisz GJ, Mareci TH, Yachnis AT, Blackband SJ (2009) Postmortem interval alters the water relaxation and diffusion properties of rat nervous tissue--implications for MRI studies of human autopsy samples. *Neuroimage* 44:820–6. doi: 10.1016/j.neuroimage.2008.09.054
31. Smith SM, Jenkinson M, Johansen-Berg H, Rueckert D, Nichols TE, Mackay CE, Watkins KE, Ciccarelli O, Cader MZ, Matthews PM, Behrens TEJ (2006) Tract-based spatial statistics: Voxelwise analysis of multi-subject diffusion data. *Neuroimage* 31:1487–1505. doi: 10.1016/j.neuroimage.2006.02.024
32. Steenwijk MD, Pouwels PJW, Daams M, van Dalen JW, Caan MWA, Richard E, Barkhof F, Vrenken H (2013) Accurate white matter lesion segmentation by k nearest neighbor classification with tissue type priors (kNN-TTPs). *NeuroImage Clin* 3:462–469. doi: 10.1016/j.nicl.2013.10.003
33. Thal DR, Griffin WST, de Vos RAI, Ghebremedhin E (2008) Cerebral amyloid angiopathy and its relationship to Alzheimer's disease. *Acta Neuropathol* 115:599–609. doi: 10.1007/s00401-008-0366-2
34. Tofts PS, Jackson JS, Tozer DJ, Cercignani M, Keir G, MacManus DG, Ridgway GR, Ridha BH, Schmierer K, Siddique D, Thornton JS, Wroe SJ, Fox NC (2008) Imaging cadavers: Cold FLAIR and noninvasive brain thermometry using CSF diffusion. *Magn Reson Med* 59:190–195. doi: 10.1002/mrm.21456
35. Weston PSJ, Nicholas JM, Lehmann M, Ryan NS, Liang Y, Macpherson K, Modat M, Rossor MN, Schott JM, Ourselin S, Fox NC (2016) Presymptomatic cortical thinning in familial Alzheimer disease. *Neurology* 87:2050–2057. doi: 10.1212/WNL.0000000000003322

SUPPLEMENTARY DATA

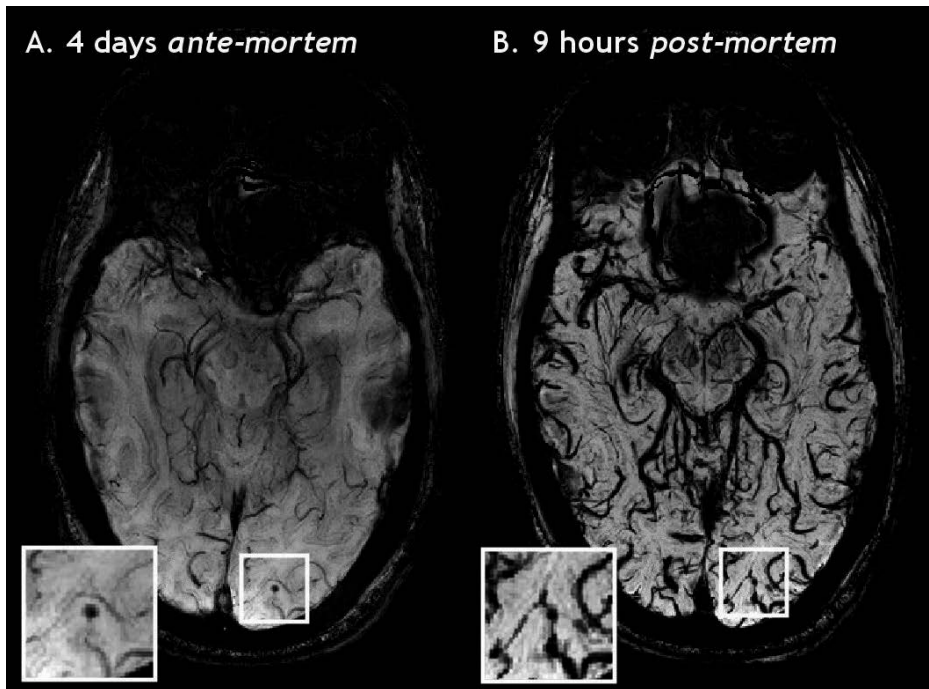


Fig. S1. Susceptibility-weighted image of the brain
Susceptibility-weighted image of the brain ante-mortem (A) and post-mortem (B). An increased vessel signal is seen after death due to blood stasis and deoxygenation. One microbleed (insets) was visible on both susceptibility-weighted images.

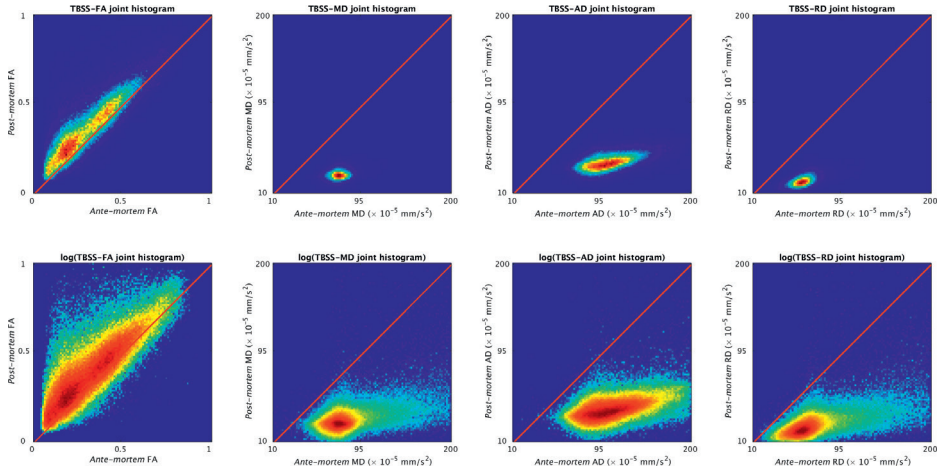


Fig. S2. Joint histogram of diffusion values within voxels of the tract-based spatial statistics skeleton

The top panel displays raw joint histograms. The bottom panel displays log-transformed joint histograms. Red line indicates the identity line. FA fractional anisotropy; MD mean diffusivity; AD axial diffusivity; RD radial diffusivity.

Video 1.

Available at: <https://academic.oup.com/braincomms/article/1/1/fcz030/5606709?searchresult=1#supplementary-data>

Section 5

Closing remarks

Chapter 10

General Summary

Alzheimer's disease (AD) is especially clinically recognized as a heterogeneous disease. Research from the past decade pointed out that the disease is also radiologically and pathologically more diverse than previously assumed. This thesis first aimed to gain more insight into the pathological diversity of different (clinical) AD subtypes. The second aim was to translate the pathological heterogeneity to radiology by studying the correlation between in vivo measurements and post mortem measurements.

The key findings of this thesis are as follows:

Aim 1: Heterogeneity in Alzheimer's disease pathology

- Although neuroinflammation is observed in and around plaque-like structures, its distribution measured by activated microglia and complement factors parallels the occurrence of pTau in typical and atypical AD.
- Atypical AD cases with an early disease onset were associated with a relative increase and aberrant distribution of neuroinflammation compared to typical AD with a late disease onset.
- Innate immune cells (e.g., microglia and astrocytes) correlate regionally differently with AD pathological hallmarks in various clinical AD subtypes.
- The distribution of reactive astrocytes differentiates the clinical atypical AD subtypes of PCA and typical AD better than pTau distribution does.
- Atypical AD cases showed increased presence of a fibrillar plaque-type we refer to as the 'coarse-grained' plaque.
- The coarse-grained plaque is especially observed in early-onset homozygous *APOE* $\epsilon 4$ AD cases, who are affected by cerebral amyloid angiopathy (CAA). The plaque is a unique fibrillar deposit located at the parenchymal border of the blood-brain barrier that shares similarities and differences with both parenchymal and vascular $A\beta$ deposits.
- Fibrillization of α -helical $A\beta$ into a β -sheet confirmation increases along the hypothesized ascending plaque-maturation stages. During plaque progression, this protein confirmation gradually increases and localizes within the plaque's center.
- The $A\beta$ β -sheet fibril confirmation is different in dense-cored compared to non-cored fibrillar plaques. Carotenoids, which are associated with inflammation, are predominantly found in the dense-cored and not in the fibrillar $A\beta$ deposits.

Aim 2: Translating pathology to the memory clinic via imaging

- A β cerebrospinal fluid (CSF) and amyloid positron emission tomography (PET) biomarker status do not per se reflect A β pathology, as inflammation may induce a positive amyloid signal. A positive A β biomarker status does not invariably equal a primary diagnosis of AD at autopsy since A β can be concomitant to other pathologies.
- In AD, A β , pTau, and activated microglia are differently associated with post mortem MRI-derived cortical thickness. A β is associated with a globally reduced cortical thinning, whereas pTau and activated microglia are regionally associated with increased cortical atrophy.
- Post mortem in situ MRI-derived cortical thickness but not volumetry measurements can be used as a proxy for ante mortem MRI, provided that the obtained measurements are corrected for within-subject.

Summary of the thesis and context

In the following paragraph, I summarize and discuss the findings of each study that make up this thesis. Research on the heterogeneity in AD pathology is described in section 2 and 3 (chapters 2-6). Chapters 2 and 3 focus on the brain regional distribution of AD pathological hallmarks and neuroinflammation in different subtypes of AD. In chapters 4-6, I focus on the heterogeneity of the A β plaque. Chapter 4 describes a divergent plaque-type that was first observed in the study described in chapter 2. The use of unconventional imaging techniques to investigate characteristics of A β plaques that cannot be studied using ordinary light microscopy is described in chapters 5 and 6. Chapter 5 describes the use of these techniques to study the common plaque-types, including the diffuse, compact, and classical cored plaque, whereas chapter 6 addresses the use of label-free imaging techniques on the classic cored plaque and the fibrillar plaque. Section 4 (chapter 7-9) aims to translate findings from pathology to the in vivo situation. Chapter 7 describes what PET and CSF biomarkers reflect in case of biomarker discordance by directly comparing the A β biomarker to A β pathology. In chapter 8, the correlation between A β , pTau, and neuroinflammation with post mortem in situ MRI-derived cortical thickness is described. Finally in chapter 9, I describe how translatable those measurements derived from post mortem in situ MRI actually are to those derived from ante mortem MRI.

Distribution of activated microglia and reactive astrocytes distinguishes between (a)typical AD subtypes

This thesis describes the heterogeneity in AD first from a neuropathological perspective by investigating the distribution of AD pathology and

neuroinflammation in a (atypical) cohort based on NFT distribution over the temporal and parietal cortex in typical and atypical AD (chapter 2). The study confirms that not all AD cases show the typical neurofibrillary tangle (NFT) distribution as proposed by Braak & Braak [1]. In the total AD cohort of 296 cases, 48% showed a typical NFT distributed, indicating that the temporal pole had more NFTs than the superior parietal; 43% showed a similar amount for NFTs in the temporal and parietal section; and 9% of the cases had an atypical NFT distribution, meaning the parietal section had more NFTs than the temporal section. Compared to the typical NFT group, this latter atypical NFT group consisted of more males (54% in the atypical; 26% in typical), who died at a younger age (72 y/o for atypical; 82 y/o for typical). Previous studies have shown that NFT pathology often aligns with clinical symptoms [2, 5, 8]. The study described in chapter 2 confirmed those findings: 90% of the cases with a typical NFT distribution presented clinically with a typical memory presentation, whereas 72% of cases with an atypical NFT distribution presented with a non-amnesic phenotype. As cohort numbers in pathology studies are generally small, an as-homogenous group-as-possible was selected for the question regarding the distribution of neuroinflammation in (a)typical AD. This meant that the atypical AD group both had an atypical NFT distribution and an atypical clinical phenotype, whereas the typical AD group had to have a typical NFT distribution and a memory-dominated presentation, resulting in a cohort of nine atypical and ten typical cases. The distribution over the temporal and parietal cortex of both activated microglia stained for CD68 and MHC-II and complement factors C3d and C4b was different in atypical AD cases. Not only did atypical AD cases show an opposite parietal-dominant distribution for all four markers, they also had relatively much higher levels of neuroinflammation compared to typical AD. In addition, an abnormal A β plaque morphology was seen in the parietal section of atypical AD cases. This plaque was characterized by a coarse-grainy appearance, and an alternative distribution of microglia and complement proteins when compared to the common classic cored plaques that were often seen in the temporal cortex of typical cases. These results support a role for activated microglia and complement factors in the atypical distribution of NFT pathology in AD subtypes.

Subsequently, I studied if the differences in neuroinflammatory distribution for AD subtypes held ground in another AD cohort, which was prospectively collected on clinical parameters (chapter 3). Since (a)typical was defined based solely on clinical symptoms and not on NFT distribution, the association of clinical symptoms with post mortem neuropathology could be investigated. The

cohort consisted of ten control cases, ten cases with typical AD, and nine cases with atypical AD. (A)typicality was based on the reported symptoms at disease onset, which means that if cases had more prominent non-memory symptoms than memory symptoms at time of disease-onset they were categorized as atypical and vice versa for typical. The atypical group was heterogeneous as it contained six cases with a behavioral/dysexecutive phenotype and three cases with posterior cortical atrophy (PCA). As expected, pTau was differently distributed between typical and atypical subtypes with a more hippocampal dominant pattern in typical AD and a more cortical dominant pattern in atypical AD. Most likely due to the small group sizes, the behavioral/dysexecutive phenotype did not differentiate in pTau distribution from that in PCA. In all AD groups, A β was more pronounced in the neocortical areas compared to the limbic areas and showed increased immunoreactivity in the middle frontal gyrus of behavioural/dysexecutive cases. Microglia marker MHC-II, but not CD68, showed a different distribution pattern in typical compared to atypical AD. Interestingly, the reactive astrocyte distribution measured with GFAP differentiated not only between typical and atypical AD, but also between atypical AD variants with an increased immunoreactivity in the parietal areas of PCA cases. This study confirmed the previous findings that an atypical distribution of neuroinflammation is associated with both clinical and pathologically defined atypical AD. Reactive astrocytic changes differentiated clinical AD subtypes better than pTau distribution, indicating a prominent role for neuroinflammation in clinical symptomatology.

The conformation of the A β peptide and the landscape of the surrounding tissue lie at the cause of A β -deposit variety

To look at the pathology from different perspectives, the focus for the next part of this thesis was shifted from a distribution- and tau-oriented view to a single deposit and A β -type of view. The ‘coarse-grained plaque’ observed in the first study was disentangled by studying its association with clinical disease as well as immunohistochemical and morphological characteristics (chapter 4). Using anti-A β immunostaining on the middle frontal gyrus we defined the coarse-grained plaque by its size (30–100 μ m), multi-cored coarse-grainy appearance, A β -devoid pores, and an ill-defined border. Increased presence of the coarse-grained plaque was related to an early disease onset in AD, a homozygous *APOE* ϵ 4 status, and the presence of amyloid deposition in the cerebral vessels, also referred to as cerebral amyloid angiopathy (CAA). The coarse-grained plaque was not observed in preclinical cases with AD neuropathologic change. Together, these results highlight the association of this plaque-type with the

clinical manifestation of AD. In-depth characterization revealed that the coarse-grained plaque contains fibrillar amyloid, was mostly composed of $A\beta_{40}$, and showed strong and divergent immunoreactivity for neuroinflammation- as well as vascular pathology-associated markers when compared to other $A\beta$ deposits. 3D assessment exposed an $A\beta_{40}$ shell structure in the larger coarse-grained plaques and a direct vascular connection. Based on the plaque's similarities and differences with both the usual parenchymal and vascular $A\beta$ deposits, I categorized the coarse-grained plaque as a separate type and hypothesize it to originate at the parenchymal border of the capillary blood-brain barrier (see Fig. 11 in chapter 4). This study provides a morphological and biochemical definition for the coarse-grained plaque, supporting that this deposit is unique, with specific clinical and etiological associations.

To study $A\beta$ plaque aspects such as the secondary protein structure that cannot be studied using ordinary (immuno)histochemistry, spectroscopy was applied on different types of $A\beta$ plaques. Spectroscopy measures the spectrum of light that is transmitted by the matter of interest (e.g., tissue, molecules, atoms) as a reaction to the exposure of electromagnetic radiation. It enables one to study the component's chemical bonds and with that the lipid, DNA, or protein content, including the protein's secondary structure. Since spectroscopy does not require secondary handling of the tissue as (immuno)histochemistry does, it facilitates that the tissue is studied in its most native form. To study the hypothesized $A\beta$ plaque-developmental stages, including diffuse, compact, and classic cored plaques in order of assumed plaque-maturity, the content and localization of fibril content was assessed with Fourier transform infrared (FTIR) and Raman spectroscopy in 160 plaques of 5 AD cases (chapter 5). The presence of plaques in the analyzed region were subsequently confirmed by anti- $A\beta$ immunohistochemistry on the same tissue section. Alongside the ascending plaque stages, plaque spectra showed a shift of the Amide I band around 1630 cm^{-1} towards lower wavenumbers and a decreasing band around 1693 cm^{-1} , indicating a shift from α -helical to β -fibril structures. This pattern was consistent across cases and showed a steady transition with increasing plaque development. Not only did $A\beta$ fibril content increase, it also seemed to centralize within the plaque with increasing plaque maturation. The spectral image analysis provides insight into the spatial distribution of $A\beta$ structure in different plaque types, contributing support for the current hypothesis on plaque development [6, 10].

In addition to the common classic cored plaques, also the fibrillar plaques were studied by spectroscopy (chapter 6). Plaque types from five AD cases

were studied using fluorescence microscopy, Raman, and stimulated Raman scattering (SRS) spectroscopy and compared to control tissue. Plaques were pre-spectroscopy identified because of their auto fluorescent characteristic with an emission peak around 540-550 nm when excited with a 488 nm laser. After spectroscopy measurements, the plaque location was confirmed by thioflavin S histochemistry. A clear peak shift in the Amide-I band of plaque areas compared to non-plaque areas was initially not detected with Raman spectroscopy as was earlier with FTIR in the previous study. In the current study, a much smaller peak-shift of only 3 cm^{-1} was detected compared to the previously mentioned $+10\text{ cm}^{-1}$. A protein peak shift from 1659 to 1666 cm^{-1} was observed when measuring with the more sensitive SRS method, but only in the classic cored plaques and not in the fibrillar plaques. A side observation was that cored plaques showed consistent Raman peaks at 1518 and 1154 cm^{-1} . These peaks are specific for carotenoid compounds and were not observed in fibrillar plaques. Carotenoids are suggested to have anti-oxidant and anti-inflammatory effects. Although only a few plaques were scanned for this study, the data adds to the evidence that the inflammatory reaction differs between various plaque-types. The above-mentioned studies implicate that associated disease mechanisms such as neuroinflammation and vascular attribution, as well as the structure and biochemical composition of $A\beta$ may lie at the cause of morphological differences between $A\beta$ deposits.

Distinct histopathological markers differently correlate with imaging and memory

For future diagnostics and therapy, it is important to understand the relation between clinical and pathological heterogeneity. Therefore, the correlation of pathology with measurements performed on the memory clinic was investigated in the next section of this thesis. To enhance the understanding of the neuropathological underpinnings of $A\beta$ biomarkers, the concordance between in vivo $A\beta$ status as measured by positron emission tomography (PET) and in the cerebrospinal fluid (CSF) was compared in a sample with neuropathological confirmation (chapter 7). Although in general both CSF and PET captured AD neuropathological change, discordance between the two modalities was found in 14% (3/21 cases). The most plausible reasons for $A\beta$ discordance in the studied sample included: neuroinflammation in a case of granulomatosis with polyangiitis with CSF+/PET- but without $A\beta$ pathology; $A\beta$ co-pathology in a case with a different primary neurodegenerative disease than AD (CSF+/PET-) but with coexisting $A\beta$ pathology; and additional factors influencing CSF $A\beta_{42}$ levels (CSF-/PET+) in a case with AD. The cohort also

contained two cases with CSF+/PET+ for A β , but without AD neuropathological diagnosis, highlighting that A β not invariably results in an AD diagnosis at autopsy. This study shows the importance in considering other comorbidities when evaluating A β biomarkers results, especially since molecular biomarkers for non-AD neurodegenerative diseases are currently lacking.

Using a combined post mortem in situ MRI and histopathology approach on the same cohort as described in chapter 3, associations between cortical thickness on MRI and the histopathological hallmarks were observed in AD, but not in controls (chapter 8). In AD, A β and pTau load contributed differently to cortical thickness. A β was weakly associated with reduced cortical atrophy globally, while increased pTau accumulation and phagocytosing microglia (CD68) strongly associated with progressive regional cortical atrophy. pTau and atrophy were strongest correlated in the temporal and frontal cortices. CD68 also correlated with atrophy but only in the parietal cortex. This CD68-atrophy correlation was driven by AD cases with an atypical clinical symptomology. Although literature tells us that various clinical AD subtypes have different cortical atrophy patterns on MRI [3, 9], the current study could not confirm this after correcting for multiple testing with mostly a temporoparietal dominant atrophy pattern, which is the classical atrophy pattern for typical AD. Explanations could be our heterogeneous group of atypical AD cases and the small sample sizes within each atypical subgroup. In addition, the largest atypical subgroup contained the behavioural/dysexecutive variant, which is known to show a more general diffusely increased atrophy pattern instead of a localized one [4, 7]. In conclusion, this study shows that distinct histopathological markers differently correlate with cortical atrophy, highlighting their different roles in the neurodegenerative process. This study contributes in understanding the pathological underpinnings of MRI atrophic patterns.

Imaging markers have been postulated to serve as a bridge between clinical measurements and histopathology. The previous study correlated MRI-derived cortical thickness to AD pathological hallmarks. Post mortem in situ MRI was used as this is close to both the in vivo and histopathological situation as one can get. However, if post mortem in situ MRI actually is comparable to ante-mortem imaging remains elusive. We had the unique opportunity to make a direct comparison between these MRI timepoints, due to the altruistic wish for brain donation of an AD patient who decided to end his life by euthanasia (chapter 9). The agonal and post mortem effects on volumetric, cortical thickness and diffusion MRI measurements were studied by comparing scans from

both ante and post mortem timepoints. The scans were performed within a four-day interval on the same scanner by the same staff. Volumetry increased disproportionately between regions with the largest expansion seen in the cerebellum and white matter. Cortical thickness decreased with 5%, which is more than could be expected from normal variance (2%). The 5% decrease was consistent for all measured cortical regions. Diffusion vectors decreased 50-60% in all compartments, being the grey matter, the white matter, and the CSF. In this study, cortical thickness and diffusion measures show compatibility for the comparison between post mortem and ante mortem MRI due to a consequent difference on whole-brain level. Based on this study, the use of post mortem cortical thickness as an intermediate between histopathology and in vivo imaging is justifiable as long as regions are compared within subjects.

Neuroinflammation might be a connecting link between $A\beta$ - pTau and clinical symptoms as its distribution not only parallels both pTau distribution and larger $A\beta$ plaques, but also differentiates between (clinical) AD subtypes. In addition, although all AD cases have plaques and tangles, the specific roles the innate immune cells play may very well differ between the various subtypes. The data provided in this thesis suggest that different types of $A\beta$ deposits are specifically associated with the type and organization of the immune cells and immune factors that surround it. The hypothesis on plaque development from compact to eventually dense-cored plaques seems plausible when looking at the fibrillar structure of $A\beta$ deposits. In aiming to translate these findings to the living patient, I described that, although $A\beta$ pathology is very well reflected by both PET and CSF markers, these two modalities are not sensitive enough for individual deposit types (CAA, classic cored, coarse-grained). Furthermore, I show that the biomarker 'cortical atrophy' on MRI is both correlated with pTau and the burden of phagocytosing microglia, confirming that neurodegeneration is associated with both tau pathology and neuroinflammation.

REFERENCES

1. Braak H, Braak E (1991) Neuropathological staging of Alzheimer-related changes. *Acta Neuropathol* 82:239–59. doi: 10.1007/BF00308809
2. Murray ME, Graff-Radford NR, Ross OA, Petersen RC, Duara R, Dickson DW (2011) Neuropathologically defined subtypes of Alzheimer’s disease with distinct clinical characteristics: a retrospective study. *Lancet Neurol* 10:785–796. doi: 10.1016/S1474-4422(11)70156-9
3. Ossenkoppele R, Cohn-Sheehy BI, La Joie R, Vogel JW, Möller C, Lehmann M, van Berckel BNM, Seeley WW, Pijnenburg YA, Gorno-Tempini ML, Kramer JH, Barkhof F, Rosen HJ, van der Flier WM, Jagust WJ, Miller BL, Scheltens P, Rabinovici GD (2015) Atrophy patterns in early clinical stages across distinct phenotypes of Alzheimer’s disease. *Hum Brain Mapp* 36:4421–37. doi: 10.1002/hbm.22927
4. Ossenkoppele R, Pijnenburg YAL, Perry DC, Cohn-Sheehy BI, Scheltens NME, Vogel JW, Kramer JH, Van Der Vlies AE, Joie R La, Rosen HJ, Van Der Flier WM, Grinberg LT, Rozemuller AJ, Huang EJ, Van Berckel BNM, Miller BL, Barkhof F, Jagust WJ, Scheltens P, Seeley WW, Rabinovici GD (2015) The behavioural/dysexecutive variant of Alzheimer’s disease: Clinical, neuroimaging and pathological features. *Brain* 138:2732–2749. doi: 10.1093/brain/awv191
5. Ossenkoppele R, Schonhaut DR, Schöll M, Lockhart SN, Ayakta N, Baker SL, O’Neil JP, Janabi M, Lazaris A, Cantwell A, Vogel J, Santos M, Miller ZA, Bettcher BM, Vessel KA, Kramer JH, Gorno-Tempini ML, Miller BL, Jagust WJ, Rabinovici GD (2016) Tau PET patterns mirror clinical and neuroanatomical variability in Alzheimer’s disease. *Brain* 139:1551–1567. doi: 10.1093/brain/aww027
6. Thal DR, Capetillo-Zarate E, Del Tredici K, Braak H (2006) The development of amyloid beta protein deposits in the aged brain. *Sci Aging Knowledge Environ* 2006:re1. doi: 10.1126/sageke.2006.6.re1
7. Townley RA, Graff-Radford J, Mantyh WG, Botha H, Polsinelli AJ, Przybelski SA, Machulda MM, Makhlof AT, Senjem ML, Murray ME, Reichard RR, Savica R, Boeve BF, Drubach DA, Josephs KA, Knopman DS, Lowe VJ, Jack CR, Petersen RC, Jones DT (2020) Progressive dysexecutive syndrome due to Alzheimer’s disease: a description of 55 cases and comparison to other phenotypes. *Brain Commun* 2. doi: 10.1093/braincomms/fcaa068
8. Vogel JW, Young AL, Oxtoby NP, Smith R, Ossenkoppele R, Strandberg OT, La Joie R, Aksman LM, Grothe MJ, Iturria-Medina Y, Weiner M, Aisen P, Petersen R, Jack CR, Jagust W, Trojanowki JQ, Toga AW, Beckett L, Green RC, Saykin AJ, Morris J, Shaw LM, Liu E, Montine T, Thomas RG, Donohue M, Walter S, Gessert D, Sather T, Jiminez G, Harvey D, Bernstein M, Fox N, Thompson P, Schuff N, DeCarli C, Borowski B, Gunter J, Senjem M, Vemuri P, Jones D, Kantarci K, Ward C, Koeppe RA, Foster N, Reiman EM, Chen K, Mathis C, Landau S, Cairns NJ, Householder E, Reinwald LT, Lee V, Korecka M, Figurski M, Crawford K, Neu S, Foroud TM, Potkin S, Shen L, Kelley F, Kim S, Nho K, Kachaturian Z, Frank R, Snyder PJ, Molchan S,

- Kaye J, Quinn J, Lind B, Carter R, Dolen S, Schneider LS, Pawluczyk S, Beccera M, Teodoro L, Spann BM, Brewer J, Vanderswag H, Fleisher A, Heidebrink JL, Lord JL, Mason SS, Albers CS, Knopman D, Johnson K, Doody RS, Meyer JV, Chowdhury M, Rountree S, Dang M, Stern Y, Honig LS, Bell KL, Ances B, Morris JC, Carroll M, Leon S, Mintun MA, Schneider S, Oliver A, Griffith R, Clark D, Geldmacher D, Brockington J, Roberson E, Grossman H, Mitsis E, deToledo-Morrell L, Shah RC, Duara R, Varon D, Greig MT, Roberts P, Albert M, Onyike C, D'Agostino D, Kielb S, Galvin JE, Pogorelec DM, Cerbone B, Michel CA, Rusinek H, de Leon MJ, Glodzik L, De Santi S, Doraiswamy PM, Petrella JR, Wong TZ, Arnold SE, Karlawish JH, Wolk D, Smith CD, Jicha G, Hardy P, Sinha P, Oates E, Conrad G, Lopez OL, Oakley MA, Simpson DM, Porsteinsson AP, Goldstein BS, Martin K, Makino KM, Ismail MS, Brand C, Mulnard RA, Thai G, McAdams Ortiz C, Womack K, Mathews D, Quiceno M, Arrastia RD, King R, Weiner M, Cook KM, DeVous M, Levey AI, Lah JJ, Cellar JS, Burns JM, Anderson HS, Swerdlow RH, Apostolova L, Tingus K, Woo E, Silverman DHS, Lu PH, Bartzokis G, Radford NRG, Parfitt F, Kendall T, Johnson H, Farlow MR, Hake AM, Matthews BR, Herring S, Hunt C, van Dyck CH, Carson RE, MacAvoy MG, Chertkow H, Bergman H, Hosein C, Black S, Stefanovic B, Caldwell C, Hsiung GYR, Feldman H, Mudge B, Past MA, Kertesz A, Rogers J, Trost D, Bernick C, Munic D, Kerwin D, Mesulam MM, Lipowski K, Wu CK, Johnson N, Sadowsky C, Martinez W, Villena T, Turner RS, Johnson K, Reynolds B, Sperling RA, Johnson KA, Marshall G, Frey M, Yesavage J, Taylor JL, Lane B, Rosen A, Tinklenberg J, Sabbagh MN, Belden CM, Jacobson SA, Sirrel SA, Kowall N, Killiany R, Budson AE, Norbash A, Johnson PL, Obisesan TO, Wolday S, Allard J, Lerner A, Ogrocki P, Hudson L, Fletcher E, Carmichael O, Olichney J, DeCarli C, Kittur S, Borrie M, Lee TY, Bartha R, Johnson S, Asthana S, Carlsson CM, Potkin SG, Preda A, Nguyen D, Tariot P, Reeder S, Bates V, Capote H, Rainka M, Scharre DW, Kataki M, Adeli A, Zimmerman EA, Celmins D, Brown AD, Pearlson GD, Blank K, Anderson K, Santulli RB, Kitzmiller TJ, Schwartz ES, Sink KM, Williamson JD, Garg P, Watkins F, Ott BR, Querfurth H, Tremont G, Salloway S, Malloy P, Correia S, Rosen HJ, Miller BL, Mintzer J, Spicer K, Bachman D, Finger E, Pasternak S, Rachinsky I, Drost D, Pomara N, Hernando R, Sarrael A, Schultz SK, Ponto LLB, Shim H, Smith KE, Relkin N, Chaing G, Raudin L, Smith A, Fargher K, Raj BA, Pontecorvo MJ, Devous MD, Rabinovici GD, Alexander DC, Lyoo CH, Evans AC, Hansson O (2021) Four distinct trajectories of tau deposition identified in Alzheimer's disease. *Nat Med* 27:871-881. doi: 10.1038/s41591-021-01309-6
9. Whitwell JL, Jack CR, Kantarci K, Weigand SD, Boeve BF, Knopman DS, Drubach DA, Tang-Wai DF, Petersen RC, Josephs KA (2007) Imaging correlates of posterior cortical atrophy. *Neurobiol Aging* 28:1051-1061. doi: 10.1016/j.neurobiolaging.2006.05.026
 10. Wisniewski HM, Terry RD (1973) Reexamination of the Pathogenesis of the Senile Plaque. In: *Progress in Neuropathology Volume II*. Grune & Stratton, Inc., New York, pp 1-26

Chapter 11

General Discussion

In this chapter, I provide an integrated overview of my standpoint based on our results discussed in the light of current literature. Subsequently, I propose suggestions for future directions to further disentangle the heterogeneity in AD pathogenesis and end this section with a conclusion.

The NFT distribution that is responsible for the clinical phenotype follows distinct trajectories

Similar to other studies, the results in chapter 2 and 3 confirm that the clinical (a)typical presentation of AD is closely correlated to the distribution of pTau [8, 22, 25]. Using a corticolimbic ratio for NFT pathology, Murray et al showed that advanced AD can be classified into three distinct AD subtypes, including a hippocampal sparing subtype, a typical subtype, and a limbic predominant subtype [22]. The hippocampal sparing subtype is characterized by a greater NFT burden in the cortex compared to the hippocampus whereas the limbic predominant subtype shows extensive NFT burden in the hippocampus compared to a relatively spared cortex. Typical AD falls between the two extreme subtypes and shows a similar NFT burden for the hippocampus as the cortex. Even though the criteria used in chapter 2 for defining an atypical NFT distribution differed from that of Murray et al. [22], our atypical AD group showed demographical similarities to the hippocampal sparing subtype. Both atypical groups comprised ~10% of all AD cases, had an earlier age at onset, a similar disease duration, more often an atypical clinical presentation, and a predominant male composition. Using the advantages for measuring in vivo tau pathology that PET imaging provides, Vogel et al. was able to unravel the heterogeneity in tau distribution even better by analyzing the largest sample ($n = 2324$) of tau PET data to date [37]. Using a data-driven algorithm that takes both disease progression and traditional clustering into account, the authors showed tau distribution can be categorized into the following four main phenotypes: 1) a limbic-predominant phenotype; 2) a medial temporal lobe sparing phenotype; 3) a predominant posterior occipitotemporal phenotype; and 4) an asymmetric temporoparietal phenotype [37]. The current hypothesis for tau spreading in AD states that tau pathology propagates from cell to cell via neuronal projections [5, 36]. Since cases in Vogel's study encompassed the whole disease progression spectrum, the authors were able to define unique tau-spreading epicenters for each distinct phenotype, being the entorhinal cortex for limbic predominant, the middle temporal gyrus for medial temporal lobe sparing, the fusiform gyrus for the posterior occipitotemporal and the inferior temporal gyrus for the asymmetric temporoparietal phenotype [37]. According to Vogel's study, the PCA cases in chapter 3 most likely follow the medial temporal lobe phenotype

trajectory [37]. Based on the high pTau burden measured in the middle temporal gyrus of PCA cases, it is tempting to assume that the highest pTau burden equals the 'earliest' pTau deposition site. However, the fact that tau burden did not translate to the tau-epicenters for the other two AD subtypes defies this assumption and confronts us with the cross-sectional aspect of post mortem. Although the difference in tau spreading epicenters for each phenotype provides an explanation for the heterogeneity in tau distribution, it does not connect the tau to the presence of A β plaques, the other AD pathological hallmark. Neuronal connectivity seems to only partly explain the distribution of tau pathology. Interestingly, the authors show that A β seems to be necessary for the pathological tau to progress its distribution from the hippocampal areas to the neocortex [36].

Glia cells as the directors of A β toxicity and subsequent clinical heterogeneity

According to the leading amyloid cascade hypothesis, AD starts with the neuronal excretion of A β . However, many elderly have brains full of A β pathology without showing any signs of neurodegeneration, let alone cognitive decline [7, 10]. The deposition of A β follows an almost opposite spatiotemporal route than that of NFTs [4, 31], and clinical trials aimed at extracting A β pathology from the brain have so far failed in saving patients from the detrimental consequences of AD [11]. These arguments imply that A β by itself is not enough for the formation of NFTs. Indeed, accumulating evidence points to a crucial role for the innate immune system in AD pathogenesis. Genome wide association studies (GWAS) show that common variants in innate immunity related genes such as CR1, TREM2, CD33, and ABCA7 are associated with a higher risk of AD, rather than genes involved in A β production or cleavage [3, 14, 17, 29]. Based to the findings in Chapter 2, 4, and 6, I hypothesize that glia cells are the directors in the formation -and the resulting morphology- of A β deposits. According to the revised amyloid hypothesis it's not only fibrillar A β that is toxic, but also the oligomeric form that is toxic. Especially this oligomeric form seems to be the instigator of synaptic toxicity [18, 27, 35]. As plaques seem to show increased fibrillar and decreased oligomeric content along the proposed plaque-development scale of diffuse to compact to classical cored plaques (chapter 5), I hypothesize plaques to become less toxic during development and that plaque formation might even be a strategy to de-escalate A β 's potential toxicity. Evidence supporting the regulating role of the innate immune system on A β deposit formation, comes from mouse models. In an APP/PS1 mouse model causing A β overproduction, knocking out the gene responsible for complement factor C3 production, resulted in a better cognition than in the APP/PS1 mouse with wildtype C3 [28]. Interestingly, the

knock-out C3 mice had more and larger plaques than the wildtypes, indicating that a higher number of plaques in this mouse model seems protective. A recent paper showed that in an AD mouse model with normal functioning microglia, especially dense-cored plaques were formed [12]. When microglia were made incapable of phagocytosis due to knocking out the Axl and Mer receptor, the knock-out mice showed less dense cored plaques, but an increase in diffuse-looking 'cotton wool' plaques and CAA compared to the wild-type mice. The microglia knock-out mice showed besides less cored plaques, a worse cognition, indicating that unsuccessful formation of dense cored plaques due to microglia-incapability caused more harm. Although mouse pathology differs from human pathology, these findings might be comparable to the human situation, where I hypothesize classic cored plaques to be 'disarmed' A β deposits and coarse-grained plaques and CAA in the capillaries to be deposits where the innate immune system failed its de-escalating approach. In case of microglia and their role in de-escalating A β toxicity, systemic infections may function as the straw that breaks the camel's back. For example, in elderly the onset of dementia is very well correlated with delirium [38], a brain state defined as an acute disorder of attention and cognition that is often the first presentation in elderly with a urinary tract or pulmonary infection [15]. Although the etiology of delirium is multifactorial, the pathophysiology is associated with an increase of pro-inflammatory markers in the brain and a stimulation of microglial activation [9, 19, 21]. The sudden change in immune regulating proteins alters brain homeostasis causing the microglia to shift their focus from de-escalating A β toxicity to dealing with a pro-inflammatory state. This subsequently may lead to their failure in compartmentalizing and removing A β , followed by increased A β toxicity causing the sequential tau hyperphosphorylation and neuronal degeneration. Very interesting data corroborating that it might not be the A β itself but rather the handling of A β that causes the neurodegeneration, comes from a case study [2]. The woman described in the study is a carrier of the *PSEN1* E280A mutation, a mutation known to cause Ab₄₂ overproduction [26]. Usually, carriers with this mutation show the first symptoms of cognitive decline at age 40 [1]. However, the woman in the case study was functioning cognitively fine until 30 years after the expected age of onset [2]. Whole exome sequencing confirmed the E280A mutation and interestingly revealed homozygosity for the rare *APOE* R136S mutation. ApoE is a protein that is very important in the lipid transport and is in the brain shown to bind A β as well as to play a role in its uptake and degradation by glial cells [20, 33]. An amyloid PET scan using the Pittsburgh Compound-B (PiB) tracer, confirmed the woman's brain was full of fibrillar amyloid pathology, even more than the 40-year-old mutation carriers

that do show cognitive decline at the expected age of onset [2]. Tau PET however showed very little pathology, mostly located around the medial temporal lobe. The authors therefore concluded that the homozygous *APOE* mutation protected the brain from developing tau pathology and neurodegeneration even in the light of high amyloid levels [2]. As PiB binds to the fibrillar form of A β , the increased amyloid signal on PiB PET could indicate increased levels of fibrillar compared to oligomeric A β . Perhaps the *APOE* mutation causes more aggregation and better compaction of the overproduced A β , e.g., plaque formation, by glial cells. This could sequentially lead to the same amount of A β in her brain as her *PSEN1* mutation carrier family members, but more in the fibrillar than oligomeric form, which could be relatively less toxic. In our opinion, the above-mentioned literature demands a change from the earlier proposed linear amyloid hypothesis starting with A β to a more immunology-based hypothesis, in which glia cells act as the gatekeepers of A β toxicity, even in autosomal dominant caused AD.

Towards ATNI criteria for AD

Before the biomarker era, the clinical diagnosis for AD was mostly based on the patient's symptomatology and required post mortem confirmation. Thanks to the major advances in the biomarker field, the current diagnosis for Alzheimer's disease has shifted from a predominantly clinical perspective to a biology-based perspective. This shift is reflected in the recent research framework for diagnosing AD based on detecting the presence of A β (A), pTau (T), and neurodegeneration (N) [13]. The modalities to measure these ATN criteria are CSF A β or amyloid PET for (A); CSF pTau or tau PET for (T); and atrophy on structural MRI, hypometabolism on FDG-PET, or total tau in CSF for (N). Although A β CSF and amyloid PET are extremely sensitive in reflecting A β pathology in the brain, these modalities are not able to detect the variability in the presence of specific types of A β deposits, nor in the underlying associated disease mechanisms. Compelling evidence shows that the brain's innate immune system, composed of microglia and astrocytes, drives AD pathology and that this system might very well be the connecting link between A β and pTau. Therefore, I propose adding an 'I' for neuroInflammation to these criteria, resulting in the ATNI criteria.

A potential neuroinflammation marker is the 18 kDa translocator protein (TSPO), a protein that is expressed on both astrocytes and microglia associated in the inflammatory process [23] and for which multiple PET ligands are available, facilitating the mapping of neuroinflammation in vivo. Binding of TSPO, measured with the ¹¹C-PBR28 ligand, was not only shown to be associated with

the severity of AD [16], but also shown to independently correlate with cognitive decline, amyloid PET, and tau PET [39], corroborating neuroinflammation as the connecting link between A β , tau and symptomatology. Furthermore, the distribution of TSPO seems to be associated with the patient's clinical AD subtype [32], making it an interesting marker in the study on clinical heterogeneity and the regional distribution of disease mechanisms.

The glial fibrillary acidic protein (GFAP), a well-known marker for reactive astrocytosis and often used in immunohistochemical studies is currently a well-investigated target. The level of GFAP in the blood is able to distinguish AD from non-AD neurodegenerative disease [24] and is associated with A β pathology, even in cognitively healthy subjects [6, 34]. The fact that GFAP can be detected in the blood makes this a promising marker.

The mentioned markers comprise only a small aspect of the process called neuroinflammation and I am very well aware that further research is necessary to depict the most important and informative markers, before the I can be reliably added to the existing ATN framework..

Future directions

Following the studies described in this thesis, I propose several future directions, which can be divided based on an etiological or biomarker translation viewpoint, of which I will mention a few in this paragraph. In order to gain more insight into the etiological diversity in AD, it is important to investigate the difference in regional deposition of specific A β deposits such as the diffuse plaques, classic cored plaques, coarse-grained plaques, cotton wool plaques, and CAA and their association with the underlying regional innate immune response of AD subtypes. To embark on this quest as efficient as possible, it would be beneficial to improve the current artificial intelligence (AI) algorithms for detecting different types of deposits in such a way that it also detects the coarse-grained plaque [30]. With the help of present techniques in digitizing pathology and AI and by combining different post mortem cohorts, we will create enough speed and statistical power to answer if there is a (regional specific) relation between distinct A β deposits, certain immune cells, and specific NFT distributions in AD subtypes. Another important step in disentangling AD etiology would be to analyse the proteome of named specific A β deposits to obtain more insights into other underlying disease mechanisms besides neuroinflammation related to the different deposits. Subsequently, by studying the presence of the deposit-specific markers in in vivo-derived blood or CSF, we could possibly predict the A β

deposit landscape in the brain, as well as the related disease mechanisms at play. Thanks to the joint forces of the Amsterdam Dementia Cohort consortium (ADC; Amsterdam, the Netherlands), the Normal Aging Brain Collection Amsterdam (NABCA; Amsterdam, the Netherlands) and the Netherlands Brain Bank (NBB; Amsterdam, the Netherlands), most of these proposed next steps can be -and are as we speak- initiated in our uniquely gathered cohort of brain donors. One of the concrete studies in the pipeline is measuring the levels of GFAP and norrin in the blood and correlate them to the levels and distribution of pathology in the brain (of the cases included in chapters 3 and 8). Another concrete study investigating that etiological diversity is to associate the underlying genome as analyzed by whole-exome sequencing to the presence and distribution of the specific A β deposits.

During the trajectory of my Ph.D., my colleagues and I set up a unique cohort of AD brain donors that have extensive clinical information, both in vivo and post mortem derived body-fluids, and both in vivo and post mortem MRI data readily available. The studies in this thesis only represent a tiny tip of the iceberg of the directly translational studies that are possible from such a valuable cohort. I believe that future pathology studies should continue to focus on prospectively gathering cohorts to enable direct translational studies, so that post mortem investigations not only add to knowledge in hindsight, but directly aid to a better disease-mechanistic stratification of patients in the memory clinic.

Conclusion

AD heterogeneity is since the first description of the disease an ongoing topic of debate. Since pathology seemed diverse within cases but similar for different types of patients, i.e., early-onset versus late-onset and sporadic versus genetic, it were in fact the pathologists who suggested to categorize AD as a single disease entity. However, in this thesis I show that various AD subtypes not only have different regional distribution patterns of AD pathological hallmarks, I also show that certain A β pathology is predominantly seen in a particular AD subgroup and that the underlying neuroinflammatory process may be a crucial factor in linking tau to A β . It seems that disease mechanisms, in particular neurodegeneration and neuroinflammation may be differently involved in various AD subtypes. Therefore, I propose a paradigm change in AD research: instead of focusing on AD as a single pathological entity, future research should acknowledge the individual differences in immunology related to AD pathology. To grow a better etiological understanding, we should start to disentangle those individual neuro-immunological differences at the immunohistochemical and

genetical level. To measure the status and progression of the innate immunity in vivo, we also need to continue our search for derivatives of this innate immune system in the CSF and blood, or by imaging. Not only will this approach help us in understanding the disease, it will also aid in 1) the categorization of patients based on their neuro-immunologic fingerprint and 2) developing personalized treatment strategies that are tailored to both anti-A β and pTau, as well as the innate immune system.

REFERENCES

1. Acosta-Baena N, Sepulveda-Falla D, Lopera-Gómez CM, Jaramillo-Elorza MC, Moreno S, Aguirre-Acevedo DC, Saldarriaga A, Lopera F (2011) Pre-dementia clinical stages in presenilin 1 E280A familial early-onset Alzheimer's disease: A retrospective cohort study. *Lancet Neurol* 10:213–220. doi: 10.1016/S1474-4422(10)70323-9
2. Arboleda-Velasquez JF, Lopera F, O'Hare M, Delgado-Tirado S, Marino C, Chmielewska N, Saez-Torres KL, Amarnani D, Schultz AP, Sperling RA, Leyton-Cifuentes D, Chen K, Baena A, Aguillon D, Rios-Romenets S, Giraldo M, Guzmán-Vélez E, Norton DJ, Pardilla-Delgado E, Artola A, Sanchez JS, Acosta-Uribe J, Lalli M, Kosik KS, Huentelman MJ, Zetterberg H, Blennow K, Reiman RA, Luo J, Chen Y, Thiyyagura P, Su Y, Jun GR, Naymik M, Gai X, Bootwalla M, Ji J, Shen L, Miller JB, Kim LA, Tariot PN, Johnson KA, Reiman EM, Quiroz YT (2019) Resistance to autosomal dominant Alzheimer's disease in an APOE3 Christchurch homozygote: a case report. *Nat Med* 25:1680–1683. doi: 10.1038/s41591-019-0611-3
3. Bertram L, Lange C, Mullin K, Parkinson M, Hsiao M, Hogan MF, Schjeide BMM, Hooli B, Divito J, Ionita I, Jiang H, Laird N, Moscarillo T, Ohlsen KL, Elliott K, Wang X, Hu-Lince D, Ryder M, Murphy A, Wagner SL, Blacker D, Becker KD, Tanzi RE (2008) Genome-wide association analysis reveals putative Alzheimer's disease susceptibility loci in addition to APOE. *Am J Hum Genet* 83:623–632. doi: 10.1016/j.ajhg.2008.10.008
4. Braak H, Alafuzoff I, Arzberger T, Kretschmar H, Tredici K (2006) Staging of Alzheimer disease-associated neurofibrillary pathology using paraffin sections and immunocytochemistry. *Acta Neuropathol* 112:389–404. doi: 10.1007/s00401-006-0127-z
5. Brettschneider J, Del Tredici K, Lee VMY, Trojanowski JQ (2015) Spreading of pathology in neurodegenerative diseases: A focus on human studies. *Nat. Rev. Neurosci.* 16:109–120
6. Chatterjee P, Pedrini S, Stoops E, Goozee K, Villemagne VL, Asih PR, Verberk IMW, Dave P, Taddei K, Sohrabi HR, Zetterberg H, Blennow K, Teunissen CE, Vanderstichele HM, Martins RN (2021) Plasma glial fibrillary acidic protein is elevated in cognitively normal older adults at risk of Alzheimer's disease. *Transl Psychiatry* 11. doi: 10.1038/s41398-020-01137-1
7. Delaère P, He Y, Fayet G, Duyckaerts C, Hauw JJ (1993) β A4 deposits are constant in the brain of the oldest old: An immunocytochemical study of 20 french centenarians. *Neurobiol Aging* 14:191–194. doi: 10.1016/0197-4580(93)90096-T
8. Galton CJ, Patterson K, Xuereb JH, Hodges JR (2000) Atypical and typical presentations of Alzheimer's disease: a clinical, neuropsychological, neuroimaging and pathological study of 13 cases. *Brain* 123:484–98
9. van Gool WA, van de Beek D, Eikelenboom P (2010) Systemic infection and delirium: when cytokines and acetylcholine collide. *Lancet* 375:773–775

10. Hedden T, Oh H, Younger AP, Patel TA (2013) Meta-analysis of amyloid-cognition relations in cognitively normal older adults. *Neurology* 80:1341–1348. doi: 10.1212/WNL.0b013e31828ab35d
11. Huang LK, Chao SP, Hu CJ (2020) Clinical trials of new drugs for Alzheimer disease. *J. Biomed. Sci.* 27
12. Huang Y, Happonen KE, Burrola PG, O'Connor C, Hah N, Huang L, Nimmerjahn A, Lemke G (2021) Microglia use TAM receptors to detect and engulf amyloid β plaques. *Nat Immunol* 1–9. doi: 10.1038/s41590-021-00913-5
13. Jack CR, Bennett DA, Blennow K, Carrillo MC, Dunn B, Haeberlein SB, Holtzman DM, Jagust W, Jessen F, Karlawish J, Liu E, Molinuevo JL, Montine T, Phelps C, Rankin KP, Rowe CC, Scheltens P, Siemers E, Snyder HM, Sperling R, Elliott C, Masliah E, Ryan L, Silverberg N (2018) NIA-AA Research Framework: Toward a biological definition of Alzheimer's disease. *Alzheimer's Dement* 14:535–562. doi: 10.1016/j.jalz.2018.02.018
14. Jonsson T, Stefansson H, Steinberg S, Jonsdottir I, Jonsson P V., Snaedal J, Bjornsson S, Huttenlocher J, Levey AI, Lah JJ, Rujescu D, Hampel H, Giegling I, Andreassen OA, Engedal K, Ulstein I, Djurovic S, Ibrahim-Verbaas C, Hofman A, Ikram MA, van Duijn CM, Thorsteinsdottir U, Kong A, Stefansson K (2013) Variant of TREM2 Associated with the Risk of Alzheimer's Disease. *N Engl J Med* 368:107–116. doi: 10.1056/nejmoa1211103
15. Kalish VB, Gillham JE, Unwin BK (2014) Delirium in Older Persons: Evaluation and Management
16. Kreisl WC, Lyoo CH, McGwier M, Snow J, Jenko KJ, Kimura N, Corona W, Morse CL, Zoghbi SS, Pike VW, McMahon FJ, Turner RS, Innis RB, Biomarkers Consortium PET Radioligand Project Team the BCPRP (2013) In vivo radioligand binding to translocator protein correlates with severity of Alzheimer's disease. *Brain* 136:2228–38. doi: 10.1093/brain/awt145
17. Lambert JC, Heath S, Even G, Campion D, Sleegers K, Hiltunen M, Combarros O, Zelenika D, Bullido MJ, Tavernier B, Letenneur L, Bettens K, Berr C, Pasquier F, Fiévet N, Barberger-Gateau P, Engelborghs S, De Deyn P, Mateo I, Franck A, Helisalmi S, Porcellini E, Hanon O, De Pancorbo MM, Lendon C, Dufouil C, Jaillard C, Leveillard T, Alvarez V, Bosco P, Mancuso M, Panza F, Nacmias B, Boss P, Piccardi P, Annoni G, Seripa D, Galimberti D, Hannequin D, Licastro F, Soininen H, Ritchie K, Blanché H, Dartigues JF, Tzourio C, Gut I, Van Broeckhoven C, Alperovitch A, Lathrop M, Amouyel P (2009) Genome-wide association study identifies variants at CLU and CR1 associated with Alzheimer's disease. *Nat Genet* 41:1094–1099. doi: 10.1038/ng.439
18. Lambert MP, Barlow AK, Chromy BA, Edwards C, Freed R, Liosatos M, Morgan TE, Rozovsky I, Trommer B, Viola KL, Wals P, Zhang C, Finch CE, Krafft GA, Klein WL (1998) Diffusible, nonfibrillar ligands derived from A β 1–42 are potent central nervous system neurotoxins. *Proc Natl Acad Sci U S A* 95:6448–6453. doi: 10.1073/pnas.95.11.6448

19. Lemstra AW, Groen in't Woud JCM, Hoozemans JJM, van Haastert ES, Rozemuller AJM, Eikelenboom P, van Gool WA (2007) Microglia activation in sepsis: A case-control study. *J Neuroinflammation* 4. doi: 10.1186/1742-2094-4-4
20. Liu CC, Kanekiyo T, Xu H, Bu G (2013) Apolipoprotein e and Alzheimer disease: Risk, mechanisms and therapy. *Nat. Rev. Neurol.* 9:106-118
21. MacLulich AMJ, Edelshain BT, Hall RJ, De Vries A, Howie SEM, Pearson A, Middleton SD, Gillies F, Armstrong IR, White TO, Cunningham C, De Rooij SE, Van Munster BC (2011) Cerebrospinal fluid interleukin-8 levels are higher in people with hip fracture with perioperative delirium than in controls. *J. Am. Geriatr. Soc.* 59:1151-1153
22. Murray ME, Graff-Radford NR, Ross OA, Petersen RC, Duara R, Dickson DW (2011) Neuropathologically defined subtypes of Alzheimer's disease with distinct clinical characteristics: a retrospective study. *Lancet Neurol* 10:785-796. doi: 10.1016/S1474-4422(11)70156-9
23. Nutma E, Stephenson JA, Gorter RP, De Bruin J, Boucherie DM, Donat CK, Breur M, Van Der Valk P, Matthews PM, Owen DR, Amor S (2019) A quantitative neuropathological assessment of translocator protein expression in multiple sclerosis. *Brain* 142:3440-3455. doi: 10.1093/brain/awz287
24. Oeckl P, Halbgebauer S, Anderl-Straub S, Steinacker P, Hussa AM, Neugebauer H, Von Arnim CAF, Diehl-Schmid J, Grimmer T, Kornhuber J, Lewczuk P, Danek A, Degeneration L, Ludolph AC, Otto M (2019) Glial fibrillary acidic protein in serum is increased in Alzheimer's disease and correlates with cognitive impairment. *J Alzheimer's Dis* 67:481-488. doi: 10.3233/JAD-180325
25. Ossenkoppele R, Schonhaut DR, Schöll M, Lockhart SN, Ayakta N, Baker SL, O'Neil JP, Janabi M, Lazaris A, Cantwell A, Vogel J, Santos M, Miller ZA, Bettcher BM, Vessel KA, Kramer JH, Gorno-Tempini ML, Miller BL, Jagust WJ, Rabinovici GD (2016) Tau PET patterns mirror clinical and neuroanatomical variability in Alzheimer's disease. *Brain* 139:1551-1567. doi: 10.1093/brain/aww027
26. Quiroz YT, Sperling RA, Norton DJ, Baena A, Arboleda-Velasquez JF, Cosio D, Schultz A, Lapoint M, Guzman-Velez E, Miller JB, Kim LA, Chen K, Tariot PN, Lopera F, Reiman EM, Johnson KA (2018) Association between amyloid and tau accumulation in young adults with autosomal dominant Alzheimer disease. *JAMA Neurol* 75:548-556. doi: 10.1001/jamaneurol.2017.4907
27. Selkoe DJ, Hardy J (2016) The amyloid hypothesis of Alzheimer's disease at 25 years. *EMBO Mol Med* 8:1-14. doi: 10.15252/emmm.201606210
28. Shi Q, Chowdhury S, Ma R, Le KX, Hong S, Caldarone BJ, Stevens B, Lemere CA (2017) Complement C3 deficiency protects against neurodegeneration in aged plaque-rich APP/PS1 mice. *Sci Transl Med* 9:eaaf6295. doi: 10.1126/scitranslmed.aaf6295
29. Sims R, van der Lee SJ, Naj AC, Bellenguez C, Badarinarayan N, Jakobsdottir J, Kunkle BW, Boland A, Raybould R, Bis JC, Martin ER, Grenier-Boley B, Heilmann-Heimbach S, Chouraki V, Kuzma AB, Sleegers K, Vronskaya M, Ruiz A, Graham RR,

Olaso R, Hoffmann P, Grove ML, Vardarajan BN, Hiltunen M, Nöthen MM, White CC, Hamilton-Nelson KL, Epelbaum J, Maier W, Choi S-H, Beecham GW, Dulary C, Herms S, Smith A V, Funk CC, Derbois C, Forstner AJ, Ahmad S, Li H, Bacq D, Harold D, Satizabal CL, Valladares O, Squassina A, Thomas R, Brody JA, Qu L, Sánchez-Juan P, Morgan T, Wolters FJ, Zhao Y, Garcia FS, Denning N, Fornage M, Malamon J, Naranjo MCD, Majounie E, Mosley TH, Dombroski B, Wallon D, Lupton MK, Dupuis J, Whitehead P, Fratiglioni L, Medway C, Jian X, Mukherjee S, Keller L, Brown K, Lin H, Cantwell LB, Panza F, McGuinness B, Moreno-Grau S, Burgess JD, Solfrizzi V, Proitsi P, Adams HH, Allen M, Seripa D, Pastor P, Cupples LA, Price ND, Hannequin D, Frank-García A, Levy D, Chakrabarty P, Caffarra P, Giegling I, Beiser AS, Giedraitis V, Hampel H, Garcia ME, Wang X, Lannfelt L, Mecocci P, Eiriksdottir G, Crane PK, Pasquier F, Boccardi V, Henández I, Barber RC, Scherer M, Tarraga L, Adams PM, Leber M, Chen Y, Albert MS, Riedel-Heller S, Emilsson V, Beekly D, Braae A, Schmidt R, Blacker D, Masullo C, Schmidt H, Doody RS, Spalletta G, Jr WTL, Fairchild TJ, Bossù P, Lopez OL, Frosch MP, Sacchinelli E, Ghetti B, Yang Q, Huebinger RM, Jessen F, Li S, Kamboh MI, Morris J, Sotolongo-Grau O, Katz MJ, Corcoran C, Dunstan M, Braddel A, Thomas C, Meggy A, Marshall R, Gerrish A, Chapman J, Aguilar M, Taylor S, Hill M, Fairén MD, Hodges A, Vellas B, Soininen H, Kloszewska I, Daniilidou M, Uphill J, Patel Y, Hughes JT, Lord J, Turton J, Hartmann AM, Cecchetti R, Fenoglio C, Serpente M, Arcaro M, Caltagirone C, Orfei MD, Ciamarella A, Pichler S, Mayhaus M, Gu W, Lleó A, Fortea J, Blesa R, Barber IS, Brookes K, Cupidi C, Maletta RG, Carrell D, Sorbi S, Moebus S, Urbano M, Pilotto A, Kornhuber J, Bosco P, Todd S, Craig D, Johnston J, Gill M, Lawlor B, Lynch A, Fox NC, Hardy J, Albin RL, Apostolova LG, Arnold SE, Asthana S, Atwood CS, Baldwin CT, Barnes LL, Barral S, Beach TG, Becker JT, Bigio EH, Bird TD, Boeve BF, Bowen JD, Boxer A, Burke JR, Burns JM, Buxbaum JD, Cairns NJ, Cao C, Carlson CS, Carlsson CM, Carney RM, Carrasquillo MM, Carroll SL, Diaz CC, Chui HC, Clark DG, Cribbs DH, Crocco EA, DeCarli C, Dick M, Duara R, Evans DA, Faber KM, Fallon KB, Fardo DW, Farlow MR, Ferris S, Foroud TM, Galasko DR, Gearing M, Geschwind DH, Gilbert JR, Graff-Radford NR, Green RC, Growdon JH, Hamilton RL, Harrell LE, Honig LS, Huentelman MJ, Hulette CM, Hyman BT, Jarvik GP, Abner E, Jin L-W, Jun G, Karydas A, Kaye JA, Kim R, Kowall NW, Kramer JH, LaFerla FM, Lah JJ, Leverenz JB, Levey AI, Li G, Lieberman AP, Lunetta KL, Lyketsos CG, Marson DC, Martiniuk F, Mash DC, Masliah E, McCormick WC, McCurry SM, McDavid AN, McKee AC, Mesulam M, Miller BL, Miller CA, Miller JW, Morris JC, Murrell JR, Myers AJ, O'Bryant S, Olichney JM, Pankratz VS, Parisi JE, Paulson HL, Perry W, Peskind E, Pierce A, Poon WW, Potter H, Quinn JF, Raj A, Raskind M, Reisberg B, Reitz C, Ringman JM, Roberson ED, Rogaeva E, Rosen HJ, Rosenberg RN, Sager MA, Saykin AJ, Schneider JA, Schneider LS, Seeley WW, Smith AG, Sonnen JA, Spina S, Stern RA, Swerdlow RH, Tanzi RE, Thornton-Wells TA, Trojanowski JQ, Troncoso JC, Van Deerlin VM, Van Eldik LJ, Vinters H V, Vonsattel JP, Weintraub S, Welsh-Bohmer KA, Wilhelmsen KC, Williamson J, Wingo TS, Woltjer RL, Wright CB, Yu C-E, Yu L, Garzia F, Golamaully F, Septier G, Engelborghs S, Vandenberghe

- R, De Deyn PP, Fernadez CM, Benito YA, Thonberg H, Forsell C, Lilius L, Kinhult-Ståhlbom A, Kilander L, Brundin R, Concaro L, Helisalmi S, Koivisto AM, Haapasalo A, Dermecourt V, Fievet N, Hanon O, Dufouil C, Brice A, Ritchie K, Dubois B, Himali JJ, Keene CD, Tschanz J, Fitzpatrick AL, Kukull WA, Norton M, Aspelund T, Larson EB, Munger R, Rotter JL, Lipton RB, Bullido MJ, Hofman A, Montine TJ, Coto E, Boerwinkle E, Petersen RC, Alvarez V, Rivadeneira F, Reiman EM, Gallo M, O'Donnell CJ, Reisch JS, Bruni AC, Royall DR, Dichgans M, Sano M, Galimberti D, St George-Hyslop P, Scarpini E, Tsuang DW, Mancuso M, Bonuccelli U, Winslow AR, Daniele A, Wu C-K, Peters O, Nacmias B, Riemenschneider M, Heun R, Brayne C, Rubinsztein DC, Bras J, Guerreiro R, Al-Chalabi A, Shaw CE, Collinge J, Mann D, Tsolaki M, Clarimón J, Sussams R, Lovestone S, O'Donovan MC, Owen MJ, Behrens TW, Mead S, Goate AM, Uitterlinden AG, Holmes C, Cruchaga C, Ingelsson M, Bennett DA, Powell J, Golde TE, Graff C, De Jager PL, Morgan K, Ertekin-Taner N, Combarros O, Psaty BM, Passmore P, Younkin SG, Berr C, Gudnason V, Rujescu D, Dickson DW, Dartigues J-F, DeStefano AL, Ortega-Cubero S, Hakonarson H, Campion D, Boada M, Kauwe JK, Farrer LA, Van Broeckhoven C, Ikram MA, Jones L, Haines JL, Tzourio C, Launer LJ, Escott-Price V, Mayeux R, Deleuze J-F, Amin N, Holmans PA, Pericak-Vance MA, Amouyel P, van Duijn CM, Ramirez A, Wang L-S, Lambert J-C, Seshadri S, Williams J, Schellenberg GD, Williams J, Schellenberg GD (2017) Rare coding variants in *PLCG2*, *ABI3*, and *TREM2* implicate microglial-mediated innate immunity in Alzheimer's disease. *Nat Genet* 49:1373-1384. doi: 10.1038/ng.3916
30. Tang Z, Chuang K V, DeCarli C, Jin LW, Beckett L, Keiser MJ, Dugger BN (2019) Interpretable classification of Alzheimer's disease pathologies with a convolutional neural network pipeline. *Nat Commun* 10:1-14. doi: 10.1038/s41467-019-10212-1
 31. Thal DR, Rüb U, Orantes M, Braak H (2002) Phases of A beta-deposition in the human brain and its relevance for the development of AD. *Neurology* 58:1791-800. doi: 10.1212/wnl.58.12.1791
 32. Tondo G, Iaccarino L, Caminiti SP, Presotto L, Santangelo R, Iannaccone S, Magnani G, Perani D (2020) The combined effects of microglia activation and brain glucose hypometabolism in early-onset Alzheimer's disease. *Alzheimer's Res Ther* 12:1-10. doi: 10.1186/s13195-020-00619-0
 33. Ulrich JD, Ulland TK, Mahan TE, Nyström S, Peter Nilsson K, Song WM, Zhou Y, Reinartz M, Choi S, Jiang H, Stewart FR, Anderson E, Wang Y, Colonna M, Holtzman DM (2018) ApoE facilitates the microglial response to amyloid plaque pathology. *J Exp Med* 215:1047-1058. doi: 10.1084/jem.20171265
 34. Verberk IMW, Thijssen E, Koelewijn J, Mauroo K, Vanbrabant J, De Wilde A, Zwan MD, Verfaillie SCJ, Ossenkuppele R, Barkhof F, Van Berckel BNM, Scheltens P, Van Der Flier WM, Stoops E, Vanderstichele HM, Teunissen CE (2020) Combination of plasma amyloid beta(1-42/1-40) and glial fibrillary acidic protein strongly associates with cerebral amyloid pathology. *Alzheimer's Res Ther* 12. doi: 10.1186/s13195-020-00682-7

35. Viola KL, Klein WL (2015) Amyloid β oligomers in Alzheimer's disease pathogenesis, treatment, and diagnosis. *Acta Neuropathol* 129:183–206. doi: 10.1007/s00401-015-1386-3
36. Vogel JW, Iturria-Medina Y, Strandberg OT, Smith R, Levitis E, Evans AC, Hansson O (2020) Spread of pathological tau proteins through communicating neurons in human Alzheimer's disease. *Nat Commun* 11:2612. doi: 10.1038/s41467-020-15701-2
37. Vogel JW, Young AL, Oxtoby NP, Smith R, Ossenkoppele R, Strandberg OT, La Joie R, Aksman LM, Grothe MJ, Iturria-Medina Y, Weiner M, Aisen P, Petersen R, Jack CR, Jagust W, Trojanowki JQ, Toga AW, Beckett L, Green RC, Saykin AJ, Morris J, Shaw LM, Liu E, Montine T, Thomas RG, Donohue M, Walter S, Gessert D, Sather T, Jiminez G, Harvey D, Bernstein M, Fox N, Thompson P, Schuff N, DeCarli C, Borowski B, Gunter J, Senjem M, Vemuri P, Jones D, Kantarci K, Ward C, Koeppe RA, Foster N, Reiman EM, Chen K, Mathis C, Landau S, Cairns NJ, Householder E, Reinwald LT, Lee V, Korecka M, Figurski M, Crawford K, Neu S, Foroud TM, Potkin S, Shen L, Kelley F, Kim S, Nho K, Kachaturian Z, Frank R, Snyder PJ, Molchan S, Kaye J, Quinn J, Lind B, Carter R, Dolen S, Schneider LS, Pawluczyk S, Beccera M, Teodoro L, Spann BM, Brewer J, Vanderswag H, Fleisher A, Heidebrink JL, Lord JL, Mason SS, Albers CS, Knopman D, Johnson K, Doody RS, Meyer JV, Chowdhury M, Rountree S, Dang M, Stern Y, Honig LS, Bell KL, Ances B, Morris JC, Carroll M, Leon S, Mintun MA, Schneider S, Oliver A, Griffith R, Clark D, Geldmacher D, Brockington J, Roberson E, Grossman H, Mitsis E, deToledo-Morrell L, Shah RC, Duara R, Varon D, Greig MT, Roberts P, Albert M, Onyike C, D'Agostino D, Kielb S, Galvin JE, Pogorelec DM, Cerbone B, Michel CA, Rusinek H, de Leon MJ, Glodzik L, De Santi S, Doraiswamy PM, Petrella JR, Wong TZ, Arnold SE, Karlawish JH, Wolk D, Smith CD, Jicha G, Hardy P, Sinha P, Oates E, Conrad G, Lopez OL, Oakley MA, Simpson DM, Porsteinsson AP, Goldstein BS, Martin K, Makino KM, Ismail MS, Brand C, Mulnard RA, Thai G, McAdams Ortiz C, Womack K, Mathews D, Quiceno M, Arrastia RD, King R, Weiner M, Cook KM, DeVous M, Levey AI, Lah JJ, Cellar JS, Burns JM, Anderson HS, Swerdlow RH, Apostolova L, Tingus K, Woo E, Silverman DHS, Lu PH, Bartzokis G, Radford NRG, Parfitt F, Kendall T, Johnson H, Farlow MR, Hake AM, Matthews BR, Herring S, Hunt C, van Dyck CH, Carson RE, MacAvoy MG, Chertkow H, Bergman H, Hosein C, Black S, Stefanovic B, Caldwell C, Hsiung GYR, Feldman H, Mudge B, Past MA, Kertesz A, Rogers J, Trost D, Bernick C, Munic D, Kerwin D, Mesulam MM, Lipowski K, Wu CK, Johnson N, Sadowsky C, Martinez W, Villena T, Turner RS, Johnson K, Reynolds B, Sperling RA, Johnson KA, Marshall G, Frey M, Yesavage J, Taylor JL, Lane B, Rosen A, Tinklenberg J, Sabbagh MN, Belden CM, Jacobson SA, Sirrel SA, Kowall N, Killiany R, Budson AE, Norbash A, Johnson PL, Obisesan TO, Wolday S, Allard J, Lerner A, Ogrocki P, Hudson L, Fletcher E, Carmichael O, Olichney J, DeCarli C, Kittur S, Borrie M, Lee TY, Bartha R, Johnson S, Asthana S, Carlsson CM, Potkin SG, Preda A, Nguyen D, Tariot P, Reeder S, Bates V, Capote H, Rainka M, Scharre DW, Katakami M, Adeli A,

- Zimmerman EA, Celmins D, Brown AD, Pearlson GD, Blank K, Anderson K, Santulli RB, Kitzmiller TJ, Schwartz ES, Sink KM, Williamson JD, Garg P, Watkins F, Ott BR, Querfurth H, Tremont G, Salloway S, Malloy P, Correia S, Rosen HJ, Miller BL, Mintzer J, Spicer K, Bachman D, Finger E, Pasternak S, Rachinsky I, Drost D, Pomara N, Hernando R, Sarrael A, Schultz SK, Ponto LLB, Shim H, Smith KE, Relkin N, Chaing G, Raudin L, Smith A, Fargher K, Raj BA, Pontecorvo MJ, Devous MD, Rabinovici GD, Alexander DC, Lyoo CH, Evans AC, Hansson O (2021) Four distinct trajectories of tau deposition identified in Alzheimer's disease. *Nat Med* 27:871-881. doi: 10.1038/s41591-021-01309-6
38. Witlox J, Eurelings LSM, De Jonghe JFM, Kalisvaart KJ, Eikelenboom P, Van Gool WA (2010) Delirium in elderly patients and the risk of postdischarge mortality, institutionalization, and dementia: A meta-analysis. *JAMA - J. Am. Med. Assoc.* 304:443-451
39. Zou J, Tao S, Johnson A, Tomljanovic Z, Polly K, Klein J, Razlighi QR, Brickman AM, Lee S, Stern Y, Kreisl WC (2020) Microglial activation, but not tau pathology, is independently associated with amyloid positivity and memory impairment. *Neurobiol Aging* 85:11-21. doi: 10.1016/j.neurobiolaging.2019.09.019

Chapter 12

Dutch Summary
Nederlandstalige Samenvatting

NEDERLANDSE SAMENVATTING

Bij de ziekte van Alzheimer denkt men vaak aan vergeetachtigheid als belangrijkste klacht. Echter, de ziekte kan ook met andere symptomen beginnen. Deze atypische ziekte van Alzheimer zien we vooral bij patiënten die de ziekte op jonge leeftijd krijgen. De klachten die patiënten ervaren van de ziekte, worden veroorzaakt door het afsterven van hersencellen, oftewel neurodegeneratie genoemd. Op de geheugenpoli kunnen we deze hersensterfte vaststellen door de hersenrimp te meten op de hersenscan. Na het overlijden zien we bij de ziekte van Alzheimer onder de microscoop iets wat we 'plaques' en 'tangles' noemen in het hersenweefsel van patiënten. Plaques zijn ophopingen van het amyloïde eiwit tussen de zenuwcellen, tangles zijn kluwen van het tau eiwit in de zenuwcellen. De plaques hopen als eerste op. We kunnen het amyloïde eiwit, waaruit de plaques bestaan, soms zelfs 20 jaar voordat patiënten klachten hebben, detecteren op iets wat we een PET hersenscan noemen. Zowel plaques als tangles worden verondersteld via een bepaalde volgorde over de hersenen te verspreiden. De plaques verspreiden zich van buiten naar binnen, dus van de hersenschors naar uiteindelijk de hersenstam. Tangles daarentegen worden vooral pas gezien wanneer patiënten klachten ervaren. Ze verspreiden zich van een hersengebied wat we de entorhinale cortex noemen, via de hippocampus, een hersengebied wat heel belangrijk is bij het geheugen, naar uiteindelijk de hersenschors. Naast plaques en tangles vinden we in de hersenen van patiënten ook veel activatie van ontstekingscellen. Het lijkt erop dat die ontstekingscellen zeer waarschijnlijk een belangrijke rol spelen in het ziekteproces.

Onderzoek van het afgelopen decennium laat zien dat de ziekte niet alleen qua klachten, maar ook op de hersenscan en onder de microscoop een stuk diverser is dan eerder werd aangenomen. Zo blijken patiënten met atypische klachten ook een atypische verdeling van de tangles te hebben. Bij patiënten die zich presenteren met vooral problemen bij het zien, vinden we bijvoorbeeld vooral tangles in de hersengebieden belangrijk bij het zien en in een stuk mindere mate in de hippocampus, het hersengebied belangrijk voor het geheugen. Echter, of er ook verschillen zijn in de verdeling van de plaques en/of de ontstekingscellen, was voordat ik met mijn promotieonderzoek begon, nog onbekend. Daarom concentreren de eerste studies uit dit proefschrift zich op de verschillen onder de microscoop van verschillende typen patiënten met de ziekte van Alzheimer. Deze studies zijn te vinden in de secties 2 (hoofdstukken 2 en 3) en 3 (hoofdstukken 4 t/m 6) van dit proefschrift. De studies beschreven in sectie 4 (hoofdstukken 7 t/m 9) onderzochten of dat wat we zien onder de microscoop,

ook te vertalen is naar wat we zien op hersenscans, zoals we die maken op de geheugenpolikliniek. In dit hoofdstuk vat ik de belangrijkste bevindingen van dit proefschrift samen.

De verdeling van geactiveerde ontstekingscellen is anders voor patiënten met de atypische vorm van de ziekte van Alzheimer

De studie beschreven in hoofdstuk 2 onderzocht het verschil in de verdeling van tangles, plaques en ontstekingscellen over de hersenen tussen typische en atypische ziekte van Alzheimer. De studie bevestigt dat niet alle patiënten de typische verdeling van tangles laten zien. In een groep van bijna 300 hersendonoren had 9% van de donoren namelijk een atypische verdeling. Deze atypische groep bestond vooral uit mannen die de ziekte voor hun 65^e levensjaar krijgen. De studie bevestigt dat de locatie van de tangles vaak overeenkomt met de klachten die patiënten ervaren. Zo hadden bijna alle patiënten met een typische tangle verdeling tijdens het leven ook de typische klachten van vergeetachtigheid, terwijl de meeste patiënten met een atypische tangle verdeling ook atypische klachten hadden tijdens het leven. De verdeling van de ontstekingsreactie leek op die van de tangles, namelijk typisch in typische patiënten en atypisch in atypische patiënten. Echter, lieten de atypische patiënten naast een andere verdeling ook een veel heftigere ontstekingsreactie zien. De verdeling van alle plaques verschilde niet. Als alleen de grotere plaques werden geteld, dan werd er opnieuw een atypische verdeling gevonden. De atypische patiënten hadden meer van deze grote plaques. De grotere plaques zagen er met hun grofkorrelige structuur anders uit dan de al bekende plaques. Tevens zag de ontstekingsreactie in de grotere plaques er anders uit dan de ontstekingsreactie in de al bekende plaques. De typische en atypische patiënten verschillen dus niet alleen van elkaar op basis van tangle verdeling, maar ook op basis van ontstekingsreactie en het aantal grotere plaques. Deze studie benadrukt dat de activatie van ontstekingscellen mogelijk een cruciale link is tussen de plaques en tangles.

Vervolgens heb ik onderzocht of de verschillen gevonden in hoofdstuk 2 ook stand hielden in een andere groep patiënten. In de studie die te lezen is in hoofdstuk 3 werden de hersendonoren enkel als typisch of atypisch gecategoriseerd op basis van hun klachten en niet op basis van de tangle verdeling. De studiegroep bestond uit tien typische Alzheimer hersendonoren en negen atypische Alzheimer hersendonoren. Als controlegroep werden tien hersendonoren zonder hersenziekten gebruikt. De atypische Alzheimer groep was erg gevarieerd met zes donoren die vooral problemen hadden van

het gedrag en drie donoren die vooral klachten hadden van de visus. Zoals te verwachten, hadden de typische donoren meer tangles in het hersengebied dat belangrijk is bij het geheugen dan de atypische donoren. De atypische donoren verschilden onderling niet in hun tangle verdeling. Dit komt meest waarschijnlijk omdat het aantal donoren in de twee atypische groepen te klein was. De atypische Alzheimer donoren met vooral de gedragsproblemen lieten vooral veel plaques zien in een hersengebied betrokken bij gedrag. Ook was de verdeling van geactiveerde ontstekingscellen wederom verschillend tussen typische en atypische donoren. Interessant is dat de verdeling van één specifieke ontstekingscel, de astrocyt, niet alleen onderscheid maakte tussen typische en atypische Alzheimer, maar ook tussen atypische Alzheimer varianten onderling. Deze studie bevestigt de eerdere bevindingen dat een atypische verdeling van ontstekingscellen geassocieerd is met atypische Alzheimer. Het feit dat de activatie van astrocyten de verschillende Alzheimer types beter onderscheidde dan de tangles, wijst wederom op een prominente rol voor de ontstekingscellen in het ziekteproces.

De variatie van plaque types wordt veroorzaakt door de verschillende celtypen die de amyloïde plaque omgeven en door verschillen in de secundaire eiwitstructuur

In de voorgaande sectie van dit thesis is vooral gekeken naar de verdeling van de microscopie bevindingen over verschillende hersengebieden. In de volgende sectie duik ik echter nog meer de diepte in, door in te zoomen op één van die microscopische bevindingen: de plaque.

De 'grofkorrelige plaque' die in de studie uit hoofdstuk 2 was ontdekt, is tot in detail uitgezocht in hoofdstuk 4. De grofkorrelige plaque werd vergeleken met andere plaques die we al kennen bij de ziekte van Alzheimer. De grofkorrelige plaque had niet alleen een andere vorm dan de andere plaques, maar bevatte ook andere eiwitten die normaal gesproken niet in plaques worden gevonden. Terwijl normale plaques ook gevonden worden in oudere mensen die niet aan dementie lijden, werd de grofkorrelige plaque alleen gezien in hersendonoren die tijdens het leven klachten van dementie hadden. Donoren met veel grofkorrelige plaques kregen de ziekte op jongere leeftijd, hadden vaker het *APOE* risico-gen en hadden het amyloïde eiwit vaak ook in de bloedvaten. Uniek aan deze studie is dat de plaque in 3D in beeld is gebracht. Hierdoor ontdekte ik dat de grofkorrelige plaque bijna altijd met een bloedvat verbonden is en dat de eiwit compositie tegenovergesteld is zoals we die zien in de al bekende plaques. Door deze resultaten concludeerde ik dat de grofkorrelige plaque een uniek plaque-

type is en dat deze op een andere manier evolueert dan de andere plaques. Dit heb ik geprobeerd te illustreren in figuur 11 van hoofdstuk 4. Deze studie biedt een morfologische en biochemische definitie voor de grofkorrelige plaque en ondersteunt dat deze plaque uniek is, met specifieke klinische en etiologische aspecten.

Eiwitten kunnen zich op een bepaalde manier vouwen. Middels de volgende metafoor probeer ik deze eiwittenvouwingen wat te verduidelijken. Vergelijk de eiwitten met bakstenen en de eiwitvouwingen met het daaruit volgende bouwsel. U kunt van dezelfde bakstenen een flatgebouw, maar ook een bungalow maken. Ook al bestaan deze bouwsels uit dezelfde bakstenen, toch hebben ze een andere vorm. Zo is het ook voor eiwitten en secundaire eiwitstructuren. Door middel van conventionele experimenten in de neuropathologie kunnen we die bakstenen, of eiwitten onderzoeken. We kunnen echter niet het verschil in uiteindelijke bouwsel, of secundaire eiwitstructuur onderzoeken. Middels de techniek genaamd spectroscopie kunnen we dit wel. Spectroscopie meet het spectrum van licht dat wordt doorgelaten door de materie van interesse (bijvoorbeeld weefsel, moleculen of atomen) als reactie op de blootstelling aan elektromagnetische straling. Op die manier kan men de chemische verbindingen bestuderen en daarmee dus ook het vet-, DNA- of eiwitgehalte, inclusief de secundaire structuur van het eiwit. In hoofdstukken 5 en 6 beschrijf ik de studies waarin verschillende typen plaques zijn onderzocht middels spectroscopie.

De amyloïde plaques zoals we die in de hersenen van patiënten met Alzheimer vinden, kunnen verschillende vormen hebben. De meest voorkomende plaque typen die we kennen zijn de diffuse plaque, de compacte plaque en de klassieke plaque. In figuur 2 van hoofdstuk 5 zijn deze verschillende typen plaques te zien. Het wordt verondersteld dat plaques in een bepaalde volgorde ontwikkelen, waarbij de diffuse plaques gezien worden als plaques in de eerste fase. De compacte plaques worden verondersteld plaques te zijn in de daaropvolgende fase met vervolgens de klassieke plaques in de daaropvolgende fase. Door middel van spectroscopie hebben we een heleboel aantal plaques uit de verschillende categorieën gescand en geanalyseerd. We vonden dat de plaques in de diffuse categorie de minst vergevorderde secundaire eiwitstructuur bevatten, oftewel ze bevatten wel bakstenen maar weinig flatgebouwen. De daaropvolgende fases bevatten in toenemende mate de vergevorderde secundaire eiwitstructuur -of flatgebouwen, met in de klassieke plaque de meeste van deze structuur gelokaliseerd in het midden van de plaque. De gevonden resultaten waren

consistent en zijn gevonden in verschillende patiënten. Deze bevindingen pleiten voor de huidige plaque-ontwikkelingshypothese.

In de studie beschreven in hoofdstuk 6 is wederom spectroscopie toegepast, maar dan op de klassieke plaque en de grofkorrelige plaque. De belangrijkste nieuwe bevinding van dit onderzoek was dat we een signaal oppikte dat specifiek past bij een bepaalde substantie die we carotenoïden noemen. Deze carotenoïden zijn door eerdere studies in verband gebracht met ontstekingsprocessen. Interessant was dat we het carotenoïde signaal alleen in de klassieke plaques oppikte en eigenlijk niet in de grofkorrelige plaque. Hoewel er voor dit onderzoek een klein aantal plaques werd gescand, dragen de resultaten bij aan het bewijs dat de ontstekingsreactie verschilt tussen verschillende typen plaques.

De bovengenoemde drie studies impliceren dat ziektemechanismen zoals ontsteking en de bijdrage van de bloedvaten, evenals de structuur en biochemische samenstelling van de plaque, allen een andere rol spelen in de verschillende plaque types.

Tangles, plaques en ontstekingscellen hebben ieder een verschillende invloed op hersenscan en hersenvocht resultaten

Tegenwoordig hebben we op de geheugenpoli twee methoden om al tijdens het leven te onderzoeken of een Alzheimerpatiënt plaques heeft in de hersenen. Door een positron emissie tomografie, afgekort PET, scan van de hersenen kunnen we het bestanddeel waaruit plaques bestaan, het amyloïde eiwit, detecteren in de hersenen. We kunnen het amyloïde eiwit ook meten in het hersenvocht, waarmee we de hoeveelheid opgehoopt amyloïd in de hersenen kunnen voorspellen. Echter, in 10-20% van de gevallen komt het resultaat van de PET scan niet overeen met het resultaat van het hersenvocht. In de studie beschreven in hoofdstuk 7, is onderzocht wat de onderliggende pathologie was bij patiënten met conflicterende PET en hersenvocht resultaten. In onze studie hadden drie van de totaal 21 patiënten een conflicterend amyloïd resultaat. In twee patiënten duidde het hersenvocht op plaques in de hersenen, maar de PET scan niet. In één patiënt duidde de PET scan op plaques, maar het hersenvocht niet. In deze laatste patiënt was de PET scan juist en vonden we plaques in de hersenen. Het hersenvocht resultaat bleek onjuist. In de eerste patient met een positief hersenvocht resultaat maar negatieve PET scan, bleek ook het hersenvocht onjuist. Er zijn dus andere factoren naast plaques die de hoeveelheid amyloïd in het hersenvocht beïnvloeden. Één van die factoren is ontsteking. Door een ontsteking in de hersenen van de eerste patiënt gaf het hersenvocht

een positief resultaat voor plaques, zonder dat er onder de microscoop plaques te zien waren. In de andere patiënt was het hersenvocht wel juist, onder de microscoop zagen we namelijk plaques in de hersenen. Deze waren nog in een te vroeg stadium om opgepikt te worden met de PET scan. Het amyloïd niveau in het hersenvocht kan plaques in de hersenen dus eerder voorspellen dan dat de PET scan dit kan. Tenslotte leerden we nog van deze studie dat iemand niet per se alleen de ziekte van Alzheimer heeft als zowel het hersenvocht als de PET scan duiden op plaques in de hersenen. Twee patiënten hadden namelijk inderdaad plaques in de hersenen, precies zoals het hersenvocht en de PET scan voorspelde, maar deze patiënten hadden naast de Alzheimer pathologie ook nog een andere neurodegeneratieve ziekte. Dit toont dus aan dat je na het doen van een hersenvochttest en PET scan niet meteen klaar bent met diagnostiek. Hoewel het heel erg zeldzaam is, kan een patiënt namelijk meerdere hersenziekten hebben.

In hoofdstuk 8 is onderzocht of de verdeling van tangles, plaques en ontstekingscellen zoals we die zien onder de microscoop, kan worden vertaald naar de dikte van de hersenschors zoals we die meten op de hersenscan gemaakt met een MRI. Patiënten met de ziekte van Alzheimer en mensen zonder hersenziekte kregen hiervoor een hersenscan ná het overlijden, maar vóórdat de hersenen uit de schedel werden genomen. Op deze manier is geprobeerd om tegelijkertijd zo dicht mogelijk bij de levende situatie te blijven, maar ook zo dicht mogelijk bij het moment van overlijden en dus het tijdstip waarop we de tangles, plaques en ontsteking meten. De dikte van de hersenschors was in patiënten, maar niet in de controlegroep, inderdaad gerelateerd aan de hoeveelheid plaques, tangles en ontstekingscellen. De tangles en de ontstekingscellen lijken op een andere manier geassocieerd met de hersenschorsdikte dan de plaques. In het geval van meer plaques lijkt de hersenschors iets dikker dan in het geval van minder plaques. In het geval van meer tangles en meer ontstekingscellen is de hersenschors dunner in specifieke hersengebieden. Met andere woorden, bij meer tangles en ontstekingscellen is er meer hersenkrimp in bepaalde hersengebieden op de hersenscan zoals deze gemaakt wordt met de MRI. De patiëntgroep bestond uit patiënten met de typische klachten van vergeetachtigheid en uit patiënten met atypische klachten. Het effect van de ontstekingscellen op de hersendikte werd vooral gevonden in de atypische patiënten. Echter, als we de typische patiënten direct vergeleken met de atypische patiënten, konden we geen statistisch significante verschillen vinden in hersenschorsdikte, plaque -, tangle - of ontstekingscel verdeling. Dit komt waarschijnlijk omdat de atypische groep een bonte verzameling aan klachten liet zien. De hersengebieden die

verantwoordelijk zijn bij deze klachten verschillen nogal van elkaar. Zo zijn bij patiënten met voornamelijk gedragsproblemen andere hersengebieden betrokken dan bij patiënten met voornamelijk problemen van de taal. Hierdoor worden de gevonden effecten kleiner en zullen grotere groepen patiënten nodig zijn om doorslaggevend resultaten te geven. Wat we wel kunnen concluderen uit deze studie is dat verschillende ziektemarkers, namelijk plaques, tangles en onstekingscellen, op een individuele manier bijdragen aan de hersenschorsdikte. Deze studie draagt bij aan het begrijpen van het onderliggende ziekteproces van hersenkrimpingpatronen zoals we die zien op de hersenscan.

In de vorige studie is onderzocht hoe metingen van de hersenscan samenhangen met bevindingen onder de microscoop. De patiënten uit deze studie hadden een hersenscan ondergaan ná het overlijden. Het is echter onbekend hoe vergelijkbaar een hersenscan gemaakt na het overlijden is met een hersenscan gemaakt tijdens het leven. Dankzij een heel bijzondere patiënt had ik in hoofdstuk 9 de unieke kans om een directe vergelijking te maken tussen deze twee hersenscan-tijdpunten. De patiënt in kwestie had besloten zijn leven te beëindigen middels euthanasie. Hij had daarnaast de altruïstische wens om zijn hersenen te doneren aan de wetenschap. De methode en workflow van deze studie zijn terug te vinden in de illustratie van het 'grafische abstract' in hoofdstuk 9. De hersenscan na het overlijden werd vier dagen later gemaakt dan de hersenscan van tijdens het leven. De scans werden op dezelfde scanner door hetzelfde personeel uitgevoerd. De hersenscan na het overlijden was anders dan de scan tijdens het leven. Terwijl na het overlijden het hersenvolume onevenredig toenam in verschillende hersenregio's, werd de hersenschorsdikte in alle regio's evenredig dunner. Naast het volume en de hersenschorsdikte werd ook de mate van diffusie van de hersenen gemeten. Met deze relatief nieuwe techniek kan de onderliggende architectuur van de hersenen in kaart worden gebracht en kunnen we de verbindingen tussen verschillende hersengebieden bestuderen. Na het overlijden daalden de diffusievectoren allen met 50-60% in alle compartimenten, namelijk de grijze stof, de witte stof en het hersenvocht. Deze studie laat zien dat een hersenscan na het overlijden andere resultaten geeft dan een hersenscan die is gemaakt tijdens het leven. Daarnaast laat deze studie zien dat de verschillen in hersenschorsdikte en de diffusiemetingen evenredig zijn. Daarom kunnen deze maten gebruikt worden als intermediair tussen de microscopie bevindingen en de hersenscan zoals die wordt gemaakt op de geheugenpoli. Omdat de verschillen in volume metingen onevenredig zijn, is deze maat minder betrouwbaar.

In dit thesis heb ik laten zien dat activatie van ontstekingscellen mogelijk de verbindende factor is tussen de pathologische kenmerken van de ziekte van Alzheimer, namelijk de plaques en tangles. Patiënten met atypische klachten zien er ook onder de microscoop anders uit dan patiënten met typische klachten. Tijdens het doen van mijn promotieonderzoek heb ik een nieuw type plaque ontdekt, de grofkorrelige plaque. Deze plaque komt vooral voor bij patiënten die de ziekte op jonge leeftijd krijgen. Als we kijken naar de mate van vergevorderde secundaire eiwitstructuren lijkt de bestaande plaque-ontwikkelingshypothese plausibel. De grofkorrelige plaque laat echter een andere ontstekingsreactie zien dan de klassieke plaque. Op de geheugenpoli kunnen we het amyloïde eiwit in de hersenen vaststellen met een PET scan of door middel van het hersenvocht. Deze methoden zijn echter niet gevoelig genoeg voor de verschillende typen van amyloïde ophopingen. Verder beschrijf ik in dit thesis dat de hersenschorsdikte zoals gemeten op de hersenscan, geassocieerd is met zowel tangles als ontstekingscellen. Dit laatste bevestigt dat neurodegeneratie, het proces dat het afsterven van zenuwcellen inhoudt, zowel is geassocieerd met tangles als met ontsteking. Tenslotte laat ik zien dat een hersenscan gemaakt na het overlijden andere resultaten laat zien dan de hersenscan gemaakt tijdens het leven, maar dat de resultaten van de scans gemaakt na het overlijden zeker wel bruikbaar zijn voor verder vervolgonderzoek.

Tijdens mijn PhD traject hebben mijn collega's en ik een uniek cohort van hersendonoren verzameld, waarbij we de beschikking hebben tot uitgebreide klinische informatie, hersenscans en hersenvocht en bloed dat zowel tijdens het leven, als na het overlijden is afgenomen. De studies die ik beschreven heb in dit thesis representeren nog maar het topje van de ijsberg van wat allemaal te onderzoeken valt op dit waardevolle studie cohort. Voor de toekomst denk ik dat pathologie studies zich moeten richten op zulke prospectief verzamelde cohorten, zodat de bevindingen niet alleen helpen bij het verbeteren van kennis ná het overlijden van de patiënt, maar direct kunnen bijdragen aan een betere ziektemechanisme-stratificatie van patiënten op de geheugenpoli.

Het lijkt erop dat de ziektemechanismen neurodegeneratie en ontsteking verschillend betrokken zijn bij de verschillende subtypen van de ziekte van Alzheimer. Daarom stel ik voor dat we de ziekte van Alzheimer in de toekomst niet meer enkel bekijken als één ziekte, maar dat we de verschillen tussen mensen met de ziekte beter gaan herkennen en onderzoeken. Ik stel voor te beginnen bij pathologie onderzoek: wat zijn nu precies al die verschillen onder de microscoop en bij wie zien we wat. Om de individuele verschillen in onder

andere ontstekingsreactie tijdens het leven vast te stellen, moeten we echter ook op zoek gaan naar de juiste markers in het hersenvocht, het bloed of op de hersenscan. Hiermee zullen we de ziekte niet alleen beter begrijpen, maar zullen we ook patiënten beter kunnen categoriseren op basis van hun onderliggende immuunsysteem en zullen we in de nabije toekomst individueel gerichte behandelingen kunnen ontwikkelen.

Addendum

List of publications
Alzheimer Center hall of fame
Acknowledgments (Dankwoord)
About the author

LIST OF PUBLICATIONS

Publications in this thesis

Lochocki B, **Boon BDC**, Verheul SR, Zada L, Hoozemans JJM, Ariese F & de Boer JF (2021) Multimodal, label-free fluorescence and Raman imaging of amyloid deposits in snap-frozen Alzheimer's disease human brain tissue. *Communications Biology* 4: 474. doi: 10.1038/s42003-021-01981-x.

Boon BDC, Bulk M, Jonker AJ, Morrema THJ, van den Berg E, Popovic M, Walter J, Kumar S, van der Lee SJ, Holstege H, Zhu X, Van Nostrand WE, Natté R, van der Weerd L, Bouwman FH, van de Berg WDJ, Rozemuller AJM, Hoozemans JJM (2020) The coarse-grained plaque: a divergent A β plaque-type in early-onset Alzheimer's disease. *Acta Neuropathologica* 140:811-830. doi: 10.1007/s00401-020-02198-8.

Röhr D, **Boon BDC**, Schuler M, Kremer K, Hoozemans JJM, Bouwman FH, El-Mashtoly SF, Nabers A, Großerueschkamp F, Rozemuller AJM & Gerwert K (2020) Label-free vibrational imaging of different A β plaque types in Alzheimer's disease reveals sequential events in plaque development. *Acta Neuropathologica Communications* 77:113-119. doi:10.1186/s40478-020-01091-5

Reimand J, **Boon BDC**, Collij LE, Teunissen CE, Rozemuller AJM, van Berckel BNM, Scheltens Ph, Ossenkoppele R, Bouwman F (2020) Amyloid- β PET and CSF in an autopsy-confirmed cohort. *Annals of Clinical and Translational Neurology* 7(11):2150-2160. doi: 10.1002/acn3.51195.

Boon BDC, Pouwels PJW, Jonkman LE, Keijzer MJ, Preziosa P, van de Berg WDJ, Geurts JJG, Scheltens Ph, Barkhof F, Rozemuller AJM, Bouwman FH, Steenwijk MD (2019) Can post-mortem MRI be used as a proxy for in-vivo? *Brain Communications* 1(1):fcz030. doi: 10.1093/braincomms/fcz030.

Boon BDC, Hoozemans JJM, Lopuhaä B, Eigenhuis KN, Scheltens P, Kamphorst W, Rozemuller AJM, Bouwman FH. (2018) Neuroinflammation is increased in the parietal cortex of atypical Alzheimer's disease. *J of Neuroinflammation* 29;15(1):170. doi: 10.1186/s12974-018-1180-y.

Frigerio I, **Boon BDC**, Lin CP, Galis-de Graaf Y, Bol JGJM, Preziosa P, Twisk J, Barkhof F, Hoozemans JJM, Bouwman FH, Rozemuller AJM, van de Berg WDJ, Jonkman LE. Amyloid- β , p-tau, and reactive microglia load are correlates of

MRI cortical atrophy in Alzheimer's disease. Accepted for publication in Brain Communications.

Boon BDC, Frigerio I, de Gooijer D, Morrema THJ, Bol JGJM, Heymans M, Van de berg WDJ, Rozemuller AJM, Jonkman LE, Bouwman FH, Hoozemans JJM. A distinct distribution of neuroinflammation, indicating a specific role for reactive astrocytes in clinical atypical Alzheimer's disease. *In preparation*.

Not in this thesis

Kenkhuis B, Jonkman LE, Bulk M, Buijs M, **Boon BDC**, Bouwman FH, Geurts JJG, van de Berg WDJ, van der Weerd L. (2019) 7T MRI allows detection of disturbed cortical lamination of the medial temporal lobe in patients with Alzheimer's disease. *Neuroimage Clinical* 5:101665. doi: 10.1016/j.nicl.2019.101665.

Groot C, Tolboom N, Ikonovic MD, Lammertsma AA, **Boon BDC**, Barkhof F, Scheltens P, Klunk WE, Rozemuller AJM, Ossenkoppele R, van Berckel BNM (2018) Quantitative PET and Histology of Brain Biopsy Reveal Lack of Selective Pittsburgh Compound-B Binding to Intracerebral Amyloidoma. *J Alzheimers Disease* 65(1):71-77. doi: 10.3233/JAD-180316.

Gami-Patel P, Scarioni M, Bouwman FH, **Boon BDC**, Van Swieten JC, Netherlands Brain Bank, Rozemuller AJM, Smit AB, Pijnenburg YAL, Hoozemans JJM, Dijkstra AA. The severity of behavioural symptoms in FTD are linked to the loss of GABRQ-expressing VENs and pyramidal neurons. *Neuropathology and Applied Neurobiology*. *In press*.

Irizarry BA, Davis J, Zhu X, **Boon BDC**, Rozemuller AJM, Van Nostrand WE, Smith SO. Anti-parallel A β 40 fibrils in human cerebral vascular amyloid. *Journal of Biological Chemistry*. *In press*.

Lin CP, Frigerio I, **Boon BDC**, Zhou Z, Rozemuller AJM, Bouwman FH, Schoonheim MM, Van de Berg WDJ, Jonkman LE. Structural (dys)connectivity associates with cholinergic cell density of the nucleus basalis of Meynert in Alzheimer's disease. *Submitted*.

Geut H, Van den Berg E, **Boon BDC**, Hoozemans JJM, Tunold JA, Pihlstrøm L, Jonkman LE, Rozemuller AJM, Lemstra EAW, Van de Berg WDJ. Alzheimer's disease copathology in dementia with Lewy bodies is associated with astroglial α -synucleinopathy. *Submitted*.

Appendices

Singleton EH, Pijnenburg YAL, Gami-Patel P, **Boon BDC**, Bouwman FH, Papma J, Seelaar H, Scheltens Ph, Grinberg LT, Rabinovic GD, Seeley WW, Ossenkoppele R, Dijkstra AA Von Economo and related neurons do not show a selective loss in the anterior cingulate cortex in the behavioral variant of Alzheimer's disease. *In preparation.*

Labuzan SA , **Boon BDC**, Ferman TJ, Duara, Matchett BJ, Kouri N, Hinkle KM, Lachner C, Ross OA, Ertekin-Taner N, Dickson DW, Graff-Radford NR , Murray ME. Minimal Atrophy Alzheimer's Disease Subtype May Reflect Co-existing Lewy Body Disease. *In preparation.*

ALZHEIMER CENTER HALL OF FAME

1. L. Gootjes: Dichotic Listening, hemispherical connectivity and dementia (14-09- 2004)
2. K. van Dijk: Peripheral nerve stimulation in Alzheimer's disease (16-01-2005)
3. R. Goekoop: Functional MRI of cholinergic transmission (16-01-2006)
4. R. Lazeron: Cognitive aspects in multiple sclerosis (03-07- 2006)
5. N.S.M. Schoonenboom: CSF markers in dementia (10-11-2006)
6. E.S.C. Korf: Medial Temporal lobe atrophy on MRI: risk factors and predictive value (22-11-2006)
7. B. van Harten: Aspects of subcortical vascular ischemic disease (22-12-2006)
8. B. Jones: Cingular cortex networks: role in learning and memory and Alzheimer's disease related changes (23-03-2007)
9. L. van de Pol: Hippocampal atrophy from aging to dementia: a clinical and radiological perspective (11-05-2007)
10. Y.A.L. Pijnenburg: Frontotemporal dementia: towards an earlier diagnosis (05-07-2007)
11. A. Bastos Leite: Pathological ageing of the brain (16-11-2007)
12. E.C.W. van Straaten: Vascular dementia (11-01-2008)
13. R.L.C. Vogels: Cognitive impairment in heart failure (11-04-2008)
14. J. Damoiseaux: The brain at rest (20-05-2008)
15. G.B. Karas: computational neuro-anatomy (19-06-2008)
16. F.H. Bouwman: Biomarkers in dementia: longitudinal aspects (20-06-2008)
17. A.A. Gouw: Cerebral small vessel disease on MRI: clinical impact and underlying pathology (20-03-2009)
18. H. van der Roest: Care needs in dementia and interactive digital information provisioning (12-10-2009)
19. C. Mulder: CSF biomarkers in Alzheimer's disease (11-11-2009)
20. W. Henneman. Advances in hippocampal atrophy measurement in dementia: beyond diagnostics (27-11-2009)
21. S.S. Staekenborg: From normal aging to dementia: risk factors and clinical findings in relation to vascular changes on brain MRI (23-12-2009)
22. N. Tolboom: Imaging Alzheimer's disease pathology in vivo: towards an early diagnosis (12-02-2010)
23. E. Altena: Mapping insomnia: brain structure, function and sleep intervention (17-03- 2010)
24. N.A. Verwey: Biochemical markers in dementia: from mice to men. A translational approach (15-04-2010)
25. M.I. Kester: Biomarkers for Alzheimer's pathology; monitoring, predicting and understanding the disease (14-01-2011)
26. J.D. Sluimer: Longitudinal changes in the brain (28-04-2011)
27. S.D. Mulder: Amyloid associated proteins in Alzheimer's disease (07-10-2011)
28. S.A.M. Sikkes: measuring IADL in dementia (14-10-2011)

Appendices

29. A. Schuitemaker: Inflammation in Alzheimer's disease: in-vivo quantification (27-01-2012)
30. K. Joling: Depression and anxiety in family caregivers of persons with dementia (02-04-2012)
31. W. de Haan: In a network state of mind (02-11-2012) (Cum Laude)
32. D. van Assema: Blood-brain barrier P-glycoprotein function in ageing and Alzheimer's disease (07-12-2012)
33. J.D.C. Goos: Cerebral microbleeds: connecting the dots (06-02-2013)
34. R. Ossenkoppele: Alzheimer PETology (08-05-2013)
35. H.M. Jochensen: Brain under pressure: influences of blood pressure and angiotensin-converting enzyme on the brain (04-10-2013)
36. A.E. van der Vlies: Cognitive profiles in Alzheimer's disease: Recognizing its many faces (27-11-2013)
37. van Rossum: Diagnosis and prognosis of Alzheimer's disease in subjects with mild cognitive impairment (28-11-2013)
38. E.I.S. Møst: Circadian rhythm deterioration in early Alzheimer's disease and the preventative effect of light (03-12-2013)
39. M.A.A. Binnewijzend: Functional and perfusion MRI in dementia (21-03-2014)
40. H. de Waal: Understanding heterogeneity in Alzheimer's disease: A neurophysiological perspective (25-04-2014)
41. W. Jongbloed: Neurodegeneration: Biochemical signals from the brain (08-05-2014)
42. E.L.G.E. Poortvliet-Koedam: Early-onset dementia: Unravelling the clinical phenotypes (28-05-2014)
43. A.C. van Harten: The road less travelled: CSF biomarkers for Alzheimer's disease (07-11-2014)
44. A.M. Hooghiemstra: Early-onset dementia: With exercise in mind (03-12-2014)
45. L.L. Sandberg-Smits: A cognitive perspective on clinical manifestations of Alzheimer's disease (20-03-2015)
46. F.H. Duits: Biomarkers for Alzheimer's disease, current practice and new perspectives (01-04-2015)
47. S.M. Adriaanse: Integrating functional and molecular imaging in Alzheimer's disease (07-04-2015)
48. C. Möller: Imaging patterns of tissue destruction - Towards a better discrimination of types of dementia (01-05-2015)
49. M. del Campo Milán: Novel biochemical signatures of early stages of Alzheimer's disease (19-06-2015)
50. M.R. Benedictus: A vascular view on cognitive decline and dementia: relevance of cerebrovascular MRI markers in a memory clinic (20-01-2016)
51. M.D. Zwan: Visualizing Alzheimer's disease pathology. Implementation of amyloid PET in clinical practice (03-03-2016)
52. E. Louwersheimer: Alzheimer's disease: from phenotype to genotype (21-06-2016)
53. W.A. Krudop: The frontal lobe syndrome: a neuropsychiatric challenge (23-09-2016)

54. E.G.B. Vijverberg: The neuropsychiatry of behavioural variant frontotemporal dementia and primary psychiatric disorders: similarities and dissimilarities (22-09-2017)
55. F.T. Gossink: Late Onset Behavioural Changes differentiating between bvFTD and psychiatric disorders in clinical practice (20-04-2018)
56. M.A. Engels: Neurophysiology of dementia (18-05-2018)
57. S.C.J. Verfaillie: Neuroimaging in subjective cognitive decline: Incipient Alzheimer's disease unmasked (12-09-2018)
58. M. ten Kate: Neuroimaging in predementia Alzheimer's disease (13-09-2018)
59. H.F.M. Rhodius-Meester: Optimizing use of diagnostic tests in memory clinics; the next step (24-09-2018)
60. E.A.J. Willemsen: Optimising biomarkers in cerebrospinal fluid. How Laboratory reproducibility improves the diagnosis of Alzheimer's disease (18-10-2018)
61. E. Konijnenberg: Early amyloid pathology – Identical twins, two of a kind? (25-06-2019)
62. A.E. Leeuwis: Connecting heart and brain; Vascular determinants of cognitive impairment and depressive symptoms (02-07-2019)
63. J. den Haan: Imaging the retina in Alzheimer's disease (12-09-2019)
64. A.C. van Loenhoud: Cognitive reserve in Alzheimer's disease. A perspective on the flourishing and whitening of the brain (18-09-2019)
65. R.J. Jutten: Capturing changes in cognition; refining the measurement of clinical progression in Alzheimer's disease (20-09-2019)
66. N. Legdeur: Determinants of cognitive impairment in the oldest-old (08-10-2019)
67. R. Slot: Subjective cognitive decline – predictive value of biomarkers in the context of preclinical Alzheimer's disease (14-11-2019)
68. N. Scheltens: Understanding heterogeneity in Alzheimer's disease – a data driven approach (17-12-2019)
69. L. Vermunt: Secondary prevention for Alzheimer's Disease – timing, selection, and endpoint of clinical trials (13-03-2020)
70. L.M.P. Wesselman: Lifestyle and brain health – exploring possibilities of an online intervention in non-demented elderly (01-04-2020)
71. I.S. van Maurik: Interpreting biomarker results in patients with mild cognitive impairment to estimate prognosis and optimize decision making (12-05-2020) (Cum Laude)
72. E. Dicks: Grey matter covariance networks in Alzheimer's disease: Edging towards a better understanding of disease progression (09-09-2020)
73. J.J. van der Zande: A sharper image of dementia with Lewy bodies: the role of imaging and neurophysiology in DLB, and the influence of concomitant Alzheimer's disease pathology (21-09-2020)
74. I. van Steenoven: Cerebrospinal fluid biomarkers in dementia with Lewy bodies – towards a biological diagnosis (22-09-2020)
75. N. Beker: Cognition in centenarians – evaluation of cognitive health and underlying factors in centenarians from the 100-plus study (02-10-2020)

Appendices

76. F. de Leeuw: Nutrition and metabolic profiles in Alzheimer's disease (30-11-2020)
77. T. Timmers: Tau PET across the Alzheimer's disease continuum (02-12-2020)
78. E.E. Wolters: Untangling tau pathology using PET (02-12-2020)
79. A.S. Doorduyn: Nutrition, the unrecognized determinant in Alzheimer's disease (12-01-2021)
80. A. de Wilde: Visualizing Brain Amyloid-beta Pathology (17-03-2021)
81. C. Groot: Heterogeneity in Alzheimer's Disease (06-04-2021)
82. D. Bertens: The use of biomarkers in non-demented AD patients for clinical trial design and clinical practice (14-04-2021)
83. J. Reimand: Disordance between amyloid-? PET and CSF biomarkers: Clinical and pathophysiological consequences (12-05-2021)
84. L.E. Colij: The AMYPAD project: Towards the next stage in amyloid PET imaging (01-07-2021)
85. C.T. Briels: Evaluation and implementation of functional cerebral biomarkers in Alzheimer's disease (15-05-2021)
86. N. Tesi: The Genetics of Cognitively Healthy Centenarians (28-09-2021)
87. L.M. Reus: Triangulating Heterogeneity in Dementia (28-09-2021)
88. R. Bapapour Mofrad: The use of Biofluid biomarkers in dementia: implementation in clinical practice and breaking new grounds (08-10-2021)
89. E.H. Thijssen: Blood-based biomarkers for Alzheimer's disease: assay development and clinical validation (15-11-2021)
90. A.C. Baakman: Innovation in cholinergic enhancement for Alzheimer's Disease (17-11-2021)
91. I.M.W. Verberk: Blood-based biomarkers for Alzheimer's disease coming to fruition (08-12-2021)
92. J.F. Leijenaar: Streamlining VCI: Heterogeneity and Treatment Response (11-01-2022)
93. B.D.C. Boon: Deciphering neuropathological heterogeneity in Alzheimer's Disease: Beyond plaques and tangles (14-01-2022)

ACKNOWLEDGMENTS

Uitkijkend over de Atlantische oceaan vanaf de Florida Keys, besef ik mij maar al te goed hoe enorm veel geluk ik heb met alle dierbare en bijzondere mensen die mij gedurende mijn promotieonderzoek hebben gesteund. Elk promotietraject is uniek en vol bepalende momenten, ook juist buiten de wetenschap om. Dat van mij was niet anders. Naast dat ik enorm veel geleerd heb over hoe je onderzoek doet, heb ik ook geleerd wat het betekent om dierbaren te verliezen. Helaas kunnen Van Eyk, mijn lieve tante Lily en oma Boon er niet meer bij zijn om de afsluiting te vieren, maar hun leven én overlijden hebben mij een rijker mens gemaakt. Sommige mensen waren er net als Van Eyk, Lily en oma Boon vanaf het begin af aan bij, anderen leerde ik gaandeweg kennen en weer anderen waren er kortstondig voor me, op de momenten dat het nodig was. De één had tips voor een bepaalde statistische analyse of filoseerde met me mee over de rol van microglia, de ander sloeg een arm om me heen als alles even te veel werd of nam me mee uit dansen om alles te vergeten. Allen zijn mij even dierbaar. In dit dankwoord doe ik een poging de meeste van jullie te noemen, maar ik kan een volledig nieuw boek schrijven als ik iedereen zou noemen die me op de één of andere manier geholpen heeft.

Allereerst wil ik alle geregistreerde hersendonoren bedanken voor hen besluit tot hersendonatie voor wetenschappelijk onderzoek. Uw bijdrage is van noodzakelijk belang om de hersenziekten beter te kunnen begrijpen. Zonder u was dit proefschrift er nooit geweest! In het bijzonder wil ik Dirk Baron en zijn echtgenote Dieke Broersma bedanken. Dankzij Dirk zijn moedige besluit zijn we iets dichterbij gekomen bij die werkelijke translatie van pathologie naar kliniek middels MRI. Dirk is voor mij een ware inspiratie. Ondanks zijn hersenziekte, kwam hij vier dagen voor zijn overlijden vanuit Friesland voor een volle dag naar het Alzheimer centrum Amsterdam om allerlei onderzoeken te ondergaan. Zelfs na zijn overlijden wist hij geld in te zamelen voor het onderzoek naar deze verwoestende ziekte. Dankzij Dirk wijdt Omrop Fryslân jaarlijks een aflevering aan de ziekte van Alzheimer. Zijn vrouw, Dieke, zet zich in voor de nabestaanden en voor het hersenonderzoek. Dirk en Dieke, dankjulliewel!

Beste professor Rozemuller, lieve Annemieke, wat heb ik enorm veel van je geleerd! Van de 'hoera' winding in het cerebellum - dank Wouter Kamphorst! - tot de uitspraak 'Zo niet, dan toch!' als de hersenblokjes dankzij jouw timmermansoog toch heus wel in de cassettes pasten. Het uitsnijden op de woensdagochtenden samen met de hersenbank (als ik weer 100 foto's moest

nemen van al die regio's), heeft enorm bijgedragen aan mijn anatomische kennis. Evenveel genoot ik van die spontane brainstormsessies, als we een case onder de microscoop bekeken en begonnen te hypothetiseren over hoe die aggregaten nu toch ontstonden. Jij hebt voor mij de liefde voor neuropathologie in vuur en vlam gezet. Ik mag mij gelukkig prijzen als mijn kennis ooit in de buurt komt van jouw encyclopedisch geheugen.

Beste professor Scheltens, beste Philip het heeft een tijdje (zes jaar..!) geduurd en het blijft mijn valkuil, maar ik realiseer me eindelijk dat een mens geen zeven truien tegelijk breit. De patronen voor de volgende tien truien, mutsen en sjaals liggen natuurlijk klaar maar jij hebt me geleerd de wol voor één project tegelijk te kiezen. Ik ben niet de snelste leerling en erg eigenwijs, maar dankjewel voor de geweldige broedplaats die jij samen met Wiesje biedt. Jouw manier van leidinggeven en tegelijkertijd zo bereikbaar zijn, is werkelijk inspirerend. Ik hoop dat we elkaar blijven tegenkomen.

Lieve Femke, dankjewel voor je tomeloze positieve spirit, ook als het allemaal niet zo lekker ging. We hebben een boel tranen gehuild, maar ook zeker hard gelachen. Weet je nog die ene keer dat ik onderweg zou gaan naar Amersfoort om donoren te werven en er een koe op het spoor stond? Of dat Jeroen en ik dankzij jou, op avontuur gingen naar Leiden om een bevroren hoofd op te halen? Jij denkt niet in beperkingen maar in mogelijkheden. Je wist me op de juiste momenten bij te sturen: deadlines zijn broodnodig bij mijn chaotische en vooral uitstellende brein. Dank! Ook voor de enorme lol, onze dansavonturen op jouw verjaardag tijdens het AAIC, dat je me aan Melissa hebt voorgesteld en dat jij altijd de angel uit het politieke conflict wist te halen. Jouw frisse en onbevooroordeelde blik hebben me menigmaal geholpen m'n ideeën in lekt taal uit te leggen en om het klinisch belang ervan te benadrukken.

Lieve Jeroen, dankjewel voor je eindeloze geduld bij het aanhoren van mijn nieuwste - en vaak ook wildste - ideeën. Koolstof bepalingen doen in plaques? 'Klinkt leuk, probeer maar uit!' Het is voornamelijk dankzij jou dat sommige van die plannen - meerdere (halve) marathons (Chicago, Egmond aan Zee, Den Haag, Rotterdam, Amsterdam, etc...), de proteomics studie en de ALZ NL grant voorstellen - ook echt tot realisatie zijn gekomen. Niets is jou te veel, zo ook niet het tot 4 uur 's nachts aanhoren van mijn op-de-valreep-toegewezen-praatje voor het BNS-congres of zoals eerdergenoemd onderzoeksmateriaal op droogijs te vervoeren. Dank voor jouw eeuwige steun en geruststelling als ik weer eens dacht 'het echt niet te kunnen', dank dat je me naar huis stuurde als het niet

ging, en dank dat je de studenten opving als ik weer eens op vakantie was... Ik heb enorme bewondering voor hoe jij mensen in hun waarde laat en hoe je anderen helpt hun eigen visie te ontwikkelen. Ik hoop dat te integreren als ik later groot ben.

Dear doctorate committee, thank you for taking the time to read and discuss my thesis. From all of your papers and our live interactions I've learned so much! Beste Yolande, het eerste wat ik van jou leerde als laatste jaar geneeskunde student, was dat het er niet om gaat dat de patiënt je een 'aardige' dokter vindt, maar dat je onderzoekt wat er met de patiënt aan de hand is. Ik heb veel geleerd van jouw scherpe observatie vermogen en ben benieuwd naar de discussie! Lieber Dietmar, ich erinnere mich noch gut an meine erste AAIC Konferenz in Toronto, als ich dich bei Bernardino Ghetti's Poster traf. Du hast mich daran erinnert, dass ich mich superglücklich schätzen kann, Annemieke als Doktermutter zu haben. Bei jedem Kongress hast du mir etwas Neues beigebracht und du warst es, der die erste Verbindung zwischen *APOE ε4* und 'the coarse-grained plaque' herstellte. Beste Charlotte dank voor jou altijd nuchtere, kritische en optimistische blik, welke ik al tijdens mijn stage bij Wilma leerde kennen. Dankzij jou hebben we de in-vivo fluids van het hele cohort kunnen reserveren! Ik ben zo ontzettend benieuwd wat we gaan vinden met de GFAP! Hopelijk zullen er nog veel meer markers (norrin) voor cross validatie volgen. Wiep, ik weet nog goed toen ik te vroeg was voor een afspraak met Jan, jij tijd had om te kletsen en filosoferen over die 'holle' cores in de plaques. Die spontane momenten zijn voor mij wat de wetenschap zo leuk maakt. Wat hebben we gelachen tijdens de ADPD-congressen in Wenen en Lissabon. Volgens mij vergeet jij die neurotische plaques van de Alzheimer meisjes nooit meer. Rik, ik vind het zo knap (en prettig) hoe relaxt jij overkomt terwijl je zo onwijs veel produceert. Naast jouw papers, leer ik zoveel van alle congressessies die jij voorziet. Jouw vragen zijn altijd helder en oprecht geïnteresseerd. Ik hoop nog veel meer van je te leren! Melissa, we met six years ago when you presented at AAIC in Toronto. Immediately I knew: she is badass, I want to learn from her! After multiple encounters all over the world, we made it happen and here I am at Mayo. Thank you for mentoring me from day one, not only on the science part of life, but on all the other aspects as well. I hope you know what it means to me.

Het PAGE-AD team (core leiders buiten de al eerder genoemde mensen: Wilma, Laura, Jeroen G, Frederik, Louise en Inge) dankjulliewel voor al jullie individuele bijdragen, soms bij de papers, soms als waardevolle commentaren tijdens de kwartaalse PAGE-AD meetings met stroopwafels en koffie (of thee met suiker

voor Laura ;-)) en vooral voor de hulp bij hoe je nu zoiets opzet en structureert. Ik ben zo trots op het bijzonder waardevolle cohort wat we hebben opgezet, waarbij directe translatie tussen in-vivo en post-mortem data mogelijk is! Daarnaast ben ik trots op alle vervolgprojecten die hieruit zijn voortgekomen en nog zullen volgen. Wilma, dankzij jou ben ik voor dit project gaan solliciteren, dankjewel! Laura, dank voor je geduld, jouw statistische kennis en je prachtige figuren. Dank aan iedereen van het post-mortem MRI-team, met onder andere Chris en Matthijs, jullie waren altijd bereid te helpen met scannen, dag en nacht! Wat was het spannend als dat telefoontje afging! Van de ANW-sectie die direct geholpen hebben bij PAGE-AD wil ik ook speciaal nog noemen Irene (thank you for always tirelessly replying to my -often double request- emails. You always took the time to -multiple times- explain to me why (and where!) certain things were saved and you went into deep with the linear mixed model!), Chen-Pei (you MRI Rockstar!), Allert (wauw wat hebben jouw prachtige free-floating kleuringen veel teweeggebracht!), Evelien (dank voor jouw geduld om met mij uit te zoeken hoe de protocollen in elkaar zaten, waar het weefsel lag, mee te denken in oplossingen), John B (de kleuringen, de organisatie en jouw kritische maar ook humoristische kijk op de methodes), Yvon (al die annotaties waar ik nog zoveel mee moet doen!). Lieve Martijn, jij hebt me echt heel veel geleerd over MRI en onderzoek doen in het algemeen, maar bent ook een vriend geweest door naar me te luisteren in die momenten dat het nodig was. Dankjewel Tijn. Daarnaast zijn er nog zoveel anderen van ANW (o.a. Piet, Angela, Hanneke G en Yasmin bijv.) die hebben bijgedragen. From ANW to O2: Marco, major thanks for helping me get those beautiful confocal videos. Besides all the sciency stuff, I love your witt and outlook on life, man you crack me up! Bedankt aan iedereen bij de NHB (Petra, Mignon, Paul, Afra, Minke, Vera, Isabell en An) onder leiding van Inge! Voor de gezellige momenten op woensdagochtend tijdens het uitsnijden, wanneer ik langskwam om coupes te kijken, of hulp via de telefoon en e-mail. Een mega special thanks gaat uit naar Michiel Kooreman, jouw relativerende vermogen hebben mij menigmaal uit de put getrokken en jouw liefde voor vogels zorgt ervoor dat ik aan je denk op alle nieuwe plekken waar ik kom en vogels spot. Hoe gaaf dat we eindelijk binnenkort samen een halve marathon gaan lopen. Vanuit Leiden wil ik Louise, Remco en ook vooral Marjolein bedanken. Marjolein dank voor het verdragen van mijn chaos. Jij kan structureren, organiseren en bent altijd flexibel. Het was een feest met jou samen te werken.

Iedereen van het immer groeiende Alzheimer centrum. Om te beginnen bij Wiesje, dankje voor de tip over de linear mixed models en ookal viel ik helemaal

niet onder jouw hoede, toch hield je altijd een oogje in het zeil. Natuurlijk iedereen van Bunker 1 (Nina, Jolien, Jort, Leonie, Aafke, Arno, Ellen en Lisa) dank voor alle gezellige uren dat we op onze stoelen ronddraaide, het staand werken uitprobeerde, samen tabellen 1 maakte, klaagde over de AAIC abstract deadlines en we bij Nien Sinterklaas vierden. Bedankt ook dat jullie me niet meteen vertelde over de vervloekte stoel, ik denk dat als ik dat vanaf het begin geweten had, er nog in zou geloven ook (placebo-effect)! Dank allen voor jullie steun! Dan zijn er nog alle anderen van het AC.. Om een aantal van jullie te noemen, dank Pieter-Jelle, Betty, en Sietske voor de gezellige brainstormsessies niet alleen tijdens werkuren, maar ook bij de borrel. Sven ik waardeer je ongezoeten mening en het feit dat je altijd beschikbaar bent voor vragen, ik heb zoveel van je geleerd! Alle jaargenootjes (met onder andere Ingrid, Tessa, Emma, Juhan, Colin met later ook Ellen en voorgaande garde Elles, Roos, Nienke, Annebeth en Astrid). Lieve Frederique, wat ben ik blij met onze vriendschap én onze samenwerk dates ondanks het tijdsverschil. Ik geniet ervan online vanuit Florida samen 'mee te eten' met Rik z'n heerlijk creaties en te worden ge-update over het laatste nieuws. Ook dank aan iedereen die deel uit maakte van het MDO met o.a. de geheugenpoli dokters Niels, Evelien en Annemieke. In het bijzonder dank aan de camper crew Roos, Nienke, Jurre en Lisa, gelukkig hebben jullie de grotto wel gezien! Roos ik kom je snel opzoeken in Boston en hoe leuk om samen met Mark Amsterdam te representen dit afgelopen AAIC! Nien, jij was ook tegen die gevlekte cheddar toch? Samen fietsen in de regen was altijd gezellig. Jurre, zo enorm veel herinneringen komen boven als ik aan jou denk: 'Dude you just hit me man!' in Canada, het hardlopen met VE en Fuikdag in Curaçao, scooter rijden door de rijstvelden op Bali, parkeerbonnen regelen door achter de kast te klimmen bij radiologie (sssst!), of al die talloze momenten bij één van ons thuis kletsend over het leven. Ik ben zo dankbaar dat jij en Kim altijd klaarstaan! Lieve Lies, dank voor je steun op alle fronten! Ik hou van onze hypothetische gesprekken waarmee we het Alzheimer mysterie hebben opgelost. Dat we de kleuringen nog moeten doen laten we even terzijde want die Vermunt toets was significant toch? Dankjewel voor de geweldige feestjes die we gehad hebben, voor de prachtige vakanties, voor jouw luisterend oor en dat je mij ondanks mijn soms niet zo nette acties (wel of niet naar Georgia / ineens een roadtrip naar California) accepteert. Zo stoer hoe jij gaat voor wetenschap! Ik ben heel erg blij dat jij in januari naast me staat.

Mega dank aan alle studenten die me geholpen hebben, jullie hebben zoveel data vergaard! Boaz, jouw tomeloze doorzettingsvermogen om al die foto's te maken in de kelder. Met je telefoon in een glas luisterend naar drum muziek kon

je uren onverstoort door. Kristel dank voor alles! Meteen legde je de vinger op de zere plek en trok je alles recht met gestructureerde excel bestanden. Wat heb ik om je gelachen met je imitaties en genoten van je kookkunsten! Ik ben trots op je, met je eigen mega PhD project bij het Erasmus. Emma, wat waren we blij toen we eindelijk die microglia in beeld kregen! Het was best een struggle, maar we hadden uiteindelijk toch een hippie festival vibe. Chris wat heb je veel kleuringen gedaan, thanks! Veerle, al dat weefsel wat je hebt uitgeschoten en wat Meike vervolgens heeft geanalyseerd, dankjulliewel! Nog een project wat (bijna) klaar is voor publicatie! Danae jij was het zonnetje van het lab. Omdat je zo proactief voor de start van je stage al begonnen was met weefsel snijden kon je gelukkig ondanks COVID-19 toch je stage met genoeg praktijkmaken afsluiten. En nu heb je een baan bij jouw lievelingsplek, de NHB!

Dank aan alle collega's bij de (neuro)pathologie. Dank voor alle gezellige tussentijdse brainstormsessies, picknicks, congressuitjes en impromptu biertjes. Lieve Anke het was niet altijd makkelijk maar ik heb veel van je geleerd en veel met je gelachen. Jouw liefde voor wetenschap en perfectie is inspirerend. Priya, my BNS-roomie, I learned so much from your politely British ways as a blunt Dutchie. Dankje Laura, voor het helpen bij structuur en organisatie en jouw (en die van Jens!) vriendschap, ik hoop net als jij (neuro)patholoog te worden. Dankjewel Regina en Kim voor alle hulp bij het snijden en kleuren. Marjolein voor je hulp bij Graphpad en onze gedeelde muzieksmaak waarbij jij altijd alle bands en nummers kent. Die Paradiso concerten waren te gek! Andrea, thanks for your sharp eye and delicious German cake! Whenever I get an earworm of the 'everything is awesome' song, I think of us dancing in the lab during our maaajor staining on your birthday. Dankjewel David, voor de gezellige kletsuurtjes met ideeën-generatie in de kelder en jouw enorme hulp bij zowel het begeleiden van Veerle als het schrijven van de scriptie van Meike tijdens de proteomics studie. Marlies! Dankjewel voor het managen van het lab en dat je toch altijd al mijn vragen (ondanks dat je er eigenlijk niet was) wist te beantwoorden! Tjado, voor alles! Ook dat ik je nu altijd nog kan bellen met vragen over antilichamen, verdunningen en protocollen. Volgens mij heb ik nog een etentje van je te goed :-p. Anna, thanks for your friendship. Besides our regular early (!) morning swim sessions in Amsterdam, we had some great holidays in the Boundary Waters (BWCAW; best vacation of my life, also thanks to Lisa!), the Gorge and Germany. Besides rules on how to set up the confocal, you taught me lots of German words, things about Berlin (oh no that was Anselm!), how to plan a hike trip, and together we came up with important rules for when canoeing in the wilderness: 'don't get your hopes up!'. Marianna, thank you for being you!

You inspire me with your expanding research lab and massive knowledge. Also thank you for the best shoes ever, I still wear them at least three times a week. Dank ook aan de andere pathologen Paul en Patrick voor het uitnemen van het kort-gefixeerd materiaal, soms (of eerder eigenlijk te vaak) diep in de nacht. Heel veel dank aan de mortuarium medewerkers Alike (jij brengt leven in de brouwerij!), Peter (die auto wil ik ook!), Michel (jep soms is het inderdaad tijd om naar huis te gaan) en Ton (ik ken geen betere photoshopper - of grappenmaker dan jij bent!!). Jullie konden altijd een hemisfeer te spoelen zetten of helpen bij het overzetten van de foto's, maar nog het meest genoot ik van de gemoedelijke sfeer met chocolademelk uit de automaat.

Dan een aantal mensen die niet geheel (meer) bij pathologie horen, maar die ik daar wel bij associeer. Ten eerste: Rob Veerhuis, dankjewel voor jouw onuitputtelijke kennis over het complementsysteem en de microglia. Het blijft me duizelen al die verschillende factoren, maar als ik met jou praat lijken de interacterende cascades allemaal zo logisch. Zelfs in de boeken die ik hier op Mayo opensla, duikt jouw naam op. Beste Wouter Kamphorst, dankjewel voor jouw uitgebreide werk op het scoren van de tangles en de paar gezamenlijke microscopie sessies, ookal kwam je eigenlijk voor andere vergaderingen naar het VUmc. Beste Piet Eikelenboom, wat heb ik veel van je geleerd! Soms duurde het even (dagen, soms maanden, soms zelfs jaren) voor ik jouw opmerkingen volledig begreep, maar altijd hebben ze me in de juiste richting geleid. Ik kwam je tegen op de momenten dat het nodig was.

Major acknowledgments to all the other great people I got the opportunity to work with! Guus, Ka Wan, Irinya en Miguel dank voor de hulp bij de proteomics projecten. Dankzij jullie en David snap ik nu een stuk beter hoe te kijken naar q-waardes en de duizenden eiwitten die we hebben gedetecteerd. Klaus, Andreas und Dominik, danke, dass ihr uns euer beeindruckendes Labor gezeigt und uns in die Welt der Spektroskopie mitgenommen habt. Ben, Freek en Johannes dank voor de altijd leerzame vergaderingen, ik ben zoveel wijzer over lichtabsorptie en reflectie! Bill van Nostrand, I can't wait for the magic angle spinning NMR spectroscopy results on different types of deposits! Jochen und Sathish, vielen Dank für eure nützlichen Einblicke und all die Antikörper und Western Blots! Die Studie zur Verteilung der Amyloid-beta-Isoform ist definitiv eines der Projekte, von denen ich hoffe, dass sie nächstes Jahr abgeschlossen werden. Juhan, thank you for your insightful questions on pathology and your valuable knowledge on PET. Even a serious hospitalization won't stop you from publishing your studies. I have the greatest respect for your unparalleled work

ethics! Eric, we hebben elkaar pas net voordat ik vertrok leren kennen, maar het klikte meteen. Ik ben ervan overtuigd dat ons hobby AI-project een geweldig project is en dat de wetenschap (of in ieder geval ik :D) er veel aan gaat hebben. Pech voor mij dat je niet ook een jaartje naar Jacksonville toe komt, maar ik wens je heel veel succes met jouw nieuwe baan bij het AvL! Thanks also to everyone from the Murray lab for making me feel so incredibly welcome here at Mayo: Sydney, Billie, Sarah, Christina, Jess, Kelly, Naomi, Christian, Tiffany, Janisse, Sabrina, Darren, and Ashley. I'm looking forward to the projects in the future!

Tim, vanaf mijn eerste kennismaking met onderzoek was jij erbij. Jouw altijd kalme energie, je engelengeduld en je vrolijke grijns hebben eraan bijgedragen dat ik ook besloot een promotie traject te doen. Samen leerde we coupes snijden van Angela en dansten we met Niki en Van Eyk tot laat in de nacht in de woonkamer. Je bent die net wat (onderzoeksleeftijd gezien!) oudere vriend waar ik naar op kijk. Ik ben dankbaar dat we altijd kunnen sparren over onze nieuwste bevindingen, maar ook vooral dat we vrienden zijn voor het leven. Zie jullie snel, of dat nu in Boston, Amsterdam, of Neptune Beach is!

Dank aan alle vrienden die, ondanks dat ze niet per se iets met onderzoek doen, mij op de één of andere manier, persoonlijk gesteund hebben. Hieronder noem ik een paar van jullie, maar er zijn nog zoveel meer vrienden die ervoor me geweest zijn op belangrijke momenten: dankjewel!

Liekie, we started off as neighbours, but became family after Lowlands, an awesome ski-trip, and an intense period in isolation. Your radiant smile instantly makes me forget the external BS. You gave me a home when I needed one and I want to thank the rest of the Van der Kaaijtes for their incredible support during not-so-easy times. Liewe Zayne, ai man! Ons het al so baie saam gesien! Dankie vir listening as ek dit nodig het, even now while I'm all the way in Florida and baie dankie vir telling me if my Afrikaans taal sucks. Ek is dankbaar vir al die major life events ons het oorleef, die spitball evenings and Sondag afternoons met Fernando, julle voel soos familie. I hope that one day we can visit SA simultaneously, give Simon a big hug, and eat roosterkoeke like we used to at Stomme Jonge. But first: penguin tattoos and kurta pyjama's!

Lieve Fen, dankje voor alle fijne hang-outs, etentjes, hardloop - en danssessies, in het Vondel-, Wester-, Ooster- of Flevopark, bij jou of mij thuis of op vakantie in de sneeuw of zon. Dankje voor jouw liefde <3!

Marcel onze zondagochtend hardloopsessies hebben mij meer dan eens uit m'n emotionele procrastinatie getrokken, dankjewel! Je zorgde ervoor dat ik niet onder m'n excuses uitkwam.

Irma, dank voor alle fijne dansfeestjes!

Richard, dankje dat je mij meenam in jouw wereld, op de vroege zaterdagochtend achterop de scooter. Dank voor jouw support en luisterend oor altijd wanneer dat nodig is.

Lieve Daaf, jouw creatieve oog heeft me meermaals geholpen, zo heeft mijn poppenhuis nu een terras, heb ik mooie video's in chapter 4, een mooie cover en weet ik dat tekst mag 'ademen', dank aap!

Dank Paul en Caroline, voor die extracurriculaire stage ;), jullie advies zodat ik geen schuld op me nam die niet van mij was, maar bovenal voor jullie steun.

An, Nien, Door en Co dank voor de jaarlijkse weekendjes weg, het was altijd feest! Volgend jaar New York?

Pascal, thanks for always being honest, providing me with the most delicious dishes, and sharing the joy of life.

Vasco thanks for the evenings you taught me 'After Effects'. Thanks even more for keeping the Willemstraat crew (Z+ John, Duncan, and Marina) together!

Megan, mijn Nederlandse steun en toeverlaat hier in het laatste stukje van m'n PhD in de USA. Ik kijk uit naar onze roommate maand in Nederland!

I also want to mention my Neptune beach family Dave, Bill & Jake for all the mental support, initiating a crossfit work-out when talking about it didn't help, a roof! A bike, the best car in the world, coffee, and lots and lots of laughter. Everyone from DOS, JT, Mr. A & Beverly, thank you for making me feel right at home here in Jacksonville. Mike, thanks for visiting me and teaching me all sorts of things about life.

Lieve Saar, dankjewel dat je me mijn eeuwige chaotiek vergeeft. Je zorgt ervoor dat ik mijn vliegtuigen haal en bent altijd beschikbaar voor de nodige reflectie. Samen met jou heb ik Amsterdam ontdekt en ik kijk uit naar de volgende jaren van onze vriendschap.

Lieve Val, dankzij onze (bijna) dagelijkse belmomenten weet jij mijn agenda en de gebeurtenissen uit het verleden, vaak beter dan ikzelf. Dikwijls heb ik (handsfree) bellend met jou, presentaties geoefend op de fiets door Amsterdam, en nu in Jacksonville. Je luistert altijd aandachtig en geeft tips voor betere zinconstructies. Het is bijzonder hoe wij al jaaaren dagelijks makkelijk een halfuur volpraten. Dankje dat je onderdeel bent van mijn ochtendritueel en dat je mij een spiegel voorhoudt wanneer dat nodig is.

Lieve Matty, dankjewel voor onze onvoorwaardelijke vriendschap sinds dag één. Alle (mooie maar ook minder mooie) life-events die jij meemaakt, volgen bij mij meestal ietsje later. Zo ook eindelijk deze promotie. Ik heb diepe bewondering voor jouw doorzettingsvermogen en ben je dankbaar voor je relativerende vermogen. Er zijn zo enorm veel momenten en reizen te noemen, maar dat gaat

hier niet passen. Naast jou wil ik ook graag iedereen van de Malistraat en Jeroen (en Stella) bedanken. Jullie way of living heeft me enorm geïnspireerd en het feit dat ik me altijd zo welkom voel, is van onschatbare waarde!

Liewe Ria, baie dankie vir jouw liefde. Ek het eintlyk geen woorde vir die liefde wat ek voel. Jy het my altyd so baie welkom laat voel en ons was familie vanaf dag één, of miskien vanaf dag drie, by die trip naar Buffels baai, toen VE hier die baie nice suite van jou gesteel het. Liewe Gerhard, dieselfde geld vir jou. Ek hoor VE wanneer ons praat en ek is so baie dankbaar vir jou onvoorwaardelyke steun. Ek geniet wanner ons praat oor politiek en mediese aangeleenthede. Daardie dae in Amsterdam is vir my goud werd. My hart lag vir jou grappies. Ek hoop ons sien mekaar snel.

Dearest Van Eykie, due to your encouragement to apply for this PhD project, we chose Amsterdam - and not Cape Town - as our home. Unfortunately, you can't celebrate the finishing of this book, but your joyful empathic spirit lives on, not only in what has been, but for me also in what will come. Both your life and passing introduced ripples to my pond. Those ripples created a swell and caused a river to rise. Since then, that river is finding its way through lots of sorts of terrain, being high snow peak mountains, sun-drenched valleys, and sometimes inevitably along the endless abyss. Your goal was to let the other person become the best version of themselves. Dearest Van Eyk, every day again, you keep on teaching me to pause for a moment and observe life's flow. By trial and error, I'll follow the natural stream and readjust course when necessary. For me, there is no greater gift than to have known you. Even though you are no longer with us, your spirit was my invisible support through all these years, and most of all, it taught me to have compassion. Thank you.

Lieve familie, pap en mam, dankjulliewel voor het vertrouwen dat ik mijn weg wel zou vinden. Ik ben jullie dankbaar voor de vrijheid die ik altijd heb mogen ervaren. Dankje mam, voor de tip dat je zelf de slingers op moet hangen en dankjewel dat je er werkelijk altijd voor me bent. Lieve Ruud, dank dat jij er voor mama bent en dat je altijd álles kunt maken. Dankje pap voor de levensles dat je moet doen waar je zelf zin in hebt en vooral niet moet zeuren, zo blijft het leven leuk! Dankje dat je me opvangt wanneer het nodig is. Dankje Karen dat jij papa gelukkig maakt.

Lieve oopie en oomie, dankjulliewel voor de fijne vakanties, Villefranche Sur Mer was er één om nooit te vergeten. Ik weet zeker dat Lily met Zil, Jon, Bor en

mij meegenoot. Lieve oomie Boon, het is me niet gelukt op tijd klaar te zijn maar ik weet zeker dat je trots bent.

Lieve Boris! De liefste broer(tje..) van de wereld, wat ben ik gek op jou! Je sleept me overal doorheen. Wanneer wij samen zijn valt er altijd wel wat te beleven: of we elkaar nu kwijtraken op Long street in Kaapstad, drie keer samen op en neer rijden naar Uluwatu om onze paspoorten terug te vinden, of dat we onze dansjes doen op Lowlands of een concert van oopie, met jou verveel ik me nooit! Ook de meer serieuze zaken kunnen we samen delen. Je nam altijd tijd voor me op de dagen dat ik alleen nog maar kon huilen. En weet je nog die thuiswerk middagen waarbij we samen over wetenschap schreven? En ik soms (iets te) kribbig sneerde dat ik nu even niet bereikbaar was voor vragen, sorry! Man, ik ben zo trots het zusje te zijn van zo'n lieve broer! Dankje, dat je ook tijdens mijn verdediging naast me staat.

ABOUT THE AUTHOR

From a young age, Baayla Dimitri Catharina Boon was fascinated by the diversity of the human mind. After her pre-university education at the Murmellius Gymnasium in Alkmaar, she initially started her medical studies in the pursuit of becoming a psychiatrist. Once she realized that the brain is the mind's blueprint, her focus shifted towards neurology. Along the way, her love for both research and neuropathology got sparked. Her scientific internship, in which she studied potential biomarkers for Parkinson's disease supervised by dr. Wilma van de Berg, lit the first spark. In September 2015, she started her PhD project under the direct supervision of dr. Femke Bouwman, dr. Jeroen Hoozemans, prof. dr. Philip Scheltens, and prof dr. Annemieke Rozemuller at the Alzheimer center Amsterdam and Department of Pathology of the Amsterdam UMC, formerly known as the VUmc. This PhD project served as fuel to a full-blown fire. She successfully set up a cohort of brain donors who undergo an in-situ 3T MRI immediately post-mortem, followed by ex-vivo 7T MRI and extensive neuropathology. Using this data, she and her collaborators set out to translate the neuropathological findings to the clinic via MRI. A coincidental side project on the discovery and characterization of a new type of plaque in Alzheimer's disease turned out to be the highlight of her PhD. To better understand what is happening on a cellular level, she initiated multiple ancillary projects and worked closely with collaborators from other (foreign) institutes. Recently, she was awarded a two-year fellowship by the Dutch Alzheimer Association to join forces with dr. Melissa Murray (Mayo Clinic, Jacksonville) on their joint interest concerning the pathology in (a)typical Alzheimer's disease. In the upcoming years, she will expand her study on the coarse-grained plaque by exploring its correlation with genetics and symptomatology in a combined cohort, consisting of donors from both the Netherlands Brain Bank (NBB, Amsterdam, the Netherlands) and the Mayo Clinic (Jacksonville, Florida, USA). Baayla currently resides in Neptune Beach, Florida, where she rides her bicycle to work and enjoys surfing, open water swimming, and scuba diving in her free time. When she isn't peeking through a microscope or with her head underwater, she loves to read up on philosophy of mind or (astro)physics. Whenever there is live music, you'll find Baayla on the dance floor.



Enjoy your happy little accidents and observe with wonder,
since the true value of Serendipity lies in the eye of its beholder

